SCIENCES

GEOSCIENCE

Dynamics of the Continental Lithosphere

The Seismic Cycle

From Observation to Modeling

Coordinated by
Frédérique Rolandone

ISTE

WILEY

The Seismic Cycle

SCIENCES

Geoscience, Field Director – Yves Lagabrielle

Dynamics of the Continental Lithosphere,
Subject Head – Sylvie Leroy

The Seismic Cycle

From Observation to Modeling

Coordinated by
Frédérique Rolandone

ISTE WILEY

First published 2022 in Great Britain and the United States by ISTE Ltd and John Wiley & Sons, Inc.

ISTE Ltd
27-37 St George's Road
London SW19 4EU
UK

www.iste.co.uk

John Wiley & Sons, Inc.
111 River Street
Hoboken, NJ 07030
USA

www.wiley.com

Library of Congress Control Number: 2022938894

British Library Cataloguing-in-Publication Data
A CIP record for this book is available from the British Library
ISBN 978-1-78945-038-5

ERC code:
PE10 Earth System Science
PE10_5 Geology, tectonics, volcanology
PE10_7 Physics of earth's interior, seismology, volcanology

Contents

Preface

Frédérique ROLANDONE
ISTeP, Sorbonne University, Paris, France

Earthquakes rank among the most destructive manifestations of the Earth's dynamics. Can they be predicted? This is often the first question students ask. To answer that right away: no, at present it is not possible to anticipate the date, site and magnitude of future seismic events. However, there does exist a general framework to describe observations related to earthquakes and understand the processes that lead to their occurrence: the seismic cycle.

The objective of this book is to discuss the state of knowledge on the seismic cycle, providing a comprehensive view of the progress made in the last three decades. These advances came from enhanced observation capabilities. Since the late 1990s, most earthquake-prone regions have been equipped with seismological, accelerometric and geodetic networks. These networks could closely monitor the large earthquakes in Indonesia in 2004, in Chile in 2010 and in Japan in 2011, capturing precise images of the earthquake rupture process. Furthermore, these new observations also made it possible to measure the evolution of surface deformation and seismicity in the period preceding and following the large earthquakes. The most surprising result was the discovery of slow, spontaneous earthquakes on the majority of large faults. This discovery, along with the observation of the rapid deformation that followed large earthquakes, revolutionized the concept of the seismic cycle, by introducing a dynamic vision of the spatio-temporal evolution of fault slips. Another development came from studies in the field of morphotectonics, geomorphology and paleo-seismology, which document the history of earthquakes over several cycles. Along with improved observations, friction laws empirically derived from laboratory experiments on rock mechanics provided a framework for

The Seismic Cycle,
coordinated by Frédérique ROLANDONE.

interpretation, and enriched numerical and analog models that aim to reproduce the observed behaviors. The coming years promise the fascinating prospect of combining observations with friction laws to validate and determine the parameters of physical models.

This book brings together different aspects of research on the seismic cycle. It is intended for students who are keen to learn about earthquakes and enhance their knowledge on observation techniques of the seismic cycle, but is also for all those who wish to quantitatively understand the underlying physics.

I would like to conclude by warmly thanking all of the authors who have contributed to this book.

June 2022

Introduction

A Kinematic Approach to the Seismic Cycle

Marianne MÉTOIS
UCBL, ENSL, UJM, CNRS, LGL-TPE, University of Lyon, Villeurbanne, France

I.1. The concept of the seismic cycle

The seismic activity along the San Andreas fault line, a spectacular and widely studied strike-slip boundary between the North American and Pacific plates, was one of the inspirations for the concept of the seismic cycle, which is studied in this book. Indeed, it was in 1910, following the devastating San Francisco earthquake (Mw ∼7.9) and the observations of the surface displacements, that Reid [REI 10] developed the "elastic rebound" theory. He postulated that in the vicinity of fault lines, the earth's crust behaved like elastic, slowly deforming, until it fractured, thus generating a relatively brutal and permanent (static) displacement between the two compartments separated by the fault line. In this simple model, near fault-lines, the most superficial layer of the earth behaved either in an elastic or brittle manner. The alternation between these two behaviors formed the basis of "the seismic cycle", a term used since the 1960s [FED 68]: the elastic deformation phase, with the slow accumulation of stresses along the fault line, called the *inter-seismic phase* (see Chapters 5 and 6), is followed by a rapid brittle deformation and the brutal release of these stresses in the form of seismic waves, heat and slipping over the fault plane.

For a color version of all the figures in this chapter, see www.iste.co.uk/rolandone/seismic.zip.

The Seismic Cycle,
coordinated by Frédérique ROLANDONE.

This is called the *co-seismic phase* (see Chapters 1 and 2), after which the elastic loading recommences.

The emergence of the plate tectonics theory and advances made in the field of imaging the earth's interior during the second half of the 20th century [LEP 68, MOR 68, RUB 01] complement the theoretical framework required to understand the seismic cycle. The relative motion of the rigid, lithospheric plates, which is of the order of a cm/year on the horizontal [DEM 94, ALT 17], generates stresses on the plate boundaries. Subject to such loading velocities, the lithosphere will deform differently depending on the pressure and temperature conditions that govern its rheology. At depth, the ductile lithospheric material will accommodate the differential movement through a deformation distributed in a more or less thick fault zone. On the other hand, on the surface, the lithosphere is primarily elastic: it undergoes elastic deformation until it ruptures, that is, until an earthquake is produced. The chief forcing of the seismic cycle is, therefore, the relatively continuous displacement of the lithospheric plates with respect to one another in the convective system in the interior of the earth.

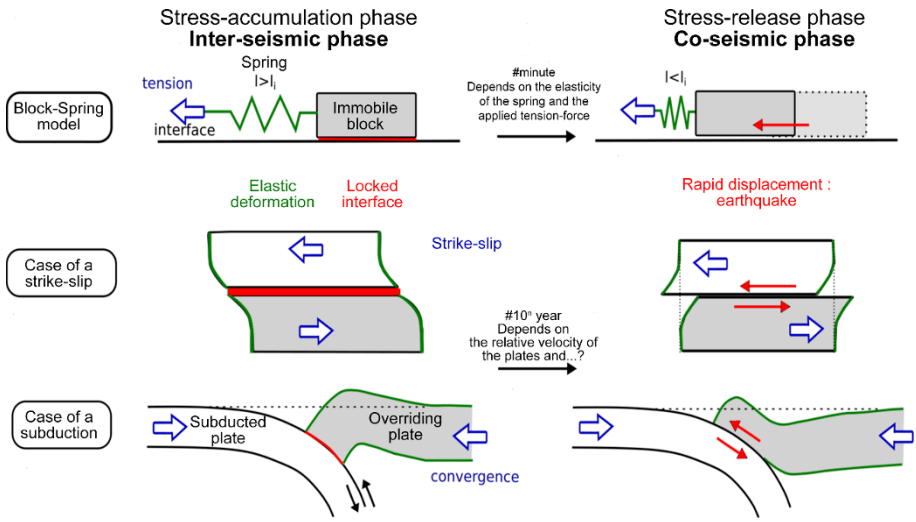

Figure I.1. *Analogy between the "spring-block" system (above) and the working of a strike-slip fault (middle) or a reverse fault (below). The seismic cycle here is composed of co-seismic and inter-seismic phases with very varied duration and functioning. The parameters that govern the passage from the co-seismic phase to the inter-seismic phase are still not well known*

In parallel, physicists studying fracture phenomena provided an analogy that is still widely used to understand and study fault mechanics: the "spring-block" system

(see Figure I.1, [BUR 67, ROS 17]). The smooth or rough interface between the block and the soil surface is analogous to the fault. For its part, the block is one of the lithospheric plates displaced by the constant traction exerted on a spring integral with this block via a pulley system. Finally, the elasticity of this spring mimics the elasticity of the lithosphere. When a traction is exerted on the spring, we observe an effect similar to the seismic cycle: the spring is increasingly deformed (inter-seismic phase) until there is a brutal displacement of the block on the interface (co-seismic phase), and then the spring begins to deform again (recommencement of the inter-seismic phase). Carrying out this experiment over time, with a constant traction velocity, shows that the displacement of the block is almost always identical and occurs quasi-periodically. This experimental observation supports the theory that *quasi-typical earthquakes* exist in nature, that is, earthquakes that are repeated identically and regularly in time. This echoes the *in situ* observations of regular rupture along certain fault segments, especially in the well-known Parkfield segment of the San Andreas fault, which has ruptured during six earthquakes of magnitude 6 or greater, between 1850 and 1966, with a recurrence time of about 20 years [BAK 85].

The example of the Parkfield segment also led the scientific community to carry out an experiment to predict future characteristic earthquakes in this zone, which was eventually in vain [BAK 05]. This was because while the "one block-one spring" system seemed to open the path to predicting earthquakes due to its quasi-periodicity, slightly more complex physical systems with two blocks in series, for example, proved chaotic (in the sense of deterministic chaos [HUA 90]). Today, scientists are well aware of the limitations of this model and no longer venture to predict individual earthquakes, given the complexity of the lithospheric system. Instead, they prefer using probabilistic approaches based on empirical laws derived from statistical analyses of earthquake catalogues [KAN 02] (the Gutenberg-Richter law, Omori law, Bäth law, see Chapter 1). However, this analogy is still useful for reflecting on the seismic cycle overall, and the theoretical physics "rate and state" formalism still offers an efficient matrix to understand the physics underlying the seismic cycle (see Chapter 4). The analogue models of fault systems have also been complexified and make it possible to better understand certain aspects of the seismic cycle (see Chapter 12).

In the context of an ideal and regular seismic cycle, the totality of the energy produced by the relative motion of the lithospheric plates in contact is first stored in the form of elastic potential energy during the inter-seismic phase, and then released entirely during the co-seismic phase in the form of heat, seismic waves, static movement on the fault plane and plastic damage to the medium. If, as assumed here, the energy balance of a seismic cycle of a given fault is effectively zero and distributed over two phases, then measuring the inter-seismic deformation allows indirect and partial access to the energy available for the next earthquake and, therefore, its magnitude, using certain hypotheses (see Chapter 1). The later is a crucial element in estimating seismic hazards. The study of plate kinematics in active

fault zones, that is, the measurement and analysis of their motion over time, even without knowing the forces involved, may thus theoretically lead to a better understanding of the seismic cycle. The following sections present an overview of this kinematic approach and the contributions it has made to the concept of the seismic cycle.

I.2. Tracking plate kinematics

I.2.1. *Recent techniques in spatial geodesy*

The scientific use of spatial geodesy techniques, from the 1990s onwards, confirmed the observations of permanent or transient deformation on the earth's surface seen before, during and after large earthquakes, with the help of conventional geodesic techniques [SMI 68, THA 84, triangulation, strain gauge etc.] (see Chapter 3). The GPS constellation, especially, has made it possible to get past the long and laborious level and triangulation campaigns (which are useful, however, in measuring metric displacements [MUR 06]) by offering the possibility of accurately following the displacement of one point on the earth's surface over its velocity approaching a millimeter per year, more or less along its horizontal components. The positioning system constellations, grouped together under the name GNSS (Global Navigation Satellite System) – within which we find the satellite systems GLONASS, Beidou or the European Galileo [BLE 15, HOF 07] – have multiplied since the 1990s. In addition to these developments in spatial technology, there are also international efforts to work within a common and regularly updated reference system (International Terrestrial Reference Frame (see http://itrf.ensg.ign.fr), partly based on the International GNSS Service [ALT 17, REB 16]), as well as the development of national surveillance systems (see, for example, the French network RENAG (see http://webrenag.unice.fr/), the Italian network RING (see http://ring.gm.ingv.it/), the Californian network (see Figure I.2(a)), etc.). All together, today, they allow precise, dense and, increasingly often, real-time or high-frequency tracking (up to 1 Hz [VIG 11, TWA 19], see Chapter 2) of the deformation around known major active faults (see Chapters 2, 3, 5, 6, 7 and 8).

Continuous or episodic GNSS measurements (see Figures I.2(b) and (c)) make it possible to have a precise knowledge and good time resolution of the displacement of a point on the earth's surface over time in three directions (east, north and vertical). However, their chief limitation is their low spatial resolution. In the densest networks of permanent stations, like the reference system in Japan (GEONET, www.gsi.go.jp), the stations are spaced 10–15 km apart. However, on the global scale, many tectonically active zones are either devoid of any networks, or the existing networks do not make their data available to researchers (for an overview of global coverage, readers can consult, for instance, the University of Nevada website, http://geodesy.unr.edu/NGLStationPages/gpsnetmap/GPSNetMap.html). Around active faults, the

deformation associated with the seismic cycle may be highly localized (see section I.3) and restricted, in some cases to a few kilometers around the active fault (a strike-slip fault blocked on the surface, for example, see Figure I.5): the GNSS benchmark systems may, thus, prove to be too loose to detect pronounced gradients in the deformation. Furthermore, in order to measure co-seismic deformation on a GNSS benchmark, the beacon must, of course, already be installed: it is impossible to measure the deformation a posteriori.

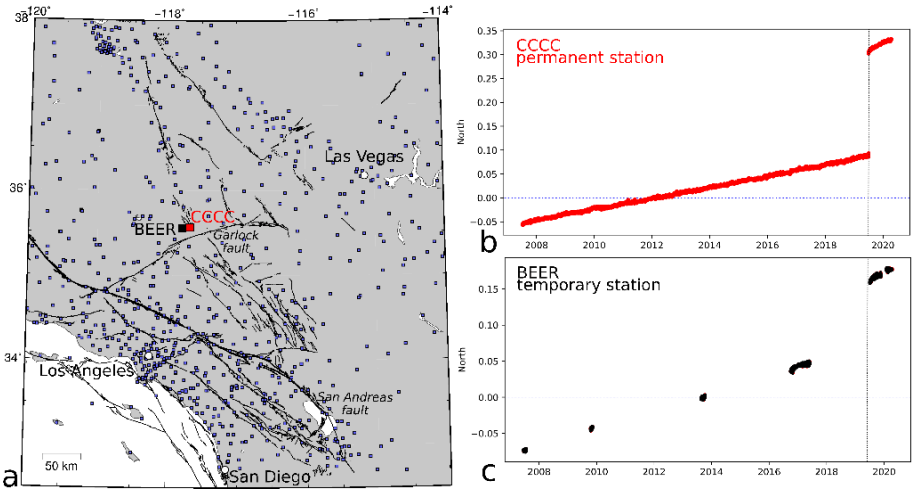

Figure I.2. *a) Networks of GNSS stations (blue squares) in California around the San Andreas fault systems. Position time series (north component, North America is fixed) of the permanent CCCC observation station b) and a temporary BBEC station c) [BLE 18]. Dotted line: RidgeCrest earthquakes (max Mw 7.1) [FLO 20]*

Satellite imaging techniques, which have been developed since the 1990s, make it possible to track deformation with a very high spatial resolution (determined by the pixel size of the image) and global coverage. Radar interferometry based on images from the ERS, Envisat, ALOS, TerraSAR-X and Sentinel-1 satellites (among others) has become an indispensable technique for analyzing earthquakes or even slow slip events [LAC 20, COR 21] (see Figure I.6(e) and Chapters 2, 3, 8). Radar interferometry provides a measurement of the displacement of the soil in the satellite's line-of-sight (LOS), and in certain cases and with latest satellites, it is also possible to get the three components of surface displacements [GRA 16]. Optical image correlation techniques also make it possible to obtain extraordinarily detailed maps of the co-seismic deformation associated with some large earthquakes [VAL 15, DEL 20] (Figure I.8(c)), including historical earthquakes, by using archived aerial photographs [MAR 18]. The time resolution of the deformation tracking using these imaging techniques is lower than that of the GNSS systems,

however it tends to improve significantly with the Sentinel-1 mission, whose revisit time in certain zones is a few days. The chief limitation of satellite imaging is the persistent difficulty in measuring large-wavelength deformation gradients, typically those that may be associated with inter-seismic deformation or movements of rigid blocks over large spatial scales, even though, in certain cases, a highly refined data processing may yield this information [DUC 12, GRA 12, BÉJ 13, DAO 19].

GNSS, InSAR and optical imaging still find it hard to detect displacements in the order of a fraction of a millimeter. However, over the course of a seismic cycle, some far-off slips, which are of very low magnitude or very deep, may generate very small displacements on the surface and certain active faults may be loaded with long-term velocities that are smaller than a millimeter per year, especially in slow deformation zones [JOM 17]. In order to detect these slow displacements, the use of inclinometers, sensitive to slope changes in the order of a nano-radiant, has become increasingly common around active faults [BOU 14] (see Chapter 6). In recent years, the fiber-optic networks developed for telecommunications have also been useful in measuring small deformations, which are sometimes of tectonic origin [LIN 17], especially in shallow underwater regions [SLA 19]. In the future, their use in local networks may enable a new cartography of deformation in a fault zone and enhance our understanding of the seismic cycle.

In the previous paragraphs we have only mentioned measurement techniques for instantaneous deformation that are relatively recent (the 1990s for GNSS systems, the first co-seismic interferogram was published in 1993 [MAS 93]). How a fault works cannot, however, be understood without knowing its behavior over the longer term. Geomorphologists and geologists quantify the deformation accumulated over several seismic cycles and the fault velocities on a scale of several thousand, or even millions of years, bringing in the perspective that is lacking with geodesic techniques for tracking the seismic cycle. These techniques will be studied in Chapters 10 and 11.

I.2.2. *Mapping deformation*

There are ever-increasing measurements of the deformation of the surface of the lithosphere: GNSS velocities over a shorter or longer term, single or cumulative co-seismic displacements, InSAR deformation maps, focal mechanisms, the direction of slip over the fault, etc. It is essential to be able to make good use of this mass of new, and often heterogeneous, observations (regular measurements, maps, 3D, 1D) and this does not always involve modeling the deformation, at least initially. Representing these deformation measurements in a coherent manner and, if possible, conjointly, is an important challenge [BIR 15, WAN 19a].

In order to do this, it may be useful to have representations of the tensors of the velocity gradients ($\nabla \mathbf{v}$) and the deformation rates ($\dot{\varepsilon}$) developed in zones with small

deformation or diffuse/distributed deformation. Using only the surface deformation measures and no direct measurement of the variations in velocity at depth ($\partial_z v_i$), we have only partial access to $\nabla\mathbf{v}$:

$$\nabla\mathbf{v} = \begin{pmatrix} \boxed{\begin{matrix}\partial_x v_x & \partial_y v_y \\ \partial_y v_x & \partial_y v_y\end{matrix}} & \partial_x v_z \\ \partial_z v_x & \partial_z v_y & \partial_z v_z \end{pmatrix}$$

The terms for the horizontal gradients of the vertical velocity $\partial_x v_z$ and $\partial_y v_z$ are generally not well known due to the poorer quality of the vertical velocities measured by GNSS. We often consider a purely 2D version of the tensor $\nabla\mathbf{v}$ (the term enclosed in a box, above), which may be obtained at any point in a given region using more or less advanced techniques for the interpolation of one-off measures [MAS 14, SHE 15, MAS 19, PAG 19]. $\nabla\mathbf{v}$ may be decomposed into a symmetric tensor of deformation rates $\dot{\epsilon}$ and an anti-symmetric matrix of rigid rotation W expressed by:

$$\dot{\epsilon}_{ij} = \frac{1}{2}(\partial_j v_i + \partial_i v_j), \text{and}$$

$$W = \begin{pmatrix} 0 & \omega \\ -\omega & 0 \end{pmatrix} \text{with } \omega = \frac{1}{2}(\partial_y v_x - \partial_x v_y).$$

We often choose to represent:

– the rotational ω to identity the rotations present in the velocity field and the movements of the independent rigid blocks;

– the horizontal divergence of $\dot{\epsilon}$, which in 2D corresponds to $d = tr(\dot{\epsilon}) = \dot{\epsilon}_{xx} + \dot{\epsilon}_{yy}$. In 3D, if we propose the hypothesis that the lithosphere is incompressible, we have $\nabla\dot{v} = 0$ or, $d = \dot{\epsilon}_{xx} + \dot{\epsilon}_{yy} = -\dot{\epsilon}_{zz}$. d, which then makes it possible to visualize the zones that are compressed or dilatated (see Figure I.3);

– an invariant of the tensor $\dot{\epsilon}$ that makes it possible to estimate the amplitude of the velocity gradients. We generally speak of a second invariant, however several definitions are used: the most conventional write $I_2 = \dot{\epsilon}_{xx}\dot{\epsilon}_{yy} - \dot{\epsilon}^2_{xy}$ while several authors use $I_2 = \sqrt{\dot{\epsilon}^2_{xx} + \dot{\epsilon}^2_{yy} + \dot{\epsilon}^2_{xy}}$ [DAG 14, MÉT 15];

– the principal directions of deformation corresponding to the vectors and eigenvalues of the 2D tensor $\dot{\epsilon}$, which make it possible to establish a relation with the focal mechanisms and the sense of motion of the faults observed on the ground (see Figure I.3).

I.3. Understanding observations via elastic modeling of the seismic cycle

What can we learn from the observations of the surface deformation of the lithosphere over faults at depth? Intuitively, and using the simple analogy of the "spring-block", given in section I.1, zones with a high deformation gradient may indicate the presence of active faults, regardless of the seismic cycle phase in which they occur. Consequently, it is important to optimally quantify and map the deformation intensity and the preferential directions of deformation, which can give us information on the relative motion on either side of a fault system (see section I.2.2). However, in order to understand the observed deformation fields, we must know what deformation to expect around an active fault in different phases of the seismic cycle: it is therefore necessary to have a theoretical model of the deformation of the lithosphere.

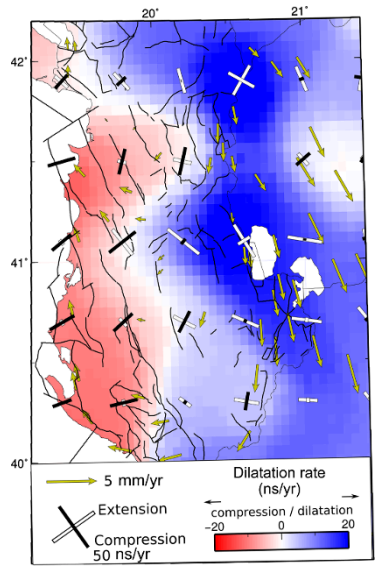

Figure I.3. *Map of the inter-seismic deformation in Albania according to Métois et al. [MÉT 15]. The GNSS velocities (yellow arrows) are interpolated to calculate the principal directions of deformation and the dilatation rate. Thin black lines: the principal active faults*

The simplest and most widely used model for modeling the observations is based on the analytical developments by Okada [OKA 85], which make it possible to calculate the deformation generated on the surface by a dislocation slipping in an infinite, elastic, isotropic and homogeneous half-space. The motion on the planar dislocation may be a horizontal slip (U1, U2), an opening/closing motion (U3, see

Figure I.5), or any combination of these motions. As per the Okada equations, the displacement of a point on the surface will depend on the depth of the dislocation (d), its size (WxL), its angle of dip (α), the amplitude of the slips (U1, U2 and U3) on the elastic parameters of the medium and on the distance, and the azimuth of the point with respect to the dislocation [OKA 85]. In the case of an earthquake, this formalism thus allows us to calculate the co-seismic displacement field expected on the surface for any kind of fault (normal, reverse, strike-slip), geometry, amplitude and sense of slip (see Figure I.4). The linear character of the elastic rheology results in the fact that it is possible to calculate the displacement produced by faults with complex geometry by summing the contributions of several unit dislocations whose geometry and slip are different from the surface deformation. Figure I.4 depicts the different theoretical displacement fields generated by the slip of reverse, normal or strike-slip faults, which may or may not emerge on the surface. In theory, it is thus possible to use surface observations to understand which fault has slipped, at what depth and in what sense: we speak of data inversion to find the model or models that can reproduce these the best.

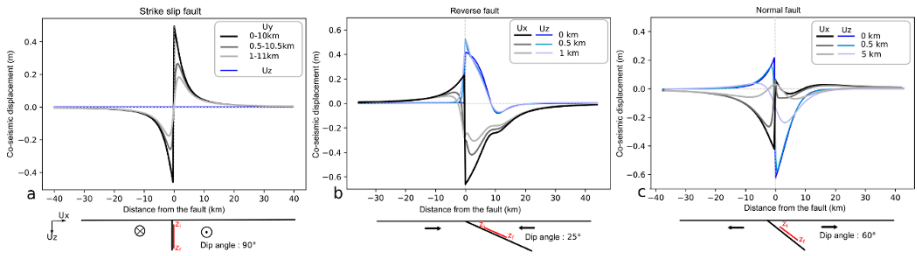

Figure I.4. *Theoretical co-seismic displacement profiles forecast by the equations put forth by Okada [OKA 85] across a fault that is strike slip a), reverse b), and normal c), this fault being 10 km wide with a coseimsic slip of 1 m. Only the depth of the dislocation varies in different cases. The caption indicates the minimum depth of the dislocation, and the angle of dip chosen for the faults is given at the bottom of the panel. Other parameters that influence the surface deformation are as follows: angle of dip, dislocation width, amplitude of the slip, elastic parameters of the medium, etc.*

It is easy to see the benefit of this elastic formalism that is relatively straightforward to implement with respect to taking into account the more complex rheologies to model slips over faults, whatever their duration. However, how can we model the deformation generated during the inter-seismic phase of the cycle during which the lithosphere is slowly deformed in response to absence of slip in the fault zone? The idea postulated by Savage [SAV 83] from the example of subduction zones was to model the deformation associated with the inter-seismic phase as being entirely complementary to the co-seismic phase in a fault zone at kinematic equilibrium. This is the *backslip theory*. Thus, the sum of the displacement accumulated during the inter-seismic phase and the co-seismic displacement must be

equal at all points on the surface with the long-term horizontal motion of the plates, given by the relative Euler poles of the plates in contact (see [KAN 10] for a detailed discussion of the terms used in the backslip model and refer to Figure I.5 for a schematic representation of this hypothesis). Under this hypothesis, it is considered that the vertical long-term motion is zero, which is obviously not very probable considering the morphologies associated with active faults. Therefore, irrespective of the fault system under consideration, we have $U_{\text{inter-seismic}} = U_{\text{long term}} - U_{\text{co-seismic}}$. According to this hypothesis and in the case of a reverse fault, for example, the surface deformation generated by a fault blocked during the inter-seismic phase is equivalent to the sum of the relative long-term motion of the plates (assumed to be known) and the deformation generated by a slip in a normal fault in this blocked zone (modeled). Figure I.5 depicts the general aspect of the inter-seismic deformation expected for strike-slip faults, reverse faults or normal faults, depending on their geometry, the extent of the blocked zone and the degree of locking during this inter-seismic phase (see section I.4). Starting from the inter-seismic velocities, measured on the surface, it is thus possible to reverse the position, the geometry and the extent of the blocked zone that generates these velocities.

In the first-order, these elastic formalisms give a very satisfactory representation of the co-seismic and inter-seismic surface observations obtained around large active faults (see the example of the Parkfield segment on the San Andreas strike-slip fault in Figure I.6, that of the Maule segment in the subduction in Chile in Figure I.7, or again that of the normal Italian faults in the Norcia region in Figure I.8). Due to their efficiency and their ease of use, they are widely used in the scientific community (see Chapters 2, 3, 5, 6 and 8). Nonetheless, it is important to note that this is *purely kinematic modeling of deformation* and that the debate over the best way to model co-seismic deformations and, above all, inter-seismic deformations, is ongoing. For example, must we use a visco-elastic rheology when the inter-seismic load times approach a few hundred years [TRU 13, LI 15, POL 10]? Is it reasonable to reduce a subduction zone to a simple dislocation, with neither the thickness nor the curvature of the sinking plate being considered [KAN 10]? Is the backslip theory truly valid [VER 01]? How can it be applied to the case of active faults in the contexts of distributed deformation, where multiple faults accommodate the movements of large blocks? Is it possible to neglect the contributions of non-elastic deformations to the energy balance equations of the seismic cycle?

I.4. Complexity of the seismic cycle

Post-seismic movements: As soon as the permanent GNSS stations increased in number and reliability, the "simple' model for the bi-phase seismic cycle (inter/co-seismic), which was already not very compatible with certain seismological observations (aftershocks, seismic swarms), was brought into question. One major complexity arose, notably, following large earthquakes (Mw>6), particularly in the

contexts of subduction, but also in strike-slip zones: the post-seismic phase [THA 83] (see Chapter 3). This is a period of instability for the entire fault system or a part of it, accompanied by aseismic and seismic slips over the fault, and a visco-elastic rebound of the neighboring mantle and lithosphere. This post-seismic phase occurs just after the co-seismic rupture phase and is expressed by a transient deformation measured on the surface, which may extend over decades [POL 01, RUE 01, VIG 05, TRU 14]. Most GNSS stations in the Chilean Patagonia that were located in the zone of the large Valdivia earthquake of 1960 (Mw 9.5) continue to move toward the west, that is, toward the subduction that slipped during this major earthquake (see Figure I.7(c); [KHA 02, MOR 08]) and not toward the east, as the inter-seismic load would indicate. It was only recently, over 50 years after the earthquake, that it became possible to observe a surface deformation compatible with a predominant inter-seismic loading phase [MEL 18].

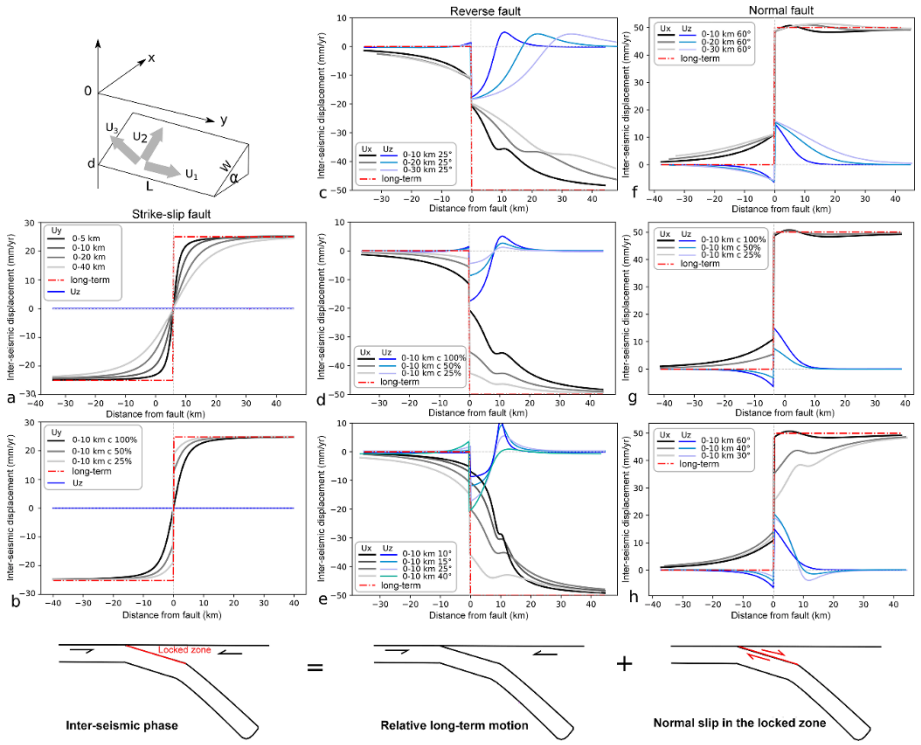

Figure I.5. *Top left: schemas for the parameters governing the dislocation as per Okada [OKA 85]. Theoretical inter-seismic deformations predicted by the backslip hypothesis (depicted at the bottom in the case of subduction) applied to the Okada equations through a strike-slip fault (a and b), reverse fault (c–e) and normal fault (f–h) separating two rigid blocks whose relative motion is 5 cm/year. Parameters tested: width of the zone blocked 100% (a, c and f), partial coupling (b, d and g) and angle of dip of the fault (e and h)*

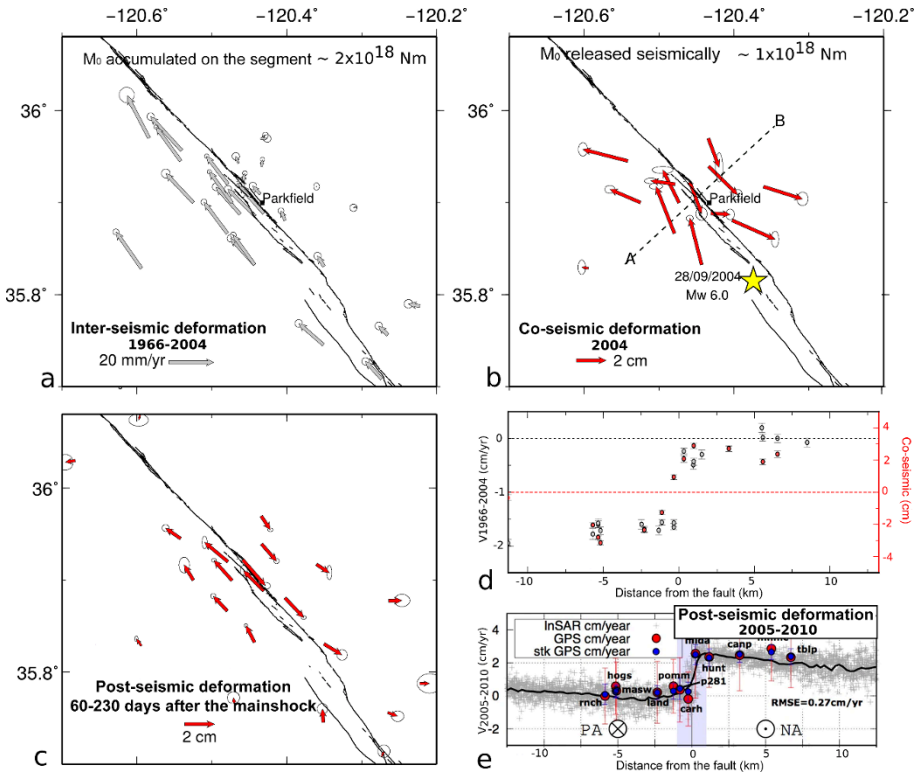

Figure I.6. *Case of a strike-slip fault: Inter-seismic deformation observed around the Parkfield segment of the San Andreas fault (a: GPS velocities obtained over the period 1966-2004 in a North America-fixed reference frame) for the co-seismic phase associated with the 2004 earthquake (b: Mw 6.0, star: epicenter USGS), and part of the post-seismic phase (c: GPS velocities calculated over the period from 60 to 230 days after the mainshock), according to Murray and Langbein [MUR 06]. (d) Inter-seismic deformation (gray) and co-seismic deformation (red) along the A-B profile perpendicular to the fault represented in (b). (e) Long-term post-seismic deformation observed by GPS and InSAR along the A-B profile (2005–2010; [BAC 18]). The plates converge at ∼2 cm/year [DEM 94]*

The three major subduction earthquakes that have occurred since the start of the 21st century (Sumatra 2004, Maule 2010, Tohoku 2011) generated transient post-seismic deformations that were recorded with great precision and unprecedented spatial coverage by the geodesic networks (see Figure I.9). The analysis of these deformations (their amplitude, spatial aspect, temporal evolution) revealed how

important this phase is in understanding the whole of the seismic cycle [POL 01, TRU 14, KLE 16, KLE 17]. How long does the post-seismic slipping phase over the fault last? How does the regional visco-elastic rebound affect the distribution of stresses over neighboring segments? How do the processes unroll during the post-seismic phase (which was relatively neglected, earlier)? Could they perturb the measurement of the long-term GNSS trends that were assumed to be totally inter-seismic, even at large distances from the fault [TRU 14]?

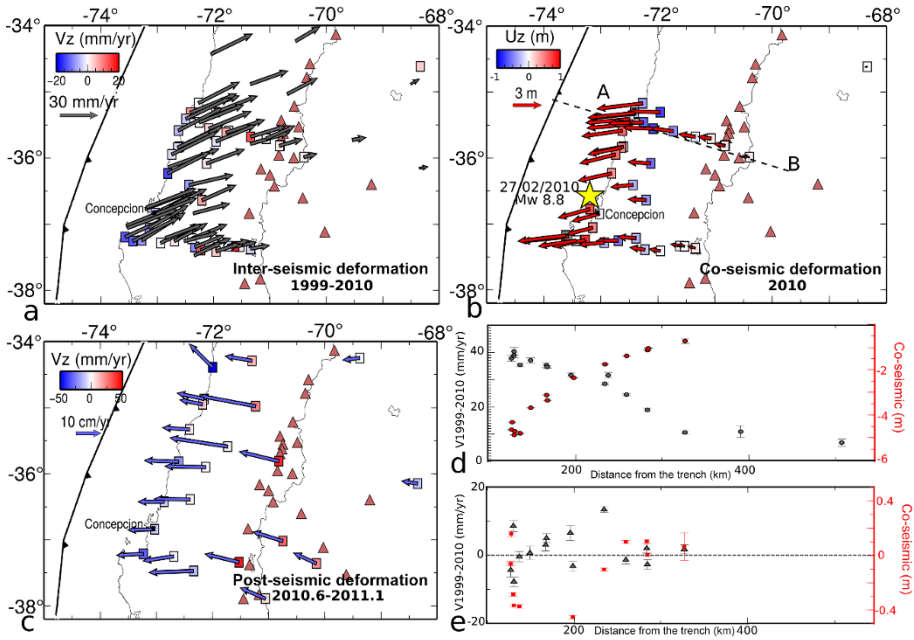

Figure I.7. *Case of a reverse fault: Deformation observed around the Maule segment of the subduction zone between the Nazca and South American plates, which converge at a rate of around 6.8 cm/year [DEM 94, ALT 17, VIG 09] during a seismic cycle. a) Vertical inter-seismic deformation (colored squares) and horizontal inter-seismic deformation (vectors) observed through GPS over the 1999–2010 period [RUE 09, VIG 11], with respect to the South America-fixed reference frame. The red triangles are the active volcanoes in the zone. b) Vertical and horizontal co-seismic deformation observed by GPS following the Maule earthquake on February 27, 2010 (Mw 8.8). c) Vertical and horizontal post-seismic deformation observed over the June 2010 to January 2011 period at the permanent stations in the zone [KLE 16]. (d and e) Co-seismic and inter-seismic deformation: horizontal d) and vertical e) observed along the A-B profile depicted in panel (b)*

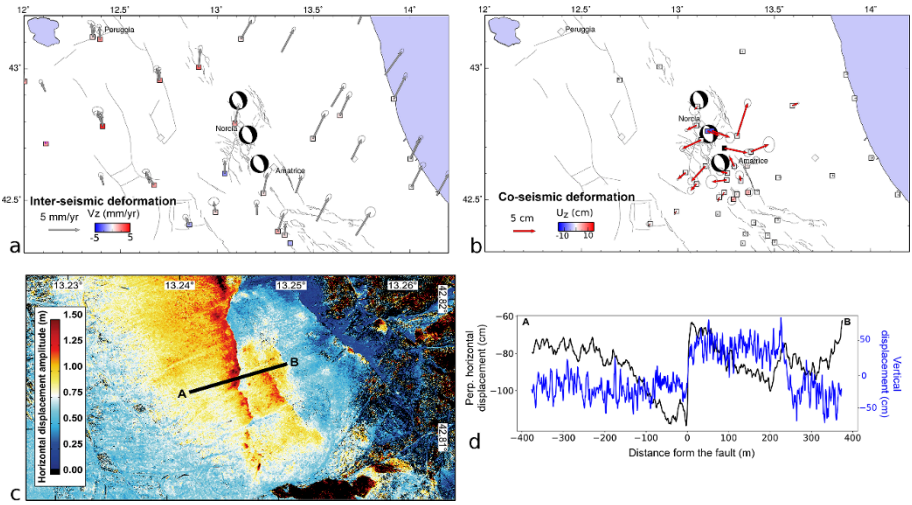

Figure I.8. *Case of a system of normal faults: Deformation observed around the system of normal Apennine faults in the Norcia-Amatrice region (Italy). Solid black lines: principal active faults [MIC 00]. a) Horizontal and vertical active inter-seismic deformation observed by GPS with respect to stable Eurasia [MÉT 15] caused by the motion of the Thyrenian and Adriatic plates. b) Horizontal and vertical co-seismic deformation following the series of earthquakes in Amatrice-Norcia (Mw 6.1, 5.9 and 6.5 represented by their focal mechanisms) as per [CHE 17]. c) Horizontal co-seismic displacement perpendicular to the principal fault seen through the correlation of optical images [DEL 20], represented with the vertical displacement along the A-B profile d). The normal faults are often segmented and complex in addition to presenting large angles of dip: it is often difficult to individualize a clear inter-seismic signal (see Figures I.5 (f)–(h))*

Transient inter-seismic movements: in the 2000s, on the border of the Cascades subduction (North America), another major discovery was made that completely overturned our understanding of the inter-seismic phase of the seismic cycle. While seismic swarms, called tremors, are regularly recorded by seismometers in this region, Rogers and Dragert [ROG 03, DRA 04] demonstrate that they are associated with centimetric displacements of the GNSS stations toward the west, that is, toward the subduction trench (see the example of the ACYA Mexican station, Figure I.9). This is a motion that resembles the motion observed in the co-seismic phase, when a rupture occurs on the subduction fault, but which lasts several weeks or even several months. And, above all, one which is not accompanied by any seismic wave other than those emitted by the very weak earthquakes that make up tremors and low-frequency earthquakes. This was the first evidence of slow slip events (SSE). These periods of aseismic, transient slip events are now quite widely identified [IDE 07], independent of the tectonic context being considered, which suggest there

is a common physical mechanism of the temporary unblocking of faults during the inter-seismic phase of the cycle [BÜR 18]. These slow slip events release part of the energy resulting from the relative motion of the plates (up to the equivalent of earthquakes of magnitude 7.5 [RAD 11]), which will not be seismically released. The discovery of these SSE thus had a major impact on how the energy balance equation of the seismic cycles is understood [CHL 14, AVO 15, MIC 19] (see Chapter 6).

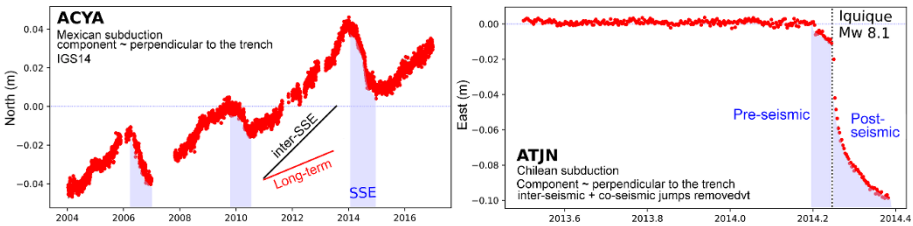

Figure I.9. *Kinematic complexities of the seismic cycle. GNSS time series [BLE 18]: ACYA (upper region, Acapulco, Mexico) records three aseismic events (SSE) lasting several months in the inter-seismic period (2004–May 2016) [VER 10, RAD 11]; ATJN (lower region, northern Chile coast), corrected from the coseismic jump the co-seismic jump associated with the Iquique earthquake (Mw 8.1, 2014) and the long-term inter-seismic trend calculated over the period 2006–2013 to reveal a phase of pre-seismic motion toward the trench, observed several weeks to several months before the mainshock [RUI 14, SOC 17, SCH 14], as well as the regional post-seismic rebound, which will last several years (toward the west, that is, toward the trench)*

Inter-seismic coupling: similarly, observations of inter-seismic surface deformations have shown that the deformation gradient could vary significantly along a fault without the geometry of the fault changing radically, and even with the relative long-term velocity of the plates in contact being unchanged [WAL 04, CHL 11, LOV 11, MCC 14, MÉT 16, HUS 18]. Figure I.10(a) depicts the large variations of the second invariant of the deformation rates tensor along the Chilean subduction (corresponding to variations in the horizontal velocity gradient, see section I.2.2) and these cannot be explained by brutal variations in the geometry of the subduction zones nor by changes in the relative velocity of the Nazca and South American plates (globally estimated to be ∼7 cm/year). In section I.3, it has been seen that the depth and size of the blocked zone during the inter-seismic period governs the aspect of the surface deformation. In the Chilean case and many other cases, the degree of locking of the interface, also called *coupling*, must also be varied over the fault to correctly explain the surface deformation (see Figure I.10(b) and Chapters 5 and 6).

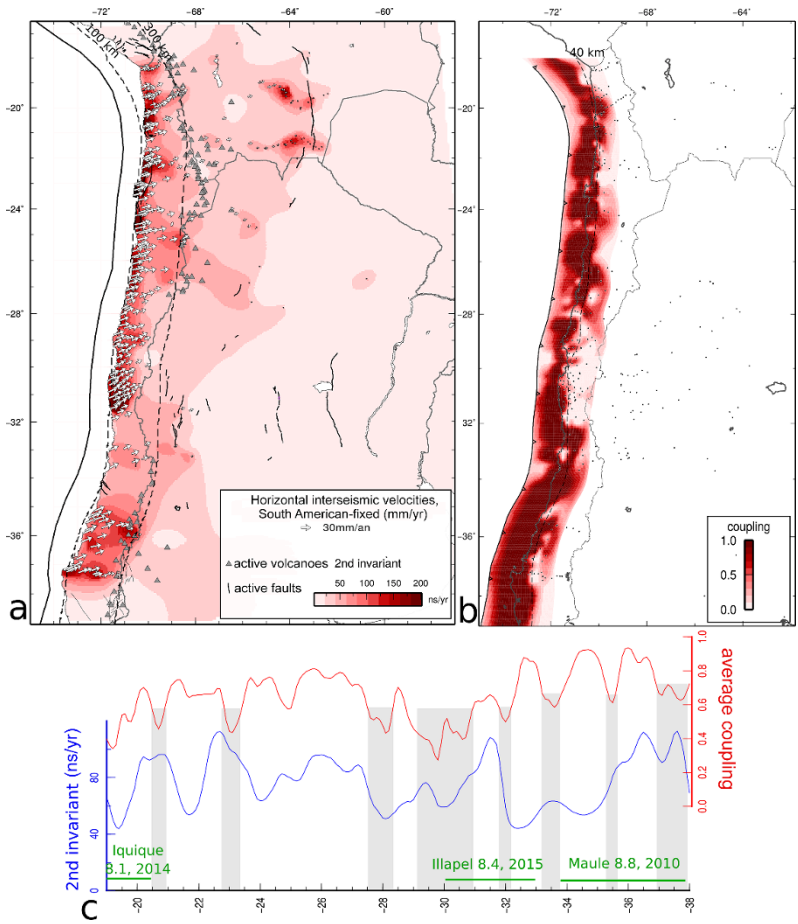

Figure I.10. *a) Vectors: inter-seismic velocities measured at the GNSS stations with respect to stable South-America. The second invariant of the deformation rates tensor calculated from this discrete velocity field is represented in color (nano strain/year). Black lines: principal active faults (Global Active Faults GEM project), including the subduction zone with the Nazca plate; gray triangles: active volcanoes; dotted lines: isodistances with the subduction trench (100 and 300 km) between which the second invariant is maximum. b) Coupling on the subduction interface, according to Métois et al. [MÉT 16]. Dotted line: isodepth 40 km on the subduction. c) Variations with latitude of the averaged coupling on the first 60 km of depth and the average second invariant between 100 and 300 km from the trench (sliding windows every 0.1°, perpendicular to the trench). Gray bands: Borders of the segments (intersegments) with weak local coupling*

This coupling coefficient ϕ is defined in a purely kinematic manner as $\phi = 1 - \frac{V_{dislocation}}{V_o}$, where V_o is the long-term horizontal velocity of the plates and $V_{dislocation}$ is the slip velocity of the fault zone that is partially locked during the interseismic phase. This must not be confused with "seismic coupling" [TIC 93], and it is important to note that the use of the same term (coupling) is debated in the community [WAN 04, LAY 04]. Some authors prefer discussing and representing the slip deficit (in mm), which corresponds to the numerator of ϕ given by $V_o - V_{dislocation}$ multiplied by the inter-seismic loading time since the last large earthquake (assumed to be known, which is far from being the case now). If $V_{dislocation} = V_o$, then the fault slips aseismically at the long-term velocity of the plates, no deformation accumulates and the coupling is zero, like the slip deficit. On the contrary, if no slip event has taken place on the fault in the inter-seismic period ($V_{dislocation} = 0$), then the elastic deformation is large, there is total coupling (100%) and the slip deficit is maximum.

What is the significance of a partial coupling, 40% for example? Kinematically, this is the same as saying that during the inter-seismic phase, 60% of the slip available for the long-term movement of the plates is released in the form of aseismic slip along the interface. The remaining 40% corresponds to the slip deficit that generates the elastic deformation of the lithospheres in contact. This aseismic slip may correspond to a continuous slow slip event in the fault zone, over several years, or a succession of small slips of very small magnitude, or in zones that are too small to be individualized. It is sometimes difficult to imagine a fault that slips and is blocked at the same time, during this inter-seismic period which is not, ultimately, a period of perfect rest.

To better understand what a coupling of 40% means, we must go down from the scale of the fault segment to that of the fault plane itself and its asperities. The fault plane is not homogeneous and smooth: (i) the materials that are in contact with it on either side may change in rheology or lithology with depth or along the fault, (ii) the roughness of the plane depends on the geological and seismic history of the fault and (iii) the circulation of fluids in this fault zone are far from being homogeneous. The fault plane can be thought of as being composed of zones that are capable of slowly slipping while others, like adhesive points or pinheads, remain immobile during the inter-seismic period and rupture brutally when the applied stress threshold is too high. The coupling coefficient maps are often interpreted based on the "rate & state" formalism [DIE 75, AVO 15]: a strong coupling could correspond to zones called "velocity-weakening" zones, while weakly coupled zones behave more like "velocity-strengthening" zones (see Chapter 4). Understanding which physical parameters govern the coupling value over a fault remains an open question that is still widely debated today [AVO 15, MOR 12]. Generally speaking, the studies tend to show that the zones that are strongly coupled during the inter-seismic period are more susceptible to rupturing during large earthquakes, while zones with weak coupling behave more like brakes (partial or total) on the propagation. The zones with a high

coupling gradient contain seismic swarms and could be conducive to the nucleation of slow earthquakes or conventional earthquakes [MOR 10, LOV 11, CHL 14, MÉT 16].

In the past few years, the increase in the surface deformation measurements has led to the publication of many coupling maps along major thrust systems (subductions [LOV 11, NOC 14, MÉT 16, CHL 08], the Himalayan arc [STE 15, MAR 16], the Alpine arc [CHE 14]) and large strike-slip faults [HUS 18, JOL 15, BLE 20]. Normal fault systems often prove to be slower, more segmented and, consequently, not very conducive to this type of approach [AND 13] (see Chapter 8). Zones with strong coupling are generally concentrated in the seismogenic zone of these faults (up to a depth of $\sim$60 km for subduction zones, much less for strike-slip or normal faults) and are surrounded by superficial or deep zones with weaker coupling. These maps present a kinematic segmentation of the faults, which can only be interpreted in relation to the seismotectonic and geological observations in the zone. However, they are, at present, one of the most efficient tools available to identify zones with high seismogenic potential [BEA 18], or even to generate rupture and tsunami scenarios by making a strong hypothesis regarding the mechanical significance of the coupling [HOK 11, YAN 19]. It is nonetheless important to remark that coupling maps have certain significant limitations:

– the coupling is poorly resolved in the superficial parts of subduction zones due to the lack of observations of deformation on the ocean floor [HAS 12];

– the value of the slip deficit depends on the fixed convergence velocity, V_o, between the two plates and, consequently, on the rigid block models used. The current motion of oceanic plates (e.g. the Caribbean or Nazca plates) is sometimes difficult to know given the absence of geodesic measurements offshore and the poor spatial distribution of networks, confined to existing islands [DEM 01]. The delineation of the rigid blocks itself may also be unclear [WAL 04, MCC 07, CHL 11]. We must therefore be careful when converting a coupling map into the maximum possible magnitude;

– the coupling is calculated over a given period (that of the surface observations), but it may evolve over the course of the inter-seismic phase or differ from one cycle to another [LOV 16, MEN 16, JAR 17];

– the alternation of decoupled and coupled zones on the same fault plane when the depth increases is considered to be mechanically unrealistic by certain authors, due to the pressure shadows associated with heavily blocked zones [ALM 18]. This particular case clearly illustrates the limitations of a purely kinematic description.

Pre-seismic motions: there has been a recent addition to this diversity of motion recorded around faults that were assumed to be inactive during the inter-seismic period, chiefly due to the large subduction earthquakes in Chile and Japan: *pre-seismic movements*, whose amplitude and very existence are still being debated [RUI 14, SCH 14, SOC 17, SOC 19, BED 20]. A fine analysis of the daily GNSS time series in the days, weeks and months preceding the large Iquique earthquake

(Chile, Mw 8.1, 2014) showed a deviation from the long-term trend before the mainshock, providing the base for a pre-seismic deformation phase (see station ATJN in Figure I.9). Some authors also think it is possible to see, in the GNSS time series or pre-seismic gravimetric time series from Maule or Tohuku, large wavelength deformations that affect a vast zone around the future epicenter [BED 20, PAN 18, WAN 19b]. This pre-seismic phase does not seem to be observed in all cases nor in all contexts. The relation between the recorded pre-seismic deformation, partially aseismic and the seismic nucleation phase is a new field of study that may allow us to better anticipate large earthquakes.

I.5. What is the current status of the "seismic cycle"?

The observations of surface deformations in the lithosphere around active faults have shown that between two earthquakes, the fault and the environment around it are not generally in a phase of quiescence. The inter-seismic period during which stresses accumulate anew around the fault zone is indeed complex and generates deformations that are of smaller amplitude than co-seismic deformations, but enhance our understanding of the seismic cycle on the whole. A partial locking of the interface, which may potentially vary over time, slow slips that release part of the accumulated energy, pre-seismic destabilization preparing the rupture, post-seismic slips that last a long time and visco-elastic relaxations of stresses in the medium: faults and the area around them are never at rest during the "inter-seismic period". The vision of a seismic cycle that is a simple succession of the spring extension phase and the brutal movement of the block, identical to one another, is today too simplistic a concept to explain all of the observations made. While the model of the characteristic earthquake can still be successfully applied to certain fault segments, this does not seem to be the rule. In addition to the co-seismic phase we now have the post-seismic and sometimes pre-seismic phases, while the inter-seismic phase is now considered in a less static manner. The high-frequency analysis of the GNSS time series following large earthquakes also begins to show us that several different phases of deformation may be identified just after the rupture, and we thus also speak of an early post-seismic phase [TWA 19].

The concept of the seismic cycle should also be adapted to the spatial and temporal scale under consideration: the seismic cycle of an asperity located on the fault plane is probably closer to the spring-block model than that of a fault segment or, even more complex, the fault segmented in its entirety, or even a fault system on a regional scale. The large-scale analysis of coupling distributions, microseismicity and historical seismicity of major faults seems to indicate that certain fault segments can rupture individually, independent of their neighbors or, more rarely but also characteristically, collectively (the concept of a seismic super-cycle [NOC 17], see Figure I.11).

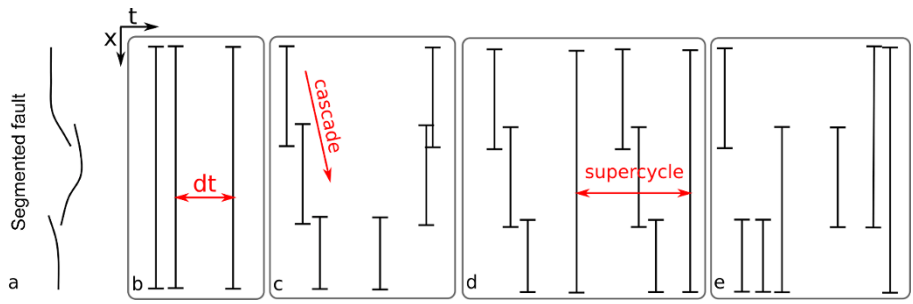

Figure I.11. *Conceptual models of cycles over a segmented fault a), according to [PHI 20]. b) Cycle blind to tectonic segmentation, the recurrence time, dt, may or may not vary (characteristic earthquake). c) Each segment ruptures alone but triggers a cascading rupture of neighboring segments at a larger or smaller timeframe. The recurrence time between two cascades may be that of a super-cycle. d) Mixed behavior: the segments can rupture in an isolated or conjoint manner. The repetition of simultaneous ruptures may be considered a super-cycle. e) Random ruptures concerning one or more segments, without any apparent repetition over time*

To conclude this introductory chapter on the concept of the seismic cycle studied through kinematics, let us return to the many strong hypotheses from simple models of the seismic cycles: (1) Let us first consider the energy equilibrium assumed to exist between the phases of the cycle (inter-seismic, pre-, co- and post-seismic) around an active fault. It is also generally considered that the elastic potential energy accumulated during the inter-seismic phase in response to the forcing of the movement of the plates is entirely released during the co-seismic phase. However, the complexities seen in section I.9 impose (i) the quantification of the energy actually released during seismic ruptures in the form of heat, seismic waves and motion, (ii) the quantification of energy released during slow slip events, (iii) considering the post-seismic slip and (iv) taking into account any eventual temporal variation in the coupling at the interface to establish an energy balance if needed. This is a difficult exercise to carry out in practice, and most often slip balance equations at the fault interface are established using surface observations only. Generally, the balance between the slip deficit, accumulated during the inter-seismic phase and the slip released during the co-seismic phase or during slow slip events is balanced to the first order. Sometimes, however, this balance must be established over several seismic cycles (equilibrium over time) or on the scale of several fault segments (equilibrium in space) to arrive at the effective equilibrium, which makes it all the more difficult to anticipate earthquakes using coupling maps, for example. (2) If we look at how faults function in the long term, it becomes difficult to neglect the fact that part of the energy coming from the relative movement of the plates is converted into topography along active faults via a plastic deformation mechanism. For example, it is striking to note that the morphology of the Chilean and Mexican coasts present segmentation

that strongly resembles the kinematic segmentation drawn through coupling: peninsulas develop wherever the coupling is weak [SAI 17, ROU 16], and high surrection rates have been recorded over the quaternary period where the coupling is strong [BÉJ 13, JOL 20]. Similarly, the analysis of the morphology of accretion prisms may be interpreted in terms of the friction on the fault interface (see Chapter 7). Where, when and how does this permanent plastic deformation occur? At what stage of the seismic cycle? This question is crucial to establish the relation between geomorphological observations and geological observation and is at the heart of current scientific discussions [MEL 16, MAL 18, JOL 20]. (3) Finally, while there is no doubt that the main forcing of the seismic cycle is related to the movement of plates in the terrestrial convection system, it seems to be increasingly necessary to take into account other factors that could influence the chronology and intensity of its different phases (erosion, hydrology and so on; see Chapter 9 and [CHA 14, CRA 17]).

I.6. References

[ALM 18] ALMEIDA R., LINDSEY E.O., BRADLEY K. et al., "Can the updip limit of frictional locking on megathrusts be detected geodetically? Quantifying the effect of stress shadows on near-trench coupling", *Geophysical Research Letters*, vol. 45, no. 10, pp. 4754–4763, 2018.

[ALT 17] ALTAMIMI Z., MÉTIVIER L., REBISCHUNG P. et al., "ITRF2014 plate motion model", *Geophysical Journal International*, vol. 209, no. 3, pp. 1906–1912, 2017.

[AND 13] ANDERLINI L., SERPELLONI E., BELARDINELLI M.E., "Kinematic model of active extension across the Umbria-Marche Apennines from GPS measurements: Fault slip-rates and interseismic coupling of the Alto Tiberina low-angle normal fault", *GNGTS*, 2013.

[AVO 15] AVOUAC J.-P., "From geodetic imaging of seismic and aseismic fault slip to dynamic modeling of the seismic cycle", *Annual Review of Earth and Planetary Sciences*, vol. 43, pp. 233–271, 2015.

[BAC 18] BACQUES G., DE MICHELE M., RAUCOULES D. et al., "Shallow deformation of the San Andreas fault 5 years following the 2004 Parkfield earthquake (Mw6) combining ERS2 and Envisat InSAR", *Scientific Reports*, vol. 8, no. 1, pp. 1–10, 2018.

[BAK 85] BAKUN W., LINDH A., "The Parkfield, California, earthquake prediction experiment", *Science*, vol. 229, no. 4714, pp. 619–624, 1985.

[BAK 05] BAKUN W., AAGAARD B., DOST B. et al., "Implications for prediction and hazard assessment from the 2004 Parkfield earthquake", *Nature*, vol. 437, no. 7061, pp. 969–974, 2005.

[BEA 18] BEAUVAL C., MARINIÈRE J., YEPES H. et al., "A new seismic hazard model for Ecuador", *Bulletin of the Seismological Society of America*, vol. 108, no. 3A, pp. 1443–1464, 2018.

[BED 20] BEDFORD J.R., MORENO M., DENG Z. et al., "Months-long thousand-kilometre-scale wobbling before great subduction earthquakes", *Nature*, vol. 580, no. 7805, pp. 628–635, 2020.

[BÉJ 13] BÉJAR-PIZARRO M., SOCQUET A., ARMIJO R. et al., "Andean structural control on interseismic coupling in the North Chile subduction zone", *Nature Geoscience*, vol. 6, no. 6, pp. 462–467, 2013.

[BIR 15] BIRD P., KREEMER C., "Revised tectonic forecast of global shallow seismicity based on version 2.1 of the Global Strain Rate Map", *Bulletin of the Seismological Society of America*, vol. 105, no. 1, pp. 152–166, 2015.

[BLE 15] BLEWITT G., "GPS and space based geodetic methods", in SCHUBERT, G. (ed.), *Treatise on Geophysics*, Elsevier, Amsterdam, available at: https://www.sciencedirect.com/science/article/pii/B9780444527486000584, 2015.

[BLE 18] BLEWITT G., HAMMOND W.C., KREEMER C., "Harnessing the GPS data explosion for interdisciplinary science", *Eos*, vol. 99, pp. 1–2, 2018.

[BLE 20] BLETERY Q., CAVALIÉ O., NOCQUET J.-M. et al., "Distribution of interseismic coupling along the North and East Anatolian Faults inferred from InSAR and GPS data", *arXiv preprint arXiv:2003.02001*, 2020.

[BOU 14] BOUDIN F., BERNARD P., ESNOULT M. et al., "Evidence for slow slip events preceeding the M8, April 1st, 2014 Pisagua Earthquake (Chile), from an underground, long base hydrostatic tiltmeter", *AGUFM*, 2014.

[BUR 67] BURRIDGE R., KNOPOFF L., "Model and theoretical seismicity", *Bulletin of the Seismological Society of America*, vol. 57, no. 3, pp. 341–371, 1967.

[BÜR 18] BÜRGMANN R., "The geophysics, geology and mechanics of slow fault slip", *Earth and Planetary Science Letters*, vol. 495, pp. 112–134, 2018.

[CHA 14] CHANARD K., AVOUAC J., RAMILLIEN G. et al., "Modeling deformation induced by seasonal variations of continental water in the Himalaya region: Sensitivity to Earth elastic structure", *Journal of Geophysical Research: Solid Earth*, vol. 119, no. 6, pp. 5097–5113, 2014.

[CHE 14] CHELONI D., D'AGOSTINO N., SELVAGGI G., "Interseismic coupling, seismic potential, and earthquake recurrence on the southern front of the Eastern Alps (NE Italy)", *Journal of Geophysical Research: Solid Earth*, vol. 119, no. 5, 4448–4468, 2014.

[CHE 17] CHELONI D., NOVELLIS V.D., ALBANO M. et al., "Geodetic model of the 2016 Central Italy earthquake sequence inferred from InSAR and GPS data", *Geophysical Research Letters*, vol. 44, no. 13, pp. 6778–6787, 2017.

[CHL 08] CHLIEH M., AVOUAC J.-P., SIEH K. et al., "Heterogeneous coupling of the Sumatran megathrust constrained by geodetic and paleogeodetic measurements", *Journal of Geophysical Research: Solid Earth*, vol. 113, no. B5, 2008.

[CHL 11] CHLIEH M., PERFETTINI H., TAVERA H. et al., "Interseismic coupling and seismic potential along the Central Andes subduction zone", *Journal of Geophysical Research*, vol. 116, no. B12, pp. 1–21, 2011.

[CHL 14] CHLIEH M., MOTHES P., NOCQUET J.-M. et al., "Distribution of discrete seismic asperities and aseismic slip along the Ecuadorian megathrust", *Earth and Planetary Science Letters*, vol. 400, 292–301, 2014.

[COR 21] CORNOU C.E.A., Jean-Paul, A., Coralie, A. et al. "Rapid response to the Mw 4.9 earthquake of November 11, 2019 in Le Teil, Lower Rhône Valley, France", *Compte rendus géoscience*, vol. 353, no. S1, pp. 1–23, 2021.

[CRA 17] CRAIG T.J., CHANARD K., CALAIS E., "Hydrologically-driven crustal stresses and seismicity in the New Madrid seismic zone", *Nature Communications*, vol. 8, no. 1, pp. 1–11, 2017.

[DAG 14] D'AGOSTINO N., "Complete seismic release of tectonic strain and earthquake recurrence in the Apennines (Italy)", *Geophysical Research Letters*, vol. 41, no. 4, pp. 1155–1162, 2014.

[DAO 19] DAOUT S., SUDHAUS H., KAUSCH T. et al., "Interseismic and postseismic shallow creep of the North Qaidam Thrust faults detected with a multitemporal InSAR analysis", *Journal of Geophysical Research: Solid Earth*, vol. 124, no. 7, pp. 7259–7279, 2019.

[DEL 20] DELORME A., GRANDIN R., KLINGER Y. et al., "Complex deformation at shallow depth during the 30 October 2016 Mw6. 5 Norcia earthquake: Interference between tectonic and gravity processes?", *Tectonics*, vol. 39, no. 2, p. e2019TC005596, 2020.

[DEM 94] DEMETS C., RICHARD, G., DONALD, F. et al. "Effect of recent revision to the geomagnetic reversal time scale on estimates of current plate motions", *Geophysical Research Letters*, vol. 21, no. 20, pp. 2191–2194, 1994.

[DEM 01] DEMETS C., "A new estimate for present-day Cocos-Caribbean plate motion: Implications for slip along the Central American volcanic arc", *Geophysical Research Letters*, vol. 28, no. 21, pp. 4043–4046, 2001.

[DIE 75] DIETERICH J.H., DECKER R.W., "Finite element modeling of surface deformation associated with volcanism", *Journal of Geophysical Research*, vol. 80, no. 29, pp. 4094–4102, 1975.

[DRA 04] DRAGERT H., WANG K., ROGERS G., "Geodetic and seismic signatures of episodic tremor and slip in the northern Cascadia subduction zone", *Earth, Planets, and Space*, vol. 56, no. 12, pp. 1143–1150, 2004.

[DUC 12] DUCRET G., DOIN M., GRANDIN R. et al., "Measurement of interseismic strain accumulation in the Southern Andes (25°-35° S) using Envisat SAR data", *EGU General Assembly Conference Abstracts*, vol. 14, p. 10391, 2012.

[FED 68] FEDOTOV S., "The seismic cycle, quantitative seismic zoning, and long-term seismic forecasting", *Seismic Zoning of the USSR*, pp. 133–166, 1968.

[FLO 20] FLOYD M., FUNNING G., FIALKO Y. et al., "Survey and continuous GNSS in the vicinity of the July 2019 Ridgecrest earthquakes", *Seismological Research Letters*, vol. 91, no. 4, pp. 2047–2054, 2020.

[GRA 12] GRANDIN R., DOIN M.-P., BOLLINGER L. et al., "Long-term growth of the Himalaya inferred from interseismic InSAR measurement", *Geology*, vol. 40, no. 12, pp. 1059–1062, 2012.

[GRA 16] GRANDIN R., KLEIN E., MÉTOIS M. et al., "Three-dimensional displacement field of the 2015 Mw8.3 Illapel earthquake (Chile) from across- and along-track Sentinel-1 TOPS interferometry", *Geophysical Research Letters*, vol. 43, no. 6, pp. 2552–2561, 2016.

[HAS 12] HASHIMOTO C., NODA A., MATSUURA M., "The Mw 9.0 northeast Japan earthquake: Total rupture of a basement asperity", *Geophysical Journal International*, vol. 189, no. 1, pp. 1–5, 2012.

[HOF 07] HOFMANN-WELLENHOF B., LICHTENEGGER H., WASLE E., *GNSS–Global Navigation Satellite Systems: GPS, GLONASS, Galileo, and More*, Springer Science & Business Media, Wien, 2007.

[HOK 11] HOK S., FUKUYAMA E., HASHIMOTO C., "Dynamic rupture scenarios of anticipated Nankai-Tonankai earthquakes, southwest Japan", *Journal of Geophysical Research: Solid Earth*, vol. 116, no. B12, 2011.

[HUA 90] HUANG J., TURCOTTE D.L., "Are earthquakes an example of deterministic chaos?", *Geophysical Research Letters*, vol. 17, no. 3, pp. 223–226, 1990.

[HUS 18] HUSSAIN E., WRIGHT T.J., WALTERS R.J. et al., "Constant strain accumulation rate between major earthquakes on the North Anatolian Fault", *Nature Communications*, vol. 9, no. 1, pp. 1–9, 2018.

[IDE 07] IDE S., BEROZA G., SHELLY D. et al., "A scaling law for slow earthquakes", *Nature*, vol. 447, no. 7140, pp. 76–79, 2007.

[JAR 17] JARA J., SOCQUET A., MARSAN D. et al., "Long-term interactions between intermediate depth and shallow seismicity in North Chile subduction zone", *Geophysical Research Letters*, vol. 44, no. 18, pp. 9283–9292, 2017.

[JOL 15] JOLIVET R., SIMONS M., AGRAM P. et al., "Aseismic slip and seismogenic coupling along the central San Andreas Fault", *Geophysical Research Letters*, vol. 42, no. 2, pp. 297–306, 2015.

[JOL 20] JOLIVET R., SIMONS M., DUPUTEL Z. et al., "Interseismic loading of subduction megathrust drives long-term uplift in northern Chile", *Geophysical Research Letters*, vol. 47, no. 8, p. e2019GL085377, 2020.

[JOM 17] JOMARD H., CUSHING E.M., PALUMBO L. et al., "Transposing an active fault database into a seismic hazard fault model for nuclear facilities – Part 1: Building a database of potentially active faults (BDFA) for metropolitan France", *Natural Hazards and Earth System Sciences*, vol. 17, no. 9, pp. 1573–1584, 2017.

[KAN 02] KANAMORI H., "Earthquake prediction: An overview", in LEE, W., KANAMORI, H., JENNINGS, P., KISSLINGER, C. (eds), *International Handbook of Earthquake and Engineering Seismology*, Academic Press, San Diego, CA, 2002.

[KAN 10] KANDA R.V.S., SIMONS M., "An elastic plate model for interseismic deformation in subduction zones", *Journal of Geophysical Research*, vol. 115, no. B3, pp. 1–19, 2010.

[KHA 02] KHAZARADZE G., WANG K., KLOTZ J. et al., "Prolonged post-seismic deformation of the 1960 great Chile earthquake and implications for mantle rheology", *Geophysical Research Letters*, vol. 29, no. 22, pp. 7–1, 2002.

[KLE 16] KLEIN E., FLEITOUT L., VIGNY C. et al., "Afterslip and viscoelastic relaxation model inferred from the large-scale post-seismic deformation following the 2010 Mw 8.8 Maule earthquake (Chile)", *Geophysical Journal International*, vol. 205, no. 3, pp. 1455–1472, 2016.

[KLE 17] KLEIN E., VIGNY C., FLEITOUT L. et al., "A comprehensive analysis of the Illapel 2015 Mw8. 3 earthquake from GPS and InSAR data", *Earth and Planetary Science Letters*, vol. 469, pp. 123–134, 2017.

[LAC 20] LACASSIN R., DEVÈS M., HICKS S.P. et al., "Rapid collaborative knowledge building via Twitter after significant geohazard events", *Geoscience Communication*, vol. 3, no. 1, pp. 129–146, 2020.

[LAY 04] LAY T., SCHWARTZ S., "Comment on 'Coupling semantics and science in earthquake research'", *Eos Trans. AGU*, vol. 85, no. 36, pp. 339–340, 2004.

[LEP 68] LE PICHON X., "Sea-floor spreading and continental drift", *Journal of Geophysical Research*, vol. 73, no. 12, pp. 3661–3697, 1968.

[LI 15] LI S., MORENO M., BEDFORD J. et al., "Revisiting viscoelastic effects on interseismic deformation and locking degree: A case study of the Peru-North Chile subduction zone", *Journal of Geophysical Research: Solid Earth*, vol. 120, no. 6, pp. 4522–4538, 2015.

[LIN 17] LINDSEY N.J., MARTIN E.R., DREGER D.S. et al., "Fiber-optic network observations of earthquake wavefields", *Geophysical Research Letters*, vol. 44, no. 23, pp. 11–792, 2017.

[LOV 11] LOVELESS J., MEADE B., "Spatial correlation of interseismic coupling and coseismic rupture extent of the 2011 MW = 9.0 Tohoku-oki earthquake", *Geophysical Research Letters*, vol. 38, p. L17306, 2011.

[LOV 16] LOVELESS J.P., MEADE B.J., "Two decades of spatiotemporal variations in subduction zone coupling offshore Japan", *Earth and Planetary Science Letters*, vol. 436, pp. 19–30, 2016.

[MAL 18] MALATESTA L., BRUHAT L., FINNEGAN N.J. et al., "Co-location of the downdip end of seismic locking and the continental shelf break", *EarthArXiv*, 2018.

[MAR 16] MARECHAL A., MAZZOTTI S., CATTIN R. et al., "Evidence of interseismic coupling variations along the Bhutan Himalayan arc from new GPS data", *Geophysical Research Letters*, vol. 43, no. 24, pp. 12–399, 2016.

[MAR 18] MARCHANDON M., VERGNOLLE M., CAVALIÉ O. et al., "Earthquake sequence in the NE Lut, Iran: Observations from multiple space geodetic techniques", *Geophysical Journal International*, vol. 215, no. 3, pp. 1604–1621, 2018.

[MAS 93] MASSONNET D., ROSSI M., CARMONA C. et al., "The displacement field of the Landers earthquake mapped by radar interferometry", *Nature*, vol. 364, no. 6433, pp. 138–142, 1993.

[MAS 14] MASSON F., LEHUJEUR M., ZIEGLER Y. et al., "Strain rate tensor in Iran from a new GPS velocity field", *Geophysical Journal International*, vol. 197, no. 1, pp. 10–21, 2014.

[MAS 19] MASSON C., MAZZOTTI S., VERNANT P. et al., "Extracting small deformation beyond individual station precision from dense Global Navigation Satellite System (GNSS) networks in France and western Europe", *Solid Earth*, vol. 10, no. 6, pp. 1905–1920, 2019.

[MCC 07] MCCAFFREY R., QAMAR A.I., KING R.W. et al., "Fault locking, block rotation and crustal deformation in the Pacific Northwest", *Geophysical Journal International*, vol. 169, no. 3, pp. 1315–1340, 2007.

[MCC 14] MCCAFFREY R., "Interseismic locking on the Hikurangi subduction zone: uncertainties from slow-slip events", *Journal of Geophysical Research: Solid Earth*, vol. 119, no. 10, pp. 7874–7888, 2014.

[MEL 16] MELNICK D., "Rise of the central Andean coast by earthquakes straddling the Moho", *Nature Geoscience*, vol. 9, no. 5, pp. 401–407, 2016.

[MEL 18] MELNICK D., LI S., MORENO M. et al., "Back to full interseismic plate locking decades after the giant 1960 Chile earthquake", *Nature Communications*, vol. 9, no. 1, pp. 1–10, 2018.

[MEN 16] MENESES G., VIGNY C., BOUDIN F., "Short and long term analysis of upper plate deformation in Northern Chile subduction zone with GPS and tiltmeter data", *AGUFM*, vol. 2016, pp. G42A–03, 2016.

[MÉT 15] MÉTOIS M., D'AGOSTINO N., AVALLONE A. et al., "Insights on continental collisional processes from GPS data: Dynamics of the peri-Adriatic belts", *Journal of Geophysical Research: Solid Earth*, vol. 120, no. 12, pp. 8701–8719, 2015.

[MÉT 16] MÉTOIS M., VIGNY C., SOCQUET A., "Interseismic coupling, megathrust earthquakes and seismic swarms along the Chilean subduction zone (38–18 S)", *Pure and Applied Geophysics*, vol. 173, no. 5, pp. 1431–1449, 2016.

[MIC 00] MICHETTI A., SERVA L., VITTORI E., "ITHACA (Italy hazard from capable faulting), a database of active capable faults of the Italian onshore territory", *Database on CD-ROM, Int. Rep. of ANPA (Agenzia Nazionale Protezione Ambiente)*, 2000.

[MIC 19] MICHEL S., GUALANDI A., AVOUAC J.-P., "Interseismic coupling and slow slip events on the Cascadia megathrust", *Pure and Applied Geophysics*, vol. 176, no. 9, pp. 3867–3891, 2019.

[MOR 68] MORGAN W.J., "Rises, trenches, great faults, and crustal blocks", *Journal of Geophysical Research*, vol. 73, no. 6, pp. 1959–1982, 1968.

[MOR 08] MORENO M.S., KLOTZ J., MELNICK D. et al., "Active faulting and heterogeneous deformation across a megathrust segment boundary from GPS data, south central Chile (36–39°S)", *Geochemistry Geophysics Geosystems*, vol. 9, no. 12, p. Q12024, 2008.

[MOR 10] MORENO M., ROSENAU M., ONCKEN O., "2010 Maule earthquake slip correlates with pre-seismic locking of Andean subduction zone", *Nature*, vol. 467, no. 7312, pp. 198–202, 2010.

[MOR 12] MORENO M., MELNICK D., ROSENAU M. et al., "Toward understanding tectonic control on the Mw 8.8 2010 Maule Chile earthquake", *Earth and Planetary Science Letters*, vol. 321, pp. 152–165, 2012.

[MUR 06] MURRAY J., LANGBEIN J., "Slip on the San Andreas fault at Parkfield, California, over two earthquake cycles, and the implications for seismic hazard", *Bulletin of the Seismological Society of America*, vol. 96, no. 4B, pp. S283–S303, 2006.

[NOC 14] NOCQUET J.-M., VILLEGAS-LANZA J., CHLIEH M. et al., "Motion of continental slivers and creeping subduction in the northern Andes", *Nature Geoscience*, vol. 7, no. 4, pp. 287–291, 2014.

[NOC 17] NOCQUET J.-M., JARRIN P., VALLÉE M. et al., "Supercycle at the Ecuadorian subduction zone revealed after the 2016 Pedernales earthquake", *Nature Geoscience*, vol. 10, no. 2, pp. 145–149, 2017.

[OKA 85] OKADA Y., "Surface deformation due to shear and tensile faults in a half-space", *Bulletin of the Seismological Society of America*, vol. 75, no. 4, pp. 1135–1154, 1985.

[PAG 19] PAGANI C., BODIN T., METOIS M. et al., "Transdimensional estimation of surface strain rates from GPS measurements: Application to California.", *AGU Fall Meeting 2019*, 2019.

[PAN 18] PANET I., BONVALOT S., NARTEAU C. et al., "Migrating pattern of deformation prior to the Tohoku-Oki earthquake revealed by GRACE data", *Nature Geoscience*, vol. 11, no. 5, pp. 367–373, 2018.

[PHI 20] PHILIBOSIAN B., MELTZNER A.J., "Segmentation and supercycles: A catalog of earthquake rupture patterns from the Sumatran Sunda Megathrust and other well-studied faults worldwide", *Quaternary Science Reviews*, vol. 241, p. 106390, 2020.

[POL 01] POLLITZ F., WICKS C., THATCHER W., "Mantle flow beneath a continental strike-slip fault: Postseismic deformation after the 1999 Hector Mine earthquake", *Science*, vol. 293, no. 5536, pp. 1814–1818, 2001.

[POL 10] POLLITZ F., MCCRORY P., WILSON D. et al., "Viscoelastic-cycle model of interseismic deformation in the northwestern United States", *Geophysical Journal International*, vol. 181, no. 2, pp. 665–696, 2010.

[RAD 11] RADIGUET M., COTTON F., VERGNOLLE M. et al., "Spatial and temporal evolution of a long term slow slip event: The 2006 Guerrero Slow Slip Event", *Geophysical Journal International*, vol. 184, no. 2, pp. 816–828, 2011.

[REB 16] REBISCHUNG P., ALTAMIMI Z., RAY J. et al., "The IGS contribution to ITRF2014", *Journal of Geodesy*, vol. 90, no. 7, pp. 611–630, 2016.

[REI 10] REID H., *The California Earthquake of April 18, 1906: The Mechanics of the Earthquake, By Harry Fielding Reid*, Carnegie Institution of Washington, Washington, DC, 1910.

[ROG 03] ROGERS G., DRAGERT H., "Episodic tremor and slip on the Cascadia subduction zone: The chatter of silent slip", *Science*, vol. 300, no. 5627, pp. 1942–1943, 2003.

[ROS 17] ROSENAU M., CORBI F., DOMINGUEZ S., "Analogue earthquakes and seismic cycles: Experimental modelling across timescales", *Solid Earth*, vol. 8, pp. 597–635, 2017.

[ROU 16] ROUSSET B., LASSERRE C., CUBAS N. et al., "Lateral variations of interplate coupling along the Mexican subduction interface: Relationships with long-term morphology and fault zone mechanical properties", *Pure and Applied Geophysics*, vol. 173, nos 10–11, pp. 3467–3486, 2016.

[RUB 01] RUBIE D.C., VAN DER HILST R.D., "Processes and consequences of deep subduction: Introduction", *Physics of the Earth and Planetary Interiors*, vol. 127, nos 1–4, pp. 1–7, 2001.

[RUE 01] RUEGG J., OLCAY M., "Co-, post-and pre (?)-seismic displacements associated with the Mw 8.4 Southern Peru earthquake of 23 June 2001 from continuous GPS measurements", *Seismological Research Letters*, vol. 72, no. 6, pp. 673–678, 2001.

[RUE 09] RUEGG J., RUDLOFF A., VIGNY C. et al., "Interseismic strain accumulation measured by GPS in the seismic gap between Constituciún and Concepciún in Chile", *Physics of the Earth and Planetary Interiors*, vol. 175, nos 1–2, pp. 78–85, 2009.

[RUI 14] RUIZ S., METOIS M., FUENZALIDA A. et al., "Intense foreshocks and a slow slip event preceded the 2014 Iquique Mw 8.1 earthquake", *Science*, vol. 345, no. 6201, pp. 1165–1169, 2014.

[SAI 17] SAILLARD M., AUDIN L., ROUSSET B. et al., "From the seismic cycle to long-term deformation: Linking seismic coupling and quaternary coastal geomorphology along the Andean megathrust", *Tectonics*, vol. 36, no. 2, pp. 241–256, 2017.

[SAV 83] SAVAGE J., "A dislocation model of strain accumulation and release at a subduction zone", *Journal of Geophysical Research*, vol. 88, no. 3, pp. 4984–4996, 1983.

[SCH 14] SCHURR B., ASCH G., HAINZL S. et al., "Gradual unlocking of plate boundary controlled initiation of the 2014 Iquique earthquake", *Nature*, vol. 512, no. 7514, pp. 299–302, 2014.

[SHE 15] SHEN Z.-K., WANG M., ZENG Y. et al., "Optimal interpolation of spatially discretized geodetic data", *Bulletin of the Seismological Society of America*, vol. 105, no. 4, pp. 2117–2127, 2015.

[SLA 19] SLADEN A., RIVET D., AMPUERO J.-P. et al., "Distributed sensing of earthquakes and ocean-solid Earth interactions on seafloor telecom cables", *Nature Communications*, vol. 10, no. 1, pp. 1–8, 2019.

[SMI 68] SMITH S.W., WYSS M., "Displacement on the San Andreas fault subsequent to the 1966 Parkfield earthquake", *Bulletin of the Seismological Society of America*, vol. 58, no. 6, pp. 1955–1973, 1968.

[SOC 17] SOCQUET A., VALDES J.P., JARA J. et al., "An 8 month slow slip event triggers progressive nucleation of the 2014 Chile megathrust", *Geophysical Research Letters*, vol. 44, no. 9, pp. 4046–4053, 2017.

[SOC 19] SOCQUET A., MARILL L., MARSAN D. et al., "Deformation transients before the 2011 Tohoku-Oki Megathrust Earthquake: What does the GPS tell?", *AGUFM*, vol. 2019, pp. T11A–07, 2019.

[STE 15] STEVENS V., AVOUAC J., "Interseismic coupling on the main Himalayan thrust", *Geophysical Research Letters*, vol. 42, no. 14, pp. 5828–5837, 2015.

[THA 83] THATCHER W., "Nonlinear strain buildup and the earthquake cycle on the San Andreas fault", *Journal of Geophysical Research: Solid Earth*, vol. 88, no. B7, pp. 5893–5902, 1983.

[THA 84] THATCHER W., "The earthquake deformation cycle at the Nankai Trough, southwest Japan", *Journal of Geophysical Research: Solid Earth*, vol. 89, no. B5, pp. 3087–3101, 1984.

[TIC 93] TICHELAAR B.W., RUFF L.J., "Depth of seismic coupling along subduction zones", *Journal of Geophysical Research*, vol. 98, no. B2, pp. 2017–2037, 1993.

[TRU 13] TRUBIENKO O., FLEITOUT L., GARAUD J.-D. et al., "Interpretation of interseismic deformations and the seismic cycle associated with large subduction earthquakes", *Tectonophysics*, vol. 589, pp. 126–141, 2013.

[TRU 14] TRUBIENKO O., GARAUD J.-D., FLEITOUT L., "Models of postseismic deformation after megaearthquakes: The role of various rheological and geometrical parameters of the subduction zone", *Solid Earth Discussions*, vol. 6, no. 1, pp. 427–466, 2014.

[TWA 19] TWARDZIK C., VERGNOLLE M., SLADEN A. et al., "Unravelling the contribution of early postseismic deformation using sub-daily GNSS positioning", *Scientific Reports*, vol. 9, no. 1, pp. 1–12, 2019.

[VAL 15] VALLAGE A., KLINGER Y., GRANDIN R. et al., "Inelastic surface deformation during the 2013 Mw 7.7 Balochistan, Pakistan, earthquake", *Geology*, vol. 43, no. 12, pp. 1079–1082, 2015.

[VER 01] VERGNE J., CATTIN R., AVOUAC J.P., "On the use of dislocations to model interseismic strain and stress build-up at intracontinental thrust faults", *Geophysical Journal International*, vol. 147, no. 1, pp. 155–162, 2001.

[VER 10] VERGNOLLE M., WALPERSDORF A., KOSTOGLODOV V. et al., "Slow slip events in Mexico revised from the processing of 11 year GPS observations", *Journal of Geophysical Research*, vol. 115, p. B08403, 2010.

[VIG 05] VIGNY C., SIMONS W., ABU S. et al., "Insight into the 2004 Sumatra–Andaman earthquake from GPS measurements in southeast Asia", *Nature*, vol. 436, no. 7048, pp. 201–206, 2005.

[VIG 09] VIGNY C., RUDLOFF A., RUEGG J.-C. et al., "Upper plate deformation measured by GPS in the Coquimbo Gap, Chile", *Physics of the Earth and Planetary Interiors*, vol. 175, nos 1–2, pp. 86–95, 2009.

[VIG 11] VIGNY C., SOCQUET A., PEYRAT S. et al., "The 2010 Mw 8.8 Maule megathrust earthquake of Central Chile, monitored by GPS", *Science*, vol. 332, no. 6036, pp. 1417–1421, 2011.

[WAL 04] WALLACE L., BEAVAN J., MCCAFFREY R. et al., "Subduction zone coupling and tectonic block rotations in the North Island, New Zealand", *Journal of Geophysical Research*, vol. 109, no. B12, p. B12406, 2004.

[WAN 04] WANG K., DIXON T., "'Coupling' semantics and science in earthquake research", *EOS Transactions*, vol. 85, p. 180, 2004.

[WAN 19a] WANG H., WRIGHT T.J., LIU-ZENG J. et al., "Strain rate distribution in South-Central Tibet from two decades of InSAR and GPS", *Geophysical Research Letters*, vol. 46, no. 10, pp. 5170–5179, 2019.

[WAN 19b] WANG L., BURGMANN R., "Statistical significance of precursory gravity changes before the 2011 M w 9.0 Tohoku-Oki earthquake", *Geophysical Research Letters*, vol. 46, no. 13, pp. 7323–7332, 2019.

[YAN 19] YANG H., YAO S., HE B. et al., "Deriving rupture scenarios from interseismic locking distributions along the subduction megathrust", *Journal of Geophysical Research: Solid Earth*, vol. 124, no. 10, pp. 10376–10392, 2019.

1

Determining the Main Characteristics of Earthquakes from Seismological Data

Martin VALLÉE
Institut de physique du globe de Paris, Paris Cité University, France

1.1. Introduction

This chapter aims to illustrate how waveform modeling of seismograms makes it possible to determine the first-order characteristics of seismic processes. These first-order characteristics are typically the mechanism, magnitude, and location, as well as other information, such as the source duration or the average rupture velocity. Thus, the finer analysis of the process, and in particular the space–time description of the slip on the fault, will not be discussed here. The reader will find this topic addressed in Chapter 2.

Section 1.2 shows the typical seismological observations, at far and close distances, which make up the data that we wish to model. Section 1.3 describes how the information from the seismic source is physically transmitted by the waves to the receiver. This section is not a complete theoretical guide to the propagation of elastic waves, but it should help the reader to better understand some fundamental concepts, especially in the case of distant body waves. These concepts are then used in section 1.4, where we present several procedures aiming to characterize seismic sources.

The Seismic Cycle,
coordinated by Frédérique ROLANDONE.

The Seismic Cycle: From Observation to Modeling,
First Edition. Frédérique Rolandone.

1.2. Observation of the elastic waves generated by earthquakes

For over a century now, earthquakes have been regularly detected and located using the elastic waves that they generate. These waves are conventionally recorded by seismometers of different kinds (velocimeters or accelerometers) and, more recently, by high-frequency GPS, when strong earthquakes occur close to the receivers. We give here a brief introduction to the evolution of seismological instrumentation in the past few decades, with an emphasis on global networks that enabled systematic earthquake studies.

A global seismological network was created in the 1960s through the WWSSN (World Wide Standardized Seismograph Network) project. One hundred stations (including long- and short-period sensors, associated with a precise clock) were deployed around the globe. Since this pioneering effort to increase and standardize seismic observations, there have been several decisive improvements. In the 1980s, the development of broadband and digital stations greatly facilitated the analysis of seismic signals. On the one hand, it became futile to try to "reconcile" the data from the older short- and long-period sensors; modern broad-band sensors faithfully record ground acceleration between a thousandth of a hertz and tens of hertz, thereby making it possible to analyze the full seismic spectrum. On the other hand, computerized analyses could be directly applied to the signals recorded by the stations, without the prior processing that was required for analog data. The 1990s and 2000s witnessed an increase in the number of broadband stations globally, with sensors installed in places that are hard to access and maintain (the Antarctic, remote islands, etc.), which improved global coverage. Today, although the distribution of sensors is uneven on the continents, the chief limitation is the absence of permanent underwater sensors at large distances from the coasts.

Improved telecommunications and data centers have also facilitated the rapid and effective analysis of large volumes of seismic data. Today, continuous signals from most global stations are accessible in real time. Data queries corresponding to thousands of earthquakes or to high-frequency time series over a long duration have become standard. Finally, as the global network evolved, free access to the data has generally continued.

1.2.1. *Observations on a global scale*

1.2.1.1. *Seismic networks*

In many types of analysis of global seismicity, there is no purpose in creating multiple observation points that are close to one another. One reason is that the seismic signal generally varies very little when the source is distant, leading to redundant information. Further, this densification of observation is always local, as the density of stations in other azimuths remains lower. This is why several networks

are only made up of high-quality stations (very broadband, if possible in sites with very little background noise, such as tunnels, wells, seismic caves, and so on), prioritizing homogeneous coverage around the world. This has always been the goal of the Geoscope network [GEO 82] from the time of its creation in the early 1980s. Today, this network has 33 stations accessible in real time. The GSN network (Global Seismic Network, [GSN 86]), which succeeded the WWSSN, is currently the chief contributor to this global observation, with about 150 accessible stations. Finally, other global networks advantageously complement terrestrial coverage, such as the Geofon network [GEO 93]. From the late 1980s, these networks were federated within the FDSN (International Federation of Digital Seismograph Networks [ROM 86]). Figure 1.1 shows the map of the reference stations in this federation. The advantage of this super network, which only gives access to a subset of available global stations, is that it provides stations with the most homogeneous density possible, and a quality that is as good as local configurations allow.

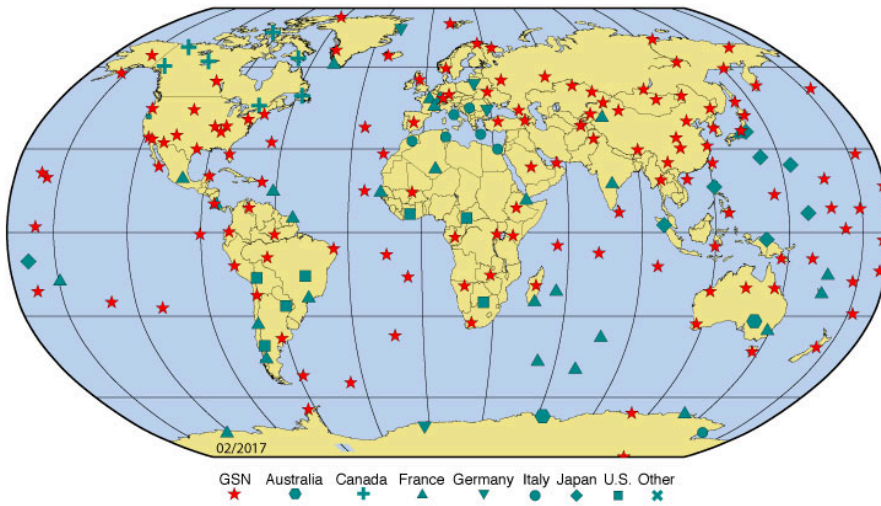

Figure 1.1. *Map of stations that make up the backbone of the FDSN (International Federation of Digital Seismograph Networks). For a color version of this figure, see www.iste.co.uk/rolandone/seismic.zip*

1.2.1.2. *Interpretation of recorded data*

Figure 1.2 illustrates the typical signals recorded on the three components of a broadband seismometer following a large, shallow earthquake observed at a teleseismic distance (between 3,000 and 10,000 km from the source). In this specific case, the figure shows the ground displacement recorded at the Geoscope SSB station (France) in the hour following the occurrence of the Pedernales earthquake (Ecuador, April 16, 2016, magnitude 7.8). Since the birth of seismology, these kinds of data

have been essential for advances in the knowledge of the Earth structure, as well as in the characterization of the seismic source. A quantitative modeling of these data requires the concepts explored in section 1.3, but an initial qualitative interpretation is given below.

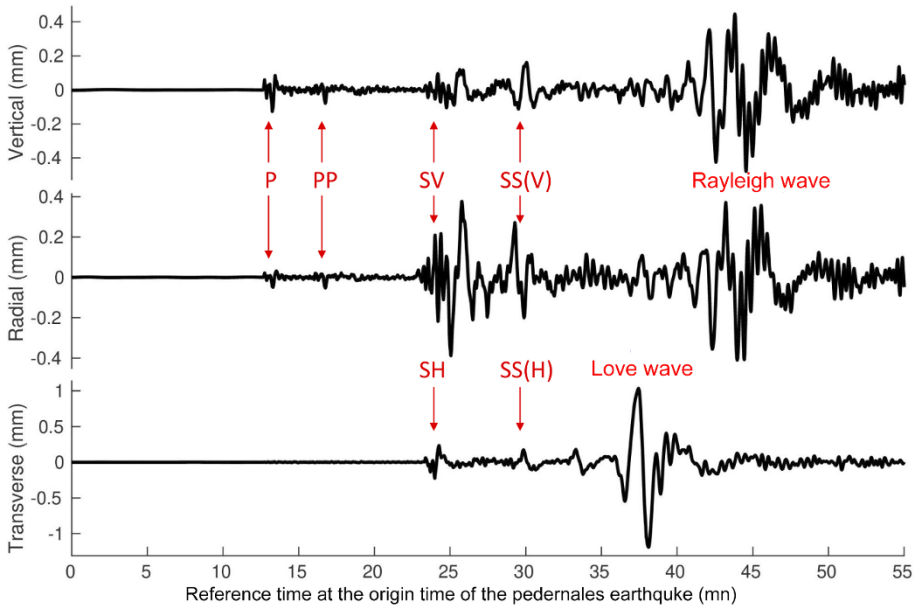

Figure 1.2. *Ground displacement following the Pedernales earthquake (Ecuador, 16 April 2016, magnitude 7.8) observed in France at the SSB station from the Geoscope network (distance along the Earth's surface of around 9500 km, corresponding to an epicentral distance, Δ, of 85.9°). For a visualization of the geometry of the observation, as well as for a discussion of the waves shown in this figure, the reader is invited to consult the text and also Figure 1.3. The displacements were obtained after correcting the instrumental response and after the destructive filtration of periods over 300 s long. The seismogram on top represents the vertical component, while the two horizontal components are depicted with respect to the earthquake-station geometry: at the bottom, the transverse component (direction orthogonal to the plane defined by the earthquake, the station and the center of the Earth); in the middle, the radial component (direction orthogonal to the plane defined by the vertical and transverse directions). This classic convention in seismology results in us seeing the waves polarized in the direction of arrival (P, PP) and the Rayleigh surface wave only on the vertical and radial components. The Love surface wave is only recorded on the transverse component. The S and SS waves, which are polarized in the plane orthogonal to the direction of arrival, are visible on the transverse component (SH wave) and on the vertical and radial components (SV wave)*

In an elastic, homogeneous medium, two types of body waves are predominant in the far field with respect to the source: a P pressure wave, and an S shear wave. This far field approximation can be made when the distance between the source and the point of observation is much greater than the wavelengths. The P wave, which is faster than the S wave, is polarized in the direction of its path. It is thus visible, as the first arrival, on the vertical and radial components in Figure 1.2. The path of the P wave, schematized in Figure 1.3, obeys the Fermat principle, which states that waves follow a path that takes either the shortest or longest time to travel (here the minimum time). Since the wave velocity increases with depth in the Earth, the seismic ray follows a curved path that leads to an incidence close to the vertical of the station. This explains why the amplitude of the P wave is greatest on the vertical component. The S wave is polarized in the plane orthogonal to the direction of its path (which is itself similar to the path taken by the P wave, since the velocities of the P and S waves vary approximately proportionally). The S wave is, therefore, visible on the three components of displacement in Figure 1.2. The projection of the S wave, denoted by SV, in the vertical–radial plane, has a greater amplitude on the radial component, and the component of the S wave in the transverse direction (denoted by SH) is the first wave arrival visible in this direction. The fact that these simple considerations correspond well with Figure 1.2 shows that the variations in seismic velocities essentially occur as a function of depth. In a different case of a medium with high lateral variations, seismograms are less easy to interpret and the P wave may also become visible on the transverse component.

During the 20th century, the progressive accumulation of measurements of arrival times of the P and S waves made it possible to determine the velocity of seismic waves in the Earth. These velocity models were optimized by requiring that each earthquake generates waves whose arrival times are compatible with those observed, which led to refinement both in the location of earthquakes and in the knowledge of the structure. The use of conventional structure models like PREM [DZI 81a] or IASP91 [KEN 95] today makes it possible to predict the arrival of the P wave with an uncertainty of a few seconds at most. For example, in the case of the Pedernales earthquake, observed at the SSB station (see Figure 1.2), the IASP91 model predicts a travel time of $12\ \mathrm{min}$ $38\ \mathrm{s}$ for the P wave and a travel time of $23\ \mathrm{min}\ 11\ \mathrm{s}$ for the S wave. For any earthquake recorded at a teleseismic distance, it is thus easy to extract the time windows of the P and S waves for later analyses (see section 1.4).

The existence of interfaces in the Earth (at the surface, between the crust and mantle, between the mantle and core, between the outer core and inner core, etc.) generates additional complexities in the wave field due to reflection and conversion of waves between P and SV waves. The effects arising from the core are particularly noticeable when we go beyond conventional teleseismic distances ($\Delta > 90°$). In this case, the core–mantle interface causes the disappearance of direct P and S waves (as can be deduced from Figure 1.3). In the conventional teleseismic range, most waves

(other than the P or S waves) visible in Figure 1.2 are a result of the highly contrasting seismic velocity (and density) across the Earth's surface.

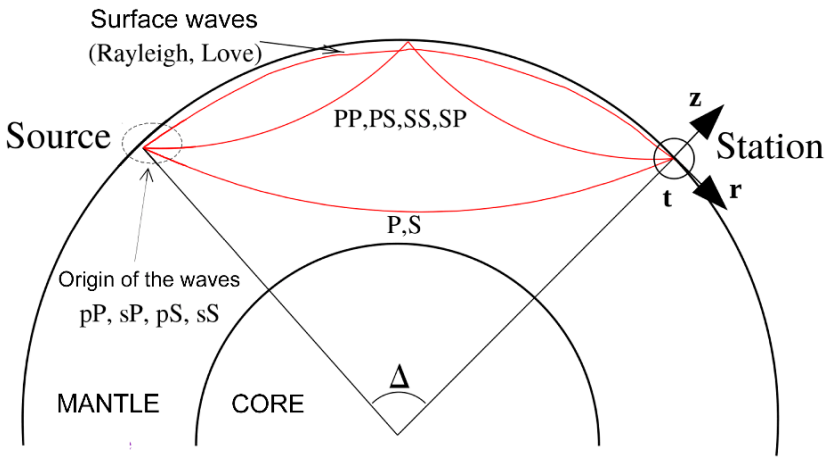

Figure 1.3. *Diagram showing the main waves recorded at a teleseismic distance in the case of a shallow source: the direct P and S waves, waves reflected off the free surface (only unique reflections are represented), and surface waves. The pP, sP, pS and sS waves are generated by wave interaction with the Earth's surface above the source (in the area indicated by the ellipse in dashed lines) and then follow approximately the same path as the P and S waves. To make the figure clear, the waves reflected off the core-mantle interface, or transmitted within the core, are not represented. The source-station distance is parameterized by the angle at the centre of the Earth, Δ (called epicentral distance). The vertical direction (z), radial direction (r) and transverse direction (t), in which the seismograms are represented in Figures 1.2 and 1.4, are also indicated*

Three important types of waves owe their existence to the Earth's surface discontinuity:

– waves reflected (PP and SP waves) or converted (PS, SP) on the Earth's surface halfway between the source and the station (see Figure 1.3). Multiple reflections (PPP, SSS, and so on) may also be visible, but in the case in Figure 1.2, only PP and SS waves are clearly identifiable;

– surface waves (Rayleigh waves on the radial and vertical components, Love waves on the transverse component). For a superficial earthquake like the Pedernales earthquake, the surface waves are the dominant signal on the displacement seismogram (at the SSB station, the Love waves attain a peak to peak amplitude of 2 mm);

– the waves that are reflected or converted on the Earth's surface above the earthquake (pP, sP, pS, sS waves), also called the depth phases. For a superficial earthquake, these waves arrive a few seconds after the direct P or S wave and cannot be individualized; with amplitude comparable to the direct P or S waves, they add to the complexity of the wave train following these direct waves. Similarly, the depth phases of the reflected waves (pPP, sPP, pSS, sSS) complexify the wave train following the PP and SS waves.

All of these waves carry information, in different and complementary ways, on the seismic source that generated them. Nonetheless, not all of these waves can be modeled with the same precision and an accurate analysis of earthquakes at teleseismic distances is based heavily on waves whose propagation can be modeled up to high frequencies. This is why direct P and S waves have been, and continue to be, the most widely used waves for analyzing a distant source.

1.2.2. *Data recorded at the regional and local scales*

Seismograms have a different appearance at local and regional distances. There are two main reasons for this. First of all, the small distance between the source and station tends to reduce the temporal gap between the different body waves, and between the body waves and surface waves. As seen in the seismogram (see Figure 1.4) recorded close to the Le Teil earthquake (Ardèche, France, November 11, 2019, magnitude 4.9), the S waves and surface waves overlap and it may be difficult to identify the arrival of the S wave on the vertical and radial components. More fundamentally, the wave field recorded close to an earthquake (even in a homogeneous medium) is not made up of only body and surface waves. Contributions said to be near field and intermediate field terms, all the more significant if analyzing long-period seismograms, take part in the wave field. These additional terms emphasize the fact that a local seismogram, unlike a teleseismic seismogram, has poorly individualized wave trains. Finally, these terms complicate the wave field: for example, the transverse component displays a non-zero signal before the arrival of the S wave, as can be seen in Figure 1.4.

It is therefore difficult, at a local distance, to study the source effects by selecting time-windows inside the seismogram, especially if the earthquake has a long duration. Consequently, it is more natural to model the complete wave field, restricting ourselves to periods for which the modeling is reliable (see section 1.4.3).

1.3. Modeling elastic waves generated by an earthquake

Preamble: This section aims to provide key elements for the modeling of elastic waves generated by an earthquake. However, it does not go into theoretical basics and does not explore certain details. There are specialized books in this field ([SHE 19, LAY 95, AKI 02]), to which we sometimes refer, and these allow a more fundamental understanding of the concepts introduced here.

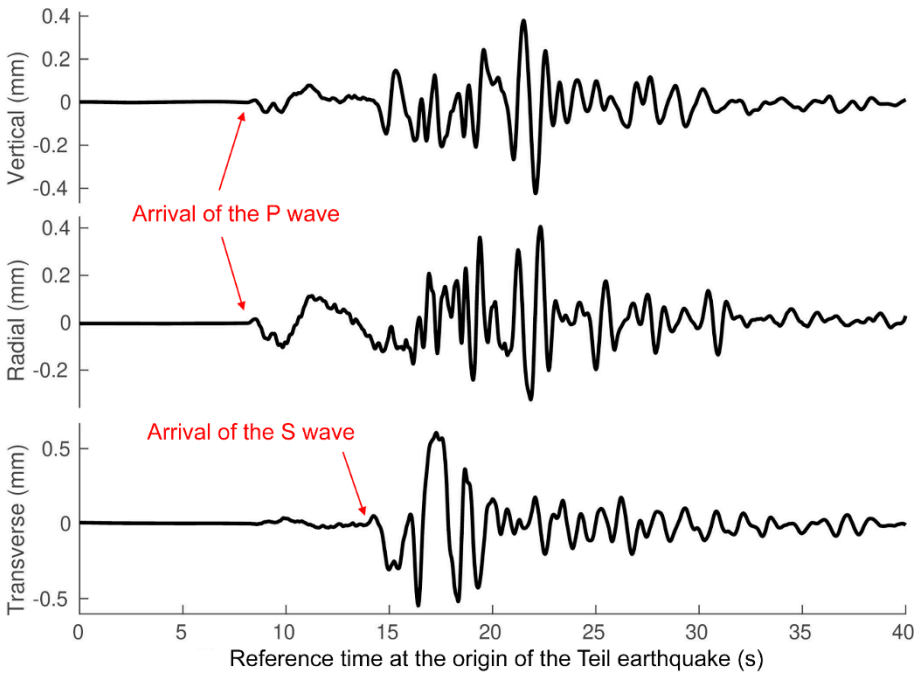

Figure 1.4. *Ground displacement observed, following the 2019 Le Teil earthquake (Ardèche, France, November 11, 2019, magnitude 5), at the BANN station of the RESIF-RLBP network (at a distance of about 42 km). The displacements were obtained after correction of the instrumental response and after the destructive filtering of periods longer than 100* s. *As in Figure 1.2, the seismograms are represented along the vertical, radial and transverse directions*

1.3.1. *Simplified representations of the seismic source*

1.3.1.1. *Point source representation*

Consider, first of all, the general case of a displacement generated by a seismic source, produced on or across a surface, S. We first introduce $\mathcal{G}_{ij}(\boldsymbol{x}, \boldsymbol{\xi}, \omega)$, called the Green's tensor, which expresses the spectral displacement generated at $\boldsymbol{x}$, in the direction i, by a unit force applied on $\boldsymbol{\xi}$, in the direction j. We also introduce $m_{jl}(\boldsymbol{\xi}, \omega)$, which is the (symmetric) tensor of seismic moment density. This source term represents the amplitude of the couples of surface forces in the direction $\pm j$, with arms along l, generated by the earthquake (it can be noted that the term "moment" is not really appropriate for the dipole terms corresponding to $j = l$). $m_{jl}(\boldsymbol{\xi}, \omega)$ thus characterizes the focal mechanism of the seismic source. The

representation theorem (equation [3.20] in [AKI 02]) teaches us that the spectral displacement, U_i, observed at $\boldsymbol{x}$, is written as:

$$U_i(\boldsymbol{x},\omega) = \int_S m_{jl}(\boldsymbol{\xi},\omega)\, \mathcal{G}_{ij,l}(\boldsymbol{x},\boldsymbol{\xi},\omega)\, d\boldsymbol{S}(\boldsymbol{\xi}) \qquad [1.1]$$

with the usual notations, given below, which we will retain for the rest of the text:

– the spatial indices, present on the right-hand side, but absent on the left-hand side (here j, l), imply the sum over the possible values of these indices (here $j = 1, 2, 3$ and $l = 1, 2, 3$);

– the notation $_{,l}$ expresses the partial derivative $\frac{\partial}{\partial \xi_l}$;

– the vector and matrix variables are written in bold.

It is further assumed that the propagation term $\mathcal{G}_{ij,l}$ has little spatial variation in the source region, which may be represented by a point $\boldsymbol{\xi^0}$ (point source model). This approximation is typically valid when the observation distance is large with respect to the size of the source, and when we are not examining very high frequencies. It is then possible to write:

$$\begin{aligned} U_i(\boldsymbol{x},\omega) &= \left(\int_S m_{jl}(\boldsymbol{\xi},\omega)\, d\boldsymbol{S}(\boldsymbol{\xi}) \right) \mathcal{G}_{ij,l}(\boldsymbol{x},\boldsymbol{\xi^0},\omega) \\ &\equiv M_{jl}(\omega)\, \mathcal{G}_{ij,l}(\boldsymbol{x},\boldsymbol{\xi^0},\omega) \end{aligned} \qquad [1.2]$$

M_{jl}, the integral over the surface of m_{jl}, is the seismic moment tensor, and thus has the same symmetry properties as m_{jl}. In theory, each of its components has a different frequency dependency, but in the case of a synchronous source mechanism:

$$U_i(\boldsymbol{x},\omega) = M(\omega)\, \mathcal{M}_{jl}\, \mathcal{G}_{ij,l}(\boldsymbol{x},\boldsymbol{\xi^0},\omega) \qquad [1.3]$$

where $\mathcal{M}_{jl}$ is the dimensionless tensor of static moment, which is also symmetric, while M describes the spectrum of the temporal function of seismic moment. It is also common to express [1.3] using the absolute source time function F, which is defined as the time derivative of the function M:

$$U_i(\boldsymbol{x},\omega) = F(\omega)\, \mathcal{M}_{jl}\, \frac{\mathcal{G}_{ij,l}(\boldsymbol{x},\boldsymbol{\xi^0},\omega)}{i\omega} \qquad [1.4]$$

If we assume that the final moment M_0 is reached instantaneously (a valid approximation for very low frequencies), the point source radiation is simply written as:

$$U_i(\boldsymbol{x},\omega) = M_0\, \mathcal{M}_{jl}\, \frac{\mathcal{G}_{ij,l}(\boldsymbol{x},\boldsymbol{\xi^0},\omega)}{i\omega} \qquad [1.5]$$

In this simple but general model, assuming that the Green's function is known, the ground displacement is therefore completely governed by nine parameters: the position of the source $\boldsymbol{\xi^0}$, the earthquake size controlled by M_0 and its mechanism $\mathcal{M}_{jl}$.

1.3.1.2. *Specific case of slip on a fault*

We will now consider that the moment density m_{jl} describes a slip on a fault plane. The slip is represented by the vector $\boldsymbol{u}$ and the normal to the fault plane is represented by the vector $\boldsymbol{\nu}$. Using the laws of elasticity [AKI 02], it can then be shown that:

$$m_{jl}(\boldsymbol{\xi},\omega) = \mu\,(u_j(\boldsymbol{\xi},\omega)\nu_l + u_l(\boldsymbol{\xi},\omega)\nu_j) \qquad [1.6]$$

where μ is the rigidity of the medium, which is assumed here to be constant in the source region. In order to simplify things, it is convenient to represent the displacement on the fault in an orthogonal basis $(\boldsymbol{e'_1}, \boldsymbol{e'_2}, \boldsymbol{e'_3})$, in which $\boldsymbol{\nu}$ is in the direction of $\boldsymbol{e'_3}$ and $\boldsymbol{u}$ is assumed to be constant in the direction of $\boldsymbol{e'_1}$. Thus:

$$\boldsymbol{m}(\boldsymbol{\xi},\omega) = \begin{pmatrix} 0 & 0 & \mu\, u_1(\boldsymbol{\xi},\omega) \\ 0 & 0 & 0 \\ \mu\, u_1(\boldsymbol{\xi},\omega) & 0 & 0 \end{pmatrix} \qquad [1.7]$$

The term m_{13} has an intuitive interpretation in the sense that a slip along $\boldsymbol{e'_1}$ creates a force couple directed along $\pm\boldsymbol{e'_1}$ with one arm along $\boldsymbol{e'_3}$. The term m_{31} may be understood by the fact that in its absence, m_{13} would induce a non-physical rotation of the source medium. These two terms make up the double couple of forces equivalent to the slip in a constant direction on a fault plane. A slip along a direction j over a fault with normal l, or a slip along a direction l over a fault with normal j therefore generate the same form of the tensor $\boldsymbol{m}$. For a point source model (equation [1.2]), this leads to a complete ambiguity between the former and the latter mechanisms.

With $\bar{u}_1(\omega)$ denoting the slip $u_1(\boldsymbol{\xi},\omega)$ averaged over a surface, S_0, equal or larger than the one affected by the earthquake, the point source representation [1.2] gives:

$$\boldsymbol{M}(\omega) = \mu\, S_0\, \bar{u}_1(\omega) \begin{pmatrix} 0 & 0 & 1 \\ 0 & 0 & 0 \\ 1 & 0 & 0 \end{pmatrix} = M(\omega)\boldsymbol{\mathcal{M}} \qquad [1.8]$$

which makes it possible to identify the spectrum of the seismic moment M, independent of the chosen basis, and the final (static) moment M_0:

$$\begin{cases} M(\omega) = \mu\, S_0\, \bar{u}_1(\omega) \\ M_0 = \mu\, S_0\, U_0 \end{cases} \qquad [1.9]$$

with U_0 being the final slip averaged over the surface of the fault S_0. Since it carries information on the surface-slip product, M_0 is a very good indicator of the size of an earthquake. Approaches using point source models at low frequency have the advantage of offering direct access to M_0 through equation [1.5]. The relevance and ease of access to this parameter [AKI 66] led to it being used to define an associated magnitude scale: the moment magnitude M_w, which is the magnitude that is most physically associated with the size of an earthquake, was defined by $M_w = 2/3(log10(M_0) - 9.1)$ [HAN 79].

$\boldsymbol{\mathcal{M}}$ may also be expressed in an orthogonal basis of eigenvectors, where the tensor is diagonal (which is always possible, since $\boldsymbol{\mathcal{M}}$ is symmetric). For example, in the basis $((\boldsymbol{e'_1} + \boldsymbol{e'_3})/\sqrt{2}, \boldsymbol{e'_2}, (\boldsymbol{e'_3} - \boldsymbol{e'_1})/\sqrt{2})$:

$$\boldsymbol{\mathcal{M}} = \begin{pmatrix} 1 & 0 & 0 \\ 0 & 0 & 0 \\ 0 & 0 & -1 \end{pmatrix} \qquad [1.10]$$

A slip in a constant direction over a fault plane may thus be represented equivalently by a double couple [1.8] or by two dipoles of orthogonal forces with opposite values. The T-axis is defined as being the direction of the eigenvector corresponding to the positive eigenvalue. Consequently, the T-axis characterizes the direction in space, in the source region, in which the shear deformation is zero and the dilatation is maximum. Similarly, the P-axis (not to be confused with the P wave), defined as the direction of the eigenvector corresponding to the negative eigenvalue, characterizes the direction in space in which the compression is maximal. The N-axis defines the direction of the eigenvector corresponding to the zero eigenvalue. These properties imply that P-wave radiation has maximum amplitude for seismic rays that leave the source in the direction of the P and T axes. When a sufficient number of seismic rays can be observed using seismometers, the amplitude and polarity of the observed P waves then make it possible to constrain the P, T and N axes, and therefore, $\boldsymbol{\mathcal{M}}$. It is interesting to note that a positive polarity in the direction of the ray (hence, in the up direction when recorded by a seismic station) is often referred to as compressive. While it is accurate that the medium around the station is compressed by such a P wave, this wave has nonetheless followed a ray that left the source in the vicinity of its T-axis with maximum dilatation. The concept of compression or dilatation thus requires us to define whether the source medium or receiver medium is being taken as reference.

A double couple moment tensor $\boldsymbol{\mathcal{M}}$, representing the slip over a fault, is completely characterized using three parameters. The conventional three parameters are the fault azimuth ϕ_s, its dip angle d and the slip angle λ (see Figure 1.5). Using this description, we make a direct relationship between the slip over a fault, as geologically observed, and $\boldsymbol{\mathcal{M}}$. ϕ_s is conventionally described clockwise with

respect to north, and d with respect to the horizontal ($d = 90°$ for a vertical fault). λ is the angle, measured in the anti-clockwise direction, of the slip vector with respect to the direction defined by ϕ_s (with the slip vector characterizing the motion of the "upper" block with respect of the "lower" block). The terms "strike, dip, rake" are often used for ϕ_s, d and λ, respectively. In any basis, the components $\mathcal{M}_{jl}$ can be expressed through trigonometric functions of ϕ_s, d and λ. In the Cartesian basis $(\boldsymbol{e_1}, \boldsymbol{e_2}, \boldsymbol{e_3})$ (with $\boldsymbol{e_1}$, $\boldsymbol{e_2}$, $\boldsymbol{e_3}$ directed in the directions north, east and vertical downward, respectively), which will be used in the rest of this text, the expression for the $\mathcal{M}_{jl}$ is given in [AKI 02, p. 12].

For any moment tensor, the analysis of its characteristics makes it possible to evaluate how well it conforms with a slip over a fault. If the trace is non-zero, at least part of the process is incompatible with a fault slip, as it involves mechanisms with volume changes (e.g. an explosion or a change in mineralogical phase). If the trace is zero, but all the eigenvalues are non-zero, the process is not compatible with a slip mechanism keeping a constant slip direction. But such a tensor may result from a combination of two double couple mechanisms with different orientations.

1.3.1.3. *Extended source and line source representations*

It is considered here that the moment tensor $\mathcal{M}_{jl}$ describes a slip in a constant direction over a fault plane, and that the earthquake process is initiated at the hypocenter, denoted by $\boldsymbol{\xi}^h$ (see Figure 1.5). Since any point on the fault is activated after the initial rupture at $\boldsymbol{\xi}^h$, the tensor of seismic moment density can be expressed as:

$$m_{jl}(\boldsymbol{\xi}, \omega) = \mu \, \mathcal{M}_{jl} \, \Delta u(\boldsymbol{\xi}, \omega) \, e^{-i\omega t_r(\boldsymbol{\xi})} \qquad [1.11]$$

Δu here describes the slip on the fault at the point $\boldsymbol{\xi}$, starting from the instant when the rupture front originating from the hypocenter $\boldsymbol{\xi}^h$ has reached this point. This shift in rupture time, with respect to the initiation time at the hypocenter, is given by the function t_r (t_r is therefore a positive function). The observed displacement is thus written using equation [1.1]:

$$U_i(\boldsymbol{x}, \omega) = \mu \int_S \mathcal{M}_{jl} \, \mathcal{G}_{ij,l}(\boldsymbol{x}, \boldsymbol{\xi}, \omega) \, \Delta u(\boldsymbol{\xi}, \omega) e^{-i\omega t_r(\boldsymbol{\xi})} \, d\boldsymbol{S}(\boldsymbol{\xi}) \qquad [1.12]$$

Equation [1.12] can be used in an optimization problem to retrieve the two-dimensional slip over the fault (see Chapter 2). In the case where one of the dimensions of the rupture over the fault is predominant, this equation can be simplified in a line source modeling framework. If the rupture in one direction has a length, L, that is much greater than the rupture in the orthogonal direction W (see Figure 1.5), which is often the case with large earthquakes, we have:

$$U_i(\boldsymbol{x}, \omega) = \mu \, W \int_L \mathcal{M}_{jl} \, \mathcal{G}_{ij,l}(\boldsymbol{x}, \boldsymbol{\xi}, \omega) \, \Delta u(\boldsymbol{\xi}, \omega) e^{-i\omega t_r(\boldsymbol{\xi})} \, d\ell(\boldsymbol{\xi}) \qquad [1.13]$$

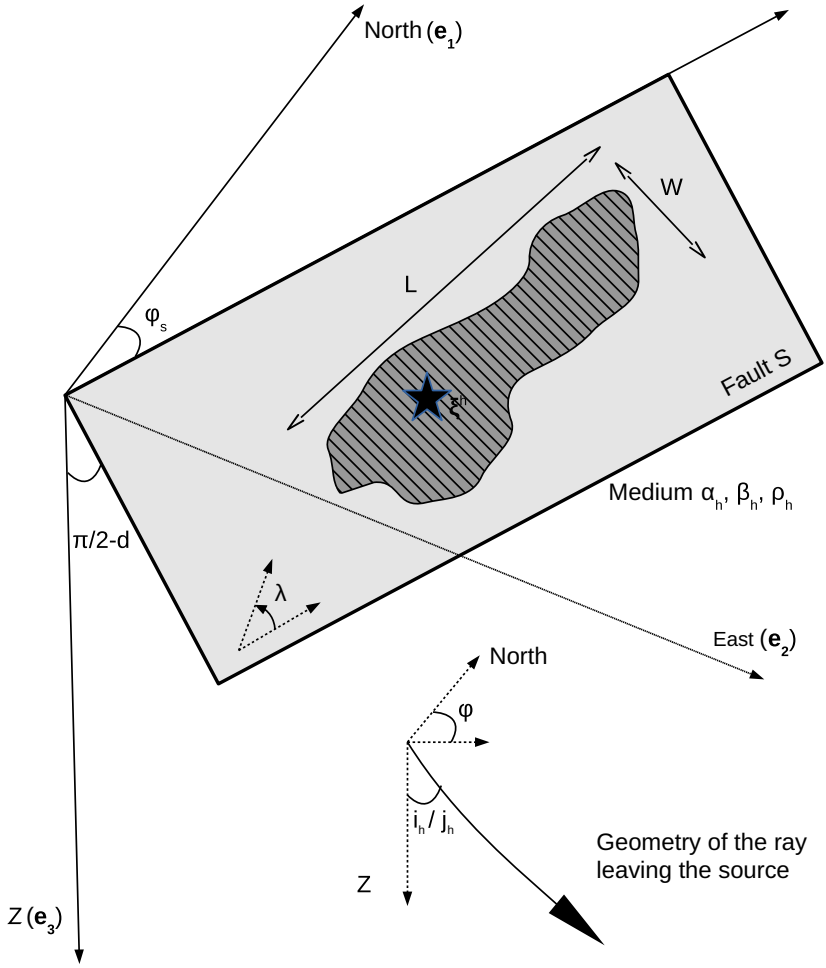

Figure 1.5. *Geometry of the rupture and of the direction of observation when using teleseismic body waves. The azimuth, ϕ_s and dip angle, d, of the fault, S, define its geometry. The slip angle λ describes how the upper block slips with respect to the lower block: the configuration represented here thus corresponds to an oblique reverse-sinistral mechanism. The earthquake is characterized by its hypocenter $\boldsymbol{\xi}^h$ and its final rupture zone is illustrated by the striped, shaded zone of characteristic dimensions $L \times W$. This earthquake is observed by a station in the azimuth ϕ (generally different from ϕ_s). The take-off angle at the source, i_h for P-waves or j_h for S-waves, is governed by the ray parameter and the wave velocities in the source region. Equations in 1.3.2 consider α_h, β_h, ρ_h as constants for the entire extent of the source and between the source and the surface, which leads to a constant i_h and j_h for P and S waves, respectively. However, this simple configuration can be adapted to a medium where α, β and ρ only depend on depth (reflectivity method; [KEN 74, MÜL 85])*

1.3.2. *Modeling body waves in the far field and at large distances: application to seismic ruptures with horizontal propagation*

This section first aims to describe the main characteristics of teleseismic P and S waves in a medium with spherical symmetry. The reflected depth phases (pP, sP, sS, pS) will be included, as they are essential for modeling the wave field of a shallow source. Indeed, as depicted in Figure 1.2, while it is often possible to isolate the P and S waves from some other phases (PP, SS, surface waves, etc.) of a seismogram, depth phases interfere with the direct arrivals. The results presented in this section are based on the properties of seismic radiation in a homogeneous medium, coupled with the reflection–transmission effects occurring at the interfaces (for plane waves), and including the intuitive concepts arising from ray theory (see Chapters 3 and 5 in [SHE 19] for the main concepts of ray theory). A more detailed review of the radiation of teleseismic body waves can be found in [OKA 92]. In the following paragraphs, we will specifically study the models of horizontal rupture propagation, which allow the source terms and propagation terms to be decoupled.

Let us consider a teleseismic P ray (see Figure 1.3) whose geometry is defined by its slowness vector $\boldsymbol{s}^P$. The modulus of this vector is the inverse of the P wave velocity, α, and its direction indicates the local direction of the ray from the source toward the station. In its propagation plane, this ray makes an angle, i, locally, with the direction of the center of the Earth. The Snell–Descartes law imposes that $p = r \sin i/\alpha$, with r being the distance to the center of the Earth, is a constant, called the "ray parameter". For a point $\boldsymbol{\xi}$ in the source region, r has very little variation, which implies that the horizontal slowness vector $\boldsymbol{s}_H^P$, with modulus $\sin i/\alpha$, is conserved. In theory, the pP wave (emitted as a P wave upwards and then reflected as a P wave by the surface) and the sP wave (emitted as an S wave upwards and then converted into a P wave by the surface) do not have exactly the same ray parameter as the P wave. Nonetheless, for a shallow source, the majority of the path is traveled in a similar manner, and the ray parameters can be considered to be the same. This imposes that these rays also share the same $\boldsymbol{s}_H^P$ in the source region. Thus, the pP ray leaves the source in the direction $(\pi - i)$ and the sP ray leaves in the direction $(\pi - j)$. The angle, j, verifies the Snell–Descartes law of conversion, that is, $j = \sin^{-1}(\beta \sin i/\alpha)$, with β being the S wave velocity. Even in the more general case of a horizontally stratified medium, all reflected or converted waves in the source region are only distinguished by the vertical component of the slowness vector ($\pm \cos i/\alpha$ for the parts of the path traveled as a P wave, and $\pm \cos j/\beta$ for the parts of the path traveled as an S wave).

For a given path originating from a source at a certain depth and recorded at an epicentral distance Δ, the ray parameter, p, is well known as it is simply related to the travel time T through the relation $p = dT/d\Delta$. At teleseismic distances, p is weakly dependent on Δ and on the depth of the source. This makes it possible to consider p as a constant for all emission points $\boldsymbol{\xi}$ of the source. In practice, i and j may still be affected by uncertainties, because α and β must be known in order to determine

them. In the following section, we will consider that α and β, as well as the density ρ, are known and constant in the source region (equal to α_h, β_h and ρ_h), as well as under the receiver (equal to α_0, β_0 and ρ_0). The take-off angles, i_h, j_h (see Figure 1.5), and incidence angles below the receiver, i_0, j_0, are thus uniquely determined. Nevertheless, using reflectivity methods [KEN 74, MÜL 85], it is possible to consider a more general case of a medium that is stratified at the source and receiver. In this case, the generated wave field does not only contain the P, pP and sP phases, but also phases corresponding to more complex paths. This approach is, however, only a refinement of what is described above, as these three waves remain the strongest and most reliable phases to analyze.

We thus consider the three waves, P, pP and sP, with the same ray parameter p, recorded in the vertical direction, defined by the unit vector $\boldsymbol{z}$. For a double couple source at $\boldsymbol{\xi}$, the far field radiation terms in equation [1.12] for the P, pP, sP waves denoted by the indices $k = 1, 2, 3$, respectively, are written as:

$$(z_i\ \mathcal{M}_{jl}\ \mathcal{G}_{ij,l}(\boldsymbol{x}, \boldsymbol{\xi}, \omega))^{(k)} = i\omega\ \mathcal{F}^{(k)}(\boldsymbol{\mathcal{M}}, p, \phi)\ R^{(k)}(p)\ B(p, \Delta, \omega)\ e^{-i\omega T^{(k)}(\boldsymbol{x}, \boldsymbol{\xi})} \quad [1.14]$$

where Δ and ϕ are the epicentral distance and the azimuth of the observation point $\boldsymbol{x}$, which are considered to be constant for any point $\boldsymbol{\xi}$ belonging to the source. The term $i\omega$ expresses the fact that a double couple radiation induces a time derivative. $\mathcal{F}^{(k)}$ describes the radiation pattern of the P, pP and sP waves and may be expressed in terms of ϕ_s, d, λ, ϕ and of the ray's take-off angle at the source, with respect to the downward direction (equation [4.89] in [AKI 02]). We must be careful, here, to evaluate $\mathcal{F}^{(1)}$ in the direction i_h, $\mathcal{F}^{(2)}$ in the direction $(\pi - i_h)$ and $\mathcal{F}^{(3)}$ in the direction $(\pi - j_h)$.

$R^{(k)}$ captures the propagation effect in the source region. As may be deduced intuitively, we have $R^{(1)} = 1$ and $R^{(2)} = R^{PP}$, with R^{PP} being the reflection coefficient on the surface for an incident P wave in the direction i_h. The term $R^{(3)}$ requires more attention as it does not only take into account R^{SP}, the reflection-conversion coefficient (in displacement) for an S incident wave, in the direction j_h. Indeed, it can be shown [OKA 92, LAN 75, KAN 76] that $R^{(3)} = R^{SP}\alpha_h^2 \cos i_h / (\beta_h^2 \cos j_h)$, the additional factors coming in because the original wave is an S wave, and it does not have the same geometric expansion [PEA 80]. $R^{(3)}$ is also naturally taken into account by the approach that uses the reciprocity of the wave field described by Bouchon [BOU 76].

$T^{(k)}$ is the travel time for each wave under consideration, which is known with a precision better than a few seconds when using the global velocity models [DZI 81a, KEN 91, KEN 95]. This precision may even be improved by the use of three-dimensional models of the Earth [SIM 12]. Finally, B represents the

propagation effects, common to all three waves, from the source region to the station. This term takes the form:

$$B(p, \Delta, \omega) = \frac{1}{4\pi\rho_h\alpha_h^3} \frac{g(p, \Delta)}{r_0} A(\omega)\, C(p) \qquad [1.15]$$

The first factor is related to the radiation of a double couple for a P wave. The factor $g(p, \Delta)/r_0$ (with r_0 being the radius of the Earth) is the geometric expansion term (equal to the inverse of the distance between the source and the receiver in a homogeneous medium). The expression for g is given in many books ([LAY 95]; equation [4] in [OKA 92], along with the associated derivation). $A(\omega)$ is the attenuation term (not to be confused with the geometric expansion) due to anelasticity or due to the diffraction during propagation. For teleseismic body waves, this attenuation is classically parameterized by a single parameter t^* (see Chapter 6.6 in [SHE 19] for details). However, certain paths in the mantle are known to be more attenuating than others. This attenuation variability is one of the principal reasons for uncertainty in modeling high frequencies (> 1Hz). Finally, C takes into account the effect of the free surface and projects the displacement onto the vertical direction. It can thus be noted that the observed P wave is never a pure P wave, as it is affected by the P-S conversion on the free surface.

Using [1.14] and [1.15], direct teleseismic waves and their depth phases can be easily modeled and with higher accuracy than the other waves visible in a distant seismogram. This characteristic is due to the fact that the majority of the path traveled by the direct teleseismic waves is in the Earth's lower mantle (see Figure 1.3), which is relatively homogeneous. On the contrary, body waves that undergo multiple reflections, and even more surface waves, strongly interact with the Earth's superficial structure. This superficial structure, where there are strong gradients of seismic velocity, causes complexities in the wave field (especially "triplications", see section 4.3 in [SHE 19]). Furthermore, the most superficial layers have high lateral variability in their elastic parameters, and modeling of surface waves, even at low frequencies (down to $\simeq 0.01$Hz), therefore requires a three-dimensional computation of the wave field.

We now consider a horizontal rupture propagation, starting from the hypocentral point $\boldsymbol{\xi}^h$ (this rupture direction hypothesis is not required for a deep earthquake, as the direct P wave can be analyzed alone, without any interference from depth phases). The case of a point source, with no explicit propagation of the rupture, is also included in this configuration. This horizontal propagation model may appear restrictive, however it makes it possible to represent a subduction earthquake, whose plane has a shallow dip, by an extended fault [1.12], or a large strike-slip earthquake by a line source

[1.13]. The travel times then do not depend on the vertical slowness (different for the P, pP and sP waves) and are written in an approximation of plane waves:

$$T^{(k)}(\boldsymbol{x},\boldsymbol{\xi}) = T^{(k)}(\boldsymbol{x},\boldsymbol{\xi}^h) - \boldsymbol{s}_H^P.(\boldsymbol{\xi}-\boldsymbol{\xi}^h) \qquad [1.16]$$

At this stage, it is useful to express the following relations in the Cartesian basis $(\boldsymbol{e_1},\boldsymbol{e_2},\boldsymbol{e_3})$ with $\boldsymbol{e_1}$, $\boldsymbol{e_2}$, $\boldsymbol{e_3}$, respectively, in the directions north, east and vertical downward. With the origin of the coordinate system chosen at the earthquake epicenter, the fault then lies in the horizontal plane with equation $\xi_3 = \xi_3^h$. The travel time $T^{(k)}(\boldsymbol{x},\boldsymbol{\xi}^h)$ can be divided into:

$$T^{(k)}(\boldsymbol{x},\boldsymbol{\xi}^h) = T^P(\boldsymbol{x},\boldsymbol{\xi}^h) + \Delta t^{(k)}(p,\xi_3^h) \qquad [1.17]$$

with T^P=$T^{(1)}$ and $\Delta t^{(k)}$ being the differential travel time with respect to the travel time of the direct P wave:

$$\begin{cases} \Delta t^{(1)}(p,\xi_3^h) = 0 \\ \Delta t^{(2)}(p,\xi_3^h) = \frac{2\xi_3^h cos(i_h)}{\alpha_h} \\ \Delta t^{(3)}(p,\xi_3^h) = \xi_3^h \left(\frac{cos(j_h)}{\beta_h} + \frac{cos(i_h)}{\alpha_h}\right) \end{cases} \qquad [1.18]$$

The complete P wave train in the vertical direction, including the phases P,pP and sP, can therefore be written as:

$$\begin{aligned} \sum_{k=1}^{3} \left(z_i\, \mathcal{M}_{jl}\, \mathcal{G}_{ij,l}(\boldsymbol{x},\boldsymbol{\xi},\omega)\right)^{(k)} = {} & i\omega\, B(p,\Delta,\omega)\, e^{i\omega \boldsymbol{s}_H^P.(\boldsymbol{\xi}-\boldsymbol{\xi}^h)}\, e^{-i\omega T^P(\boldsymbol{x},\boldsymbol{\xi}^h)} \\ & \times \sum_{k=1}^{3} \mathcal{F}^{(k)}(\boldsymbol{\mathcal{M}},p,\phi) R^{(k)}(p) e^{-i\omega \Delta t^{(k)}(p,\xi_3^h)} \end{aligned} \qquad [1.19]$$

Inserting [1.19] into [1.12] leads to the expression of the vertical P wave train generated by an extended source on a horizontal plane (a similar form can be found in [BOA 80]):

$$\begin{aligned} U_z^P(\boldsymbol{x},\omega) = {} & B(p,\Delta,\omega)\, e^{-i\omega T^P(\boldsymbol{x},\boldsymbol{\xi}^h)} \\ & \times \left(\sum_{k=1}^{3} \mathcal{F}^{(k)}(\boldsymbol{\mathcal{M}},p,\phi)\, R^{(k)}(p)\, e^{-i\omega \Delta t^{(k)}(p,\xi_3^h)}\right) \\ & \times \mu \int_S \Delta\dot{u}(\boldsymbol{\xi},\omega) e^{i\omega(\boldsymbol{s}_H^P.(\boldsymbol{\xi}-\boldsymbol{\xi}^h) - t_r(\boldsymbol{\xi}))} d\xi_1 d\xi_2 \end{aligned} \qquad [1.20]$$

In the time domain, for an observed P wave displacement corrected from the instrumental response and shifted to the arrival of the P wave (by theoretical or observed picking), [1.20] can be written:

$$U_z^P(\boldsymbol{x}, t + T^P(\boldsymbol{x}, \boldsymbol{\xi}^h)) = G^P_{\phi_s,d,\lambda,\xi_3^h}(t) * F^P(t) \quad [1.21]$$

with $*$ denoting convolution,

$$G^P_{\phi_s,d,\lambda,\xi_3^h}(t) = B(p,\Delta,t) * \left(\sum_{k=1}^{3} \mathcal{F}^{(k)}(\boldsymbol{\mathcal{M}}, p, \phi) R^{(k)}(p) \delta(t - \Delta t^{(k)}(p, \xi_3^h)) \right) \quad [1.22]$$

and

$$F^P(t) = \mu \int_S \Delta\dot{u}(\boldsymbol{\xi}, t + \boldsymbol{s}_H^P.(\boldsymbol{\xi} - \boldsymbol{\xi}^h) - t_r(\boldsymbol{\xi}))\, d\xi_1 d\xi_2 \quad [1.23]$$

$G^P_{\phi_s,d,\lambda,\xi_3^h}$ is the wave train of P waves, shifted by the arrival time P, generated by an instantaneous point source with the mechanism (ϕ, d, λ) at depth ξ_3^h. We always know (even approximately), using location techniques where the P wave has been emitted from, that $G^P_{\phi_s,d,\lambda,\xi_3^h}$ can be computed without any information apart from these four parameters. As shown by [1.22], this term is made up of three impulses, whose relative time shift is governed by the depth at which the earthquake occurs, and whose form will be "enlarged" by the attenuation operator present in B.

F^P is the apparent source time function seen by the P wave. The term "apparent" refers to the fact that F^P is affected by the wave type and the location of the observation point, through the influence of the slowness vector $\boldsymbol{s}_H^P$. We will return to the apparent source time function to learn more about its potential for rupture imaging in section 1.4.

Very similar reasoning can be followed to simulate the SH wave train (relative to the arrival time, T^S, of the S wave) in the transverse direction $\boldsymbol{t}$:

$$U_t^{SH}(\boldsymbol{x}, t + T^S(\boldsymbol{x}, \boldsymbol{\xi}^h) = G^{SH}_{\phi,d,\lambda,\xi_3^h}(t) * F^{SH}(t) \quad [1.24]$$

$G^{SH}_{\phi,d,\lambda,\xi_3^h}$ is the SH wave train, shifted by the arrival time S, generated by a point source with mechanism (ϕ, d, λ) at the depth ξ_3^h. This term includes a single depth phase (the sS wave) since there is no coupling between the P wave and the SH wave in a medium with spherical symmetry. F^{SH}, the apparent source time function seen by the SH wave, is written as:

$$F^{SH}(t) = \mu \int_S \Delta\dot{u}(\boldsymbol{\xi}, t + \boldsymbol{s}_H^S.(\boldsymbol{\xi} - \boldsymbol{\xi}^h) - t_r(\boldsymbol{\xi}))\, d\xi_1 d\xi_2 \quad [1.25]$$

with $\boldsymbol{s}_H^S$ being the horizontal slowness vector of the S and sS waves in the source region. These apparent source time functions are written as follows in a line source model:

$$\begin{cases} F^P(t) = \mu\, W \int_L \Delta\dot{u}(\boldsymbol{\xi}, t + \boldsymbol{s}_H^P.(\boldsymbol{\xi} - \boldsymbol{\xi}^h) - t_r(\boldsymbol{\xi}))\, d\ell(\boldsymbol{\xi}) \\ F^{SH}(t) = \mu\, W \int_L \Delta\dot{u}(\boldsymbol{\xi}, t + \boldsymbol{s}_H^S.(\boldsymbol{\xi} - \boldsymbol{\xi}^h) - t_r(\boldsymbol{\xi}))\, d\ell(\boldsymbol{\xi}) \end{cases} \quad [1.26]$$

Similarly, the wave train of the SV waves in the radial direction $\boldsymbol{r}$ may be written in the form of a convolution between the point source radiation $G^{SV}_{\phi,d,\lambda,\xi_3^h}$ and the apparent source time function F^{SV}. However, $F^{SV} = F^{SH}$, which implies that the SV wave does not bring in any additional information on the source. The SV wave is also practically more difficult to analyze for several reasons: first of all, it arrives following multiply reflected and converted phases of the P wave (unlike the SH wave, which is the first significant wave on the transverse component) and its first motion may consequently be difficult to determine. This phase also has an arrival time that is close to that of other phases with a large amplitude (e.g. the SP phase, or the SKS core phase), which complexifies its analysis. More fundamentally, the SV radiation is affected by additional radiation complexities, both at the source and receiver [LAN 85].

Finally, depending on the applications, the considered earthquakes or the observation distances, it may be necessary to model the teleseismic waves that follow the P wave (on the vertical component) and the SH wave (on the transverse component). An example of this is the $ScS(H)$ wave, which is the SH wave reflected at the core-mantle interface. This phase usually has a large amplitude (due to its complete reflection at the interface) and closely follows the SH wave train for far teleseismic distances (epicentral distances of 60°-90°). The equivalent wave for the P wave (the PcP phase) is less critical, as its relative amplitude is much smaller. In the case of earthquakes with very long source duration, there may also be interference between the P wave and the PP wave, which leads us to model the latter wave. The PP wave can be modeled using a formalism similar to the one discussed earlier, but in addition to the adaptation of the coefficients that depend on the geometry of the rays, the reflection coefficient at the surface and a $\pi/2$ phase-shift (Hilbert transform) have to be taken into account. Before including additional waves, which makes it possible to expand the analyzable section of the seismogram, we must be aware that the precision of their high-frequency modeling is lower, since they have greater interaction with complexities in the terrestrial structure. And because these three-dimensional complexities are also not as well known as the average spherical structure, more accurate methods than the ray theory (used here) may not be able to bring in more reliable information at high frequency.

1.3.3. *Empirical Green's function*

Previous sections show that there are two configurations where the wave field of a superficial earthquake may take the form of a convolution between the point source radiation and a source time function: the general case of the point source (equation 1.4) with an absolute source time function, F, and the case of teleseismic body waves generated by a rupture with small vertical extension, in which the source time function is apparent. Although we have not discussed this here, the radiation of surface waves at a large distance may also be written in this form.

One of the advantages of this convolutive form is that it is sometimes possible to avoid the numerical computation of the radiation generated by a point source. Indeed, the earthquake being studied may be preceded or followed (which frequently occurs, with the aftershocks) by a "small" earthquake that is similar and close by. That is, with mechanism and depth very close to $\boldsymbol{\mathcal{M}}$ and ξ_3^h, and with hypocenter $\boldsymbol{\xi'}^h$ belonging to the source region of the earthquake being studied. In this case, the displacement, u, of the small earthquake of source time function f is written as:

$$u^{(i)}(\boldsymbol{x}, t + T^P(\boldsymbol{x}, \boldsymbol{\xi'}^h)) = G^{(i)}_{\phi_s, d, \lambda, \xi_3^h}(t) * f^{(i)}(t) \qquad [1.27]$$

where the index $^{(i)}$ refers to any wave train for which the convolutive form is applicable. u is called the 'empirical Green's function'[1] [HAR 78], as it directly provides the point source radiation and thus avoids its numerical computation. Relation [1.27] shows that the smaller the earthquake, the more closely u approximates G, a true empirical Green's function being obtained in the ideal case where f is similar to a Dirac delta function. In practice, u provides a smoothened version of G, as periods shorter than the duration of the small earthquake are not faithfully transcribed. Without needing to calculate G, we have access to the apparent source time functions, $F^{(i)}$, of the large earthquake:

$$\begin{aligned} F^{(i)}(t) &= \left(U^{(i)}(\boldsymbol{x}, t + T^{(i)}(\boldsymbol{x}, \boldsymbol{\xi}^h)) * f^{(i)}(t)\right) *^{-1} u^{(i)}(\boldsymbol{x}, t + T^{(i)}(\boldsymbol{x}, \boldsymbol{\xi'}^h)) \\ &= \left(U^{(i)}(\boldsymbol{x}, t - \boldsymbol{s}_H^{(i)}.(\boldsymbol{\xi}^h - \boldsymbol{\xi'}^h)) * f^{(i)}(t)\right) *^{-1} u^{(i)}(\boldsymbol{x}, t) \end{aligned} \qquad [1.28]$$

where $*^{-1}$ indicates deconvolution. In the case where the source time function f cannot be precisely evaluated, or where it is of a negligible duration with respect to F, the following approximation is often made:

$$F^{(i)}(t) = U^{(i)}(\boldsymbol{x}, t - \boldsymbol{s}_H^{(i)}.(\boldsymbol{\xi}^h - \boldsymbol{\xi'}^h)) *^{-1} u^{(i)}(\boldsymbol{x}, t) \qquad [1.29]$$

1 The term, "Green's function" is inaccurate as u is more exactly related to the spatial derivatives of the Green's function.

Methods using the empirical Green's function are particularly recommended in the following conditions:

– The mechanism and depth of the earthquake being studied have already been determined and the goal is to characterize the absolute source time function, or the apparent source time functions.

– A smaller earthquake exists in the region of study, with similar mechanism and depth. Its magnitude must be chosen as the smallest possible, while also being strong enough to generate waves with a good signal–noise ratio, over the largest possible range of frequencies. Practically, an earthquake of magnitude $(M_w - 2)$ is typically chosen to analyze an earthquake of magnitude M_w. If possible, its source time function, f, will be calculated in order to use [1.28]; if not, the effect of the approximation used in [1.29] has to be evaluated.

– It is difficult to numerically model the considered waves over the desired periods (i.e. periods shorter than the source duration). Surface waves are a typical case of this: while they can bring in valuable information about the source, the complex nature of their propagation at high frequency reduces the benefit of using numerical modeling approaches.

– We make use of a method that manages the intrinsic numerical instability of the deconvolution. For example, the direct extraction of $F^{(i)}$ through spectral division is too sensitive to small values of the denominator. Simple methods such as the "water level" method [MUE 85], or more evolved ones, like the Landweber projection [BER 97], make it possible to stabilize the obtained source time function.

When all of these conditions are met, the apparent source time functions obtained through the empirical Green's function are highly valuable for the analysis of the seismic source. For example, the rupture length (see section 1.4.2.2) can be directly determined using these functions.

1.3.4. *Complete modeling of the elastic wave field*

The expression of the observed displacement as a convolution between a point source radiation and an apparent source time function (equation [1.21]) requires the hypothesis of a distant source (small variation of Δ and ϕ across the entire source), as well as the far-field hypothesis (distance to the source much greater than the wavelength). These hypotheses may remain valid, even at near distances, for high-frequency radiation from small earthquakes. However, additional difficulties do arise at proximity to the source. While a primary P or S wave always exists, there are other paths, with similar travel times but different ray parameters, that can interfere with these first arrivals. These multiple arrivals tend to hide the end of the P or S waves in the seismograms (see Figure 1.4); moreover, even if a time window that contains all of these waves is extracted and if the associated point source

radiation is calculated, the concept of the apparent source time function (which requires a single ray parameter) cannot be used in these conditions.

Consequently, the most natural approach for studying the source of a local earthquake is to model the entire wave field, using the general point source formulation [1.3], line source formulation [1.13] or extended source formulation [1.12]. The complete Green's function, $\mathcal{G}$, can be calculated using several approaches, which require a more complex formalism than that used for the Green's functions of teleseismic body waves. We must take into account the interaction between the spherical expansion of the waves at the source and the layers in the medium (at least the free surface), and the geometric ray methods are not appropriate in this case. This configuration is generically called a "Lamb problem", referring to the first study [LAM 04] that provided a complete analytical solution of the radiation generated by a force applied to the free surface of a half-space. In the case of a vertically stratified medium, semi-analytical solutions do exist and there is no need to use purely numerical methods that require volume discretization (finite differences, finite elements).

A widely used semi-analytical method is the discrete wave number method [BOU 81, BOU 03] coupled with the reflectivity method [KEN 74, MÜL 85]. The generic technique for solving Lamb problems is to represent spherical waves as a superimposition of plane waves, the advantage being that the reflection-transmission-conversion behavior at the interfaces of each of these plane waves is known [AKI 02]. The solution is then obtained by integrating over the ray parameters of these plane waves. The discrete wave number method simplifies this problem by replacing the integration by a discrete sum, which is possible by bringing in a spatial periodization of the source. The obtained seismogram is thus unrealistic at long times, as soon as the effect of the closest periodized source is visible. However, it is accurate when restricted to shorter times. A periodization that is adapted to the distance between the source and the station makes it possible to obtain the complete wave field as accurately as desired (by adapting a convergence criterion). It must be noted that even the final static displacement (originating from the zero frequency contribution of the near-field term) is correctly modeled using this approach. The accuracy of this method should not be confused with the accuracy of the Green's function itself. At high frequency, the latter depends on the details of the Earth structure, that are not well known, and the structure model with laterally homogeneous layers is unable to reflect these complexities anyway. The simulation of the Green's function will, therefore, typically be imprecise for periods shorter than a few seconds at close distances (a few kilometers to a few tens of kilometers), and the precision further decreases for larger distances.

1.4. Approaches used to determine the global characteristics of the seismic source

1.4.1. *Methods based on the analysis of long-period waves at far distances*

1.4.1.1. *The Global CMT method*

The Global CMT method [DZI 81b, EKS 12] has enabled the analysis of the moment tensor for tens of thousands of earthquakes since 1976 (the catalog can be accessed at https://www.globalcmt.org/CMTsearch.html). It is based on the analysis of long-period body and surface waves, such that the details of the seismic source do not dominate the seismograms. The Green's functions are calculated by summing the eigenmodes [SAI 67, GIL 71], which is an efficient method for the simulation of the waves with periods greater than 40 s (lower limit used in Global CMT). The term "long period" depends on the magnitude of the earthquakes. For moderate earthquakes of magnitudes of about 6, body waves with a period of 40 s can be considered as long-period data. However, the Tohoku earthquake (Japan, March 11, 2011, M_w = 9.1) required the analysis of surface waves with periods longer than 300 s. In such long-period configurations, it is appropriate to consider a point source model (equation [1.3]) and use a very simple form for the function M: the Global CMT method chooses, for M, the time integral of a triangle function whose area is M_0 and whose duration τ only depends on M_0. This function has a classic analytical Fourier transform, which we will call $T_{M_0}(\omega)$. The method uses an estimation of the location $\tilde{\boldsymbol{\xi}}^h$ and origin time of the earthquake (e.g. based on the location derived from the first arrivals), and this origin time is chosen as the reference time. The equation that relates the observed displacements, $\boldsymbol{U}^{obs}$, with the model, can be written as:

$$U_i^{obs}(\boldsymbol{x},\omega) = T_{M_0}(\omega)\, \mathcal{M}_{jl}\, \mathcal{G}_{ij,l}(\boldsymbol{x}, \tilde{\boldsymbol{\xi}}^h + \boldsymbol{\Delta\xi}_c, \omega)\, e^{-i\omega\Delta t_c} \qquad [1.30]$$

Theoretically, there are therefore 10 parameters for the model: M_0, the non-dimensionalized moment tensor, $\boldsymbol{\mathcal{M}}$ (five parameters), the variation in location $\boldsymbol{\Delta\xi}_c$ with respect to $\tilde{\boldsymbol{\xi}}^h$ (three parameters), and the modification of the origin time Δt_c. The form of [1.30] seems to lead to a completely nonlinear inversion. In reality, the Global CMT formalism, which is not fully described here, makes it possible to solve this optimization problem through iterative linear inversions.

In practice, the trace of $\boldsymbol{\mathcal{M}}$ is constrained to zero (since the isotropic component is difficult to resolve), which leads to the search of only nine parameters. The inversion thus leads to a tensor that is called a deviatoric tensor, whose deviation from a double couple mechanism can be evaluated (see section 1.3.1.2). The Global CMT catalog shows that in the majority of cases, the eigenvalue with minimum absolute value is not significantly different from zero. The mechanism is therefore compatible with a slip in a constant direction over the fault.

$\boldsymbol{\Delta\xi}_c$ and Δt_c can be seen as the correction terms leading to the determination of an optimal point source, representing the characteristics integrated over space and time of all the earthquake complexity (this optimal point source is thus generally different from the earthquake origin). Formally, the modified location and time minimize the first-order moments of $\dot{m}_{jl}$, that is, they are the "center of gravity" or spatial and temporal "centroids" of the rupture. For large earthquakes, if the difference between the centroid, $\boldsymbol{\xi}^c$ $(= \tilde{\boldsymbol{\xi}}^h + \boldsymbol{\Delta\xi}_c)$, and the hypocentral position $\tilde{\boldsymbol{\xi}}^h$ is greater than their absolute uncertainties, this information is very useful: we can easily learn the preferential direction in which the rupture propagated. For example, the centroid of the Kokoxili earthquake (Tibet, November 14, 2001, M_w = 7.8) was located 200 km to the east, with respect to its hypocenter. This observation removes the ambiguity of the moment tensor on the activated fault plane, and testified to a rupture length of over 200 km, toward the east. Similarly, the centroid time Δt_c made it possible to identify some original earthquakes: a significant deviation between $\tau/2$ and Δt_c reveals an abnormally fast or slow rupture process. The latter is a typical indicator of tsunamigenic earthquakes (see, for example, the M_w= 7.7 Java earthquake, July 17, 2006).

1.4.1.2. *The W phase method*

The W phase method [KAN 08] may be seen as an approach that is similar to the Global CMT method, but in which the waves used are of even lower frequency. At large distances, the time window between the P wave and the surface waves contains all arrivals of the waves reflected at the surface (PP, PPP, PS, PPS, SS, etc.). While these waves are considered as individual arrivals in ray theory, they can also be viewed as a wave train whose low-frequency component can be analyzed. This wave train equivalently corresponds to the higher modes of the surface waves. Unlike the fundamental mode, which dominates the seismogram (see Figure 1.2), the higher modes have a higher propagation velocity (due to their propagation at greater depth) and a smaller amplitude. In order to refer to this wave train, Kanamori [KAN 93] coined the term "W phase", since it was analogous to the whispering gallery phenomenon.

The W phase has first been used to determine the first-order characteristics of major earthquakes [KAN 08]. In this context, it offers several advantages:

– Since the W phase arrives early in seismograms, its potential to serve as an early warning (of a possible tsunami, in particular) is greater than the fundamental modes of surface waves (used in the Global CMT method).

– As the analysis is carried out at very low frequencies (between 0.001 Hz and 0.005 Hz), the obtained characteristics represent the earthquake in its globality. This kind of determination is harder using P waves, especially when the source duration causes them to interfere with other waves in the seismogram.

– At these very low frequencies, the W phase mostly propagates in the upper mantle, which is relatively homogeneous. Modeling this propagation is thus simple and particularly reliable.

– Its small amplitude is an asset for very strong earthquakes recorded at relatively close distances (between 1,500 and 3,000 km): seismometers may get saturated during the arrival of the fundamental modes of the surface waves, but remain usable for the wave trains that precede them, which includes the W phase.

Subsequent developments [DUP 12, HAY 09] have shown that this method is able to analyze most earthquakes whose magnitude is greater than 5.8–6. The W phase method determines the moment tensor, as well as the spatial and temporal centroids of the rupture. For strong earthquakes, this approach thus provides the same type of information as the Global CMT method in a shorter time. The advantage of the W phase for early warning has also led to it being used at regional distances [RIQ 16]. However, at these distances, the W phase, strictly speaking, is no longer used as the time windows used tend to analyze the whole seismogram [ZHA 17]. In this sense, the method is thus based on the analysis of the entire field, like other approaches for local or regional distances (section 1.4.3).

1.4.2. *Methods based on the broadband analysis of teleseismic body waves*

1.4.2.1. *Point source approach and absolute source time function*

The propagation of teleseismic P and SH body waves can be modeled up to high frequencies of the order of 1 Hz (see section 1.3.2), which offers the possibility of capturing details of the seismic rupture. In theory, in addition to the influence of the point source radiation, signals differ between stations due to the apparent source time function. In the case of the P wave, for a dominantly horizontal rupture:

$$F^P(t) = \mu \int_S \Delta\dot{u}(\boldsymbol{\xi}, t + \boldsymbol{s}_H^P.(\boldsymbol{\xi} - \boldsymbol{\xi}^h) - t_r(\boldsymbol{\xi}))\, d\xi_1 d\xi_2 \qquad [1.31]$$

In [1.31], it is interesting to evaluate the phase shifts related to the slowness term $\boldsymbol{s}_H^P$, with modulus $(\sin i_h/\alpha_h)$. Using typical ray parameter values for a classic teleseismic P wave (coming from a source at the surface at an epicentral distance of $60°$), we obtain $||\boldsymbol{s}_H^P|| \simeq 0.06\mathrm{s/km}$. The steepness of the ray at the source and the high velocity of the P waves are the reasons for the small amplitude of this term. Thus, for a source propagating radially over 20 km around the hypocenter (which corresponds to an earthquake of magnitude 6–6.5), the maximum phase shift is of the order of ± 1 s, and its average value over all the observation azimuths is zero for horizontal propagation. In this same case, the phase shift related to the rupture time is of the order of 8 s, considering a conventional rupture velocity of $2.5\,\mathrm{km/s}$. These moderate earthquakes can thus be analyzed, even for frequencies that are quite high, approaching 1 Hz, using the absolute source time function F:

$$F(t) = \mu \int_S \Delta\dot{u}(\boldsymbol{\xi}, t - t_r(\boldsymbol{\xi}))\, d\xi_1 d\xi_2 \qquad [1.32]$$

It must be noted that this approximation is less precise for SH waves, due to their greater slowness. By using [1.32], we are thus brought back to a point source type approximation, where the P or SH wave observations are related to the model through:

$$U^{obs,P/SH}(\boldsymbol{x}, t + T^{P/SH}(\boldsymbol{x}, \boldsymbol{\xi}^h)) = G^{P/SH}_{\phi_s,d,\lambda,\xi_3^h}(t) * F(t) \qquad [1.33]$$

In an optimization perspective, the unknown quantities related to the time discretization of F will thus be added to the four unknowns of the point source radiation functions. F is conventionally parameterized by a sum of elementary functions (triangles, for example) that are regularly time shifted [LAN 81, NAB 85]. The duration of each elementary function and their number are defined a priori, while their amplitudes are inversed. The simplest case, which considers a single triangle to parameterize F, reproduces the Global CMT strategy and is therefore only valid for long periods. In practice, the observation of the data U^{obs}, in the range of frequencies that is used, governs the number and duration of the elementary functions that allow us to reproduce both the total duration and the complexity of the signals. If we work at relatively high frequency (up to 1Hz), the teleseismic body waves then provide a very good characterization of the duration, τ, of the earthquake, as soon as it exceeds a few seconds (i.e. from around magnitude 6). And when the earthquake is even longer, F can illuminate the existence of complexities inside the seismic rupture.

1.4.2.2. *Integration of the space–time effects in the point source approach*

The approach described earlier may have its limitations when the earthquake is of very high magnitude, or when the mechanism is modified over the course of the rupture. In this latter case, a classical method is to use several point sources, each associated with its own mechanism, location and source time function [NAB 85]. As [KIK 82, KIK 91] proposed, this idea may also be implemented in an iterative manner: after modeling the dominant point source in the waveforms, its contribution is subtracted from the seismograms in order to highlight the effect of other point sources. The approach can then be repeated until the seismogram is completely explained. In practice, however, this technique may lead to biases, as parasite signals may be introduced during the subtraction operations. Furthermore, the interpretation of multiple point sources may not be very clear in terms of physical rupture process [IHM 98].

In the case of a large earthquake (with constant mechanism), propagating preferentially in a horizontal direction, simple modifications can be made to the point source model. The following description corresponds to the Haskell model [HAS 64]: let us assume that the rupture propagates as a line source along the azimuth θ, at constant velocity v_r, and over the length L_0 (θ is necessarily equal to $\pm\phi_s$ in the case of a significant dip angle d, but can take an arbitrary value for an

almost flat fault). For any point ℓ on this line source of width W, we also consider that the spatial and temporal dependencies of the local slip are decoupled, that is, $\Delta\dot{u}(\boldsymbol{\xi}, t) = \Delta u_0(\ell) f_u(t)$. Δu_0 is the final slip, zero outside the segment $[0\ L_0]$, and f_u is the time function describing the local slip velocity. The absolute source time function in this model is thus written as:

$$F(t) = \mu\, W \int_0^{L_0} \Delta u_0(\ell) f_u(t - \frac{\ell}{v_r})\, d\ell = \mu\, W v_r \int_{-\infty}^{+\infty} \Delta u_0(v_r(t-\eta)) f_u(\eta)\, d\eta$$
$$= \mu\, W v_r\, \Delta u_0(v_r t) * f_u(t) \qquad [1.34]$$

By explicitly writing the phase shift related to the slowness $\boldsymbol{s}_H^P$, the apparent source time function for the P wave (see equation [1.26]) is written in terms of i_h and ϕ in the form:

$$F^P(t) = \mu\, W \int_0^{L_0} \Delta u_0(\ell) f_u(t + \frac{\ell \sin i_h \cos(\phi - \theta)}{\alpha_h} - \frac{\ell}{v_r})\, d\ell \qquad [1.35]$$

[BEN 61, BEN 62] have shown the importance of the term $\gamma = 1 - \cos(\phi - \theta) v_r \sin i_h / \alpha_h$, which controls the "directivity" of the earthquake (which will appear in the following derivations). For the P wave, $\gamma > 0$ regardless of the observation azimuth ϕ, as the velocity of the P wave is the upper limit of the rupture velocity v_r. For the SH waves, in the limiting case where $v_r = \alpha_h$, the cancellation of γ requires that $\sin j_h = \beta_h / \alpha_h \simeq 1/\sqrt{3}$. For a crustal source at a teleseismic distance, the ray parameter imposes that $\sin j_h$ is always smaller, which implies that we also always have $\gamma > 0$ for teleseismic SH waves. Relation [1.35] can be thus be expressed and rewritten as:

$$F^P(t) = \mu\, W \int_0^{L_0} \Delta u_0(\ell) f_u(t - \frac{\ell\gamma}{v_r})\, d\ell$$
$$= \frac{\mu\, W v_r}{\gamma} \int_{-\infty}^{+\infty} \Delta u_0(v_r(t-\eta)/\gamma) f_u(\eta)\, d\eta \qquad [1.36]$$
$$= \frac{\mu\, W v_r}{\gamma}\, \Delta u_0(v_r t/\gamma) * f_u(t)$$

Many studies show that the local duration of slip is much shorter than the total duration τ of the earthquake [HEA 90]. In other words, the seismic rupture, at least for strong earthquakes, tends to propagate as a "pulse". Therefore, in the equations above, it is instructive to neglect the duration of f_u and model f_u as a Dirac impulse. In this case, $F^P(t) = F(t/\gamma)/\gamma$. For a station in the direction of rupture ($|\phi - \theta| < \pi/2$), $\gamma < 1$, the apparent source time function has the same form as the absolute source

time function, but contracted in time and amplified in amplitude. The station is then said to be "directive". On the other hand, if ($\pi/2 < |\phi - \theta| < \pi$), the apparent source time function is dilated in time and reduced in amplitude, and the station is said to be "anti-directive". Both effects are all the more marked when γ varies over a large range. They are therefore amplified for fast rupture velocity v_r, and stronger for S waves than for P waves.

In an inversion process, owing to the modest effect of f_u, this function is often modeled as a simple triangle with duration τ_u, called the "rise time". τ_u itself may be difficult to solve and is thus frequently empirically fixed based on the magnitude of the earthquake. In this case, the addition of two parameters (θ and v_r) to a conventional point source analysis (section 1.4.2.1) makes it possible to explore the relevance of a unilateral rupture to explain the data. The rupture length ($L_0 = (\tau - \tau_u)v_r$) is then also known. The analysis can be refined by considering a bilateral rupture or a variable rupture velocity; however, it generally becomes necessary to discretize the line source model and this kind of modeling falls beyond the scope of this chapter (see Chapter 2).

The apparent source time functions can also be directly obtained using an empirical Green's function approach (section 1.3.3). A widespread technique is then to measure the apparent duration τ_a^j ($1 \leq j \leq N$, where N is the number of source time functions) of each source time function. Using the slowness $\boldsymbol{s}_H^j$, the theoretical value τ_a^j can be derived from relation [1.36]:

$$\begin{aligned} \tau_a^j = \frac{L_0\gamma}{v_r} + \tau_u &= \frac{L_0}{v_r} + \tau_u - L_0||\boldsymbol{s}_H^j|| \cos(\phi - \theta) \\ &= \tau - L_0||\boldsymbol{s}_H^j|| \cos(\phi - \theta) \end{aligned} \qquad [1.37]$$

This relation involves the rise time and rupture velocity only through the total duration τ, and thus remains true, even if v_r and τ_u vary over the course of the rupture. The rupture direction, θ, can be directly obtained by maximizing the linearity of τ_a as a function of $||\boldsymbol{s}_H|| \cos(\phi - \theta)$. The slope and intercept of the resulting linear equation then provide access to the rupture length L_0 and rupture duration τ, respectively [AMM 93, HAR 96].

1.4.2.3. *The SCARDEC method*

The previous inversion approaches make it necessary to impose or parameterize the source time functions of the earthquake. When the functions are parameterized, the information obtained on the source is controlled by the chosen number of elementary functions: increasing their number characterizes the temporal behavior more finely, but also leads to a larger number of parameters, which makes the inversion more complex and less stable. Furthermore, parameterization assumes a model (point source(s), unilateral propagation) that may inadequately represent the earthquake's space–time complexity.

The SCARDEC method [VAL 11] does not impose any parameterization of the source time function, as it remains based on a general formulation of an apparent source time function (for a dominantly horizontal rupture). Let us consider a collection of N observations of P or SH waves. For an observation j, the apparent source time function F^j for a wave of slowness $\boldsymbol{s}_H^j$ is written in the form:

$$F^j(t) = \mu \int_S \Delta\dot{u}(\boldsymbol{\xi}, t + \boldsymbol{s}_H^j.(\boldsymbol{\xi} - \boldsymbol{\xi}^h) - t_r(\boldsymbol{\xi}))\, d\xi_1 d\xi_2 \quad [1.38]$$

Before the analysis of a specific earthquake, F^j is an unknown function, but it has several intrinsic properties due to the positivity of $\Delta\dot{u}$ and γ (section 1.4.2.2) and to the finite duration τ of the earthquake. Furthermore, even if the source time function is apparent, its time integral is always equal to the seismic moment of the earthquake. The following four properties must therefore be respected for any observation j:

$$\begin{cases} \forall t,\ F^j(t) \geq 0 \\ \forall t < 0,\ F^j(t) = 0 \\ \exists \tau^j > 0, \forall t > \tau^j, F^j(t) = 0 \\ \int_0^{\tau^j} F^j(t)dt = M_0 \end{cases} \quad [1.39]$$

Furthermore, F^j is the result of the deconvolution of the observed signals from the point source radiation:

$$F^j(t) = U^j(\boldsymbol{x}, t + T^j(\boldsymbol{x}, \boldsymbol{\xi}^h)) *^{-1} G^j_{\phi_s, d, \lambda, \xi_3^h}(t) \quad [1.40]$$

We can thus develop the following optimization procedure, with the aim of simultaneously determining the mechanism (ϕ_s, d, λ), the depth (ξ_3^h) and the apparent source time functions of the earthquake. For a set of test parameters $(\phi'_s, d', \lambda', \xi_3'^h)$, $G^j_{\phi'_s, d', \lambda', \xi_3'^h}$ is calculated for all of the P and SH waves under consideration. Each observation, U^j, is then deconvoluted from its corresponding radiation $G^j_{\phi'_s, d', \lambda', \xi_3'^h}$, using a method (e.g. [VAL 04]) that imposes that all four properties [1.39] are respected. The source time functions that have been constrained to respect these properties are denoted by F'^j. The ability of $(\phi'_s, d', \lambda', \xi_3'^h)$ to explain the data is then evaluated using the norm of differences between the observed signals and the signals obtained through reconvolution. In this optimization problem, the function Q to be minimized is therefore:

$$Q(\phi'_s, d', \lambda', \xi_3'^h) = \sum_{j=1}^{N} \left\| U^j(\boldsymbol{x}, t + T^j(\boldsymbol{x}, \boldsymbol{\xi}^h)) - F'^j(t) * G^j_{\phi'_s, d', \lambda', \xi_3'^h}(t) \right\| \quad [1.41]$$

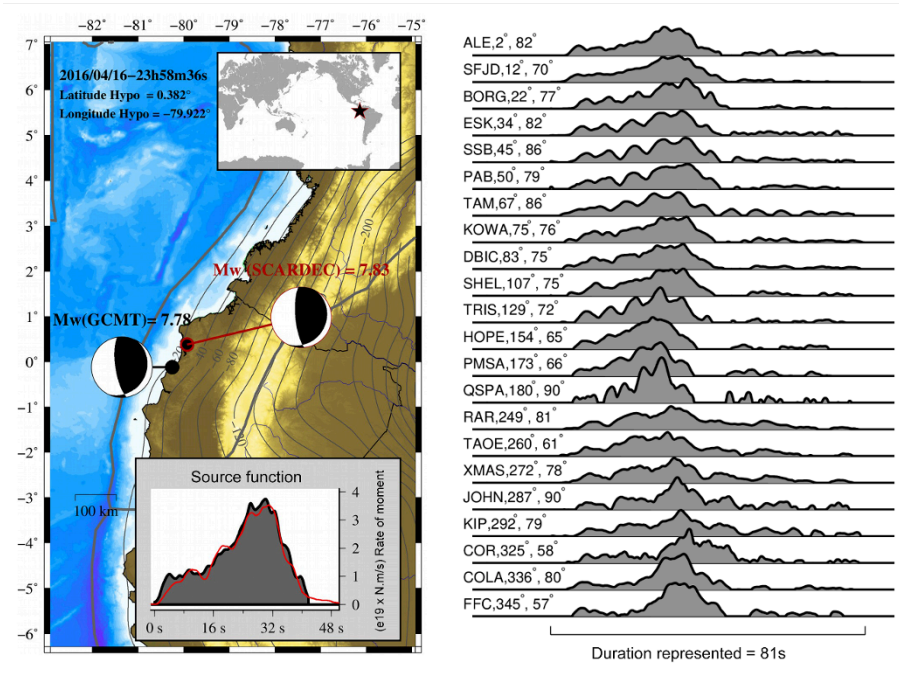

Figure 1.6. *Model of the Pedernales earthquake using the SCARDEC method. The map on the left summarizes the SCARDEC source parameters and compares them with the Global CMT solution. (ϕ, d, λ) is visualized by the usual representation of the focal mechanism, and the magnitudes corresponding to each method are given. The locations of the earthquake using SCARDEC and Global CMT correspond, respectively, to the hypocentral position $\boldsymbol{\xi}^h$ and to the position of the centroid $\boldsymbol{\xi}^c$. $(\phi, d, \lambda, \xi_3^h)$ is equal to $(29°, 19°, 123°, 16$ km) using SCARDEC and $(\phi, d, \lambda, \xi_3^c)$ is equal to $(27°, 21°, 124°, 22$ km) using Global CMT (best double couple solution). The formal uncertainty of SCARDEC is of the order of a few degrees for the angles of the mechanism, and up to 10 km for depth. The apparent source time functions of the P wave, associated with the SCARDEC mechanism and depth, are shown in the figure on the right. Each source time function is referenced by the name of the station, its azimuth ϕ, and its epicentral distance Δ. From top to bottom, they are thus represented starting from the north, in clockwise direction, and include the SSB station whose data are shown in Figure 1.2. Their shape and apparent duration reveal a directivity effect toward the south, which is consistent with the position of $\boldsymbol{\xi}^c$ with respect to $\boldsymbol{\xi}^h$. The source time functions shown in gray and red in the inset of the map have been deduced from all the apparent source time functions, and are representative of the absolute source time function of the earthquake. For a color version of this figure, see www.iste.co.uk/rolandone/seismic.zip*

The minimization of Q is a nonlinear problem, but owing to the very small number of parameters (4), an exhaustive search of the parameter space is possible. A guided search approach (SCARDEC method uses the Neighborhood Algorithm from [SAM 99]) further helps the rapid convergence toward models with a low Q value. When a sufficient number of P and SH waveforms are used, the optimal model leads to a simultaneous estimation of $(\phi, d, \lambda, \xi_3^h)$ and of the apparent source time functions F^j.

The details of, and limitations in, applying the SCARDEC method are described in [VAL 16]. The method is illustrated here by its application to the Pedernales earthquake (Ecuador, April 16, 2016, M_w = 7.8). The observations from this earthquake at a teleseismic distance were presented in section 1.2. Figure 1.6 shows the compatibility of the mechanism, magnitude and depth determined using the SCARDEC and Global CMT methods. The apparent source time functions highlight the duration of the earthquake (40–45 s) and the propagation of the rupture toward the south. These characteristics are confirmed by the detailed analysis of the earthquake, using a rich collection of geodetic and seismological data [NOC 17].

1.4.3. *Methods based on full wavefield modeling at local or regional distances*

In this section, the "large distance" hypothesis (size of the source much smaller than the observation distance) is assumed to be verified. Indeed, any analysis at a local or regional distance requires this hypothesis in order to avoid discretizing the seismic fault. Since the development of broadband networks in the vicinity of seismic sources, several methods have aimed to analyze the observed wave field in order to extract the source characteristics (e.g. TDMT-INVC ([DRE 93], ISOLA [SOK 08], FMNEAR [DEL 14], RAPIDINV [CES 10], MECAVEL [VAC 19]). These approaches enabled the analysis of earthquakes whose magnitude is too small for a study at teleseismic distances (where the magnitude limit is about 5–5.5). In the cases where very dense networks exist around a well-identified target (a volcano, for example), even very low magnitudes, of the order of 0 or 1, can be analyzed.

A very common geometry of observation is that of an earthquake recorded by a set of stations located at distances ranging from a few tens to a few hundreds of kilometers. In this configuration, the complete Green's function modeling at all stations is usually accurate only for frequencies lower than 0.1 Hz or even 0.05 Hz. This limitation precludes the analysis of small earthquakes (typically below a magnitude of 3.5), whose signal-to-noise ratio is not sufficient. The most suitable range of magnitudes is typically located between magnitudes 4 and 5.5. The signal-to-noise ratio in this range is generally good for frequencies between 0.01–0.02 Hz and 0.03–0.04 Hz. For these frequencies and magnitudes, the Green's function is reliable (if using an Earth model adapted to the area under study), the

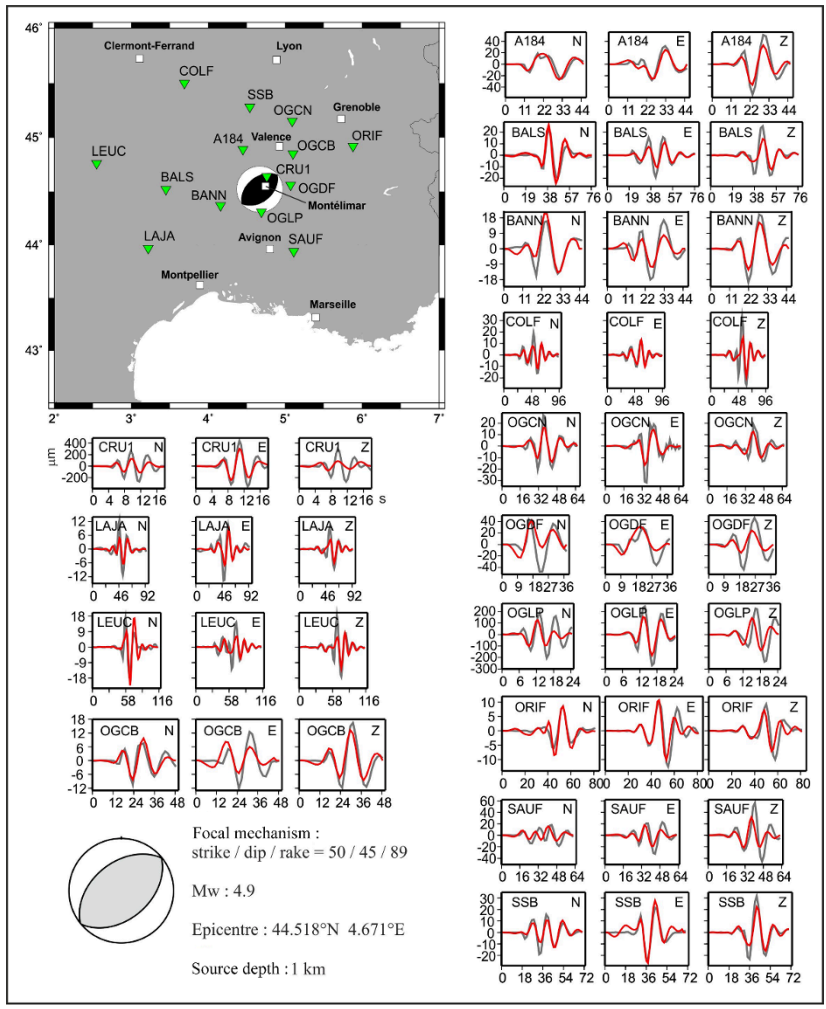

Figure 1.7. *Analysis of the 2019 Le Teil earthquake using the FMNEAR method [DEL 14] for a point source. The seismological stations used are indicated on the map by green triangles, and the obtained focal mechanism is centered on the epicenter. For each station, the data (in gray) and the synthetics (in red) are represented on the three components (N for the north component, E for the east component and Z for the vertical component) as a function of time (s). The signals have been converted into displacement (μm) and filtered between 0.03 and 0.08 Hz, except for the CRU1 station (between 0.15 and 0.3 Hz). The indicated epicenter is a fixed parameter of the inversion. After testing a number of other values, the shallow depth of 1 km was shown to provide the best adjustment to the waveforms. The indicated moment magnitude (M_w) and focal mechanism correspond to the best solution found for this depth (figure from [DEL 14])*

point source model is satisfactory, and the time complexity of the source does not perturb the seismograms. The simple point source equation [1.5] associated with the calculation of the Green's function (section 1.3.4) adequately relate the data with the parameters of the model (location, magnitude and source mechanism).

Figure 1.7 illustrates the determination of the source characteristics of the 2019 Le Teil earthquake (Ardèche, France, November 11, 2019, M_w = 4.9). The recording of this earthquake at BANN station (RESIF-RLBP network) was already shown in Figure 1.4. The method used here is the FMNEAR method [DEL 14] and the data are made up of complete three-component seismograms recorded at local and regional distances. The minimization of the differences between the data and the synthetics reveals a compressive mechanism ($(\phi, d, \lambda) = (50°, 45°, 89°)$) and a very shallow depth.

1.5. Conclusion

This chapter introduced different strategies for extracting the first-order characteristics of earthquakes from seismological data. At the global scale, these approaches determine the focal mechanism, depth and magnitude of all earthquakes whose magnitude is greater than 5–5.5. At the regional scale, the instrumentation now available in many seismic areas frequently make it possible to bring this magnitude threshold down to about 3.5–4.

Such comprehensive and systematic analyses are valuable for the study of the seismic cycle. For example, the amount of strain that is accommodated seismically can be estimated, and compared with the total strain predicted by plate tectonics. The types of seismic deformation, characterized by the moment tensor, provide rich information on the geometry of the stresses to which the Earth is subjected. Finally, the earthquake depths delimit the thickness of the seismogenic zone, which can be compared with the total thickness in which deformations are expected.

In the case of strong earthquakes, more detailed information on the seismic source, such as the duration, rupture length and rupture velocity can be estimated using the methods described in this chapter. However, for a more precise spatial-temporal image of major events, we must use fault-discretization methods, which are discussed in Chapter 2.

1.6. References

[AKI 66] AKI K., "Generation and propagation of G waves from the Niigata earthquake of June 16, 1964: Part 2. Estimation of earthquake moment, released energy, and stress-strain drop from the G wave spectrum", *Bulletin of the Earthquake Research Institute*, vol. 44, no. 1, pp. 73–88, 1966.

[AKI 02] AKI K., RICHARDS P., *Quantitative Seismology*, University Science Books, Sausalito, CA, 2002.

[AMM 93] AMMON C.J., VELASCO A.A., LAY T., "Rapid estimation of rupture directivity: Application to the 1992 Landers (Ms = 7.4) and Cape Mendocino (Ms = 7.2), California earthquakes", *Geophysical Research Letters*, vol. 20, no. 2, pp. 97–100, 1993.

[BEN 61] BEN-MENAHEM A., "Radiation of seismic surface-waves from finite moving sources", *Bulletin of the Seismological Society of America*, vol. 51, no. 3, pp. 401–435, 1961.

[BEN 62] BEN-MENAHEM A., "Radiation of seismic body waves from a finite moving source in the earth", *Journal of Geophysical Research*, vol. 67, no. 1, pp. 345–350, 1962.

[BER 97] BERTERO M., BINDI D., BOCCACCI P. et al., "Application of the projected Landweber method to the estimation of the source time function in seismology", *Inverse Problems*, vol. 13, no. 2, p. 465, 1997.

[BOA 80] BOATWRIGHT J., "Preliminary body-wave analysis of the St. Elias, Alaska earthquake of February 28, 1979", *Bulletin of the Seismological Society of America*, vol. 70, no. 2, pp. 419–436, 1980.

[BOU 76] BOUCHON M., "Teleseismic body wave radiation from a seismic source in a layered medium", *Geophysical Journal International*, vol. 47, no. 3, pp. 515–530, 1976.

[BOU 81] BOUCHON M., "A simple method to calculate Green's functions for elastic layered media", *Bulletin of the Seismological Society of America*, vol. 71, no. 4, pp. 959–971, 1981.

[BOU 03] BOUCHON M., "A review of the discrete wavenumber method", *Pure and Applied Geophysics*, vol. 160, nos 3–4, pp. 445–465, 2003.

[CES 10] CESCA S., HEIMANN S., STAMMLER K. et al., "Automated procedure for point and kinematic source inversion at regional distances", *Journal of Geophysical Research: Solid Earth*, vol. 115, no. B6, 2010.

[DEL 14] DELOUIS B., "FMNEAR: Determination of focal mechanism and first estimate of rupture directivity using near-source records and a linear distribution of point sources", *Bulletin of the Seismological Society of America*, vol. 104, no. 3, pp. 1479–1500, 2014.

[DRE 93] DREGER D.S., HELMBERGER D.V., "Determination of source parameters at regional distances with three-component sparse network data", *Journal of Geophysical Research: Solid Earth*, vol. 98, no. B5, pp. 8107–8125, 1993.

[DUP 12] DUPUTEL Z., RIVERA L., KANAMORI H. et al., "W phase source inversion for moderate to large earthquakes (1990–2010)", *Geophysical Journal International*, vol. 189, no. 2, pp. 1125–1147, 2012.

[DZI 81a] DZIEWONSKI A., ANDERSON D.L., "Preliminary reference Earth model", *Physics of the Earth and Planetary Interiors*, vol. 25, no. 4, pp. 297–356, 1981.

[DZI 81b] DZIEWONSKI A., CHOU T.-A., WOODHOUSE J., "Determination of earthquake source parameters from waveform data for studies of global and regional seismicity", *Journal of Geophysical Research: Solid Earth*, vol. 86, no. B4, pp. 2825–2852, 1981.

[EKS 12] EKSTRÖM G., NETTLES M., DZIEWOŃSKI A., "The global CMT project 2004–2010: Centroid-moment tensors for 13,017 earthquakes", *Physics of the Earth and Planetary Interiors*, vol. 200, pp. 1–9, 2012.

[GEO 82] GEOSCOPE, GEOSCOPE – French Global Network of broadband seismic stations, Institut de Physique du Globe de Paris and École et Observatoire des Sciences de la Terre de Strasbourg (IPGP/EOST), 1982.

[GEO 93] GEOFON DATA CENTRE, GEOFON seismic network, GDC, 1993.

[GIL 71] GILBERT F., "Excitation of the normal modes of the Earth by earthquake sources", *Geophysical Journal International*, vol. 22, no. 2, pp. 223–226, 1971.

[GSN 86] GSN, Global seismic network, Albuquerque Seismological Laboratory (USGS/ASL) and IDA project at UC San Diego (IRIS/IDA), 1986.

[HAN 79] HANKS T.C., KANAMORI H., "A moment magnitude scale", *Journal of Geophysical Research: Solid Earth*, vol. 84, no. B5, pp. 2348–2350, 1979.

[HAR 78] HARTZELL S.H., "Earthquake aftershocks as Green's functions", *Geophysical Research Letters*, vol. 5, no. 1, pp. 1–4, 1978.

[HAR 96] HARTOG J.R., SCHWARTZ S.Y., "Directivity analysis of the December 28, 1994 Sanriku-oki earthquake (Mw= 7.7), Japan", *Geophysical Research Letters*, vol. 23, no. 16, pp. 2037–2040, 1996.

[HAS 64] HASKELL N., "Total energy and energy spectral density of elastic wave radiation from propagating faults", *Bulletin of the Seismological Society of America*, vol. 54, no. 6A, pp. 1811–1841, 1964.

[HAY 09] HAYES G.P., RIVERA L., KANAMORI H., "Source inversion of the W-Phase: Real-time implementation and extension to low magnitudes", *Seismological Research Letters*, vol. 80, no. 5, pp. 817–822, 2009.

[HEA 90] HEATON T.H., "Evidence for and implications of self-healing pulses of slip in earthquake rupture", *Physics of the Earth and Planetary Interiors*, vol. 64, no. 1, pp. 1–20, 1990.

[IHM 98] IHMLÉ P.F., "On the interpretation of subevents in teleseismic waveforms: The 1994 Bolivia deep earthquake revisited", *Journal of Geophysical Research: Solid Earth*, vol. 103, no. B8, pp. 17919–17932, 1998.

[KAN 76] KANAMORI H., STEWART G.S., "Mode of the strain release along the Gibbs fracture zone, Mid-Atlantic Ridge", *Physics of the Earth and Planetary Interiors*, vol. 11, no. 4, pp. 312–332, 1976.

[KAN 93] KANAMORI H., "W phase", *Geophysical Research Letters*, vol. 20, no. 16, pp. 1691–1694, 1993.

[KAN 08] KANAMORI H., RIVERA L., "Source inversion of W phase: Speeding up seismic tsunami warning", *Geophysical Journal International*, vol. 175, no. 1, pp. 222–238, 2008.

[KEN 74] KENNETT B., "Reflections, rays, and reverberations", *Bulletin of the Seismological Society of America*, vol. 64, no. 6, pp. 1685–1696, 1974.

[KEN 91] KENNETT B., ENGDAHL E., "Traveltimes for global earthquake location and phase identification", *Geophysical Journal International*, vol. 105, no. 2, pp. 429–465, 1991.

[KEN 95] KENNETT B., ENGDAHL E., BULAND R., "Constraints on seismic velocities in the Earth from traveltimes", *Geophysical Journal International*, vol. 122, no. 1, pp. 108–124, 1995.

[KIK 82] KIKUCHI M., KANAMORI H., "Inversion of complex body waves", *Bulletin of the Seismological Society of America*, vol. 72, no. 2, pp. 491–506, 1982.

[KIK 91] KIKUCHI M., KANAMORI H., "Inversion of complex body waves III", *Bulletin of the Seismological Society of America*, vol. 81, no. 6, pp. 2335–2350, 1991.

[LAM 04] LAMB H., "I. On the propagation of tremors over the surface of an elastic solid", *Philosophical Transactions of the Royal Society of London. Series A*, vol. 203, no. 359–371, pp. 1–42, 1904.

[LAN 75] LANGSTON C.A., HELMBERGER D.V., "A procedure for modelling shallow dislocation sources", *Geophysical Journal International*, vol. 42, no. 1, pp. 117–130, 1975.

[LAN 81] LANGSTON C.A., "Source inversion of seismic waveforms: The Koyna, India, earthquakes of 13 September 1967", *Bulletin of the Seismological Society of America*, vol. 71, no. 1, pp. 1–24, 1981.

[LAN 85] LANGSTON C.A., BAAG C.-E., "The validity of ray theory approximations for the computation of teleseismic SV waves", *Bulletin of the Seismological Society of America*, vol. 75, no. 6, pp. 1719–1727, 1985.

[LAY 95] LAY T., WALLACE T.C., *Modern Global Seismology*, Academic Press, Elsevier, San Diego, 1995.

[MUE 85] MUELLER C.S., "Source pulse enhancement by deconvolution of an empirical Green's function", *Geophysical Research Letters*, vol. 12, no. 1, pp. 33–36, 1985.

[MÜL 85] MÜLLER G., "The reflectivity method: A tutorial", *Journal of Geophysics*, vol. 58, nos 1–3, pp. 153–174, 1985.

[NAB 85] NABELEK J., "Geometry and mechanism of faulting of the 1980 El Asnam, Algeria, earthquake from inversion of teleseismic body waves and comparison with field observations", *Journal of Geophysical Research: Solid Earth*, vol. 90, no. B14, pp. 12713–12728, 1985.

[NOC 17] NOCQUET J.-M., JARRIN P., VALLÉE M. et al., "Supercycle at the Ecuadorian subduction zone revealed after the 2016 Pedernales earthquake", *Nature Geoscience*, vol. 10, no. 2, pp. 145–149, 2017.

[OKA 92] OKAL E.A., "A student's guide to teleseismic body wave amplitudes", *Seismological Research Letters*, vol. 63, no. 2, pp. 169–180, 1992.

[PEA 80] PEARCE R., "Fault plane solutions using relative amplitudes of P and surface reflections: Further studies", *Geophysical Journal International*, vol. 60, no. 3, pp. 459–487, 1980.

[RIQ 16] RIQUELME S., BRAVO F., MELGAR D. et al. "W phase source inversion using high-rate regional GPS data for large earthquakes", *Geophysical Research Letters*, vol. 43, no. 7, pp. 3178–3185, 2016.

[ROM 86] ROMANOWICZ B.A., DZIEWONSKI A., "Toward a federation of broadband seismic networks", *Eos, Transactions American Geophysical Union*, vol. 67, no. 25, pp. 541–542, 1986.

[SAI 67] SAITO M., "Excitation of free oscillations and surface waves by a point source in a vertically heterogeneous earth", *Journal of Geophysical Research*, vol. 72, no. 14, pp. 3689–3699, 1967.

[SAM 99] SAMBRIDGE M., "Geophysical inversion with a neighbourhood algorithm I. Searching a parameter space", *Geophysical Journal International*, vol. 138, no. 2, pp. 479–494, 1999.

[SHE 19] SHEARER P.M., *Introduction to Seismology*, Cambridge University Press, Cambridge, New York, 2019.

[SIM 12] SIMMONS N.A., MYERS S.C., JOHANNESSON G. et al., "LLNL-G3Dv3: Global P wave tomography model for improved regional and teleseismic travel time prediction", *Journal of Geophysical Research: Solid Earth*, vol. 117, no. B10, 2012.

[SOK 08] SOKOS E.N., ZAHRADNIK J., "ISOLA a Fortran code and a Matlab GUI to perform multiple-point source inversion of seismic data", *Computers & Geosciences*, vol. 34, no. 8, pp. 967–977, 2008.

[VAC 19] VACA S., VALLÉE M., NOCQUET J.-M. et al., "Active deformation in Ecuador enlightened by a new waveform-based catalog of earthquake focal mechanisms", *Journal of South American Earth Sciences*, vol. 93, pp. 449–461, 2019.

[VAL 04] VALLÉE M., "Stabilizing the empirical Green function analysis: Development of the projected Landweber method", *Bulletin of the Seismological Society of America*, vol. 94, no. 2, pp. 394–409, 2004.

[VAL 11] VALLÉE M., CHARLÉTY J., FERREIRA A.M. et al., "SCARDEC: A new technique for the rapid determination of seismic moment magnitude, focal mechanism and source time functions for large earthquakes using body-wave deconvolution", *Geophysical Journal International*, vol. 184, no. 1, pp. 338–358, 2011.

[VAL 16] VALLÉE M., DOUET V., "A new database of source time functions (STFs) extracted from the SCARDEC method", *Physics of the Earth and Planetary Interiors*, vol. 257, pp. 149–157, 2016.

[ZHA 17] ZHAO X., DUPUTEL Z., YAO Z., "Regional W-phase source inversion for moderate to large earthquakes in China and neighboring areas", *Journal of Geophysical Research: Solid Earth*, vol. 122, no. 12, pp. 10–52, 2017.

2

Co-Seismic Phase: Imaging the Seismic Rupture

Zacharie DUPUTEL
Observatoire Volcanologique du Piton de la Fournaise,
CNRS, Institut de physique du globe de Paris, Paris Cité University, France

2.1. Introduction

Most earthquakes correspond to a fault rupture inside the Earth. These phenomena are caused by the relative motion of tectonic plates on the terrestrial surface. When tectonic stresses increase and finally exceed the resistance of the fault, a rupture occurs with an abrupt deformation of the surrounding environment, releasing seismic waves (see the Introduction to this book). Although this description is generally correct, today we know that there are a variety of ways in which earthquakes occur [KAN 04a]. First of all, the size of earthquakes varies over several orders of magnitude. The smallest earthquakes last for only a fraction of a second, while the largest ruptures can occur over hundreds of kilometers in a few minutes. Furthermore, while earthquakes often correspond to "brittle ruptures", releasing seismic waves, other "slow slip events" occur silently (see Chapter 6). Some earthquakes involve dissipative processes with a large amount of heat release. Others are not even caused by the activity of tectonic faults but rather by large landslides or volcanic processes.

This wide diversity of seismic sources observed in nature is still poorly understood. Why do some earthquakes stop quickly, after a few meters, while others

The Seismic Cycle,
coordinated by Frédérique ROLANDONE.

The Seismic Cycle: From Observation to Modeling,
First Edition. Frédérique Rolandone.

continue to rupture a fault over several hundreds of kilometers? Why are some ruptures catastrophic, generating seismic waves, while others involve the slow slip of a fault? What is the interaction between seismic and aseismic slip modes? Several models have been developed to try and explain the diversity of rupture behaviors observed on faults. Over the past few decades, one dominant vision has consisted of considering faults as being segmented into large regions with different frictional properties governing the seismic or aseismic character of slip [LAY 81]. This conceptual asperity model suggests an exclusive partitioning between slip modes and, notably, predicts the concept of "characteristic earthquakes" that always rupture the same asperity in a periodic time-predictable or slip-predictable fashion (see the introduction to this book as well as [SHI 80]). However, today much observation suggests an overlap between seismic and aseismic fault slip (e.g., [JOH 12]). Furthermore, a fault region may be entirely ruptured by a single large earthquake, but may also rupture sequentially, in a series of smaller earthquakes, as observed in Japan, Sumatra or Ecuador [SIM 11, LAY 15, NOC 17]. This diversity is likely associated with a wide heterogeneity of frictional properties on faults (see Chapter 4), with conditionally stable slip zones to explain the occurrence of seismic ruptures in areas that are usually associated with slow continuous slip [SCH 98]. This spatial variability may also explain certain complex behaviors observed during the seismic cycle, such as the variability in the size of earthquakes in the same region [KAN 10].

In order to understand fault activity and rupture dynamics, we must describe what happens during ruptures by determining the spatial and temporal slip evolution. We should then characterize co-seismic slip during earthquakes along with slip distributions producing slow transient deformations, and fault coupling in the interseismic period. Slip inversion makes it possible to evaluate the partitioning between seismic and aseismic slips, which is an essential parameter in seismotectonics since it determines the seismogenic potential of faults. The characterization of rupture processes is also important for the realistic simulation of strong motions generated by earthquakes. The seismic rupture is usually represented as a model describing the slip distribution over the fault, usually referred to as slip models or finite fault models. Since these models describe the rupture history without an explicit reference to the underlying forces, they are also called kinematic models. The estimation of slip models is complicated by observational noise, the complexity of rupture processes and our limited knowledge of the Earth's structure. Since the pioneering studies carried out in the 1970s, different approaches have been developed to obtain images of the spatiotemporal distribution of fault slip. The 1971 San Fernando earthquake ($M_W = 6.7$, California) is the first earthquake for which a slip model could be established using seismological data [TRI 74]. Today, slip models are routinely calculated for every large earthquake, which is facilitated by the rapid availability of a large volume of data. The increase in computation capabilities has also led to significant improvements, especially to solve nonlinear inverse problems and to simulate waveforms in heterogeneous media.

Slip inversion methods are the central theme of this chapter. Chapter 1 discusses the determination of first-order characteristics of earthquakes (focal mechanism, source function, etc.). Here, we will first summarize the main types of data used today in seismic rupture imaging. Next, we will examine the forward problem, that is, the formulation to predict surface observations for a given seismic source. We will then deal with the inverse problem, consisting of finding the slip distribution from surface data. Finally, we will discuss certain implications of slip models on the dynamics of seismic ruptures.

2.2. Surface observations

The number of measurements available to study earthquake sources has evolved considerably over the last few decades. In this section, we summarize the main geophysical data used today to image the seismic rupture. In particular, we will examine in detail the seismological data that are essential components in determining the temporal evolution of slip. These observations are generally combined with different types of geodetic data (GNSS, high-rateGNSS, radar interferometry, image correlation). Tsunami data can also bring significant constraints in rupture areas located offshore. In addition to these measurements, earthquake studies have also benefited from field observations. These observations make it possible, for example, to map the trace of faults or even directly measure slip at the surface.

2.2.1. *Seismological data*

Seismometers are the most widely used instrument for quantifying seismic displacements. These sensors are made up of a mass attached to the ground through a spring and a damping device. For a long time, ground movement was measured through the displacement of the mass relative to the ground. Modern instruments are based on the same inertial system, but with an electromagnetic feedback mechanism that prevents the mass from moving. The correction signal required to prevent the mass from moving is recorded. This system makes it possible to have a compact instrument recording signals over a large range of frequencies and amplitudes, conserving the linearity of the sensor. For more information on seismometry, the reader may consult Chapter 12 of [AKI 02].

Seismological waveforms provide essential information to estimate the time history of seismic ruptures. Two types of seismological sensors are widely used today to characterize the seismic source: broadband seismometers and strong motion sensors. Seismological data may be seen as the convolution product of ground displacement in the recorded direction and the sensor's transfer function. Thus, in the frequency domain, the seismological recordings $S(\omega)$ may be described as:

$$S(\omega) = I_D(\omega)U(\omega) \qquad [2.1]$$

where ω is the angular frequency, $U(\omega)$ is the ground displacement and $I_D(\omega)$ is the displacement transfer function of the sensor. Alternatively, the instrument response with respect to the ground displacement velocity ($I_V(\omega)$) or to its acceleration ($I_A(\omega)$) can be used in the above equation $S(\omega) = I_V(\omega)\dot{U}(\omega) = I_A(\omega)\ddot{U}(\omega)$, where $\dot{U}(\omega)$ and $\ddot{U}(\omega)$ correspond, respectively, to the ground velocity and acceleration. Figure 2.1 presents the responses of a broadband seismometer (Dumont d'Urville station in Antarctica) and a strong motion sensor in New Zealand. The broadband instrument presents a velocity transfer function ($I_V(\omega)$) that is almost flat over a large frequency range, that is, a response that is proportional to ground velocity up to a period of 360 s. For longer periods, the amplitude of the instrumental response decreases proportional to ω^2. The strong motion sensor depicted in Figure 2.1 is an accelerometer, that is, with a "flat" acceleration response from zero frequency up to its corner frequency (here 200 Hz).

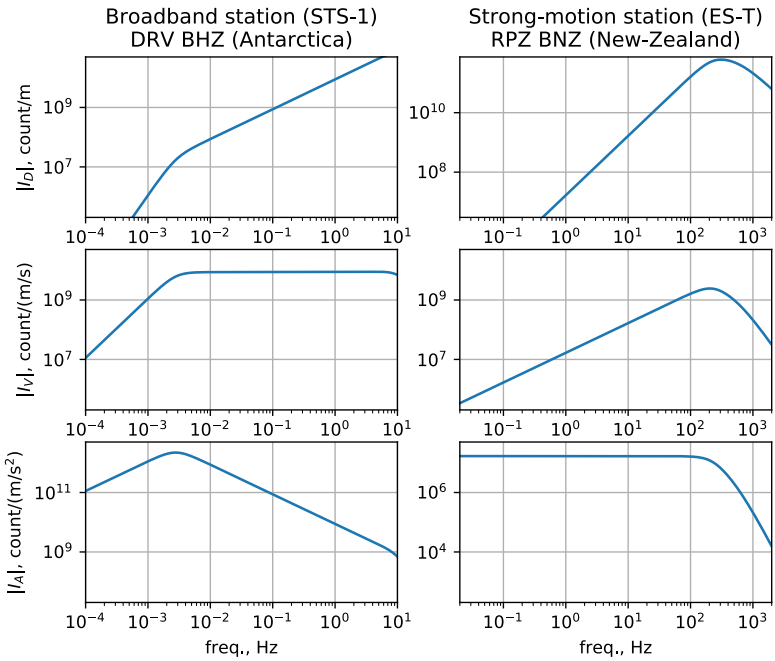

Figure 2.1. *Examples of instrumental responses for a broadband seismometer (left) and for an accelerometer (right). The spectral amplitude of transfer functions in displacement I_D, velocity I_V and acceleration I_A is shown for each case. The broadband station is equipped with a Streckeisen STS-1 sensor, with a corner frequency at 2.7 mHz. The strong motion sensor is an EpiSensor (ES-T) kinemetrics accelerometer with a corner frequency at 200 Hz. Both of these sensors are force-feedback sensors*

In order to work with data that can be physically interpreted, the recorded signals must be corrected from the instrumental response. For example, if we wish to extract the ground displacement:

$$U(\omega) \sim F(\omega)\frac{S(\omega)}{I_D(\omega)} \quad [2.2]$$

During this deconvolution, we use a filter $F(\omega)$ that filters the data in a pass band similar to the one that is used for inversion.

Figure 2.2 presents examples of signals that were recorded during the 2016 Kaikoura earthquake (New Zealand, $M_W = 7.8$) by the broadband station DRV (the Dumont d'Urville station in Antarctica) and the strong-motion station RPZ (Rata Peaks in New Zealand), whose responses are depicted in Figure 2.1. The raw data are on top, and the data after instrument correction is presented below (for ground displacement velocity and acceleration). It can be clearly seen that the acceleration and velocity data have higher frequency than the displacement data. This effect is related to the time derivative relationship between these signals, translated by a factor $i\omega$ in the spectral domain (where i is the imaginary unit). Acceleration or velocity waveforms are therefore more sensitive to rupture complexities visible at high frequency. These data are also more sensitive to heterogeneities in the propagation medium, which are not necessarily adequately considered in the velocity model that is employed for slip inversion. In practice, we often use displacement or velocity data (since ground acceleration is usually difficult to model).

As broadband stations are very sensitive to ground displacement, they make it possible to observe seismic waves over large distances (over 3,000 km from the epicenter in Figure 2.2). At these teleseismic distances, body waves are conventionally used (generally P and SH waves) to determine the time history of the rupture. In Figure 2.2 on the left, the teleseismic P waves emerge weakly until there is a large amplitude arrival around 60 s after the first arrival. This arrival corresponds to large slip that occurred ∼60 s after the earthquake origin time in the northern part of the Kaikoura earthquake rupture (e.g., [WAN 18]). We can also use surface waves (Rayleigh and Love waves), which can constrain first-order source parameters such as the seismic moment and rupture directivity (e.g., [DUP 17]). Unlike broadband seismometers, accelerometers are usually much less sensitive (see Figure 2.1), allowing us to record very strong motions without data clipping. On the right of Figure 2.2, we once again see that the signal emerges weakly and that the energetic arrivals come later (∼60 s after the first arrival as in teleseismic data). For more details on seismological data recorded at global and regional scales, the reader is referred to Chapter 1.

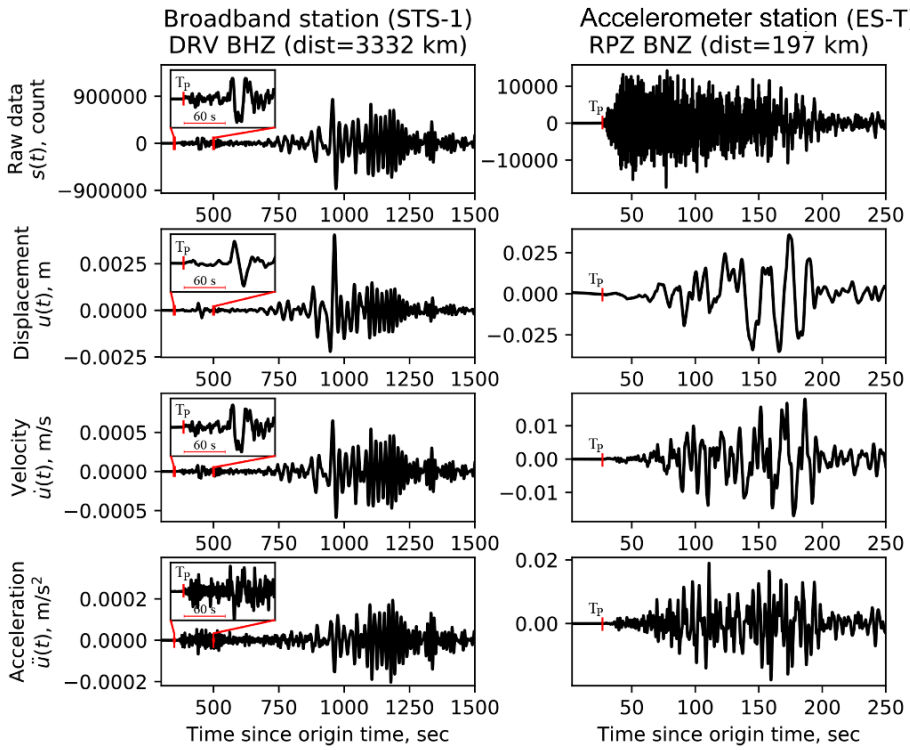

Figure 2.2. *Seismological recordings during the 2016 Kaikoura earthquake ($M_W = 7.8$, New Zealand). The waveforms presented here correspond to the broadband seismometer (STS-1, on the left) and to the accelerometer (EpiSensor ES-T) whose responses are given in Figure 2.1. In each case, we show the raw data, $s(t)$, the displacement data $u(t)$, the velocity data $\dot{u}(t)$ and the acceleration data $\ddot{u}(t)$. The correction of the instrumental response is carried out between periods of 5 and 125 s (0.008–0.2 Hz). The insets on the left of the figures show an enlargement of the teleseismic P arrival at the DRV station (T_P indicates P-wave arrival times)*

2.2.2. *GNSS data: from geodesy to seismo-geodesy*

GNSS (Global Navigation Satellite System) data are among the most widely used data to study earthquakes. This includes the global positioning system (GPS), the Russian system GLONASS or the European Galileo system. By estimating the position of a point with respect to a reference system defined by a constellation of satellites, these data allow the measurement of co-seismic displacements in three directions (vertical, east and north). Two types of measurements may be acquired: campaign measurements or measurements from continuous stations. In the first case, the measured displacements may contain a large part of the inter- and post-seismic

displacements, or motions related to aftershocks, which may be corrected by combining the observations with other available data (e.g., [KLE 17]). In the case of continuous measurements from continuous stations for which a daily position is estimated, co-seismic displacements can be estimated from the offset between the estimated positions before and after the event. Daily co-seismic data may also be affected by the post-seismic deformations [TWA 19] or by earthquakes occurring immediately before or after the mainshock [SIM 11].

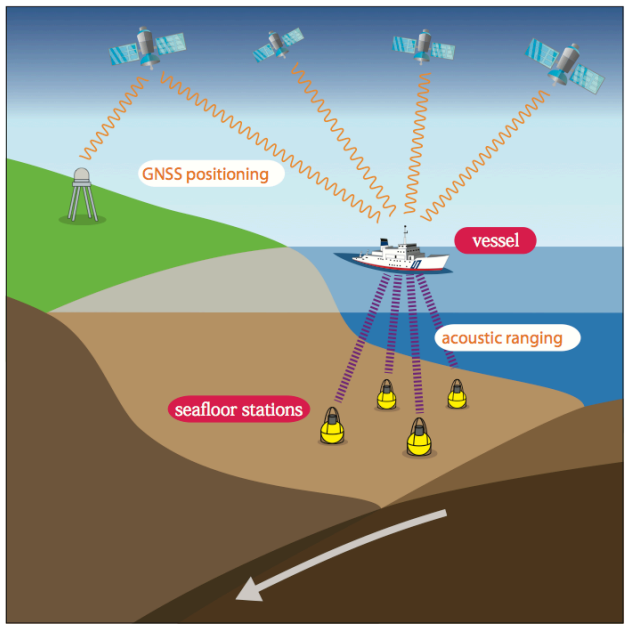

Figure 2.3. *The GNSS-A seafloor geodesic observation system. This system combines the GNSS positioning of a boat (or an autonomous robot) and acoustic ranging for the relative positioning of transponders placed on the seafloor. This figure is modified according to [YOK 20]. For a color version of this figure, see www.iste.co.uk/rolandone/seismic.zip*

Along subduction zones, land-based geodetic data are almost insensitive to deformation processes off the coast. To mitigate this problem, several seafloor geodetic approaches have been developed from the 1980s onwards [BÜR 14]. One approach in particular, combining GNSS observations and acoustics ranging (GNSS-A; Figure 2.4), is used today in various regions [YOK 20]. This method is based on the GNSS positioning of a boat (or an autonomous robot) from which the transponders placed on the seafloor are located through acoustic ranging. Another widespread method is the deployment of pressure sensors that measure vertical

displacements. Many other approaches have also been suggested, such as the installation of seafloor inclinometers, repetitive SONAR mapping, or fiber optic deformation measurement [BÜR 14].

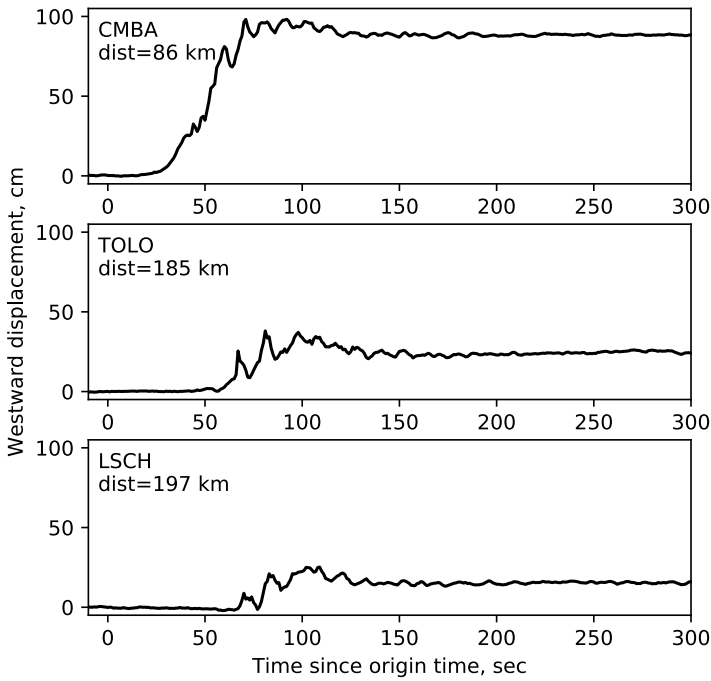

Figure 2.4. *High-frequency GNSS displacements during the 2015 Illapel earthquake in Chile ($M_W = 8.3$). The westward displacements are presented for three GPS stations at various epicentral distances (indicated in each case). The time-series sampled at 1 Hz were obtained at the Jet Propulsion Laboratory using the GIPSY-OASIS code in Precise Point Positioning mode (data processed by S. Owen, A. Moore and M. Simons)*

Over the last decade, there have also been significant efforts to obtain GNSS measurements sampled at higher frequency, that is, $\geq$1 Hz, [LAR 03]. With such sampling, these measurements correspond, in reality, to seismograms but there are three main differences: (1) high-rate GNSS data directly measures the ground displacement, which eliminates the problem of the integration of seismological data; (2) there is no waveform clipping (unlike conventional seismograms); (3) GNSS stations are much less sensitive to seismological data (which limits their use to the largest earthquake at small epicentral distances). An example of high-rate GNSS data is presented in Figure 2.4 for the 2015 Illapel earthquake (Chile, $M_W = 8.3$). We can clearly see the superimposition of the dynamic wave field (short period oscillations)

and the static displacement (long-period ramp). These data are very useful in the near field as it yields information on both the final slip and the rupture time history.

2.2.3. *Satellite and aerial imaging*

Data from satellite and aerial imaging has considerably improved our view of the displacement field associated with active faults. Satellite data are especially useful as it gives us a global view of the surface deformation, even in regions that are poorly equipped with instruments. These imaging methods are based on the combination of satellite or aerial images acquired before and after the earthquake being studied. In addition to the co-seismic signal, these measurements may contain a non-negligible part of inter- and post-seismic signals along with displacements induced by aftershocks (see Introduction and Chapter 3).

Radar interferometry is particularly useful to measure the displacement field generated by earthquakes [MAS 93, SIM 07]. This approach is based on the use of two SAR (Synthetic-Aperture Radar) images taken before and after an earthquake. The SAR images are obtained by emitting a series of electromagnetic pulses from a lateral antenna on a satellite or airborne system [SIM 07]. The echoes of each pulse are combined to obtain an image of the observed zone. By measuring the phases differences for each point captured before and after an earthquake, it is possible to generate a map of the co-seismic displacement in the line-of-sight of the satellite. This method is commonly called Interferometric Synthetic-Aperture Radar (InSAR). It must be noted that when the displacement is too large, InSAR data suffers from a loss of coherence, which can sometimes affect measurements in the vicinity of the rupture. Many sources of noise may also contaminate InSAR data. In particular, the atmosphere and ionosphere can induce propagation delays in the SAR signal resulting in phase shifts in the interferogram (e.g. due to variations in tropospheric water vapor content). The amplitude of these errors can be large and can sometimes even exceed the tectonic signal. While the ionospheric effect is more difficult to estimate, several techniques have been developed to evaluate the signal originating in the troposphere and to correct for these effects in the interferogram (e.g., [JOL 11]). Another source of noise is due to the poor knowledge of the satellite orbit, inducing a large-wavelength signal in the image. An orbital correction can thus be estimated to limit the impact on slip models [SIM 07].

Figure 2.5 shows an example of an InSAR image of the 1992 Landers earthquake ($M_W = 7.2$). This was the first earthquake imaged using radar interferometry [MAS 93]. The image is dominated by the co-seismic displacement associated with the mainshock, but also includes 2 days of post-seismic deformation as well as an aftershock of magnitude $M_W = 6.5$, which occurred a few hours after the mainshock (in the southern part of the image).

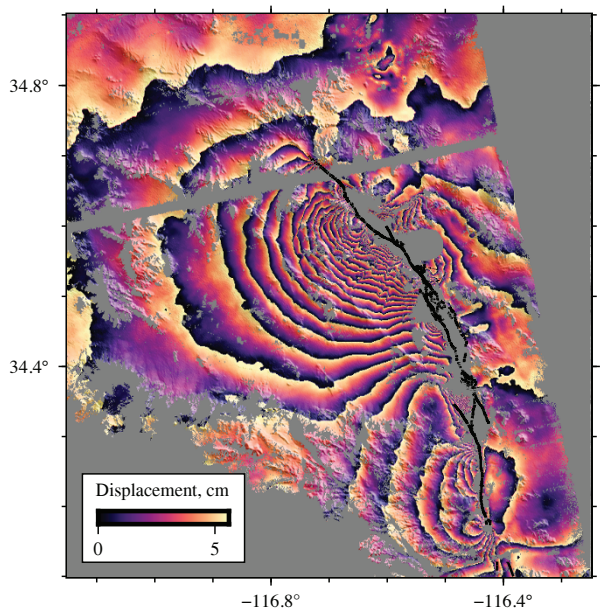

Figure 2.5. *Interferogram showing the deformation associated with the 1992 Landers earthquake (California, $M_W = 7.2$). These data have been obtained from two SAR images acquired by the ERS-1 satellite in an ascendant orbit on May 26 and June 30, 1992 (see [GOM 18a]). The colors indicate the displacement measured in the satellite's line-of-sight. The phase was unwrapped and then re-wrapped at 5.17 cm per fringe. The fault trace of the Landers earthquake is shown in black. For a color version of this figure, see www.iste.co.uk/rolandone/seismic.zip*

Another widely used approach is the correlation of images taken before and after an earthquake. These images may correspond to optical satellite images [AVO 14], aerial photographs [GOM 18a] or again to SAR amplitude images [SIM 07]. Unlike with SAR, which illuminates the zone under study, cloud cover is a limiting parameter when optical images are used. Although this method is not very sensitive to atmospheric disturbances, the main difficulties are due to the co-recording of two images along with orbital nuisances that may affect one or both images. The correlation of images is a method that is complementary to InSAR as it allows horizontal displacements and can also provide measurements close to faults, where InSAR often suffer from incoherent phase returns.

2.2.4. *Tsunami data*

Subduction earthquakes can generate large displacements of the seafloor. Such large seafloor motions result in a change of the sea-level with respect to its equilibrium,

thus creating tsunami waves. Tsunami data are therefore a significant asset as they provide important information on the seafloor displacements, where few observations are available.

Tsunami data are measured by estimating variations in height of the ocean surface. From the 2000s onwards, a network of Deep-ocean Assessment and Reporting of Tsunamis (DART) buoys has been deployed in the open sea by the National Oceanic and Atmospheric Administration (NOAA). These buoys transmit real-time recordings from a pressure sensor placed on the seafloor to estimate variations in the height of the water column. Tsunamis can also be recorded on the coast using tide gauges, providing data which are generally more sensitive to local bathymetry. Other tools can also be used. In 2004, for example, the Jason altimetry satellite was able to measure the tsunami generated by the Sumatra-Andaman earthquake ($M_W = 9.0$, [SLA 08])

2.3. The forward problem

We will now introduce the formulation to relate the earthquake source to surface observations (listed in section 2.2). We consider that a seismic rupture corresponds to a displacement discontinuity $\Delta\mathbf{u}(\boldsymbol{\xi}, \tau)$ over a duration T through one or more faults corresponding to a surface denoted by Σ. The function $\Delta\mathbf{u}(\boldsymbol{\xi}, \tau)$ thus describes the slip over time (τ) and space ($\boldsymbol{\xi}$) on the considered fault (see Figure 2.6). It is also assumed that over the considered timescale, the medium behaves in a linear elastic manner. The displacement discontinuity $\Delta\mathbf{u}(\boldsymbol{\xi}, \tau)$ over the fault Σ may thus be related to the observed displacement $\mathbf{u}(\mathbf{x}, t)$ via the following expression:

$$u_i(\mathbf{x}, t) = \int_0^T d\tau \int_\Sigma \Delta u_j(\boldsymbol{\xi}, \tau)\, c_{jkpq}(\boldsymbol{\xi})\, \nu_k(\boldsymbol{\xi})\, G_{ip,q}(\mathbf{x}, t; \boldsymbol{\xi}, \tau)\, d\Sigma \qquad [2.3]$$

where G_{ip} is the Green's function describing the displacement component i at the receiver at $(\mathbf{x}, t)$ due to an impulse force at $(\boldsymbol{\xi}, \tau)$ acting in the direction p. The index q in $G_{ip,q}$ indicates the derivative of the Green's function G_{ip} with respect to direction ξ_q. In this equation, we also have the elastic constants c_{ijpq} and the normal to the fault surface $\boldsymbol{\nu}(\boldsymbol{\xi})$. We will restrict ourselves here to the case where the displacement discontinuity $\Delta\mathbf{u}(\boldsymbol{\xi}, \tau)$ is perpendicular to $\nu(\boldsymbol{\xi})$. For more details on this representation of the seismic source, the reader can refer to Chapters 2 and 3 in [AKI 02]. Equivalently, we can rewrite equation [2.3] as:

$$u_i(\mathbf{x}, t) = \int_0^T d\tau \int_\Sigma \Delta \dot{u}_j(\boldsymbol{\xi}, \tau)\, c_{jkpq}(\boldsymbol{\xi})\, \nu_k(\boldsymbol{\xi})\, H_{ip,q}(\mathbf{x}, t; \boldsymbol{\xi}, \tau)\, d\Sigma \qquad [2.4]$$

where $\Delta\dot{\mathbf{u}}$ is the slip velocity and $H_{ip,q}$ is the Earth response to a step function:

$$H_{ip,q}(\mathbf{x}, t; \boldsymbol{\xi}, \tau') = \int_0^{\tau'} G_{ip,q}(\mathbf{x}, t; \boldsymbol{\xi}, \tau)\, d\tau. \qquad [2.5]$$

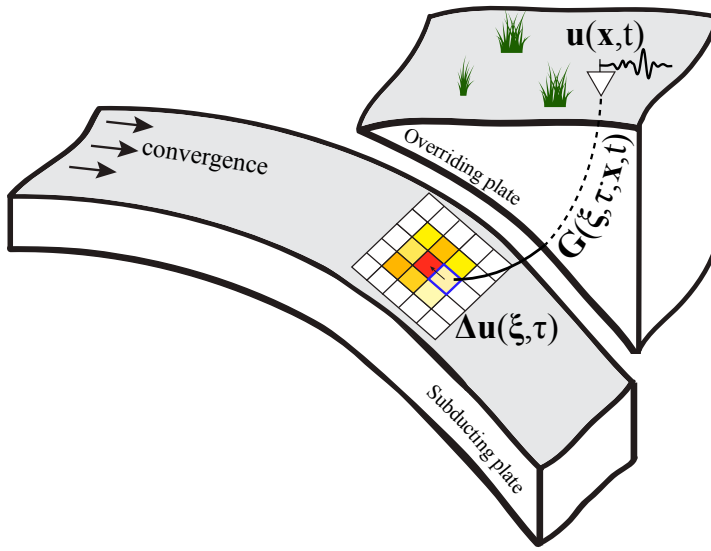

Figure 2.6. *Forward problem in the case of a subduction earthquake. In this example, the fault is spatially discretized with rectangular sub-faults (here colored according to the amplitude of slip). The slip distribution $\Delta\mathbf{u}(\boldsymbol{\xi},\tau)$ in space ($\boldsymbol{\xi}$) and in time (τ) is linked to surface observations $\mathbf{u}(\mathbf{x},t)$ using the Green's function $\mathbf{G}(\mathbf{x},t;\boldsymbol{\xi},\tau)$ as indicated in equation [2.3]. Figure modified as per [GOM 18c]. For a color version of this figure, see www.iste.co.uk/rolandone/seismic.zip*

We wish to describe slip distribution in time and space. This is done by parameterizing the slip velocity by decomposing it over N_s spatial basis functions in the following manner [IDE 07]:

$$\Delta\dot{u}_i(\xi,\tau) = \sum_{j=1}^{N_s} p^j\, \hat{u}_i^j(\tau)\, \phi^j(\xi)\, h^j(\xi,\tau) \qquad [2.6]$$

where we define:

– $\Delta\dot{u}_i$ the ith component of the slip velocity vector on the fault;

– $\phi^j(\xi)$ the jth spatial basis function associated with the coefficient p^j;

– p^j a coefficient whose dimension is the product of slip and area;

– $h^j(\xi,\tau)$ a function describing the temporal evolution of the rupture;

– $\hat{u}_i^j(\tau)$ a unit vector representing slip direction at time τ.

The functions $\phi^j(\xi)$ and $h^j(\xi,\tau)$ are normalized so that $\int\int_\Sigma \phi^j(\xi)d\Sigma(\xi) = 1$ and $\int_{-\infty}^{+\infty} h^j(\xi,\tau)\,d\tau = 1$.

A common choice for the spatial parameterization of slip is to discretize the fault with sub-faults in which final slip is considered constant. Rectangular sub-faults (as in Figure 2.6) or triangular sub-faults are commonly used in the literature. In previous equations, we thus define $\phi^j(\mathbf{x})$ as a boxcar function on the fault surface. For the jth sub-fault, we then have

$$\begin{aligned} &\phi^j(\xi) = 1/\Sigma^j \text{ when } \xi \in \Sigma^j \\ &\phi^j(\xi) = 0 \text{ otherwise} \end{aligned} \qquad [2.7]$$

where Σ^j corresponds to the area of the sub-fault j. In this case, the coefficients p^j correspond directly to the product of the slip and the area of each sub-fault, which is commonly referred to as "seismic potency". Alternatively, one may define $\phi^j(\xi) = 1$ in Σ^j so that p^j corresponds directly to average slip in the j-th subfault.

2.3.1. *The static case: modeling geodetic data*

If we are only interested in the final slip distribution, we can use co-seismic geodetic data, which is only sensitive to static slip. For moderate sized earthquakes, this also includes tsunami data, as these usually have low sensitivity to rupture history. Earthquakes of magnitude $M_W > 8$ have a long rupture duration ($T > 1$ min), which must generally be taken into account when modeling tsunami data. Static data are modeled by integrating previous equations over time up to the rupture duration T. We then obtain:

$$\Delta u_i(\xi) = \sum_{j=1}^{N_s} p^j\, \hat{u}_i^j\, \phi^j(\xi) \qquad [2.8]$$

where $\hat{u}_i^j$ represents the final direction of slip over the fault. It is then possible to decompose the slip vector into two components:

$$\Delta u_i(\xi) = \sum_{j=1}^{N_s} (p^{j1} v_i^1 + p^{j2} v_i^2)\, \phi^j(\xi) \qquad [2.9]$$

where p^{j1} and p^{j2} are the components of $p^j \hat{u}_i^j$ in the direction of the two unit orthogonal vectors $\mathbf{v}^1$ and $\mathbf{v}^2$. For example, $\mathbf{v}^1$ and $\mathbf{v}^2$ can correspond to directions

along the fault dip and along the fault strike. By replacing this formulation in equation [2.3], we obtain:

$$u_i(\mathbf{x}) = \sum_{l=1}^{N_s} (p^{l1} v_j^1 + p^{l2} v_j^2)\, \mathcal{G}_{ij}^l(\mathbf{x}) \qquad [2.10]$$

where:

$$\mathcal{G}_{ij}^l(\mathbf{x}) = \int\int_{\Sigma} \phi^l(\xi)\, c_{jkpq}(\xi)\, \nu_k(\xi)\, G_{ip,q}(\mathbf{x};\xi)\, d\Sigma(\xi) \qquad [2.11]$$

In the case where a sub-fault parameterization is used, we have:

$$\mathcal{G}_{ij}^l(\mathbf{x}) = \frac{1}{\Sigma^l} \int\int_{\Sigma^l} c_{jkpq}(\xi)\, \nu_k(\xi)\, G_{ip,q}(\mathbf{x};\xi)\, d\Sigma(\xi) \qquad [2.12]$$

where Σ^l corresponds to the area of the sub-fault l for which $\phi^l(\xi) = 1/\Sigma^l$ (see equation [2.7]). In the above equations, $\mathcal{G}_{ij}^l(\mathbf{x})$ describes the surface displacement (at $\mathbf{x}$) caused by a unit slip potency over sub-fault l. In a homogeneous half-space, this function can be calculated analytically [OKA 85]. For a heterogeneous medium, there are various tools to numerically calculate the response of a tabular medium (e.g., [ZHU 02]) or a 3D medium (e.g., [AAG 13]).

In the static case, it is thus possible to describe the final slip distribution using two slip potency components, p^{l1} and p^{l2}, for each sub-fault l (i.e. for each basis function ϕ^l). This is a linear problem:

$$\mathbf{d}_s = \mathbf{G}_s\, \mathbf{m}_s \qquad [2.13]$$

where $\mathbf{d}_s$ is the data vector containing geodetic observations, $\mathbf{m}_s$ corresponds to the model vector containing the coefficients p^{l1} and p^{l2}, and $\mathbf{G}_s$ is the matrix containing the functions $\mathcal{G}_{ij}^l(\mathbf{x})$ defined in equations [2.11] and [2.12].

2.3.2. *The kinematic case: modeling seismological data and high-frequency GNSS data*

If we wish to examine how ruptures propagate along faults, we must choose the parameterization that will describe the temporal evolution of slip. Traditionally, there are two approaches, which are detailed below.

2.3.2.1. *Linear approach using multiple time windows*

As depicted in Figure 2.7, a parameterization using multiple windows consists of expanding the function $\hat{u}_i^j(\tau)\, h^j(\xi,\tau)$ in equation [2.6] using a series of N_t coefficients:

$$\Delta\dot{u}_i(\xi,\tau) = \sum_{j=1}^{N_s}\sum_{k=1}^{N_t}(p^{jk1}v_i^1 + p^{jk2}v_i^2)\,\phi^j(\xi)\, f(\tau-(k-1)\Delta\tau-\tau_0(\xi)) \qquad [2.14]$$

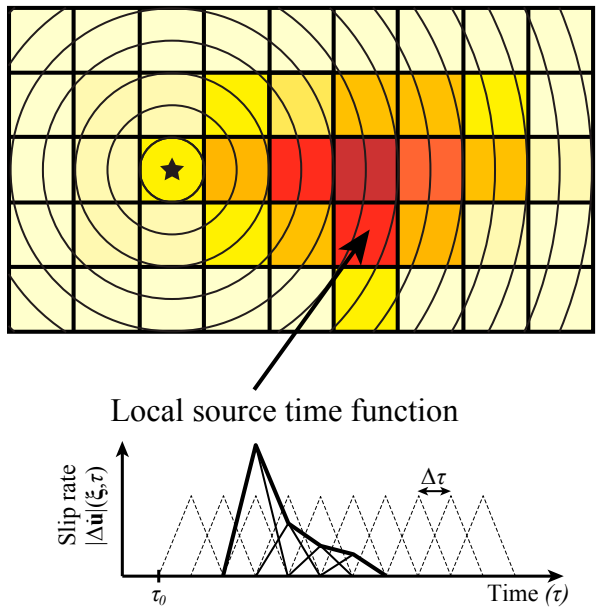

Figure 2.7. *Multiple time window parameterization. Example of a formulation based on the use of triangular basis functions in time and rectangular basis functions in space. The color of each sub-fault indicates the amplitude of slip. The minimum rupture times τ_0 are shown by time isocontours on the fault. The slip velocity is presented in black for one of the sub-faults after summing up the time functions (dotted triangles). For a color version of this figure, see www.iste.co.uk/rolandone/seismic.zip*

In this equation, $f(\tau)$ is a temporal basis function that is zero for $\tau < 0$ with unit integral and a finite support. A typical choice for $f(\tau)$ is a boxcar function or a triangular function [OLS 82]. These functions represent a series of windows all spaced apart by $\Delta\tau$ between a minimum rupture time $\tau = \tau_0(\xi)$ and a maximum rupture time $\tau = \tau_0(\xi) + (N_t - 1)\Delta\tau$. This parameterization thus decomposes the slip velocity

$\Delta\dot{\mathbf{u}}$ into a series of coefficients p^{jkl} associated with the lth direction of slip velocity over the jth spatial basis function, and a time window offset by $(k-1)\Delta\tau + \tau_0(\xi)$ (see Figure 2.7).

Substituting this equation in [2.3] yields an expression that is quite similar to the static case. By considering a rectangular function $\phi^j(\xi)$ for the jth sub-fault and an initial rupture time $\tau_0(\xi \in \Sigma^j) = \tau_0^j$:

$$u_i(\mathbf{x},t) = \sum_{l=1}^{N_s}\sum_{k=1}^{N_t}(p^{lk1}v_j^1 + p^{lk2}v_j^2)\,\mathcal{G}_{ij}^{lk}(\mathbf{x}, t-(k-1)\Delta\tau - \tau_0^j) \qquad [2.15]$$

with:

$$\mathcal{G}_{ij}^{lk}(\mathbf{x},t) = \frac{1}{\Sigma^l}\int_0^T d\tau \int\int_{\Sigma^l} f(\tau)\, c_{jkpq}(\xi)\, \nu_k(\xi)\, H_{ip,q}(\mathbf{x},t;\xi,\tau)\, d\Sigma(\xi) \qquad [2.16]$$

As in the static case, we obtain a linear problem:

$$\mathbf{d}_k = \mathbf{G}_k\mathbf{m}_k \qquad [2.17]$$

where $\mathbf{d}_k$ is the data vector, $\mathbf{m}_k$ includes the coefficients p^{jkl} and $\mathbf{G}_k$ is the matrix containing the waveforms calculated for each basis function in space and in time (see equation [2.16]).

This parameterization is often used as it results in a system of linear equations that can be resolved using conventional approaches such as the least squares method. The multiple time window model is also advantageous because it allows some flexibility in the slip time history. However, one major drawback of this formulation is that it relies on a large number of parameters to be estimated. For large earthquakes occurring over large faults, with long rupture durations, there can easily be several thousands of parameters. To reduce the dimension of the problem, we generally consider a limited number of time windows starting from a minimum rupture time $\tau_0(\xi) = |\xi - \xi_0|/V_R^{max}$, determined by a rupture velocity V_R^{max} and the position of the hypocenter ξ_0 on the fault (which is fixed *a priori*).

2.3.2.2. *Nonlinear approach*

In the nonlinear approach to kinematic inversion, rupture times are treated as parameters to be determined. We thus have:

$$\Delta\dot{u}_i(\xi,\tau) = \sum_{j=1}^{N_s}(p^{j1}v_i^1 + p^{j2}v_i^2)\,\phi^j(\xi)\, f(\tau-\tau^j, r^j) \qquad [2.18]$$

with:

– $f(\tau, r)$ being a function that is zero for $\tau < 0$ and $\tau > r$ and with unit integral;

– τ^j corresponding to the rupture time for sub-fault j (or the function ϕ^j);

– r^j is the local duration of slip, called "rise-time".

In the nonlinear approach, the shape of the local source function $f(\tau, r)$ is identical for all sub-faults (unlike the multiple time window linear approach). It is possible to use different shapes for the function $f(\tau, r)$: boxcar and triangular functions are the typical choices (see Figure 2.8). It is also possible to use expressions that best represent the rupture dynamic (e.g., the Yoffe function depicted in Figure 2.8, [TIN 05b]).

By integrating this parameterization into equation [2.3], we obtain a nonlinear forward problem:

$$\mathbf{d}_k = \mathbf{G}_k(\mathbf{m}_k) \qquad [2.19]$$

In this equation, the model vector $\mathbf{m}_k$ includes the coefficients p^{jl}, the rise time r^j and rupture time τ^j. $\mathbf{G}_k$ represents the nonlinear function that relates these parameters to the data vector $\mathbf{d}_k$. Some approaches describe the rupture velocity V_R^j in each sub-fault instead of the rupture time τ^j (e.g., [MIN 13]). The forward calculation $\mathbf{G}_k(\mathbf{m}_k)$ then includes the solution to the eikonal equation

$$|\nabla \tau^j| = 1/V_R^j \qquad [2.20]$$

to derive the rupture times τ^j (with $\tau^j = 0$ at the hypocenter of the earthquake) from the rupture velocities V_R^j. This kind of approach is particularly useful to impose the causality of the rupture front.

A nonlinear parameterization allows us to significantly reduce the dimension of the problem. Using this formulation, the number of parameters is $4 \times N_s$, which is generally much lower than the $2 \times N_s \times N_t$ parameters used in the multiple time window approach (see equation [2.15]). A major drawback is the nonlinear nature of the forward problem, which complicates the solution of the inverse problem and may lead to the existence of local minima.

2.3.3. *Computing the Green's functions*

The formulations of the forward problem given above are based on the spatial derivatives of the Green's functions (i.e., $G_{ip,q}$ and $H_{ip,q}$ in equations [2.3] and [2.4]), which must be calculated at every point of the fault. Different strategies may be used for that purpose depending on the parameterization and data used.

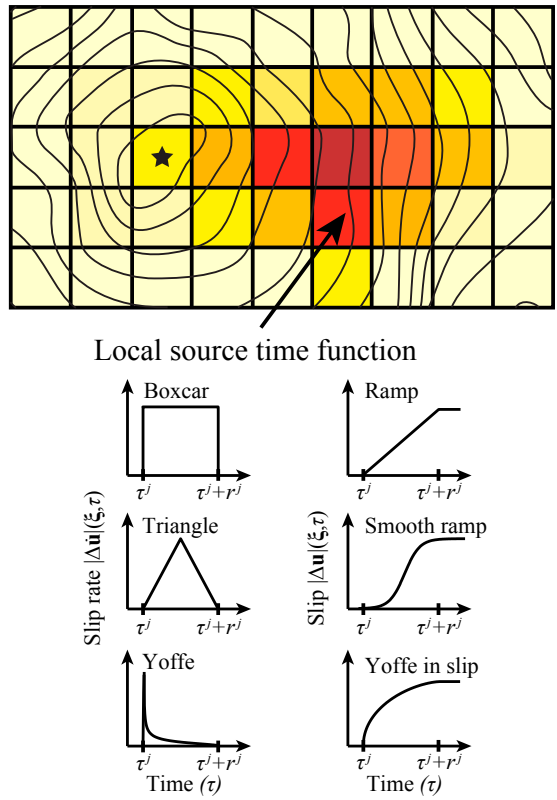

Figure 2.8. *Nonlinear parameterization: Nonlinear formulation where the temporal evolution of slip is parameterized with a rupture time τ^j and a rise time r^j. We consider a sub-fault spatial parameterization where the color indicates the amplitude of the slip. The rupture times are indicated on the fault using isocontours. Different choices for the function $f(\tau, r)$ are presented below in terms of slip velocity on the left (boxcar, triangular and Yoffe functions) with their equivalent in slip on the right (linear ramp, smooth ramp, Yoffe function in slip). For a color version of this figure, see www.iste.co.uk/rolandone/seismic.zip*

As described in section 2.3.1 for the static case, there are analytical solutions to calculate the Green's functions in a homogeneous half-space [OKA 85]. There are also different numerical tools to simulate the static displacements in a 2D or 3D medium [ZHU 02, AAG 13]. When tsunami data is used, these static Green's functions must be coupled with models describing tsunami propagation for a given displacement field on the seafloor [SAT 07]. Since the tsunami wavelength is generally much greater than the depth of the water and its amplitude is small compared to

the ocean depth in open sea, tsunami modeling is usually carried out by considering approximations called “shallow water” and “small-amplitude wave” conditions. One of the most popular codes based on these approximations is COMCOT (COrnell Multi-grid COupled Tsunami Model [LIU 98]). Although this code is well suited to model DART data in the open ocean, it is generally not appropriate for coastal tide-gauge data, for which the small-amplitude wave hypothesis is often not valid. In addition, dispersive effects related to the elasticity of the seafloor and to variations in water density are generally neglected [TSA 13]. These effects can cause delays up to several minutes in tsunami propagation. Codes have been developed to model these effects [ALL 14] and it is also possible to apply first-order corrections to the travel time [TSA 13] or to the oceanic depth [INA 13].

The modeling of seismological data is generally based on the simulation of waveforms for a tabular medium. Teleseismic data are generally modeled using the propagator matrix method coupled with ray theory [BOU 76, KIK 91]. The teleseismic P and S waves are thus modeled by considering the tabular media at the source, at the receivers and at the points of reflection of PP waves if these phases are used. To predict seismic waveforms at near field distances, it is common to use methods based on the wavenumber integration approach [BOU 81], which is available in several widely distributed codes (e.g. [HER 13]). It is increasingly more common in studying seismic sources to take into account the 3D structure [HJÖ 09]. This can be done using different 3D waveform simulation methods, such as the finite difference method or spectral elements method [KOM 99]. Although it is important to consider lateral heterogeneities to improve the characterization of the source, detailed models of the 3D structure are not always available. In order to minimize the impact of any imprecision in the Earth model, certain approaches are based on the empirical calibration of Green’s functions [WEI 13]. A good alternative is to use empirical Green’s functions (EGF), which consists of using recordings of small earthquakes that are co-located with the earthquake being studied [HAR 78]. Nonetheless, EGF coverage is not always sufficient to cover the entire fault and this approach is based on the hypothesis that the earthquake being studied and the EGFs are associated with the same focal mechanism. The question of modeling the seismic wave field (especially at teleseismic distances) is described in detail in Chapter 1.

Imprecisions in the velocity model used to calculate Green’s functions can have a large impact on slip inversion results. As described in the following section, the uncertainty associated with the Earth model can be taken into account in the inverse problem. In order to mitigate the impact of inaccuracies in the velocity model, a common practice is to align predicted and observed wave arrivals to minimize differences between the corresponding seismic phases. However, this approach remains complex in the near field since S wave arrivals often overlap with P waves for large earthquakes. A poor alignment of P and/or S arrivals may have a considerable impact on the inversion result and may partly explain the variability of

certain source models. It is therefore essential to use a reliable velocity model to limit its impact on the final result.

2.4. The inverse problem

The inverse problem consists of finding a slip model $\mathbf{m}$ given the data $\mathbf{d}_{\text{obs}}$, given our formulation of the forward problem and our prior knowledge of the model. There are many books describing the different approaches used to solve inverse problems. We present here only a few approaches to introduce regularized optimization and Bayesian inference for slip inversion. For further details, the reader can for example refer to [TAR 05].

Here, we consider approaches where an L^2 norm is used to characterize data residuals. We define the data misfit function as:

$$\chi(\mathbf{m}) = \|\mathbf{d}_{\text{obs}} - \mathbf{G}(\mathbf{m})\|_2^2 \qquad [2.21]$$

The data vector $\mathbf{d}_{\text{obs}}$ is generally constructed by concatenating seismic waveforms and other observations (geodetic data, tsunami waveforms, etc.). The problem can also be solved by representing seismological data in the frequency domain. However, as we will see in section 2.4.3, modeling data in the frequency domain is theoretically identical to modeling it in the time domain [IDE 07].

Since data is affected by measurement errors and our limited knowledge of the Earth structure, the solution to the inverse problem is usually non-unique. There are usually several slip models associated with a similar data misfit $\chi(\mathbf{m})$. Even when the uncertainty is small, the use of data collected at the Earth's surface to characterize complex ruptures at depth is a fundamentally ill-posed problem. For example, if we consider the linear Gaussian case $\mathbf{G}(\mathbf{m}) = \mathbf{G}\mathbf{m}$, considering independent and identically distributed data, the minimization of $\chi(\mathbf{m})$ leads to the least squares solution:

$$\widetilde{\mathbf{m}} = (\mathbf{G}^t\mathbf{G})^{-1}\mathbf{G}^t\mathbf{d}_{\text{obs}} \qquad [2.22]$$

where the superscript t denotes the transposition of a matrix. During slip inversion, the matrix $\mathbf{G}^t\mathbf{G}$ is generally poorly conditioned such that there exists an infinite number of solutions $\widetilde{\mathbf{m}}$ minimizing the data misfit. This variability in the inversion results is depicted in Figure 2.9 in the case of the 1999 Izmit (Turkey) earthquake ($M_W = 7.6$). The 1999 Izmit earthquake is not an isolated case. For many events, small differences in the data set or in the formulation of the problem lead to large differences in the slip distributions [MAI 12]. A widely used practice to mitigate the non-uniqueness of the solution is to regularize the inversion to obtain a well-conditioned optimization

problem. An alternative approach is to characterize the ensemble of plausible models that fit the observations while considering the prior knowledge we already have on the rupture. Both of these approaches are described below.

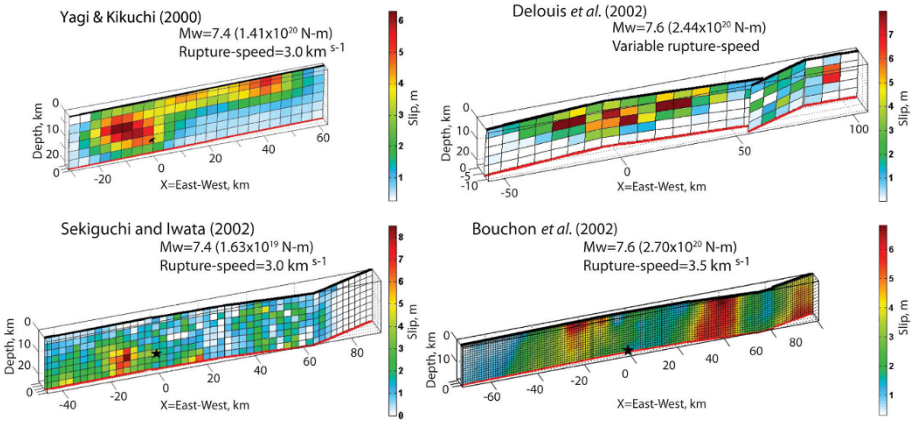

Figure 2.9. *An illustration of the variability in kinematic source models: Slip inversion results obtained by different teams for the 1999 Izmit earthquake. These source models are available through the SRCMOD database [MAI 12]. Figure modified from [DUP 14]. For a color version of this figure, see www.iste.co.uk/rolandone/seismic.zip*

2.4.1. *Tikhonov regularization approach*

Tikhonov regularization is a widely used regularization method used to solve ill-posed inverse problems. This method is also known as the "ridge regression" method. To limit the non-uniqueness of the solution, a regularization term is introduced into the minimization. The solution is then given by:

$$\widetilde{\mathbf{m}} = \arg\ \min(\|\mathbf{d}_{\text{obs}} - \mathbf{G}(\mathbf{m})\|_2^2 + \lambda^2 \|\mathbf{\Gamma}\mathbf{m}\|_2^2) \qquad [2.23]$$

where $\mathbf{\Gamma}$ is the Tikhonov matrix and λ is a damping parameter. In the above equation, "arg $\min(f(\mathbf{m}))$" defines the value of $\mathbf{m}$ minimizing the cost function $f(\mathbf{m})$. The matrix $\mathbf{\Gamma}$ can take different forms depending on which model characteristics we wish to emphasize. A conventional choice is $\mathbf{\Gamma} = \mathbf{I}$, which favors models with a low L_2 norm (e.g., [OLS 82]). In the context of slip inversion, this regularization may however bias the models toward low moment magnitudes (by artificially reducing the amplitude of fault slip). Another popular choice is the spatial Laplacian operator $\mathbf{\Gamma} = \nabla^2$, which consists of minimizing the model's "roughness" in order to obtain a relatively smooth slip distribution over the fault.

We now consider a linear case $\mathbf{d} = \mathbf{Gm}$ as in the static case (section 2.3.1) or when using a multiple time window parameterization (section 2.3.2.1). To deal with the inverse problem, consider the weighted case $\mathbf{Wd} = \mathbf{WGm}$ with $\mathbf{W}$ being a diagonal matrix whose elements W_{ii} give the weight associated with the ith data sample. Equation [2.23] then becomes:

$$\widetilde{\mathbf{m}} = (\mathbf{G}^t\mathbf{W}^2\mathbf{G} + \lambda^2\boldsymbol{\Gamma}^t\boldsymbol{\Gamma})^{-1}\mathbf{G}^t\mathbf{W}^2\mathbf{d}_{\text{obs}} \quad [2.24]$$

This equation is not used much in practice as it often leads to solutions that incorporates slip in the negative direction (i.e. in the direction opposite to the average slip over the fault). Although the existence of such a phenomenon is debated, it is difficult to imagine such a radical reversal in the slip direction in an stressed environment like the Earth's crust. To limit such oscillations in the model, we then integrate positivity constraints: the minimization of equation [2.23] can then be solved using optimization approaches like non-negative least squares, conjugate gradients or simulated annealing [TAR 05].

The solution to equation [2.23] is a trade-off between data misfit $\|\mathbf{d}_{\text{obs}} - \mathbf{G}(\mathbf{m})\|_2^2$ and model regularization $\|\boldsymbol{\Gamma}\mathbf{m}\|_2^2$ whose relative weight is controlled by the damping parameter (λ). The choice of λ thus has a direct impact on the solution. As illustrated in Figure 2.10, a high value of λ will lead to a very smooth model while a lower value of λ will favor a better fit to the data. The most widely used approach consists of using an *L*-curve representing the data misfit $\|\mathbf{d}_{\text{obs}} - \mathbf{G}(\mathbf{m})\|_2^2$ as a function of the model regularization $\|\boldsymbol{\Gamma}\mathbf{m}\|_2^2$ obtained for various values of λ. The idea is then to choose a value of λ at the corner of the curve (offering an acceptable compromise). This choice however remains quite arbitrary and has a significant impact on the resulting slip model (see [CAU 10]).

2.4.2. *Bayesian approach*

The Tikhonov regularization is a convenient tool to quickly solve slip inversion as an optimization problem. However, this approach is based on model damping, which has no real physical basis. Furthermore, this regularization can also significantly impact the solution (see Figure 2.10). The Bayesian approach is a different way to tackle the non-uniqueness of the solution. The idea is to characterize the whole set of models that can fit the data taking into account the different sources of uncertainty and our *a priori* knowledge of the model. The resulting model ensemble is then considered to be the solution to the inverse problem.

This approach is based on Bayes' theorem to characterize the posterior probability density of the model $\mathbf{m}$ given our observations $\mathbf{d}_{\text{obs}}$:

$$p(\mathbf{m}|\mathbf{d}_{\text{obs}}) = \frac{p(\mathbf{d}_{\text{obs}}|\mathbf{m})p(\mathbf{m})}{p(\mathbf{d}_{\text{obs}})} \quad [2.25]$$

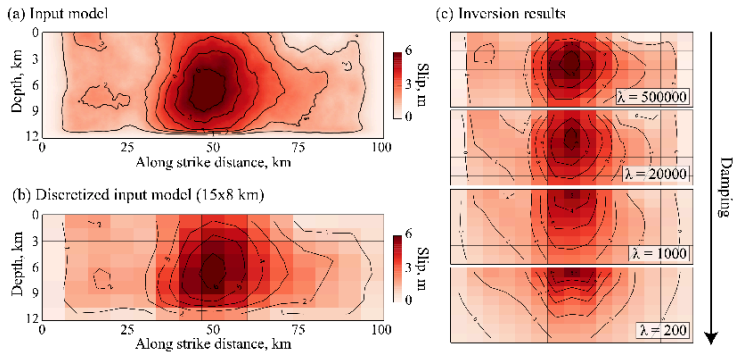

Figure 2.10. *Impact of regularization on the slip models: (a) Synthetic model describing a heterogeneous slip distribution. (b) Synthetic model discretized into rectangular subfaults of 15 x 8 km. (c) Result of the inversion considering an increasing level of damping. This test was carried out assuming a regularly spaced network of GNSS stations every 10 km around the fault. The smoothing is controlled by the damping λ as indicated in equation [2.23]. For a color version of this figure, see www.iste.co.uk/rolandone/seismic.zip*

In this equation, $p(\mathbf{m})$ is the probability distribution representing our *a priori* knowledge of the model $\mathbf{m}$. The term $p(\mathbf{d}_{\text{obs}}|\mathbf{m})$ is the data likelihood, representing the plausibility of our observations $\mathbf{d}_{\text{obs}}$ for different models $\mathbf{m}$. Although the data likelihood is a function of $\mathbf{m}$, it is not a probability density on $\mathbf{m}$ (its integral over $\mathbf{m}$ is also not necessarily equal to one). The denominator in equation [2.25] is a normalization constant that can be defined as:

$$p(\mathbf{d}_{\text{obs}}) = \int p(\mathbf{d}_{\text{obs}}|\mathbf{m})p(\mathbf{m})d\mathbf{m} \qquad [2.26]$$

In a Bayesian framework, the solution to the problem is therefore the *a posteriori* probability distribution $p(\mathbf{m}|\mathbf{d}_{\text{obs}})$. This distribution characterizes the information on the model $\mathbf{m}$ given the observations $\mathbf{d}_{\text{obs}}$, the forward formulation of the problem $\mathbf{G}(\mathbf{m})$, the associated uncertainties and our hypotheses about the model. Formally, the forward problem can be rewritten by taking into account the associated uncertainties:

$$\mathbf{d}_{\text{obs}} = \mathbf{G}(\mathbf{m}) + \mathbf{e}_d + \mathbf{e}_p \qquad [2.27]$$

where $\mathbf{e}_d$ represents observational uncertainty (i.e. the measurement error) and $\mathbf{e}_p$ corresponds to the uncertainty associated with the forward problem (due to modeling inaccuracies). Although the uncertainty over a forward problem $\mathbf{e}_p$ is generally neglected, its amplitude may be greater than the data uncertainty $\mathbf{e}_d$. $\mathbf{e}_p$ may arise

from the imprecisions in the Earth model used to calculate the Green's function, from an over-simplistic fault geometry, or approximations during the parameterization of the rupture process (see section 2.3). The uncertainties $\mathbf{e}_d$ and $\mathbf{e}_p$ are commonly considered as Gaussian (a choice that can be justified through the principle of maximum entropy, given the corresponding covariances [JAY 03]). The likelihood function $p(\mathbf{d}_{\rm obs}|\mathbf{m})$ in equation [2.25] can thus be written as [TAR 05]:

$$p(\mathbf{d}_{\rm obs}|\mathbf{m}) = \frac{1}{(2\pi)^{N/2}|\mathbf{C}_\chi|^{1/2}} e^{-\frac{1}{2}[\mathbf{d}_{\rm obs}-\mathbf{G}(\mathbf{m})]^t \mathbf{C}_\chi^{-1}[\mathbf{d}_{\rm obs}-\mathbf{G}(\mathbf{m})]} \qquad [2.28]$$

where N is the number of observations (the size of the vector $\mathbf{d}_{\rm obs}$) and $\mathbf{C}_\chi$ is the covariance matrix, defined by:

$$\mathbf{C}_\chi = \mathbf{C}_d + \mathbf{C}_p \qquad [2.29]$$

where $\mathbf{C}_d$ and $\mathbf{C}_p$ are the covariance matrices associated with $\mathbf{e}_d$ and $\mathbf{e}_p$, respectively. By using this Gaussian form of the likelihood function, the deviation from the data is characterized by a norm, L^2, as in equation [2.21]. The covariance matrix $\mathbf{C}_d$ associated with the observational uncertainties $\mathbf{e}_d$ can take different forms depending on the data being considered. For example, in the case of seismological data, $\mathbf{C}_d$ characterizes the level of noise at each station as well as the temporal correlation for the filtered data (e.g., [DUP 12]). Different approaches have been developed to construct the covariance matrix, $\mathbf{C}_p$, associated with modeling uncertainties $\mathbf{e}_p$, in particular to account for inaccuracies in the Earth model [DUP 14] and the fault geometry [RAG 18].

Let us now consider the linear case (as in sections 2.3.1 and 2.3.2.1), with an *a priori* Gaussian of the form:

$$p(\mathbf{m}) = \frac{1}{(2\pi)^{M/2}|\mathbf{C}_m|^{1/2}} e^{-\frac{1}{2}(\mathbf{m}-\mathbf{m}_{\rm prior})^t \mathbf{C}_m^{-1}(\mathbf{m}-\mathbf{m}_{\rm prior})} \qquad [2.30]$$

where M is the number of model parameters (i.e. the size of the vector $\mathbf{m}$), $\mathbf{m}_{\rm prior}$ is the average prior model and $\mathbf{C}_m$ is the *a priori* covariance matrix. In this configuration, the posterior distribution is Gaussian [TAR 05]:

$$p(\mathbf{m}|\mathbf{d}_{\rm obs}) = \frac{1}{(2\pi)^{M/2}|\widetilde{\mathbf{C}}_m|^{1/2}} e^{-\frac{1}{2}(\mathbf{m}-\widetilde{\mathbf{m}})^t \widetilde{\mathbf{C}}_m^{-1}(\mathbf{m}-\widetilde{\mathbf{m}})} \qquad [2.31]$$

where $\widetilde{\mathbf{m}}$ is the posterior average model (also corresponding to the *maximum a posteriori* model) and $\widetilde{\mathbf{C}}_m$ is the posterior covariance, which are, respectively, written as:

$$\begin{aligned} \widetilde{\mathbf{m}} &= (\mathbf{G}^t\mathbf{C}_\chi^{-1}\mathbf{G} + \mathbf{C}_m^{-1})^{-1}(\mathbf{G}^t\mathbf{C}_\chi^{-1}\mathbf{d}_{\rm obs} + \mathbf{C}_m^{-1}\mathbf{m}_{\rm prior}) \\ \widetilde{\mathbf{C}}_m &= (\mathbf{G}^t\mathbf{C}_\chi^{-1}\mathbf{G} + \mathbf{C}_m^{-1})^{-1} \end{aligned} \qquad [2.32]$$

The linear Gaussian case is useful as it offers an analytical solution to the Bayesian formulation of the inverse problem. The term $\mathbf{C}_m^{-1}$ in equation [2.32] acts as a regularization term. It is interesting to note that by considering $\mathbf{m}_{\text{prior}} = \mathbf{0}$, $\mathbf{C}_\chi^{-1} = \mathbf{W}^2$ and $\mathbf{C}_m^{-1} = \lambda^2 \mathbf{\Gamma}^t \mathbf{\Gamma}$, we obtain the regularized least squares solution in equation [2.24]. In the linear Gaussian case, there is thus a clear link between the Bayesian formulation and the Tikhonov regularization. If the weighing matrix $\mathbf{W}$ is chosen in an ad hoc manner, the damping parameter λ can also be seen as the ratio between the *a priori* variance in the model and the uncertainty over the data. Furthermore, one of the pieces of information that we have *a priori* is the positivity of fault slip in a given direction (from long-term observations or from the slip orientation expected from the relative motion of the tectonic plates). Some of our parameters are thus associated with a non-Gaussian prior $p(\mathbf{m})$ (typically a uniform distribution defined to be positive), which prevents the use of equations [2.31] and [2.32]. Furthermore, there is no analytical form for $p(\mathbf{m}|\mathbf{d}_{\text{obs}})$ in the case of a nonlinear problem, like when we invert for rupture velocity and rise time when dealing with kinematic data (see section 2.3.2.2).

To solve the problem in the general (nonlinear and/or non-Gaussian) case, a sampling approach can be used. Bayesian sampling consists of generating a population of models that will be statistically distributed according to $p(\mathbf{m}|\mathbf{d}_{\text{obs}})$. The solution is thus composed of a set of models distributed with a probability density that is greater when these models fit the observations and are plausible with respect to the *a priori* information $p(\mathbf{m})$. The *a posteriori* distribution will be obtained by generating a large number of samples of models for which $p(\mathbf{m}|\mathbf{d}_{\text{obs}})$ is evaluated. Despite a high cost in terms of computation time, this approach is of interest for badly posed problems as it does not require the evaluation of the inverse of $\mathbf{G}$ (or of $\mathbf{G}^t\mathbf{G}$). Unlike what is described in equations [2.24] and [2.32], it is thus not necessary to regularize the inversion of $\mathbf{G}$ by smoothing the model or minimizing its L_2 norm. The prior information contained in $p(\mathbf{m})$ must include all physical constraints applicable to the model. Let us take the example of an earthquake for which we wish to find the fault slip distribution. If long-period seismic moment tensor solutions reveal that this is a strike-slip earthquake of magnitude 7, we can choose an *a priori* distribution for the slip in the rake direction such as $p(\mathbf{m}) = \mathcal{U}(-1m, 15m)$, that is, a uniform distribution between -1 and 15 m of slip. We do not expect to have more than 15 m of slip for this magnitude and the fault is forbidden from slipping more significantly in the opposite direction. All slip values between -1 and 15 m are, *a priori*, equiprobable. This choice of an *a priori* that gives very little information allows us to reduce the explored model space while still allowing the data to drive the posterior solution. This is one of the advantages of Bayesian sampling. For further information on Bayesian sampling for slip inversion, the reader can consult [MIN 13].

2.4.3. *Modeling data in the frequency domain or as wavelets*

In most slip inversion approaches, the data vector $\mathbf{d}_{\text{obs}}$ is constructed by concatenating seismological waveforms with other data sets (GNSS, InSAR, tsunami, etc.). The problem can also be solved by representing seismological data in the frequency domain [OLS 88, COT 95] or after wavelet transform [JI 02]. It is shown here that modeling seismological data in these different domains (time, frequency or wavelet) should lead to identical slip models [IDE 07].

We begin by rewriting the misfit function in equation [2.21] in the form:

$$\chi(\mathbf{m}) = [\mathbf{d}_{\text{obs}} - \mathbf{G}(\mathbf{m})]^t \, \mathbf{C}_\chi^{-1} \, [\mathbf{d}_{\text{obs}} - \mathbf{G}(\mathbf{m})] \qquad [2.33]$$

In the following, the inverse of the covariance matrix $\mathbf{C}_\chi$ can invariably be replaced by the weighing matrix $\mathbf{W}^2$ used in equation [2.24]. It must also be noted that $\chi(\mathbf{m})$ appears in the Gaussian likelihood function introduced in equation [2.28]. The Fourier transform or wavelet transform can be represented by a linear operator $\mathbf{T}$. We can then define:

$$\begin{aligned} \hat{\mathbf{d}}_{\text{obs}} &= \mathbf{T}\mathbf{d}_{\text{obs}} \\ \hat{\mathbf{G}}(\mathbf{m}) &= \mathbf{T}\mathbf{G}(\mathbf{m}) \end{aligned} \qquad [2.34]$$

In this equation, $\hat{\mathbf{d}}_{\text{obs}}$ and $\hat{\mathbf{G}}(\mathbf{m})$ correspond to the Fourier/wavelet transform of the data $\mathbf{d}_{\text{obs}}$ and predictions $\mathbf{G}(\mathbf{m})$ in the time domain. It is considered here that $\mathbf{T}$ is an orthonormal operator, such that:

$$\mathbf{T}^t\mathbf{T} = \mathbf{T}\mathbf{T}^t = \mathbf{I} \qquad [2.35]$$

where $\mathbf{I}$ is the identity matrix. This is indeed the case for the Fourier transform and also usually the case with the wavelet transforms commonly used in source inversion. The misfit function can thus be defined in the frequency/wavelet domain as:

$$\hat{\chi}(\mathbf{m}) = \left[\hat{\mathbf{d}}_{\text{obs}} - \hat{\mathbf{G}}(\mathbf{m})\right]^t \mathbf{C}_{\hat{d}}^{-1} \left[\hat{\mathbf{d}}_{\text{obs}} - \hat{\mathbf{G}}(\mathbf{m})\right] \qquad [2.36]$$

where $\mathbf{C}_{\hat{d}}$ is the frequency/wavelet covariance matrix that can be obtained from the covariance $\mathbf{C}_d$ in the time domain by using:

$$\mathbf{C}_{\hat{d}} = \mathbf{T}\mathbf{C}_d\mathbf{T}^t \qquad [2.37]$$

By inserting equations [2.34] and [2.37] into equation [2.36] and then using equation [2.35], it can be shown that:

$$\begin{aligned}\hat{\chi}(\mathbf{m}) &= \left[\mathbf{T}\mathbf{d}_{\text{obs}} - \mathbf{T}\mathbf{G}(\mathbf{m})\right]^t \left(\mathbf{T}\mathbf{C}_d\mathbf{T}^t\right)^{-1} \left[\mathbf{T}\mathbf{d}_{\text{obs}} - \mathbf{T}\mathbf{G}(\mathbf{m})\right] \\ &= \left[\mathbf{d}_{\text{obs}} - \mathbf{G}(\mathbf{m})\right]^t \mathbf{T}^t\mathbf{T}\mathbf{C}_d^{-1}\mathbf{T}^t\mathbf{T} \left[\mathbf{d}_{\text{obs}} - \mathbf{G}(\mathbf{m})\right] \\ &= \left[\mathbf{d}_{\text{obs}} - \mathbf{G}(\mathbf{m})\right]^t \mathbf{C}_d^{-1} \left[\mathbf{d}_{\text{obs}} - \mathbf{G}(\mathbf{m})\right] \\ &= \chi(\mathbf{m})\end{aligned} \quad [2.38]$$

The equality between the misfit functions $\chi(\mathbf{m}) = \hat{\chi}(\mathbf{m})$ for the same model $\mathbf{m}$ shows that the data inversion in the time domain or frequency domain theoretically lead to identical solutions. Of course, this is only valid if the covariance matrices $\mathbf{C}_{\widehat{d}}$ and $\mathbf{C}_d$ are statistically consistent (i.e. if equation [2.37] is true). Representing the data in frequency/wavelets makes it possible to easily associate different weights with different frequency bands [JI 02]. In practice, this is done by constructing $\mathbf{C}_{\widehat{d}}$ in the frequency domain. However, it is still possible to carry out the inversion in the time domain by using equation [2.37] to calculate the corresponding covariance matrix $\mathbf{C}_d$.

2.5. Characterization of the source and implications on the physics of earthquakes

The slip models obtained using the methods described above present certain generic properties that are actively debated in the literature. In this section, we will examine, in particular, the rupture propagation mode, the rupture velocity, the stress-drop and the energy partitioning of earthquakes.

An interesting property of kinematic models is that they generally show the existence of a slip pulse, corresponding to a narrow slipping band propagating on the fault with a width that is small with respect to the total rupture size [HEA 90]. This observation has important implications on the stress state and friction of faults. Figure 2.11 depicts an example in the case of the 2017 Ezgeleh earthquake in Iran ($M_W = 7.3$). This model shows that a slip pulse quickly appears: in less than 4 s and less than 7 km away from the epicenter (Figure 2.11d). If this pulse were controlled by the rupture size, we would get a rise time of $r = 0.5 \times W/V_R$, where W is the fault width [DAY 82]. Figure 2.11(b) shows that we systematically have $r < 0.5 \times W/V_R$, which indicates that the pulse appears before the rupture front reaches the edges of the fault. This is known as a self-healing slip pulse [HEA 90]. These narrow pulses can be caused by different factors such as the fault frictional properties, stress heterogeneities, or wave reflections in the low velocity zone around the fault [COC 94, PEY 01, HUA 11]. The existence of pulse-like ruptures also has implications in terms of seismic hazard and the generation of strong motions. In the case of the Ezgeleh earthquake, the high slip rate, short rise-time and strong directivity of the rupture toward the south seem to have exacerbated the damage to

the south of the hypocenter (see Figure 2.11c). These slip pulses can be difficult to stop as they involve large dynamic stresses at the rupture front. These ruptures can thus propagate in weakly loaded regions or re-rupture fault zones that were recently broken by another earthquake [VAL 14].

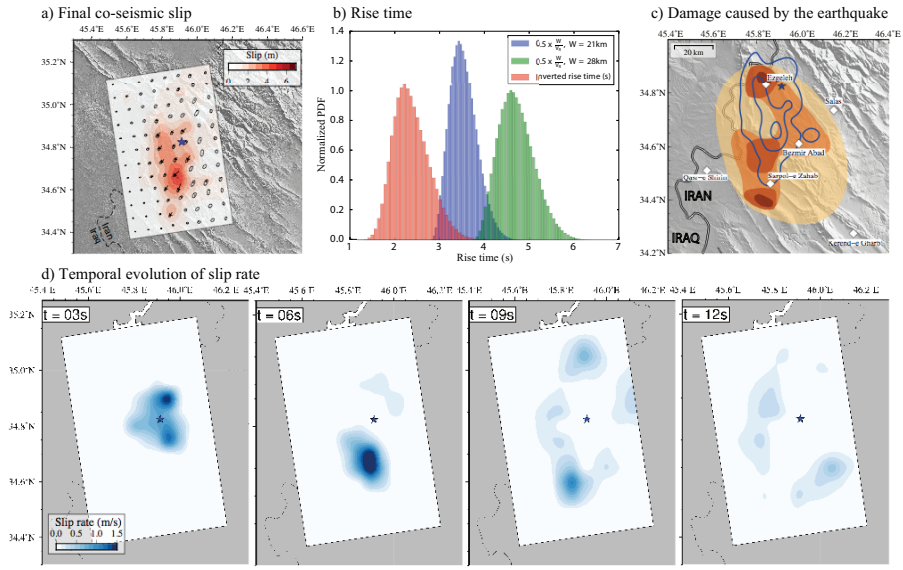

Figure 2.11. *Slip pulse during the 2017 Ezgeleh earthquake in Iran ($M_W = 7.3$). a) Final slip. The colors and arrows indicate slip amplitude and direction. The ellipses represent 95% of posterior uncertainties. The star indicates the location of the hypocenter. b) Comparison of the estimated rise time with the prediction by [DAY 82]. The histogram in red is the a posteriori distribution of rise-time r averaged along the rupture. The histograms in blue and green correspond to predictions according to $r = 0.5 \times W/V_R$ with V_R being the estimated rupture velocity along the rupture, and W being the width of the fault. Two cases are considered: $W = 21\,km$ (corresponding to three sub-faults) and $W = 28\,km$ (corresponding four sub-faults). c) Damage caused by the earthquake. The colors indicate the level of damage estimated by the Iranian geological department. The darkest colors indicate the most severe damage. The blue lines correspond to contour lines of the final slip distribution (every 1.5 m). (d) Evolution of the slip velocity over the fault 3, 6, 9 and 12 s after the origin time. Figure modified from [GOM 19]. For a color version of this figure, see www.iste.co.uk/rolandone/seismic.zip*

The rupture velocity V_R is also a parameter that can be extracted from kinematic models and which can provide interesting information on the rupture dynamics. However, V_R and the associated rupture times τ are often estimated with high uncertainty. Figure 2.12 depicts an example of the Bayesian kinematic model

obtained for the 2016 Pedernales earthquake ($M_W = 7.8$, Ecuador). We clearly see a tradeoff between rupture time τ and rise-time r with a negative correlation between the two parameters. This is due to the fact that the centroid time of the slip pulse is relatively well constrained, while band-pass filtered data have a limited sensitivity to the initial rupture time and to the local slip duration. While it is generally difficult to restrain the local rupture velocity, the average rupture speed is generally easier to characterize (especially if observations are available at small epicentral distances). Typically, the observed rupture velocities are of the order of 70% of the velocity of the S wave speed around the fault [IDE 07]. However, for certain earthquakes, we see rupture velocities that exceed the S wave velocities. This is theoretically possible for mode II ruptures, that is, when the fault slips in the same direction as the rupture propagation. In practice, these *supershear* ruptures were mainly observed for strike-slip earthquakes [BOU 08, SOC 19] but have also been reported for other kinds of focal mechanisms [ZHA 14].

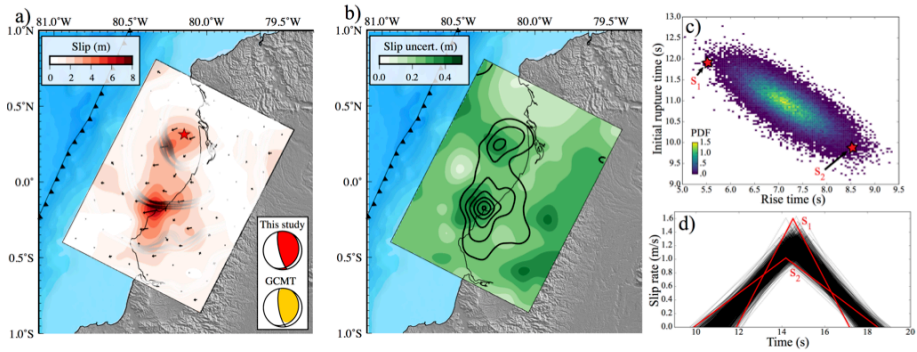

Figure 2.12. *Bayesian model of the 2016 Pedernales earthquake in Ecuador ($M_W = 7.8$). a) Final slip. The colors and arrows indicate the amplitude and direction of slip. The gray lines indicate the stochastic rupture fronts derived from the posterior ensemble of models and displayed at 10, 20 and 30 s. The red star indicates the hypocenter location. b) Final slip uncertainty. c) Marginal a posteriori distribution of rise-time and rupture time in the first slip asperity (located close to the epicenter). d) Corresponding posterior ensemble of local slip rate functions. The source time functions denoted s_1 and s_2 correspond to the rupture time and rise-time indicated by red stars in c). Figure modified from [GOM 18b]. For a color version of this figure, see www.iste.co.uk/rolandone/seismic.zip*

For periods smaller than 2 s (i.e. wavelengths smaller than $\sim$5 km), the heterogeneity of the medium and the rupture complexities produce waveforms that are too complex to be explained by simple models [KAN 04b]. In particular, the observation of complex waveforms at stations located very close to the source suggests significant heterogeneities in the rupture process [ZEN 94]. Given the use of

data filtered at low frequency and the spatial smoothing of slip distributions, many kinematic models inform us about the large wavelength distribution of fault slip. Moreover, sources of high-frequency radiation are not necessarily co-localized with zones with large slip on the fault. For example, the emission of high-frequency waves can be associated with variations in rupture velocity [MAD 77]. Dynamic damage caused by seismic ruptures around the fault may also explain part of the high-frequency content observed at short epicentral distances [THO 17]. At the level of the subduction zones, several studies report the existence of high-frequency sources in the deeper part of the seismogenic domain [SIM 11, LAY 15, GRA 15]. This observation potentially expresses an increased level of frictional and stress heterogeneity at depth [LAY 15].

The final slip distribution gives direct information on the stress drop caused by the rupture. The final slip distribution is thus commonly used to characterize the average drop in the static stress $\overline{\Delta\sigma}$ associated with an earthquake. A widely used approach in seismological is based on the seismic moment M_0 and the rupture area A:

$$\overline{\Delta\sigma} = C\frac{M_0}{A^{3/2}} \qquad [2.39]$$

where C is a geometric parameter depending on the shape of the ruptured zone [NOD 13]. However, in practice, it is often difficult to determine the ruptured area A. For example, the spatial smoothing of the model ($\|\boldsymbol{\Gamma}\mathbf{m}\|$ in equation [2.23]) can induce zones with low slip, which are generally poorly constrained. The area A is thus often defined from the regions where the slip exceeds a fraction s_{th} of the maximum slip. Nonetheless, this approach remains problematic as the estimated value of $\overline{\Delta\sigma}$ strongly depends on the chosen threshold s_{th}. An alternative approach is to calculate the co-seismic change in traction $\Delta\sigma$ at the center of each sub-fault (using the [OKA 92] formulation, for example). In the case where the parameterization is based on continuous and differentiable base function, the continuous distribution of $\Delta\sigma$ can also be evaluated. We then express the average stress drop [NOD 13]:

$$\overline{\Delta\sigma} = \frac{\int \boldsymbol{\Delta}\mathbf{u}\,\boldsymbol{\Delta}\boldsymbol{\sigma}\, d\Sigma}{\int \boldsymbol{\Delta}\mathbf{u}\,\mathbf{e}_1\, d\Sigma} \qquad [2.40]$$

where $\mathbf{e}_1$ is the unit vector along the mean slip direction, and $\boldsymbol{\Delta}\mathbf{u}$ is the final distribution of the co-seismic slip. An example of estimation of $\overline{\Delta\sigma}$ based on this approach is presented for the 2014 Iquique earthquake ($M_w = 8.1$) in Figure 2.13. Despite a non-negligible uncertainty, the values estimated between 5 and 25 MPa indicate that the earthquake source is quite compact (the global stress drop average being situated around 3 MPa [ALL 09]).

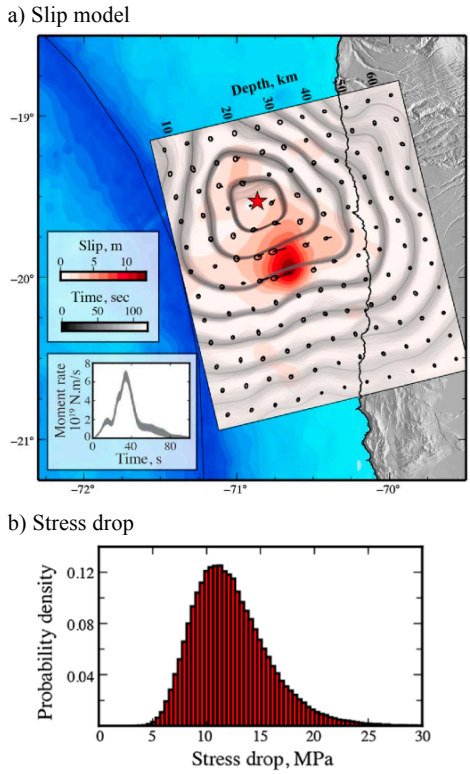

Figure 2.13. *Kinematic model of the 2014 Iquique earthquake in Chile ($M_W = 8.1$): a) Final slip. Colors and arrows indicate the amplitude and direction of slip. The ellipses represent 95% of a posteriori uncertainty. Gray lines indicate the stochastic rupture fronts derived from the posterior ensemble of models (the gray colormap indicate the corresponding rupture time). The red star indicates the location of the hypocenter. The lower left inset shows the posterior ensemble of moment rate functions. b) A posteriori distribution of the average stress drop (see equation [2.40]). Modified from [DUP 15]. For a color version of this figure, see www.iste.co.uk/ rolandone/seismic.zip*

The spatiotemporal distribution of slip can also be used as a boundary condition for calculating the evolution of stress change during the rupture [BOU 97]. This makes it possible to analyze slip-stress relationships and thus to explore the fault weakening. However, several studies show that the detail of this relation is actually poorly constrained using bandpass filtered data and the parameterization used for kinematic modeling [GUA 00]. On the other hand, the fracture energy E_G, which corresponds to the integral of the stress–slip curve above the level of dynamic friction, is often well characterized by seismic observations [TIN 05a]. E_G

corresponds to the energy dissipated by many processes, such as plastic deformation at the head of the fissure, the creation of micro-cracks outside the fault, fluid pressurization, etc. [KAN 06]. Similarly, slip models allow us to estimate the energy E_R radiated by earthquakes in the form of seismic waves [RIV 05]. By combining these observables, it is possible to evaluate energy partitioning during seismic ruptures. During an earthquake, the potential energy (elastic strain energy and gravitational energy) stored in the Earth during the inter-seismic period is released in the form of radiated energy E_R, fracture energy E_G and frictional energy E_F [KAN 06]. The frictional energy E_F corresponds to the work against the resistance to slip on the fault and is mainly dissipated as heat. There is little information available on E_F, since the seismological data does not provide information regarding the level of absolute stress on the fault. For this reason, we generally focus on the partitioning of the energy available for the rupture propagation $E_{T0} = E_R + E_G$ in terms of radiated energy E_R and fracture energy E_G. In particular, we can estimate the ratio between radiated energy E_R and this available energy E_{T0} from the different parameters that can be derived from slip models:

$$\eta_R = \frac{E_R}{E_R + E_G} \sim \frac{2\mu}{\overline{\Delta\sigma}} \frac{E_R}{M_0} \qquad [2.41]$$

where μ is the shear modulus around the fault, $\overline{\Delta\sigma}$ is the average stress drop (see equation [2.40]) and M_0 is the scalar seismic moment. This parameter, η_R, called the radiation efficiency, is useful in characterizing the overall dynamic behavior of an earthquake. If $\eta_R = 1$, the earthquake is very efficient at radiating seismic energy. If $\eta_R = 0$, the available energy (E_{T0}) is fully dissipated mechanically and there is no radiated energy (such as for slow-slip events discussed in Chapter 6). Figure 2.14 shows η_R for different earthquakes for which this parameter could be estimated. It can be seen that most earthquakes have η_R values greater than 0.25. However, some earthquakes have a very low radiation efficiency ($\eta_R < 0.25$). This is the case with tsunami earthquakes, which correspond to very slow ruptures that generate tsunamis that are abnormally large with respect to their magnitude. These earthquakes could thus be associated with large dissipative processes. One possible interpretation is that most tsunami earthquakes involve ruptures in deformable sediments at a shallow depth and that a large part of available energy is used for the deformation of these materials. Certain deep earthquakes (at depths > 600 km) are also associated with a $\eta_R < 0.25$, like the 1994 Bolivia earthquake. The mechanics of these earthquakes is not yet well understood, but these events could involve significant dissipation related to plastic deformation [KAN 98]. On the other hand, high values of η_R for many superficial earthquakes suggests low fracture energy E_G, with important implications concerning these ruptures. In a velocity weakening model, these high values of η_R suggest a small weakening distance (in other words, rapid weakening in terms of slip [KAN 04b]). This also suggests easy runaway ruptures that can easily grow and are difficult to stop.

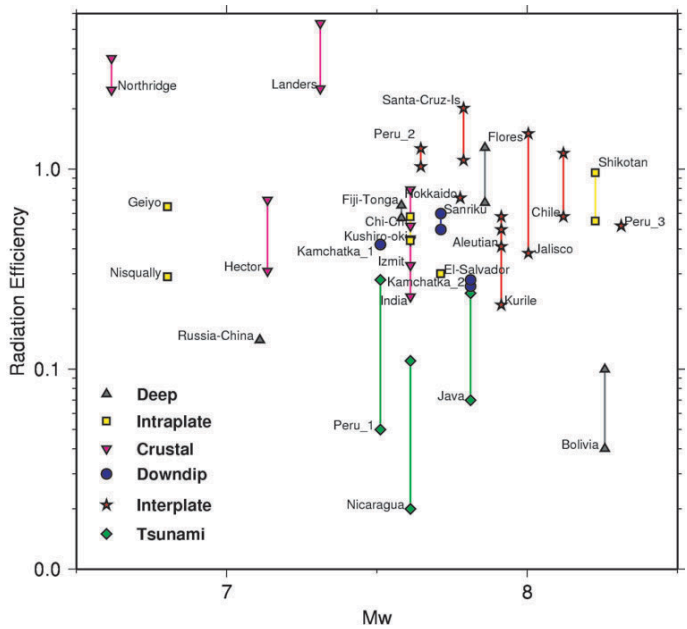

Figure 2.14. *Radiation efficiency estimated for several large earthquakes. The radiation efficiency* $\eta_R = \frac{E_R}{E_R+E_G}$ *is presented in terms of the moment magnitude* M_W*. The different symbols correspond to different types of earthquakes (deep, inter-plate, crustal etc.). Figure modified from [VEN 04]. For a color version of this figure, see www.iste.co.uk/rolandone/seismic.zip*

2.6. Conclusion

In this chapter, we have introduced the most common methods for characterizing the spatiotemporal history of seismic ruptures. There are two broad categories of approaches to describe the evolution of slip on the fault. The first category is based on the linear decomposition of slip evolution into a series of basis functions. This method, called the multiple time window method, is very flexible, but is based on a large number of parameters and can therefore lead to artificially complex models [IDE 07]. The second category of methods is based on the estimation of rupture times and the local duration of slip over the fault. Despite the nonlinearity of this approach, possibly associated with the existence of local minima, it usually promotes relatively simple models that can appropriately fit the data. To make optimal use of both types of approaches, certain methods combine the multiple time window method with the nonlinear inversion of rupture times in each sub-fault [DEL 02].

Despite using an increasing amount of data to constrain models, slip inversion remains a fundamentally badly posed problem. Indeed, it is common to have several

slip models that fit the observations equally well. Different strategies exist to address such non-uniqueness of the solution. A widely used approach consists of regularizing the inversion through spatial and/or temporal smoothing of the slip distribution to obtain a well-conditioned optimization problem. This approach is convenient as it allows us to rapidly solve the inverse problem. However, it is based on model damping that may have a large impact on the solution. An alternative approach is to restrict ourselves to hypotheses that are *a priori* simple and physically justified, but which do not necessarily guarantee the uniqueness of the solution. This then requires characterizing the set of plausible models that fit the data, given these *a priori* constraints. Although this Bayesian approach makes it possible to characterize the uncertainty of the models, it remains computationally expensive and the ensemble of models is often difficult to visualize in practice.

Slip inversion approaches are commonly used today to characterize earthquake sources. Preliminary kinematic models are now published just a few hours after the occurrence of a large earthquake. These rapid estimates are generally based only on teleseismic data, with a limited resolution of the rupture process. Obtaining better constrained results requires the incorporation of additional data, particularly in the near field. Models now incorporate a large amount of observations, such as broadband and strong-motion seismological data, as well as GNSS, InSAR and optical data, that yield detailed information about ground deformation. An important limitation for underwater earthquakes is the loss of resolution when we move farther away from the coast (most observations being on land). To overcome this problem, it is important to incorporate tsunami data that provides essential information on seafloor displacements. Additionally, the deployment of seafloor observational networks is an important task to improve our understanding of the seismic source.

The improvement of observational and modeling methods enables a constant improvement of slip models and thereby a better understanding of seismic ruptures. Despite these improvements, slip inversion results remain uncertain, leading to variability in the models obtained by different teams. For many earthquakes, the accuracy of the estimated source parameters is not enough to draw definitive conclusions on the rupture dynamics. In this context, the estimation of model uncertainty is essential to objectively assess the robustness of our information about the rupture process. A better understanding of earthquake dynamics also requires the development of models that can fit observations over a wide range of frequencies (from static displacements to the high-frequency wavefield).

2.7. References

[AAG 13] AAGAARD B.T., KNEPLEY M.G., WILLIAMS C.A., "A domain decomposition approach to implementing fault slip in finite-element models of quasi-static and dynamic crustal deformation", *J. Geophys. Res.: Solid Earth*, vol. 118, no. 6, pp. 3059–3079, 2013.

[AKI 02] AKI K., RICHARDS P.G., *Quantitative Seismology*, 2nd ed., University Science Books, Sausalito, 2002.

[ALL 09] ALLMANN B.P., SHEARER P.M., "Global variations of stress drop for moderate to large earthquakes", *J. Geophys. Res.*, vol. 114, no. B1, p. B01310, 2009.

[ALL 14] ALLGEYER S., CUMMINS P., "Numerical tsunami simulation including elastic loading and seawater density stratification", *Geophys. Res. Lett.*, vol. 41, no. 7, pp. 2368–2375, 2014.

[AVO 14] AVOUAC J.-P., AYOUB F., WEI S. et al., "The 2013, Mw 7.7 Balochistan earthquake, energetic strike-slip reactivation of a thrust fault", *Earth Planet. Sci. Lett.*, vol. 391, pp. 128–134, 2014.

[BOU 76] BOUCHON M., "Teleseismic body wave radiation from a seismic source in a layered medium", *Geophys. J. Int.*, vol. 47, no. 3, pp. 515–530, 1976.

[BOU 81] BOUCHON M., "A simple method to calculate Green's functions for elastic layered media", *Bull. Seism. Soc. Am.*, vol. 71, no. 4, pp. 959–971, 1981.

[BOU 97] BOUCHON M., "The state of stress on some faults of the San Andreas system as inferred from near-field strong motion data", *J. Geophys. Res.*, vol. 102, no. B6, pp. 11731–11744, 1997.

[BOU 08] BOUCHON M., KARABULUT H., "The aftershock signature of supershear earthquakes", *Science*, vol. 320, pp. 1323–1325, 2008.

[BÜR 14] BÜRGMANN R., CHADWELL D., "Seafloor Geodesy", *Annual Review of Earth and Planetary Sciences*, vol. 42, no. 1, pp. 509–534, 2014.

[CAU 10] CAUSSE M., COTTON F., MAI P.M., "Constraining the roughness degree of slip heterogeneity", *J. Geophys. Res.*, vol. 115, no. B5, p. B05304, 2010.

[COC 94] COCHARD A., MADARIAGA R., "Dynamic faulting under rate-dependent friction", *Pure Appl. Geophys.*, vol. 142, no. 3, pp. 419–445, 1994.

[COT 95] COTTON F., CAMPILLO M., "Frequency domain inversion of strong motions: Application to the 1992 Landers earthquake", *J. Geophys. Res.*, vol. 100, p. 3961, 1995.

[DAY 82] DAY S.M., "Three-dimensional finite difference simulation of fault dynamics: Rectangular faults with fixed rupture velocity", *Bull. Seism. Soc. Am.*, vol. 72, no. 3, pp. 705–727, 1982.

[DEL 02] DELOUIS B., GIARDINI D., LUNDGREN P. et al., "Joint inversion of InSAR, GPS, teleseismic, and strong-motion data for the spatial and temporal distribution of earthquake slip: Application to the 1999 İzmit Mainshock", *Bull. Seism. Soc. Am.*, vol. 92, no. 1, pp. 278–299, 2002.

[DUP 12] DUPUTEL Z., RIVERA L., FUKAHATA Y. et al., "Uncertainty estimations for seismic source inversions", *Geophys. J. R. Astr. Soc.*, vol. 190, no. 2, pp. 1243–1256, 2012.

[DUP 14] DUPUTEL Z., AGRAM P.S., SIMONS M. et al., "Accounting for prediction uncertainty when inferring subsurface fault slip", *Geophys. J. Int.*, vol. 197, no. 1, pp. 464–482, 2014.

[DUP 15] DUPUTEL Z., JIANG J., JOLIVET R. et al., "The Iquique earthquake sequence of April 2014: Bayesian modeling accounting for prediction uncertainty", *Geophys. Res. Lett.*, vol. 42, no. 19, pp. 7949–7957, 2015.

[DUP 17] DUPUTEL Z., RIVERA L., "Long-period analysis of the 2016 Kaikoura earthquake", *Phys. Earth Planet. Inter.*, vol. 265, pp. 62–66, 2017.

[GOM 18a] GOMBERT B., DUPUTEL Z., JOLIVET R. et al., "Revisiting the 1992 Landers earthquake: A Bayesian exploration of co-seismic slip and off-fault damage", *Geophys. J. Int.*, vol. 212, no. 2, pp. 839–852, 2018.

[GOM 18b] GOMBERT B., DUPUTEL Z., JOLIVET R. et al., "Strain budget of the Ecuador-Colombia subduction zone: A stochastic view", *Earth Planet. Sci. Lett.*, vol. 498, pp. 288–299, 2018.

[GOM 18c] GOMBERT B., Vers une nouvelle génération de modèles de glissements cosismiques : analyse stochastique et approche multi-données, PhD Thesis, Université de Strasbourg, 2018.

[GOM 19] GOMBERT B., DUPUTEL Z., SHABANI E. et al., "Impulsive source of the 2017 MW = 7.3 Ezgeleh, Iran, earthquake", *Geophys. Res. Lett.*, vol. 46, no. 10, pp. 5207–5216, 2019.

[GRA 15] GRANDIN R., VALLÉE M., SATRIANO C. et al., "Rupture process of the Mw = 7.9 2015 Gorkha earthquake (Nepal): Insights into Himalayan megathrust segmentation", *Geophys. Res. Lett.*, vol. 42, no. 20, pp. 8373–8382, 2015.

[GUA 00] GUATTERI M., SPUDICH P., "What can strong-motion data tell us about slip-weakening fault-friction laws?", *Bull. Seism. Soc. Am.*, vol. 90, no. 1, pp. 98–116, 2000.

[HAR 78] HARTZELL S.H., "Earthquake aftershocks as Green's functions", *Geophys. Res. Lett.*, vol. 5, no. 1, pp. 1–4, 1978.

[HEA 90] HEATON T.H., "Evidence for and implications of self-healing pulses of slip in earthquake rupture", *Phys. Earth Planet. Inter.*, vol. 64, no. 1, pp. 1–20, 1990.

[HER 13] HERRMANN R.B., "Computer programs in seismology: An evolving tool for instruction and research", *Seismol. Res. Lett.*, vol. 84, no. 6, pp. 1081–1088, 2013.

[HJÖ 09] HJÖRLEIFSDÓTTIR V., KANAMORI H., TROMP J., "Modeling 3-D wave propagation and finite slip for the 1998 Balleny Islands earthquake", *J. Geophys. Res.*, vol. 114, p. B03301, 2009.

[HUA 11] HUANG Y., AMPUERO J.-P., "Pulse-like ruptures induced by low-velocity fault zones", *Journal of Geophysical Research: Solid Earth (1978–2012)*, vol. 116, no. B12, p. B04301, 2011.

[IDE 07] IDE S., "Slip inversion", *Treatise on Geophysics*, vol. 4, pp. 193–223, 2007.

[INA 13] INAZU D., SAITO T., "Simulation of distant tsunami propagation with a radial loading deformation effect", *Earth Planets Space*, vol. 65, no. 8, pp. 835–842, 2013.

[JAY 03] JAYNES E.T., *Probability Theory: The Logic of Science*, Cambridge University Press, New York, 2003.

[JI 02] JI C., WALD D.J., HELMBERGER D.V., "Source description of the 1999 Hector Mine, California, earthquake, part I: wavelet domain inversion theory and resolution analysis", *Bull. Seism. Soc. Am.*, vol. 92, no. 4, pp. 1192–1207, 2002.

[JOH 12] JOHNSON K.M., FUKUDA J., SEGALL P., "Challenging the rate-state asperity model: Afterslip following the 2011 M9 Tohoku-oki, Japan, earthquake", *Geophys. Res. Lett.*, vol. 39, no. 20, p. L20302, 2012.

[JOL 11] JOLIVET R., GRANDIN R., LASSERRE C. et al., "Systematic InSAR tropospheric phase delay corrections from global meteorological reanalysis data", *Geophys. Res. Lett.*, vol. 38, no. 17, p. L17311 , 2011.

[KAN 98] KANAMORI H., ANDERSON D.L., HEATON T.H., "Frictional melting during the rupture of the 1994 Bolivian earthquake", *Science*, vol. 279, no. 5352, pp. 839–842, 1998.

[KAN 04a] KANAMORI H., "The diversity of the physics of earthquakes", *Proc. Jpn. Acad.*, vol. 80, no. 1, pp. 297–316, 2004.

[KAN 04b] KANAMORI H., BRODSKY E.E., "The physics of earthquakes", *Reports on Progress in Physics*, vol. 67, no. 8, pp. 1429–1496, 2004.

[KAN 06] KANAMORI H., RIVERA L., "Energy partitioning during an earthquake", *Radiated Energy and the Physics of Faulting, Geophys. Monogr. Ser.*, pp. 3–13, American Geophysical Union, Washington DC, 2006.

[KAN 10] KANEKO Y., AVOUAC J.-P., LAPUSTA N., "Towards inferring earthquake patterns from geodetic observations of interseismic coupling", *Nature Geosci.*, vol. 3, no. 5, pp. 363–369, 2010.

[KIK 91] KIKUCHI M., KANAMORI H., "Inversion of complex body waves–III", *Bull. Seism. Soc. Am.*, vol. 81, no. 6, p. 2335, 1991.

[KLE 17] KLEIN E., VIGNY C., FLEITOUT L. et al., "A comprehensive analysis of the Illapel 2015 Mw8.3 earthquake from GPS and InSAR data", *Earth Planet. Sci. Lett.*, vol. 469, pp. 123–134, 2017.

[KOM 99] KOMATITSCH D., TROMP J., "Introduction to the spectral element method for three-dimensional seismic wave propagation", *Geophys. J. Int.*, vol. 139, no. 3, pp. 806–822, 1999.

[LAR 03] LARSON K.M., BODIN P., GOMBERG J., "Using 1-Hz GPS data to measure deformations caused by the Denali fault earthquake", *Science*, vol. 300, no. 5624, pp. 1421–1424, 2003.

[LAY 81] LAY T., KANAMORI H., "Earthquake prediction: An international review, Volume 4", in SIMPSON, D.W., RICHARDS, P.G. (eds), *An Asperity Model of Large Earthquake Sequences*, American Geophysical Union, Washington, D.C., 1981.

[LAY 15] LAY T., "The surge of great earthquakes from 2004 to 2014", *Earth Planet. Sci. Lett.*, vol. 409, pp. 133–146, 2015.

[LIU 98] LIU P.L.F., WOO S.-B., CHO Y.-S., Computer programs for tsunami propagation and inundation, Paper, Cornell University, New York, 1998.

[MAD 77] MADARIAGA R., "High-frequency radiation from crack (stress drop) models of earthquake faulting", *Geophys. J. R. Astr. Soc.*, vol. 51, no. 3, pp. 625–651, 1977.

[MAI 12] MAI M., "Source inversion validation (SIV): Current results & developments", *SCEC Source Inversion Validation Workshop*, 2012.

[MAS 93] MASSONNET D., ROSSI M., CARMONA C. et al., "The displacement field of the Landers earthquake mapped by radar interferometry", *Nature*, vol. 364, pp. 138–142, 1993.

[MIN 13] MINSON S.E., SIMONS M., BECK J.L., "Bayesian inversion for finite fault earthquake source models I – Theory and algorithm", *Geophysical Journal International*, vol. 194, no. 3, pp. 1701–1726, 2013.

[NOC 17] NOCQUET J.M., JARRIN P., VALLÉE M. et al., "Supercycle at the Ecuadorian subduction zone revealed after the 2016 Pedernales earthquake", *Nature Geosci.*, vol. 10, no. 2, pp. 145–149, 2017.

[NOD 13] NODA H., LAPUSTA N., KANAMORI H., "Comparison of average stress drop measures for ruptures with heterogeneous stress change and implications for earthquake physics", *Geophys. J. Int.*, vol. 193, no. 3, pp. 1691–1712, 2013.

[OKA 85] OKADA Y., "Surface deformation due to shear and tensile faults in a half-space", *Bull. Seism. Soc. Am.*, vol. 75, pp. 1135–1154, 1985.

[OKA 92] OKADA Y., "Internal deformation due to shear and tensile faults in a half-space", *Bull. Seism. Soc. Am.*, vol. 82, pp. 1018–1040, 1992.

[OLS 82] OLSON A.H., APSEL R.J., "Finite faults and inverse-theory with applications to the 1979 imperial-valley earthquake", *Bull. Seism. Soc. Am.*, vol. 72, no. 6, pp. 1969–2001, 1982.

[OLS 88] OLSON A.H., ANDERSON J.G., "Implications of frequency-domain inversion of earthquake ground motions for resolving the space-time dependence of slip on an extended fault", *Geophys. J. Int.*, vol. 94, no. 3, pp. 443–455, 1988.

[PEY 01] PEYRAT S., OLSEN K., MADARIAGA R., "Dynamic modeling of the 1992 Landers earthquake", *Journal of Geophysical Research: Solid Earth (1978–2012)*, vol. 106, no. B11, pp. 26467–26482, 2001.

[RAG 18] RAGON T., SLADEN A., SIMONS M., "Accounting for uncertain fault geometry in earthquake source inversions I: Theory and simplified application", *Geophys. J. Int.*, vol. 214, no. 2, pp. 1174–1190, 2018.

[RIV 05] RIVERA L., KANAMORI H., "Representations of the radiated energy in earthquakes", *Geophys. J. Int.*, vol. 162, no. 1, pp. 148–155, 2005.

[SAT 07] SATAKE K., "4.17 – Tsunamis", in SCHUBERT, G. (ed.), *Treatise on Geophysics*, Elsevier, Amsterdam, 2007.

[SCH 98] SCHOLZ C.H., "Earthquakes and friction laws", *Nature*, vol. 391, no. 6662, pp. 37–42, 1998.

[SHI 80] SHIMAZAKI, K., NAKATA, T., "Time-predictable recurrence model for large earthquakes". *Geophys. Res. Lett.*, vol. 7, no. 4, pp. 279–282, 1980.

[SIM 07] SIMONS M., ROSEN P.A., "3.12 – Interferometric synthetic aperture radar geodesy", in SCHUBERT, G. (ed.), *Treatise on Geophysics*, Elsevier, Amsterdam, 2007.

[SIM 11] SIMONS M., MINSON S.E., SLADEN A. et al., "The 2011 magnitude 9.0 Tohoku-Oki earthquake: Mosaicking the megathrust from seconds to centuries", *Science*, vol. 332, no. 6036, pp. 1421–1425, 2011.

[SLA 08] SLADEN A., HÉBERT H., "On the use of satellite altimetry to infer the earthquake rupture characteristics: Application to the 2004 Sumatra event", *Geophysical Journal International*, vol. 172, no. 2, pp. 707–714, 2008.

[SOC 19] SOCQUET A., HOLLINGSWORTH J., PATHIER E. et al., "Evidence of supershear during the 2018 magnitude 7.5 Palu earthquake from space geodesy", *Nature Geosci.*, vol. 12, no. 3, pp. 192–199, March 2019.

[TAR 05] TARANTOLA A., *Inverse Problem Theory and Methods for Model Parameter Estimation*, SIAM, Philadelphia, 2005.

[THO 17] THOMAS M.Y., BHAT H.S., KLINGER Y., "Effect of brittle off-fault damage on earthquake rupture dynamics", in THOMAS, M.Y., MITCHELL, T.M., BHAT, H.S. (eds), *Fault Zone Dynamic Processes*, John Wiley & Sons, Inc., Hoboken, 2017.

[TIN 05a] TINTI E., SPUDICH P., COCCO M., "Earthquake fracture energy inferred from kinematic rupture models on extended faults", *J. Geophys. Res.: Solid Earth*, vol. 110, p. B12303, 2005.

[TIN 05b] TINTI E., FUKUYAMA E., PIATANESI A. et al., "A kinematic source-time function compatible with earthquake dynamics", *Bull. Seism. Soc. Am.*, vol. 95, no. 4, pp. 1211–1223, 2005.

[TRI 74] TRIFUNAC M.D., "A three-dimensional dislocation model for the San Fernando, California, earthquake of February 9, 1971", *Bull. Seism. Soc. Am.*, vol. 64, no. 1, pp. 149–172, 1974.

[TSA 13] TSAI V.C., AMPUERO J.-P., KANAMORI H. et al., "Estimating the effect of Earth elasticity and variable water density on tsunami speeds", *Geophys. Res. Lett.*, vol. 40, no. 3, pp. 492–496, 2013.

[TWA 19] TWARDZIK C., VERGNOLLE M., SLADEN A. et al., "Unravelling the contribution of early postseismic deformation using sub-daily GNSS positioning", *Scientific Reports*, vol. 9, no. 1, pp. 1–12, 2019.

[VAL 14] VALLÉE M., SATRIANO C., "Ten year recurrence time between two major earthquakes affecting the same fault segment", *Geophys. Res. Lett.*, vol. 41, no. 7, pp. 2312–2318, 2014.

[VEN 04] VENKATARAMAN A., KANAMORI H., "Effect of directivity on estimates of radiated seismic energy", *J. Geophys. Res.*, vol. 109, no. B4, p. 1265, 2004.

[WAN 18] WANG T., WEI S., SHI X. et al., "The 2016 Kaikoura earthquake: Simultaneous rupture of the subduction interface and overlying faults", *Earth Planet. Sci. Lett.*, vol. 482, pp. 44–51, 2018.

[WEI 13] WEI S., HELMBERGER D., ZHAN Z. et al., "Rupture complexity of the Mw 8.3 sea of okhotsk earthquake: Rapid triggering of complementary earthquakes?", *Geophys. Res. Lett.*, vol. 40, no. 19, pp. 5034–5039, October 2013.

[YOK 20] YOKOTA Y., ISHIKAWA T., "Shallow slow slip events along the Nankai Trough detected by GNSS-A", *Science Advances*, vol. 6, no. 3, p. 5786, 2020.

[ZEN 94] ZENG Y., ANDERSON J.G., YU G., "A composite source model for computing realistic synthetic strong ground motions", *Geophys. Res. Lett.*, vol. 21, no. 8, pp. 725–728, 1994.

[ZHA 14] ZHAN Z., HELMBERGER D.V., KANAMORI H. et al., "Supershear rupture in a Mw 6.7 aftershock of the 2013 Sea of Okhotsk earthquake", *Science*, vol. 345, no. 6193, pp. 204–207, 2014.

[ZHU 02] ZHU L., RIVERA L.A., "A note on the dynamic and static displacements from a point source in multilayered media", *Geophys. J. Int.*, vol. 148, no. 3, pp. 619–627, 2002.

3

The Post-seismic Phase: Geodetic Observations and Mechanisms

Frédérique ROLANDONE
ISTeP, Sorbonne University, Paris, France

3.1. The initial observations of the post-seismic deformation

The seismic cycle has long been described as a two-phase process: the inter-seismic phase, with a slow accumulation of stresses on a fault, and the co-seismic phase, during which these stresses are released abruptly during a large earthquake (see Introduction). This book discusses many observations from the inter- and co-seismic phases (see Introduction and Chapters 2, 5 and 6). A third phase in the seismic cycle has been revealed: the post-seismic phase. Following a large earthquake, an increase in seismicity is recorded in and around the rupture zone. These are aftershocks of a smaller magnitude than the mainshock. However, the amplitude of the post-seismic phase was not revealed by seismicity, but geodesy, as the deformation in this phase is aseismic above all. Observations of the deformation of the Earth's surface have shown that large earthquakes (magnitude > 6) were followed by a deformation whose spatial and temporal characteristics were different from those in the inter-seismic and co-seismic phases. The first observations were made using conventional geodesy techniques, such as triangulation and leveling measurements, before the advent of spatial geodesy in the 1990s.

The Seismic Cycle,
coordinated by Frédérique ROLANDONE.

The Seismic Cycle: From Observation to Modeling,
First Edition. Frédérique Rolandone.

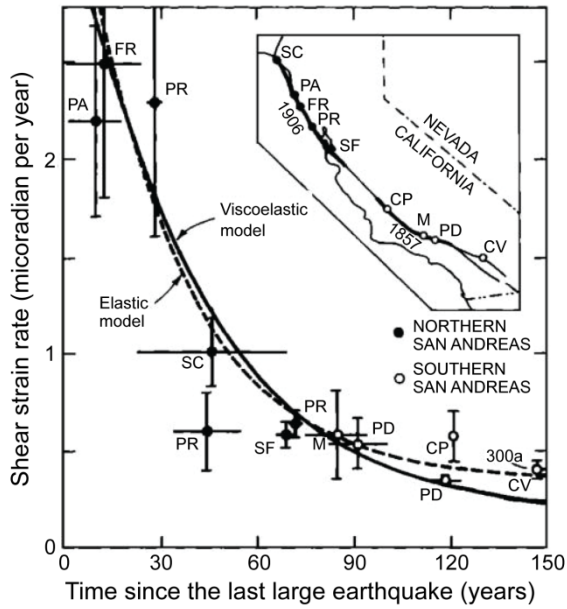

Figure 3.1. *Shear strain rate as a function of the time since the last large earthquakes on the San Andreas Fault: the 1906 San Francisco earthquake in northern California and the 1857 Fort Tejon earthquake in southern California. The triangulation stations are located along the San Andreas fault in the inset. The black circles indicate the stations in northern California and the white circles indicate the stations in southern California. Two models (solid line and dotted line) have been proposed to explain the data [THA 83]*

A transient post-seismic signal was first observed following the 1906 San Francisco earthquake from triangulation measurements [THA 75]. Triangulation measurements make it possible to determine the horizontal shear strain rate, which reflects deformation in the crust. Thatcher shows that following the 1906 earthquake, the deformation rate is four times greater than the inter-seismic deformation rate. Figure 3.1 is taken from Thatcher's article [THA 83] and shows the change in shear strain rate in terms of the time since the last large earthquakes on the San Andreas fault: the 1906 San Francisco earthquake in northern California and the 1857 Fort Tejon earthquake in southern California. Despite the fact that the data are dispersed with large error bars, a transient post-seismic signal is observed with a significant decrease following the earthquake on a time scale of a few decades [THA 83].

Two post-seismic deformation processes have been proposed to explain the observed deformation. The first process stipulates that the slow post-seismic slip, called the "afterslip", takes place in the fault plane below the fault zone where the co-seismic slip happened. The second postulates that the post-seismic deformation could be due to the relaxation of a viscoelastic layer that is deeper than the fault zone. These different mechanisms that could explain post-seismic deformation will be examined in greater detail in section 3.3. We will also look at the ongoing debates around the dominant processes between a localized aseismic slip, the afterslip, and a more distributed viscous flow. It must be noted here that following Thatcher's conclusions, the curves representing these two models (simple, one-dimensional models) are very close and that very varied physical mechanisms can produce similar displacements on the earth's surface. However, Thatcher highlights the inherent benefit of the post-seismic phase in probing the deep rheology. Regardless of the deformation model used, another important conclusion is that the strong post-seismic signal makes it necessary to consider the post-seismic phase in a seismic cycle model and in the estimation of recurrence times of large earthquakes.

Staying with the San Andreas Fault: a strong post-seismic signal was also observed following the 1966 Parkfield earthquake at the northern end of the segment, which ruptured in 1857 (see inset in Figure 3.1). Since 1857, five magnitude 6 earthquakes have been recorded close to Parkfield (1881, 1901, 1922, 1934, 1966). The periodicity of the earthquakes was one of the motivations for equipping the Parkfield segment with instruments and testing different predictions (see Introduction). The last earthquake here to date is the 2004 earthquake, which will be discussed in section 3.2.4. It occurred 15 years later than predicted by a simple seismic cycle model. Like the 1966 earthquake, it had a strong post-seismic signal. The post-seismic displacement observed in the year following the 1966 earthquake is the first observation of an afterslip. The displacement shows a rapid initiation following the earthquake and a logarithmic decrease over time. It was larger than the co-seismic displacement observed [SMI 68]. Here again, this observation highlights the role of the post-seismic deformation in the seismic cycle balance.

Other post-seismic deformations have been seen in subduction contexts due to the vertical measurements of deformation. Using leveling measurements, Prescott and Lisowski [PRE 80] observed an uplift in the Gulf of Alaska, which they interpreted as being related to the post-seismic deformation following the earthquake of magnitude 9.2 in Alaska in 1964. Leveling measurements were carried out in Japan, as well as tide gauge measurements off the Nankai Trough, marked in Figure 3.2 [THA 84]. These measurements were taken before and after the large earthquakes in Tonankai (1944) and Nankaido (1946), whose magnitudes were

estimated to be 8.0 and 8.2, respectively. Figure 3.3 depicts an example of the vertical measurements obtained on one of the profiles. Uplifts and subsidences can be observed depending on the time periods considered and the distance from the Trough. Following the 1944 and 1946 earthquakes, the post-seismic phase in the period 1947/1948–1967 (see Figure 3.3(b)) shows a large uplift up to 160 km from the Trough, with a peak at 130 km from the Trough (where the main subsidence of the co-seismic displacement is located) and then a subsidence when we continue to move away from the Trough. The vertical post-seismic motion observed is opposite to the co-seismic motion.

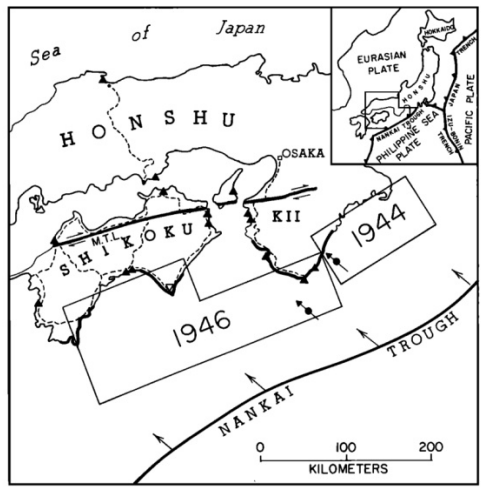

Figure 3.2. *Map of the Nankai subduction zone in Japan. The ruptures from the 1944 and 1946 earthquakes are indicated by rectangles. The dotted lines indicate the location of the leveling measurements taken. The black triangles indicate the tide gauges [THA 84]*

To explain the strong post-seismic signal that followed the Nankaido earthquake, Nur and Mavko [NUR 74] proposed a viscoelastic rebound model, analogous to post-glacial rebound. They showed that the duration of the post-seismic signal could be related to the viscosity of the asthenosphere. Nur and Mavko conclude that studying deformation that follows a large earthquake may provide new constraints on the rheology of the upper mantle.

The initial measurements of post-seismic deformations highlight the significance of the post-seismic phase in constraining the rheological properties of the lithosphere and the important role played by this phase in the seismic cycle balance.

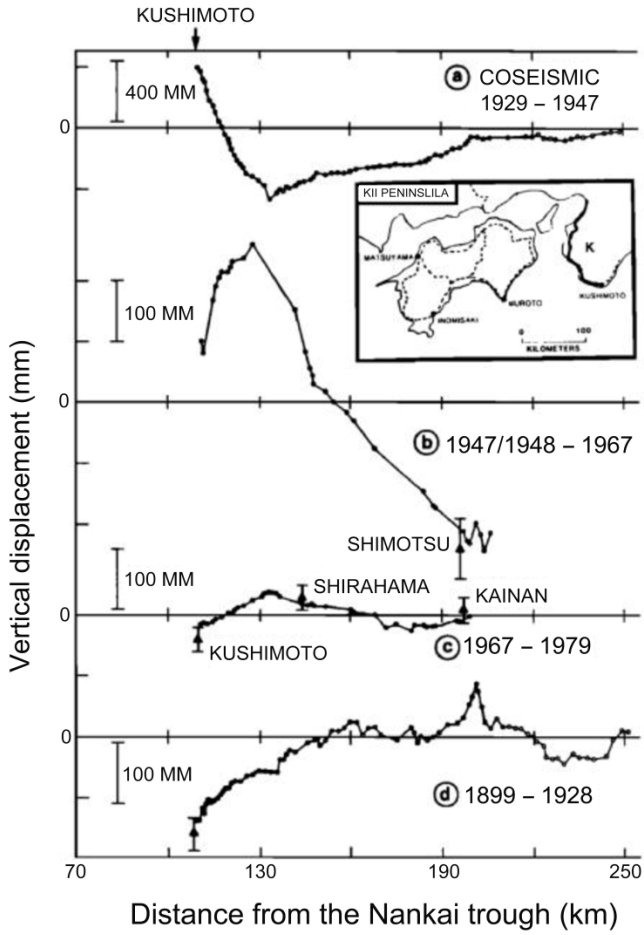

Figure 3.3. *Example of vertical measurements based on the distance to the Nankai Trough (see Figure 3.2) for different time periods. The leveling measurements were carried out along the profile K, whose location is indicated in the inset. The triangles represent the tide gauge measurements: a) co-seismic phase, (b and c) post-seismic phase and d) inter-seismic phase [THA 84]*

3.2. Using spatial geodesy for imaging post-seismic deformation

Spatial geodesy techniques, Global Navigation Satellite Systems (GNSS), including Global Positioning Systems (GPS), and radar interferometry Interferometric Synthetic Aperture Radar (InSAR) have enabled a more detailed observation of post-seismic deformation thanks to greater accuracy in the

measurements, and greater spatial and temporal coverage. These techniques have made it possible to enhance our ability to detect and track surface deformations over time, thus highlighting transient deformation processes at depth. These techniques are described in Segall and Davis's [SEG 97] review article for GPS, and Bürgmann et al.'s [BUR 00] review article for InSAR. These techniques image the deformation during the entire seismic cycle (see Introduction and Chapters 2, 5, 6 and 8).

3.2.1. *Post-seismic phenomena of the Sanriku-Haruka-Oki earthquake*

Heki et al. [HEK 97] made the first GPS observation of a transient post-seismic signal. This was in Japan, following the Sanriku-Haruka-Oki earthquake (magnitude 7.6), which took place in Japan's subduction zone on December 28, 1994. Japan's GPS network had just been established in October 1994. Following this earthquake, the displacements recorded by 16 GPS stations showed, in the year following the earthquake, a post-seismic signal whose amplitude was comparable to that of the signal recorded during the earthquake. Figure 3.4 shows the evolution over time of the position of the east and north components of the Kuji GPS station. Each point corresponds to a daily calculation of the position of the GPS station with its error bar. The coordinates vary very little before the Sanriku-Haruka-Oki earthquake (time t = –0.2 to 0.0 years). We then observe a co-seismic jump, a discontinuity in the time series at t = 0. The displacement is 9.2 cm on the east component. A post-seismic displacement is then observed, characterized by a rapid start following by a decrease over an observation period of one year. A second co-seismic jump is also observed, on the east component alone, corresponding to the largest aftershock of magnitude 6.9, which took place nine days after the mainshock. The associated co-seismic displacement is of 2.6 cm. Other aftershocks took place, 22 of which were of a magnitude greater than 5, but their co-seismic displacements are not visible in the time series. After removing the co-seismic jump associated with the strongest aftershock, the post-seismic displacement observed at the Kuji station is 5.8 cm in one year. The post-seismic displacement takes place in the same direction as the co-seismic displacement, that is, for a subduction zone it is toward the trench, unlike the inter-seismic displacement. Heki et al. [HEK 97] modeled the post-seismic deformation by the afterslip, the slow slip on the subduction fault plane close to the rupture zone of the earthquake.

The energy released in the post-seismic phase is estimated to be equivalent to a magnitude of 7.7. To estimate the energy released post-seismically, we apply the

same formula as used for earthquakes, namely the seismic moment defined by Mo = μ S U (in Nm), with S being the fault slip surface, U being the average slip on the fault, μ the shear modulus and the magnitude defined by Mw = 2/3 log(M_0) – 6.07. The energy released by the afterslip in the post-seismic phase is of an order of magnitude greater than the energy released by the aftershocks, emphasizing that this phase is chiefly aseismic. Further, the energy released in the post-seismic phase (magnitude 7.7) is greater than the co-seismic magnitude (7.6). The authors conclude that their observations in the post-seismic phase have significant implications in terms of the slip budget on the subduction plane, and in terms of energy for the seismic cycle balance, and consequently for estimating the seismic hazard.

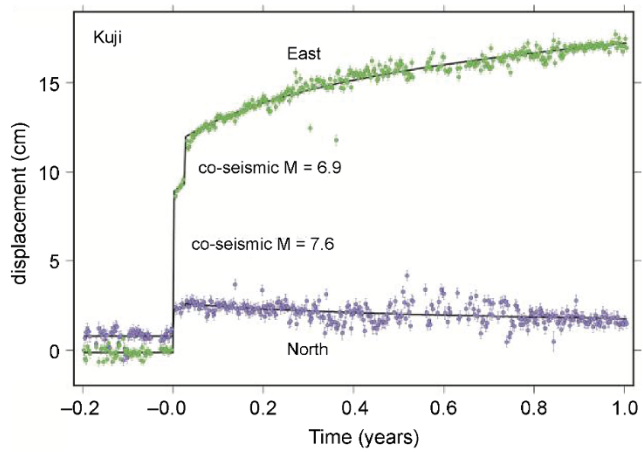

Figure 3.4. *Time series for the Kuji GPS station before and after the 1994 Sanriku-Haruka-Oki earthquake (Japan). The horizontal axis indicates the time in years after the earthquake and the vertical axis indicates the coordinates with respect to an arbitrary reference. The green dots and purple dots are the east and north components, respectively. Two co-seismic jumps are visible: that of the mainshock (magnitude 7.6) and that of the strong aftershock (magnitude 6.9). The post-seismic phase is rapidly initiated just after the earthquake and then decreases logarithmically. Figure reproduced with the kind permission of Kosuke Heki. For a color version of this figure, see www.iste.co.uk/rolandone/seismic.zip*

3.2.2. *Post-seismic phenomena of the Landers earthquake*

In the months and years following the Landers earthquake (magnitude 7.3), the post-seismic deformation was measured using triangulation networks and GPS stations, as well as radar interferometry techniques (InSAR). The Landers

earthquake occurred on June 28, 1992 in the Mojave Desert in southern California. It ruptured a series of dextral strike-slip faults over a length of around 80 km. The co-seismic deformation of the Landers earthquake, imaged by InSAR, is reproduced in Figure 2.5 in Chapter 2. Figure 3.5 shows the post-seismic deformation observed by InSAR over a period of more than three years after the earthquake. The color code in the figure indicates the ground motion toward the satellite. We thus have access to a single component of the deformation, while the GPS provides two horizontal components and one vertical component. As a result of its geometry, InSAR is more sensitive to vertical motions and offers better spatial coverage of the deformation. Several signals can be identified in this image. The first is related to a strong deformation gradient, identified at three locations where the fault segments are discontinuous. From south to north, considering the motion is purely vertical, we observe two uplift zones (the ground moves toward the satellite) and one subsidence zone (the ground moves away from the satellite). These vertical movements, measuring a few centimeters, are localized and observed in sites where the dextral strike-slip fault segments change direction, highlighting the tectonic structures in the two pull-apart basins to the south, and a compression, or push-up, relay to the north. During the Landers earthquake, the pull-apart basins accommodated the extension with a subsidence motion, while the push-up accommodated the compression with a vertical co-seismic displacement of about a meter, showing an uplift. Thus, the vertical motions observed in the post-seismic phase are opposite to the motions observed in the co-seismic phase.

Peltzer et al. [PEL 96] interpret these signals as resulting from the diffusion of fluids induced by the Landers earthquake. This is the poro-elastic rebound model. In this model, the earthquake causes a change in the pore pressure of fluids, following by a circulation of the fluids, which leads to a re-equilibrium of hydrostatic pressure. In a push-up, the compression due to the earthquake is expressed by an increase in the pore pressure of the fluids, following by a diffusion of the fluids beyond this zone in the post-seismic phase. This will result in the subsidence. On the other hand, in a pull-apart basin, in extension in the co-seismic phase, the fluid deficit is compensated in the post-seismic phase by a transfer of fluids toward this region. This results in an uplift.

While the poro-elastic rebound can explain the post-seismic observations close to the rupture zone, other processes have been used to explain the GPS data and the deformation field on a larger scale. Among the processes discussed in many publications on the post-seismic phenomena of Landers, we find the afterslip on the fault plane, or at depth, below the seismogenic zone, and the viscoelastic relaxation of the lower crust or upper mantle, in response to an increase in co-seismic stress.

These different processes contribute in varying degrees to the post-seismic deformation field. The red lobe to the northwest, in Figure 3.5, cannot be explained only by the afterslip. However, it can be reproduced by a combination of afterslip and poro-elastic rebound. Viscoelastic relaxation models make it possible to both explain this red lobe and also take into account GPS data over 100 km from the rupture zone, which indicate a large-scale post-seismic horizontal deformation. These models support a relaxation chiefly in the upper mantle (see the article by Pollitz [POL 00] and the references therein for a discussion on the different processes).

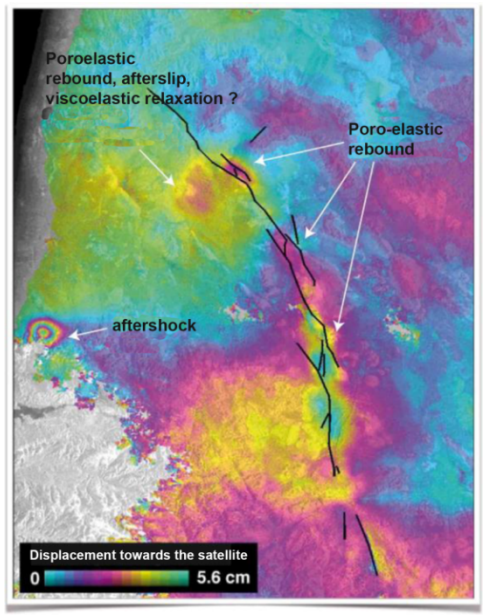

Figure 3.5. *Interferogram of post-seismic deformation following the Landers earthquake over the time period from September 27, 1992 to January 23, 1996, from the ERS-1 satellite. The color code represents the ground movement in the direction of the satellite. The black lines indicate faults with a surface rupture associated with the Landers earthquake. Different post-seismic signals have been identified. Image reproduced with the kind permission of Gilles Peltzer. For a color version of this figure, see www.iste.co.uk/rolandone/seismic.zip*

3.2.3. *Post-seismic phenomena of the Hector Mine earthquake*

The Hector Mine earthquake (magnitude 7.1), occurred on October 16, 1999 in the Mojave desert, on a dextral strike-slip fault. Its epicenter was located 50 km

northwest of the epicenter of the Landers earthquake. The ruptures in both these earthquakes are indicated in Figure 3.6. The post-seismic deformation for this earthquake can also be explained through different processes. Owen et al. [OWE 02] postulate that the afterslip occurs below the co-seismic rupture zone, to explain the GPS data at the 32 campaign sites, measured over the 170 days following the earthquake. Pollitz et al. [POL 01] use three interferograms covering a period of nine months. An example of one such interferogram is given in Figure 3.6. The observations show four deformation lobes, two in subsidence (marked "down") and two in uplift (marked "up"). These vertical movements are of the order of 15–20 mm. The GPS data indicate a horizontal post-seismic velocity that is four times greater than the inter-seismic velocity.

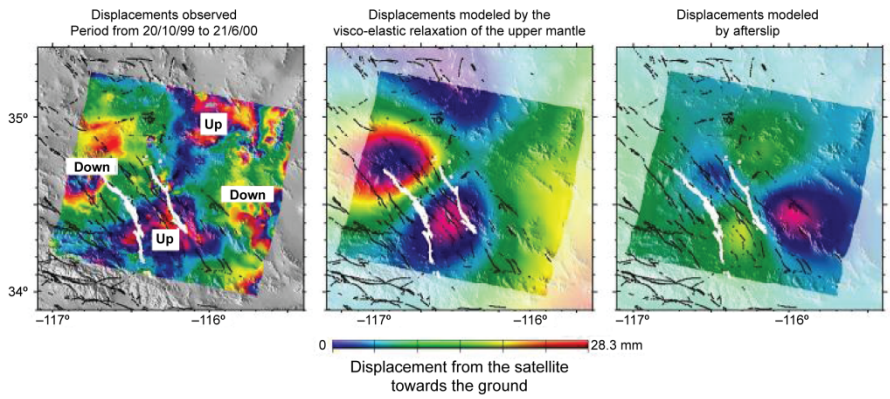

Figure 3.6. *Interferograms observed by the ERS-2 satellite (on the left) and modeled (the two on the right) relating to the post-seismic deformation of the Hector Mine earthquake. The faults are shown in white, those on the left represent the Landers earthquake rupture, while those on the right represent the Hector Mine earthquake rupture. Image reproduced with the kind permission of Fred Pollitz. For a color version of this figure, see www.iste.co.uk/rolandone/seismic.zip*

To explain the observed deformation, Pollitz et al. [POL 01] went on to test two models: an afterslip model, where they considered a slip on the fault plane at depth, and a viscoelastic relaxation model, for which they considered viscoelastic lower crust and mantle with different viscosities. While these two models explained the horizontal GPS velocities, the vertical component proved to be the discriminant. Both interferograms modeled in Figure 3.6 show opposite signals. The afterslip model is anti-correlated with the observed deformation. The viscoelastic relaxation model, with creep in the upper mantle, appears to be the dominant process in the post-seismic phase of the Hector Mine earthquake.

3.2.4. *Post-seismic phenomena of the Parkfield earthquake*

Another example of an earthquake that has been extensively studied is the magnitude 6.0 Parkfield earthquake, which occurred on September 28, 2004 on the San Andreas Fault. Figure I.6 in Introduction illustrates the deformation observed around the Parkfield segment for the inter-, co- and post-seismic phases of the 2004 earthquake. Parkfield is a zone well-equipped with instruments due to the (more or less) regular occurrence of earthquakes of magnitude 6, since 1857. The 1966 earthquake was discussed in section 3.1. The 40 km long Parkfield segment is a transition zone between the aseismic creeping segment to the north-west and the locked Cholame segment to the south-east, which ruptured during the 1857 Fort Tejon earthquake (see inset in Figure 3.1). The creeping segment is aseismic, that is, it is characterized by many small earthquakes (magnitude < 4) and devoid of large earthquakes, while the Cholame segment ruptured during large earthquakes. The Parkfield segment is made up of creeping and locked asperities and presents a degree of heterogeneous coupling (see Introduction for the definition of coupling). The spatial variations in the frictional properties seem to make up the major factor controlling the spatial extension and timing of seismic ruptures (see Chapter 4).

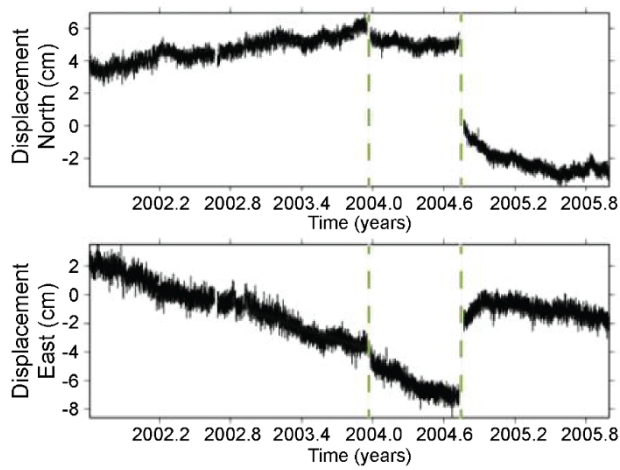

Figure 3.7. *Time series (north component on the top and east component at the bottom) of the GPS HUNT station in the ITRF reference frame (data from USGS: https://earthquake.usgs.gov/monitoring/gps/CentralCalifornia/hunt). The green lines indicate the co-seismic jumps related to two earthquakes: the San Simeon earthquake in December 2003 and the Parkfield earthquake in September 2004. Note the large post-seismic deformation following the Parkfield earthquake. For a color version of this figure, see www.iste.co.uk/rolandone/seismic.zip*

Johanson et al. [JOH 06] used GPS and InSAR data to study the co-seismic and post-seismic displacements associated with the 2004 Parkfield earthquake. Figure 3.7 shows the time series for a GPS station located about 1 km from the San Andreas Fault. Two co-seismic jumps are observed: the first is that of the San Simeon earthquake (magnitude 6.5) which occurred in December 2003, 50 km to the west of the Parkfield earthquake. The second co-seismic jump corresponds to the Parkfield earthquake (the two earthquakes are localized in Figure 3.8). A large post-seismic deformation was observed in the GPS time series after the Parkfield earthquake. Figure 3.8 shows an interferogram of the deformation over the period from September 14, 2004 to November 23, 2004 containing the contribution of co-seismic and post-seismic signals. The deformation is chiefly horizontal and dextral.

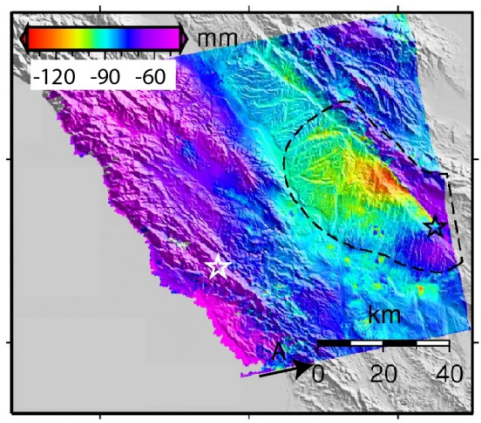

Figure 3.8. *Interferogram of the co-seismic and post-seismic deformation of the Parkfield earthquake from September 14, 2004 to November 23, 2004 by the Envisat satellite in ascending orbit. The white star indicates the epicenter of the San Simeon earthquake and the black star shows the epicenter of the Parkfield earthquake. The zone marked out in dotted lines indicates the data used for the modeling. Image reproduced with the kind permission of Ingrid Johanson. For a color version of this figure, see www.iste.co.uk/rolandone/seismic.zip*

Johanson et al. [JOH 06] modeled the deformations by combining the data from eight interferograms with the GPS data from 17 campaign stations and 22 continuous stations. The fault is discretized, and the aim is to find a slip model that will best account for the surface data. Figure 3.9 shows the result of their inversions. The co-seismic slip modeled by the geodesy represents the instantaneous slip during the earthquake and one day of post-seismic, that is, early post-seismic.

This slip chiefly occurs over two asperities, one of which is close to the hypocenter and the other 15 km to the north-west. The post-seismic slip, modeled by afterslip, is estimated by considering an exponential decrease. Thus, it is the total afterslip that is estimated and represented. It touches its maximum 25 km to the north-west of the hypocenter, at a depth of 10 km. It includes another asperity at depth, close to the hypocenter. The post-seismic slip also takes place in the superficial part of the fault plane close to the rupture zone. A spatial complementarity is observed between the co-seismic slip and the post-seismic slip. The 2004 earthquake was followed by a strong post-seismic slip and the authors suggest that 66–75% of the total moment occurred aseismically. This study underlines the importance of the aseismic slip in the total slip balance in the Parkfield area.

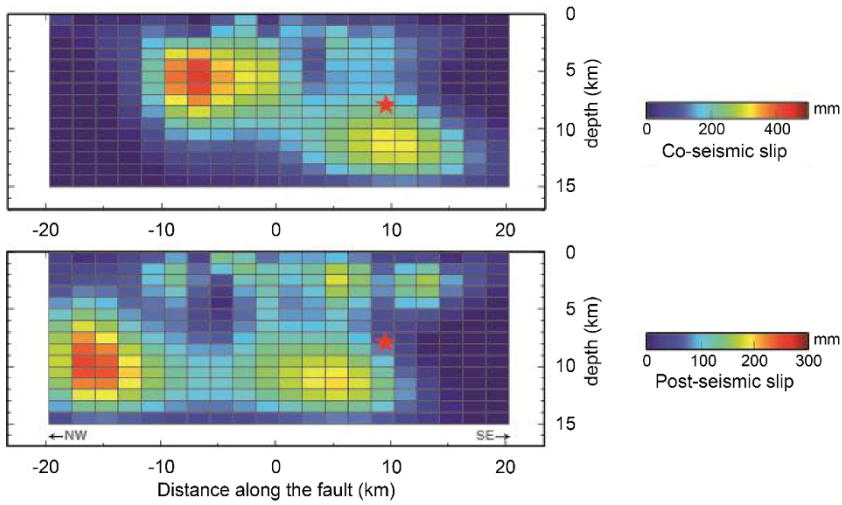

Figure 3.9. *Co-seismic and early post-seismic (one day) slip on top, and estimated total post-seismic slip at the bottom. The red star indicates the hypocenter of the Parkfield earthquake. Image reproduced with the kind permission of Ingrid Johanson. For a color version of this figure, see www.iste.co.uk/rolandone/seismic.zip*

3.3. Post-seismic deformation processes and the mechanical behavior of the lithosphere

As seen in the previous sections, there are different processes that can cause post-seismic deformation, including fluid circulation through the poro-elastic effect, the frictional slip (the afterslip on the fault plane in and around the rupture zone of the earthquake), or the viscoelastic relaxation in deeper layers such as the lower

crust or upper mantle. These deformations, triggered by the earthquake, are characterized by different spatial and temporal scales. These different processes are not mutually exclusive and each may contribute something to the post-seismic deformation field. An earthquake can be seen as a large experiment on deformation of rocks for which the co-seismic stresses induce a variety of post-seismic mechanisms that yield information on the rheology of the fault zone, the lithosphere and the asthenosphere. As we have seen in the previous sections, the post-seismic processes induce deformations that can be accurately observed on the surface through spatial geodesy. These are used in numerical models and bring in constraints on the frictional properties in the fault zone, the permeability of the crust and the viscosity of the lower crust and upper mantle.

3.3.1. *Poroelastic deformation and fluid circulation*

The poro-elastic rebound, an example of which was seen in the Landers earthquake (see Figure 3.5), is a process that is highly localized in space (in the order of 10 km around the fault) and time (in the order of a few days to a few months). The creeping of fluids in the fault zone may be intuitively understood through an analogy of a sponge saturated with water. If the sponge is rapidly compressed, the space between the pores is compacted, thereby increasing the water pressure in the pores. An earthquake can thus cause a rise in pore pressure in the compressed zones, and a reduction in this pressure in the extension zones. These pressure gradients induce a circulation of fluids and a deformation that depends on time. The poro-elastic rebound results in post-seismic uplift in zones with co-seismic extension, and post-seismic subsidence in zones with co-seismic compression.

A simple model helps in understanding this process by relating the displacement to the change in the Poisson's ratio. The co-seismic perturbation will change hydrological conditions by modifying fluid pressure. The co-seismic displacement is proportional to the Poisson's ratio of the deformed volumes of rock under undrained conditions, since the co-seismic stress rapidly changes with respect to the diffusion time of the fluids. The Poisson's ratio is denoted by ν_u (u for undrained). There is then a readjustment of hydrological conditions to reach a drained state and achieve a new hydrostatic balance with slip proportional to the Poisson's ratio ν. The post-seismic poro-elastic slip is thus proportional to $(\nu_u - \nu)$. Since the Poisson's ratio ν_u is higher than ν, the post-seismic vertical displacement is in the opposite direction to the co-seismic displacement. Surface observations make it possible to constrain the difference between the undrained and drained Poisson's ratio $(\nu_u - \nu)$. If the reader is interested in the equations for the poro-elastic process, they can consult Chapter 10 in the book by Paul Segall [SEG 10]. The equations make it possible to determine surface displacements

caused by drainage of a permeable layer of rock. The analysis of the poro-elastic process following the Landers earthquake (see section 3.2.2) has shown that the surface deformation may be explained through a difference of about 13% in the Poisson's ratio for the drained (value of 0.27) and undrained crustal rocks (value of 0.3) over a depth of 15 km. By studying the poro-elastic process, it is therefore possible to characterize the permeability of the upper crust.

3.3.2. *Afterslip and frictional properties of faults*

The afterslip is an aseismic frictional slip on the fault plane. With respect to the inter-seismic slip, which is relatively constant (Introduction), the afterslip is a transient slip triggered by an increase in stress due to an earthquake. The afterslip is observed to have a strong initial slip rate, followed by a decrease with a logarithmic temporal evolution. Spatially, the afterslip is observed mainly around the co-seismic rupture zone and the seismic and aseismic slips complement each other spatially for most earthquakes, as we have seen for the Parkfield earthquake (see Figure 3.9). Thus, on the fault plane we observe locked or coupled regions, which will slip seismically during an earthquake, while other regions show stable or transient slow slips. These differences in the slip mode are chiefly related to variations in frictional properties and friction laws that change over time and with the slip velocity (see Chapter 4). These laws are called rate-and-state laws [SCH 98]. Two opposite behaviors are observed: either (1) the friction increases as slip velocity increases. The friction is then said to be velocity-strengthening, that is, friction hardening with slip velocity and causing an aseismic slip, or (2) the friction decreases as velocity increases. This is called the velocity-weakening regime, that is, softening with slip velocity, and it allows the nucleation of earthquakes. Friction laws may be more complex and involve, for example, additional softening mechanisms. The dominant conceptual model is that of velocity-weakening asperities surrounded by an aseismic velocity-strengthening region (Lay and Kanamori's "rate-state asperity model" [LAY 80]). This rate-and-state formalism originates in laboratory experiments [MAR 98]. Chapter 4 details the friction law equations, laboratory measurements and their application to seismic and aseismic slips over faults.

From the time of the first observations made by Smith and Wyss [SMI 68] following the 1966 Parkfield earthquakes (see section 3.1), afterslip has been observed for a large number of earthquakes. These observations are becoming more and more precise and dense. In addition to these, we have advances in modeling methods based on the increasing computing power of computers. It is therefore possible to image the temporal evolution of the afterslip on fault planes discretized into a large number of sub-faults, and to thus temporally and spatially study the afterslip process. The observation and modeling of the afterslip have revealed the

heterogeneity in frictional properties on the fault plane. We thus obtain an anatomy of the fault plane with velocity-weakening and velocity-strengthening zones. Avouac's [AVO 15] review article gives many examples of afterslip in subduction zones. Avouac postulates a conceptual model of the spatially heterogeneous subduction interface made up of interwoven velocity-weakening and velocity-strengthening asperities. The structure in terms of friction laws will determine the first-order mechanical behavior of different zones in terms of inter-seismic coupling, seismic rupture and afterslip. In the majority of cases, we can observe a complementarity between the afterslip zones with aseismic slip and those with co-seismic slip, as for example in the 2007 Pisco earthquake of magnitude 7.8 [PER 10]. Does this mean that both these slip modes, seismic and aseismic, are distinct and cannot coincide spatially? The afterslips of the mega-earthquakes in Maule in 2010 [BED 13] and Tohuku in 2011 [JOH 12] took place in zones that coincided with the seismic rupture. Therefore, the two modes, aseismic slip and seismic slip, can co-exist. It seems therefore that it is essential to accurately image seismic and aseismic slip zones to better understand friction laws and the processes in play in the accumulation and release of stresses along fault planes.

3.3.3. *Viscoelastic relaxation and upper mantle viscosity*

The viscoelastic relaxation process corresponds to the response in deep layers following an increase in stress due to an earthquake. A relatively strong earthquake (magnitude > 7) is needed for the change in co-seismic stresses to be strong enough to stimulate the viscoelastic response in the lower crust or upper mantle and produce effects that are detectable on the surface. The co-seismic stresses generated by the earthquake propagate and relax in these layers that behave in a viscoelastic manner. Although the afterslip will be observed in the near field and localized around the co-seismic rupture, the viscoelastic relaxation mechanism produces deformations that can be observed over very large distances (several hundred kilometers) and over durations that could go as high as several decades after the earthquake that initiated them. In the continental domain, the increase in co-seismic stress will stimulate the lower crust and/or the upper mantle. In a subduction context, earthquakes will cause viscoelastic relaxation in the asthenosphere, that is in the upper mantle, below the lithosphere. In the temperature and pressure conditions of the lower crust or upper mantle, the deformation includes both the initial elastic behavior, as well as a viscous behavior. These behaviors are described by laws that relate stress and deformation (or deformation rate). The viscoelastic properties of the lithosphere or the asthenosphere are modeled using a combination of linear elastic elements in series or in parallel with linear viscous elements. Bürgmann and Dresen's [BÜR 08] review article gives the constitutive laws of viscoelastic rheologies and their

equations. The article summarizes the results of laboratory experiments in constraining the deformation mechanisms and the viscosities of minerals and rocks that are representative of the lower crust and upper mantle. It is still difficult to extrapolate these laboratory experiments to conditions prevailing in the Earth, as the laboratory parameters are separated from those prevailing in nature by several orders of magnitude. One way of directly characterizing the viscoelastic deformation parameters is to study post-seismic deformation.

We have seen examples of viscoelastic relaxation in the post-seismic deformation of the 1992 magnitude 7.4 Landers earthquake, and the 1999 magnitude 7.1 Hector Mine earthquake in California, in the Mojave desert (see sections 3.2.2 and 3.2.3). In order to explain the horizontal and vertical geodetic data, Pollitz et al. [POL 00, POL 01] and Freed and Bürgmann [FRE 04] showed that for both these earthquakes, the post-seismic deformation is chiefly due to the relaxation of the upper mantle. As we have seen earlier, the post-seismic deformation observed through spatial geodesy shows a rapid decrease. From their models, Pollitz et al. [POL 00, POL 01] deduced that the viscosity of the mantle increases with time, with an initial value of 1-8 $\times 10^{17}$ Pa·s in the first few months and a viscosity of a greater order of magnitude of 1–6 $\times 10^{18}$ Pa·s from between three months to three years after these two earthquakes. The authors explain these observations by suggesting a time-dependent rheology in the upper mantle, with a weaker and transient rheology, and a stronger, long-term rheology. Freed and Bürgmann [FRE 04] explain the temporal variation of viscosity by a nonlinear rheology. A nonlinear rheology implies that the viscosity decreases as the stress increases, which is the case following an earthquake, and it then regains its long-term value when the stresses are released by viscous relaxation. Another case of a slip-strike earthquake is that of the 1999 magnitude 7.4 Izmit earthquake in Turkey, on the North Anatolian fault. The initial deformation is controlled by the afterslip, but this mechanism does not explain the observations made in the years following the earthquake. A viscoelastic relaxation model [HEA 09] makes it possible to constrain the transient viscosity of the mantle, which is of the order of 2–5 $\times 10^{19}$ Pa·s, and a long-term viscosity greater than 2 $\times 10^{20}$ Pa·s. The relaxation of the lower crust contributes to the post-seismic deformation, but it is still difficult to distinguish this from deformation in a weak shear zone localized below the co-seismic rupture. The viscosity of the lower crust, estimated from geodetic measurements, is between 1 to >10 $\times 10^{19}$ Pa·s, indicating a lower crust in continental contexts stronger than the upper mantle (see Supplemental Table 2 in [BÜR 08]).

Since the duration and spatial extension of the post-seismic deformation are linked to the increase in co-seismic stress, subduction earthquakes of a large

magnitude will be followed by a deformation on a large spatial and temporal scale. The Valdivia earthquake, the largest instrumental earthquake, with a magnitude of 9.5, occurred in 1960 in Chile (see Chapter 5). This mega-earthquake resulted in a post-seismic deformation observable in GPS data over several decades, and over distances between 300 to 400 km from the rupture zone [KHA 02]. Indeed, the GPS velocity field still shows regions where the velocities are oriented towards the trench (like the post-seismic displacement field that immediately follows an earthquake) contrary to the inter-seismic velocity field. Several viscoelastic relaxation models in subduction contexts that consider linear rheology make it possible to constrain the viscosity of the upper mantle. Using the vertical uplift data from the Chilean coast, Piersanti [PIE 99] proposes a viscosity in the mantle of the order of 8–10 $\times$ 10^{19} Pa·s. To reproduce the GPS data, the model by Khazaradze et al. [KHA 02] suggests a viscosity of 3 $\times$ 10^{19} Pa·s, while the model from Hu et al. [HU 04] suggests a viscosity of 2.5 $\times$ 10^{19} Pa·s. In Chile again, the post-seismic modeling of the 2010 Maule earthquake (magnitude 8.8) using a model that combined afterslip and viscoelastic relaxation in the asthenosphere and in a deep, low viscosity channel (<10^{18} Pa·s), can explain the horizontal GPS deformation field, as well as the observed vertical field [KLE 16]. Wang's [WAN 07] review article compiles the estimations of the rheology in the upper mantle, the asthenosphere or mantle wedge located above the subduction zone. Based on the post-seismic study of different subduction earthquakes, this article gives viscosity values in the range $0.1^{-10} \times 10^{19}$ Pa·s. Analyses of mega-earthquakes of the 21st century, for which there are dense spatial geodesy data before and after the earthquake, as well as occasional seafloor geodesy data (see Chapter 2), has made it possible to better constrain the rheology of the mantle. The deformation is governed by the mantle's viscous behavior, both in the short-term (months-years) and the long term (decades). Sun et al. [SUN 18] propose a comparative study of the post-seismic deformation for 10 subduction earthquakes with a magnitude greater than 8. They estimate a transient viscosity in the upper mantle of the order of 2.5 $\times$ 10^{17} to 2.5 $\times$ 10^{18} Pa·s and a long-term viscosity between 7 $\times$ 10^{17} and 2 $\times$ 10^{19} Pa·s. Studying the viscoelastic relaxation thus makes it possible to bring in constraints on the rheology of the upper mantle and the temporal variations in its viscosity.

3.4. Conclusions: the importance of post-seismic deformation in the seismic cycle balance

We have seen examples of post-seismic deformations that show that this phase of the seismic cycle can release more energy than the co-seismic phase. The

post-seismic signal for the 1966 Parkfield earthquake is larger than the co-seismic displacement recorded for this earthquake (see section 3.1). The post-seismic phenomena of the 2004 Parkfield earthquake (see section 3.2.4) also shows a strong aseismic slip, suggesting that the energy released aseismically is thrice as much as the energy released in the co-seismic phase. In a subduction context, for the Sanriku-Haruka-Oki earthquake (see section 3.2.1), the energy released in the post-seismic phase (magnitude 7.7) is greater than that released in the co-seismic phase (magnitude 7.6). Pritchard and Simons [PRI 06] have compiled the ratio between post-seismic and co-seismic moment for 12 large subduction earthquakes. They consider the post-seismic deformation in the initial months or the year following the earthquake, and model this deformation in terms of afterslip. They show that the moment released by the afterslip is very different depending on the earthquakes, and varies from below 10% to more than 100% of the co-seismic moment (see Table 2 in [PRI 06]). Pritchard and Simons neglect viscoelastic deformation, but the significant duration of the post-seismic phase, several decades for the viscoelastic relaxation of large earthquakes, also underlines how important this process is in the seismic cycle. Further, Sun et al. [SUN 14] use seafloor geodesy data to show that this viscoelastic relaxation was strong immediately after the 2011 Tohoku mega-earthquake.

Finally, it is important to evaluate the partitioning between the seismic and aseismic slips on faults in order to constrain the contributions of the seismic and aseismic deformations in the seismic cycle balance. Several hypotheses can explain the variations in the amplitude of the afterslip and, among them, the variations in the frictional properties of faults [MAR 98, AVO 15] (see Chapter 4). To better constrain these variations (see section 3.3.2), it is necessary to have detailed and accurate imaging of seismic (see Chapter 2) and aseismic slips on faults. In addition to the fundamental aspects regarding the physics of friction, anticipating the seismogenic potential of faults, that is, anticipating the size and location of future earthquakes, has considerable implications on the evaluation of seismic hazards. This evaluation requires the precise quantification of inter-seismic, co-seismic and post-seismic deformations in the seismic cycle balance. The seismic cycle is further complicated by the recent discovery of other types of transient aseismic slip, namely slow earthquakes or slow slip events (SSE, see Chapter 6). In the case of the 2016 Pedernales earthquake (magnitude 7.8) in Ecuador, the areas prone to SSE blocked the propagation of the seismic rupture and were conducive to a strong post-seismic slip [ROL 18]. These transient slow slip events are important not only in understanding frictional properties, but also in estimating the seismic hazards.

3.5. References

[AVO 15] AVOUAC J.-P., "From geodetic imaging of seismic and aseismic fault slip to dynamic modeling of the seismic cycle", *Ann. Rev. Earth Planet. Sci.,* vol. 43, pp. 233–271, 2015.

[BED 13] BEDFORD J., MORENO M., BAEZ J.C. et al., "A high-resolution, time-variable afterslip model for the 2010 Maule Mw = 8.8, Chile megathrust earthquake", *Earth Planet. Sci. Lett.,* vol. 383, pp. 26–36, 2013.

[BÜR 00] BÜRGMANN R., ROSEN P.A., FIELDING E.J., "Synthetic aperture radar interferometry to measure Earth's surface topography and its deformation", *Annu. Rev. Earth Planet. Sci.*, vol. 28, pp. 169–209, 2000.

[BÜR 08] BÜRGMANN R., DRESEN G., "Rheology of the lower crust and upper mantle: Evidence from rock mechanics, geodesy, and field observations", *Annu. Rev. Earth Planet. Sci.*, vol. 36, pp. 531–567, 2008.

[FRE 04] FREED A.M., BÜRGMANN R., "Evidence of power-law flow in the Mojave desert mantle", *Nature*, vol. 430, pp. 548–551, 2004.

[HEA 09] HEARN E.H., MCCLUSKY S., ERGINTAV S. et al., "Izmit earthquake postseismic deformation and dynamics of the North Anatolian Fault Zone", *J. Geophys. Res.*, vol. 114, p. B08405, 2009.

[HEK 97] HEKI K., MIYAZAKI S., TSUJI H., "Silent fault slip following an interplate thrust earthquake at the Japan Trench", *Nature*, vol. 386, no. 6625, pp. 595–598, 1997.

[HU 04] HU Y., WANG K., HE J. et al., "Three-dimensional viscoelastic finite element model for postseismic deformation of the great 1960 Chile earthquake", *J. Geophys. Res.*, vol. 109, no. B12, pp. B12403, 2004.

[JOH 06] JOHANSON I.A., FIELDING E.J., ROLANDONE F. et al., "Coseismic and postseismic slip of the 2004 Parkfield earthquake from space-geodetic data", *Bull. Seism. Soc. Am.*, vol. 96, no. 4B, pp. S269–S282, 2006.

[JOH 12] JOHNSON K.M., FUKUDA J., SEGALL P., "Challenging the rate-state asperity model: Afterslip following the 2011 M9 Tohoku-oki, Japan, earthquake", *Geophys. Res. Lett*., vol. 39, no. 20, pp. L20302, 2012.

[KHA 02] KHAZARADZE G., WANG K., KLOTZ J. et al., "Prolonged post-seismic deformation of the 1960 great Chile earthquake and implications for mantle rheology", *Geophys. Res. Lett*., vol. 29, no. 22, pp. 7–1–7–4, 2002.

[KLE 16] KLEIN E., FLEITOUT L., VIGNY C. et al., "Afterslip and viscoelastic relaxation model inferred from the large-scale post-seismic deformation following the 2010 Mw 8.8 Maule earthquake (Chile)", *Geophysical Journal International*, vol. 205, pp. 1455–1472, 2016.

[LAY 80] LAY T., KANAMORI H., "An aperity model of large earthquake sequences", in SIMPSON D., RICHARDS P. (eds), *Earthquake Prediction, An International Review*, AGU, Washington, DC, 1980.

[MAR 98] MARONE C., "Laboratory-derived friction laws and their application to seismic faulting", *Annu. Rev. Earth Planet. Sci*., vol. 26, pp. 643–696, 1998.

[NUR 74] NUR A., MAVKO G., "Postseismic viscoelastic rebound", *Science*, vol. 183, pp. 204–206, 1974.

[OWE 02] OWEN S., ANDERSON G., AGNEW D.C. et al., "Early Postseismic deformation from the 16 October 1999 Mw7.1 Hector Mine, California, earthquake as measured by survey-mode GPS", *Bull. Seism. Soc. Am*., vol. 92, pp. 1423–1432, 2002.

[PEL 96] PELTZER G., ROSEN P., ROGEZ F. et al., "Postseismic rebound in fault step-overs caused by pore fluid flow", *Science*, vol. 273, no. 5279, pp. 1202–1204, 1996.

[PER 10] PERFETTINI H., AVOUAC J.-P., TAVERA H. et al., "Seismic and aseismic slip on the Central Peru megathrust", *Nature*, vol. 465, pp. 78–81, 2010.

[PIE 99] PIERSANTI A., "Postseismic deformation in Chile: Constraints on the asthenospheric viscosity", *Geophys. Res. Lett.*, vol. 26, no. 20, pp. 3157–3160, 1999.

[POL 00] POLLITZ F., PELTZER G., BÜRGMANN R., "Mobility of continental mantle: Evidence from postseismic geodetic observations following the 1992 Landers earthquake", *J. Geophys. Res.*, vol. 105, pp. 8035–8054, 2000.

[POL 01] POLLITZ F., WICKS C., THATCHER W., "Mantle flow beneath a continental strike-slip fault: Postseismic deformation after the 1999 Hector Mine earthquake", *Science*, vol. 293, no 5536, pp. 1814–1818, 2001.

[PRE 80] PRESCOTT W.H., LISOWSKI M., "Vertical deformation at Middleton Island, Alaska", *Bull. Seismol. Soc. Am*., vol. 70, pp. 1887–1892, 1980.

[PRI 06] PRITCHARD M.E., SIMONS M., "An aseismic slip pulse in northern Chile and along-strike variations in seismogenic behavior", *J. Geophys. Res*., vol. 111, p. B08405, 2006.

[ROL 18] ROLANDONE F., NOCQUET J.M., MOTHES P.A. et al. "Areas prone to slow slip events impede earthquake rupture propagation and promote afterslip", *Science Advances*, vol. 4, no. 1, p. 6596, 2018.

[SCH 98] SCHOLZ C., "Earthquakes and friction laws", *Nature*, vol. 391, pp. 37–42, 1998.

[SEG 97] SEGALL P., DAVIS J.L., "GPS applications for geodynamics and earthquake studies", *Annu. Rev. Earth Planet. Sci*., vol. 25, pp. 301–336, 1997.

[SEG 10] SEGALL P., *Earthquake and Volcano Deformation*, Princeton University Press, NJ, 2010.

[SMI 68] SMITH S. W., WYSS M., "Displacements on the San Andreas fault subsequent to the 1966 Parkfield earthquake", *Bull. Seismol. Soc. Am.*, vol. 58, pp. 1955–1973, 1968.

[SUN 14] SUN T., WANG K., IINUMA T. et al., "Prevalence of viscoelastic relaxation after the 2011 Tohoku-oki earthquake", *Nature*, vol. 514, pp. 84–87, 2014.

[SUN 18] SUN T., WANG K., HE J., "Crustal deformation following great subduction earthquakes controlled by earthquake size and mantle rheology", *J. Geophys. Res*., vol. 123, pp. 5323–5345, 2018.

[THA 75] THATCHER W., "Strain accumulation and release mechanism of the 1906 San Francisco Earthquake", *J. Geophys. Res.*, vol. 80, pp. 4862–4872, 1975.

[THA 83] THATCHER W., "Nonlinear strain buildup and the earthquake cycle on the San Andreas fault", *J. Geophys. Res*., vol. 88, pp. 5893–5902, 1983.

[THA 84] THATCHER W., "The earthquake deformation cycle on the Nankai trough, southwest Japan", *J. Geophys. Res*., vol. 89, pp. 5674–5680, 1984.

[WAN 07] WANG K., "Elastic and viscoelastic models of crustal deformation in subduction earthquake cycles", in DIXON T.H., MOORE J.C. (eds), *The Seismogenic Zone of Subduction Thrust Faults*, Columbia University Press, New York, 2007.

4

Friction Laws and Numerical Modeling of the Seismic Cycle

Marion THOMAS[1] and Harsha BHAT[2]
[1]*ISTeP, Sorbonne University, Paris, France*
[2]*Laboratoire de géologie, ENS, Paris, France*

4.1. Friction laws

4.1.1. *Historical notions about friction*

Friction is resistance to motion that appears when two surfaces in contact slide against one another. Generally speaking, the concept of "friction" describes the dissipation of energy that occurs. Most phenomena associated with sliding friction can be understood from observations made by Leonardo da Vinci. He was the first to note, based on his experiments, that friction is proportional to one-fourth of the applied pressure and that it is independent of the area of contact between two active surfaces. This latter observation was inspired by the fact that the resistance to sliding of a coil of rope is the same as for a stretched piece of rope.

Almost two centuries later, in the 18th century, Guillaume Amontons and Charles-Augustin de Coulomb, carried out rigorous experiments on friction, with the aim of obtaining quantitative results. The collective work by da Vinci, Amontons and de Coulomb led to the two fundamental "laws" of friction. These statements, simple and still valid, are widely applicable:

The Seismic Cycle,
coordinated by Frédérique ROLANDONE.

The Seismic Cycle: From Observation to Modeling,
First Edition. Frédérique Rolandone.

– the friction force acting between two sliding surfaces is proportional to the load pressing the surfaces together. That is, these two forces have a constant ratio, often called the coefficient of friction;

– the sliding force is independent of the apparent area of contact between the two surfaces.

The discoveries that followed (see Introduction) led researchers to revisit these laboratory experiments in order to better understand earthquakes. In 1966, in a now-famous paper, Brace and Byerlee showed that the creation of new fractures was not the only model that could explain the existence of seismic faults [BRA 66]. In their experimental protocol, they pre-cut a rock sample and loaded its extremities, while also applying confining pressure. They observed that the sliding between the two pieces of rock was not continuous, but a jerky motion with accelerations and decelerations. This was the origin of the theory, which is widely accepted today, that earthquakes are governed by frictional forces.

4.1.2. *From static friction to dynamic friction*

If we go back to the fundamental laws of friction stated by Amonton-Coulomb, they are mathematically expressed as follows. The frictional force $\mathbf{F}_{fric} = \tau A$ is independent of the contact area A (τ being the shear stress). $\mathbf{F}_{fric}$ is proportional to the applied normal force $\mathbf{F}_n = \overline{\sigma_{eff}} A$ through the constant μ ($\overline{\sigma_{eff}}$ corresponds to the effective normal stress). We thus have:

$$\mu = \frac{\mathbf{F}_{fric}}{\mathbf{F}_n} = \frac{\tau}{\overline{\sigma_{eff}}} \qquad [4.1]$$

Let us now consider an object of mass M placed on a table. The force $\mathbf{F}_n = Mg$ is, therefore, normal to the surface. We apply a tangential force $\mathbf{F}_t$ parallel to the surface of the table. If the object is initially at rest, a motion may be produced if a force $\mathbf{F}_t$, greater than $\mathbf{F}_{fric}$, is applied. In this case, the coefficient μ_s is called the coefficient of static friction.

$$\mathbf{F}_{fric} = \mathbf{F}_s = \mu_s \mathbf{F}_n \qquad [4.2]$$

Now, if the object is displaced at a finite velocity over the surface, it has been experimentally found that the frictional force is also proportional to the normal force, through the coefficient μ_d, called the coefficient of dynamic friction:

$$\mathbf{F}_{fric} = \mathbf{F}_d = \mu_d \mathbf{F}_n \qquad [4.3]$$

Early experiments showed that the coefficient of static friction is different from the coefficient of dynamic friction [RAB 58]. Static friction has the property of increasing logarithmically with time, and dynamic friction depends on the velocity V.

From the classic work carried out by Kostrov [KOS 64, KOS 66] and Eshelby [ESH 69], it soon became clear that friction also played a fundamental role in the initiation, rupture development and "healing" of faults. The classic Amonton-Coulomb model, however, led to an impasse. Among other physical problems, it postulated the hypothesis of an instantaneous modification of the coefficient of friction, from its static value to its dynamic value. This brings in singularities (infinite stresses) at the rupture front (red model in Figure 4.1).

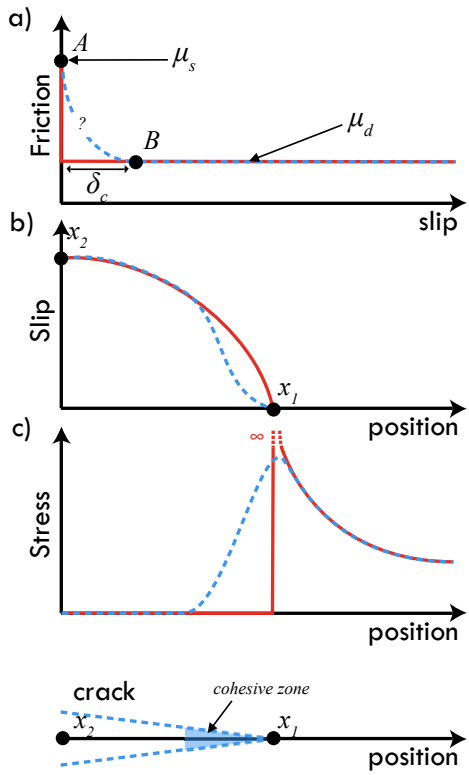

Figure 4.1. *Comparison between the rupture model hypothesizing linear elasticity (red curve) and the cohesive zone model (dotted blue curve). a) Coefficient of friction in terms of the quantity of slip. b) Quantity of slip in terms of the position along the fracture. The point x_1 is in the position A on the friction curve and the point x_2 is at position B. c) Stress field close to the rupture front. For a color version of this figure, see www.iste.co.uk/rolandone/seismic.zip*

This model lacks a scale of length that makes it possible to define a finite quantity of energy released at the rupture front. There are two possible options. One consists of defining the characteristic quantity of slip (between the two surfaces) required to move from static friction to dynamic friction. The other consists of introducing a characteristic time in which friction decreases from μ_s to μ_d. In this second case, a scale of characteristic length emerges when the characteristic time is related to the slip velocity. For example, to explain his experiments on friction, Rabinowicz [RAB 58] introduced the concept of a "critical distance" d_c during which the gap between the static friction and the dynamic friction is closed. He related this critical distance to the velocity, $V = D_c/t_w$. Here, t_w is called *weakening time*.

In general, the laws called *weakening friction laws* were thus developed to reproduce seismic behavior. We speak of *weakening* because the friction reduces with slip (or rate of slip) and these laws can thereby produce instabilities [BOC 13, ZHU 13, ROM 17]. This ingredient is required to anticipate seismic velocities (m/s) in the models. We will now present the most commonly used models in the following sections.

4.1.3. *Slip weakening friction law*

In fracture mechanics, the model where friction weakens with distance, also known as the *cohesive zone model*, postulates that:

– the rupture process, which causes the shift from static friction to dynamic friction, is confined to the fracture plane;

– inelastic deformation begins when the stresses on the rupture front reach a certain critical level;

– we reach the value of the coefficient of dynamic friction when the displacement on the fracture plane exceeds a critical value δ_c [LEO 59, BAR 59, DUG 60].

This law was introduced in the context of a study of tension fractures, in order to solve the problem of singularities arising (infinite stresses) on the rupture front (blue model in Figure 4.1).

The slip weakening friction law was introduced by Ida [IDA 72] and Andrews [AND 76] to model dynamic ruptures for 2D models, and by Day [DAY 82] for 3D models. This is analogous to the cohesive zone model, but for mode II fractures, that is, for shear fractures. In this law, the slip is zero until the shear stress τ reaches a maximum value (elasticity limit) that will be denoted by τ_f^s. Once this stress is attained, the slip starts and the resistance to the sliding τ_f decreases linearly until the value τ_f^d, that is, when the plane has slipped with a critical value δ_c:

$$\tau_f(\delta) = \begin{cases} (\tau_f^s - \tau_f^d)\left(1 - \dfrac{\delta}{\delta_c}\right) + \tau_f^d & ;\delta < \delta_c \\ \tau_f^d & ;\delta > \delta_c \end{cases} \qquad [4.4]$$

If this law is combined with the Amonton–Coulomb law (equation [4.1]), we have:

$$\tau_f(\delta) = \begin{cases} \left[(\mu_s - \mu_d)\left(1 - \dfrac{\delta}{\delta_c}\right) + \mu_d\right]\overline{\sigma_{eff}} & ;\delta < \delta_c \\ \mu_d\overline{\sigma_{eff}} & ;\delta > \delta_c \end{cases} \qquad [4.5]$$

where $\mu_d < \mu_s$. In their article, Palmer and Rice [PAL 73] presented a law that is very close to this for which they could derive a complete analytical solution for the rupture front. They showed that this law made it possible to regularize the numerical model by distributing the stresses and the slip over a distance controlled by the length scale in the friction law.

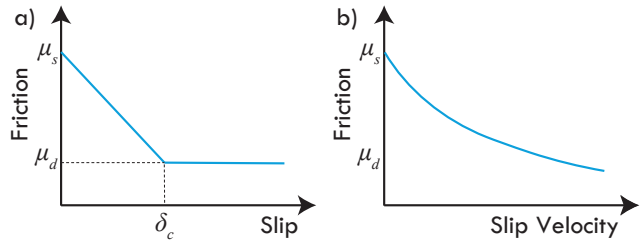

Figure 4.2. *Schematic illustration of a) the slip weakening friction law, b) the velocity weakening friction law*

A few nuanced but important points with respect to the slip weakening law:

1) This friction law describes the start and growth of a seismic rupture. The more the fault slips, the weaker its resistance. If the shear stress on the fault, τ, is uniform, then this law implies that the fault will continue to slip indefinitely until $\tau < \tau_f$. This does not match the observations. There are therefore two possibilities: the first is that τ is heterogeneous along the fault due to its geometric complexity (branches, nonlinear plane, fault jump, etc.) or related to past earthquakes. The second possibility, since faults have finite length, is that the rupture stopped because the earthquake ruptured the entire slip plane. Consequently, when it arrived at the geometric limit of the fault, the friction resistance τ_f, is infinite by definition. For most small earthquakes, it seems likely that the first case is the applicable one. For larger earthquakes, it may be assumed that the second case is applicable.

2) This law does not explain how the next earthquake will occur. Following an earthquake, the entire fault plane that re-ruptured should, logically, have a shear stress equal to the dynamic friction multiplied by the effective normal stress, that is, $\tau = \tau_f^d = \mu_d\overline{\sigma_{eff}}$. Further, for the nucleation and propagation of the next earthquake, τ must again increase and reach the value τ_f^s. We talk about a fault plane "healing",

but the slip-weakening law does not allow this. It is thus well suited to model a single rupture, but not to simulate the seismic cycle, where inter-seismic periods and earthquakes succeed one another over a long period of time.

3) If we go back to law 4.4, but with $\mu_s < \mu_d$, we will then have an increase in friction with the slip, which does not produce instabilities. We then talk of *slip-hardening* behavior, which leads to "creep" type behavior.

4.1.4. *Rate weakening friction law*

In order to respond to the problem of the fault plane "healing", that is, to allow the shear value τ to return to the value τ_f^s, Burridge and Knopoff [BUR 67] propose a new model. They base it on a key observation made in the laboratory: once the plane has slipped from the critical value δ_c, the friction becomes a function of the slip rate V:

$$\tau_f(V) = (\tau_f^s - \tau_f^d)\frac{V_0}{V_0 + V} + \tau_f^d \qquad [4.6]$$

where V_0 corresponds to the characteristic slip velocity. When the slip velocity is much smaller than V_0, the fault's resistance to slip corresponds to the static friction (μ_s) multiplied by the effective normal stress ($\overline{\sigma_{eff}}$), that is, τ_f^s. Conversely, when the slip velocity is much greater than V_0, the fault's resistance to slip corresponds to $\tau_f^d = \mu_d\overline{\sigma_{eff}}$. Therefore, during an earthquake, the resistance decrease as the slip velocity is large (of the order of 1 m/s). On the other hand, it rises again quickly as the slip on the fault slows down, when it reaches loading velocities of the order of an mm/year to cm/year. Thus, this law cannot only model an earthquake individually, but also model the entire seismic cycle. Burridge and Knopoff [BUR 67] applied this friction law over a series of connected block-spring systems used as a proxy for an elastic medium hosting a fault (see section 4.2.1.1).

4.1.5. *Rate-and-state type friction law*

Building on the work started by Brace and Byerlee [BRA 66], new experimental protocols have emerged. In particular, researchers wished to explore the effect of the sudden change in velocity observed in nature when there is a shift from aseismic velocities (∼cm/yr) to seismic velocities (∼m/s). Experiments with velocity jumps in the loading of the system were carried out (Figure 4.3).

In his seminal 1998 paper, Marone [MAR 98] offered an exhaustive review of these works. There are four key observations from this (Figure 4.4):

– a sudden change in slip rate first leads to a sudden increase in the coefficient of friction. This is called the direct effect;

– a transient adjustment is then seen toward a new, stationary value of the coefficient of friction;

– the coefficient of dynamic friction depends on the slip velocity;

– the coefficient of static friction increases with time when there is no motion between the two surfaces in contact.

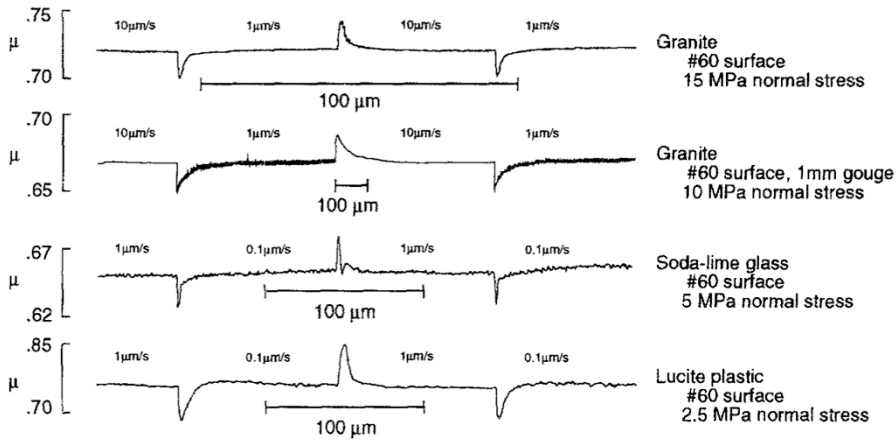

Figure 4.3. *Experiments on friction, by applying velocity jumps, for different types of materials, published by Dieterich in 1994 [DIE 94]*

James H. Dieterich was the first person to propose an empirical law that could reproduce these observations both qualitatively and quantitatively [DIE 79a, DIE 79b]. He based this, notably, on his own friction experiments, with velocity jumps, that involved two ground blocks of granodiorite. He also based it on his earlier experiments, demonstrating that the coefficient of static friction increased with time [RAB 58]. He thus interpreted the decrease of the coefficient of friction with velocity as an effect of the reduction of the mean contact time. And so, in his friction law, the coefficient of friction goes from μ_s to μ_d over a distance D_c, which relates the contact time t to the slip velocity V in the following manner: $V = D_c/t$. With this, he adopted an approach that was similar to that proposed by E. Rabinowicz (section section 4.1.2). The law that he put forward made it possible to bring together the different coefficients of static and dynamic friction into a single coefficient, which depended on the slip rate. It was later refined by Ruina [RUI 83] through the introduction of a state variable θ, which followed a law of evolution. A common way to interpret θ is to relate it to the lifespan of the asperities present on the surfaces in contact. The law was thus called the *rate-and-state* law, due to the existence of this *state* variable, and the dependence of the coefficient of friction on the velocity or *rate*.

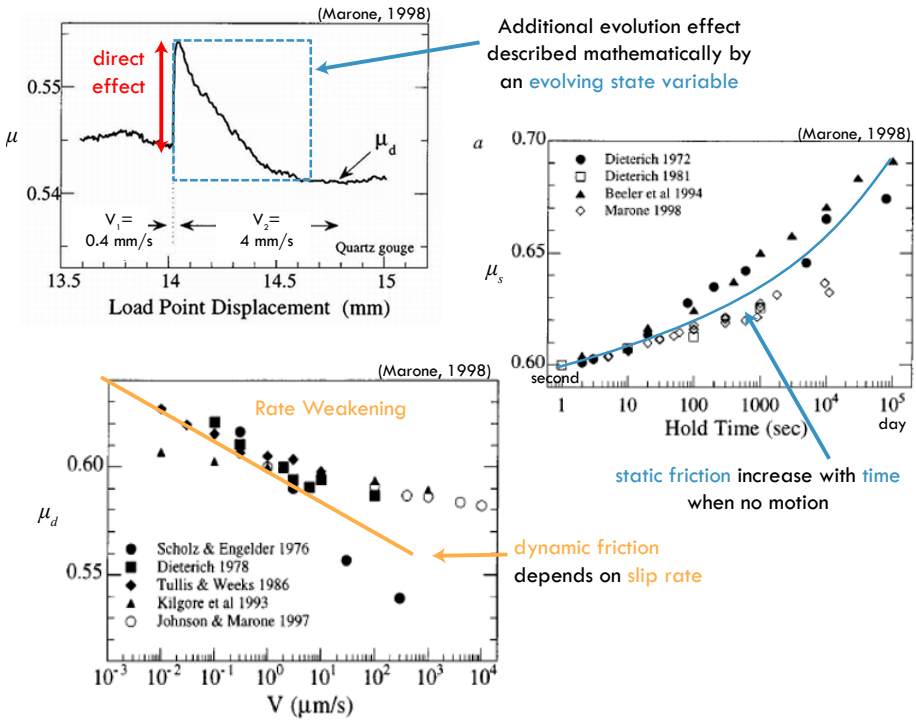

Figure 4.4. *Experiments on friction. Figures modified from Marone [MAR 98]*

A modern form of the rate-and-state law was given by [MAR 98]:

$$\tau_f(V,\theta) = \left[\mu_0 + a\log\left(\frac{V}{V_0}\right) + b\log\left(\frac{\theta V_0}{D_c}\right)\right]\overline{\sigma_{eff}} \qquad [4.7]$$

By associating this either with a law called the *aging law*:

$$\dot{\theta} = 1 - \frac{\theta V}{D_c} \qquad [4.8]$$

or with a state law called *slip evolution*:

$$\dot{\theta} = -\frac{V\theta}{D_c}\log\left(\frac{V\theta}{D_c}\right) \qquad [4.9]$$

Here, $a > 0$ and b are state parameters, of an order of magnitude of $\sim 10^{-2}$, associated, respectively, with the direct effect and the transient change in the

coefficient of friction (Figure 4.5). f_0 corresponds to the reference coefficient of friction at the reference velocity V_0.

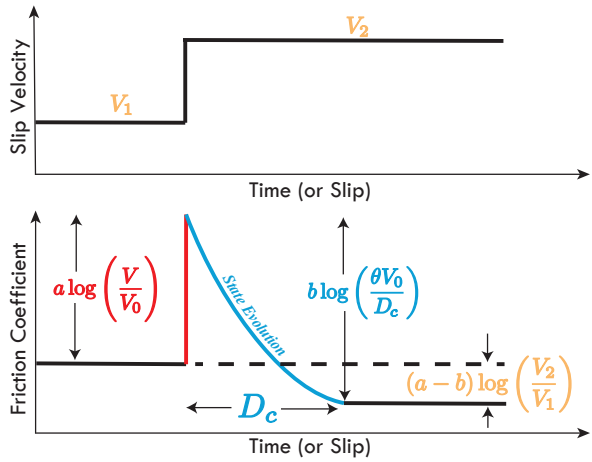

Figure 4.5. *Schematic illustration of the rate-and-state law*

At constant slip velocity, V, the coefficient of friction and the state variable evolve toward a stationary value, f_{ss} and θ_{ss}. It is thus possible to rewrite the rate-and-state law as follows:

$$\theta_{ss} = D_c/V \quad \& \quad f_{ss} = f_0 + (a-b)\log\frac{V}{V_0} \qquad [4.10]$$

Thus, when $(a-b) < 0$, the coefficient of friction decreases with the increase in slip velocity. We then speak of a *rate-weakening* material. If $(a-b) > 0$, then a *rate-strengthening* behavior is obtained.

Today, none of the state laws (equations [4.8] and [4.9]) reproduce the full set of experimental data. The slip evolution law does not reproduce the logarithmic time dependence of the coefficient of static friction (Figure 4.4). If $\dot{\delta} = 0$, θ does not evolve over time. This is probably why the models tend to favor the *aging law* [AMP 08]. However, this law offers a non-symmetric response according to which a positive (increase) or negative (decrease) velocity jump is introduced [BLA 98, AMP 08]. Several modifications were proposed to improve the state law, for example, by introducing a dependency for the normal stress [LIN 92], proposing a completely different evolution of the parameter θ [PER 95, KAT 01] or adding a dependency to the shear rate [BHA 15] . However, none of these laws led to a consensus. On the other hand, other promising modifications made it possible to

come close to observations made in nature (see section 4.3.2). Some of those include additional friction mechanisms that increase friction through dilatancy [SEG 95, SEG 12], or lead to a decrease in effective friction through the pressurization of pore fluids [RIC 06, SCH 11].

4.2. Modeling fault behavior: the "spring-block slider" model

In the brittle part of the crust, the deformation is essentially accommodated along faults in response to the tectonic plate movement in the earth's crust. Along these faults two main behaviors are observed: either the fault creeps continuously at a velocity comparable to the plate velocity (mm/yr to cm/yr), or it remains locked for years, or even centuries, and slips suddenly in a very short time, of the order of several seconds, thus resulting in an earthquake. An earthquake of magnitude M_w 4–5 corresponds to an average slip of a few centimeters, an M_w 7 corresponds to a slip of a few meters and an M_w 9–10 to a slip of 20 m. It is thus observed that slips of the order of m/s cause destructive seismic waves that propagate in the surrounding medium. A simple analogy to represent the behavior of faults on the Earth's surface is the "spring-block slider" model (Figure 4.6), which is described in the following section.

4.2.1. *Modeling the slip on a fault: creep or earthquake*

4.2.1.1. *Block-spring model*

In the spring-block slider model, the force that pulls on the spring attached to the block in a constant manner represents the plate motion. The stiffness constant k of the spring represents the rock's elastic properties, the weight of the spring represents the compression and the basal friction of the block represents the friction of the fault plane (Figure 4.6). There is therefore competition between the shear force pulling the block, $\mathbf{F}_{spr}$, and the force of the friction that resists the shear force, $\mathbf{F}_{fric}$, defined as follows:

$$\mathbf{F}_{spr} = \tau \times A = k \times x \qquad [4.11]$$

$$\mathbf{F}_{fric} = \mu \times \overline{\sigma_{eff}} \times A = \mu \times \mathbf{F}_n \qquad [4.12]$$

As a reminder, τ is to the shear stress, A is the contact area, k is the spring's stiffness coefficient, $\overline{\sigma_{eff}}$ is the effective normal stress and μ is the coefficient of friction. Depending on the law applicable to μ, for example *slip-hardening* or *slip-weakening*, "creep" or "earthquakes" can be reproduced as observed in nature (see section 4.1.3).

In the case of faults that produce earthquakes, we speak of *stick-slip* behavior, that is, alternating between long periods where the fault does not move but stress

accumulates (stick) and periods where the accumulated stress exceeds the fault's resistance to slip, which results in a slip displacement.

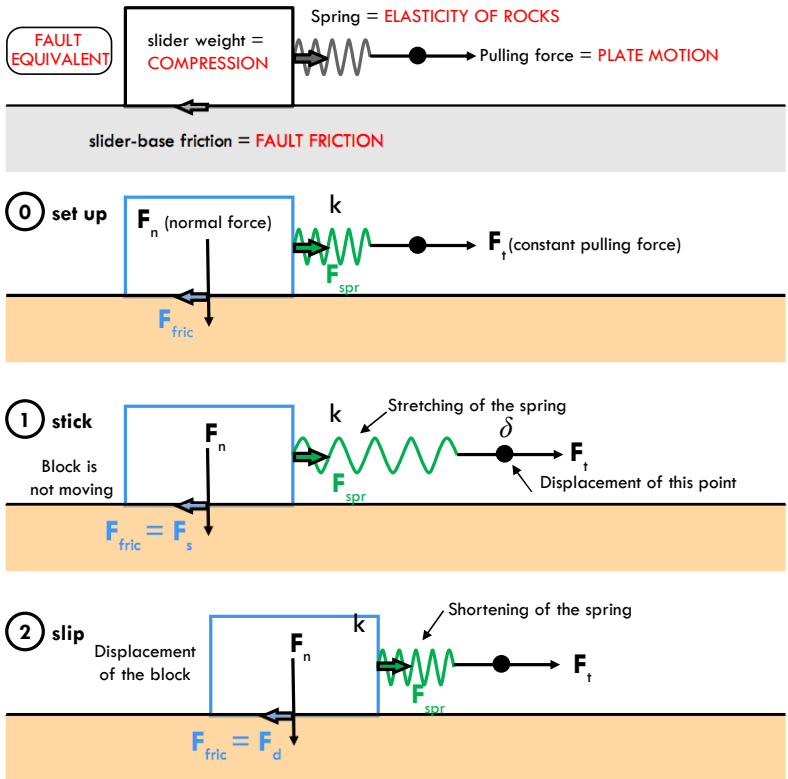

Figure 4.6. *Block-spring model. For a color version of this figure, see www.iste.co.uk/rolandone/seismic.zip*

4.2.1.2. *Earthquake and instability condition*

By applying a slip-weakening law to the block-spring model, it is therefore possible to reproduce stick-slip behavior and deduce the instability condition that will lead to a rapid, "earthquake" type slip.

Initially, the spring is pulled over a distance x but the block does not move (phase 1 in Figures 4.6 and 4.7). We thus have:

$$F_{spr} + F_{fric} = 0 \qquad [4.13]$$

Next, when the shear stress, τ, which is equal to the fault's resistance to slip, $\tau_f^s = \mu_s \overline{\sigma_{eff}}$, the block begins to move. Since the block slips in the direction parallel to $\mathbf{F}_{spr}$, this force decreases, just like $\mathbf{F}_{fric}$ because we applied a slip-weakening type friction to the model (see equation [4.4]). When $\mathbf{F}_{spr}$ exceeds $\mathbf{F}_{fric}$, the block accelerates (phase 2a in Figure 4.7). We therefore add an inertial force to equation [4.13].

$$\mathbf{F}_{spr} + \mathbf{F}_{fric} = m\ddot{x} \qquad [4.14]$$

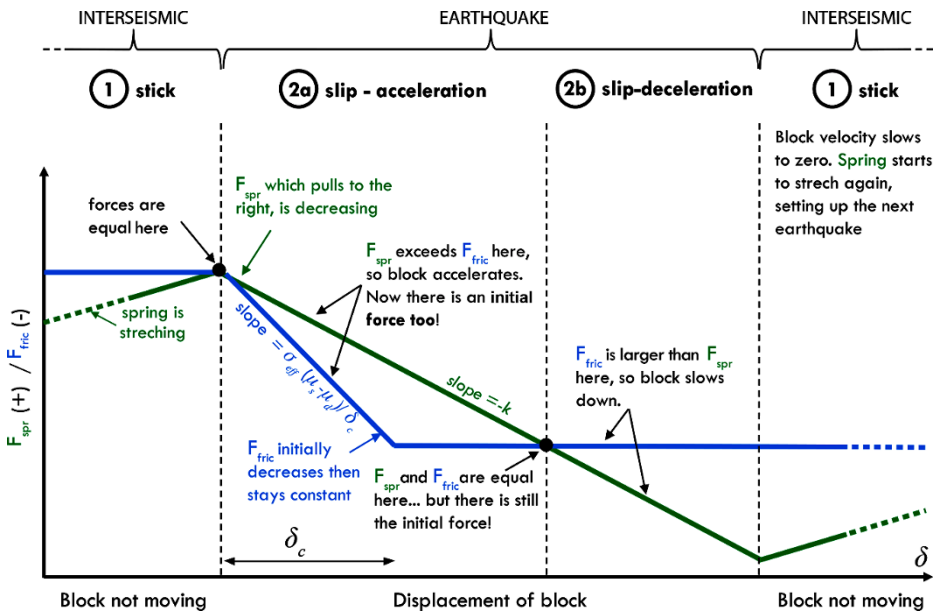

Figure 4.7. *Balance equation of forces for the block-spring model with a slip-weakening friction law. For a color version of this figure, see www.iste.co.uk/rolandone/seismic.zip*

When the coefficient of friction μ reaches its dynamic value μ_d, $\mathbf{F}_{fric}$ remains constant, while $\mathbf{F}_{spr}$ continues to decrease (phase 2b in Figure 4.7). The block finally decelerates. After it completely stops, phase 1 (the stretching of the spring) resumes.

There is therefore an instability, that is, an acceleration in slip, when $\mathbf{F}_{fric}$ decreases faster than $\mathbf{F}_{spr}$ during the slip. The instability condition is thus defined through the following relation, where k, the stiffness of the spring, must be smaller than a critical value k_c:

$$k < k_c = \left| \frac{\overline{\sigma_{eff}}(\mu_s - \mu_d)}{\delta_c} \right| \qquad [4.15]$$

Conversely, creep is produced if $k > k_c$, that is, if the system is "rigid" (a high k) or if the normal stress is low.

4.2.1.3. *Representation of a subduction zone*

A simple way of representing a subduction zone, therefore, consists of combining several blocks, connected to each other through springs, as proposed by Burridge and Knopoff in 1967 [BUR 67]. The aseismic zone at depth is represented by a block whose basal friction responds to a slip-hardening law, and the seismogenic zone is represented by a block whose basal friction follows a slip-weakening law (Figures 4.8(a) and (b)). Researchers then observed that for the seismogenic zone, the slip accumulates in "steps" (Figure 4.8(c)). This is expressed by jagged variations in the shear stress, which is accumulated over long periods of time and then released in a few seconds (Figure 4.8(d)). We then speak of a *stress-drop*. For the aseismic zone, after going through a plateau, which corresponds to the time required for the shear stress to reach the block's value of resistance to slip, that is, τ_d^s (Figure 4.8(d)), the slip accumulates continuously and therefore there is indeed creep (Figure 4.8(c)).

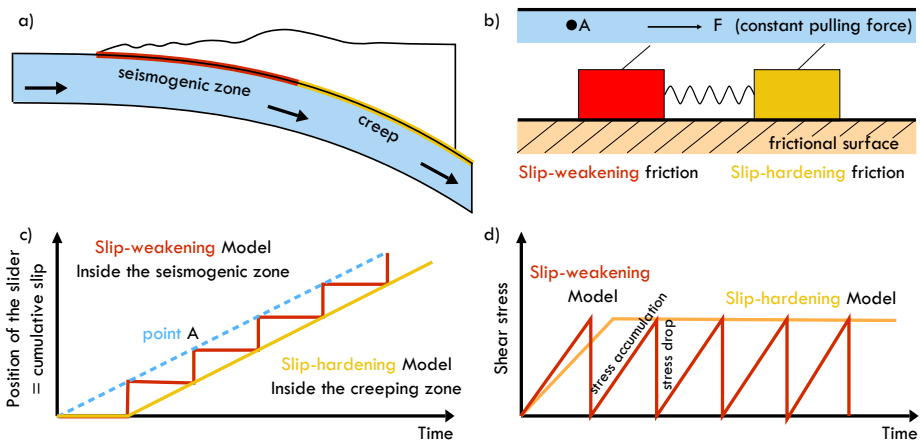

Figure 4.8. *Modeling of a subduction using the block-spring method. a) Schematic representation of a subduction. b) Conceptual model. c) Accumulation of slip over time. d) State of shear stress over time. For a color version of this figure, see www.iste.co.uk/rolandone/seismic.zip*

4.2.2. *Modeling the seismic cycle*

4.2.2.1. *Shifting to the rate-and-state law*

As discussed in section 4.1.3, while the earlier model makes it possible to reproduce the essential steps that lead to the seismic slip, it does not allow multiple

events to be chained, since μ does not return to its static value μ_d (Figure 4.7). On the other hand, the R&S law, with the state variable θ, takes into account the healing of the fault plane (Figure 4.9).

If we go back to the spring-block slider model and replace the slip weakening friction law with a rate-and-state friction law, it is possible to derive a new instability condition. In this second case, during the acceleration phase (2a in Figure 4.9), the slope of F_{fric} is approximately equal to $\overline{\sigma_{eff}}(b-a)/D_c$. Consequently, for an instability, and potentially an earthquake, to be generated, we must have the following relation:

$$k < k_c \approx \left| \frac{\overline{\sigma_{eff}}(b-a)}{D_c} \right| \qquad [4.16]$$

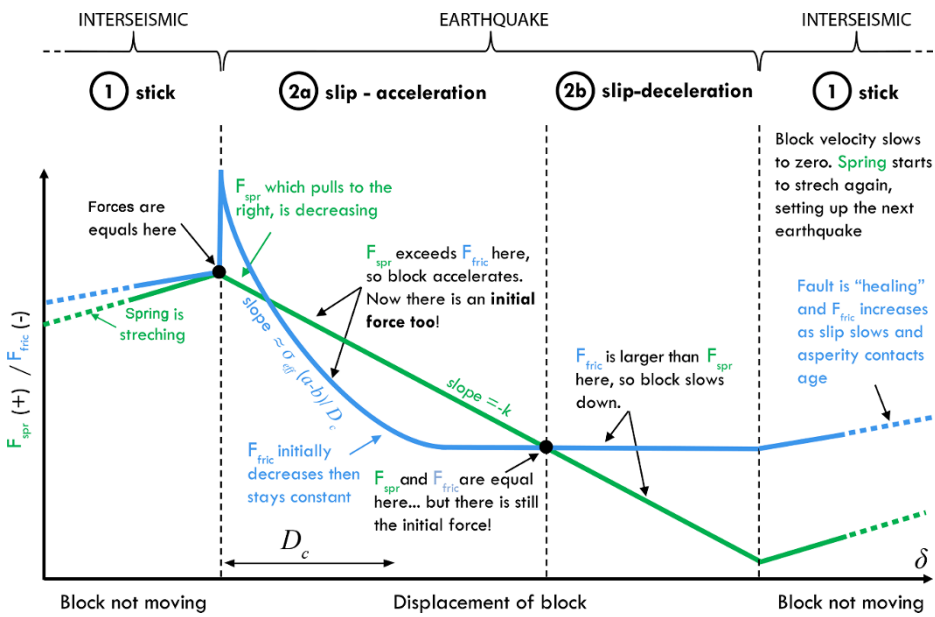

Figure 4.9. *Assessment of forces for the block-spring model with a rate-weakening friction law (rate-and-state law). For a color version of this figure, see www.iste.co.uk/rolandone/seismic.zip*

4.2.2.2. *Implications for the nucleation size of earthquakes*

To move from the spring-block slider model to a slightly more realistic Earth model with elastic behavior, we use elasticity to determine the k value of an elliptical crack:

$$k = \frac{G}{(1-\nu)L} \qquad [4.17]$$

where G is the shear modulus, ν is Poisson's ratio and L is the length of the zone that slips over the fault plane (Figure 4.10). In this case, the instability occurs when the decrease in the frictional force is greater than the decrease in elastic force, and equation [4.16] is rewritten as:

$$\frac{G}{(1-\nu)L} < k_c \approx \left| \frac{\overline{\sigma_{eff}}(b-a)}{D_c} \right| \qquad [4.18]$$

Consequently, the zone that slips must be greater than a critical size L_c in order to become unstable and generate earthquake nucleation:

$$L > L_c \approx \left| \frac{D_c G}{(1-\nu)\overline{\sigma_{eff}}(b-a)} \right| \qquad [4.19]$$

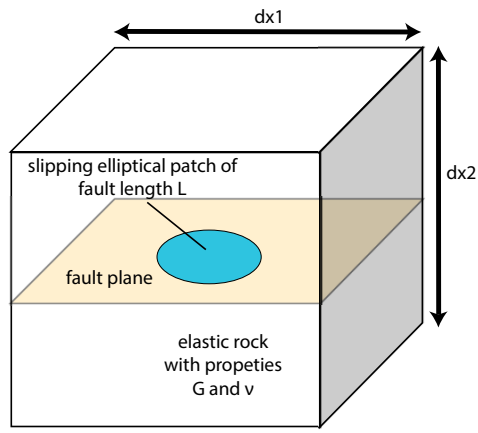

Figure 4.10. *Nucleation model*

4.2.2.3. *Continuum model*

In his seminal 1993 article [RIC 93], J. R. Rice highlights the importance of moving from "spring-block slider" models to continuous medium models. He notably demonstrated that

> "while the equations of Newtonian dynamics are solved exactly in these Burridge-Knopoff models, it has not been generally acknowledged that the dynamical solution for rupture along a chain of lumped masses,or a string of concentrated mass in the continuous limit, bears a presently uncertain relation to dynamical solutions for rupture along a fault embedded in a surrounding elastic continuum. For example, the response of B-K models to an instantaneous change in stress τ along the rupture is an instantaneous change in the acceleration $\partial^2\delta/\partial t^2$, but there is no instantaneous change in $\partial\delta/\partial t$".

This is true, on the other hand, in continuum models. The other major drawback is that "since there is no analogue to energy radiation as seismic waves in the normal implementation of the B-K models (an exception is the recent work of Knopoff et al.), all potential energy lost to the system during a rupture is fully account- able as frictional work; the same is not true for rupture in a continuum".

It is therefore essential to highlight, in this text, that while the block-spring model makes it possible to qualitatively reproduce the phenomena observed in nature, it is essential to shift to a continuum model if we wish to develop robust numerical models. Interested readers can consult [BIZ 12].

4.3. A more complex physical reality

4.3.1. *Spatial and temporal variability in the slip mode on faults*

Until recently deformation in fault zones, in the brittle part of the crust, was attributed either to earthquakes or to the slow continuous slip during the inter-seismic period (creep) or post-seismic period. This latter phenomenon is called the *afterslip* and corresponds to a logarithmic acceleration in the aseismic slip on the fault, which can be observed after large earthquakes. However, this paradigm of two "extreme" behaviors is being questioned today.

Advances in technology and methodology in the field of geodesy and in seismology have significantly improved our capacity to measure deformation rates and given us higher resolutions. These observations have enabled us to document a large variability in the slip dynamic in the seismogenic zone (Figure 4.11). Faults may have chiefly seismic behavior, have a slow, stable slip [THO 14a] or a transient slip [ROU 16]. In addition to this, one of the most significant discoveries in the last decade has been the revelation of the existence of "slow earthquakes" (see Chapter 7). These encompass several phenomena. *Slow slip events* rupture the fault very

slowly over several hours or even days, at velocities that are higher than the inter-seismic creep (cm/yr), but slower than earthquakes, such that no detectable seismic waves are radiated [DRA 01]. They are generally (though not always) accompanied by weak seismic signals of a long duration (a few minutes to a few weeks) called *non-volcanic tremors* [OBA 02]. *Low-frequency earthquakes*, with a duration close to a second, and *very low frequency earthquakes*, which can last a hundred seconds, are commonly observed within *non-volcanic tremors* [IDE 07, ITO 07]. As a result, it is known today that slip velocities on faults cover a continuum going from a millimeter per year to a meter per second [PEN 10]. This is therefore an essential parameter to take into consideration when modeling active faults. However, the physics behind the processes that govern this behavior is still unknown and is the subject of much active debate in the community.

In addition to the large range of deformation velocities, there is a spatial and temporal variability in the slip mode. Contrary to what the schematic representation in Figure 4.11 might suggest, the phenomena described here are not restricted to a specific depth. On some faults creep may be recorded over the entire seismogenic zone, that is, from the surface up to the maximum depth where earthquakes are observed [TIT 06, THO 14a]. Further, while slow earthquakes were first located beyond the seismogenic zone [OBA 02, IDE 07], non-volcanic tremors and slow slip events have recently been observed at depths of less than 10 km, as well as in the sub-surface [ITO 06, OUT 10]. Moreover, geodetic data has shown that the seismic or aseismic behavior is not necessarily stable over time, and that the same zone may creep and slide seismically [JOH 12, THO 17a]. These observations lead to two hypotheses: (1) These different phenomena can occur under varied pressure/temperature conditions and/or result from various deformation mechanisms. (2) They correspond to particular mechanical and rheological properties, but which vary over time. Consequently, they also vary over space, depending on what seismic cycle phase the observed site is undergoing.

4.3.2. *Additional mechanisms that can come into play during earthquakes*

The standard formulation of the rate-and-state law (section 4.1.5) allows a numerical reproduction of a large number of the phenomena discussed above. However, this formulation was based on slip velocity experiments ranging from 10^{-9} to 10^{-3} m/s. While comparable to aseismic velocities (10^{-10} to 10^{-9} m/s), they are still slow when compared to seismic velocities ($\sim$ 1 m/s). There is increasing experimental and theoretical proof that larger slip velocities and quantity of slip also come into play [LAP 12]. This has the effect of drastically reducing the dynamic friction. Wibberley and co-authors [WIB 08] have compiled laboratory values for different kinds of rocks and at different loading velocities (Figure 4.12).

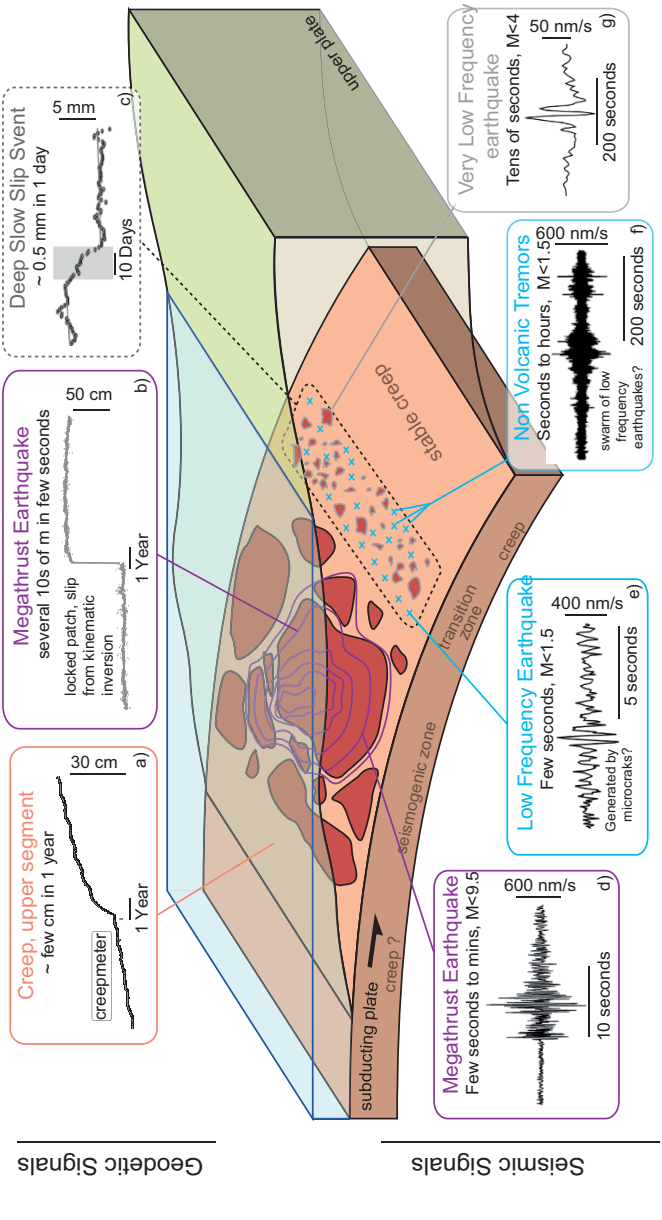

Figure 4.11. *Schematic representation of a subduction zone and the distribution of sources potentially responsible for the observed phenomena. GEODESY: a) creep recorded by an extensometer; b) slip during a major earthquake; c) slow slip events (SSE). SEISMOLOGY: seismograms registering d) earthquakes, e) Low Frequency Earthquakes, f) non-volcanic tremors and g) Very Low Frequency Earthquakes. The red patches represent asperities blocked during inter-seismic periods. The mauve isocontours represent the co-seismic slip which would have ruptured several adjacent patches. Data from a) and b): [THO 14]; data from c), d), e), f): [PEN 10]. For a color version of this figure, see www.iste.co.uk/rolandone/seismic.zip*

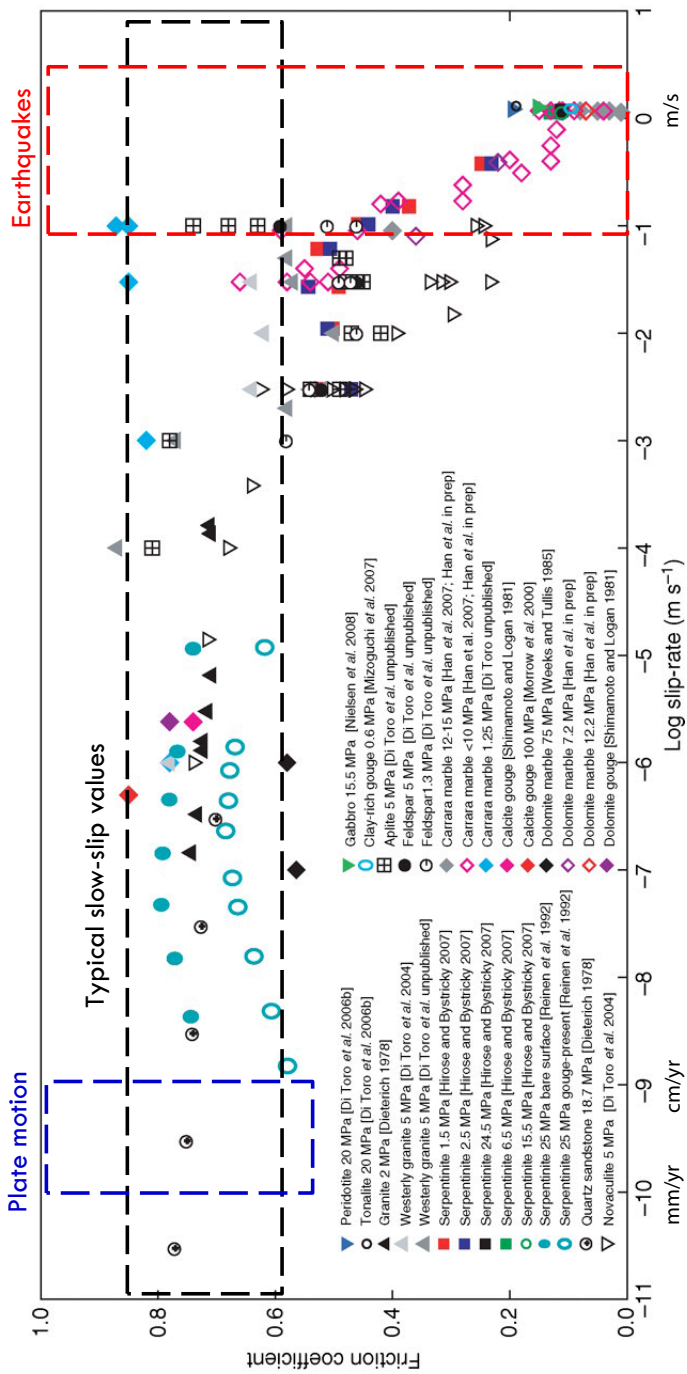

Figure 4.12. *Dependence of the coefficient of dynamic friction, in a continuous regime, on the slip velocity. Figure modified from [WIB 08]. For a color version of this figure, see www.iste.co.uk/rolandone/seismic.zip*

The lack of experimental data on the properties of friction that are applicable to earthquakes is due to the difficulty of carrying out experiments in conditions similar to earthquakes. A laboratory experiment that would reproduce the conditions that exist during seismic slip would simultaneously involve high slip rates (1–10 m/s), with large displacements (0.1–20 m), a resulting effective normal stress (50–200 MPa), high pore pressure (0.4–1 times the normal stress) and high temperature (ambient temperatures of 100–300°C, but potentially as high as 1,500° C in the slip zone). Although considerable progress has been made over the last decade, there is as yet no device that is capable of simultaneously responding to all these requirement. It is therefore necessary to compromise on one or more factors. Tullis and Schubert highlighted this difficulty and proposed a complete review of the processes that could lead to substantial reductions in the friction coefficient with respect to its typical experimental value of 0.6 [TUL 15]. The proposed mechanisms include:

– dynamic reduction in the normal stress or loss of contact due to the vibrations perpendicular to the interface;

– dynamic reduction in the normal stress due to the contrast in elastic properties, or permeability, on either side of the fault;

– acoustic fluidization;

– elasto-hydrodynamic lubrication;

– thermal pressurization of pore fluids;

– pressurization of pore fluids induced by the degradation of minerals;

– local heating/melting of the point of contact between the asperities;

– lubrication of the fault through fusion, in response to frictional processes;

– lubrication of the fault through the creation of a thixotropic silica gel;

– superplastic deformation of fine grains.

These highlight the difficulty of proving which mechanism is responsible for the observed experimental behavior and to design experiments that can clearly prove or refute a mechanism proposed in theory. Nonetheless, since it is likely that one or more of these processes is activated at high slip rates, the rate-and-state law described in section 4.1.5 does not adequately reproduce this strong fall in the coefficient of dynamic friction. Indeed, for seismic velocities ($\sim$ 1 m/s) is a typical value for $(a - b)$ equal to -0.005, we obtain a μ_d of $\sim$ 0.54. Further, based on laboratory experiments, the effective μ_d, that is, $\tau/\overline{\sigma_{eff}}$, can reach very low values (0–0.2) during co-seismic slip. This observation has many implications for our understanding of the mechanism of earthquakes: on the amplitude of the stress drop, on the propensity of earthquakes to propagate in pulse form, on the amplitude of ground movements, and on the orientation of stresses in the crust. N. Lapusta and S. Barbot propose two ways of modifying the *rate-and-state* law to take into account these additional weakening mechanisms [LAP 12]. Interested readers may refer to their publication for more details.

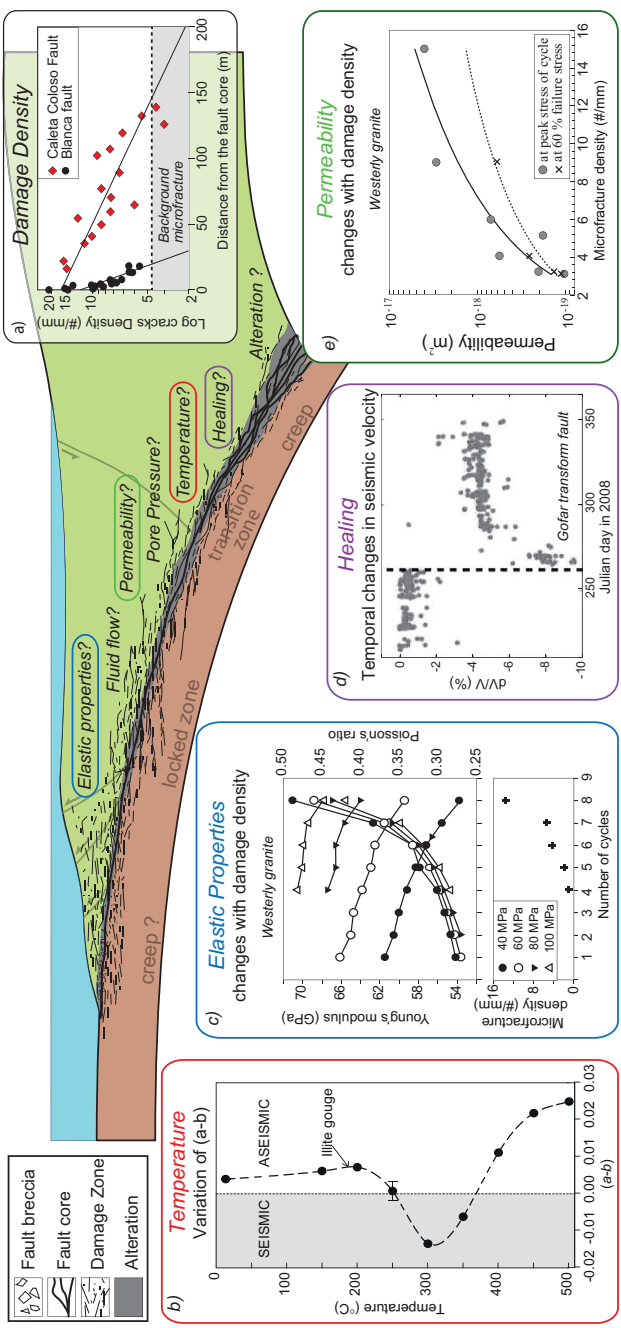

Figure 4.13. *Schematic representation of a subduction zone from a mechanical point of view. The interface between the subducting plate and the overriding plate is a complex zone that includes a fault breccia, principal fault cores and a damage zone. The deformation depends on several factors with their own temporal evolution throughout the seismic cycle. a) Damage decreases exponentially with distance to the fault [MIT 09]. b) Friction parameters (ab) depend on temperature [HAR 12]. c) Elastic properties vary with damage [FAU 06]. d) The velocity of seismic waves changes after an earthquake [FRO 14]. The dotted line marks the date of a 6.0 Mw earthquake. e) Permeability evolves depending on the density of the microfracture [MIT 12]. For a color version of this figure, see www.iste.co.uk/rolandone/seismic.zip*

4.3.3. *Going beyond the elastic Earth model*

Many ground studies, geophysical observations and laboratory experiments have highlighted the strong coupling that exists between the main rupture plane and the surrounding medium. The faults zones are not made up only of a major plane where the majority of slip occurs, but also make up a complex group, surrounded by a zone where surrounding rock is fractured intensively (Figure 4.13). Seismic ruptures result in damage around the faults with an exponential decrease in the density of microfractures perpendicular to the main slip plane [AND 94, MIT 09]. The damage modifies the microstructure and changes the elastic properties of the rocks at the level of the fault breccia and in the adjacent medium [WAL 65a, WAL 65b, FAU 06]. These changes, in return, modify the extension and dynamic of the rupture as well as the radiation of seismic waves [THO 17b]. They also influence seismic processes during the post-seismic period, such as aftershocks, with the minimum size of the nucleation zone depending chiefly on the elastic modulus [RUB 05]. In their experimental study, Gratier et al. [GRA 14] have also demonstrated that the co-seismic damage would promote aseismic slip through pressure-dissolution, thus explaining the afterslip recorded following large earthquakes. Co-seismic damage also increases permeability (Figure 4.13(e)), which results in a variation in the fluid pressure [SIB 94] that modifies the fault's resistance to slip. Geophysical observations suggest that this effect is transient (Figure 4.13(d)), because a gradual and partial recovery of the elastic properties after the earthquake has been recorded [HIR 05, FRO 14]. This evolution is probably related to the healing of microfractures and faults through the precipitation of dissolved substances, products of alteration and/or the development of clayey minerals [MIT 08]. In their model, den Hartog and Spiers [DEN 14] propose that the compaction through pressure-dissolution leads in turn to the recovery of seismogenic behavior.

Moreover, several studies have demonstrated the influence of the properties of the surrounding rock on the behavior of faults. Audet and co-authors have shown a direct relationship between the physical properties of the interlocking plate in the subduction zone and the recurrence of slow earthquakes [AUD 14]. In my microstructure study of Taiwan's longitudinal valley fault, Thomas and co-authors were able to demonstrate the aseismic behavior of the fault was controlled by inherited microstructure [THO 14b]. Perrin et al. [PER 16] proposed the influence of the "maturity" of the faults on the accumulation of slip. A study of 27 earthquakes concluded that the more damage the fault presents (mature fault), the greater the quantity of slip during an earthquake.

4.4. Transition toward a new generation of models

The usual way of looking at the fault restricts the deformation in the brittle part of the crust to slip along the interface (fault plane), loaded with creep at depth, whose

behavior is controlled by its frictional properties [SCH 98]. According to these properties, when the resistance threshold is exceeded, the stress accumulated when the fault is locked is released through seismic slip or creep, or again during slow earthquakes. Further, as the previously cited studies have highlighted, while the behavior of the fault zones is intrinsically related to the properties of the main slip plane, it also depends on the properties of the surrounding rock. In parallel, the displacement on the faults induces a modification of the physical properties of the surrounding medium. These observations suggest the existence of a second "cycle" where the properties of the fault zone evolve with respect to the slip dynamic, which in turn influences the deformation mode.

However, the majority of models used today do not take into account this complex feedback. By attributing constant properties (pressure, temperature, petrology, microstructure) that do not evolve with deformation, we neglect to take into account how seismic/aseismic fault behavior is impacted by temporal variations of the physical properties of the volume and the interface. It is thus useful to develop a new generation of models that take into account spatial-temporal evolution of physical properties in fault zones. New models are being developed and have already shown the importance of these interactions from a seismic point of view [THO 17b, THO 18, OKU 19].

4.5. References

[AMP 08] AMPUERO J.-P., RUBIN A.M., "Earthquake nucleation on rate and state faults – Aging and slip laws", *J. Geophys. Res.*, vol. 113, no. B1, 2008.

[AND 76] ANDREWS D.J., "Rupture velocity of plane strain shear cracks", *J. Geophys. Res.*, vol. 81, no. B32, pp. 5679–5689, 1976.

[AND 94] ANDERS M., WILTSCHKO D.V., "Microfracturing, paleostress and the growth of faults", *Journal of Structural Geology*, vol. 16, no. 6, pp. 795–815, June 1994.

[AUD 14] AUDET P., BURGMANN R., "Possible control of subduction zone slow-earthquake periodicity by silica enrichment", *Nature*, vol. 510, pp. 389–392, 2014.

[BAR 59] BARENBLATT G.I., "The formation of equilibrium cracks during brittle fracture. General ideas and hypotheses. Axially-symmetric cracks", *J. Appl. Math. Mech.-USSR.*, vol. 23, no. 3, pp. 622–636, 1959.

[BHA 15] BHATTACHARYA P., RUBIN A.M., BAYART E. et al., "Critical evaluation of state evolution laws in rate and state friction: Fitting large velocity steps in simulated fault gouge with time-, slip-, and stress-dependent constitutive laws", *J. Geophys. Res.*, vol. 120, no. 9, pp. 6365–6385, 2015.

[BIZ 12] BIZZARRI A., BHAT H., *The Mechanics of Faulting: From Laboratory to Real Earthquakes*, Research Signpost, Trivandrum, 2012.

[BLA 98] BLANPIED M., MARONE C., LOCKNER D. et al., "Quantitative measure of the variation in fault rheology due to fluid-rock interactions", *J. Geophys. Res.*, vol. 103, no. B5, pp. 9691–9712, 1998.

[BOC 13] BOCQUET L., "Friction: An introduction, with emphaisis on some implications in winter sports", CLANET C., (ed.), *Sports Physics*, Editions de l'Ecole Polytechnique, Palaiseau, 2013.

[BRA 66] BRACE W.F., BYERLEE J.D., "Stick-slip as a mechanism for earthquakes", *Science*, vol. 153, no. 3739, pp. 990–992, 1966.

[BUR 67] BURRIDGE L.K.R., "Model and theoretical seismicity", *Bulletin of the Seismological Society of America*, vol. 57, no. 3, pp. 341–371, 1967.

[DAY 82] DAY S.M., "Three-dimensional simulation of spontaneous rupture: The effect of nonuniform prestress", *Bull. Seism. Soc. Am.*, vol. 72, no. 6A, pp. 1881–1902, 1982.

[DEN 14] DEN HARTOG S.A.M., SPIERS C.J., "A microphysical model for fault gouge friction applied to subduction megathrusts", *Journal of Geophysical Research: Solid Earth*, vol. 119, no. 2, pp. 1510–1529, 2014.

[DIE 79a] DIETERICH J.H., "Modeling of rock friction 1: Experimental results and constitutive equations", *J. Geophys. Res.*, vol. 84, no. B5, pp. 2161–2168, 1979.

[DIE 79b] DIETERICH J.H., "Modeling of rock friction 2: Simulation of preseismic slip", *J. Geophys. Res.*, vol. 84, no. B5, pp. 2169–2175, 1979.

[DIE 94] DIETERICH J.H., KILGORE B., "Direct observation of frictional contacts: New insights for state-dependent properties", *Pure Appl. Geophys.*, vol. 143, no. 1, pp. 283–302, 1994.

[DRA 01] DRAGERT H., WANG K.L., JAMES T.S., "A silent slip event on the deeper Cascadia subduction interface", *Science*, vol. 292, no. 5521, pp. 1525–1528, 2001.

[DUG 60] DUGDALE D., "Yielding of steel sheets containing slits", *J. Mech. Phys. Solids*, vol. 8, pp. 66–75, 1960.

[ESH 69] ESHELBY J.D., "The elastic field of a crack extending non-uniformly under general anti-plane loading", *J. Mech. Phys. Solids*, vol. 17, no. 3, pp. 177–199, 1969.

[FAU 06] FAULKNER D.R., MITCHELL T.M., HEALY D. et al., "Slip on 'weak' faults by the rotation of regional stress in the fracture damage zone", *Nature*, vol. 444, no. 7121, pp. 922–925, December 2006.

[FRO 14] FROMENT B., MCGUIRE J.J., VAN DER HILST R.D. et al., "Imaging along-strike variations inmechanical properties of the Gofar transform fault, East Pacific Rise", *Journal of Geophysical Research-solid Earth*, vol. 119, no. 9, pp. 7175–7194, September 2014.

[GRA 14] GRATIER J.P., RENARD F., VIAL B., "Postseismic pressure solution creep: Evidence and time-dependent change from dynamic indenting experiments", *Journal of Geophysical Research-solid Earth*, vol. 119, no. 4, pp. 2764–2779, 2014.

[HIR 05] HIRAMATSU Y., HONMA H., SAIGA A. et al., "Seismological evidence on characteristic time of crack healing in the shallow crust", *Geophys. Res. Lett.*, vol. 32, no. 9, 2005.

[IDA 72] IDA Y., "Cohesive force across tip of a longitudinal-shear crack and Griffiths specific surface-energy", *J. Geophys. Res.*, vol. 77, pp. 3796–3805, 1972.

[IDE 07] IDE S., SHELLY D.R., BEROZA G.C., "Mechanism of deep low frequency earthquakes: Further evidence that deep non-volcanic tremor is generated by shear slip on the plate interface", *Geophysical Research Letters*, vol. 34, 2007.

[ITO 06] ITO Y., OBARA K., "Very low frequency earthquakes within accretionary prisms are very low stress-drop earthquakes", *Geophys. Res. Lett.*, vol. 33, no. 9, 2006.

[ITO 07] ITO Y., OBARA K., SHIOMI K. et al., "Slow earthquakes coincident with episodic tremors and slow slip events", *Science*, vol. 315, no. 5811, pp. 503–506, 2007.

[JOH 12] JOHNSON K.M., FUKUDA J., SEGALL P., "Challenging the rate-state asperity model: Afterslip following the 2011 M9 Tohoku-oki, Japan, earthquake", *Geophysical Research Letters*, vol. 39, no. 20, p. L20302, 2012.

[KAT 01] KATO N., TULLIS T.E., "A composite rate-and state-dependent law for rock friction", *Geophys. Res. Lett.*, vol. 28, no. 6, pp. 1103–1106, 2001.

[KOS 64] KOSTROV B., "Selfsimilar problems of propagation of shear cracks", *J. Appl. Math. Mech.-USS.*, vol. 28, no. 5, pp. 1077–1087, 1964.

[KOS 66] KOSTROV B., "Unsteady propagation of longitudinal shear cracks", *J. Appl. Math. Mech.-USS.*, vol. 30, pp. 1241–1248, 1966.

[LAP 12] LAPUSTA N., BARBOT S., "Models of earthquakes and aseismic slip based on laboratory-derived rate and state friction laws", BIZZARRI A., BHAT H.S. (eds), *The Mechanics of Faulting: From Laboratory to Earthquakes*, Research Signpost, Trivandrum, 2012.

[LEO 59] LEONOV M.Y., PANASYUK V.V., "Development of the smallest cracks in a solid", *Prikl. Mekh.*, vol. 5, no. 4, pp. 391–401, 1959.

[LIN 92] LINKER M., DIETERICH J.H., "Effects of variable normal stress on rock friction: Observations and constitutive equations", *J. Geophys. Res.*, vol. 97, no. B4, pp. 4923–4940, 1992.

[MAR 98] MARONE C., "Laboratory-derived friction laws and their application to seismic faulting", *Ann. Rev. Earth Planet. Sci.*, vol. 26, no. 1, pp. 643–696, 1998.

[MIT 08] MITCHELL T.M., FAULKNER D.R., "Experimental measurements of permeability evolution during triaxial compression of initially intact crystalline rocks and implications for fluid flow in fault zones", *Journal of Geophysical Research-solid Earth*, vol. 113, no. B11, p. B11412, November 2008.

[MIT 09] MITCHELL T.M., FAULKNER D.R., "The nature and origin of off-fault damage surrounding strike-slip fault zones with a wide range of displacements: A field study from the Atacama fault system, northern Chile", *Journal of Structural Geology*, vol. 31, no. 8, pp. 802–816, August 2009.

[OBA 02] OBARA K., "Nonvolcanic deep tremor associated with subduction in southwest Japan", *Science*, vol. 296, no. 5573, pp. 1679–1681, 2002.

[OKU 19] OKUBO K., BHAT H.S., ROUGIER E. et al., "Dynamics, radiation, and overall energy budget of earthquake rupture with coseismic off-fault damage", *Journal of Geophysical Research: Solid Earth*, vol. 124, no. 11, pp. 11771–11801, 2019.

[OUT 10] OUTERBRIDGE K.C., DIXON T.H., SCHWARTZ S.Y. et al., "A tremor and slip event on the Cocos-Caribbean subduction zone as measured by a global positioning system (GPS) and seismic network on the Nicoya Peninsula, Costa Rica", *Journal of Geophysical Research: Solid Earth*, vol. 115, no. B10, B10408, 2010.

[PAL 73] PALMER A.C., RICE J.R., "Growth of slip surfaces in progressive failure of over-consolidated clay", *Proc. R. Soc. Lond. Ser-A*, vol. 332, pp. 527–548, 1973.

[PEN 10] PENG Z., GOMBERG J., "An integrated perspective of the continuum between earthquakes and slow-slip phenomena", *Nature Geoscience*, vol. 3, pp. 599, August 2010.

[PER 95] PERRIN G., RICE J.R., ZHENG G., "Self-healing slip pulse on a frictional surface", *J. Mech. Phys. Solids*, vol. 43, no. 9, pp. 1461–1495, 1995.

[PER 16] PERRIN C., MANIGHETTI I., AMPUERO J.-P. et al., "Location of largest earthquake slip and fast rupture controlled by along-strike change in fault structural maturity due to fault growth", *Journal of Geophysical Research: Solid Earth*, vol. 121, no. 5, pp. 3666–3685, 2016.

[RAB 58] RABINOWICZ E., "The intrinsic variables affecting the stick-slip process", *Proc. Phys. Soc.*, vol. 71, no. 4, p. 668, 1958.

[RIC 93] RICE J.R., "Spatio-temporal complexity of slip on a fault", *J. Geophys. Res.*, vol. 98, no. B6, pp. 9885–9907, 1993.

[RIC 06] RICE J.R., "Heating and weakening of faults during earthquake slip", *J. Geophys. Res.*, vol. 111, no. B05311, 2006.

[ROM 17] ROMANET P., Fast algorithms to model quasi-dynamic earthquake cycles in complex fault networks, PhD Thesis, Institut de Physique du Globe de Paris, 2017.

[ROU 16] ROUSSET B., JOLIVET R., SIMONS M. et al., "An aseismic slip transient on the North Anatolian Fault", *Geophysical Research Letters*, vol. 43, no. 7, pp. 3254–3262, 2016.

[RUB 05] RUBIN A.M., AMPUERO J.P., "Earthquake nucleation on (aging) rate and state faults", *Journal of Geophysical Research-solid Earth*, vol. 110, no. B11, p. B11312, November 2005.

[RUI 83] RUINA A., "Slip instability and state variable friction laws", *J. Geophys. Res.*, vol. 88, no. 10, pp. 359–370, 1983.

[SCH 98] SCHOLZ C.H., "Earthquakes and friction laws", *Nature*, vol. 391, pp. 37–42, 1998.

[SCH 11] SCHMITT S., SEGALL P., MATSUZAWA T., "Shear heating-induced thermal pressurization during earthquake nucleation", *J. Geophys. Res.*, vol. 116, no. B6, 2011.

[SEG 95] SEGALL P., RICE J.R., "Dilatancy, compaction, and slip instability of a fluid-infiltrated fault", *J. Geophys. Res.*, vol. 100, no. B11, pp. 22155–22171, 1995.

[SEG 12] SEGALL P., BRADLEY A.M., "The role of thermal pressurization and dilatancy in controlling the rate of fault slip", *J. Appl. Mech.*, vol. 79, no. 3, p. 031013, 2012.

[SIB 94] SIBSON R.H., "Crustal stress, faulting and fluid flow", *Geological Society, London, Special Publications*, vol. 78, no. 1, pp. 69–84, 1994.

[THO 14a] THOMAS M.Y., AVOUAC J.-P., CHAMPENOIS J. et al., "Spatiotemporal evolution of seismic and aseismic slip on the Longitudinal Valley Fault, Taiwan", *Journal of Geophysical Research-solid Earth*, vol. 119, pp. 5114–5139, 2014.

[THO 14b] THOMAS M.Y., AVOUAC J.-P., GRATIER J.-P. et al., "Lithological control on the deformation mechanism and the mode of fault slip on the Longitudinal Valley Fault, Taiwan", *Tectonophysics*, vol. 632, pp. 48–63, 2014.

[THO 17a] THOMAS M.Y., AVOUAC J.-P., LAPUSTA N., "Rate-and-state friction properties of the Longitudinal Valley Fault from kinematic and dynamic modeling of seismic and aseismic slip", *Journal of Geophysical Research-solid Earth*, vol. 122, pp. 3115–3137, 2017.

[THO 17b] THOMAS M.Y., BHAT H.S., KLINGER Y., "Effect of brittle off-fault damage on earthquake rupture dynamics", in THOMAS M.Y., MITCHELL T.M., BHAT H.S. (eds), *Fault Zone Dynamic Processes: Evolution of Fault Properties During Seismic Rupture*, American Geophysical Union and John Wiley & Sons, Hoboken, NJ, 2017.

[THO 18] THOMAS M.Y., BHAT H.S., "Dynamic evolution of off-fault medium during an earthquake: A micromechanics based model", *Geophysical Journal International*, vol. 214, issue 2, pp. 1267–1280, 2018.

[TIT 06] TITUS S.J., DEMETS C., TIKOFF B., "Thirty-five-year creep rates for the creeping segment of the San Andreas fault and the effects of the 2004 Parkfield earthquake: Constraints from alignment arrays, continuous global positioning system, and creepmeters", *Bulletin of the Seismological Society of America*, vol. 96, no. 4, pp. S250–S268, 2006.

[TUL 15] TULLIS T.E., SCHUBERT G., "4.06 – Mechanisms for friction of rock at earthquake slip rates", in SCHUBERT, G. (ed.), *Treatise on Geophysics (Second Edition)*, Elsevier, Amsterdam, 2015.

[WAL 65a] WALSH J.B., "The effect of cracks in rocks on Poisson's ratio", *J. Geophys. Res.*, vol. 70, no. 20, pp. 5249–5257, 1965.

[WAL 65b] WALSH J.B., "The effect of cracks on the compressibility of rock", *J. Geophys. Res.*, vol. 70, no. 2, pp. 381–389, 1965.

[WIB 08] WIBBERLEY C.A., YIELDING G., DI TORO G., "Recent advances in the understanding of fault zone internal structure: A review", *Geological Society, London, Special Publications*, vol. 299, no. 1, pp. 5–33, 2008.

[ZHU 13] ZHURAVLEV V.P., "On the history of the dry friction law", *Mechanics of Solids*, vol. 48, no. 4, pp. 364–369, 2013.

5

The Seismic Cycle of the Chilean Subduction: Mega-earthquakes, Seismic Gap and Coupling

Christophe VIGNY and Emilie KLEIN
Laboratoire de géologie CNRS UMR 8538,
Ecole normale supérieure – PSL University, Paris, France

5.1. The seismo-tectonic context

Chile's seismicity essentially results from the high-velocity convergence (7 cm/year according to the GPS measurements carried out in recent decades) of the Nazca Plate toward the South American Plate. While the movement is slightly oblique over a length of more than 2,000 km, from the Peruvian border to Patagonia, it is almost entirely absorbed on a single fault at sea. Along this fault, the Nazca Plate passes under the South America Plate and then sinks into the Earth's mantle in what is called a subduction motion (Figure 5.1, see Introduction). The situation changes south of 40°S, with the presence of a third plate (the Antarctic Plate) and then a fourth (the Scotia Plate), which introduces great complexity with different movements that are less well known and new faults on land. The Chilean subduction zone experiences intense seismic activity. On average, there is a magnitude 8 earthquake every 10 years and a magnitude 9 earthquake at least once a century

For a color version of all of the figures in this chapter, see www.iste.co.uk/rolandone/seismic.zip.

The Seismic Cycle,
coordinated by Frédérique ROLANDONE. © ISTE Ltd 2022.

The Seismic Cycle: From Observation to Modeling,
First Edition. Frédérique Rolandone.

(Table 5.1). Finally, the largest earthquake ever recorded (since the advent of seismographs), with a magnitude of about 9.4–9.5, occurred in Chile, just south of Concepción (37°S): the Valdivia earthquake of May 22, 1960.

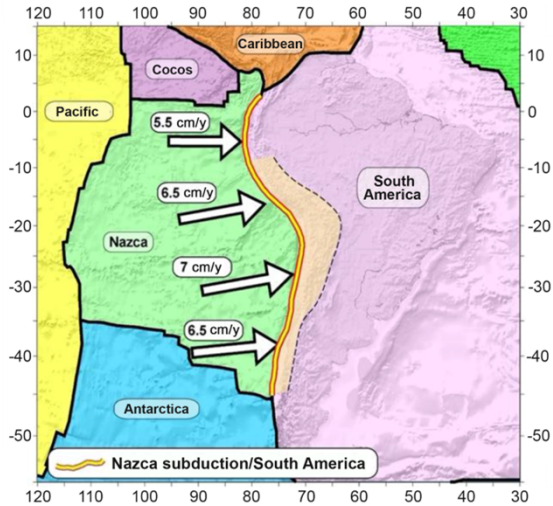

Figure 5.1. *Plate tectonics of the region. The thick red/yellow line shows the subduction of the Nazca Plate under the South American Plate; the dashed line follows the eastern border of the Andes; the orange-shaded area between the two lines covers the high topography of the mountain range. Arrows show the direction and velocity of the convergence between the two tectonic plates, determined using GPS*

Three types of earthquakes: Different types of earthquakes occur in Chile (Figure 5.2):

1) *Subduction earthquakes*: they occur on the subduction interface, due to the friction between the two plates. These are generally the largest earthquakes and can reach a magnitude of 9. Since ruptures largely occur at sea, the damage on land is often relatively moderate. However, they trigger major tsunamis that are responsible for most of the victims and destruction (examples around the world: Sumatra 2004 and Japan 2011; examples from Chile: Valdivia 1960, Maule 2010 and Illapel 2015).

2) *Intra-plate earthquakes* of two sorts occur either in the upper plate or in the lower plate due to the stresses that accumulate there. Although they are often smaller (magnitudes ranging between 5.5 and 8, typically), since they are limited to the thickness of the plate, they can be very destructive: they are closer to the surface and/or located just below inhabited regions. Furthermore, for the same magnitude, the ground accelerations may vary significantly both in amplitude and frequency

content. In particular, the spectrum of emitted waves may contain more or fewer high frequencies. Buildings are more likely to be affected if more high frequencies are present (see Chapter 1).

Date	Name	M_w	Type	max g
1939	Chillan	7.8	Deep intra-slab	0.2 g
1958	Las Melosas	6.8	Superficial crustal	0.2 g
1960	Valdivia	9.5	Subduction	1.2 g
1966	TalTal	7.7	?	1.9 g
1985	Valparaiso	8.0	Subduction	0.5 g
1987	Antofagasta	7.6	?	0.4 g
1995	Antofagasta	8.0	Subduction	0.8 g
1997	Punitaqui	7.1	Deep intra-slab	0.4 g
2005	Tarapaca	7.8	Deep intra-slab	0.9 g
2007	Tocopilla	7.7	Subduction	0.3 g
2010	Maule	8.8	Subduction	0.9 g
2010	Pichilemu	7.0	Superficial crustal	0.2 g
2014	Iquique	8.1	Subduction	0.6 g
2015	Illapel	8.3	Subduction	0.7 g
2019	Tongoy	6.7	? (complex)	0.3 g

Table 5.1. *Non-exhaustive summary of significant earthquakes in central and northern Chile in recent decades. The maximum accelerations given come from USGS models*

5.2. The seismic gap theory applied to Chile

In the late 1960s, tectonic plate theory prevailed. It provided a simple conceptual framework to understand the occurrence of earthquakes (see Introduction). The plates move, but the faults are locked due to friction and consequently deformation slowly accumulates around the edges of the plate. A rupture occurs when the deformation exceeds the resistance. Therefore, at a given site we see an accumulation-rupture cycle, which is constantly repeated. This leads to a simple observation: if at a given site, there has been no earthquake for a long time (called a gap or seismic gap), a lot of deformation has accumulated here and a large earthquake may occur. Conversely, a zone that has recently ruptured must wait a long time for enough deformation to accumulate before it ruptures again. This is the seismic gap theory as formulated by [KEL 72] and applied to South America by [NIS 85]. This theory can be quantified by measuring plate velocity and the deformation released by an earthquake.

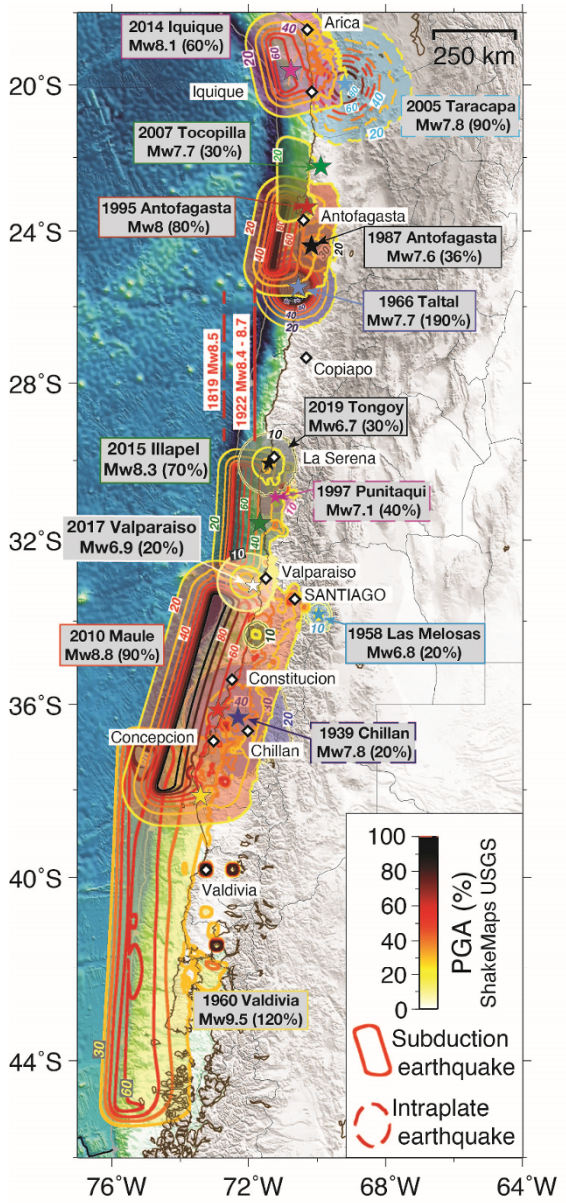

Figure 5.2. *Example of recent significant earthquakes in Chile (non-exhaustive list). The stars indicate the epicenters, the colored contour lines indicate the ground acceleration produced by earthquakes as a percentage of g, according to the scale (yellow ~20% g, red ~60% g, black ~100% g), source USGS*

If two plates converge at 10 cm/year and a magnitude 8 earthquake releases 5 m of deformation over a 100 km long segment, this zone would see such an earthquake every 50 years. The gap theory works quite well in Chile: the Maule earthquake (33°S–38°S) of February 27, 2010 (Mw 8.8) released the deformation accumulated since the last earthquake in 1835, described by Darwin [MAD 10, VIG 11, MET 12]. GPS stations positioned on the coast measured up to 6 m of co-seismic displacement, which corresponds quite well to the slow accumulation observed earlier by the stations: 40 mm/year during the 175 years that elapsed between the two earthquakes, that is, around 7 m in total. Even better, the 2015 Illapel earthquake (30°S–32°S) of magnitude 8.4 repeated the ruptures of 1943 and 1880, thus establishing a 70-year recurrence for an earthquake releasing 4–5 m of deformation accumulated at the velocity of 6 cm/year over this duration. Finally, the Atacama desert region experienced very large earthquakes, where magnitudes approached 9, that occurred in 1819 and 1922 [WIL 29]. The fact that the region was quiet for the following 100 years corresponds well with the need to re-accumulate the necessary deformation before rupturing again. In all these regions, the observed co-seismic slip corresponds well, quantitatively, to the slow accumulation over the time-interval between the earthquakes.

5.3. Coupling/seismicity correspondence

Precise spatial geodesy positioning observations, like GPS, have revealed that deformation does not accumulate homogeneously along the subduction. While there are indeed zones where the friction is very high, therefore where the locking is total (100% of the convergence between plates is converted into deformation in the plates), there are also zones where plates in contact undergo little or no deformation, which seems to indicate that coupling between the plates is weak or non-existent (Figure 5.3, see Introduction). As a result, GPS measurements enable us to not only quantify plate velocity, but also map the extent of the zones where deformation accumulates. These are zones where, as per gap theory, future earthquakes will occur. A very good correspondence is seen between coupling maps recorded nowadays and the most recent seismic ruptures [MET 16] (see Introduction). Recent earthquakes indeed always occurred in zones where the coupling is strong and did not propagate into zones with weak coupling (Figure 5.3). These low coupling zones (LCZ) act as barriers to the propagation of the seismic rupture through a very simple mechanism: there is nothing to break since no deformation accumulates here. These LCZ may be more or less wide and, therefore, more or less efficient at stopping the propagation of earthquakes. For example, the low coupling zone of La Serena (30°S) is about 100 km long and it appears that no earthquake with a magnitude of 8 or more has ever passed through it. The 1992 earthquake that occurred in the north, the

magnitude of which was greater than 8.5, stopped here, just like any earthquake that occurred in the Illapel region (in the south), the magnitude of which was greater than 8. Conversely, the low coupling zone of Baranquilla, further north (28°S), is narrower (~50 km) and several large earthquakes (1819, 1922) are likely to have crossed it.

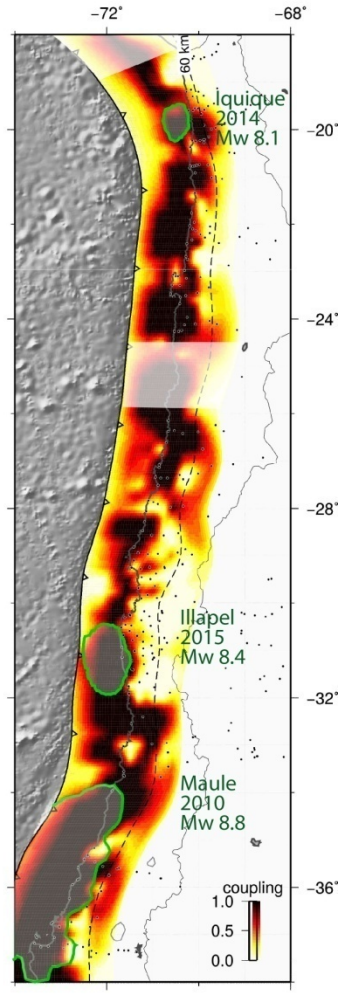

Figure 5.3. *Correspondence between the coupling revealed by GPS measurements and the most recent seismic ruptures, according to [MET 16]. The colored contours show the intensity of the coupling (white = minimum, orange/red = intermediate, black = maximum) as revealed by the distribution of the plate deformation on the surface. The green curves show the extent of the last three large seismic ruptures in Chile*

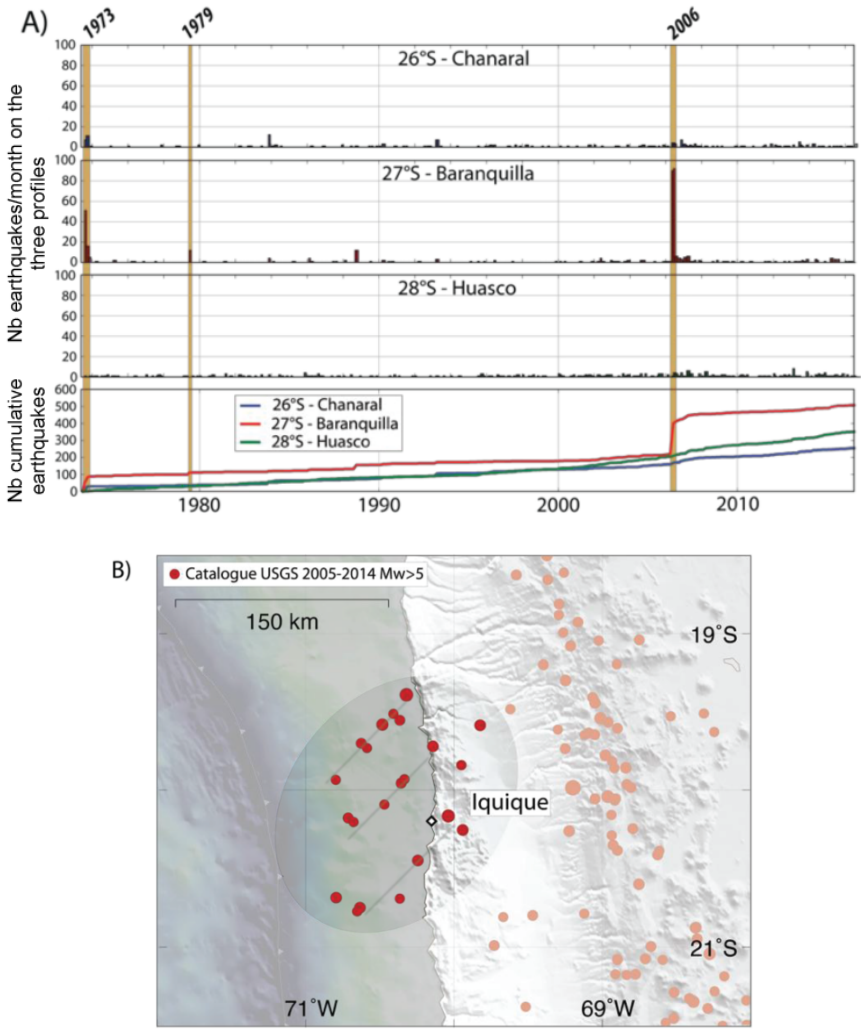

Figure 5.4. *A) Seismicity in the low coupling zone of Baranquilla (Copiapo region – 27°S). The first three frames depict the temporal evolution of seismicity (number of earthquakes per month) over more than 40 years, at three different latitudes (26°S, 27°S and 28°S). Seismicity peaks (up to 100 earthquakes per month in 2006) occur at the center of the decoupled zone. Other seismicity peaks appear, not labeled "swarms", corresponding to the classic sequences of mainshock–aftershocks. The fourth frame depicts the evolution of the cumulative seismicity according to the three profiles. B) Seismicity (Mw > 5) in the low coupling zone of Iquique (20.2°S) between 2005 and 2014 (before the 8.1 magnitude earthquake, USGS catalog) following a linear geometry, called "streaks"*

In low coupling zones, we regularly observe a particular seismicity in the form of swarms. That is, an increase of abnormal seismicity in space and/or time, without a mainshock (something that differs from the standard sequence governed by Omori's law during which a large main shock is followed by a series of smaller aftershocks). Temporal anomaly means more earthquakes during a particular period, or a "seismic crisis", such as those observed repeatedly in the low coupling zone of Baranquilla (Copiapo region – 27°S) in 1973, 1979, and 2006 [HOL 11] (Figure 5.4(A)). Spatial anomaly means there is a concentration of seismicity in a specific region, sometimes following a particular geometry. This is what was observed in the low coupling zone of Iquique (20.2°) before the 2014 earthquake, with seismicity lines oblique to the coast (*streaks*, Figure 5.4(B)).

5.4. Evaluation of the current seismic hazard in Chile

Along the linear part of the subduction (between 20°S and 40°S), there is at least one significant earthquake (magnitude approaching 7 or greater) every 5 years (Table 5.1). These earthquakes occur almost everywhere on this portion of the subduction, with the notable exception of the region between 26°S and 30°S (the Atacama desert region). As previously mentioned, two very large subduction earthquakes occurred here in the past, 200 years ago (1819, Mw 8.5) and 100 years ago (1922, Mw 8.7). It is easy to extrapolate a recurrence of 100 years and to imagine that a large subduction earthquake with a magnitude greater than or equal to 8.5 should occur soon. GPS observations corroborate this information both with regard to the size of the zone where deformation accumulates as well as the quantity of accumulated deformation required to produce an earthquake with a magnitude of well above 8, every 100 years.

5.4.1. *From the hazards to the risk*

"Hazard" is defined as the probability of an earthquake of a certain size occurring at a given place at a given time. The "risk" is the exposure of a population or infrastructure to this hazard. A large, strongly coupled zone in which no earthquake has occurred for a long time poses a large hazard, but the risk is low if there is nothing around it. Conversely, a small fault located very close to a large, poorly built city, may present a low hazard but definitely poses a large risk. Things get even more complicated if we consider that the ground acceleration (in % of g) caused by the passage of seismic waves is only partially related to the size of the earthquake. According to the descriptions given by people who have experienced these firsthand,

large subduction earthquakes tend to produce large but "smooth" movements in the inhabited continent, while continental earthquakes generally produce movements that are more "dry" and more "violent". The maximum acceleration predicted by identified seismic sources varies greatly: between 0.3 g and 1.9 g (Table 5.1). In general, the strongest accelerations correspond to earthquakes that combine large size and shallow depth. Some mysteries remain, such as the 1966 Taltal earthquake, which could have produced maximum accelerations of the order of 190% of g, although it was located relatively deep on the subduction interface.

5.4.2. *"Standard" subduction earthquakes along the Chilean segments from North to South*

a) *The far north segment* (between 18°S and 24°S) ruptured in 1877 (Mw 9+) and only very partially in front of the cities of Tocopilla in 2008 (Mw 7.8) and Iquique in 2014 (Mw 8.1). The deformation has thus been accumulating here for over 150 years and many seismologists have predicted the imminent occurrence of a large earthquake in this region [MAD 91]. We now know (see inset**)** how spatial geodesy has thrown fresh light on this zone by showing that the 1877 rupture and the coupled zone are actually shorter than the whole segment and that producing such a large earthquake...may take much longer, perhaps 300 years in total, that is, still over a century from now.

b) *The Antofagasta segment* (between 24°S and 26°S) ruptured in 1995 (Mw 8, max acceleration ~0.8 g). It appears that this earthquake only ruptured the deep part of the subduction interface. It is possible that this segment will be involved in a subsequent earthquake, which would either complete the rupture of 1995 (an example can be seen in the Bengkulu-Pagai sequence in Sumatra from 2007 to 2010 with three earthquakes, of magnitudes 8.4, 7.9 and 7.7), or would widen the rupture of 1995 (an example of this is the 2010 Maule earthquake that resumed but also enlarged the 1835 rupture described by Darwin).

c) *The Atacama segment* (between 26°S and 30°S) has not ruptured since 1922, though it seemed to rupture every 100 years (1819, Mw 8.5 and 1922, Mw 8.7). The imminent occurrence of a magnitude 8.5 earthquake could therefore be plausible. The worst scenario could feature a simultaneous rupture in the Atacama and Antofagasta segments (perhaps the 1922 situation, as far as we know). If we are to believe the general statistics of a single, very large Chilean earthquake every century, then this catastrophic scenario is not likely to take place in the near

future, since a magnitude 8.8 earthquake has already occurred in the 21st century (Maule, 2010). On the contrary, it seems likely that a repetition of the 1819 earthquake, which was significantly smaller, might occur imminently.

d) *The Illapel segment* (between 30°S and 32°S) ruptured in 2015, following ruptures of equivalent magnitudes in 1943 and 1880. This segment could be a good example of the seismic gap theory, with a characteristic earthquake of magnitude 8–8.5 occurring every 70 years or so. The next one would be 2080–2100.

e) *The Valparaiso segment* (between 32°S and 34°S) generated an earthquake in 1985 (Mw ~ 8), which only partially released the stresses accumulated since the devastating 1906 earthquake (Mw 8.2). Many observers therefore fear the imminence of a large earthquake in the region, where the country's second largest city and most important port is located. In fact, it should already have occurred (at 6–7 cm/year, enough deformation accumulates to produce an earthquake with magnitude well beyond 8 every 100 years, cf. the neighboring Illapel segment), especially as the zone is assumed to have been "weakened" by the 2010 rupture in the south and the 2015 rupture in the north. However, nothing has happened here apart from "aborted seismic crises", such as the one in 2017 (intense seismicity for 2 days, preceding a magnitude 6.9 earthquake). One reason that might explain the non-recurrence of such a large earthquake could be the release of stresses generated by the post-seismic deformations following the 2010 Maule earthquake (see Introduction and Chapter 3).

f) *The Maule segment* (34°S–40°S) ruptured in 2010, after the historic 1835 rupture described by Darwin. Displacements observed by GPS show that the deformation released by the 2010 earthquake corresponds quite well to the deformation accumulated over the 175 years separating the two earthquakes. The zone is in a post-seismic phase for a long time to come and there would thus be nothing significant left to release – on the subduction interface – for at least another century.

5.4.3. *"Deep" subduction earthquakes*

In contrast to the giant earthquakes that rupture the entire subduction interface (from the surface to the transition zone), "smaller" earthquakes (Mw < 8) also occur on the subduction interface but are limited to greater depths (between 40 and 60 km). The ruptures are smaller but the damage may be significant since, first of all, epicenters are close to the coast, and second, seismic waves arrive directly from below. The 1966, 1987 and 2007 earthquakes (all three in North Chile) seem to fall

into this category. The recurrence is unknown, but similar earthquakes can occur several times in a century. Thus, ruptures regularly occur at the level of the city of Taltal (100 km to the south of the astronomical sites of the *Very Large Telescope* (VLT) and the *Extremely Large Telescope* (ELT)), though they have not been precisely located, as this is a rather inaccessible part of the Chilean desert.

5.4.4. *Intra-plate earthquake*

Whether in the slab (part of the already subducted, downward dipping plate) or in the continental crust, superficial earthquakes are rarer. Almost entirely absent in the north, a few superficial earthquakes have occurred in central and southern Chile over the past century (Las Melosas, close to Santiago, in 1958; or more recently, Pichilemu to the south of Valparaiso in 2010) and there were probably some others before the Spanish colonization (e.g. on the San Ramon fault in the Santiago region). However, we have almost no information on any of these. On the contrary, deep intra-slab earthquakes occurred in the north in 2005 (Tarapaca 20°S), in central Chile in 1997 (Punitaqui 31°S) and in the south in 1935 (Chillan 37°S). They reveal the presence of high stresses in the slab at these depths and may perhaps herald large subduction earthquakes, since the earthquakes in Iquique (2014), Illapel (2015) and Maule (2010) occurred in precisely these zones.

5.5. Giant earthquakes and the super-cycle

On May 22, 1960, Chile experienced the largest earthquake ever recorded by seismographs: the 9.5 magnitude Valdivia earthquake [KAN 74, CIF 89, OKA 91]. This earthquake ruptured a portion of the subduction interface nearly 1000 km long, between 36°S and 56°S. It was preceded, on May 21, by a magnitude 8.1 earthquake in the Concepción region, and two other precursors, of magnitude 7.1 and 7.8, in the preceding hours and minutes. This exceptional magnitude was confirmed through comparison with waveforms of the Sumatra earthquake (Mw 9.2) recorded by the same seismographs, more than 40 years apart (Kanamori, pers. Com.). The 1960 earthquake produced much larger signals than the 2004 earthquake. This earthquake also had several other exceptional features. Contrary to standard subduction earthquakes that correspond to a slip on the interface that is perpendicular to the subduction, it included a large shear component [KAN 19]. The extremely large rupture surface, which may explain the magnitude, was so large that it may have exceeded standard seismogenic depths and have extended into the mantle (Kanamori, pers. Com.). Finally, this earthquake triggered a very large-scale

post-seismic deformation that was still detectable 50 years later [KHA 02] (see Chapter 3). For the following 50 years, the segment was seismically silent and was reactivated only very recently, in 2016, with the Chiloé earthquake (Mw 7.6). The fact that this earthquake occurred seems to indicate a return to the accumulation of deformation on the Valdivia segment [RUI 17]. Because of all these exceptional characteristics, this earthquake falls into the category of giant earthquakes.

Earthquakes of magnitude close to 9 and above are truly in a different category. They are much more powerful than those of magnitude 8–8.5, with rupture lengths that can reach 1000 km and produce destructive trans-Pacific tsunamis in Japan. These are rare: 1960 in southern Chile, 1730 in central Chile [UDI 12], 1922 in the Atacama desert [WIL 29] and 1877 in far north Chile [KAU 86, COM 91]. Their long recurrence (300 years?) seems independent from that of many earthquakes of magnitude 8–8.5, which occur almost every 100 years in a given region [RUI 18]. Therefore, the 1960 earthquake covered the smaller seismic ruptures, with magnitudes of the order of 8, from 1737 (Temuco ~39°S) and 1837 (Chiloé ~43°S). The 1730 earthquake, which ruptured the interface from Concepción (37°S) to Huasco (28°S), and maybe even up to Copiapo (27°S), covered the ruptures of an entire series of earthquakes (with a magnitude of around 8) (Talca 1928; Valparaiso 1822, 1906, 1985; Illapel 1880, 1943, 2015). Therefore, the giant earthquake follows a cycle of its own and occurs when its segment is ripe and ready to rupture, involving one or more independent segments, regardless of whether they have ruptured previously. On the contrary, the Valdivia case suggests that they may release enough deformation to produce a period of quiescence for several decades after their occurrence. We thus speak of giant earthquakes that are likely to follow a supercycle, independent of the normal cycle. Such a supercycle was also observed on the Sumatra subduction thanks to the coral reefs, which record co-seismic displacements in their growth rings [SIE 08].

SUMMARY: SCENARIOS OF CONCERN IN CHILE

1) A medium-sized subduction earthquake, slightly deep, located below the coast and at the latitude of one of the large cities or port infrastructures. Unknown recurrence. Accelerations greater than 1 g highly probable.

2) A very large subduction earthquake that could rupture several hundred kilometers of the interface. With a rupture length reaching 500 km, it would correspond to a magnitude close to 9.This is a possible scenario for the Atacama region if we go by the recurrence established by the events of 1819 and 1922.

3) A super-subduction earthquake that would rupture a length of 1000 km like the 2004 Sumatra earthquake. This might have been the case of the 1730 earthquake that is likely to have ruptured from Concepcion to La Serena. This kind of event is undoubtedly very exceptional and we have very little information on its recurrence time and the conditions required for its occurrence.

4) A deep intra-slab earthquake like the 1939 Chillan, 1997 Punitaqui or 2005 Tarapaca events. These earthquakes are relatively infrequent, but not exceptional. They are destructive as inhabited areas are located directly above their epicenter, hence where ground accelerations are strong and the shaking severe. Because they correspond to stresses at depth in the subducting plate, which we have no means of directly quantifying, their occurrence and recurrence is still very difficult to quantify.

5) A crustal earthquake on a continental fault, like San Ramon in the Santiago area. This is an extremely slow fault (maximum 1 mm/year to be compared to the 70 mm/year of the subduction), therefore extremely rare earthquakes (maybe one every 1000–10,000 years), thus with a recurrence probability that is very diluted over time. Such an earthquake would be highly destructive, even with a modest magnitude, because its epicenter would be very close to the surface and perhaps even below the city. The 2010 earthquake in Haiti, which was of moderate magnitude but caused an extremely high level of destruction and close to 300,000 deaths, is a typical example of such an event.

INSET: THE TANGLED HISTORY OF THE SEISMIC GAP IN THE FAR NORTH OF CHILE

A major earthquake, of the order of magnitude 9, occurred in 1877 on the subduction in North Chile. This earthquake is known as the “far north earthquake” or the “Arica bend” earthquake (Arica is a Chilean city close to the Peruvian border). Since no other large earthquake has occurred in this region since this date, it is considered to be a seismic gap worth monitoring: with deformation accumulating here at the rate of around 6–7 cm/year for almost 150 years, the gap seems ready for the imminent occurrence of a very large earthquake, capable of immediately releasing 10 m of the deformation accumulated since 1877. At first glance, the location of the gap seems to correspond to the strong coupling evaluated in the area, confirming the theory: earthquakes occur where the subduction is locked, because this is where the deformation accumulates. However, in reality, the strong coupled zone does not correspond at all to the assumed rupture of the 1877 event. It is much shorter, measuring about 250 km instead of 500 km. This observation has raised doubts about the accuracy of coupling maps and even challenged the seismic gap hypothesis. In fact, the problem lies in the estimation of the 1877 rupture. A careful reading of scientific literature shows how the size of the rupture was “increased” over time....in the literature (Table 5.2, Figure 5.5).

In [KAU 86], the 1877 rupture first extends from Cobija (22.5°S) to Tarapaca (20°S), corresponding to a length of about 285 km. This length (A1 – Table 5.2) is obtained from the size of the zone affected by intensity greater than or equal to VIII (significant destruction on the Mercalli scale) and as per the hypothesis that was in vogue at the time, relating rupture length to intensity VIII [DOR 90]. Intensities are estimated based on the descriptions from that time, reported in [MON 19; Figure 5.5]. However, these estimates are tricky. It is not uncommon for different intensities to be reported in nearby villages, for abnormally high intensities to be reported far from the epicenter or, on the contrary, for abnormally low intensities to be reported closer. It is thus difficult to establish the north and south termination of the rupture. Consequently, in a second step, [KAU 86] extends the rupture up to Pisagua in the north (19.5°S) and takes its length to ~350 km (A2 – Table 5.2) based on more or less dubious information reported by a contemporary Peruvian journalist: large subsidence seemed to have occurred on a coastal strip around Pisagua, as attested by the fact that the sea flooded into this area. In his article, [KAU 86] does write that he is doubtful about this contradictory information, given the low level of destruction observed in Pisagua, but takes it into account anyway. In a third step, he again extends the rupture by 40 km south of Cobija and takes the length to 390 km (A3 – Table 5.2). It was on the basis of these successive extensions that he mapped out the iso-intensity VIII zone (Figure 5.5). Finally, he used a length of 400 km (A4 – Table 5.2) for his calculations. In reality, the "need" for a longer rupture arose from Abe's formula (Abe was a contemporary Japanese seismologist), which related magnitude (M) to rupture length (L) in a simple manner: $M \sim L^3$ [ABE 79]. According to this formula, a rupture length of 285 km is highly insufficient to obtain a magnitude of 9. A rupture length of 400 km is required. Nowadays, we know that this formula is incorrect. It attributes a magnitude 10 to the 2004 Sumatra earthquake (1300 km long) instead of 9.2, and a magnitude 8.5 to the 2011 Japan earthquake (250 km long), instead of 9.0.

In a second, later article ([COM 91], Figure 1e), the rupture goes from south of Cobija to north of Pisagua, that is, ~425 km in length (B – Table 5.2). The article combines two slightly incongruous pieces of information from [KAU 86]: a length from Cobija (22.5°S) to Pisagua (19.5°S), but an epicentral zone extending from 22.5°S to 19°S. This article, written and published in English in an international journal, unlike the article by [KAU 86], written in Spanish and published a Chilean journal, would be a landmark article. Unfortunately, as it describes many other earthquakes in Chile, the paragraph on 1877 is simply a brief summary of the conclusions from [KAU 86] and his doubts and imprecisions are not mentioned.

In a third article ([BEJ 13], Figure 1), the rupture goes from Mejillones (23°S) to northern Arica (18.5°S), that is ~500 km in length (C – Table 5.2). The authors cited the landmark paper [COM 91] and make no mention of additional data. This is a slightly different picture. Indeed, the rupture that occurred in Peru in 1968 is also depicted, presented as disjointed from the 1877 rupture in Chile, just like in [COM 91]; however, the border between the two earthquakes has moved further north by over 50 km (Figure 5.5).

In a final article ([JAR 18], Figure 1), the rupture also reaches the Peruvian border around 18°S with a length of the same order of magnitude (~510 km) (D – Table 5.2), however above all, it overlaps the Peruvian earthquake of 1868 (Figure 5.5). The authors do not cite the preceding articles and do not indicate why they have drawn a different rupture.

To summarize, in 30 years of scientific literature on the topic, the rupture has practically doubled in size, going from the initial 285 km to the 510 km finally described. The very first estimation of the rupture (established over the size of the region affected by intensity VIII (or greater) destruction) was 270 km positioned between Cobija (22.5°S) and south of Iquique (20.5°S), corresponding well with the coupling evaluated nowadays by GPS. This coupling map reveals a more complex segmentation than two large contiguous segments that ruptured in 1868 (Peru) and 1877 (Chile), which would be ready to rupture again imminently. In reality, the two large historic earthquakes are separated by at least 200 km between Arica and Iquique, with this portion itself being made up of two segments: the bend itself, strictly speaking, between Arica and Pisagua, poorly coupled with low seismicity, and the Pisagua-Iquique segment, which is highly coupled and broke precisely in 2014. The seismic hazard in the region must be completely reviewed in light of the coupling revealed by GPS and a close re-examination of scientific literature. If the Arica segment (poorly coupled) and the Pisagua segment (already ruptured in 2014) were not involved in the 1877 earthquake and are not involved in the recurrence to come, then these earthquakes correspond to a length that is twice as short, over which twice as much deformation must accumulate to produce the same magnitude. At the same velocity (6 cm/year for the inter-plate convergence), twice as much time is needed, that is 300 years instead of the 150 years mentioned earlier. The next magnitude 9 earthquake in the region would thus be expected during the 22nd century rather than the 21st century.

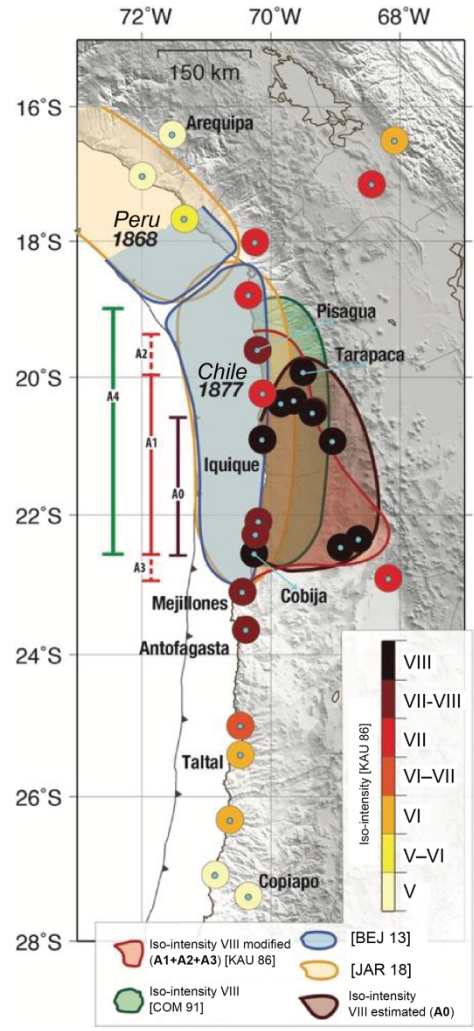

Figure 5.5. *Epicentral area and rupture length of the 1877 earthquake as described in the scientific literature (Table 5.2). Intensities of destruction due to the 1877 earthquake according to the Mercalli scale modified after [KAU 86]. The colored circles indicate the intensities attributed by [KAU 86] according to the analyses of the descriptions of the destruction compiled by [MON 19]. The original epicentral zone corresponds to the geographical zone where the destruction is greater than or equal to level VIII (zone delineated by the brown curve). This zone is considerably smaller than the ruptures described in scientific literature and correspond to the rupture length A0 of the order of 270 km*

	Reference/figure/text	Rupture length	Observation
A1	[KAU 86], text, p. 9 *[intensidades VIII o mayor : lat min Cobija, lat max Tarapaca]*	285 km	Original iso intensities greater than or equal to VIII
A2	[KAU 86], text, p. 10 *[hundimiento costa Pisagua ... incluir este punto dentro de la zone epicentral a pesar de intensida menor que VIII]*	350 km	Iso intensities VIII extended northward using the "information" of subsidence at Pisagua
A3	[KAU 86], Figure 2	390 km	Iso intensities VIII extended southward beyond Cobija, toward Mejillones
A4	[KAU 86], text, p. 12 *[Utilizando esta relacion hemos estimado la magnitude con longitude de falla de 400 km]*	400 km	Value used to calculate the magnitude according to Abe's formula
B	[COM 91], Figure 1(e)	425 km	Cite A. Combine the length of 400 km and the information from the abstract of [KAU 86] [from 19°S to 21.5°S]
C	[BEJ 13], Figure 1(a)	505 km	No explanation, cite B. The 1877 and 1868 ruptures are separated.
D	[JAR 18], Figure 1	510 km	No explanation, cite C. The rupture zones of the 1877 and 1868 overlap.

Table 5.2. *Summary (non-exhaustive) of the rupture length of the 1877 earthquake reported in scientific literature (since 1986)*

5.6. References

[ABE 79] ABE K., "Size of great earthquakes of 1837–1974 inferred from tsunami data", *Journal of Geophysical Research*, vol. 84, pp. 1561–1568, 1979.

[BEJ 13] BEJAR-PIZARRO M., SOCQUET A., ARMIJO R. et al., "Andean structural control on interseismic coupling in the North Chile subduction zone", *Nature Geoscience*, vol. 6, pp. 462–467, 2013.

[CIF 89] CIFUENTES I., SILVER P., "Low-frequency source characteristics of the great 1960 Chilean earthquake", *Journal of Geophysical Research*, vol. 94, pp. 643–663, 1989.

[COM 91] COMTE D., PARDO M., "Reappraisal of great historical earthquakes in the northern Chile and southern Peru seismic gaps", *Nat. Hazards*, vol. 4, pp. 23–44, 1991.

[DOR 90] DORBATH L., CISTERNAS A., DORBATH C. et al., "Assessment of the size of large and great historical earthquakes in Peru", *Bulletin of Seismological Society of America*, vol. 80, pp. 551–576, 1990.

[HOL 11] HOLTKAMP S.G., PRITCHARD M.E., LOHMAN R.B. et al., "Earthquake swarms in South America", *Geophysical Journal International*, vol. 187, no. 1, pp. 128–146, 2011.

[JAR 18] JARA J., SANCHES-REYES H., SOCQUET A. et al., "Kinematic study of Iquique 2014 Mw8.1 earthquake: Understanding the segmentation of the seismogenic zone", *Earth and Planetary Science Letters*, vol. 503, pp. 131–143, 2018.

[KAN 74] KANAMORI H., CIPAR J., "Focal process of the great Chilean earthquake May 22, 1960", *Physics of the Earth and Planetary Interiors*, vol. 9, pp. 128–136, 1974.

[KAN 19] KANAMORI H., RIVERA L., LAMBOTTE S. et al., "Evidence for a large strike-slip component during the 1960 Chilean earthquake", *Geophysical Journal International*, vol. 218, pp. 1–32, 2019.

[KAU 86] KAUSEL E., "Los Terremotos de Agosto de 1868 y Mayo de 1877 que Afectaron el Sur del Peru y Norte de Chile", *Boletin de la Academia Chilena de Ciencias*, vol. 3, pp. 8–12, 1986.

[KHA 02] KHAZARADZE K., WANG K., KLOTZ J. et al., "Prolonged post-seismic deformation of the 1960 great Chile earthquake and implications for mantle rheology", *Geophysical Research Letters*, vol. 29, no. 22, pp. 2050, 2002.

[KEL 72] KELLEHER J.A., "Rupture zones of large South American earthquakes and some predictions", *Journal of Geophysical Research*, vol. 77, no. 11, pp. 2087–2103, 1972.

[MAD 91] MADARIAGA R., "Chili : l'œil sur le séisme", *Le Provençal*, 3 March 1991.

[MAD 10] MADARIAGA R., METOIS M., VIGNY C. et al., "Central Chile finally breaks", *Science*, vol. 328, no. 5975, pp. 181–182, 2010.

[MET 12] METOIS M., VIGNY C., SOCQUET A. et al., "Interseismic coupling, segmentation and mechanical behavior of the central Chile subduction zone", *Journal of Geophysical Research*, vol. 117, pp. B03406, 2012.

[MET 16] METOIS M., VIGNY C., SOCQUET A., "Interseismic coupling, megathrust earthquakes and seismic swarms along the Chilean subduction zone (38_–18_S)", *Pure and Applied Geophysics*, vol. 173, pp. 1431–1449, 2016.

[MON 19] MONTESSUS DE BALLORE F., *Bibliografia general de Temblores y Terromotos*, Imprenta Universitaria, Santiago de Chile, 1915–1919.

[NIS 85] NISHENKO S., "Seismic potential for large and great interplate earthquakes along the Chilean and Southern Peruvian margins of South America: A quantitative reappraisal", *Journal of Geophysical Research*, vol. 90, pp. 3589–3615, 1985.

[OKA 91] OKAL A., TALANDIER J., "Single-station estimates of the seismic moment of the 1960 Chilean and 1964 Alaskan earthquakes, using the mantle magnitude Mm", *Pure and Applied Geophysics*, vol. 136, pp. 103–126, 1991.

[RUI 17] RUIZ S., MORENO M., MELNICK D. et al., "Reawakening of large earthquakes in south central Chile: The 2016 Mw 7.6 Chiloé event", *Geophysical Research Letters*, vol. 44, no. 13, pp. 6633–6640, 2017.

[RUI 18] RUIZ, S., MADARIAGA R., "Historical and recent large megathrust earthquakes in Chile", *Tectonophysics*, vol. 733, pp. 37–56, 2018.

[SIE 08] SIEH K., NATAWIDJAJA D.H., MELTZNER A.J. et al., "Earthquake supercycles inferred from sea-level changes recorded in the Corals of West Sumatra", *Science*, vol. 322, no. 5908, pp. 1674–1678, 2008.

[UDI 12] UDIAS A., MADARIAGA R., BUFORN E. et al., "The large Chilean historical earthquakes of 1647, 1657, 1730, and 1751 from contemporary documents", *Bulletin of Seismological Society of America*, vol. 102, pp. 1639–1653, 2012.

[VIG 11] VIGNY C., SOCQUET A., PEYRAT S. et al., "The 2010 Mw 8.8 Maule mega-thrust earthquake of Central Chile, monitored by GPS", *Science*, vol. 332, pp. 1417–1421, 2011.

[WIL 29] WILLIS B., *Studies in Comparative Seismology: Earthquake Conditions in Chile*, Carnegie Institution of Washington, 1929.

6

The Mexican Subduction Seismic Cycle: Highlighting the Key Role Played by Transient Deformations

Mathilde RADIGUET
ISTerre, Grenoble Alpes University, France

Subductions are convergence zones between tectonic plates, known for being the regions where the largest earthquakes in the world occur. These earthquakes are related to the brutal release of stresses that accumulate slowly in the contact area between the subducted and upper plate as a result of tectonic movements. Understanding the mechanisms through which convergence is accommodated is essential for a better assessment of the seismic hazard.

The past two decades have seen an explosion in the number of deformation measurements at the level of the plate boundaries, especially with the rise in continuous GNSS stations and, more recently, satellite radar imaging with a revisit time of a few days. These observations shed light on the diversity in deformation modes in fault zones (see the Introduction and Chapters 2, 3, 5 and 8).

This chapter will look specifically at the seismic cycle on the Mexican Pacific margin, which corresponds to the subduction of the Cocos/Riviera oceanic plates

For a color version of all the figures in this chapter, see www.iste.co.uk/rolandone/seismic.zip.

The Seismic Cycle,
coordinated by Frédérique ROLANDONE. © ISTE Ltd 2022.

The Seismic Cycle: From Observation to Modeling,
First Edition. Frédérique Rolandone.

beneath the North American plate. This Mexican subduction zone is known for causing destructive earthquakes, the best known being the 1985 Michoacán earthquake of magnitude 8.1. This earthquake is tragically notorious for the tens of thousands of victims and the extensive damage it caused, chiefly in Mexico City. Because of the diverse processes that take place there, which will be detailed in this chapter, this region is of particular interest when it comes to studying the different modes of stress accumulation and release, which govern the seismic cycle in a subduction zone. In this chapter, we will place particular emphasis on the different slip modes, seismic and aseismic, observed in this subduction zone and their interrelations, both spatial and temporal.

6.1. The geo-dynamic context of the region

6.1.1. *Convergence of plates and geometry of the subduction*

The Middle American Trench extends over almost 3,000 km and marks the boundary between the oceanic plates of Rivera/Cocos (in the north) and Nazca (in the south), which are subducted beneath the North American and Caribbean plates. This chapter is limited to studying the subduction between the Rivera/Cocos and North American plates, between -106 and -92° of longitude, that is, the Mexican portion of this subduction zone. The Cocos plate corresponds to a fragment of the Farralon plate, formed around 23 Mya (million years ago), when it separated from the Nazca plate in the south. The Rivera microplate is the most recently broken fragment of the Cocos plate, and has moved independently for at least 10 million years [DEM 00]. These two plates are relatively young, about 5–25 million years old, with ages that vary suddenly at the location of the oceanic fracture zones. The convergence velocity between the Cocos and North American plates varies from west to east between 55 mm/year and 75 mm/year [DeMets 2000]. The Rivera-North American plate convergence velocities are quite poorly defined [BAN 95], but estimations give velocities of 20–40 mm/year.

The southern limit of the study region is the triple point between the Cocos, Caribbean and North American plates, characterized by the Polochiv–Motagua system of sinistral strike-slip faults. At its northwest end, the Mexican subduction zone ends in the Gulf of California. The boundary between the Rivera plate and the Cocos plate is poorly defined. It is marked by a 100-km-wide seismicity band at the El Gordo Graben in the sea [DEM 00]. This depression extends inland with the Colima Graben, which has been active for 5 million years [BAN 95]. Extensive motions affect the upper plate, both at the location of the Colima Graben and further north on the Tepic-Zacoalco rift. These two graben zones delimit the Jalisco block. The origin of this extension is attributed to the roll-back motion of the Rivera plate [MAN 13] and, sometimes, to the obliquity of the convergence 5 million years ago having induced a dextral strike-slip and extensive stresses in the upper plate [DEM 00].

Since the direction of convergence between the Cocos and North American plates has an obliquity of around 10° with respect to the trench, a trench-parallel strike-slip component of around 8 mm/year is yet to be accommodated [GAI 16]. It was proposed that there was a partitioning of the deformation: according to recent studies based on available geodetic observations, the Xolopa sliver is currently active and accommodates a sinistral motion of 3-6mm/year on the La Venta Chacalapa sinistral strike-slip fault system (LVC, see Figure 6.1) [KAZ 20]. While the spatial continuity of this fault network is not clearly established, it has been proposed that this strike-slip fault system was active during the Eocene (to the east) and the Oligocene (to the west) [GAI 16]. One consequence of this subduction is the existence of the Trans-Mexican Volcanic Belt (TMVB), going from east to west around the latitude 21° north (see the white triangles in Figure 6.1). This chain is not parallel to the trench as its orientation is governed by the specific subduction configuration in this region. Many studies have examined the geometry of the interface between the two plates, based on seismicity [PAR 95], seismicity and gravity [KOS 96], or on receiver function imaging [PÉR 08]. All of these studies agree on the existence of a flat slab in the states of Guerrero and Oaxaca (between the latitudes -102 and -96°), at a depth of 40 km (see the depth iso-contours in Figure 6.1). On either side of this zone, the subduction occurs with a high dip angle, around 50° in the Jalisco and Chiapas regions [PAR 95]. In the Chiapas region, there is active volcanic activity closer to the coast. The distance between the trench and the coast is short, around 40–60 km, which is favorable for the observation of the subduction seismic cycle on land.

6.1.2. *Seismicity*

6.1.2.1. *Guerrero seismic gap*

The large earthquakes ($M_w > 7$) that have hit the region since 1900 are depicted in Figure 6.1 with the approximate contours of the zones affected in each case. Almost the entire subduction interface ruptured during earthquakes that occurred in the last century, with the notable exception of a segment between 100°W and 101.2°W, conventionally referred to in the literature as the Guerrero seismic gap [SIN 81]. The last probable earthquake in this zone dates back to 1911, but its location is not accurate. The zone between 99° W and 100° W is sometimes included in this seismic gap, because the earthquakes that occurred there for the last century have been of moderate magnitude. Given the absence of any recent large earthquakes, the Guerrero seismic gap is considered as one of the zones that is most likely to rupture during a major earthquake in the Mexican subduction. It has been widely studied and equipped with instruments in order to assess the possible rupture scenarios and their impact on the regional seismic hazard.

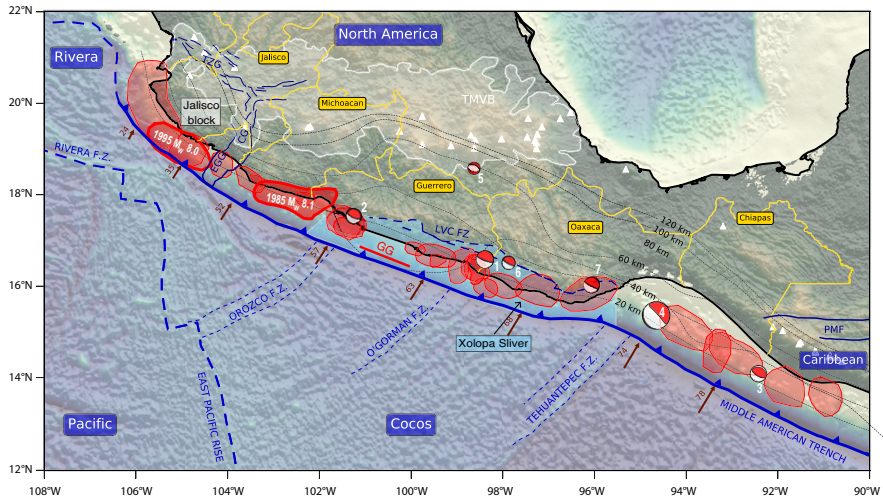

Figure 6.1. *Geodynamic context of the subduction zone in southern Mexico. The Rivera and Cocos ocean plates subduct below the North American plate at a velocity of 25–78 mm/year (brown vectors from the PVEL model [DEM 10]). The chief tectonic structures of the subducting plates are represented by the blue dashed lines. The black dashed lines are the iso-contours of the subduction interface. The yellow contours correspond to the Mexican states. The main volcanoes are represented by the white triangles. The red contours correspond to the main earthquakes with magnitude greater than 7 since 1900. The mechanisms of 7 earthquakes of M_w> 7 between 2010 and 2020 are indicated: 1 = Ometepec M_w7.5-2012/03/20 ; 2 =M_w7.3-2012/11/07; 3 = Papanoa M_w7.2-2014/04/18; 4 = Chiapas M_w8.2-2017/09/08; 5 = Puebla M_w7.1-2017/09/19; 6 = Pinotepa M_w7.2-2018/02/16; 7 =M_w7.4-2020/06/23. The main crustal fault networks are given in blue: EGG = El Gordo Graben; CG = Colima Graben; TZG = Tepic-Zacoalco Graben; LFC-FZ = the La Venta Chacalapa fault zone; PMF = the Polochiv-Motagua Faults. GG = Guerrero Gap; TMVB = Trans Mexican Volcanic Belt*

6.1.2.2. *Two major earthquakes: Michoacán 1985 and Colima 1995*

Among the destructive earthquakes that have affected this region over the last 30 years, the major one is the 1985 Michoacán earthquake (19-09-1985, Mw 8.1), which was located to the west of the Guerrero seismic gap. This was followed by a major aftershock (21-09-1985, Mw 7.5). This earthquake led to considerable damage, largely in Mexico city, which has around 20 million inhabitants, and in which around 10,000 people died, 1,000 buildings were destroyed and close to 300,000 people were rendered homeless. This severe damage occurred despite the epicenter being located almost 400 km away from Mexico City and is attributed to strong site effects. The city is built on lacustrine sediments and consequently, the superficial layers of the basin are very soft, with very low wave propagation velocities. The resonance in

this sedimentary basin led to an amplification of waves and an increase in the signal duration for frequencies between 0.3 and 0.5 Hz, these frequencies being critical for constructions [SIN 88]. Other factors may have played a role, such as source effects, with abnormally large radiations in the frequency range around 0.5 Hz, and the effects of propagation [SIN 90]. More recently, the 1995 Colima-Jalisco earthquake (M_w8.0) also ruptured the subduction interface in the region of the triple point between the Cocos, Rivera and North American plates. This earthquake caused major damage in the coastal cities in Jalisco and Colima. The seismological and geodetic studies [MEN 99, MEL 97], as well as tsunami data [ORT 98], have made it possible to characterize this earthquake that ruptured the superficial part of the interface at a depth of less than 15 km, over a length of 150 km.

6.1.2.3. *Seismic activity between 2010 and 2020*

In addition to the major earthquakes described earlier, we present some information about the five earthquakes with magnitude greater than 7 that affected the region between 2010 and 2020 (see Figure 6.1). We will discuss these events again later in the text, as well as their potential links with the aseismic slip that affect these regions. First of all, two earthquakes with reverse mechanisms ruptured the subduction interface: the Ometepec earthquake, $M_w7.4$ on March 20, 2012 (no. 1 in Figure 6.1) [UNI 13], and the Papanoa earthquake, $M_w7.4$, on April 18, 2014 (no. 2) to the west of the Guerrero gap [UNA 15]. In 2017, two earthquakes occurred, 10 days apart, with a mechanism of normal intra-slab faulting at depths of around 50 km: the Tehuantepec earthquake, $M_w8.2$, on September 9, 2017 (no. 4) [OKU 17] and the Puebla earthquake, M_w 7.1, on September 19, 2017 (no. 5) [MEL 18] near Mexico City. This event caused a lot of damage and many hundreds of fatalities in Mexico City [SIN 18]. On February 16, 2018, a M_w 7.2 earthquake (no. 6, interface earthquake, reverse faulting mechanism) occurred in Oaxaca, to the east of the 2012 earthquake.

6.2. Observation of the seismic cycle: the evolution of networks and the history of discoveries

The observation of the seismic cycle and its complexity is inseparable from the evolution of observation networks that enable us to characterize it (see the Introduction and Chapter 1). By 2020, the Mexican National Seismological Service had around 60 sites around the country equipped with broadband seismological sensors and accelerometers, enabling the study of seismicity on a regional level. To characterize the surface deformation, several complementary GNSS networks exist, notably the TLALOCNet and SSN-TLALOCNet networks, the COCONet network (for the western part) and the sites of the UNAM Institute of Geophysics, with a total of a hundred continuous GNSS stations over the entire network. Radar interferometry is also used to characterize the deformations associated with major earthquakes [LI 20, ATZ 19] or to characterize aseismic deformations [CAV 13, MAU 20]. The

characterization of inter-seismic deformations or slow earthquakes using InSAR in a subduction zone is promising, as it makes it possible to improve spatial coverage of the deformations with respect to GNSS data. It is still difficult, however, because of the anticipated low amplitudes of the deformation (a few cm/year), and the large wavelength of the expected signal, in a region where there are large atmospheric disturbances [MAU 20]. In addition to the continuous networks, it must be noted that between January 2005 and August 2007 a temporary but dense seismic network (MASE) was deployed over a transect perpendicular to the subduction, starting from the coast (Acapulco) and going across Mexico City. This network also allowed a detailed characterization of the geometry of the subduction interface in this region [PÉR 08], and the identification of tremors, and consequently of low-frequency earthquakes (LFEs), over this time period.

The first observation related to the existence of a slow, transient slip in Mexico, in the Guerrero region, was made by Lowry et al. [LOW 01], and published just a few months after the first silent earthquake was observed in the Cascades [DRA 01]. The only available continuous GNSS station (CAYA) recorded a transient deformation signal corresponding to a displacement of 26 mm to the south, over a 6 month period in 1998 (see Figure 6.2(C)). The observation from a single station prevents a more rigorous analysis of the source of the signal, but the authors suggest that it is unlikely that the measured signal can be explained by measurement errors or external causes (linked to precipitation). They also suggest that this signal may be modeled by a dislocation of reverse mechanism on the subduction interface.

The subsequent, growing densification of the GNSS network led to improved observations and in 2001–2002, a second transient deformation event was recorded by seven GNSS stations. This allowed the source to be better characterized [KOS 03]. The same event was also detected by a long base inclinometer [KOS 02] located close to the coast, making it possible to measure deformations more precisely than the GNSS stations.

The attention given to the different regions along the subduction varies. The majority of studies focus on the Guerrero and Oaxaca regions, because this is where the transient deformations were first observed and are the largest. These regions are also the earliest to have been equipped with instruments. Other regions, notably the Michoacán region, were not given as much attention and the geodetic networks there are less dense. This does not allow the detection of transient, low-amplitude signals. This study lists the main observations of transient deformations made between 2000 and 2020 across the Mexican subduction, but it is likely that enhanced networks and observation techniques will, in the coming years, further refine the picture presented here.

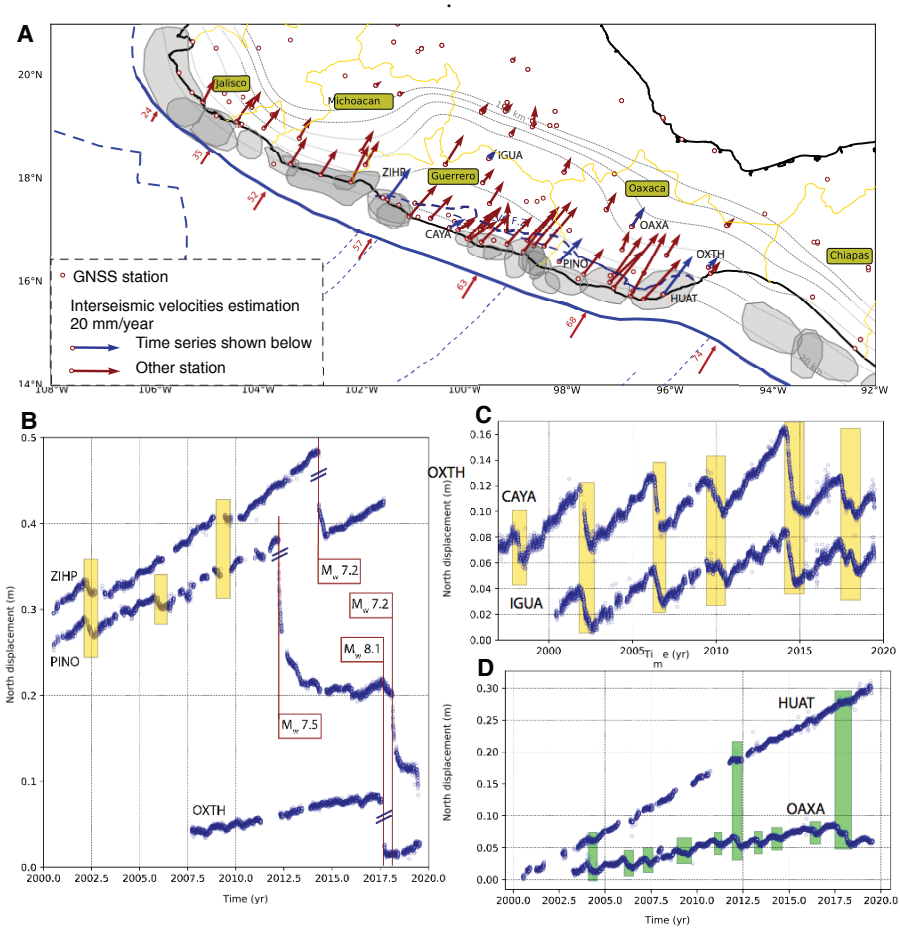

Figure 6.2. *A) Map of GNSS stations (red points) with interseismic velocities (vectors) according to Kazachkina et al. [KAZ 20]. Only the stations that have a time series that is long enough to allow an estimation of interseismic velocities are indicated. The blue vectors are of stations whose time series are presented in B, C and D. B) Examples of GNSS time series that recorded large earthquakes. On the PINO station, the 2012 Oaxaca earthquake ($M_w 7.5$), with large post-seismic displacement, and the 2018 Pinotepa earthquake ($M_w 7.2$). The Papanoa earthquake ($M_w 7.2$) on the ZIHP station and that of the Chiapas earthquake ($M_w 8.1$) on the OXTH station. C) Time series that recorded the major SSEs in Guerrero, which occur roughly every 4 years (yellow rectangles). The IGUA station, further from the coast, also records short-term SSEs with smaller amplitudes (difficult to detect over a single time series). D) Time series recording the Oaxaca SSEs, which occur every 1–2 years (green rectangles). The OAXA station records all SSEs in Oaxaca, and the HUAT station only records some of the largest events*

6.3. Characterization of major slow earthquakes and the relationship with coupling

The densification and the increase in the surveillance period of ground deformation through GNSS time series in Mexico has made it possible to highlight the characteristics of the seismic cycle in this region for the past 20 years or so. Figure 6.2A depicts the average inter-seismic velocities observed over a period of 5–20 years (depending on the stations), estimated using continuous GNSS measures. For coastal stations, the amplitude of horizontal velocities varies between 10 mm/year to the west and 30 mm/year to the east, and is oriented NNE, compatible with the convergence vectors. It can also be seen that there are particularly low velocities in the region of the Guerrero seismic gap. A detailed time series for different stations reveals the large temporal variability in the deformations affecting the upper plate. Figure 6.2(B) presents time series for the stations affected by co-seismic displacements. It must be noted that there are linear displacements toward the north in the inter-seismic period, and instantaneous displacements in the opposite direction during the different earthquakes, sometimes followed by a period of post-seismic displacement. Figures 6.2(C) and (D) depict time series affected by transient aseismic movements. These transient movements accommodate a large part of the inter-seismic deformation and explain the low values for the estimated inter-seismic velocities (especially for the CAYA station). These events (marked by yellow rectangles in Figures 6.2(C) and (D)) correspond to slow slip events (SSEs). They are observed at several stations and the following paragraph describes their main characteristics.

6.3.1. *Characteristics and location of SSEs*

The largest SSEs observed in Mexico occur in the Guerrero region (see time series Figure 6.2(C), yellow rectangles). The surface displacements are of the order of 5 cm on the north component (which records the signal the strongest, since its orientation is close to the orientation of the convergence), and 4 cm on the vertical components. The oldest GNSS time series, on the CAYA station, has made it possible to identify six events between 1998 and 2019. The events have a periodicity close to 4 years (plus or minus 0.5 years), and a variable duration between 8 and 18 months. In the Oaxaca region, the SSEs (OAXA station, Figure 6.2(D), green rectangles) produce weaker surface displacements, and occur every 1 or 2 years.

It is possible to estimate the location and amplitude of the slip on the subduction interface by inverting the surface displacement. In order to do this, slip at depth is modeled by a set of dislocations located on the subduction interface and transfer functions relate the slip at depth to the surface displacement. This is generally done using analytical formulas for the elastic half-space [OKA 92] or stratified elastic media. This inverse problem is regularized so that the solutions become physically acceptable.

Figure 6.3 compiles the estimated locations of the main slow earthquakes recorded in the Guerrero region (between 2002 and 2014) [RAD 16] and the Oaxaca region between 2006 and 2010 [GRA 16]. The estimation of the *equivalent magnitude* of the SSEs makes it possible to compare the seismic moment released by these events with the seismic moments of ordinary earthquakes. For SSEs at Guerrero, taking the example of the 2006 SSE, the average slip on the interface is of the order of 10 cm, over a zone of 300 km $\times$ 150 km or 45 $\times$ 10^3 km^2, the equivalent magnitude of this event is 7.5 [RAD 11], and varies for the events observed between 7.4 and 7.6 [RAD 12]. In the Oaxaca region, the events are generally of smaller amplitude than at Guerrero, for example, the 2004 and 2006 events had a slip area of 100 km $\times$ 50 km and an average slip of the order of 7 cm, which gives an equivalent magnitude of 6.6. The stress drops of the Guerrero SSEs are from 10 to 20 kPa, and around 30 kPa for the Oaxaca SSEs [COR 08], that is, two orders of magnitude smaller than ordinary earthquakes [GAO 12].

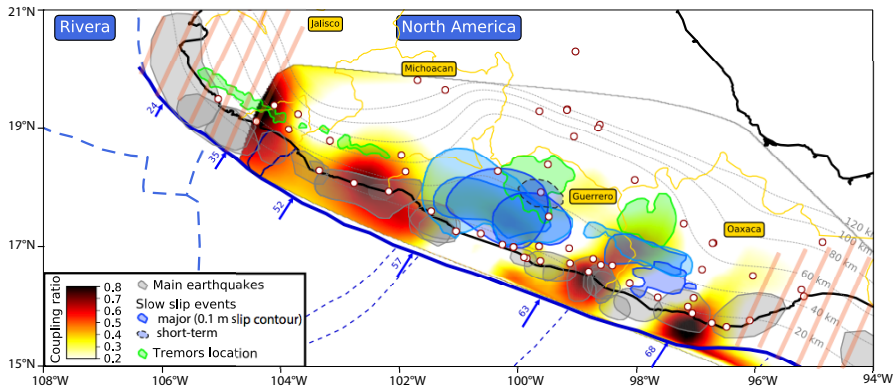

Figure 6.3. *Coupling, location of SSEs and tremors along the subduction. The background colors represent the inter-seismic coupling as per [RAD 16]. In the cross-hatched region, the coupling is poorly defined or not defined. The SSEs in the Guerrero region (2002–2014), from [RAD 16] and Oaxaca region (2006–2010) from [GRA 16] are represented by the blue curves (0.1 m of slip). The contours of the tremors (in green) are taken from Maury et al. [MAU 18]*

In the Oaxaca region, the SSEs are located between a depth of 20–40 km [COR 08]. In Guerrero, they are shallower and go up to depths of around 15 km. This question of location, especially with respect to the minimum depth, is an essential one when it comes to understanding the relationship between slow slip zones and earthquake asperities. To go even further, it is possible to estimate how the

occurrence of these phenomena can modify the inter-seismic loading over a few SSE cycles by studying the coupling.

6.3.2. *Connection to plate coupling*

The GNSS observations available for the past 20 years make it possible to estimate the degree of locking between the upper plate and the subducting plate, by inverting the average deformation velocities over a given period, under the *back-slip hypothesis* [SAV 83]. The ratio between the slip-deficit (estimated through inversion) and the long-term plate-convergence velocity is called "interseismic coupling". An inter-seismic coupling value of 1 corresponds to a perfectly locked interface, a value of 0 corresponds to a slip on the interface at the convergence velocity (see the Introduction for concepts of *back-slip* and coupling). In the Mexican subduction, where tectonic activity is dominated by large-amplitude transient deformations, the estimated coupling varies strongly over the observation period. Figure 6.3 presents the coupling over the 2000–2014 period, taken from [RAD 16], and corresponds to *long-term* coupling, that is, it includes the periods of major slow earthquakes, but excludes co-seismic displacements in the calculation of inter-seismic velocities. If the inter-SSE periods are considered, the displacement velocities measured on the surface would be higher and the apparent, *short-term* coupling will be stronger in zones that slip during the SSEs.

The comparison between the coupling map, the locations of historical earthquakes and the main SSEs (see Figure 6.3) reveal that the SSE zones (in blue) have low long-term coupling (<0.2). With the SSEs accommodating the majority of the movements associated with convergence in these zones, the accumulation of stresses here is either very low or absent. On the contrary, coupling is generally high (>0.7) in the rupture zones of historical earthquakes: these zones thus accumulate stresses that will be released during earthquakes. However, the estimated coupling is weak in the Guerrero seismic gap, above the SSE zone. This observation, which would indicate a weak accumulation of stresses in the Guerrero gap, is yet to be confirmed, especially for the section in the sea, as the resolution of terrestrial data is limited to constrain the coupling in this zone. Nevertheless, these observations demonstrate that the slip deficit that accumulates in the Guerrero seismic gap is much weaker than in the adjacent regions and, consequently, the recurrence time for large earthquakes in the Guerrero gap will probably be greater.

There are, thus, large lateral variabilities in the behavior of this subduction, with changes in coupling and clearly identified SSE zones. In the following paragraph, we will look at the diversity in low-amplitude seismic activity that can be observed there.

6.4. Seismic activity

6.4.1. *The different signal types identified*

Until now, we have chiefly described geodetic observations that make it possible to characterize SSEs. These transient deformations are also associated with seismological signals falling within the slow earthquakes spectrum (see Figure 6.4). We identify tectonic tremors (also called non-volcanic tremors, as opposed to those observed in volcanic zones), which correspond to low-amplitude seismic signals of long duration, whose energy is dominant in the frequency range between 1 and 8 Hz. These signals are emergent and the arrival of P and S waves are not easily identifiable (see Figure 6.4(A)): they are thus generally located by cross-correlation of their seismic envelope. Within these tremor signals, it is possible to identify impulsive and repetitive seismic events, called LFEs. They last a few seconds and are characterized by a low-frequency content, compared to regular earthquakes of similar magnitude [BER 11]. Multiple LFEs can be detected automatically from a LFE signal template using a match filter search method. Because of their impulsive nature, these LFEs are easier to locate than the tremors and may be used as a proxy to characterize tremors [SHE 06, FRA 13]. Finally, note the characterization of signals called *Very Low Frequency Earthquakes* (VLFEs) in the frequency range 0.02–0.05 Hz. These events are generally detected during tremor periods and the sum of waveforms at very low frequency allows us to characterize focal mechanisms for these events, which are compatible with reverse mechanism along the subduction interface [MAU 16, MAU 18].

6.4.2. *Global characteristics of tremors in the subduction zone*

Tectonic tremors have been observed in four main zones in the Mexican subduction (see the green contour lines in Figure 6.3). To the north-west of the subduction, tremors have been mainly identified at Jalisco and also in Michoacán [BRU 16]. They form a band that is about 10 kilometers wide, close to the subduction interface, and their depth varies between 40 km to the east and 20 km to the west [MAU 18]. There is no geodetic deformation signal clearly associated with these seismic signals. The tremors in the Guerrero and Oaxaca region occur in a larger zone, about 50 km wide, at a depth of 40 km. This corresponds to the sub-horizontal part of the subduction interface. The Guerrero tremors are the most widely studied, especially because of the presence of temporary networks that allow their enhanced detection and location, as well as the identification of LFEs. Thus, in Guerrero, it is possible to differentiate between a region where tremors occur consistently (called the *sweet spot*) at around 215 km from the trench, and a zone closer to the trench in which higher energy tremors occur in an episodic manner (see Figure 6.5). Spatially, the transient tremor zone is located at greater depth than the main slow slip zone (see the profile in Figure 6.5(D)).

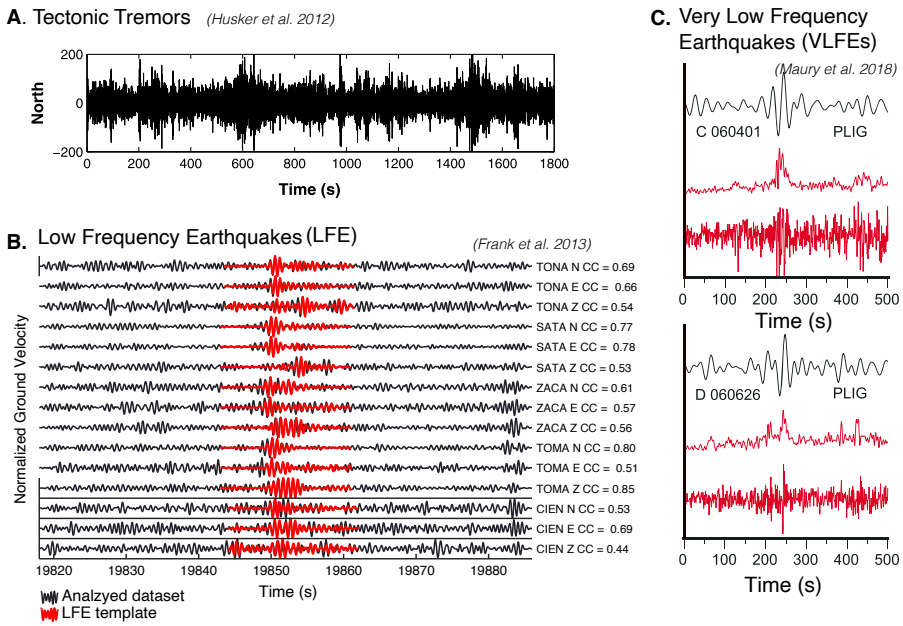

Figure 6.4. *Example of the different types of seismological signals associated with slow slip. A) Tectonic tremors over a duration of 30 min. The signal is emergent, without the arrival of distinct waves, and has low amplitude. Modified from [HUS 12]. B) Low-frequency earthquake (LFE), of 15-s duration, detected by the template matching method. The red signal corresponds to the template (model signal), detected in the continuous series (in black) through correlation. The different traces correspond to different components and stations. CC = correlation coefficients computed between the red and black curves. Modified from [FRA 13]. C) Example of very low frequency earthquakes (VLFEs) over a period of 500 seconds. The traces in red correspond to the frequency band of the tremors (filtered between 2 and 8Hz), the envelopes are indicated just above. The black curves correspond to the VLFE signal, in the frequency range between 0.02 and 0.05 Hz. Modified from [MAU 16]*

A complete catalog of LFEs was constructed over the MASE period. These LFEs confirm the observations of tremors made in the same zone. That is, the existence of a *sweet spot* where many LFEs are continuously active between 200 and 250 km from the trench, and a zone located between 140 and 170 km from the trench, called the transient zone, where LFEs occur in a more episodic manner (see Figures 6.6(A) and (B)). LFEs in this transient zone were very active during the 2006 SSE.

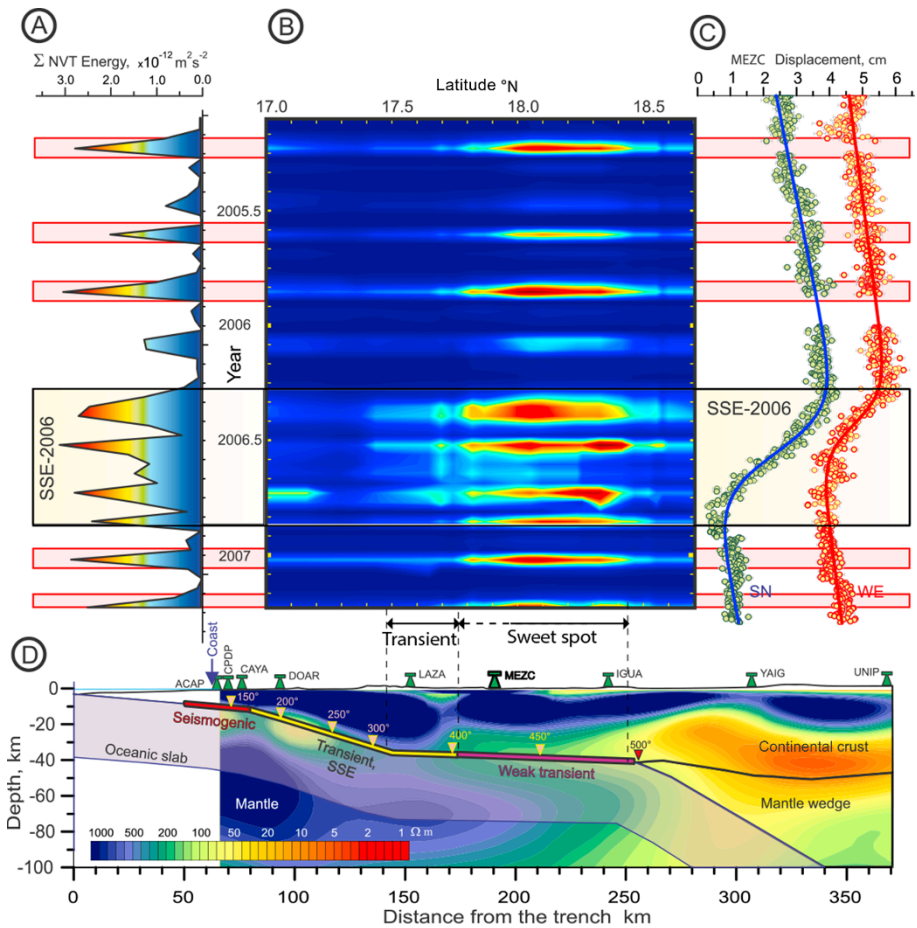

Figure 6.5. *Characterization of tremors at Guerrero between 2005 and 2007, during the Middle America Subduction Experiment (dense seismic profile). Modified from Kostoglodov et al. [KOS 10]. A) Energy of the tremors (frequency band 1–2 Hz) as a function of time. The yellow and red rectangles correspond to peaks of activity related to the major SSE in 2006 and the small SSEs, respectively. B) Spatial-temporal distribution of the energy of tremors (temporal smoothing of 15 days) along a profile perpendicular to a trench. Note the episodic nature of this tremor activity, as well as their locations between 140 and 220 km from the coast. C) Daily time series for the GNSS MEZC station (indicated in bold in profile figure D). Note the large displacement during the 2006 SSE, associated with strong tremor activity. D) Cross-section of the subduction interface aligned with figure B above. The background color corresponds to electrical conductivity. The temperature predicted by a thermal model is given. The locations of the GNSS stations along the profile are given in green. From surface to depth, the interface includes a seismogenic zone (in red), a transient zone with major, long-term SSEs (in yellow) and, at greater depth, a zone with transient, low-amplitude events (the "sweet spot" for tremors). The "transient" and "sweet-spot" LFE zones in Figure 6.6 defined by Frank et al. [FRA 14] are marked*

6.4.3. *Relations between tremor activity, LFEs and SSEs*

No clear relation has been established between tremor activities and the GNSS deformation signals for the tremors occurring in the Jalisco and Michoacan regions. This may be due to the low density of the GNSS station network in these zones. In the Oaxaca region, tremor activity is strongly correlated with an increase in velocities measured by GNSS, which are markers of aseismic slip [HUS 19]. In the Guerrero region (the most widely studied), the link between tremor activity or LFEs and slow slip is clearly established. Figure 6.5 compares the activity of tremors (cumulative energy) and the GNSS displacements measured on the surface. The tremor activity is very espisodic and the period of the slow earthquake in 2006 corresponds to a period of intense activity. Spatially, the main slip zone during the SSEs (in yellow, in Figure 6.5(D)) is shallower than the tremor zone. There is no perfect spatial overlapping between tremors and SSEs in Guerrero, unlike the proposed correspondence between *Episodic Tremor and Slip* in the Cascades [ROG 03]. The observations made from LFEs confirm what we observe from tremors: an increase in their activity during SSE periods, but located at greater depth with respect to the main slip zone of the SSEs (Figures 6.6(A) and (B)).

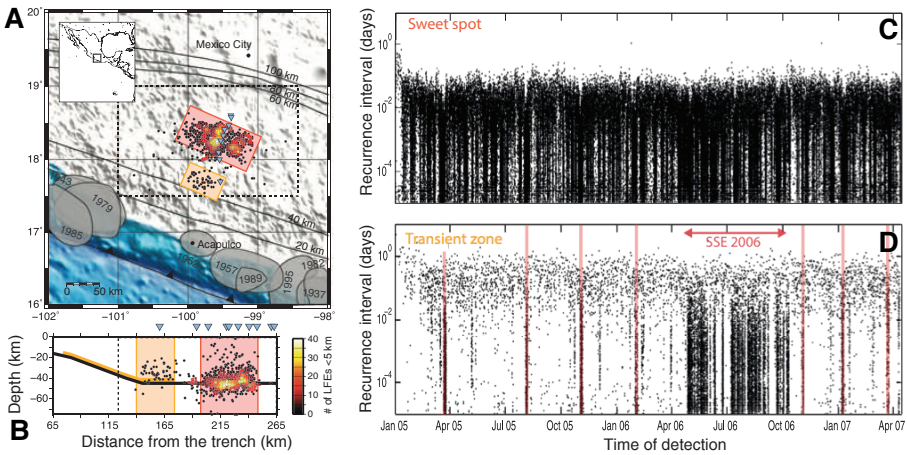

Figure 6.6. *LFE activity in Guerrero during the 2005–2007 period, from stations in the MASE network. (A) A map depicting the location of the LFEs and the stations used to study them. (B) Profile perpendicular to the trench between Acapulco and Mexico City. The colors correspond to the density of LFEs in a region of 5 km. The red and yellow rectangles in figures A and B correspond, respectively, to the transient and near-continuous LFE zones (sweet spot). (C and D) The recurrence intervals for the LFEs over time in the two source regions given in A. The greater the LFE activity, the smaller the recurrence intervals. In the sweet spot, LFE activity is nearly-continuous; in the transient zone, the activity is more episodic. The peaks of activity associated with the small SSEs are highlighted in red [FRA 15a])*

A detailed study of the dynamic of tremors and LFEs (see Figures 6.5 and 6.6) also makes it possible to show periods of high activity, lasting a few days, at regular intervals outside the SSE periods clearly identified by GNSS. There are five to seven activity peaks (marked in red) detected outside the 2006 SSE period. These periods are associated with SSEs of lower amplitude, described in the following paragraph.

6.4.4. *Characterization of small SSEs: joint seismo-geodetic analyses*

Based on the observation of deformation signals correlated with the time series at different stations [VER 10], it was proposed that there may be SSEs with smaller amplitudes than the major SSEs at Guerrero. However, since the geoedetic signature of these small SSEs are still difficult to identify as the surface displacement is millimetric, several approaches have been proposed to detect and characterize these small events. With a network-based method, Rousset et al. [ROU 17] showed that it is possible to detect low-amplitude transient events in the GNSS time series, and they were able to characterize about 30 events with M_w greater than 6.

Using the seismological signature of slow slips, marked by an increase in LFE activity, Frank et al. [FRA 15b] showed that it is possible to detect small events identified by an increase in LFE activity. Over the 2005–2007 period, seven small events occurred with a recurrence period of the order of 3 months (see Figure 6.6(D)), which is much smaller than the periodicity of 4 years observed for major SSEs. Using the activity peaks of LFEs as a temporal guide and by summing the geodetic signal corresponding to each event, it is possible to estimate an average surface displacement of 1–2 mm for these small SSE episodes. This displacement would be difficult to estimate on individual events due to the low signal-to-noise ratio in GNSS measurements. A slip inversion makes it possible to estimate the location and average magnitude of these small SSEs. They are situated at greater depth with respect to the major SSEs (see the dotted contours in Figure 6.3), and their equivalent magnitude is of the order of $M_w 6.4$, that is, an average slip of one centimeter over a 100 km $\times$ 100 km zone (the slip area is poorly constrained). These events thus occur at greater depth than long-term SSEs, at the same depth as the LFE transient activation zone. They are still rather imprecisely located, as Figure 6.3 gives an average location.

6.5. Interactions between seismic and aseismic slips in Mexico

Several studies across the world postulated the existence of spatial or temporal interactions between aseismic slips and earthquakes. The most widely studied, undoubtedly, is the existence of post-seismic slip (especially the afterslip), discussed in Chapter 3. Afterslip is aseismic slip, often accompanied by aftershocks, whose amplitude decreases over time, and which allow a relaxation of the stresses in zones adjacent to the co-seismic rupture. We will give one example of this phenomenon,

without entering into details, as the process is described elsewhere (see Chapter 3). We will, however, focus on interactions between SSEs and earthquakes in Mexico, giving detailed examples of SSEs that precede major earthquakes and examples of tremors or SSEs triggered by seismic waves.

6.5.1. *Slow slip events preceding major earthquakes*

From the earliest observations of SSEs in the subduction zone, Mazzotti and Adams [MAZ 04] hypothesized that the occurrence of SSEs in the transition zone could induce a build up in shear stress in the seismogenic zone, increasing the probability of a strong earthquake occurring during a SSE period. The existence of aseismic slip in epicentral zones before large subduction zones was also revealed by several studies, notably for the 2011 Tohoku earthquake [KAT 12] or the 2014 Iquique earthquake [RUI 14, SOC 17] (see Introduction). In this paragraph, we will detail the observations of this type that were made at the Mexican subduction.

The existence of an active SSE in the weeks and months preceding the occurrence of a large earthquake has been documented in the Mexican subduction by several studies: before the 2012 Ometepec earthquake ($M_w 7.5$) [GRA 14], where an SSE located below the co-seismic slip zone was revealed (see Figures 6.7(A) and (B)), and also in 2014 before the Papanoa earthquake ($M_w 7.2$) [RAD 16] (see Figures 6.7((C) and (D)), and finally in 2018, before the Pinotepa earthquake [LI 20]. In each case, the authors propose that there is a causal link between the occurrence of the SSE and the triggering of the earthquake, arguing there is spatial and temporal proximity between the aseismic slip zones and the earthquake's epicenter. In Figure 6.7, the epicenters of the earthquakes (indicated by the focal mechanisms) are adjacent to the SSE zone (dark blue). However, the mechanisms that cause this possible triggering are not clearly established.

It is possible to test the hypothesis of triggering through static stress transfer by estimating the *Coulomb failure stress change* ($\Delta CFS = \Delta\tau - \mu\Delta\sigma_N$). ΔCFS represents the relative contributions of the normal stress changes $\Delta\sigma_N$ and tangential stress changes $\Delta\tau$ induced by the slow slip in the epicentral zone; μ corresponds to the estimated coefficient of friction. For the three cases mentioned above, the estimated ΔCFS are small but positive, between 10 and 50 kPa, with large uncertainties related to the smoothing in the inversion used to estimate slip distributions. The triggering of earthquakes through variations in static stresses is, therefore, a possible hypothesis. Nonetheless, the values of the increased ΔCFS are smaller than the variations in stress that are generally reported for static interactions between earthquakes (at least 1 bar, i.e., 100 kPa, [KIN 94]). Other mechanisms that have been proposed take into account the dynamic effects to explain a possible triggering. In this context, the slow slip participates in the earthquake nucleation phase, by inducing a weakening of the interface in the epicentral zone. This has been proposed in numerical models that

link thermal pressurization and dilatancy [SEG 12], or in certain studies based on observations and suggesting that the SSE facilitates the propagation of fluids from deep zones toward the epicentral zones, thereby promoting earthquake nucleation [VOS 18].

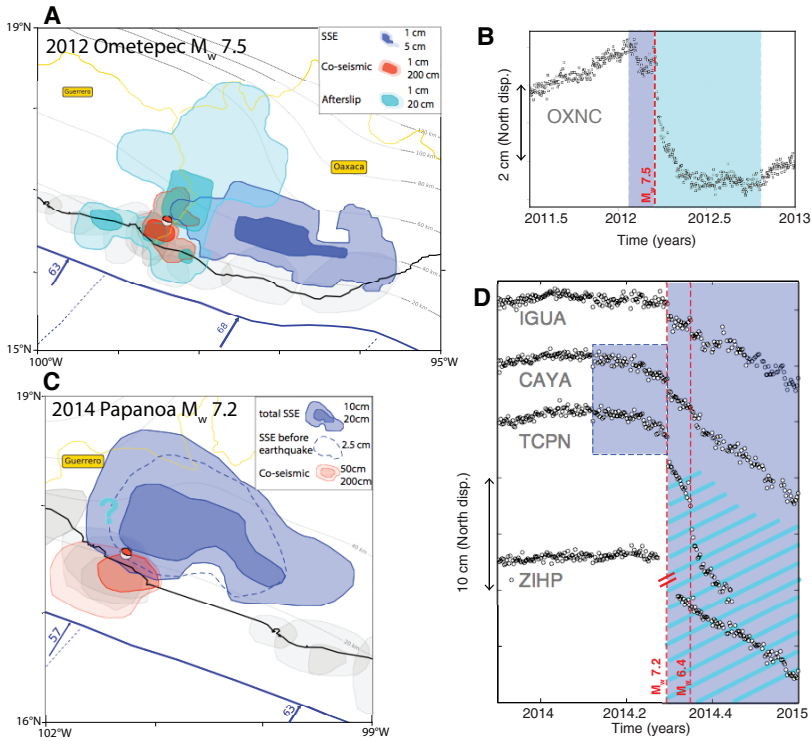

Figure 6.7. *Examples of spatial-proximity between slow slips and earthquakes. (A and B) The SSE-earthquake sequence from Ometepec to Oaxaca in 2012; (C and D) the SSE-earthquake sequence from Papanoa to Guerrero in 2014. (A and C) The distribution of the SSE slip (in dark blue), co-seismic slip (red) and post-seismic slip (sky blue). For the Papanoa earthquake, the study does not differentiate between the SSE and post-seismic slip. (B and D) Examples of the time series that make it possible to distinguish between the different phases of the sequence. The earthquakes are shown by red lines, the displacements associated with the SSEs and post-seismic slips are marked, respectively, by dark blue boxes and sky-blue boxes. For Papanoa, the cross-hatched zone corresponds to the combination of the SSE signal and post-seismic signal, which are not differentiated in the study*

6.5.2. *SSE and post-seismic slip*

For the two examples given in Figure 6.7, a large part of the aseismic slip occurs after the earthquake. In this case, it is not always easy to distinguish the post-seismic displacement that decreases rapidly over time and the SSE that initiated before the earthquake and continues to propagate. Both phenomena correspond to aseismic slip on the subduction interface. In one case the initiation is spontaneous (SSE), in the second it is related to stress loading due to the earthquake. In the case of the Ometepec earthquake, the high amplitude and characteristic decrease in displacements after the earthquake (see Figure 6.7(B)) lead us to think that the majority of the slip after the earthquake corresponds to the post-seismic slip. For this earthquake, there is also great spatial complementarity between the SSE zone, the co-seismic slip and that of the post-seismic slip, with different zones of the interface having been activated in each case (see Figure 6.7(A)). In the case of the Papanoa earthquake, it is difficult to clearly separate the SSE from the post-seismic slip: the large amplitudes of displacement after the earthquake at certain stations (TCPN, ZHIP) indicates that in certain zones at least the slow slip has been accelerated by a post-seismic slip contribution (see Figure 6.7(D)).

6.5.3. *Sensitivity of aseismic slips to seismic waves*

The modulation in the activity of the tremors, LFEs and slow slips by small perturbations in static or dynamic stresses was studied in many regions around the world. We will not talk here about modulation in tremor activity through tidal effects, but we will focus on a few examples in which earthquakes could have contributed to the triggering of slow slips. In 2010, Zigone et al. [ZIG 12] revealed the triggering of tremor activity associated with the passage of waves from the M_w 8.8 Maule earthquake that occurred in Chile, 5000 km away. They also postulated that the second phase of the 2009–2010 slow earthquake in Guerrero, which took place after a quiet period visible in the time series, was also related to a dynamic triggering of this SSE by waves associated with the earthquake. More recently, the 2017 Chiapas earthquake was also responsible for triggering tremors or possibly even SSEs in Guerrero and Oaxaca [CRU 21], this triggering being related to dynamic effects.

All of these interactions show that aseismic slips are very sensitive to low stress perturbations, and are thus close to a critical stress state.

6.6. Conclusion

This chapter presents the main observations and discoveries made during the last 20 years on the seismic cycle in the Mexican subduction zone. During this period, a large increase in continuous observations made it possible to characterize the

complexity of this seismic cycle and the different modes through which stresses are released. The Mexican subduction zone offers quite a complete picture of the diversity in these processes, especially since slow slip events (or SSEs) are frequent there, and among the largest in the world. In this chapter, we have placed particular emphasis on these transient processes, SSEs, tremors and LFEs, undoubtedly ignoring some other processes, such as a detailed look at co-seismic or post-seismic phases.

In the Guerrero zone, major slow slips have been identified, with duration in the order of a year. These release energy equivalent to magnitude 7.5 earthquakes, with a periodicity of around 4 years. In the neighboring Oaxaca region, SSEs are more frequent, occurring every 1–2 years, and have smaller equivalent magnitudes, around 6.5. These SSEs are largely detected through GNSS observations. A large variety of seismological signals (tremors, LFEs) are observed and associated with these slow slips detected through geodesy. Studying these signals brings in additional information on the characterization of slip mechanisms around the subduction interface. The observation of tremors and LFEs makes it possible to reveal a dynamic on a smaller time-scale. At Guerrero, low-amplitude SSEs are detected that are more frequent than the major SSEs, with a duration of a few days and located at greater depth on the subduction.

The distribution of different slip modes at the subduction interface has been described: first, there exists a spatial complementarity between the different slip modes and a succession (from the surface to depth) between the most superficial seismogenic zone, the zone of major SSEs and, at greater depth, SSEs of smaller amplitudes, as well as tremor and LFE zones. However, strong lateral variations are also seen, with SSEs and tremors being localized in specific zones. This indicates that the frictional behavior along this subduction zone is heterogeneous. Finally, all of the slip modes on the faults interact with one another and we have given a few examples of temporal interactions between earthquakes, tremors and SSEs.

This chapter is essentially descriptive in nature and the study of the mechanisms behind these different slip modes falls beyond the scope of this text, but are partly discussed in Chapters 3 and 7. Due to the diversity of the processes described here, the Mexican subduction zone is an excellent natural laboratory to understand the mechanisms behind the various slip modes and the observations that may be correlated with predictions from numerical models (see Chapter 3), analytical models (see Chapter 7), or analog models (see Chapter 12).

6.7. References

[ATZ 19] ATZORI S., ANTONIOLI A., TOLOMEI C. et al., “InSAR full-resolution analysis of the 2017–2018 M>6 earthquakes in Mexico”, *Remote Sensing of Environment*, vol. 234, p. 111461, December 2019.

[BAN 95] BANDY W., MORTERA–GUTIERREZ C., URRUTIA–FUCUGAUCHI J. et al., "The subducted Rivera-Cocos plate boundary: Where is it, what is it, and what is its relationship to the Colima Rift?", *Geophysical Research Letters*, vol. 22, no. 22, pp. 3075–3078, 1995.

[BER 11] BEROZA G.C., IDE S., "Slow earthquakes and nonvolcanic tremor", *Annu. Rev. Earth Planet. Sci.*, vol. 39, no. 1, pp. 271–296, 2011.

[BRU 16] BRUDZINSKI M.R., SCHLANSER K.M., KELLY N.J. et al., "Tectonic tremor and slow slip along the northwestern section of the Mexico subduction zone", *Earth and Planetary Science Letters*, vol. 454, pp. 259–271, November 2016.

[CAV 13] CAVALIÉ O., PATHIER E., RADIGUET M. et al., "Slow slip event in the Mexican subduction zone: Evidence of shallower slip in the Guerrero seismic gap for the 2006 event revealed by the joint inversion of InSAR and GPS data". *Earth Planet. Sci. Lett.*, vol. 367, pp. 52–60, April 2013.

[COR 08] CORREA-MORA F., DEMETS C., CABRAL-CANO E. et al., "Interplate coupling and transient slip along the subduction interface beneath Oaxaca, Mexico", *Geophysical Journal International*, vol. 175, no. 1, pp. 269–290, 2008.

[CRU 21] CRUZ-ATIENZA, V.M., TAGO, J., VILLAFUERTE, C. et al., "Short-term interaction between silent and devastating earthquakes in Mexico", *Nature Communications*, vol. 12, p. 2171, available at: https://doi.org/10.1038/s41467-021-22326-6, 2021.

[DEM 00] DEMETS C., TRAYLEN S., "Motion of the Rivera plate since 10 Ma relative to the Pacific and North American plates and the mantle", *Tectonophysics*, vol. 318, no. 1, pp. 119–159, 2000.

[DEM 10] DEMETS C., GORDON R.G., ARGUS D.F., "Geologically current plate motions", *Geophys. J. Int.*, vol. 181, no. 1, pp. 1–80, 2010.

[DRA 01] DRAGERT H., WANG K., JAMES T.S., "A silent slip event on the deeper cascadia subduction interface", *Science*, vol. 292, no. 5521, pp. 1525–1528, 2001.

[FRA 13] FRANK W.B., SHAPIRO N.M., KOSTOGLODOV V. et al., "Low-frequency earthquakes in the Mexican Sweet Spot", *Geophysical Research Letters*, vol. 40, no. 11, pp. 2661–2666, 2013.

[FRA 14] FRANK W.B., SHAPIRO N.M., HUSKER A.L. et al., "Using systematically characterized low-frequency earthquakes as a fault probe in Guerrero, Mexico", *Journal of Geophysical Research: Solid Earth*, vol. 119, no. 10, pp. 7686–7700, 2014.

[FRA 15a] FRANK, W.B., SHAPIRO, N.M., HUSKER, A.L. et al. "Along-fault pore-pressure evolution during a slow-slip event in Guerrero, Mexico", *Earth and Planetary Science Letters*, no. 413, pp. 135–143, 2015.

[FRA 15b] FRANK W.B., RADIGUET M., ROUSSET B. et al., "Uncovering the geodetic signature of silent slip through repeating earthquakes", *Geophysical Research Letters*, vol. 42, no. 8, pp. 2774–2779, 2015.

[GAI 16] GAIDZIK K., RAMÍREZ-HERRERA M.T., KOSTOGLODOV V., "Active crustal faults in the forearc region, Guerrero Sector of the Mexican Subduction Zone", *Pure and Applied Geophysics*, vol. 173, no. 10, pp. 3419–3443, 2016.

[GAO 12] GAO H., SCHMIDT D.A., WELDON R.J., "Scaling relationships of source parameters for slow slip events", *Bulletin of the Seismological Society of America*, vol. 102, no. 1, pp. 352–360, 2012.

[GRA 14] GRAHAM S.E., DEMETS C., CABRAL-CANO E. et al., "GPS constraints on the 2011–2012 Oaxaca slow slip event that preceded the 2012 March 20 Ometepec earthquake, southern Mexico", *Geophysical Journal International*, vol. 197, no. 3, pp. 1593–1607, 2014.

[GRA 16] GRAHAM S., DEMETS C., CABRAL-CANO E. et al., "Slow slip history for the MEXICO subduction zone: 2005 through 2011", *Pure and Applied Geophysics*, vol. 173, no. 10, pp. 3445–3465, 2016.

[HUS 12] HUSKER, A.L., KOSTOGLODOV, V., CRUZ-ATIENZA, V.M. et al., "Temporal variations of non-volcanic tremor (NVT) locations in the Mexican subduction zone: Finding the NVT sweet spot," *Geochem. Geophys. Geosyst.*, vol. 13, p. Q03011, 2012.

[HUS 19] HUSKER A.L., FRANK W.B., GONZALEZ G. et al., "Characteristic tectonic tremor activity observed over multiple slow slip cycles in the Mexican subduction zone", *Journal of Geophysical Research: Solid Earth*, vol. 124, no. 1, pp. 599–608, 2019.

[KAT 12] KATO A., OBARA K., IGARASHI T. et al., "Propagation of slow slip leading up to the 2011 Mw 9.0 Tohoku-Oki earthquake", *Science*, vol. 335, no. 6069, pp. 705–708, 2012.

[KAZ 20] KAZACHKINA E., KOSTOGLODOV V., COTTE N. et al., "Active 650-km long fault system and Xolapa Sliver in Southern Mexico", *Frontiers in Earth Science*, vol. 8, available at: https://www.frontiersin.org/article/10.3389/feart.2020.00155, 2020.

[KIN 94] KING G.C.P., STEIN R.S., LIN J., "Static stress changes and the triggering of earthquakes", *Bull. Seismol. Soc. Am.*, vol. 84, no. 3, pp. 935–953, 1994.

[KOS 96] KOSTOGLODOV V., BANDY W., DOMINGUEZ J. et al., "Gravity and seismicity over the Guerrero seismic gap, Mexico", *Geophys. Res. Lett.*, vol. 23, no. 23, pp. 3385–3388, 1996.

[KOS 02] KOSTOGLODOV V., BILHAM R., SANTIAGO J.A. et al., "Long-baseline fluid tiltmeter for seismotectonic studies of Mexican subduction zone", *Geofísica Internacional*, vol. 41, no. 1, pp. 11–25, 2002.

[KOS 03] KOSTOGLODOV V., SINGH S., SANTIAGO J.A. et al., "A large silent earthquake in the Guerrero seismic gap, Mexico", *Geophys. Res. Lett.*, vol. 30, no. 15, p. 1807, 2003.

[KOS 10] KOSTOGLODOV V., HUSKER A.L., SHAPIRO N.M. et al., "The 2006 slow slip event and nonvolcanic tremor in the Mexican subduction zone", *Geophysical Research Letters*, vol. 37, no. L24301, 2010.

[LI 20] LI Y., SHAN X., ZHU C. et al., "Geodetic model of the 2018 Mw 7.2 Pinotepa, Mexico, earthquake inferred from InSAR and GPS data", *Bulletin of the Seismological Society of America*, vol. 110, no. 3, pp. 1115–1124, June 2020.

[LOW 01] LOWRY A., LARSON K., KOSTOGLODOV V. et al., "Transient slip on the subduction interface in Guerrero, southern Mexico", *Geophys. Res. Lett.*, vol. 28, no. 19, pp. 3753–3756, 2001.

[MAN 13] MANEA V.C., MANEA M., FERRARI L., "A geodynamical perspective on the subduction of Cocos and Rivera plates beneath Mexico and Central America", *Tectonophysics*, vol. 609, pp. 56–81, 2013.

[MAU 16] MAURY J., IDE S., CRUZ–ATIENZA V.M. et al., "Comparative study of tectonic tremor locations: Characterization of slow earthquakes in Guerrero, Mexico", *Journal of Geophysical Research: Solid Earth*, vol. 121, no. 7, pp. 5136–5151, 2016.

[MAU 18] MAURY J., IDE S., CRUZ–ATIENZA V.M. et al. "Spatiotemporal variations in slow earthquakes along the Mexican subduction zone", *Journal of Geophysical Research: Solid Earth*, vol. 123, no. 2, pp. 1559–1575, 2018.

[MAU 20] MAUBANT L., PATHIER E., DAOUT S. et al., "Independent component analysis and parametric approach for source separation in InSAR time series at regional scale: Application to the 2017–2018 slow slip event in Guerrero (Mexico)", *Journal of Geophysical Research: Solid Earth*, vol. 125, no. 3, p. e2019JB018187, 2020.

[MAZ 04] MAZZOTTI S., ADAMS J., "Variability of near-term probability for the next great earthquake on the Cascadia subduction zone", *Bull. Seismol. Soc. Am.*, vol. 94, no. 5, pp. 1954–1959, 2004.

[MEL 97] MELBOURNE T., CARMICHAEL I., DEMETS C. et al., "The geodetic signature of the M8.0 Oct. 9,1995, Jalisco subduction earthquake", *Geophysical Research Letters*, vol. 24, no. 6, pp. 715–718, 1997.

[MEL 18] MELGAR D., PÉREZ–CAMPOS X., RAMIREZ–GUZMAN L. et al., "Bend faulting at the edge of a flat slab: The 2017 Mw7.1 Puebla-Morelos, Mexico earthquake", *Geophysical Research Letters*, vol. 45, no. 6, pp. 2633–2641, 2018.

[MEN 99] MENDOZA C., HARTZELL S., "Fault-slip distribution of the 1995 Colima-Jalisco, Mexico, earthquake", *Bulletin of the Seismological Society of America*, vol. 89, no. 5, pp. 1338–1344, 1999.

[OKA 92] OKADA Y., "Internal deformation due to shear and tensile faults in a half-space", *Bull. Seismol. Soc. Am.*, vol. 82, no. 2, p. 1018, 1992.

[OKU 17] OKUWAKI R., YAGI Y., "Rupture process during the Mw 8.1 2017 Chiapas Mexico earthquake: Shallow intraplate normal faulting by slab bending", *Geophysical Research Letters*, vol. 44, no. 23, p. 2017GL075956, December 2017.

[ORT 98] ORTIZ M., SINGH S.K., PACHECO J. et al., "Rupture length of the October 9, 1995 Colima-Jalisco Earthquake (Mw 8) estimated from tsunami data", *Geophysical Research Letters*, vol. 25, no. 15, pp. 2857–2860, 1998.

[PAR 95] PARDO M., SUAREZ G., "Shape of the subducted Rivera and Cocos plates in southern Mexico: Seismic and tectonic implications", *J. Geophys. Res.*, vol. 100, no. B7, pp. 12357–12373, 1995.

[PÉR 08] PÉREZ-CAMPOS X., KIM Y., HUSKER A.L. et al., "Horizontal subduction and truncation of the Cocos Plate beneath central Mexico", *Geophys. Res. Lett.*, vol. 35, no. 18, p. L18303, 2008.

[RAD 11] RADIGUET M., COTTON F., VERGNOLLE M. et al., "Spatial and temporal evolution of a long term slow slip event: The 2006 Guerrero slow slip event", *Geophys. J. Int.*, vol. 184, no. 2, pp. 816–828, 2011.

[RAD 12] RADIGUET M., COTTON F., VERGNOLLE M. et al., "Slow slip events and strain accumulation in the Guerrero gap, Mexico", *J. Geophys. Res.*, vol. 117, no. B4, p. B04305, 2012.

[RAD 16] RADIGUET M., PERFETTINI H., COTTE N. et al., "Triggering of the 2014 Mw7.3 Papanoa earthquake by a slow slip event in Guerrero, Mexico", *Nature Geoscience*, vol. 9, no. 11, pp. 829–833, 2016.

[ROG 03] ROGERS G., DRAGERT H., "Episodic tremor and slip on the Cascadia subduction zone: The chatter of silent slip", *Science*, vol. 300, no. 5627, pp. 1942–1943, 2003.

[ROU 17] ROUSSET B., CAMPILLO M., LASSERRE C. et al., "A geodetic matched filter search for slow slip with application to the Mexico subduction zone", *Journal of Geophysical Research: Solid Earth*, vol. 122, no. 12, pp. 10,498–10,514, 2017.

[RUI 14] RUIZ S., METOIS M., FUENZALIDA A. et al., "Intense foreshocks and a slow slip event preceded the 2014 Iquique Mw 8.1 earthquake", *Science*, vol. 345, no. 6201, pp. 1165–1169, 2014.

[SAV 83] SAVAGE J., "A dislocation model of strain accumulation and release at a subduction zone", *J. Geophys. Res.*, vol. 88, no. B6, pp. 4984–4996, 1983.

[SEG 12] SEGALL P., BRADLEY A.M., "The role of thermal pressurization and dilatancy in controlling the rate of fault slip", *Journal of Applied Mechanics*, vol. 79, no. 3, pp. 031013–031013, 2012.

[SHE 06] SHELLY D.R., BEROZA G.C., IDE S. et al., "Low-frequency earthquakes in Shikoku, Japan, and their relationship to episodic tremor and slip", *Nature*, vol. 442, no. 7099, pp. 188–191, 2006.

[SIN 81] SINGH S.K., ASTIZ L., HAVSKOV J., "Seismic gaps and recurrence periods of large earthquakes along the Mexican subduction zone: A reexamination", *Bull. Seismol. Soc. Am.*, vol. 71, no. 3, p. 827, 1981.

[SIN 88] SINGH S.K., MENA E., CASTRO R., "Some aspects of source characteristics of the 19 September 1985 Michoacan earthquake and ground motion amplification in and near Mexico City from strong motion data", *Bull. Seismol. Soc. Am.*, vol. 78, no. 2, pp. 451–477, 1988.

[SIN 90] SINGH S.K., MORI A., MENA E. et al., "Evidence for anomalous body-wave radiation between 0.3 and 0.7 Hz from the 1985 September 19 Michoacan, Mexico earthquake", *Geophys. J. Int.*, vol. 101, no. 1, pp. 37–48, 1990.

[SIN 18] SINGH S.K., REINOSO E., ARROYO D. et al., "Deadly intraslab Mexico earthquake of 19 September 2017 (Mw 7.1): Ground motion and damage pattern in Mexico City", *Seismological Research Letters*, vol. 89, no. 6, pp. 2193–2203, November 2018.

[SOC 17] SOCQUET A., VALDES J.P., JARA J. et al., "An 8-month slow slip event triggers progressive nucleation of the 2014 Chile megathrust", *Geophysical Research Letters*, vol. 44, no. 9, pp. 4046–4053, May 2017.

[UNA 15] UNAM SEISMOLOGY GROUP, "Papanoa, Mexico earthquake of 18 April 2014 (Mw 7.3)", *Geofísica Internacional*, vol. 54, no. 4, pp. 363–386, 2015.

[UNI 13] Universidad Nacional Autónoma de México Seismology Group, "Ometepec-Pinotepa Nacional, Mexico Earthquake of 20 March 2012 (Mw 7.5): A preliminary report", *Geofísica Internacional*, vol. 52, no. 2, pp. 173–196, 2013.

[VER 10] VERGNOLLE M., WALPERSDORF A., KOSTOGLODOV V. et al., "Slow slip events in Mexico revised from the processing of 11-year GPS observations", *J. Geophys. Res.*, vol. 115, p. B08403, 2010.

[VOS 18] VOSS N., DIXON T.H., LIU Z. et al., "Do slow slip events trigger large and great megathrust earthquakes?", *Science Advances*, vol. 4, no. 10, p. 8472, October 2018.

[ZIG 12] ZIGONE D., RIVET D., RADIGUET M. et al., "Triggering of tremors and slow slip event in Guerrero, Mexico, by the 2010 Mw 8.8 Maule, Chile, earthquake", *J. Geophys. Res.*, vol. 117, no. B9, p. B09304, 2012.

7

Forearc Topography: Mirror of Megathrust Rupture Properties

Nadaya CUBAS
ISTeP, Sorbonne University, Paris, France

7.1. Introduction

Subductions generate earthquakes along their megathrust, the interface between the subducting and overriding plates. They occur in the brittle domain that extends from the trench to the fragile/ductile transition. Until relatively recently, the deformation related to the seismic cycle was considered as purely elastic and therefore non-permanent [SAV 83]. The elastic deformation acquired during the inter-seismic phase was assumed to be entirely counterbalanced by the deformation of the co-seismic and post-seismic phases [PLA 70] (see Chapter 1). However, the large subduction earthquakes of the 21st century have challenged this classical view. The morphology and deformation of the overriding plate partly respond to the mechanical and seismic behavior of the megathrust [SON 03]. In this chapter, we will study how large subduction earthquakes impact the forearc topography. With this objective, we will recall the critical taper theory, which describes the deformation of brittle wedges. We will then replace this theory in a forearc context with megathrusts composed of seismic and aseismic patches. We will finally see how the study of the deformation and topography of forearcs can help in estimating the seismic and tsunamigenic hazards.

For a color version of all the figures in this chapter, see www.iste.co.uk/rolandone/seismic.zip.

The Seismic Cycle,
coordinated by Frédérique ROLANDONE.

The Seismic Cycle: From Observation to Modeling,
First Edition. Frédérique Rolandone.

7.2. Mechanical analysis: the critical taper theory

The critical taper theory was established in the early 1980s, from the analogy between accretionary prisms and sand pushed by a moving bulldozer [DAV 83]. In a compressive setting, sand, sediments or rocks are deformed by a sequence of thrusts, above a basal décollement to form a prism, or wedge (see Figure 7.1(a)). Once the wedge reaches a certain critical taper, formed by the topographic slope α and the décollement dip β, it slides along its décollement. If no material is encountered at the front, the wedge slides without internal deformation. In the contrary case, the wedge grows self-similarly to maintain the critical taper. For a non-cohesive prism, the critical taper relates to the angle formed by the maximum principal stress σ_1 and the topography ψ_0, and the angle formed by σ_1 and the décollement ψ_b (see Figure 7.1(a)) [DAH 84]:

$$(\alpha + \beta)_c = \Psi_B - \Psi_0 \qquad [7.1]$$

with

$$\Psi_B = \frac{1}{2} arcsin\left(\frac{sin\phi'_b}{sin\phi_b}\right) - \frac{1}{2}\phi'_b \,, \qquad [7.2]$$

$$\Psi_0 = \frac{1}{2} arcsin\left(\frac{sin\alpha'}{sin\phi_{int}}\right) - \frac{1}{2}\alpha', \qquad [7.3]$$

with ϕ_{int} as the internal friction of the prism and ϕ_b as the friction of the décollement, such that $\mu_{int} = tan\phi_{int}$ and $\mu_b = tan\phi_b$, and:

$$\phi'_b = arctan\left[\left(\frac{1-\lambda_b}{1-\lambda}\right) tan\phi_b\right] , \qquad [7.4]$$

$$\alpha' = arctan\left[\left(\frac{1-\rho_w/\rho}{1-\lambda}\right) tan\alpha\right] . \qquad [7.5]$$

The ratio between the Hubbert–Rubbey fluid pressures λ and λ_b are defined as: [RUB 59, DAV 83]

$$\lambda = \frac{P - \rho_w g D}{|\sigma_z| - \rho_w g D} \,, \qquad [7.6]$$

$$\lambda_b = \frac{P_b - \rho_w g D}{|\sigma_z| - \rho_w g D} \,, \qquad [7.7]$$

with ρ and ρ_w as the density of the prism and of water, respectively, and D as the water depth. The solution is exact if $\lambda = \lambda_b$ [WAN 06], but the approximation is valid for small angles $\alpha + \beta$, as in our case study.

In a topographic slope α versus slab dip β graph, this relation corresponds to the lower branch of the envelope (see Figure 7.1(b)). For other branches, the solution differs based on the system of active or passive stresses [LEH 86].

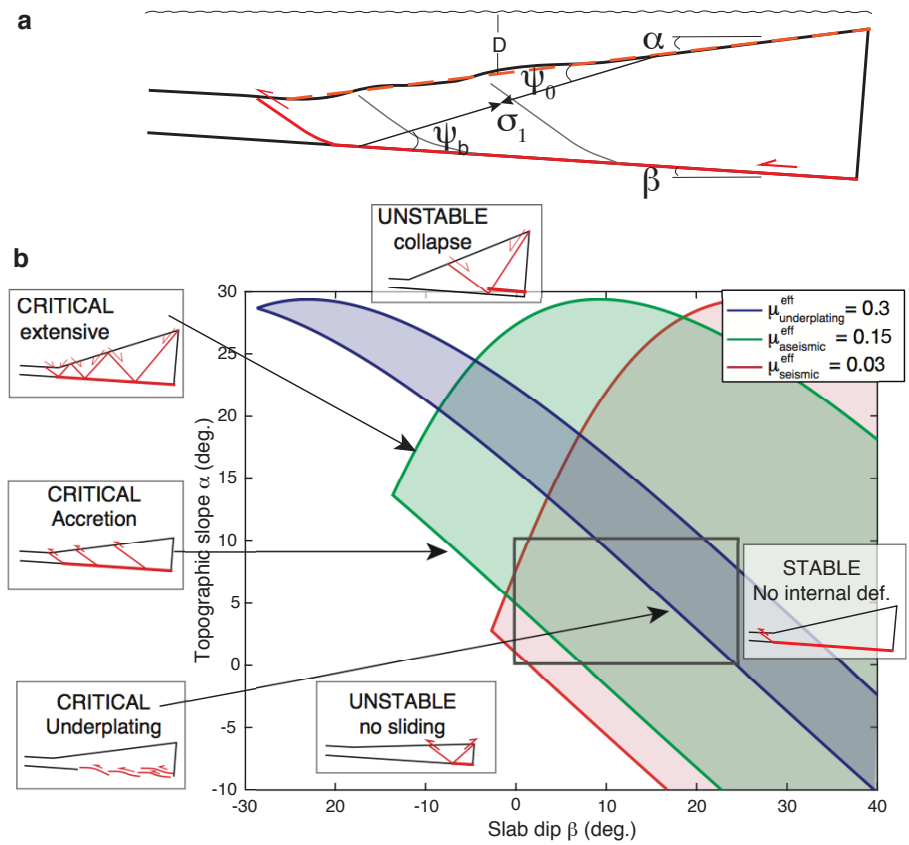

Figure 7.1. *a) Critical taper theory. The critical taper is formed by the topographic slope α and the décollement dip β, which depends on the angles Ψ_0 and Ψ_b. b) Critical envelopes, mechanical states and associated deformation for different décollement frictions and for $\lambda = 0.4$. For the blue curve, $\phi_{int}^{eff} - \phi_b^{eff} = 1^o$. The subduction zones usually fall in the gray rectangle*

If the angle formed by $\alpha + \beta$ is smaller than the critical taper represented by the envelope, the décollement cannot be activated. A thrust fault forms at the back of

the wedge to increase the topographic slope and reach the critical envelope. If the critical taper is reached, the wedge is on the verge of Coulomb failure in its whole volume. However, since no geological structure is ever perfectly homogeneous, the critical state involves the activation of the décollement and of internal thrust faults, which generally correspond to pre-existing structures. If the topographic slope is larger than the critical taper, the wedge enters a stability domain. The wedge slides along its décollement without inducing any internal deformation, and with a single active thrust fault at the front. With steeper slopes, the wedge can reach the upper branch of the critical envelope, and be on the verge of extensional Coulomb failure. In the conditions given in Figure 7.1(b), while sliding along its décollement, the wedge collapses through a series of normal faults that bring the prism back into the stable domain. If the topographic slope exceeds the envelope, the prism collapses under its own weight. The lower branch of the critical envelope corresponds to the least-effort mechanical state. Consequently, this branch is the preferred mechanical state.

As shown by equations [7.1] and [7.2], the critical taper depends on the décollement friction. The smaller the basal friction, the larger the envelope. Consequently, the smaller the basal friction, the smaller the critical taper (see Figure 7.1(b)). It also depends on the fluid pressure: as the fluid pressure increases, the slope of the envelope decreases. Moreover, the difference between the internal and basal effective friction controls the dip of internal thrusts: the larger the difference, the larger the dip between internal thrusts and décollement. For very small differences, like the blue curve in Figure 7.1(b), internal thrust faults parallel the décollement allowing for underplating [CUB 22].

7.3. Application to subduction forearcs

7.3.1. *Relations between seismic behavior and frictional properties*

In the previous chapters (see Chapters 4, 5 and 6), we have seen that megathrusts are composed of patches that either slip at slow slip rate and thus aseismically, or during earthquakes. This segmentation seems to have a certain persistence through time and space [SON 03]. In the chapter on friction laws, we have seen that the behavior along the megathrust, as well as the alternation between slow slip or seismic slip, can be formalized using the rate-and-state friction laws [DIE 78, RIC 83] (see Chapter 4). Aseismic zones are described with a rate-strengthening friction, and the seismogenic zone with a rate-weakening behavior. We have also seen that during the seismic event, other weakening mechanisms come into play, such as thermal-pressurization or flash heating. These additional mechanisms cause a dynamic decrease of the friction, bringing it down to extremely low values [DIT 11]. The effective friction of aseismic megathrusts is estimated to vary around $\mu_{aseis.} = 0.15 \pm 0.1$ [GAO 14], consistent with relatively weak minerals under some fluid overpressure. Along the seismogenic zone, slip only occurs during the co-seismic

phase. Since the slip necessary to reach the dynamic friction is extremely small (of the order of mm) (see Chapter 4), displacement mostly occurs under dynamic friction. According to the measurements and modeling of heat flow, the apparent friction of seismogenic megathrusts is of the order of $\mu_{seism.} \sim 0.01$–0.03 [GAO 14].

7.3.2. *Relations between seismic behavior and critical state*

In a subduction zone, the décollement corresponds to the megathrust and β to the dip angle of the slab. As a general rule, the slab dip increases as we move away from the trench, except in a flattening case. Consequently, if the subduction forearc is at the critical state, it will follow a critical envelope as represented in Figure 7.1(b).

Figure 7.1(b) represents the envelopes corresponding to a seismic effective friction (in red) and an aseismic effective friction (in green). The difference in friction is significant enough to induce a difference of mechanical state. Aseismic segments can reach a critical state, undergo internal deformation and hence maintain a relatively steep slope. On the contrary, due to their extremely low friction, the seismogenic segments always fall in the stable domain. No topography building or internal deformation is necessary to activate the megathrust.

This difference in mechanical state is particularly striking in the Central Chile region (see Figure 7.2). Two large subduction earthquakes occurred during the last 60 years (see Chapter 5): the 1960 Mw 9.5 Valdivia earthquake in the southern region and the 2010 Mw 8.8 Maule earthquake in the north (see Figure 7.2(a)). Forearc sections at accretionary critical state are represented in green in Figure 7.2(b) [CUB 13b]. They are characterized by internal deformation, as predicted by the theory. Forearc segments located above the rupture zone are at stable state. Along these segments, deformation is only accommodated by the megathrust. The seismic ruptures are limited up-dip by segments at accretionary critical state. After the down-dip of the Maule and 2015 Mw 8.2 Illapel earthquakes, the forearc is again at critical state, but internal deformation occurs along the plate interface, leading to underplating, and a slow coastal uplift [SAI 17] (see Figure 7.3).

7.3.3. *Impact on the trench-coast distance*

The difference in friction between seismic and aseismic segments also impacts the trench-coast distance. High effective basal frictions generate high topographic slopes, and hence short trench-to-coast distances (see Figure 7.4(a)). Along a profile that is perpendicular to the trench, the trench-coast distance therefore depends on the proportion of the segment that is seismic versus aseismic, that is, the average coupling, as observed in the Guerrero region of Mexico (see Figure 7.4(b) and Chapter 6) [ROU 16], or along the Chilean and Peruvian subduction [SAI 17].

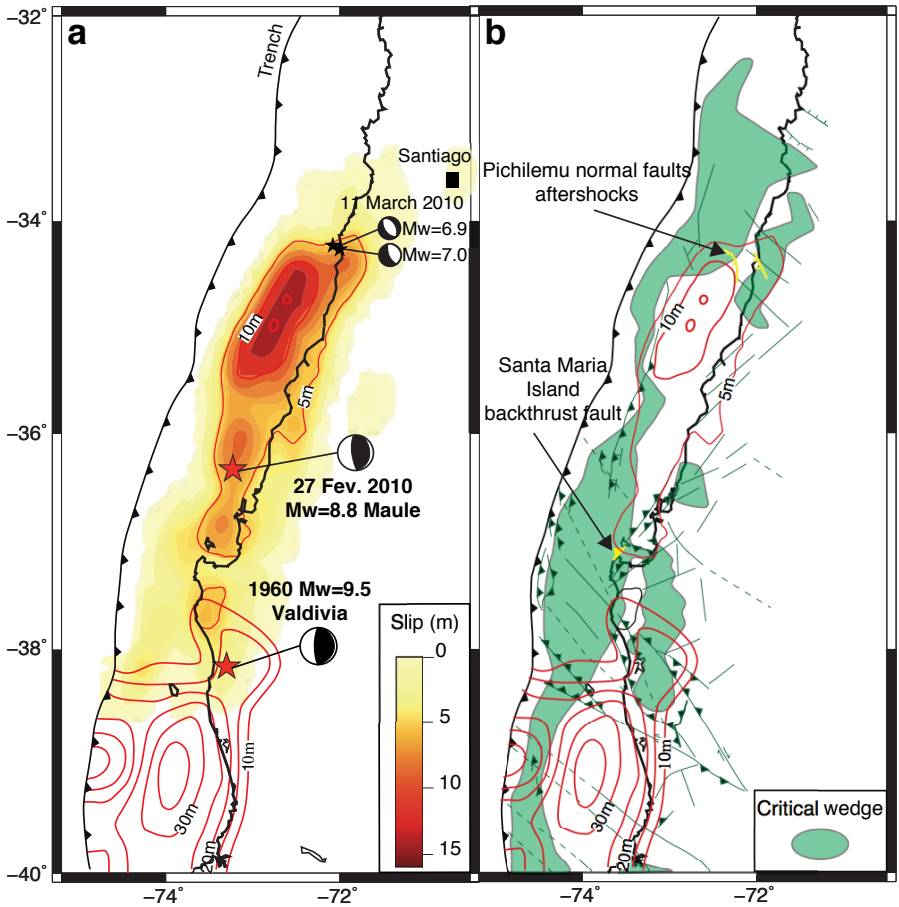

Figure 7.2. *a) Co-seismic displacement of the 2010 Mw 8.8 Maule earthquake [LIN 13], and the 1960 Mw 9.5 Valdivia earthquake (in red) [MOR 09]. b) Segments at accretionary critical state (in green). Known faults are represented in dark green. The crustal faults activated right after the Maule earthquake are represented in yellow. Modified from [CUB 13b]*

7.4. Splay faults: transition faults

The difference in friction also implies different displacement quantities between aseismic and seismic segments. The smaller the effective basal friction, the lower the resistance to motion and the larger the displacement. These differences are accommodated by splay faults (see Figure 7.5, [CUB 13a]). The type of splay fault, normal or reverse, depends on the difference in effective friction and the position of

the prism with respect to the critical envelope. Close to the compressive branch, splay faults are reverse; close to the extensional branch, faults are normal. Two splay faults have been activated after the Maule earthquake (see Figure 7.2(b)). The Santa Maria island, located at the up-dip seismic/aseismic transition zone, was uplifted by a backthrust [MEL 12]. Two weeks after the earthquake, two normal fault aftershocks (the Pichilemu earthquakes) were recorded north-east of the rupture. The micro-seismicity associated with these events revealed a crustal normal fault, located at the down-dip seismic/aseismic transition zone [FAR 11].

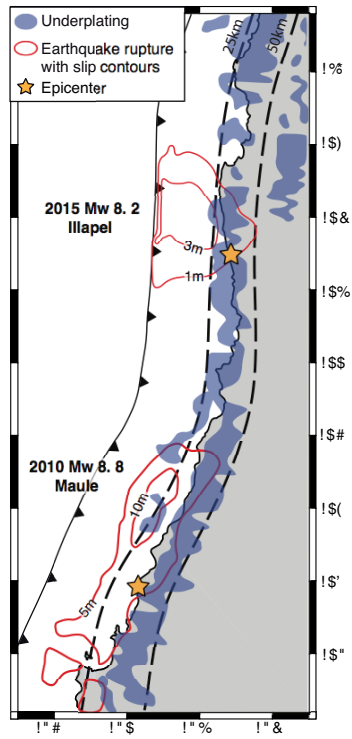

Figure 7.3. *Co-seismic displacement of the 2010 Mw 8.8 Maule earthquake [LIN 13] and the 2015 Mw 8.2 Illapel earthquake (in red) [TIL 16] and segments at underplating critical state (in blue). Dashed black lines show the slab depths [HAY 18]. Modified from [CUB 22]*

Splay faults can also take place within the seismic zone, as observed for the 2011 Mw 9.0 Tohoku-Oki earthquake (see Figure 7.6(a)). Gauges placed on the seafloor measured a displacement of the order of 20–30 m, at a depth of 10–15 km, while the frontal part close to the trench underwent 50 m of slip [ITO 11]. This difference

induced the activation of a large normal fault [TSU 11], explained by a variation of basal friction (see Figure 7.6(b)) [CUB 13a].

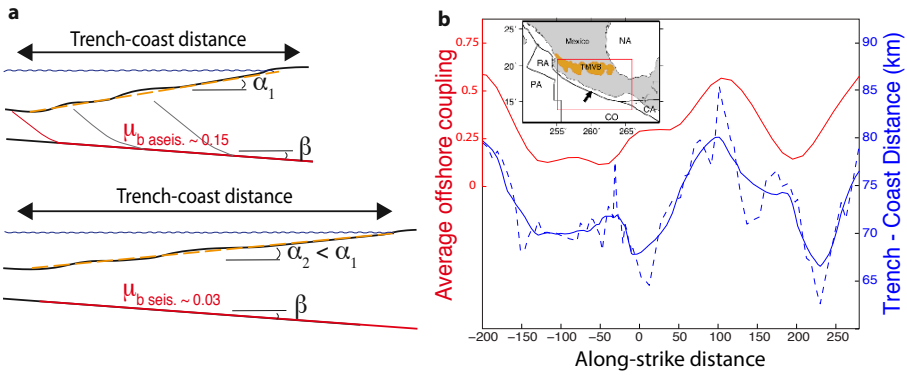

Figure 7.4. *a) Scheme representing the trench-coast distance for segments with aseismic or seismic effective basal friction. b) Example of the Guerrero subduction in Mexico. The trench-coast distance (in blue) correlates with the average coupling (in red). Modified from [ROU 16]*

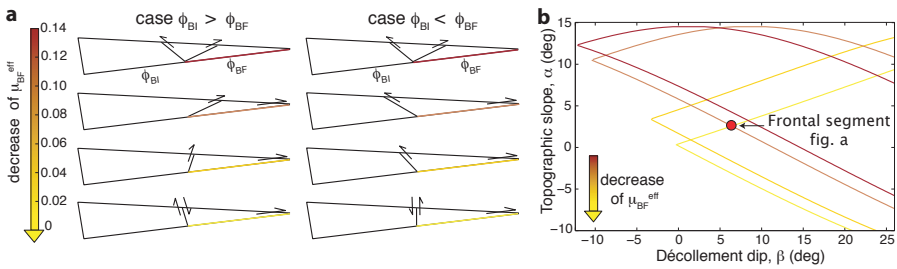

Figure 7.5. *a) Splay faults related to varying basal frictions between a deep (μ_{BI} = 0.1) and a frontal (μ_{BF} = 0.135, 0.13, 0.037 and 0.003) segment. b) Critical envelope for each value of μ_{BF} (0.135, 0.13, 0.037 and 0.003). Modified from [CUB 13a]*

7.5. Deformation of accretionary prisms: evidence for rupture propagating up to the trench

From the 2011 Mw 9.0 Tohoku-Oki [KOD 12] (see Figure 7.6(a)) and the 2004 Mw 9.15 Sumatra earthquakes [CHL 07] (see Figure 7.7(a)), we have also learned that ruptures can propagate up to the trench.

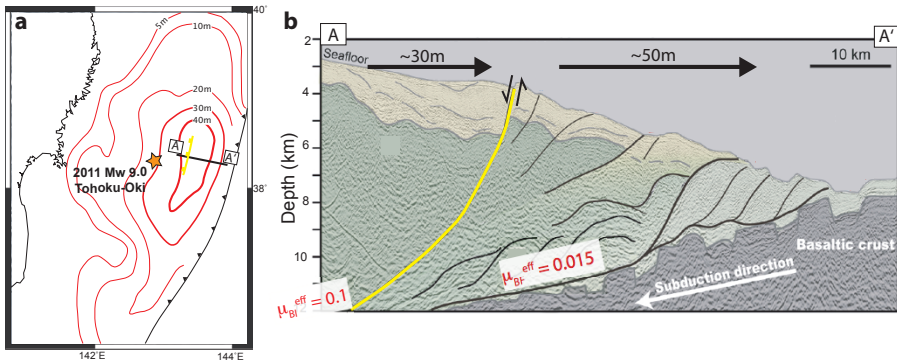

Figure 7.6. *a) Slip contours of the 2011 Tohoku-Oki earthquake, Mw 9.0 (Japan) and location of the normal splay fault that was activated during the earthquake. b) Seismic profile recorded before the earthquake [TSU 11]; 30 m and 50 m: displacements measured by gauges placed on the seafloor on either side of the normal fault [ITO 11]. μ_{BI}, μ_{BF}: effective basal frictions estimated from the observed displacements [CUB 13a]. Modified from [CUB 13a]*

The critical taper theory can again help to identify characteristic structures of a frontal propagation. An aseismic accretionary prism, with a typical aseismic friction, should be at or close to critical state, and develop thrust faults with seaward vergence (see Figure 7.8(a)). If earthquakes systematically propagate toward the trench, then the frontal prism should be at stable state, within the critical envelope. The vergence of the frontal fault depends on its position in the envelope (see Figure 7.9). Close to the extensional limit, the frontal thrust has a landward vergence (see Figure 7.8(d)). With extremely low basal friction, a prism can even reach the extensional critical limit (see Figure 7.8(e)). Consequently, if the seismogenic zone extends up to the trench, we should expect accretionary prisms with either frontal landward thrust or normal faults. In the case of occasional propagation of the earthquake toward the surface, the prism could be at critical state over the long term, but develop structures associated with this occasional propagation, such as landward thrusts or normal faults (see Figure 7.8(b-c)).

In the Sumatra region, where the rupture is strongly suspected to have reached the trench, thrust faults with a landward vergence are observed at the front of high slip patches (see Figures 7.7(a) and 7.10(a)). The Cascadia subduction zone experienced a Mw 9 earthquake in 1700, causing an enormous tsunami across the Pacific [WAN 13]. It is also known for its accretionary prism with landward vergent thrusts. All of these landward prisms correlate with the maximum slip zones estimated for the 1,700 earthquake (see Figures 7.7(b) and 7.10(b)). In the southern Sumatra

region, the prism shows seaward and landward faults, suggesting a mixed (seismic/aseismic) behavior (see Figure 7.10(c)). The Tohoku prism shows both reverse faults with seaward vergence and a large normal fault, revealing the occasional propagation of earthquakes up to the trench (see Figure 7.6(b)).

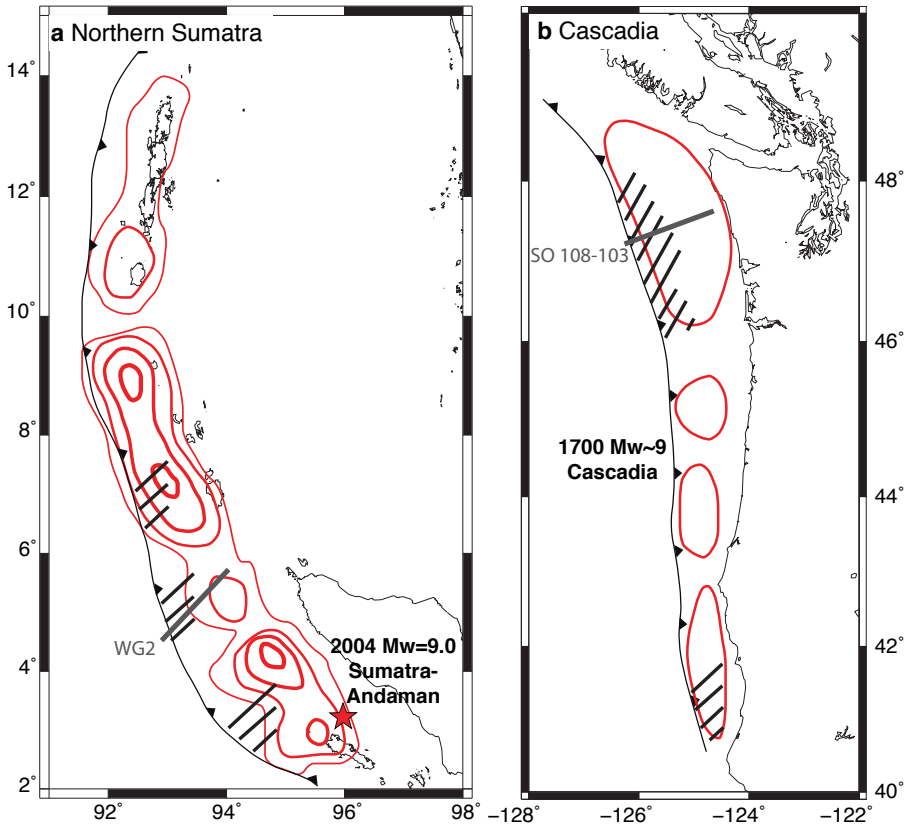

Figure 7.7. *a) Location of landward thrust faults in the northern region of Sumatra (black lines: compilation from [DEA 10, MOE 14]) and co-seismic slip of the 2004 Mw 9.1 Sumatra-Andaman earthquake (in red, contours every 5 m, [CHL 07]). WG2: Seismic profile, Figure 7.10(a). b) Landward thrust faults in Cascadia (black lines; compilation from [MAC 95, GUL 98, ADA 04]) and estimated slip contours for the 1700 Cascadia earthquake, considering a frontal rupture scenario with a Mw 8.9 [WAN 13]. SO-108-103: Seismic profile, Figure 7.10(b). Modified from [CUB 16]*

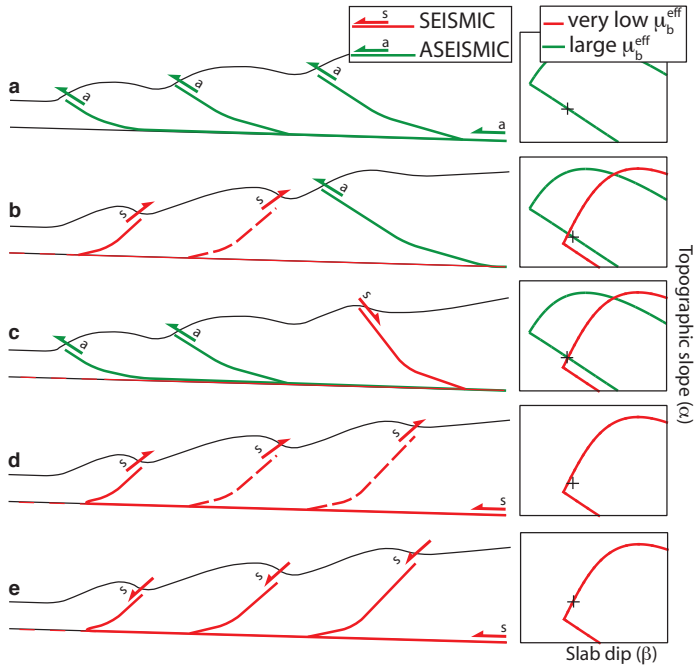

Figure 7.8. *Relation between deformation in accretionary prism (seaward and landward vergence, reverse and normal faults) and seismic behavior of the megathrust, in terms of the position of the prism with respect to the critical envelope. Modified from [CUB 16]*

7.6. Conclusion

The differences in frictional properties between seismic and aseismic segments imply differences in morphology (different slopes) and deformation (no deformation in the upper plate above a seismic segment, distributed deformation above an aseismic segment).

They can also lead to the activation of splay faults, whose type and vergence depend on the spatial distribution of effective friction.

The study of forearc morphology and splay faults can therefore contribute to identify the extent of seismic asperities and, consequently, to improve seismic hazard assessment. The deformation of accretionary prisms provides information on past propagation of earthquakes to the surface, essential for tsunamigenic hazard assessment. These studies are particularly important in regions where geodetic coupling models are either absent or limited.

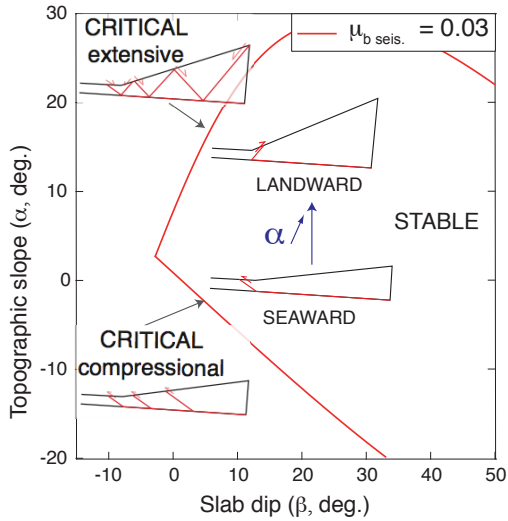

Figure 7.9. *Change in vergence of the frontal fault in the stability domain depending on its position in the envelope*

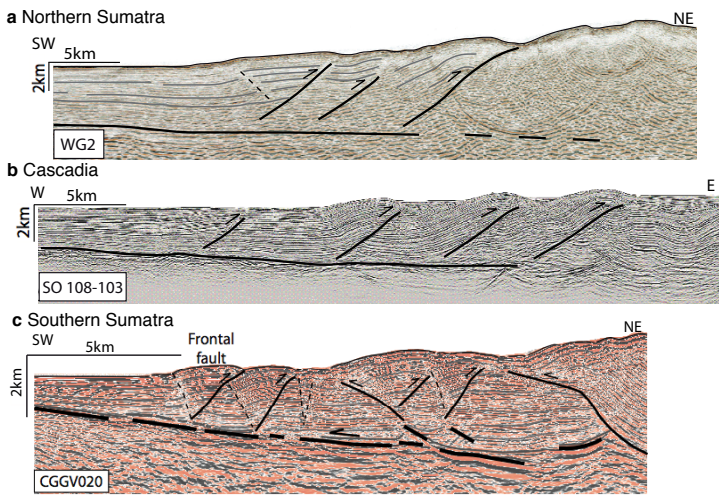

Figure 7.10. *Landward deformation in accretionary prisms, a) North Sumatra , profile WG2 [MOE 14], location Figure 7.7(a). b) Cascades, profile SO-108-103 [ADA 04], location Figure 7.7b). c) South Sumatra, profile CGGV20 [SIN 11]. Modified from [CUB 16]*

7.7. References

[ADA 04] ADAM J., KLAESCHEN D., KUKOWSKI N. et al., "Upward delamination of Cascadia Basin sediment infill with landward frontal accretion thrusting caused by rapid glacial age material flux", *Tectonics*, vol. 23, no. 3, 2004.

[CHL 07] CHLIEH M., AVOUAC J.-P., HJORLEIFSDOTTIR V. et al., "Coseismic slip and afterslip of the great Mw 9.15 Sumatra–Andaman earthquake of 2004", *Bulletin of the Seismological Society of America*, vol. 97, no. 1A, pp. S152–S173, 2007.

[CUB 13a] CUBAS N., AVOUAC J.-P., LEROY Y.M. et al., "Low friction along the high slip patch of the 2011 Mw 9.0 Tohoku-Oki earthquake required from the wedge structure and extensional splay faults", *Geophysical Research Letters*, vol. 40, no. 16, pp. 4231–4237, 2013.

[CUB 13b] CUBAS N., AVOUAC J.-P., SOULOUMIAC P. et al., "Megathrust friction determined from mechanical analysis of the forearc in the Maule earthquake area", *Earth and Planetary Science Letters*, vol. 381, pp. 92–103, 2013.

[CUB 16] CUBAS N., SOULOUMIAC P., SINGH S.C., "Relationship link between landward vergence in accretionary prisms and tsunami generation", *Geology*, vol. 44, no. 10, pp. 787–790, 2016.

[CUB 22] CUBAS N., AGARD P., TISSANDIER R., "Earthquake ruptures and topography of the Chilean margin controlled by plate interface deformation", *Solid Earth*, vol. 13, no. 3, pp. 779–792, 2022.

[DAH 84] DAHLEN F., SUPPE J., DAVIS D., "Mechanics of fold-and-thrust belts and accretionary wedges: Cohesive Coulomb theory", *Journal of Geophysical Research: Solid Earth*, vol. 89, no. B12, pp. 10087–10101, 1984.

[DAV 83] DAVIS D., SUPPE J., DAHLEN F., "Mechanics of fold-and-thrust belts and accretionary wedges", *Journal of Geophysical Research: Solid Earth*, vol. 88, no. B2, pp. 1153–1172, 1983.

[DEA 10] DEAN S.M., MCNEILL L.C., HENSTOCK T.J. et al., "Contrasting décollement and prism properties over the Sumatra 2004–2005 earthquake rupture boundary", *Science*, vol. 329, no. 5988, pp. 207–210, 2010.

[DIE 78] DIETERICH J.H., "Time-dependent friction and the mechanics of stick-slip", *Rock Friction and Earthquake Prediction*, vol. 116, pp. 790–806, 1978.

[DIT 11] DI TORO G., HAN R., HIROSE T. et al., "Fault lubrication during earthquakes", *Nature*, vol. 471, no. 7339, pp. 494–498, 2011.

[FAR 11] FARÍAS M., COMTE D., ROECKER S. et al., "Crustal extensional faulting triggered by the 2010 Chilean earthquake: The Pichilemu seismic sequence", *Tectonics*, vol. 30, no. 6, 2011.

[GAO 14] GAO X., WANG K., "Strength of stick-slip and creeping subduction megathrusts from heat flow observations", *Science*, vol. 345, no. 6200, pp. 1038–1041, 2014.

[GUL 98] GULICK S.P., MELTZER A.M., CLARKE JR. S.H., "Seismic structure of the southern Cascadia subduction zone and accretionary prism north of the Mendocino triple junction", *Journal of Geophysical Research: Solid Earth*, vol. 103, no. B11, pp. 27207–27222, 1998.

[HAY 18] HAYES G.P., MOORE G.L., PORTNER D.E. et al., "Slab2, a comprehensive subduction zone geometry model", *Science*, vol. 362, no. 6410, pp. 58–61, 2018.

[ITO 11] ITO Y., TSUJI T., OSADA Y. et al., "Frontal wedge deformation near the source region of the 2011 Tohoku-Oki earthquake", *Geophysical Research Letters*, vol. 38, no. 7, 2011.

[KOD 12] KODAIRA S., NO T., NAKAMURA Y. et al., "Coseismic fault rupture at the trench axis during the 2011 Tohoku-oki earthquake", *Nature Geoscience*, vol. 5, no. 9, pp. 646–650, 2012.

[LEH 86] LEHNER F., "Comments on 'Noncohesive critical Coulomb wedges: An exact solution' by FA Dahlen", *Journal of Geophysical Research: Solid Earth*, vol. 91, no. B1, pp. 793–796, 1986.

[LIN 13] LIN Y.-N.N., SLADEN A., ORTEGA-CULACIATI F. et al., "Coseismic and postseismic slip associated with the 2010 Maule Earthquake, Chile: Characterizing the Arauco Peninsula barrier effect", *Journal of Geophysical Research: Solid Earth*, vol. 118, no. 6, pp. 3142–3159, 2013.

[MAC 95] MACKAY M.E., "Structural variation and landward vergence at the toe of the Oregon accretionary prism", *Tectonics*, vol. 14, no. 6, pp. 1309–1320, 1995.

[MEL 12] MELNICK D., MORENO M., MOTAGH M. et al., "Splay fault slip during the Mw 8.8 2010 Maule Chile earthquake", *Geology*, vol. 40, no. 3, pp. 251–254, 2012.

[MOE 14] MOEREMANS R., SINGH S.C., MUKTI M. et al., "Seismic images of structural variations along the deformation front of the Andaman–Sumatra subduction zone: Implications for rupture propagation and tsunamigenesis", *Earth and Planetary Science Letters*, vol. 386, pp. 75–85, 2014.

[MOR 09] MORENO M.S., BOLTE J., KLOTZ J. et al., "Impact of megathrust geometry on inversion of coseismic slip from geodetic data: Application to the 1960 Chile earthquake", *Geophysical Research Letters*, vol. 36, no. 16, 2009.

[PLA 70] PLAFKER G., SAVAGE J.C., "Mechanism of the Chilean earthquakes of May 21 and 22, 1960", *Geological Society of America Bulletin*, vol. 81, no. 4, pp. 1001–1030, 1970.

[RIC 83] RICE J.R., RUINA A.L., "Stability of steady frictional slipping", *Journal of Applied Mechanics*, vol. 50, no. 2, pp. 343–349, 1983.

[ROU 16] ROUSSET B., LASSERRE C., CUBAS N. et al., "Lateral variations of interplate coupling along the Mexican subduction interface: Relationships with long-term morphology and fault zone mechanical properties", *Pure and Applied Geophysics*, vol. 173, nos 10–11, pp. 3467–3486, 2016.

[RUB 59] RUBEY W.W., KING HUBBERT M., "Role of fluid pressure in mechanics of overthrust faulting II: Overthrust belt in geosynclinal area of western Wyoming in light of fluid-pressure hypothesis", *Geological Society of America Bulletin*, vol. 70, no. 2, pp. 167–206, 1959.

[SAI 17] SAILLARD M., AUDIN L., ROUSSET B. et al., "From the seismic cycle to long-term deformation: Linking seismic coupling and quaternary coastal geomorphology along the Andean megathrust", *Tectonics*, vol. 36, no. 2, pp. 241–256, 2017.

[SAV 83] SAVAGE J.C., "A dislocation model of strain accumulation and release at a subduction zone", *Journal of Geophysical Research: Solid Earth*, vol. 88, no. B6, pp. 4984–4996, 1983.

[SIN 11] SINGH S.C., HANANTO N., MUKTI M. et al., "Seismic images of the megathrust rupture during the 25th October 2010 Pagai earthquake, SW Sumatra: Frontal rupture and large tsunami", *Geophysical Research Letters*, vol. 38, no. 16, 2011.

[SON 03] SONG T.-R.A., SIMONS M., "Large trench-parallel gravity variations predict seismogenic behavior in subduction zones", *Science*, vol. 301, no. 5633, pp. 630–633, 2003.

[TIL 16] TILMANN F., ZHANG Y., MORENO M. et al., "The 2015 Illapel earthquake, central Chile: A type case for a characteristic earthquake?", *Geophysical Research Letters*, vol. 43, no. 2, pp. 574–583, 2016.

[TSU 11] TSUJI T., ITO Y., KIDO M. et al., "Potential tsunamigenic faults of the 2011 off the Pacific coast of Tohoku earthquake", *Earth, Planets and Space*, vol. 63, no. 7, p. 58, 2011.

[WAN 06] WANG K., HE J., HU Y., "A note on pore fluid pressure ratios in the Coulomb wedge theory", *Geophysical Research Letters*, vol. 33, no. 19, 2006.

[WAN 13] WANG P.-L., ENGELHART S.E., WANG K. et al., "Heterogeneous rupture in the great Cascadia earthquake of 1700 inferred from coastal subsidence estimates", *Journal of Geophysical Research: Solid Earth*, vol. 118, no. 5, pp. 2460–2473, 2013.

8

The Diking Cycle at Divergent Plate Boundaries

Cécile DOUBRE
ITES, EOST, University of Strasbourg, France

8.1. Introduction

The densification of geophysical monitoring networks and the continuous recording of geodetic and seismological data, complemented by satellite observations, marked a decisive step in the understanding of convergent and strike-slip plate boundaries, especially when evaluating seismic hazard in these regions. The concept of the seismic cycle makes it possible to describe the evolution of these boundaries over the short term and medium term (10^2 to 10^5 years) to account for loading periods (inter-seismic phase), stress release periods (co-seismic phase) and the period that follows this (post-seismic phase) (see Introduction and Chapters 1, 2 and 3). While this concept is now commonly used for convergent and strike-slip plate boundaries, it is not easily applicable to divergent plate boundaries. Indeed, magmatism is often strongly involved in extensional deformation along these boundaries, and so they cannot be understood in the same way as others, where the forces causing this deformation result primarily from plate tectonics. Nonetheless, at the level of magmatic continental rifts or ocean ridges in the emerged domain, the increase in geophysical observations, especially terrestrial and spatial geodesy measurements, as well as seismological data makes it possible to describe a cycle called the *diking* cycle, which occurs over a timescale similar to that

For a color version of all of the figures in this chapter, see www.iste.co.uk/rolandone/seismic.zip.

The Seismic Cycle,
coordinated by Frédérique ROLANDONE.

The Seismic Cycle: From Observation to Modeling,
First Edition. Frédérique Rolandone.

of the seismic cycle. For the boundaries of plates diverging at low or intermediary velocities (<4 cm/year) especially, the evolution of the boundary may often be described to the first order by following this concept of a *diking cycle.*

8.2. Boundaries of diverging plates

It was only from the late 1950s onwards that technological developments enabled marine geophysical investigations of ocean ridges. For several thousand kilometers on the ocean floor (Figure 8.1), volcanic and hydrothermal activity is concentrated in a central valley across bathymetric highs (underwater mountain chains). Tectonic activity here is more developed when the spreading rate is low. Thus, for slow spreading ocean ridges, the central valley is formed by large escarpments of normal faults. Measuring magnetic anomalies on either side of these ridges was essential to validate the concept of plate tectonics. The conveyor-belt model, as it was then called, shed light on the importance of the contribution of deep and molten products in the functioning of diverging plate boundaries. This model corresponds to the formation of a new oceanic crust concentrated along the ridge and moving away from this ridge over time. Nonetheless, the roles played by tectonics and magmatism, respectively, in accommodating plate divergence have always been debated, especially when we study the active, extensional deformation of the crust.

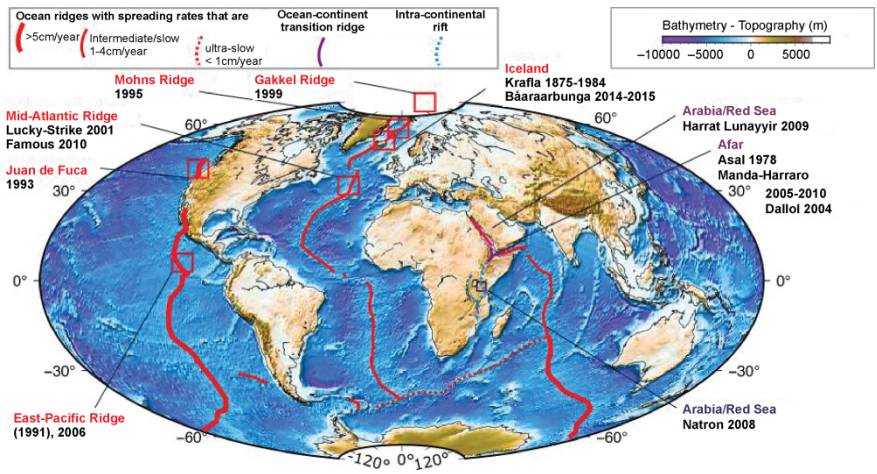

Figure 8.1. *Diverging plate boundaries in the oceanic (red), transitional (purple) and continental (blue) domains. The diking events observed through seismology and/or geodesy are indicated (non-exhaustive list). The chapter cites diking events that affected plate boundaries with low expansion rates and in emerged domains and these are indicated in the figure in bold*

The vast majority of diverging plate boundaries correspond to ocean ridges and are found in submerged environments (Figure 8.1). Geodetic instrumentation in the sea is still not developed enough to measure surface deformation here and provide information on the processes involved in crustal extension. Only seismological data can be used. However, some sites offer the chance to carry out geophysical measurements on land to track the spatial-temporal evolution of the extensional deformation (Figure 8.2). These sites include Iceland, where the North Atlantic mantle plume causes a bathymetric anomaly: the North Atlantic Ocean ridge that separates the North American and Eurasian plates crosses the island (Figure 8.2(c)). The intra-continental rifts (where continental lithosphere rupture is not yet complete) are also largely in the emerged regions. The East African Rift (EAR) is the best example of this, as it separates the Nubian and Somalian plates for over 5,000 km, from Mozambique to northern Ethiopia (Figure 8.2(b)). Finally, the Afar region, at the northern end of this rift, is also located on an abnormal topographic level, partly due to the presence of a plume under the African lithosphere, from ~35 to 30 Ma (million years ago). Three diverging plate boundaries outcrop here, allowing the observation of deformation along rifts above sea level associated with the Red Sea and Aden ocean ridges and the East African Rift (Figure 8.2(a)). The extension rates in Afar (~10 mm/year) are much higher than those measured along the East African rift (~1 mm/year), making it possible to track the evolution of the deformation across shorter time scales and thus understand the dynamics on these boundaries.

Magmatism is inherent to the evolution of the boundary and thus this border cannot be understood in the same way as the others. Unlike back-arc volcanism, the fusion products are found on the boundary itself. Magmatism induces point-like pressure sources, and therefore local stress fields and transient motions caused by the non-stationary activity of magmatic and/or geothermal reservoirs. In addition to a complex lithospheric structure dominated by a thinned lithosphere and large heat flow, the border of diverging plates does not correspond to a single interface where all the tectonic loading is concentrated during the inter-seismic period. Along the most evolved continental rifts, like those north of the REA and in Afar, or along the Icelandic ridges (Figure 8.2), the brittle deformation is further distributed in a network of small faults, both laterally and vertically. These faults are therefore not likely to generate large earthquakes (low seismogenic depth).

The examples in this chapter are the three aforementioned sites: Iceland, Afar, and the East African Rift (Figure 8.2). Although each of these has their own intrinsic features, especially their structural inheritance that influences the rifting, the observations and measurements carried out here in the last few decades shed light on the spatial-temporal organization of the deformation of diverging plate boundaries with low expansion rates. These examples enable us to better understand the

respective roles played by magmatism and tectonics, as well as how they interact in the accommodation of regional extension. It must also be noted that these three sites are located in proximity to ancient mantle plumes. The presence of these plumes plays a role in modifying the physical and chemical properties of the magma, the thermal conditions in the lithosphere and has an influence on the location, propagation (if any) and morphology of extensional deformation zones [COU 99].

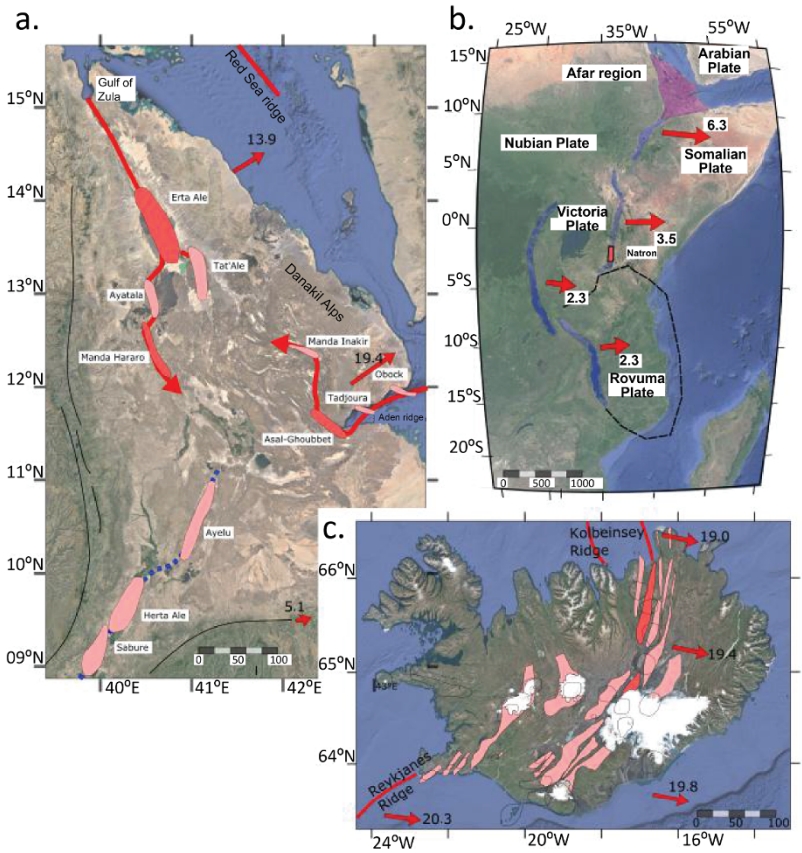

Figure 8.2. *a) Spreading segments in the Afar Depression [BAR 77]. b) Location of the East African Rift. The velocities are indicated with respect to the Nubian plate. c) Spreading segments of the mid-Atlantic ocean ridge in Iceland, with the location of volcanic centers [SIG 06]. The rift zones where normal faults and fissures are concentrated are given in pink. The segments indicated in red in (a) and (c) are those that have experienced rifting events observed through geophysics (see text). Velocities in mm/year are expressed relative to the Nubian plate in (a) and (c), and relative to the North American plate in (b)*

8.3. Magmato-tectonic interactions in rift zones

At the regional level, many geodynamic and structural studies have been carried out on the evolution in a continental lithosphere leading to rupture. They show the link between the surface extension and magmatic processes at depth. This evolution is traditionally viewed through the concept of two rifting modes [SEN 78, WHI 89, BOT 85]:

– active rifting mode, where the upward migration of material at depth to the base of the lithosphere are due to the presence of a thermal anomaly in the mantle. This causes thinning through thermal erosion, doming and the extension of the lithosphere, which is accompanied by crustal magmatism and volcanism;

– passive rifting mode, in which extensional tectonic forces cause the stretching and thinning of the lithosphere. The asthenospheric rise due to decompression and convective changes in the mantle at the base of the thinned lithosphere causes magmatism and volcanic activity at the crustal level.

Conventionally, the long-term evolution of rifting is described based on geophysical imaging data from passive continental margins, which give access to the finite deformation. It is essential to identify pre-rift, syn-rift and post-rift lithospheric and crustal structures across a margin in order to reconstitute the steps from continental rifting to oceanic accretion, that is, over a timescale of ~20 million years. A large number of observations has been made on many margins and both current or aborted rifts, showing the variety and complexity of the structures and mechanisms of continental lithosphere thinning and stretching [BUC 91, BRU 99]. These also show that magmatism is involved in extension budgets, especially during the ocean-continent transition. The amount of melted products during continental break-up is a crucial parameter with respect to the structure of the basins being formed and the rift margins [WHI 89, GEO 05].

The width of the rift zone may be narrower or wider, depending on the regions. The more evolved the rift is, the narrower it is transversely. The spatial organization of the volcanic center (or centers), the fault systems, and the basins define a longitudinal segmentation. Along the East African Rift, the segments associated with young intra-continental rifting are mainly structured by large, asymmetric basins whose characteristic length is ~200 km and whose development is controlled by one or two major faults, that are long and deep [BOS 85]. The volcanic systems and magmatism are concentrated in the transfer zones of the extensional deformation between the basins that form the segments [HAY 96]. The structural evolution of the longitudinal segmentation of the EAR will depend on the variations in the mechanical properties of the lithosphere, especially with respect to the

presence of the mantle plume in the north and also because basin development is not synchronous across the EAR. In the north, the most evolved rift segments, like in Afar, share many structural and morphological similarities with segments of slow-spreading ocean ridges (Figure 8.3). With a length of ~150 km and width of ~15-20 km, these segments are usually structured by a narrow rift zone that develops on either side of a central volcanic, magmatic and/or hydrothermal system. The rift zone is formed by a system made up of many small, normal faults that often have high dip angles toward the rift axis, growing smaller as they move away from this. This difference in rift structure between the EAR and Afar also indicates the relative importance of tectonics and magmatism in the extension dynamics. The comparison of seismic and geodetic moments along the EAR also reveals an evolution from south to north [DÉP 13]. To the south, the extensional deformation is dominated by tectonics, that is, the slip of normal seismic faults. In the north, it is dominated by magmatism, that is, the magma intrusions into the crust, associated with low seismicity and, consequently, largely aseismic spreading.

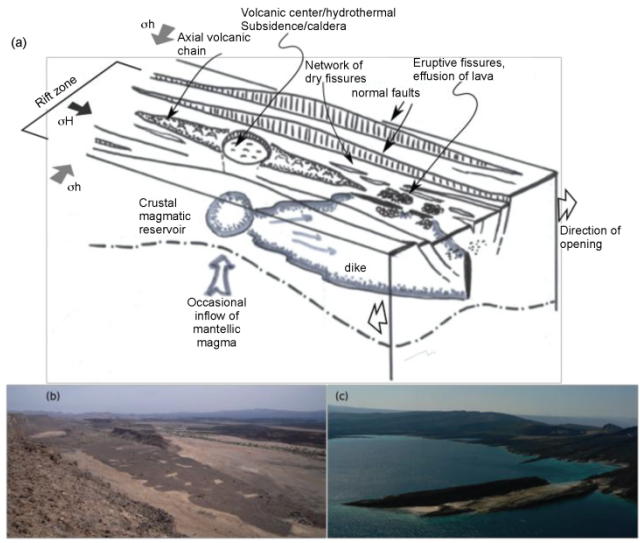

Figure 8.3. *a) Sketch of the rift segment with slow spreading ridge. Views of the rift zone b) in the Manda Hararo segment in Afar (Ethiopia) and (c) the Asal-Ghoubbet segment in Afar (Djibouti). Location in Figure 8.2. Photos @ C. Doubre*

The overall structure of the most evolved rift, like in Afar, or along slow-spreading ocean ridges, like in Iceland, or in submerged zones (known because of

marine geophysical observations), shows the importance of both normal faults and magmatism (Figure 8.3). The conventional view was that in the presence of magmatism, plate divergence was accommodated in the narrow rift zone though magmatic dilatation, because of magmatic intrusions (veins, dikes) into the crust. In the absence of magmatism, the divergence is likely to result in tectonic extension, that is, the involvement of the normal faults that make up the rift. This view was modified based on many recent observations in rifts affected by diking episodes, as well as those which currently have limited volcanic and magmatic activity.

8.4. The diking cycle

Several regions were equipped early on with instruments as part of geophysical measurement networks (geodetic and seismological) to quantify the crustal deformation associated with the boundaries of diverging plates. From the 1990s onward, these regions could also be observed through satellite imaging. The associated remote sensing techniques give access to the displacement field for the entire region, and no longer only for a few measurement points. They also allow accurate tracking over time in regions that may be hard-to-reach. Today, there are measurement time series that are long enough to describe the behavior of the boundary, or the future boundary, over the course of the "diking cycle". It must be noted that several cyclicities in rift zones, occurring over different time scales, may be interlinked. Here, we will examine short cycles, whose duration (an order of magnitude of 10^2 years) essentially depends on the plate velocity at the boundaries and, as will be seen, on the presence of magma. The term "rifting cycle" is also often used for the time scales that we are studying, but this may be confused with the cycle that includes the pre-, syn- and post-rifting periods identified across passive continental margins, which occur over a timescale of ~20 million years [LER 12]. Magmato-tectonic alternations have also been demonstrated on time scales of ~10^5 years in slow- and intermediate-spreading ocean ridges, and also in emerged opening segments [MED 16].

The "diking cycle" serves as a reminder of the concept of "seismic cycle", used for transform and convergent boundaries (see Introduction and Chapter 5), where the interface between plates remains amagmatic. The intrusion of a dike thus corresponds to a transient event that could cause significant displacements of the ground surface. The *co-diking* phase would therefore correspond to the co-seismic phase of the seismic cycle. Extending the analogy, the period that follows this will then be called the *post-diking* phase, while the deformation of the ground surface in the absence of any strong movements will be seen in the *inter-diking* phase. For each of these periods, there are specific characteristics that can be highlighted. These

reveal both the similarities and differences with respect to the mechanisms that control the dynamics on other plate boundaries. Even in Iceland, where several diking events have been observed and experienced by the population from the 18th and 19th centuries onwards, it has not been possible to carry out quantitative monitoring of the deformation throughout the diking cycle [SIG 06].

8.4.1. *The co-diking phase*

8.4.1.1. *Magmatic intrusion*

We use the "co-diking" phase to refer to the period during which transient displacements in the crust are large enough to entirely or partially compensate for the spreading deficit along the plate boundary, with respect to the far field velocities imposed by plate tectonics. A dike is a vertical planar intrusion, that is, a fissure in which magma circulates before solidifying. From a mechanical point of view, the dike will be set up in the direction of the maximal horizontal stress, and its opening, which is usually normal to the intrusion plane, will be in the direction of the minimal horizontal stress (Figure 8.3). Dikes can thus also serve as indicators of ancient stress fields. Such structures are observed in ancient volcanic zones, where erosion has stripped the upper layers, causing an outcropping of these hypovolcanic rocks in the surrounding rocks, which may or may not be of a different nature.

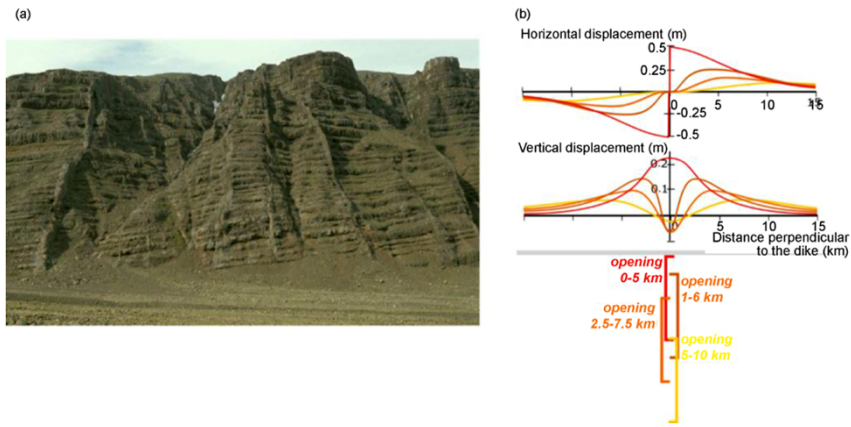

Figure 8.4. *a) Photo of basaltic dikes intruded into the basaltic lava pile in Tertiary Iceland. b) Horizontal and vertical displacements of the surface, associated with a 1 m opening of a vertical dislocation (5 m in height, top of the dislocation at 0, 1, 2.5 and 5 km depth) in an elastic half-space [OKA 85]. Photo @ C. Doubre*

When we look at active processes, the establishment of a sufficiently large and superficial dike in the crust is accompanied by vertical and horizontal displacements on the ground surface. If the dike reaches the topographic surface, allowing magmatic products to spread across the surface, a fissural eruption can be observed (Figure 8.3). At a distance from a local pressure source, the direction of this planar intrusion is perpendicular to the spreading velocity of the plates. The opening of such a magma-filled fissure accommodates plate movement along this rift segment.

8.4.1.2. *Monitoring diking episodes*

All along the submerged ocean ridges, the only observations that make it possible to detect and track a diking event are basically seismological records, which may be complemented by other geophysical observations and/or in situ observations if submersible missions are possible [TOL 06]. It has also been possible to acquire data from the temporary hydrophone networks [GIU 18] or Ocean Bottom Seismometers (OBS) [SCH 17], or by using signals from the global network of seismometers on land [TOL 01], or regional networks located close by [AHM 16]. It must be noted that many diking episodes take place in different volcanic contexts, but they will not be discussed here [TOD 02, SMI 19], since we are only studying episodes along diverging boundaries with low extension rates.

In Afar, in the EAR, and in Iceland, several diking events have been observed using seismology and geodesy, enabling a description and understanding of the activity and processes involved in this phase (Figure 8.1). On land, diking events in the Krafla segment in Iceland, between 1975 and 1985 [BJÖ 85], and in the Asal-Ghoubbet segment in Afar, in 1978 [ABD 79] could be intensively tracked using the geophysical means available at the time (Figure 8.1). With regard to crustal deformation, there was largely seismology and terrestrial geodesy (distanciometry, leveling) complemented by measurements and observations obtained through tectonics, geochemistry or other geophysical methods such magnetotellurics and gravimetry. In addition to many geological, geochemical or petrological investigations, crustal deformation associated with the most recent events have been studied through modern tracking methods, notably spatial geodesy (GNSS, radar interferometry – InSAR – and correlation of optical or radar images) (see Introduction). The most striking event was the 2005 Manda-Hararo episode in Afar [GRA 09] (Figure 8.5(a)). Other events in Afar and in Iceland, of smaller amplitude, were detected thanks to the use of radar images (SAR) and seismic activity. We must also note the episode that affected the Natron continental segment in Tanzania along the EAR in 2008 [CAL 18]. A particular diking event, observed in Saudi Arabia in 2010, in the Harrat Lunayyir volcanic region, drew a lot of attention

as it was located more than 200 km away from the oceanic spreading ridge of the Red Sea [PAL 10]. This activity, which is consistent with crustal extension onto land, suggested that the passive continental margin could be active [EBI 10]. Table 8.1 lists the characteristics of these events as well as the main studies that focus on them.

8.4.1.3. *The deformations associated with the co-diking phase*

The beginning of the co-diking phase has attracted the attention of geophysicists through the sudden increase in seismic activity, the recording of a series of low-magnitude earthquakes, low-frequency signals (tremors) and/or the occurrence of moderate-magnitude earthquakes (M~5). Magnitudes greater than 5.0 are significant in magmatic diverging boundaries, especially when excluding transfer zones between rifts that are likely to be affected by earthquakes of greater magnitudes.

When volcanic activity does not necessarily take place within the rift zone and/or in the vicinity of the volcanic center(s), the co-diking phase is revealed mainly through movements of the ground surface, which can be plurimetric in magnitude (Figures 8.5 (a) and (b)). Although the amplitude of the vertical displacements (deduced from leveling measures and/or InSAR) and horizontal displacements (deduced through distanciometry, GNSS, InSAR and displacement fields measured through correlation of high-resolution radar or optical images) vary from case to case (Table 8.1), the main characteristics of the co-diking phase are as follows:

– the collapse of the rift zone over all or part of the segment: the collapsed zone is narrow (Figures 8.5 (a) and (b)). The 2005 event in the Manda-Hararo segment in Afar is quite exceptional in length, as the inner floor collapsed across a width of barely 5 km, but over a length of 65 km along the rift axis (Figure 8.5 (b));

– the uplift of rift shoulders: it should be noted that the uplift of rift shoulders is a characteristic of the rift structure observed over the long term, since it results from the elastic behavior of the crust. The larger the collapse in the rift zone, the greater the uplift. The relative displacements between the rift zone and the shoulders can be of several meters during a single diking episode. Large gradients in vertical displacement across the rift are consistent with normal fault activity;

– the horizontal opening across the rift can be as large as several meters. When the density of measurements is sufficient, as was the case in Asal-Ghoubbet in 1978, or at Manda-Hararo in 2005 (Figure 8.5), the horizontal displacement shows that the amplitude of this opening also varies longitudinally in this segment;

– a subsidence located in the central part of the segment, where hydrothermal activity and/or a magmatic reservoir are identified.

Diking episode	Number of intrusions	Number of eruptions	Doformation measurements	Surface observations	Horizontal opening measured	Maximum vertical displacement measured	Dimension of the intrusion	Depth of the crustal reservoir	Geodetic moment (N.m)	Seismic moment (N.m)	Post-diking deformation
Sequence for Krafla (Iceland) 1975-1984 Vpl = 19.2 mm/yr	20	9	Leavelling Distanciometry	-Tension fractures -Seismicity	2 m over 50 km 6 m over 30 km						Yes
Dyke - Dec. 1975		1 minor eruption				Caldera subsidence:	Length: 60 km				
Islande = Iceland 2014 Vpl = 18.5 mm/an		Probably but under the glacier	InSAR GNSS	45 km long	1.3 m max	Central caldera subsidence 70m	Length: 48 km	1.5 km		1.9	
Asal-Ghoubbet episode (Afar) 1978-79 Vpl=16 mm/yr	2	1	Levelling Distanciometry	-Tension fractures -Normal fault slips	2m	70cm centreal subsidence 20 cm shoulder uplift	Length: 21 km Depth; 4 km Opening: 1.7-3.8 m Volume: 0.2x10(9)?	~5 km			Yes
Manda Hararo sequence (Afar) 2005-2010 Vpl=18,5 mm/yr	13		InSAR GNSS								Yes
Dyke - Sept 2005	3 dikes	Minor eruption	InSAR	-Tension fractures -Normal fault slips			1.1-2 km3	10 km	3.5x10 (19)(?)	3.5x10 (18)(?)	Yes
****											
Dallol episode Oct-Nov 2004 Vpl=?? mm/yr	1		InSAR	-Mw_max=5.5		Caldera subsidence:	Length: 9 km Depth: between 2 and 6 km Vol: 0.058 km^3	1.5 - 3.3 km	22x10 (17)(?)	2.3x10 (17)	
Natron episode (Tanzania) 2008 Vpl=3-4 mm/yr	1		InSAR GNSS	-Tension fractures -Seismicity -Normal fault slips			Length: 12 km Depth: 2-6 km Opening: <2 m	3 km 10 km	2.7x10 (17)(?)	16.5x10 (16)	

Table 8.1. *Main features of the diking events cited in the text*

A)

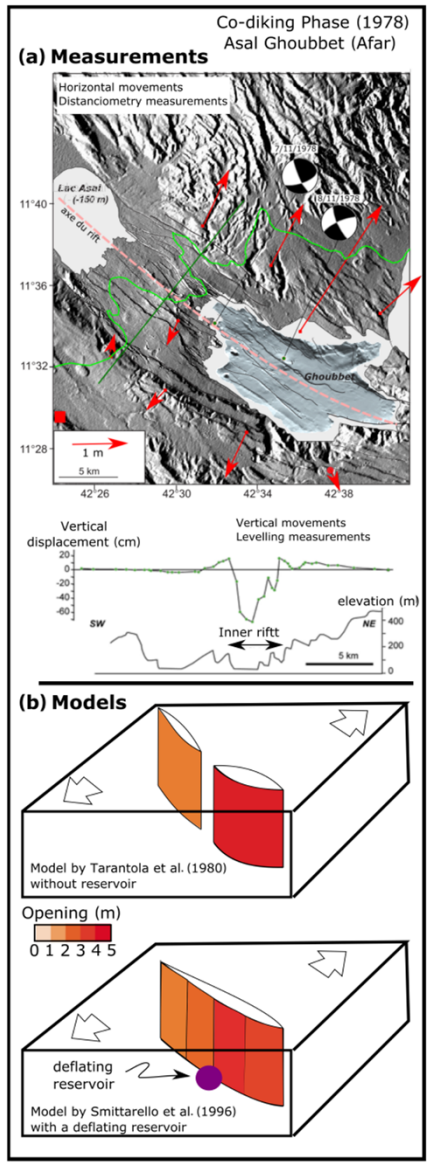

Figure 8.5A. *a) Measurements of horizontal and vertical movements (green leveling line) of the co-diking phase in the Asal-Ghoubbet rift (Afar) in 1978 (based on [RUE 79]). b) Models of the opening of vertical dislocations in an elastic half-space. On top: model from Tarantola et al. [TAR 79b], with the homogeneous opening of two, disconnected dikes. Bottom: model of [SMI 16] with a single dike, an opening varying laterally, and the deflation of a reservoir at a depth of 5 km at the center of the segment*

B)

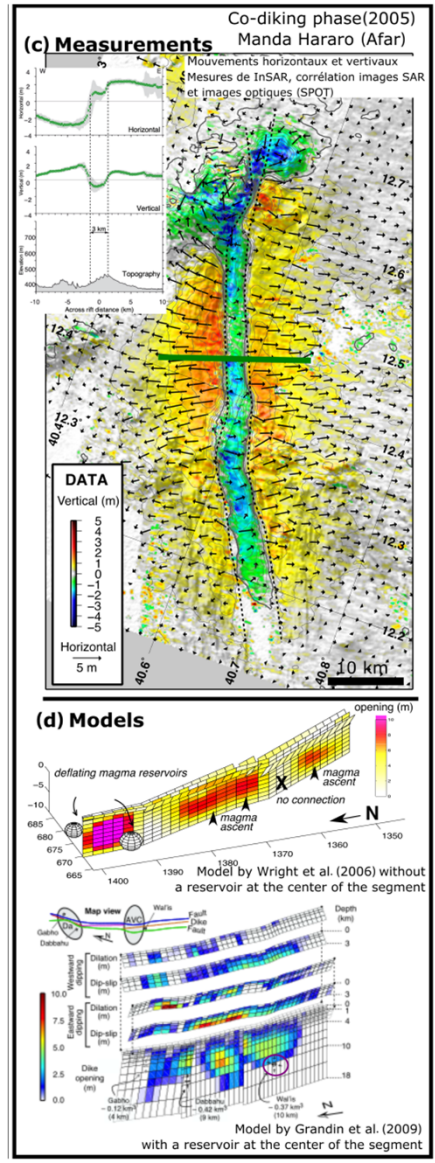

Figure 8.5B. *c) Measurements of horizontal movements and the co-diking phase in the Manda Hararo rift (Afar) in 2005. d) Models of the spreading of vertical dislocations and slips over normal faults in an elastic half-space. On top: model from [WRI 06] with the opening of two disconnected dikes. Bottom: model from [GRA 09] with a single dike and deflation of a reservoir at a depth of 10 km at the center of the segment. Images (c and d) reproduced with the kind permission of R. Grandin and T. Wright*

The observations on land and the interpretations of satellite images, including interferograms, are essential for the mapping of surface ruptures. These correspond to the opening of dry (no magma) fissures and normal fault slips. The relative vertical motion between the collapsed rift zone and its margins is accommodated by near-vertical normal faults that form the edges of the rift zone or are found in proximity to it (Figure 8.5(d)).

The seismic or micro-seismic activity associated with these deformations is recorded by the regional or local networks. Earthquakes occur in sequence during each event. Despite the low accuracy of certain catalogs (due to the absence of nearby seismic stations), the epicenters are concentrated in the rift zone, close to where the deformation is most intense. Seismic events also draw alignments parallel to the rift axis. The temporal analysis of this activity reveals a migration of seismic activity from the center of the segment in one or two directions, at velocities of 2–3 km/h.

8.4.1.4. *Processes involved during the co-diking phase*

The observed surface displacements are consistent with the opening of a near-vertical fissure at depth in an elastic medium. Simple mechanical models show that such an opening causes diverging displacements on the surface on either side of the fissure, and an uplift at the height of the fissure (Figure 8.4 (b)). In the case of a deeper fissure, a collapsed zone is observed at the level of the fissure. The induced extensional local stresses concentrated at the top of the dike favor the relative movement between the collapse at the center of the rift zone and the uplift of the shoulders [POL 83, RUB 98]. The amplitude and spatial distribution of horizontal and vertical ground surface movements are thus crucial constraints to determine the geometry (dimensions, depth, any eventual dip angle) and the amplitude of the source at depth (distribution of the opening over the entire dike) that induced the surface deformation.

The earliest inverse surface slip models were developed by Tarantola et al. [TAR 79a, 79b] to determine the characteristics of the dike associated with the Asal-Ghoubbet rift event in Afar in 1978 (Figure 8.5(b)). The displacement data associated with each diking event is also inverted using a similar approach. More elaborate inversions take into account a more complex rheology of the surrounding rock or estimate the distribution of the amplitude of the opening on the discretized plane, and not a homogeneous opening of the dike (Figures 8.5 (b) and (d)). Surface displacements, like the subsidence measured during the co-diking phase or local uplifts during the post-diking phase for several events, reveal the existence of one or more crustal reservoirs, especially at the center of the rift (Figure 5 (b) and (d)). Therefore, the models can also include point-like pressure sources (Mogi types)

[MOG 58] to determine the parameters related to the magmatic reservoirs, such as their depth, their size and the associated loss of volume/pressure (deflation) during the co-diking phase.

The geophysical observations, mainly geodetic and seismological, and the results from the models make it possible to describe the processes that are involved in the co-diking phase and finally to better understand the short-term dynamics of the plate boundaries.

– The main source of the magmatic products that allow the magmatic dilatation and crustal spreading is concentrated at the center of the segment. The difference in density between the low-density material and its surrounding rock allows the vertical ascension of material from depth toward the crustal reservoir. The seismic data suggest a magmatic chamber roof less than 3 km from the center of the Krafla segment, a depth similar to that in the Asal-Ghoubbet segment, where the hypocenters of the earthquakes are concentrated at the roof of the chamber. Mechanical models match the Manda-Hararo segment (10 km; [GRA 09]) or the Asal Ghoubbet segment (5 km; [SMI 16]). The non-uniqueness of models resulting from inversions is well illustrated in the case of Asal-Ghoubet. Indeed, the observed deformation field can be reproduced by the opening of two unconnected dikes, or dikes connected by reservoir deflation (Figures 8.5 (b) and (d)). Taking such a source into account in the models has a significant implication, since it involves a primarily vertical circulation in the first case [TAR 79a, 79b, WRI 06], while it seems likely to be lateral, from the reservoir toward the ends of the segment beneath the rift zone [GRA 09, SMI 16].

– The opening of a dike propagates from the crustal reservoir in the direction of the maximum horizontal stress. The hydraulic fracturing mechanism, observed around boreholes, would allow extensional stresses to be concentrated in the neighborhood of the over-pressurized magma reservoir. The lateral propagation in the rift zone is accompanied by the migration of seismic events. These events take place mainly in the surrounding rock and are associated with the deformation of rocks around the intrusion and at the front of the propagating dyke. The sequence also describes the growth of the dyke over time. While the lateral propagation under shield volcanos is explained by the lateral variations in lithostatic pressure, such differences in topography are not always observed in rifts, especially the most evolved rifts. The propagation could then follow a level of lithostatic equilibrium (the same distance from the topographic surface) or follow the ductile-brittle transition, shallow in the center of the segment (strong geothermal gradient), deepening toward the “colder” extremities [GRA 12, BUC 06].

– The budget of volumes between the magma that left the reservoir and of the magma circulating in the dike(s) is not necessarily zero. The difference may also be due to the variations in the compressibility of the magma [RIV 08].

– The comparison between the seismic deformation (measured from the energy released by earthquakes recorded during the seismic phase) and the geodetic deformation (measured from the opening estimated by the inversion of surface data) shows that a large part of the deformation occurs aseismically.

– Large movements have been observed on the faults during the co-diking phase and suggest that most of the slip on the faults takes place during this phase.

8.4.2. *The post-diking phase*

Geodetic observations have shown that these diking events are very often followed by a significant, largely aseismic, deformation. Measurements of horizontal velocity indicate an opening rate of the rift zone (local field) that can exceed the plate velocity (far field, Figures 8.6(a)). In addition to horizontal movements, in many cases vertical movements have been observed, corresponding to an uplift in the rift zone. The amplitude of both horizontal and vertical displacements tends to decrease with time (Figure 8.6(b)).

Thus, as in the case of transform or convergent plate boundaries, the post-seismic deformation evolving over time can be explained either as the environment's response to the seismic deformation (after-slip, relaxation, rebound) (see Chapter 3) or by an active mechanism related to a source of deformation at depth, even in a purely elastic medium, with no involvement of more complex rheology. It can be noted that the poroelastic rebound (see Chapter 3) is not the favored mechanism in the case of a rift zone where the rocks are mainly volcanic, and that the associated deformation is rarely longer than a few months or years. Thus, two explanations are generally cited to account for the mainly aseismic deformation of the post-diking phase: (1) the redistribution of stresses in the generally shallow upper mantle in the rift zones, or even in the lower crust, with viscoelastic rheology and (2) a continuous injection of magma into the rift zone. The discrimination between the two mechanisms is not always possible due to the quality of available data, which is not spatially or temporally dense enough to differentiate the origin of the deformation. Nevertheless, the sequence of intrusions in the Icelandic segment of Krafla (1975–1985), the Asal-Ghoubbet episode (1978) and the Manda-Hararo sequence (2005–2010) in Afar are the three main sites where the large amount of data gathered during the months and years following the intrusions made it possible to investigate both mechanisms. Unfortunately, in the case of the Manda-Hararo segment, because radar images (SAR) were no longer acquired by

the Envisat satellite beyond 2010, it was no longer possible to track the post-diking deformation over many years as precisely as over the whole active sequence.

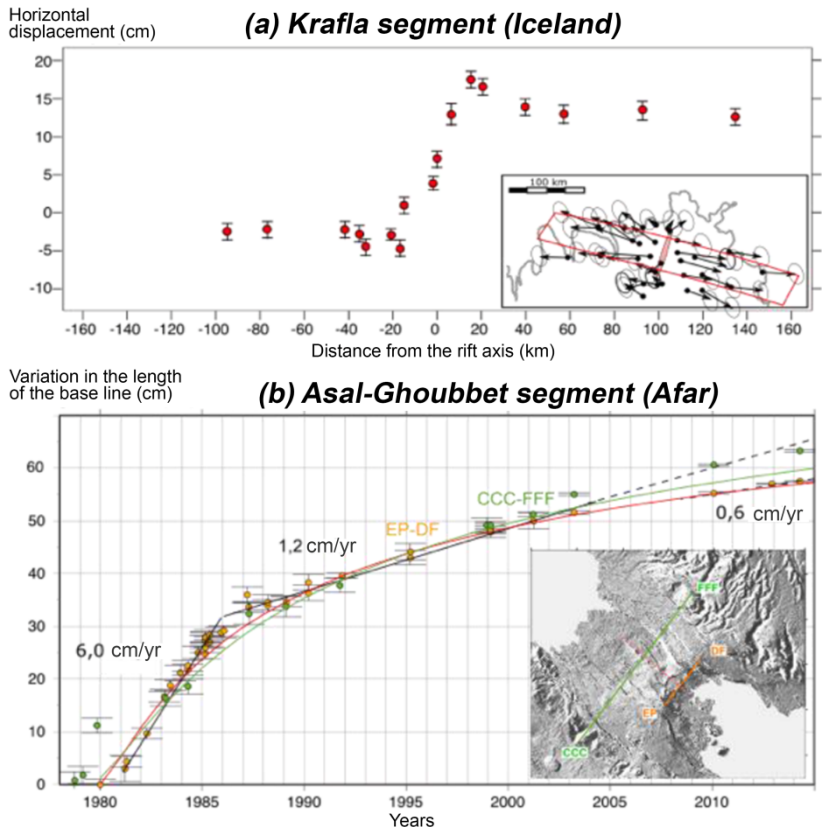

Figure 8.6. *a) GNSS horizontal displacements between 1987 and 1992, projected on a profile perpendicular to the axis of the Krafla segment affected by a diking sequence between 1975 and 1984 [HOF 96]. b) Variations of the length of two baselines across the Asal-Ghoubbet segment since the 1978 diking event (modified from [VIG 07])*

In the case of a post-diking deformation due to the redistribution of stresses in a half-space with viscoelastic rheology below an elastic layer, the different observations are consistent with high viscosity of the order of 10^{18}-10^{19} Pa·s, and an elastic layer thickness of between 10 and 20 km, depending on the case. This is often greater than the crust thickness measured using other geophysical methods (receiver function, MT, seismogenic layer etc.).

However, the two scenarios are not necessarily mutually exclusive, and may take place at the same time. The post-diking viscoelastic relaxation is not necessarily enough to explain the amplitude of the deformation and it may be necessary to bring in the magmatic dilatation (dike opening) to explain the surface deformation data. Several observations support the arguments in favor of an active process, such as the opening of a dike or a sill (horizontal, planar intrusion) at depth, in relation to the activity of the magmatic and hydrothermal crustal reservoir or the deep feeding system. The placement of magma at depth could indeed be favored by the existence of extensional stresses at the base of the dyke established during the sequence, that is, at the base of the brittle layer. In several cases, especially in the Asal-Ghoubbet rift, the amplitude of the spreading velocities, higher than the extension velocities in the far field measured just after the diking episode, fell dramatically in 1985 (Figure 8.6(b); [CAT 05]). This evolution cannot be explained simply by viscoelastic deformation and must involve a rapid evolution of a deep source [SMI 16]. Further, the regions that are most deformed in the post-diking periods are not necessarily those where the strongest deformation was observed in the co-diking period. In several cases, the large deformation observed on the rift axis is also accompanied by movements in the center of the segment at the level of the crustal reservoir. The observed movements show an uplift in the ground, which can be accompanied by radial horizontal displacements, consistent with an inflow of magma into the crustal reservoir and also at a greater depth. Thus, the modeling of displacements, velocities and their temporal variations require the inflow of magma at depth. This inflow can be mainly focused and related to the replenishment of magma in the central reservoir at the crustal level and also the sub-crustal level, or they could affect a larger region in the segment with the emplacement of deep vertical dike(s) or even horizontal dike(s).

8.4.3. *The inter-diking phase*

It is difficult to carry out geodetic and seismological monitoring over the entire inter-diking period. Indeed, with the co-diking openings (between 1 and 8 m) in regions where the expansion rates are low or intermediate (~1 cm/year), the expected recurrence times will be greater than 100 years. Nevertheless, as in the case of the inter-seismic phase (see Introduction and Chapter 5), the surface movements recorded between the major transient events bring in information on the location, the geometry and behavior of the boundary. Long time series of displacement are therefore required to estimate the displacement velocities on either side of the boundary and the deformation at the level of the reservoirs. Only a few of the sites considered as examples, like Iceland and the Asal-Ghoubbet rift, were equipped early enough with instruments by geophysical networks for these

movements to be interpreted. Terrestrial geodetic networks and then the GNSS have been installed on these sites for almost 50 years. These measurements make it possible to describe the deformation occurring transversely with respect to the boundary as well the longitudinal deformation within the length of the segment. In the case of the AG segment and the Krafla segment, the networks were densified after the occurrence of the diking events in the late 1970s. The more recent monitoring of inter-diking deformation was carried out through radar interferometry (InSAR). Although this offers the advantage of quantifying the evolution in the displacement field around a segment, radar interferometry is subject to the same limitations as the inter-seismic phase and requires a particular processing methodology. The expected displacements are small and not always oriented in a direction suitable to being measured in the satellite's line of sight and thus deducing the displacement field for the two divergent plates. Further, over long observation periods, the ground reflectivity properties are prone to change which induces decorrelation in interferograms (snow in Iceland, significant changes to vegetation, water runoff). InSAR is not necessarily best-suited to tracking distributed deformation as in the case of inter-diking periods, when the relative velocities of the plates evolve slowly across the border. Nevertheless, the arrival of a new generation of satellites, like the Sentinel-1, raised fresh hopes. The orbital stability and high repetition of acquisitions of the Sentinel-1 promote both good coherence and an accurate monitoring of the evolution of the displacement field over time. As concerns seismological monitoring, it is not always easy to maintain dense microseismic monitoring networks over many decades, especially in remote regions, such as in Afar or Iceland.

A few studies make it possible to study the deformation over the inter-diking phase, characterized by small movements and low-magnitude earthquakes (generally smaller than 3.0).

Seismological monitoring reveals little activity. This seems irregular, with the occurrence of small swarms associated with small slips over the faults. Activity being concentrated close to, or even above, the magmatic or hydrothermal reservoir may be observed. It is interpreted as transient variations in pressure within the reservoir [DOU 07a]. These variations could be responsible for non-double-couple mechanisms, that is, the seismic rupture includes an opening component [ARN 94]. Tension fractures are probably filled by hydrothermal products or even melts. Slips along caldera faults have also been seen at the level of the reservoir (Figure 8.7(a)). These pressure variations in the reservoir locally disturb the regional stress field. Peaks of activity in the reservoir seem to also influence the activity of normal faults that have already developed or are incipient in the rift zone.

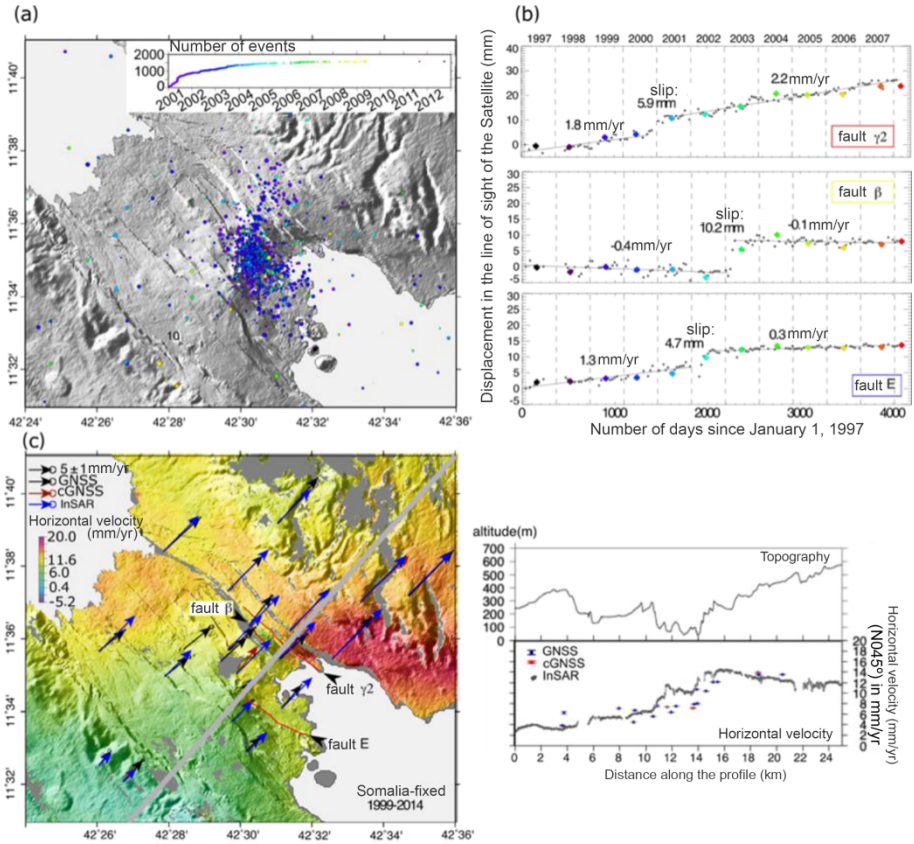

Figure 8.7. *Activity in the Asal-Ghoubbet rift during the inter-diking period. a) Map and temporal evolution of seismicity recorded by the Arta Geophysical Observatory (Djibouti) for the period 2001–2012 (magnitude Ml < 2.0). b) Temporal evolution of the relative displacement (in the satellite's line of sight) of two points located on either side of faults y2, b and E (location at c). These evolutions show the mainly aseismic and continuous slip on the faults and periods of acceleration of the slip that coincide with peaks of seismic activity near the volcanic center. c) Horizontal velocities measured by GNSS (1999–2014) and InSAR (1997–2008). Map and InSAR horizontal velocity profile obtained by assuming that the horizontal movements are only in the direction N045°E, matching the measured GNSS velocities*

Geodetic monitoring confirms there is a homogeneous velocity field across the segments (Figure 8.7(c)) and also confirms the existence of movements close to the reservoirs during the inter-diking period. This would suggest that availability of magma is an essential parameter in the dynamics of these boundaries. Fault slip

monitoring can be carried out either through in situ measurements using extensometers or high repetition of leveling measurements or through InSAR. InSAR monitoring in Afar, especially the high temporal resolution (24 days) Radarsat-1 images for the 1998–2008 period, reveal the slow slip on the faults [DOU 07b]. These faults can, indeed, slip largely aseismically at a rate of several mm/year over several years (Figure 8.7(b)). Periods of slip over locked faults, or periods with slip acceleration over creep faults occur when low-magnitude earthquakes are concentrated close to the main volcanic center (Figure 8.7(a)). There is thus a connection between the reservoir and faults, whose slip may be induced through the circulation of magmatic or hydrothermal fluids at the base of the crust.

The functioning of the boundary during the inter-diking period is explained using an approach similar to that used for inter-seismic deformation. The evolution of plate velocity parallel to the spreading direction is deduced from the repetition of baseline measurements, GPS positioning or InSAR measurements. From about 50-100 km from the rift axis, the velocities correspond to the relative movement of the plates. The evolution of the velocity across the boundary will depend on how this boundary behaves at the crustal level. We arrive again at the sigmoid form (arctan [SAV 73]) for the variation in the spreading velocity between both sides of the boundary (Figure 8.7(c)) (see Introduction). Analogous to other boundaries, the measured velocities can be modeled by (1) a back-slip mechanism, or (2) slips at the base of the elastic brittle crust on either side. The boundary itself corresponds to an opening vertical dislocation from a certain depth onwards, which is superficially locked. Velocity measurements thus make it possible to estimate the rate of opening at depth, as well as the locking depth. A viscoelastic parameter in the upper mantle can also be evaluated. Regardless of the modeling strategy used, different studies agree on a relatively shallow locking depth (4 km in the Asal rift, between 4 and 15 km in Iceland, depending on the segment). In each example, the estimated value of the locking depth corresponds to the depth of the ductile-brittle transition that is derived either from mechanical models, or from the seismogenic depth taken from seismicity catalogs. Nonetheless, it has been seen, notably in Asal, that there is an evolution in spreading velocities over time. Although it is difficult to precisely determine the date of the shift from the post-diking period to the inter-diking period (i.e. the end of the diking episode's influence on the rift deformation), a regular decrease is observed, over time, in the spreading rate, and a spreading out of the variations in velocity. Thus, the evolution of the opening of the segment suggests that depth of the locked layer keeps increasing, which would be consistent with a gradual decrease in magmatic inflow. Recent GNSS measurements confirm the absence of an observed opening at the level of the Manda-Inakir segment, which was nevertheless affected by a magmato-tectonic episode in 1929 [DOU 17]. The

Afar region is complex, not only because the plate boundaries are young (especially the Manda Inakir boundary) and the segments are not fully established, but also because they can overlap and the accommodation of extensional deformation may take place in another segment. Nonetheless, these recent measurements suggest that in the absence of any focused magma inflow in the rift, the inter-plate deformation is no longer located in the segment. Several tectonic extension events, or magmatic dilatation outside the axis, have also been observed far from rift zones.

8.5. Conclusion

Tracking recent deformation along divergent plate boundaries is only possible for submerged regions. Recent studies on several magmato-tectonic segments, whether or not affected or not by diking events in the last decades have shown that the short-term evolution of these boundaries can be considered like those of the other boundaries with which they share similarities and differences. When speaking of the diking cycle, the analogy with the seismic cycle is justified by the distinct presence of three phases in which the deformation is consistent with the accumulation of elastic deformation, which is entirely or partially released at the boundary itself during the transient event of the formation of magmatic intrusions (Figure 8.8).

As with seismic rupture (Chapter 3), the surface movements and seismicity show that the dimension of the magmatic intrusion is spatially limited, that is, laterally in the axis of the segment and also in depth. It affects a part of the segment or the whole segment. Nonetheless, it appears that the boundary cannot be considered as a unique and fixed interface in space and time. The available datasets do not make it possible to show that the spreading zone in the co-diking phase corresponds to the highly coupled zone related to the presence of an asperity as was shown for subduction interfaces. On the contrary, the length of the intrusion seems to depend on the structure of the segment. Thus, in terms of seismic and volcanic hazard, it is essential to know the crustal structure along the segment, the variations in seismogenic depth, and the depth of the ductile-brittle transition and the lithospheric mantle in order to constrain the dimensions of the zone that will potentially be affected by a magmatic intrusion.

Geophysical monitoring of diking events has clearly demonstrated the importance of aseismic deformation. The estimate of the ratios between the seismic energy released during the events and the “geodetic energy” measured on the surface makes it possible to obtain orders of magnitude, which can be applied to events at sea, for which there are no surface deformation measurements. Thus, seismological recordings and the alignment of epicenters provide information on the dimensions of the dike in terms of length and opening amplitude.

There are ongoing debates over the origin of the deformation observed after a diking event. As is often the case with amagmatic boundaries, the datasets remain insufficient to allow us to clearly differentiate between the environment's response and the setting up of a dike, or progressive opening process that evolves over time, involving slow magmatic activity.

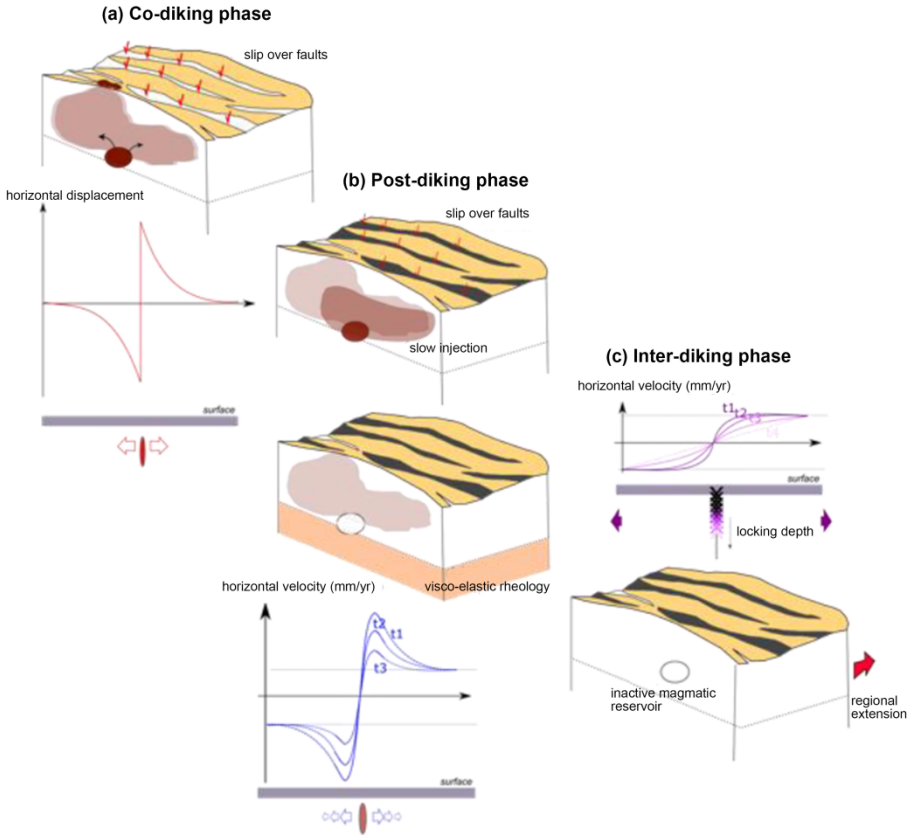

Figure 8.8. *Schematic representation of the evolution of the segment during the diking cycle*

Finally, the inter-diking period is characterized by small deformation on either side of the boundary, that is the rift axis, suggesting the localization and accumulation of elastic deformation. However, in the case of young rifts, as in Afar, in the absence of magmatic inflows, there is a smaller and smaller deformation concentrated in the segment and this is distributed over a wider zone. Off-axis magmatism or normal faulting can take on the role of accommodating extensional

deformation. Thus, the evolution of the plate boundary is strongly dependent on the available magma supply from the mantle, feeding the crustal reservoir(s) from which the intrusions are initiated.

All these studies agree on the fact that we must revise the conventional vision according to which magmatic activity and tectonic activity alternate in the short term in the evolution of boundary. On the scale of the diking cycle (100–200 years), crustal extension through normal faulting seems to have a limited impact on rift development. Magmatism plays the main role, with tectonic activity in the rift zone mainly induced by the emplacement of dikes. Topography reconstructions, making it possible to estimate the long-term deformation, confirm the major role played by the magmatic dilation on the extension. Geophysical measurements must continue in order to better estimate the relative importance of tectonic and magmatic processes in the construction and evolution of rifts over the short and long term.

8.6. References

[ABD 79] ABDALLAH A., COURTILLOT V., KASSER K. et al., "Afar seismicity and volcanism: Relevance to the mechanics of accreting plate boundaries", *Nature*, vol. 282, pp. 17–23, 1979.

[AHM 16] AHMED A., DOUBRE C., LEROY S. et al., "Seafloor spreading event in western Gulf of Aden during the November 2010 – March 2011 period captured by regional seismic networks: Evidence for diking events and interactions with a nascent transform zone", *Geophys. J. Int.*, vol. 205, pp. 1244–1266, 2016.

[ARN 94] ARNOTT S.K., FOULGER G.R. "The Krafla spreading segment, Iceland: 1. Three-dimensional crustal structure and the spatial and temporal distribution of local earthquakes", *J. Geophys. Res.*, vol. 99, pp. 23801–23825, 1994.

[BAR 77] BARBIERI F., VARET J., "Volcanism of Afar: Small-scale plate tectonics implications", *Geol. Soc. Amer. Bull.*, vol. 88, pp. 1251–1266, 1977.

[BJÖ 85] BJÖRNSSON A., "Dynamics of crustal rifting in NE Iceland", *J. Geophys. Res.*, vol. 90, pp. 151–162, 1985.

[BOS 85] BOSWORTH W., "Geometry of propagating continental rifts", *Nature*, vol. 316, pp. 625–627, 1985.

[BOT 85] BOTT M.H.P., "Mechanisms of rifting: Geodynamic modeling of continental rift systems", *Continental Rifts: Evolution, Structure, Tectonics. Developments in Geotectonics*, vol. 25, pp. 27–43, 1985.

[BRU 99] BRUN J.-P., "Narrow rifts versus wide rifts: Inferences for the mechanics of rifting from laboratory experiments", *Philos. Trans. R. Soc. A*, vol. 357, pp. 695–712, 1999.

[BUC 91] BUCK W.R., "Modes of continental lithospheric extension", *J. Geophys. Res.*, vol. 96, pp. 20161–20178, 1991.

[BUC 06] BUCK W.R., EINARSSON P., BRANDSDOTTIR B., "Tectonic stress and magma chamber size as controls on dike propagation: Constraints from the 1975–1984 Krafla rifting episode", *J. Geophys. Res*., vol. 111, issue B12, doi: 10.1029/2005JB003879, 2006.

[CAL 18] CALAIS E., D'OREYE N. et al., "Strain accommodation by slow slip and dyking in a youthful continental rift, East Africa", *Nature*, vol. 456, pp. 783–787, 2018.

[CAT 05] CATTIN R., DOUBRE C., DE CHABALIER J.-B. et al., "Numerical modelling of quaternary deformation and post-rifting displacement in the Asal-Ghoubbet rift (Djibouti, Africa)", *Earth Planet. Sci. Lett.*, doi:10.1016/j.epsl.2005.07.028, 2005.

[COU 99] COURTILLOT V., JAUPART C., MANIGHETTI I. et al., "On causal links between flood basalts and continental breakup", *Earth Planet. Sci. Lett.*, vol. 166, pp. 177–195, 1999.

[DÉP 13] DÉPREZ A., DOUBRE C., MASSON F. et al., "Seismic and aseismic deformation along the East African Rift System from a reanalysis of the GPS velocity field of Africa", *Geophys. J. Int.*, doi:10.1093/gli/ggt085, 2013.

[DOU 07a] DOUBRE, C., MANIGHETTI I., DORBATH C. et al., "Crustal structure and magmato-tectonic processes in an active rift (Asal-Ghoubbet, Afar, East-Africa). Part 1: Insights from a five-month seismological experiment", *J. Geophys. Res*, 112, doi:10.1029/2005JB003940, 2007.

[DOU 07b] DOUBRE C., PELTZER G., "Fluid-controlled faulting process in the Asal Rift, Djibouti, from 8 yr of radar interferometry observations", *Geology*, vol. 35, pp. 69–72, 2007.

[DOU 17] DOUBRE C., DÉPREZ, A., MASSON, F. et al., "Current deformation in Central Afar and triple junction kinematics deduced from GPS and InSAR measurements", *Geophys. J. Int.*, vol. 208, pp. 936–953, 2017.

[EBI 10] EBINGER C., BELASHEW M., "Active passive margins", *Nat. Geosc.*, vol. 3, pp. 670–671, 2010.

[GEO 05] GEOFFROY L., "Volcanic passive margins", *C.R. Geoscience*, vol. 337, pp. 1395–1408, 2005.

[GIU 18] GIUSTI M., PERROT J., DZIAK R. et al., "The August 2010 earthquake swarm at North FAMOUS–FAMOUS segments, Mid-Atlantic Ridge: Geophysical evidence of dike intrusion", *Geophys. J. Int.*, vol. 215, pp. 181–195, 2018.

[GRA 09] GRANDIN R., SOCQUET A., BINET R. et al., "September 2005 Manda Hararo–Dabbahu rifting event, Afar (Ethiopia): Constraints provided by geodetic data", *J. Geophys. Res.*, vol. 114, pp. B08404, 2009.

[GRA 12] GRANDIN R., SOCQUET A., DOUBRE C. et al., "Elastic thickness control of lateral dyke intrusion at mid-ocean ridges", *Earth Plant. Sci. Let.*, vol. 319–320, pp. 83–95, 2012.

[HAY 96] HAYWARD N.J., EBINGER C.J., "Variations in the along-axis segmentation of the Afar Rift system", *Tectonics*, vol. 15, pp. 244–257, 1996.

[HOF 96] HOFTON M.A., FOULGUER G.R., "Postrifting anelastic deformation around the spreading plate boundary, North Iceland 1: Modeling of the 1987–1992 deformation field using a viscoelastic Earth structure", *J. Geophys. Res*., vol. 101, pp. 25403–25421, 1996.

[LER 12] LEROY S., RAZIN P., AUTIN J. et al., "From rifting to oceanic spreading in the Gulf of Aden: A synthesis", *Arab J. Geosci.*, vol. 5, pp. 859–901, 2012.

[MED 16] MEDYNSKI S., PIK R., BURNARD P. et al., "Magmatic cycles pace tectonic and morphological expression of rifting (Afar depression, Ethiopia)", *Earth Planet. Sci. Lett.*, vol. 446, pp. 77–88, 2016.

[MOG 58] MOGI K., "Relations between the eruptions of various volcanoes and the deformation of ground surface around them", *Bull. Earthquake Res. Inst.*, vol. 36, pp. 99–135, 1958.

[OKA 85] OKADA Y., "Surface deformation due to shear and tensile faults in a half-space", *Bull. Seismo. Soc. Amer.*, vol. 75, pp. 1135–1154, 1985.

[PAL 10] PALLISTER J., MCCAUSLAND W., JONSSON S. et al., "Broad accommodation of rift related extension recorder by dyke intrusion in Saudi Arabia", *Nature Geosci*., vol. 3, pp. 705–712, 2010.

[POL 83] POLLARD D., DELANEY P., DUFFIELD W. et al., "Surface deformation in volcanic rift zones", *Tectonophysics*, vol. 94, pp. 541–584, 1983.

[RIV 08] RIVALTA E., SEGALL P., "Magma compressibility and the missing source for some dike intrusions", *Geophys. Res. Lett.*, vol. 35, pp. L04306, doi:10.1029/2007GL032521, 2008.

[RUB 98] RUBIN A., POLLARD D.D., "Dike-induced faulting on rift zones of Iceland and Afar", *Geology*, vol. 16, pp. 413–417, 1998.

[RUE 79] RUEGG J.-C., LÉPINE J.-C., TARANTOLA A., "Geodetic measurements of rifting associated with a seismo-volcanic crisis in Afar", *Geophys. Res. Lett.*, vol. 6, pp. 817–820, 1979.

[SAV 73] SAVAGE J.C., BURFORD R.O., "Geodetic determination of relative plate motion in central California", *J. Geophys. Res.*, vol. 78, pp. 832–845, 1973.

[SCH 17] SCHMID, F., SCHLINDWEIN V., KOULAKOV I. et al., "Magma plumbing system and seismicity of an active mid-ocean ridge volcano", *Sci Rep.*, vol. 7, pp. 42949, 2017.

[SEN 78] SENGOR A., BURKE K., "Relative timing of rifting and volcanism on Earth and its tectonic implications", *Geophys. Res. Lett*., vol. 6, pp. 419–421, 1978.

[SIG 06] SIGMUNDSSON F., *Iceland Geodynamics: Crustal Deformation and Divergent Plate Tectonics*, Springer, Berlin, Heidelberg, available at: https://doi.org/10.1007/3-540-37666-6_6, 2006.

[SMI 16] SMITTARELLO D., GRANDIN R., DE CHABALIER J.-B. et al. "Transient deformation in the Asal-Ghoubbet Rift (Djibouti) since the 1978 diking event: Is deformation controlled by magma supply rates?", *J. Geophys. Res.*, vol. 121, doi: 10.1002/2016JB013069, 2016.

[SMI 19] SMITTARELLO D., CAYOL V., PINEL V. et al., "Magma propagation at Piton de la Fournaise from joint inversion of InSAR and GNSS", *J. Geophys. Res.*, vol. 124, pp. 1361–1387, 2019.

[TAR 79a] TARANTOLA A., RUEGG J.-C., LÉPINE J.-C., "Geodetic evidence for rifting in Afar: A brittle-elastic model of the behaviour of the lithosphere", *Earth Planet. Sci. Lett.*, vol. 45, pp. 435–444, 1979.

[TAR 79b] TARANTOLA A., RUEGG J.-C., LÉPINE J.-C., "Geodetic evidence for rifting in Afar 2: Vertical displacements", *Earth Planet. Sci. Lett.*, vol. 48, pp. 363–370, 1979.

[TOD 02] TODA S., STEIN R., SAGIYA T., "Evidence from the AD 2000 Izu islands earthquake swarm that stressing rate governs seismicity", *Nature*, vol. 419, pp. 58–61, 2002.

[TOL 01] TOLSTOY M., BOHNENSTIEHL D., EDWARDS M. et al., "Seismic character of volcanic activity at the ultraslow-spreading Gakkel Ridge", *Geology*, vol. 29, pp. 1139–1142, 2001.

[TOL 06] TOLSTOY M., COWENE, J.P., BAKER, T. et al., "A sea-floor spreading event captured by seismometers", *Science*, vol. 314, pp. 1920–1922, 2006.

[VIG 07] VIGNY C., DECHABALIER J.B., RUEGG J.C. et al., "25 years of geodetic measurements along the Tadjoura-Asal rift system, Djibouti, East Africa", *J. Geophys. Res.*, vol. 112, doi:10.1029/2004JB003230, 2007.

[WRI 06] WRIGHT T.J., EBINGER C., BIGGS J. et al., "Magma maintained rift segmentation at continental rupture in the 2005 Afar dyking episode", *Nature*, vol. 442, pp. 291–294, 2006.

[WHI 89] WHITE R., MCKENZIE D., "Magmatism at rift zones: The generation of volcanic continental margins and flood basalts", *J. Geophys. Res*., vol. 94, pp. 7685–7729, 1989.

9

Interactions Between Tectonic Deformation and Erosion During the Seismic Cycle in Mountain Ranges

Philippe STEER
CNRS, Géosciences Rennes, University of Rennes, France

9.1. Introduction

The topography of mountain ranges is the result of a competition, integrated over time, between tectonic uplift and erosion processes. For example, a topography under construction will have uplift rates greater than rates of erosion, while a declining topography will have erosion greater than uplift rates. However, uplift rates and erosion rates do not evolve strictly independently. On geologic time scales (>100 kyr), uplift allows for an increase in topography relief and slopes, which in turn increases erosion rates. This reflects the "action" of tectonics on erosion and is explained in particular by the fact that river erosion (e.g. incision) and hillslope erosion (e.g. landslides) are highly sensitive to gravity and, therefore, to the slope (e.g. [AHN 70, BON 03]). In addition, many studies suggest a "feedback" effect of erosion on tectonics, notably through isostasy and through the modification of the stress tensor resulting from erosion-induced topographic unloading (e.g. [WIL 99, VER 13, THI 14]). These principles of action and feedback, between tectonic and

For a color version of all of the figures in this chapter, see www.iste.co.uk/rolandone/seismic.zip.

The Seismic Cycle,
coordinated by Frédérique ROLANDONE.

The Seismic Cycle: From Observation to Modeling,
First Edition. Frédérique Rolandone.

erosion processes, favor the development of a dynamic balance between uplift and erosion rates [GIL 77, WHI 09]. A corollary feature of this dynamic equilibrium is a state characterized by a constant mean-elevation topography that can be sustained on geological time scales. The foundations of modern quantitative geomorphology have thus been built around this paradigm of steady-state landscapes responding to progressive changes in climatic or tectonic conditions (e.g. [WHI 99, 02]). In recent decades, numerous studies have used this idea to explore the long-term signature of climate and tectonics on the landscapes (e.g. [KIR 12, WIL 14]).

However, this view is challenged by the observation of landscape dynamics on the scale of the seismic cycle (<1 kyr). While mountain landscapes are the result of a long geological history, their dynamics are marked by a series of discrete and potentially extreme disturbances during earthquakes or storms [DAD 03, LAG 05, PAR 11, HOV 11]. During these events, elementary geomorphic processes become active and are catalyzed by the disturbances. For example, in August 2009, Typhoon Morakot generated up to 3 m of rain in Taiwan in 3 days, triggered more than 10,000 landslides [LIN 11, MAR 18] and led to a large increase in sedimentary flows [HUA 13]. This discrete erosion event could correspond to 10 to 100 years of erosion at the 10-year average rate [DAD 03]. Large magnitude earthquakes represent the second type of landscape disturbance, as evidenced by the ~200,000 landslides potentially induced by the 2008 Wenchuan (China) earthquake of magnitude Mw 7.9 [PAR 11, LI 14, FAN 18]. It is even suggested that the total volume of landslides produced during such an earthquake could equal or even exceed the volume of uplifted rock resulting from co-seismic displacement [PAR 11, MAR 16a, MAR 16b, LI 19].

In addition, these elementary processes occur in chains or cascades of events, resulting in major changes in the mechanical properties of hillslopes, the rate of landslides [KEE 84, MAL 04, MAR 15], the rate of rock alteration [EMB 16], inorganic sediment fluxes [HOV 11, CRO 17a] and organic sediment fluxes [HIL 08, FRI 18], river morphology [YAN 10, CRO 17b] and hydrological and hydrogeological flows [MON 03, MOH 17]. These rapid erosion events, in turn, induce potential feedback with tectonic and even seismic activity [CAL 10, STE 14, STE 20]. Such elementary processes and chains of events, on a short time scale, are currently not taken into account by numerical models studying the evolution of mountain landscapes (e.g. [TUC 01, CRA 01, BRA 13, CAM 17]). As a result, we do not know what the impact of these extreme events is on landscape form and dynamics, whether a steady-state can be maintained following these disturbances [PEI 01, FIN 14], or how to interpret landscape form in terms of the frequency and magnitude of these disturbances, which are the cause of major natural disasters.

In this section, we will first present a current synthetic view of landscape dynamics based on the paradigm of landscapes reaching a state of dynamic

equilibrium. We will then summarize the results and evidence from field observations, satellite and geophysical imagery, and numerical simulations challenging this paradigm and supporting the idea of landscapes constantly disturbed by extreme events, especially during the seismic cycle. We will focus on the impact earthquakes have on landscapes through the triggering of numerous landslides during the co-seismic phase. Since these landslides are the starting point of many secondary geomorphological processes, we will try to understand the link between the number or volume of these landslides and the characteristics of the earthquake and the impacted topography. We will then describe the evolution of these landslides and disturbed landscapes during the post-seismic relaxation phase of the topography. This will allow us to quantify the topographic balance of the seismic cycle. This article is mainly a non-exhaustive synthesis of the existing literature on the subject and the choice of works and interpretations may sometimes be personal or subjective.

9.2. The paradigm of steady-state landscapes

In ice-free landscapes, the evolution of continental landforms over large time scales (> 10 kyr) is generally described by a competition between tectonic uplift and erosion of rivers and hillslopes. In the absence of sedimentation, the evolution of topographic height h is thus controlled by the imbalance between the topographic uplift rate U and the erosion rate E:

$$\frac{\partial h}{\partial t} = U - E \qquad [9.1]$$

In its simplest formulation, it is proposed that the rate of river erosion E is a function of the local slope S and the specific river discharge Q_w, and thus of the precipitation P:

$$E = K {Q_w}^m S^n, \qquad [9.2]$$

where K is a coefficient of erosion efficiency, which depends on riverbed lithology and sediment discharge, among other factors, and m and n are positive exponents [HOW 83, HOW 94, WHI 99, LAG 14]. The m/n ratio, called the concavity index, should be close to 0.5 based on river profile geometry, and the pair $m = 0.5$ and $n = 1$ is often chosen for non-alluvial rivers. In the simple modeling approach that we develop here, hydrological flows at the surface of the topography, resulting from precipitation P, are routed gradually in the direction of the steepest slope until they reach an outlet. Slope dynamics are generally modeled either by a diffusion law or by a maximum threshold on the local slope corresponding to the resting slope beyond which gravitational movements are activated. In the following, we will consider the latter approach by setting the maximum slope at 30°. Numerically,

equation [9.2] is solved by an implicit scheme with the finite difference method [BRA 13].

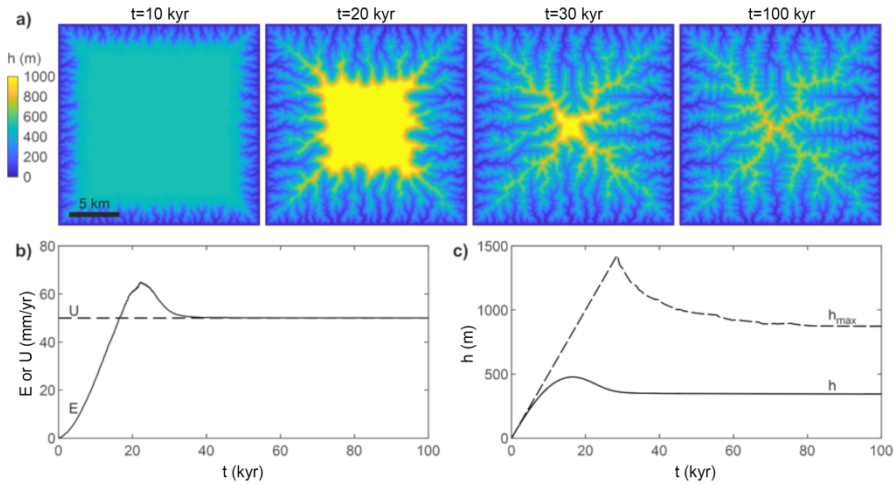

Figure 9.1. *a) Maps of the temporal evolution of the topography, h, of a relief subject to tectonic uplift and erosion by rivers and slopes. b) Temporal evolution of the rates of uplift, U, and erosion, E, averaged over the whole model. c) Temporal evolution of the mean elevation, h, and maximum elevation, h_{max}, of the topography. Erosion rates higher than the uplift rate are obtained around 20 kyr and are explained in particular by a transient imbalance of the planar hydrological flow network during the incision of the plateau (e.g. [CAR 09])*

In the presence of a uniform uplift rate combined with a constant base level, such a system of equations results in the progressive building of relief (see Figure 9.1). The initial plateau is first incised at its edges, following the initiation of uplift (see Figure 9.1(a)). Rivers associated with preferential flows quickly emerge and favor the propagation of the regressive erosion wave from downstream to upstream. Following the dissection of these valleys, the hillslopes gradually increase their slopes until they reach the angle of repose. The increase in the slopes of the hillslopes and rivers leads to an erosion rate increase, which is then balanced with the uplift rate (see Figure 9.1(b)). The resulting relief and topography reach a dynamic steady-state (see Figure 9.1(c)). This dynamic steady-state can be maintained as long as the boundary conditions of the model, including its base level, uplift rates and precipitation rates, remain unchanged.

Any disturbance of these boundary conditions leads to a transient phase of rebalancing of the relief with the new boundary conditions. The duration of this transient phase:

$$\tau = \beta U^{\frac{1}{n}-1} P^{-\frac{m}{n}} \qquad [9.3]$$

is a function of the precipitation rate P and the uplift rate U, with a proportionality constant β, which depends, among other things, on the characteristic size of the catchment areas and K [WHI 99]. In the example model, the duration of this transitional phase is several tens of thousands of years (see Figures 9.1(b) and (c)). In active orogens such as Taiwan, the duration of this transient phase is probably of the order of one million years [WHI 01]. This transient phase is therefore much longer than the classical duration of a seismic cycle, about 50–1000 years, and even longer than the periodicity of some climatic cycles, such as those referred to as Milanković periodicities.

9.3. Earthquakes and co-seismic landslides

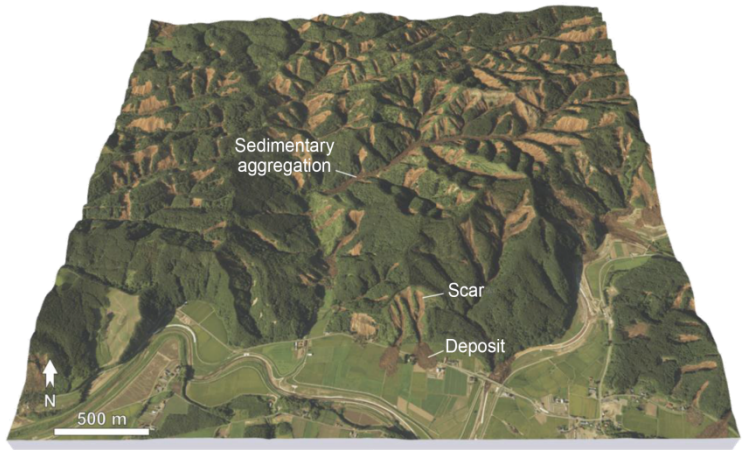

Figure 9.2. *3D block representing the epicentral zone of the Hokkaido (Japan) earthquake of magnitude 6.6, which took place on September 6, 2018, where numerous co-seismic landslides were observed. Landslide scars, depositional zones and sedimentary aggregation in the valleys are visible in this figure. A satellite image is draped over the topography. Source: https://maps.gsi.go.jp/#16/42.766793/141.962703/&base=std&ls=std%7C20180906hokkaido_atsuma_0906do&blend=0&disp=11&lcd=20180906hokkaido_atsumachiku_0906suichoku&vs=c0j0h0k0l0u0t0z0r0s1m0f0&vs2=f0&sync=1&base2=ort&ls2=ort%7Cexperimental_anno&disp2=11&reliefdata=0G000000*

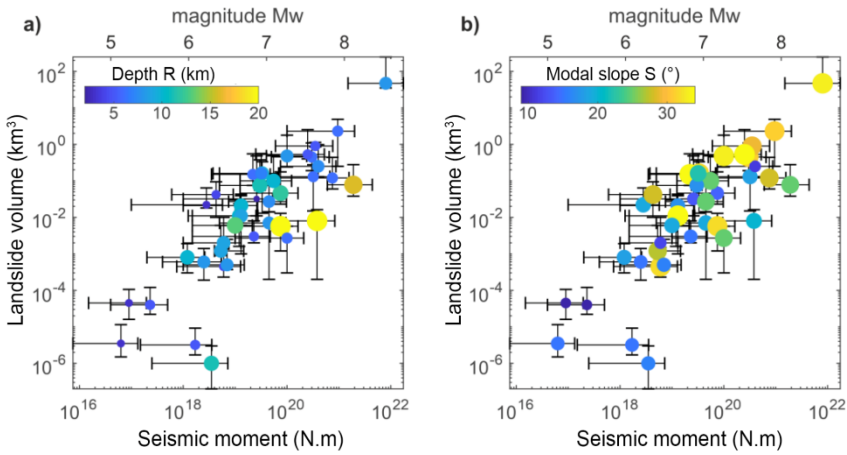

Figure 9.3. *a) Influence of the magnitude MW, the seismic moment M0 and the depth of an earthquake R on volume V of co-seismic landslides. b) Influence of the modal slope S of the topography of the epicentral zone on volume V of co-seismic landslides. Modified from [MAR 16a]*

However, this simplistic view of the long-term dynamics (>10 kyr) of continental landscapes fails to take into account many processes and forcings that generate perturbations on shorter time scales [DAD 04]. For example, numerous studies have demonstrated the significant role of earthquakes in landscape dynamics [KEE 84, HOV 11, PAR 11, LI 14, MAR 16a,b]. Large magnitude earthquakes (see Figure 9.2), such as the 7.9 magnitude Wenchuan earthquake in 2008, are capable of potentially triggering up to several hundred thousand landslides in the vicinity of the fault that ruptured during the earthquake [LI 14, FAN 18]. In terms of order of magnitude, the mass of sediment produced by landslides during the Wenchuan earthquake, ~7.4 Gt [ZHA 19], represents ~40% of the annual global sediment flow from the continents to the ocean, or 19 Gt [MIL 13]. In addition to this earthquake, two other events mentioned by Hovius et al. [HOV 11] provide insight into the erosive potential of earthquakes: (1) the Assam 8.6 magnitude earthquake in 1950 possibly triggered a total landslide volume close to 47 km^3, with a total mass close to ~120 Gt [MAT 53] and, (2) the 7.9 magnitude earthquake in Papua New Guinea in 1937 potentially caused between 74 and 400 mm of erosion [SIM 67]. These co-seismic landslides include both shallow landslides, deep-seated landslides, rockfalls and avalanches. The initiation of co-seismic landslides is generally attributed to the passage of seismic waves, and in particular to the peak ground

acceleration (PGA) associated with volume waves. In addition to physical predictions (e.g. [NEW 65]), this inference is consistent with the observation of a spatial correlation between PGA and landslide spatial density [MEU 07]. However, the triggering mechanism is subject to debate, and some authors observe an influence of the distance to the fault [MAS 18] or the maximum speed of displacements induced by the passage of seismic waves.

The development of satellite imagery, especially at high resolution (~1 m), has led to numerous inventories of landslides triggered by earthquakes [TAN 17] or intense rainfall events [MAR 18]. These inventories provide a better understanding of the characteristics of earthquakes that trigger numerous landslides [MAR 16a,b]. First, the seismic moment M_0 or the magnitude of the earthquakes:

$$M_W = \frac{2}{3}\log_{10}(M_0) - 6.07 \qquad [9.4]$$

emerges empirically as the predominant factor controlling the total volume V of co-seismic landslides [KEE 84, 99, MAR 16a,b]. Below a threshold magnitude close to 5, earthquakes are no longer able to generate a sufficiently large PGA, greater than ~0.2 g, to trigger a significant number of landslides. Above a magnitude of ~5, it is empirically observed that PGA increases exponentially with the seismic moment until it saturates beyond a magnitude of ~7 [BOO 08]. Combined with the increase in fault rupture length with seismic moment [LEO 10] and therefore of the surface area of the landscape subjected to high PGA, it is observed that V increases more than linearly with M_0 (see Figure 9.2) [MAR 16a]. For magnitudes greater than ~7, the increase in V with M_0 is only allowed to exist due to the increase in the length of the fault rupture with M_0. Second, the depth, R, of the earthquakes also has a fundamental impact on the number of co-seismic landslides and on V. Indeed, the deeper the seismic rupture, the lower the acceleration induced by the surface seismic waves will be. This is a direct result of the attenuation of the seismic waves during their geometric propagation and of possible inelastic or dispersion effects. Third, the presence of slopes close to mechanical instability in the epicentral zone favors the number of landslides.

However, this empirical view of the role of the magnitude and depth of the earthquake and the slope of the reliefs on the triggering of landslides should be confronted with physical modeling of these processes. Indeed, the propensity of a slope to generate a landslide is governed, among other things, by the mechanical state of the rocks that form the slope, inherited from the geological nature of the rocks; the deformations and fatigue processes expressed over geological time, by the

shape of the slope, inherited from a morphological history over several thousand years; and from a hydrogeological state, developed over the previous months and years. For example, the Hokkaido (Japan) earthquake of magnitude 6.6, which occurred on September 6, 2018, triggered about 6000 landslides (see Figure 9.2), while the earthquake nucleated at a depth of 37 km [YAM 18, ZHA 19]. Such a depth is empirically considered to be unsuitable for the initiation of so many landslides. This being said, (1) the volcanic nature of the rocks with the presence of pumice stones at the base of the landslide surfaces, having a low threshold of resistance to mechanical shear and liquefaction [LI 20], (2) the possible saturation of the soils induced by the accumulation of 200–300 mm of precipitation during the previous month [ZHA 19] and (3) the occurrence of the Jebi supertyphoon, 1 day before the earthquake, associated with significant atmospheric depression and less than 20 mm of precipitation, are all elements that placed the slopes of the epicentral zone close to a critical mechanical state, even before the earthquake occurred.

9.4. Landslide size distributions

Earthquakes trigger landslides, with the number and total volume of these varying greatly from one event to another. However, it is noteworthy that all of these landslides follow a common distribution law of landslide size (see Figure 9.4). This distribution is characterized by a negative power distribution for landslides of intermediate to large size, and an exponential rollover for smaller landslides [STA 01, GUZ 02]. This type of distribution can be approximated by an inverse-gamma [MAL 04] or double-Pareto distribution. The size of landslides is currently characterized by the planar surface of the landslide, which can be systematically measured, thanks notably to the contribution of high-resolution satellite images (e.g. [MAR 15a, MAS 18]). The volume of landslides is then generally obtained using empirical scaling laws with their area [LAR 10]. More recent work (e.g. [BER 20]) extends this approach to the volume of landslides through a pre- and post-earthquake comparison of high-resolution topographic data (e.g. Lidar). In all cases, a power law emerges from the surface or volume-based distributions of landslides [BER 20]. This raises the question of the mechanical and topographic properties of the slopes, allowing the universal emergence of this power law. This is all the more motivated (1) by the consequences of such a distribution on the topographic impact of earthquakes [PAR 11, MAR 16b], (2) by the changes in hazard and risk brought in by deviation from this law and (3) by the observation that other physical processes and mechanical instabilities, such as earthquakes, respond to distribution laws of similar size or magnitude.

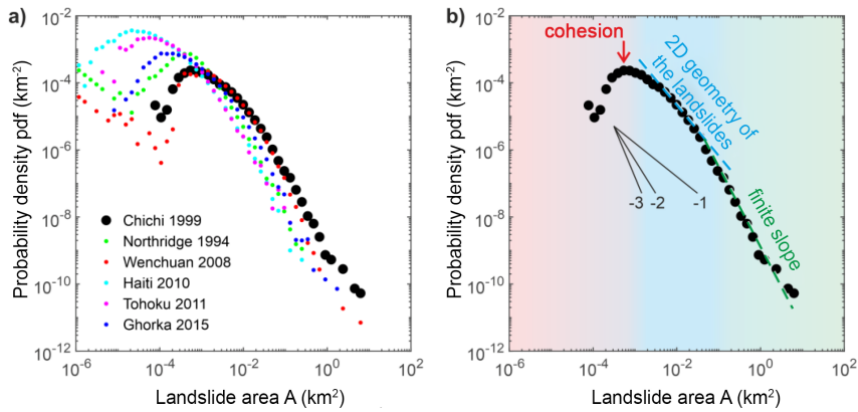

Figure 9.4. *Landslide size distribution. a) Probability densities of landslide areas from several co-seismic landslide inventories [TAN 17]. b) According to [JEA 19], the rollover of the distribution (small sizes) is associated with the role of cohesion, the power law behavior (intermediate sizes) is related to the presence of a scaling law between landslide depth and area, and the deviation of the power law (large sizes) can be explained by a finite slope size effect*

While the size distribution law of landslides is considered a universal property of landscapes [MAL 04], the origin of the power law behavior and its variability, with an exponent between -1.42 and -3.36 [VAN 07], remain open questions (see Figure 9.4(a)). Similarly, the conditions allowing the existence of a rollover and the variability of its position, between ~10 and ~1000 m^2, are debated [TEB 20]. Reasons given for the under-representation of small landslides include (1) detectability due to the resolution of satellite images [STA 01], (2) amalgamation of small landslides [TAN 19] or even (3) satellite coverage too widely spaced in time [BAR 12, WIL 18].

To explain the shape of landslide size distribution, [JEA 19] proposes a novel probabilistic model, integrating a criterion of the mechanical strength of slopes and a topographic criterion, which we summarize here (see Figure 9.4(b)). In this model, the mechanical resistance of hillslopes is inferred from a Mohr-Coulomb criterion, integrating a slope cohesion C and a friction coefficient μ, applied to a potential rupture plane. The safety factor:

$$F = \frac{C+\mu\sigma_n}{\tau} \qquad [9.5]$$

of such a plane is the ratio between the mechanical resistance, with σ_n being the normal stress, and the driving stress, here the tangential stress τ induced by the

potential landslide weight force. A point of the topography is considered unstable if it is associated with at least one potential failure plane (1) that intersects downstream the surface of the hillslope upstream of the river and (2) whose safety factor is unstable $F < 1$. In addition to the above parameters, the depth of the plane and its dip appear to be two essential factors that favor gravitational instability.

This model naturally predicts the occurrence of a rollover for small landslide sizes, due to the dominant role of cohesion relative to friction for shallow depths. Beyond a certain depth, cohesion becomes negligible and the safety factor can be approximated by $\mu\sigma_n/\tau$, which becomes relatively invariant with depth as τ and σ_n are proportional. Thus, landslides of intermediate size have the same probability of failing. By considering a sampling without replacement (i.e. a large landslide prevents the occurrence of several smaller landslides), the probabilistic model naturally leads to a power law behavior for the landslide size distribution. This is referred to as self-similar statistical behavior. The exponent of the power law is directly related to the scaling law between the depth and area of landslides. For large landslides, i.e. those close to the size of the hillslope considered, the probability of failure is limited by the topographic criterion. This criterion is unfavorable for large landslides associated with failure planes that are too deep or too steep, with little chance of intersecting the hillslope upstream of the river. For natural landscapes, this finite-size effect is, of course, subject to great variability due to the variability of hillslope lengths and heights. It promotes a deviation in power law behavior for large landslides and imposes a maximum potential landslide size for a given landscape.

Thus, [JEA 19] offers a single, relatively simple, and mechanical-based model to explain the whole spectrum of landslide size distribution. As the total volume of triggered landslides is highly dependent on the volume of the largest landslides, this model highlights the predominant role of hillslope size in the topographic impact of large magnitude earthquakes. Moreover, apart from the role of cohesion, this model presents a certain similarity with the probabilistic models explaining the magnitude distribution of earthquakes [JEA 18]. Indeed, it is generally proposed that the exponent (b-value) of Gutenberg-Richter's law emerges from the scaling law relating the seismic moment of earthquakes to the area and displacement of earthquake ruptures. Moreover, finite-size effects, controlled here by the depth of the seismogenic zone or by the size distribution of faults in a medium, could lead to a deviation of the distribution and limit the maximum magnitude allowed on a fault [SCH 97].

9.5. Post-seismic relaxation of landscapes

Co-seismic landslides have a geomorphological impact that goes beyond the co-seismic phase. Indeed, sediments mobilized by landslides, which reach rivers or are redeposited on hillslopes can generate sedimentary disturbances over the entire watershed draining the epicentral zone. This disturbance is characterized in particular by an increase in sediment discharge downstream of the landslides and by a phase of sediment aggregation in the valleys. The Chi-Chi earthquake of M_w 7.6 in Taiwan in 1999, which triggered more than 20,000 landslides in the epicentral zone, provided a well-documented case study thanks to a dense network of hydrological and sediment gauging stations [DAD 03, DAD 04]. Following the Chi-Chi earthquake, concentrations of suspended sediments measured in rivers downstream of the epicentral zone increased by up to a factor of ~5 in the Choshui River watershed [HOV 11]. This positive anomaly of suspended sediment discharge fades over a period of about 6 years until it reaches the pre-Chi-Chi "background" sediment discharge. This 6-year period constrains a phase of post-seismic geomorphological relaxation of the landscapes, analogous to the post-seismic geodynamic phase of the seismic cycle. This post-seismic phase does not allow the evacuation of all the sediments resulting from co-seismic landslides, but it does allow a return to a form of equilibrium in terms of sediment transport.

The duration of this post-seismic relaxation phase of the landscapes seems to present a certain variability. A duration of close to 6 years is also deduced from measurements of suspended sediment concentration (less than 0.25 mm in diameter) after the Wenchuan earthquake [WAN 15]. Similar values are obtained using a post-seismic dilution of the detrital cosmogenic signal for larger sediments between 0.25 and 1 mm in size [WES 14, WAN 17]. The distal sedimentary deposits of the Zingpu Reservoir, downstream of the epicentral zone of the Wenchuan earthquake, recorded an increase in median particle size from 8 to 12–24 μm for ~6 years, starting 2 years after the earthquake [ZHA 19]. However, [HOW 12, 14] suggests a relaxation time of around 50 years from measurements of sediment cores obtained from two lakes near the Alpine Fault in New Zealand. It is also important to note that the post-seismic sediment fluxes associated with coarser grain sizes and transport modes are currently poorly known. However, this particle size represents a non-negligible part, possibly 10 to 90% by mass (e.g. [DAD 03]; Fei, personal communication), of the sediments mobilized following an earthquake. Furthermore, while sediment discharge offers the advantage of providing a quantitative and integrative measure, it does not make it possible to discriminate between the processes at work during the post-earthquake phase.

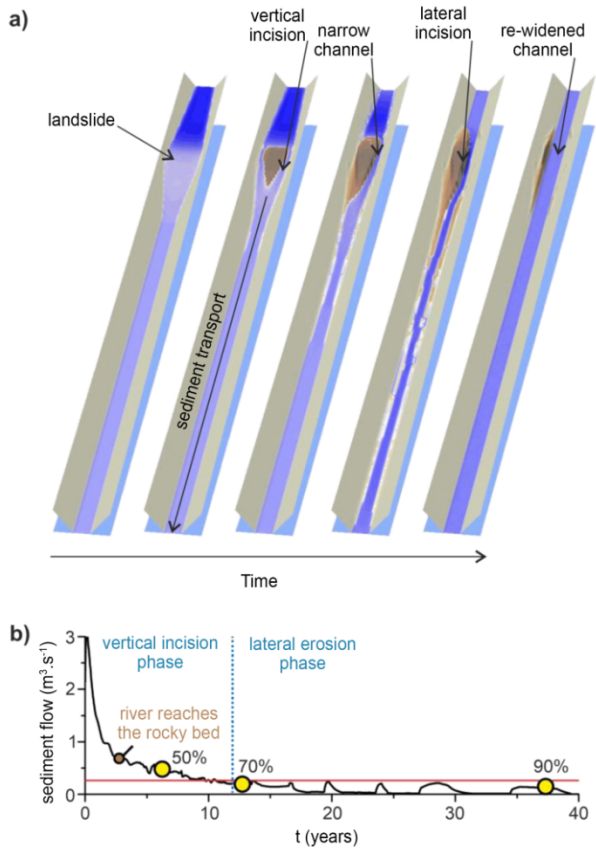

Figure 9.5. *Numerical modeling of the temporal evolution of a bedrock river located in a confined gorge following the deposition of a landslide, modified from [CRO 17a]. The numerical model used, Eros, includes the 2D resolution of hydraulic flows, vertical and lateral erosion, and sediment transport [DAV 17]. a) The scenario considered is that of a large volume landslide depositing in a river with a low sediment transport capacity. The river (in blue) first forms a dam lake upstream of the landslide and then vertically re-incises the sediments (in brown) from the landslide. This rapid incision phase is associated with a very efficient sediment transport due to the reduction of the active channel width and the increase in the transport capacity of the river. This is followed by a slower phase of lateral erosion, leading to a progressive re-widening of the active channel and a less intense sediment transport, until the channel regains its initial geometry. b) Temporal evolution of the sediment discharge resulting from the landslide and measured downstream of the landslide in the river. The yellow dots indicate the percentage of the initial mass of the landslide that has been evacuated. The red line indicates the initial transport capacity of the river*

Conceptual, experimental, and numerical models thus offer a relevant tool to better understand the dynamics of the post-seismic geomorphological phase. [YAN 10] develop a conceptual model to constrain the transport of the mass M of the sediment pulse delivered by co-seismic landslides. In this approach, the river, which is assumed to maintain its sediment transport capacity Q_T, exports away from the sediment pulse in a time:

$$t = M/Q_T \qquad [9.6]$$

For the Peikang River in Taiwan, which drains the epicentral zone of the Chi-Chi earthquake, the evacuation time is several decades to several centuries and thus potentially greater than or equal to the duration of the seismic cycle. This value is highly dependent on the frequency of large flow events allowing efficient transport of sedimentary grain size and increases with the median grain size. [CRO 17a] takes advantage of the conceptual framework of [YAN 10], but develops a numerical model taking into account the 2D resolution of hydraulic discharges, vertical and lateral erosion, and sediment transport to study the duration of sediment export from a landslide (see Figure 9.5). Above all, the sediment transport capacity, Q_T, of the river is free to adjust to the geometry of the river, itself modified by erosion and sedimentation processes. This addition is particularly important, as [CRO 17a] demonstrates that rivers incise landslide deposits by forming a relatively narrow alluvial channel that concentrates the flow, greatly increasing the river's transport capacity and thus reducing sediment removal time to a few years or decades. This effect is even more marked when the volume of the landslide is large or when the initial transport capacity (i.e. before the landslide) of the river is low. It is also important to note that the models of [CRO 17a] predict a rapid evacuation of sediments, while the landslide represents a morphological disturbance for the river. However, given that the sediment transport capacity of the river decreases during the evacuation of sediments and the re-widening of its channel, the evacuation of the remaining sediments falls back on export dynamics close to that predicted by [YAN 10] with a duration of around a few decades to a few centuries.

An export time, for most sediments, of a few decades instead of a few hundred years, has strong implications for post-seismic geomorphological dynamics. Indeed, a duration of a few centuries implies that river activity during the seismic cycle is mainly limited to evacuating the sediment and eroding its alluvial cover, without allowing a phase of erosion of the rocky bottom. A duration of a few decades, less than or equal to the duration of the seismic cycle, suggests the possibility of a phase

of re-incision of the valleys, allowing the hillslopes, in turn, to redevelop a significant proportion of unstable slopes, before the next major earthquake occurs. This difference in duration also leads to (1) a difference in interpretation between the formation of geomorphological markers, particularly rocky (i.e. strath) or alluvial terraces, and the seismic cycle [YAN 10], and (2) a difference in temporality for hazards and hydro-sedimentary risks induced by the sedimentary pulse, which can lead to lateral mobility, avulsion of river channels and flooding [CRO 2017b]. In addition, it is important to note that a major uncertainty remains about the initial state of connectivity of landslide-generated sediments to the river system. Several studies suggest that this initial state of connectivity of the sediments to the river ranges from 8%, with most of the sediments deposited on the hillslopes, to almost 100% [DAD 04, LI 16, WES 11]. Moreover, landslide sediments deposited on hillslopes can be remobilized by surface flow during future landslides, debris avalanches, and other gravity processes [ZHA 19, FAN 18]. These processes control the effectiveness of sediment dynamic connectivity to the river network. The post-seismic sediment export time is therefore the sum of the duration of the dynamic connectivity phase along the hillslopes and the sediment transport phase by river transport (see Figure 9.6). [CRO 19] thus shows that, following a scenario for the expected future high magnitude earthquake on the Alpine Fault, the sediment transport dynamics for the New Zealand Alps would be limited by the time of connection of landslide sediments to rivers and not by river transport (see Figure 9.6).

However, the induced post-seismic geomorphological disturbance is not limited to increased sedimentary fluxes. It is observed that debris flows are more likely to be triggered (i.e. for a lower daily precipitation threshold) in the years following a major earthquake [LIN 04, ZHA 17, FAN 19], possibly due to the presence of easily mobilized sediments along the hillslopes. In addition, the number of landslides triggered after a major earthquake is also abnormally high [MAR 15, FAN 19]. This anomaly is certainly partially amplified by the occurrence of intense rainfall events, but seems to diminish over a period of 1–4 years after the earthquake. In addition to the possible impact of rainfall or aftershocks, post-seismic mechanical weakening of the hillslopes, particularly through damage and fracturing triggered during the earthquake, seems to be the main mechanism involved [MAR 15]. This state of transient mechanical weakness is consistent with the observation of subsurface attenuation of seismic wave propagation velocity following a high magnitude earthquake [BRE 08], although the depths considered differ.

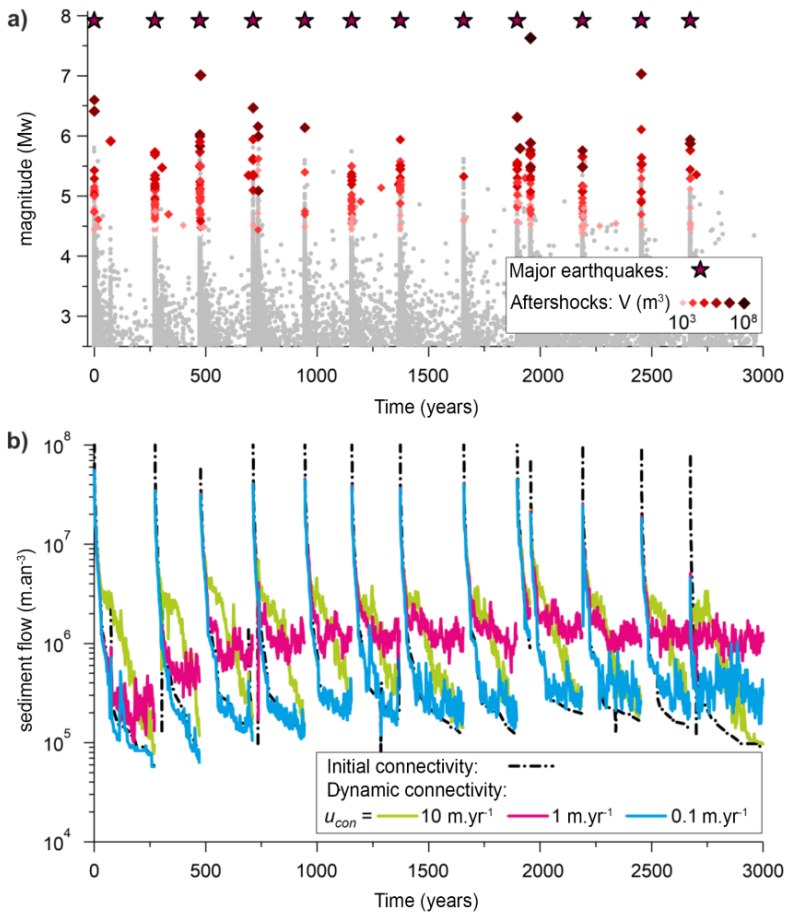

Figure 9.6. *Evolution of sediment flux from co-seismic landslides over several seismic cycles, modified from [CRO 19]. a) Time series of major earthquakes (red stars) and their aftershocks (grey dots), possibly generating a total volume of landslides indicated by color-coding (diamonds), stochastically modeled by [CRO 19]. The scenario is based on the seismogenic dynamics of the Alpine Fault in New Zealand. b) Temporal evolution of sediment fluxes according to four scenarios of landslide connectivity to rivers: no dynamic connectivity (black dashed line), dynamic connectivity of 10 (green line), 1 (purple line) and 0.1 m/yr (blue line)*

Last, the post-seismic geomorphological phase is also characterized by the dynamics of the retreat of knickpoints, formed co-seismically along the trace of the ruptured fault. These co-seismic knickpoints can reach a height of several meters

(e.g. [YAN 10]) and their retreat rate, averaged over several thousand years, is observed to range between about 1 mm/yr and 1 m/yr (e.g. [VAN 01]). Co-seismic knickpoints are thus generally considered as geomorphological objects relevant to landscape dynamics on large time scales beyond the duration of a seismic cycle. However, more recent results document retreat rates potentially reaching ~100 $m.yr^{-1}$ over a few years [YAN 10, COO 13], favored in particular by the frequency of high water flow events and the presence of bedload sediments [COO 13]. Such velocities qualify co-seismic knickpoints as fundamental geomorphological objects for understanding landscape dynamics at the scale of a seismic cycle, particularly upstream of faults [YAN 10]. However, the propagation during the seismic cycle of co-seismic knickpoints and their interaction with the alluvial cover remain poorly understood, despite recent works [CAR 05, FIN 13, SCH 17, MAL 18, STE 19].

9.6. Discussions: topographic budget of earthquakes and the seismic cycle

It is now well established, thanks to field observations and semi-empirical models, that the total volume of co-seismic landslides in an active mountain range increases non-linearly with the seismic moment M_0 [KEE 84, MAR 16a, CRO 19]. This result should be related to the quasi-linear increase in the volume of rocks uplifted by co-seismic displacement [OKA 85, MAR 16b, CRO 19]. A comparison between the volume of co-seismically uplifted rocks and the total volume of co-seismic landslides makes it possible to infer the topographic budget of an earthquake. For example, the 2008 Wenchuan (China) earthquake of magnitude 7.9 triggered ~2.8 km^3 of landslides for ~2.6 km^3 of uplifted rock volume [LI 14]. Assuming that landslide-driven sediments are evacuated over a duration shorter than the seismic cycle, the topographic budget of the Wenchuan earthquake could be considered almost neutral. A systematic comparison between the volume of landslides and the volume of uplifted rock suggests that earthquakes of magnitude between 6 and 7.3 can potentially be topographically destructive, or have a neutral budget [MAR 16b]. In other words, these earthquakes of intermediate magnitude do not contribute to the relief building of mountain ranges. Such behavior is theoretically only possible for relief with relatively steep modal slopes (>30°) and/or a shallow depth of earthquake nucleation (< 10 km). Earthquakes of magnitude less than ~6 induce PGAs that are too weak to generate a high spatial density of landslides. Earthquakes of magnitude greater than 7 have PGAs that saturate, and the total landslide volume increases less than linearly with M_0, and thus increases less rapidly with M_0 than the volume of uplifted rock. We invite the reader to refer to [MAR 16a] and [LI 19] for more details on the topographic budget of earthquakes.

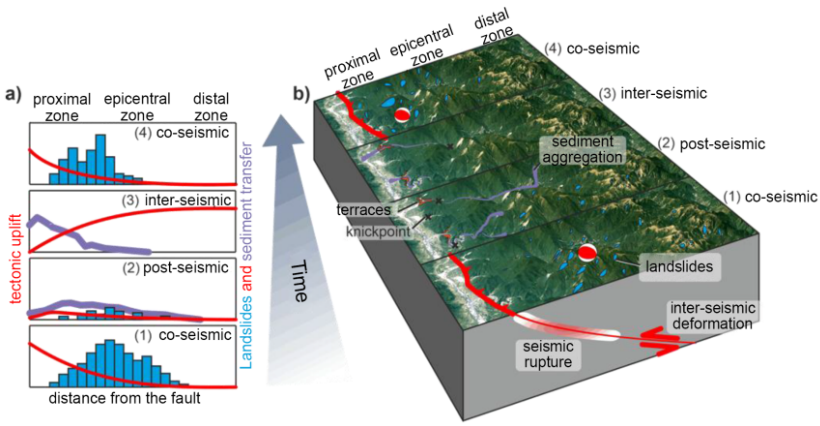

Figure 9.7. *Schematic scheme describing the spatial-temporal evolution of landscapes during the seismic cycle. a) Evolution in the profile of tectonic uplift (red), the number of landslides (histogram in blue) and the induced sedimentary pulse during the co-, post- and inter-seismic phases (from bottom to top). b) Evolution in the map of landscape dynamics and of the tectonic and geomorphological processes related to panel (a) during the seismic cycle*

While the impact of earthquakes on the evolution of landscapes during the co- and post-seismic phases has been well studied, particularly following the Chi-Chi and Wenchuan earthquakes, the geomorphological impact of earthquakes on the whole seismic cycle remains relatively poorly known. Although data are lacking, conceptual and numerical models suggest that the geomorphological perturbations induced directly (e.g. landslides, knickpoints) and indirectly (e.g. sedimentary aggradation, high sediment fluxes) by large magnitude earthquakes can control all or part of the landscape dynamics on the scale of the seismic cycle [YAN 10, CRO 19]. However, the frequency of high magnitude earthquakes, the inter-seismic distribution of tectonic displacements, climatic conditions, variability of hydrological discharges, lithology, drainage density, and the state of equilibrium of the landscape are all probably first order-factors whose role remains largely unexplored. The principle of a landscape at a steady state, with a balance between the rates of erosion and uplift, needs to be reconsidered due to the amplitude and variability of tectonic and geomorphological processes during the seismic cycle. However, it is possible that the landscape may develop a morphological state that allows it (i) to produce an average rate of erosion that is spatially balanced over the long term (t >> seismic cycle) with the uplift rate, and (ii) to digest the

geomorphological disturbances induced by large earthquakes in a duration of less than one seismic cycle. A necessary condition for the achievement of this last point (ii) is (1) the evacuation of a significant part of the sediments mobilized by the co-seismic landslides during a seismic cycle allowing (2) rivers to incise their bedrock, (3) to redevelop the slope and height of surrounding hillslopes, destabilized during the previous earthquake and (4) to recover the potential for triggering new landslides during the next major earthquake, at the beginning of the future seismic cycle (see Figure 9.7). To maintain a long-term steady-state and condition (i), the spatial distributions of co-, post- and inter-seismic uplift must be compensated by equivalent erosion of rivers and hillslopes. We have not mentioned the role of horizontal tectonic displacement, which is largely ignored in the literature despite probably having a first-order influence on landscape dynamics.

Despite the variability of natural systems and the large uncertainties concerning the dynamics of landscapes during the seismic cycle, we depict here a quantitative and qualitative view of the topographic budget of earthquakes and the seismic cycle (see Figure 9.7). On the hanging wall of the thrust fault, co-seismic uplift generally increases with proximity to the trace of the fault (proximal zone), whereas inter-seismic uplift increases with distance to the fault (distal zone) (e.g. [CAT 00]). Moreover, the spatial density of co-seismic landslides is generally highest at the epicenter [MEU 07], in a transition zone (epicentral zone) between the proximal and distal zones. The re-incision of rivers in the proximal zone is probably favored by the presence of co-seismic knickpoints, which can rapidly migrate upstream (e.g. [YAN 10]), notably favored by the increase in post-seismic sedimentary discharge [COO 13]. This suggests a re-incision of rivers in the proximal part of the river on a scale of a few decades after the earthquake [YAN 10]. In the distal and epicentral zones, the incision can only start again after the evacuation of the sedimentary input from the co-seismic landslides. The time scales involved are probably a few decades to a few centuries after the earthquake [YAN 10, CRO 17] and, thus, correspond well to the inter-seismic phase. However, in order to maintain such a condition, rivers in the epicentral zone must have a higher sediment transport capacity than in the distal zone, as they are subject to a higher spatial density of landslides and additionally receive the products of sediment transport from the distal zone. This increase in transport capacity can occur either (1) permanently, due to the geometric properties of the riverbed, as suggested for example, for the Peikang River in the epicentral zone of the Chi-Chi earthquake [YAN 10] or (2) dynamically, by morphodynamic feedback in response to the abrupt sediment input following the earthquake [CRO 17]. Thus maintaining a river incision rate balanced with the uplift rate over the entire catchment area is possibly achieved by two quite distinct mechanisms: on the one hand the upstream migration of the co-seismic knickpoints

and subsequent incision waves in the zone proximal to the fault, and on the other hand the downstream evacuation of sediments from the landslides in the epicentral and distal zones, allowing a gradual return to detachment-limited conditions [YAN 10]. For hillslopes, the high density of landslides in the epicentral zone contrasts with the low density generally observed in the distal and proximal zones [MEU 07]. The paradigm of topography in a state of dynamic equilibrium thus implies that major earthquakes are not necessarily the trigger for landslides and hillslope erosion in the distal and proximal zones. In the proximal zone, landslides triggered by frequent shallow earthquakes of moderate magnitude could partially compensate for this erosion deficit. Whereas in the distal zone, landslides not triggered by earthquakes or triggered by heavy rainfall events and other erosion processes (e.g. soil creeping) could dominate hillslope dynamics. But such hypothetical scenarios imply close relationships, still poorly understood, between (1) the organization of landscapes, built on geological time scales (10 Kyr-10 Myr, and (2) the capacity of these landforms to respond to disturbances on a time scale of a few decades or centuries, shorter than the return time of these disturbances. Numerical modeling of geomorphological and tectonic processes during the seismic cycle thus offers a unique approach to understanding how landscapes behave on these different time scales.

9.7. Prospects: impact of erosion on fault and earthquake dynamics

Acknowledging the role of extreme events and the high variability of short-scale erosion rates on landscape dynamics has implications that go beyond purely geomorphological considerations. Indeed, numerical models, coupling tectonic deformation and erosion processes on geological time scales (1–10 Myr), suggest that the spatial distribution of erosion significantly impacts the distribution and intensity of tectonic deformation in mountain ranges (e.g. [WIL 99, THI 14]). On intermediate time scales (10 kyr–1 Myr), erosion and induced isostatic rebound can promote sliding along certain faults [CAL 10, VER 13]. At the scale of the seismic cycle (<1000 yr), erosion and induced mass unloading at the surface may contribute to elastically loading stresses on underlying thrust faults (see Figure 9.8; [STE 14]). This effect is all the more marked at shallow depths (<5 km), since the static Coulomb stress ΔCFF induced by surface erosion, evaluated at depth z, has an amplitude that decreases in z^{-2}. Moreover, for a point unload F, the change in ΔCFF is directly proportional to the value of F and thus increases linearly with the amount of erosion. It is also important to point out that erosion, unlike other external forcings with a certain periodicity (i.e. hydrological load or tidal effect), generates a temporal accumulation of stresses on a fault plane in an elastic environment on the scale of the seismic cycle.

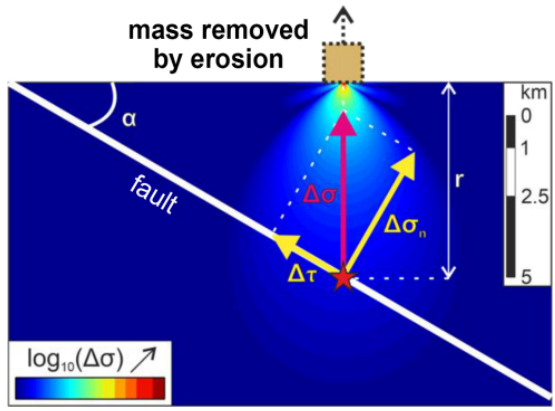

Figure 9.8. *Schematic scheme illustrating the spatial distribution of the stress increment Δσ (here purely illustrative) induced by surface point erosion, increasing both the tangential stress Δτ and the normal stress Δσn. Modified from [STE 14]*

[STE 14] suggests that such dependence of the stress state of the faults on the spatial and temporal distribution of surface erosion is conducive to the occurrence of shallow earthquakes triggered by erosion. [STE 14] proposes two particularly favorable cases: (1) extreme events, such as large magnitude earthquakes and intense rainfall events, triggering a large volume of landslides and rapid export of sediments and (2) the extraction of large volumes of rock from quarries. For example, the magnitude 5 Le Teil earthquake (southern France) of November 11, 2019, with a ruptured fault plane located between the surface and about 1.5 km of depth, could have been triggered by the extraction of rock from a quarry located just above the rupturing fault. In this particular case, the ~0.03 km^3 of rock extracted from the quarry between 1946 and 2019 could have induced a ΔCFF of around 1.5–2 bar, compared with the stress drop induced by the earthquake, possibly around 10 bar. Moreover, quasi-dynamic numerical models of the seismic cycle, considering frictional faults following a rate-and-state law, suggest that variations in normal stresses induced by surface erosion can affect seismicity [JEA 20]. More specifically, a rapid variation, i.e. shorter than the duration of the seismic cycle, of the normal stress can lead to more frequent earthquakes associated with lower magnitudes (i.e. a higher *b*-value for the Gutenberg-Richter law). Taking advantage of theoretical frameworks, [STE 20] demonstrates that the frequency of shallow earthquakes in Taiwan increased for 2.5 years following Typhoon Morakot in 2009, which triggered a large number of landslides, corresponding to a volume of 1.2 km^3, and relatively rapid and intense erosion of the landscape. Such results illustrate once

again the need to better constrain sedimentary evacuation after a geomorphological disturbance triggered by a major earthquake or intense rainfall event.

9.8. References

[AHN 70] AHNERT F., "Functional relationships between denudation, relief, and uplift in large, mid-latitude drainage basins", *American Journal of Science*, vol. 268, no. 3, pp. 243–263, 1970.

[BAR 12] BARLOW J., LIM M., ROSSER N. et al., "Modeling cliff erosion using negative power law scaling of rockfalls", *Geomorphology*, vol. 139, pp. 416–424, 2012.

[BER 20] BERNARD T., LAGUE D., STEER P., "3D point cloud LiDAR differencing method apply to region scale landslide detection and volume estimation: Application to the Kaikoura region, New Zealand", *Earth Surface Dynamics*, submitted, 2020.

[BON 03] BONNET S., CRAVE A., "Landscape response to climate change: Insights from experimental modeling and implications for tectonic versus climatic uplift of topography", *Geology*, vol. 31, no. 2, pp. 123–126, 2003.

[BOO 08] BOORE D.M., ATKINSON G.M., "Ground-motion prediction equations for the average horizontal component of PGA, PGV, and 5%-damped PSA at spectral periods between 0.01 s and 10.0 s", *Earthquake Spectra*, vol. 24, no. 1, pp. 99–138, 2008.

[BRA 13] BRAUN J., WILLETT S.D., "A very efficient O (n), implicit and parallel method to solve the stream power equation governing fluvial incision and landscape evolution", *Geomorphology*, vol. 180, pp. 170–179, 2013.

[BRE 08] BRENGUIER F., CAMPILLO M., HADZIIOANNOU C. et al., "Postseismic relaxation along the San Andreas fault at Parkfield from continuous seismological observations", *Science*, vol. 321, no. 5895, pp. 1478–1481, 2008.

[CAL 10] CALAIS E., FREED A.M., VAN ARSDALE R. et al., "Triggering of New Madrid seismicity by late-Pleistocene erosion", *Nature*, vol. 466, no. 7306, pp. 608–611, 2010.

[CAM 17] CAMPFORTS B., SCHWANGHART W., GOVERS G., "Accurate simulation of transient landscape evolution by eliminating numerical diffusion: The TTLEM 1.0 model", *Earth Surface Dynamics*, vol. 5, no. 1, pp. 47–66, 2017.

[CAR 05] CARRETIER S., LUCAZEAU F., "How does alluvial sedimentation at range fronts modify the erosional dynamics of mountain catchments?", *Basin Research*, vol. 17, no. 3, pp. 361–381, 2005.

[CAR 09] CARRETIER S., POISSON B., VASSALLO R. et al., "Tectonic interpretation of transient stage erosion rates at different spatial scales in an uplifting block", *Journal of Geophysical Research: Earth Surface*, vol. 114, no. F2, 2009.

[CAT 00] CATTIN R., AVOUAC J.P., "Modeling mountain building and the seismic cycle in the Himalaya of Nepal", *Journal of Geophysical Research: Solid Earth*, vol. 105, no. B6, pp. 13389–13407, 2000.

[COO 13] COOK K.L., TUROWSKI J.M., HOVIUS N., "A demonstration of the importance of bedload transport for fluvial bedrock erosion and knickpoint propagation", *Earth Surface Processes and Landforms*, vol. 38, no. 7, pp. 683–695, 2013.

[CRA 01] CRAVE A., DAVY P., "A stochastic 'precipiton' model for simulating erosion/sedimentation dynamics", *Computers and Geosciences*, vol. 27, no. 7, pp. 815–827, 2001.

[CRO 17a] CROISSANT T., LAGUE D., STEER P. et al., "Rapid post-seismic landslide evacuation boosted by dynamic river width", *Nature Geoscience*, vol. 10, no. 9, pp. 680–684, 2017.

[CRO 17b] CROISSANT T., LAGUE D., DAVY P. et al., "A precipiton-based approach to model hydro-sedimentary hazards induced by large sediment supplies in alluvial fans", *Earth Surface Processes and Landforms*, vol. 42, no. 13, pp. 2054–2067, 2017.

[CRO 19] CROISSANT T., STEER P., LAGUE D. et al., "Seismic cycles, earthquakes, landslides and sediment fluxes: Linking tectonics to surface processes using a reduced-complexity model", *Geomorphology*, vol. 339, pp. 87–103, 2019.

[DAD 03] DADSON S.J., HOVIUS N., CHEN H. et al., "Links between erosion, runoff variability and seismicity in the Taiwan orogeny", *Nature*, vol. 426, no. 6967, pp. 648–651, 2003.

[DAD 04] DADSON S.J., HOVIUS N., CHEN H. et al., "Earthquake-triggered increase in sediment delivery from an active mountain belt", *Geology*, vol. 32, no. 8, pp. 733–736, 2004.

[DAV 17] DAVY P., CROISSANT T., LAGUE D., "A precipiton method to calculate river hydrodynamics, with applications to flood prediction, landscape evolution models, and braiding instabilities", *Journal of Geophysical Research: Earth Surface*, vol. 122, no. 8, pp. 1491–1512, 2017.

[EMB 16] EMBERSON R., HOVIUS N., GALY A. et al., "Chemical weathering in active mountain belts controlled by stochastic bedrock landsliding", *Nature Geoscience*, vol. 9, no. 1, pp. 42–45, 2016.

[FAN 18] FAN X., JUANG C.H., WASOWSKI J. et al., "What we have learned from the 2008 Wenchuan Earthquake and its aftermath: A decade of research and challenges", *Engineering Geology*, vol. 241, pp. 25–32, 2018.

[FAN 19] FAN X., SCARINGI G., KORUP O. et al., "Earthquake-induced chains of geologic hazards: Patterns, mechanisms, and impacts", *Reviews of Geophysics*, vol. 57, no. 2, pp. 421–503, 2019.

[FIN 13] FINNEGAN N.J., BALCO G., "Sediment supply, base level, braiding, and bedrock river terrace formation: Arroyo Seco, California, USA", *Bulletin*, vol. 125, nos 7–8, pp. 1114–1124, 2013.

[FIN 14] FINNEGAN N.J., SCHUMER R., FINNEGAN S., "A signature of transience in bedrock river incision rates over timescales of 10(4)–10(7) years", *Nature*, vol. 505, no. 7483, pp. 391–394, 2014.

[FRI 18] FRITH N.V., HILTON R.G., HOWARTH J.D. et al., "Carbon export from mountain forests enhanced by earthquake-triggered landslides over millennia", *Nature Geoscience*, vol. 11, no. 10, pp. 772–776, 2018.

[GIL 77] GILBERT G.K., Report on the geology of the Henry Mountains, Dept. of the Interior, US Geographical and Geological Survey of the Rocky Mountain Region, Washington, D.C., 1877.

[GUZ 02] GUZZETTI F., MALAMUD B.D., TURCOTTE D.L. et al., "Power-law correlations of landslide areas in central Italy", *Earth and Planetary Science Letters*, vol. 195, nos 3–4, pp. 169–183, 2002.

[HIL 08] HILTON R.G., GALY A., HOVIUS N. et al., "Tropical-cyclone-driven erosion of the terrestrial biosphere from mountains", *Nature Geoscience*, vol. 1, no. 11, pp. 759–762, 2008.

[HOV 11] HOVIUS N., MEUNIER P., LIN C.W. et al., "Prolonged seismically induced erosion and the mass balance of a large earthquake", *Earth and Planetary Science Letters*, vol. 304, nos 3–4, pp. 347–355, 2011.

[HOW 83] HOWARD A.D., KERBY G., "Channel changes in badlands", *Geological Society of America Bulletin*, vol. 94, no. 6, pp. 739–752, 1983.

[HOW 94] HOWARD A.D., DIETRICH W.E., SEIDL M.A., "Modeling fluvial erosion on regional to continental scales", *Journal of Geophysical Research: Solid Earth*, vol. 99, no. B7, pp. 13971–13986, 1994.

[HOW 12] HOWARTH J.D., FITZSIMONS S.J., NORRIS R.J. et al., "Lake sediments record cycles of sediment flux driven by large earthquakes on the Alpine fault, New Zealand", *Geology*, vol. 40, no. 12, pp. 1091–1094, 2012.

[HOW 14] HOWARTH J.D., FITZSIMONS S.J., NORRIS R.J. et al., "Lake sediments record high intensity shaking that provides insight into the location and rupture length of large earthquakes on the Alpine Fault, New Zealand", *Earth and Planetary Science Letters*, vol. 403, pp. 340–351, 2014.

[HUA 13] HUANG M.Y.F., MONTGOMERY D.R., "Altered regional sediment transport regime after a large typhoon, southern Taiwan", *Geology*, vol. 41, no. 12, pp. 1223–1226, 2013.

[JEA 18] JEANDET L., Modélisation numérique des liens entre séismes et glissements de terrain au cours du cycle sismique : processus déclencheurs, distributions de tailles et implications géologiques, Doctoral dissertation, Université Rennes 1, 2018.

[JEA 19] JEANDET L., STEER P., LAGUE D. et al., "Coulomb mechanics and relief constraints explain landslide size distribution", *Geophysical Research Letters*, vol. 46, no. 8, pp. 4258–4266, 2019.

[JEA 20] JEANDET RIBES L., CUBAS N., BHAT H. et al., "The impact of large erosional events and transient normal stress changes on the seismicity of faults", *Geophysical Research Letters*, submitted, 2020.

[KEE 84] KEEFER D.K., "Landslides caused by earthquakes", *Geological Society of America Bulletin*, vol. 95, no. 4, pp. 406–421, 1984.

[KEE 99] KEEFER D.K., "Earthquake-induced landslides and their effects on alluvial fans", *Journal of Sedimentary Research*, vol. 69, no. 1, pp. 84–104, 1999.

[KIR 12] KIRBY E., WHIPPLE K.X., "Expression of active tectonics in erosional landscapes", *Journal of Structural Geology*, vol. 44, pp. 54–75, 2012.

[LAG 05] LAGUE D., HOVIUS N., DAVY P., "Discharge, discharge variability, and the bedrock channel profile", *Journal of Geophysical Research: Earth Surface*, vol. 110, no. F4, pp. 1–17, 2005.

[LAG 14] LAGUE D., "The stream power river incision model: Evidence, theory and beyond", *Earth Surface Processes and Landforms*, vol. 39, no. 1, pp. 38–61, 2014.

[LAR 10] LARSEN I.J., MONTGOMERY D.R., KORUP O., "Landslide erosion controlled by hillslope material", *Nature Geoscience*, vol. 3, no. 4, pp. 247–251, 2010.

[LEO 10] LEONARD M., "Earthquake fault scaling: Self-consistent relating of rupture length, width, average displacement, and moment release", *Bulletin of the Seismological Society of America*, vol. 100, no. 5A, pp. 1971–1988, 2010.

[LI 14] LI G., WEST A.J., DENSMORE A.L. et al., "Seismic mountain building: landslides associated with the 2008 Wenchuan earthquake in the context of a generalized model for earthquake volume balance", *Geochemistry Geophysics Geosystems*, vol. 15, no. 4, pp. 833–844, 2014.

[LI 16] LI G., WEST A.J., DENSMORE A.L. et al., "Connectivity of earthquake-triggered landslides with the fluvial network: Implications for landslide sediment transport after the 2008 Wenchuan earthquake", *Journal of Geophysical Research: Earth Surface*, vol. 121, no. 4, pp. 703–724, 2016.

[LI 19] LI G., WEST A.J., QIU H., "Competing effects of mountain uplift and landslide erosion over earthquake cycles", *Journal of Geophysical Research: Solid Earth*, vol. 124, no. 5, pp. 5101–5133, 2019.

[LI 20] LI R., WANG F., ZHANG S., "Controlling role of Ta-d pumice on the coseismic landslides triggered by 2018 Hokkaido Eastern Iburi Earthquake", *Landslides*, vol. 17, no. 5, pp. 1233–1250, 2020.

[LIN 04] LIN C.W., SHIEH C.L., YUAN B.D. et al., "Impact of Chi-Chi earthquake on the occurrence of landslides and debris flows: Example from the Chenyulan River watershed, Nantou, Taiwan", *Engineering Geology*, vol. 71, nos 1–2, pp. 49–61, 2004.

[LIN 11] LIN C.W., CHANG W.S., LIU S.H. et al., "Landslides triggered by the 7 August 2009 Typhoon Morakot in southern Taiwan", *Engineering Geology*, vol. 123, nos 1–2, pp. 3–12, 2011.

[MAL 04] MALAMUD B.D., TURCOTTE D.L., GUZZETTI F. et al., "Landslide inventories and their statistical properties", *Earth Surface Processes and Landforms*, vol. 29, no. 6, pp. 687–711, 2004.

[MAL 18] MALATESTA, L.C., LAMB, M.P., "Formation of waterfalls by intermittent burial of active faults", *GSA Bulletin*, vol. 130, nos 3–4, pp. 522–536, 2018.

[MAR 15a] MARC O., HOVIUS N., "Amalgamation in landslide maps: Effects and automatic detection", *Natural Hazards and Earth System Sciences*, vol. 15, no. 4, pp. 723–733, 2015.

[MAR 15b] MARC O., HOVIUS N., MEUNIER P. et al., "Transient changes of landslide rates after earthquakes", *Geology*, vol. 43, no. 10, pp. 883–886, 2015.

[MAR 16a] MARC O., HOVIUS N., MEUNIER P., "The mass balance of earthquakes and earthquake sequences", *Geophysical Research Letters*, vol. 43, no. 8, pp. 3708–3716, 2016a.

[MAR 16b] MARC O., HOVIUS N., MEUNIER P. et al., "A seismologically consistent expression for the total area and volume of earthquake-triggered landsliding", *Journal of Geophysical Research: Earth Surface*, vol. 121, no. 4, pp. 640–663, 2016b.

[MAR 18] MARC O., STUMPF A., MALET J.P. et al., "Initial insights from a global database of rainfall-induced landslide inventories: The weak influence of slope and strong influence of total storm rainfall", *Earth Surface Dynamics*, vol. 6, no. 4, pp. 903–922, 2018.

[MAS 18] MASSEY C., TOWNSEND D., RATHJE E. et al., "Landslides triggered by the 14 November 2016 Mw 7.8 Kaikōura Earthquake, New Zealand", *Bulletin of the Seismological Society of America*, vol. 108, no. 3B, pp. 1630–1648, 2018.

[MAT 53] MATHUR L.P., "Assam earthquake of 15th August 1950 – A short note on factual observations", in RAO M.B.R. (ed.), *A Compilation of Papers on the Assam Earthquake of August 15, 1950*, National Geophysical Research Institute, Hyderabad, 1953.

[MEU 07] MEUNIER P., HOVIUS N., HAINES, A.J., "Regional patterns of earthquake-triggered landslides and their relation to ground motion", *Geophysical Research Letters*, vol. 34, no. 20, p. L20408, 2007.

[MIL 13] MILLIMAN J.D., FARNSWORTH K.L., *River Discharge to the Coastal Ocean: A Global Synthesis*. Cambridge University Press, Cambridge, 2013.

[MOH 17] MOHR C.H., MANGA M., WANG C.Y. et al., "Regional changes in streamflow after a megathrust earthquake", *Earth and Planetary Science Letters*, vol. 458, pp. 418–428, 2017.

[MON 03] MONTGOMERY D.R., MANGA M., "Streamflow and water well responses to earthquakes", *Science*, vol. 300, no. 5628, pp. 2047–2049, 2003.

[NEW 65] NEWMARK N.M., "Effects of earthquakes on dams and embankments", *Geotechnique*, vol. 15, no. 2, pp. 139–160, 1965.

[OKA 85] OKADA Y., "Surface deformation due to shear and tensile faults in a half-space", *Bulletin of the Seismological Society of America*, vol. 75, no. 4, pp. 1135–1154, 1985.

[PAR 11] PARKER R.N., DENSMORE A.L., ROSSER N.J. et al., "Mass wasting triggered by the 2008 Wenchuan earthquake is greater than orogenic growth", *Nature Geoscience*, vol. 4, no. 7, pp. 449–452, 2011.

[PEI 01] PEIZHEN Z., MOLNAR P., DOWNS W.R., "Increased sedimentation rates and grain sizes 2–4 Myr ago due to the influence of climate change on erosion rates", *Nature*, vol. 410, no. 6831, pp. 891–897, 2001.

[SCH 97] SCHOLZ C.H., "Size distributions for large and small earthquakes", *Bulletin of the Seismological Society of America*, vol. 87, no. 4, pp. 1074–1077, 1997.

[SCH 17] SCHEINGROSS J.S., LAMB M.P., "A mechanistic model of waterfall plunge pool erosion into bedrock", *Journal of Geophysical Research: Earth Surface*, vol. 122, no. 11, pp. 2079–2104, 2017.

[SIM 67] SIMONETT D.S., "Landslide distribution and earthquakes in the Bavani and Torricelli Mountains, New Guinea", in JENNINGS, J.A., MABBUTT, J.A. (eds), *Landform Studies from Australia and New Guinea*, Cambridge University Press, Cambridge, 1967.

[STA 01] STARK C.P., HOVIUS N., "The characterization of landslide size distributions", *Geophysical Research Letters*, vol. 28, no. 6, pp. 1091–1094, 2001.

[STE 14] STEER P., SIMOES M., CATTIN R. et al., "Erosion influences the seismicity of active thrust faults", *Nature Communications*, vol. 5, no. 1, pp. 1–7, 2014.

[STE 19] STEER P., CROISSANT T., BAYNES E. et al., "Statistical modelling of co-seismic knickpoint formation and river response to fault slip", *Earth Surface Dynamics*, vol. 7, no. 3, pp. 681–706, 2019.

[STE 20] STEER P., JEANDET L., CUBAS N. et al., "Earthquake statistics changed by typhoon-driven erosion", *Scientific Reports*, vol. 10, no. 1, pp. 1–11, 2020.

[TAN 17] TANYAŞ H., VAN WESTEN C.J., ALLSTADT K.E., et al., "Presentation and analysis of a worldwide database of earthquake-induced landslide inventories", *Journal of Geophysical Research: Earth Surface*, vol. 122, no. 10, pp. 1991–2015, 2017.

[TAN 19] TANYAŞ H., VAN WESTEN C.J., ALLSTADT K.E. et al., "Factors controlling landslide frequency–area distributions", *Earth Surface Processes and Landforms*, vol. 44, no. 4, pp. 900–917, 2019.

[TEB 20] TEBBENS S.F., "Landslide scaling: A review", *Earth and Space Science*, vol. 7, no. 1, p. e2019EA000662, 2020.

[THI 14] THIEULOT C., STEER P., HUISMANS R.S., "Three-dimensional numerical simulations of crustal systems undergoing orogeny and subjected to surface processes", *Geochemistry Geophysics Geosystems*, vol. 15, no. 12, pp. 4936–4957, 2014.

[TUC 01] TUCKER G.E., LANCASTER S.T., GASPARINI N.M. et al., "An object-oriented framework for distributed hydrologic and geomorphic modeling using triangulated irregular networks", *Computers and Geosciences*, vol. 27, no. 8, pp. 959–973, 2001.

[VAN 01] VAN HEIJST M.W.I.M., POSTMA G., "Fluvial response to sea-level changes: A quantitative analogue, experimental approach", *Basin Research*, vol. 13, no. 3, pp. 269–292, 2001.

[VAN 07] VAN DEN EECKHAUT M., POESEN J., GOVERS G. et al., "Characteristics of the size distribution of recent and historical landslides in a populated hilly region", *Earth and Planetary Science Letters*, vol. 256, nos 3–4, pp. 588–603, 2007.

[VER 13] VERNANT P., HIVERT F., CHERY J.A. et al., "Erosion-induced isostatic rebound triggers extension in low convergent mountain ranges", *Geology*, vol. 41, no. 4, pp. 467–470, 2013.

[WAN 15] WANG J., JIN Z., HILTON R.G. et al., "Controls on fluvial evacuation of sediment from earthquake-triggered landslides", *Geology*, vol. 43, no. 2, pp. 115–118, 2015.

[WAN 17] WANG W., GODARD V., LIU-ZENG J. et al., "Perturbation of fluvial sediment fluxes following the 2008 Wenchuan earthquake", *Earth Surface Processes and Landforms*, vol. 42, no. 15, pp. 2611–2622, 2017.

[WES 11] WEST A.J., LIN C.W., LIN T.C. et al., "Mobilization and transport of coarse woody debris to the oceans triggered by an extreme tropical storm", *Limnology and Oceanography*, vol. 56, no. 1, pp. 77–85, 2011.

[WES 14] WEST A.J., HETZEL R., LI G. et al., "Dilution of 10Be in detrital quartz by earthquake-induced landslides: Implications for determining denudation rates and potential to provide insights into landslide sediment dynamics", *Earth and Planetary Science Letters*, vol. 396, pp. 143–153, 2014.

[WHI 99] WHIPPLE K.X., TUCKER G.E., "Dynamics of the stream-power river incision model: Implications for height limits of mountain ranges, landscape response timescales, and research needs", *Journal of Geophysical Research: Solid Earth*, vol. 104, no. B8, pp. 17661–17674, 1999.

[WHI 01] WHIPPLE K.X., "Fluvial landscape response time: How plausible is steady-state denudation?", *American Journal of Science*, vol. 301, nos 4–5, pp. 313–325, 2001.

[WHI 02] WHIPPLE K.X., TUCKER G.E., "Implications of sediment-flux-dependent river incision models for landscape evolution", *Journal of Geophysical Research: Solid Earth*, vol. 107, no. B2, p. ETG-3, 2002.

[WHI 09] WHIPPLE K.X., "The influence of climate on the tectonic evolution of mountain belts", *Nature Geoscience*, vol. 2, no. 2, pp. 97–104, 2009.

[WIL 99] WILLETT S.D., "Orogeny and orography: The effects of erosion on the structure of mountain belts", *Journal of Geophysical Research: Solid Earth*, vol. 104, no. B12, pp. 28957–28981, 1999.

[WIL 14] WILLETT S.D., MCCOY S.W., PERRON J.T. et al. "Dynamic reorganization of river basins", *Science*, vol. 343, no. 6175, p. 1248765, 2014.

[WIL 18] WILLIAMS J.G., ROSSER N.J., HARDY R.J. et al., "Optimising 4-D surface change detection: An approach for capturing rockfall magnitude–frequency", *Earth Surface Dynamics*, vol. 6, no. 1, pp. 101–119, 2018.

[YAM 18] YAMAGISHI H., YAMAZAKI, F., "Landslides by the 2018 Hokkaido Iburi-Tobu Earthquake on September 6", *Landslides*, vol. 15, no. 12, pp. 2521–2524, 2018.

[YAN 10] YANITES B.J., TUCKER G.E., MUELLER, K.J. et al., "How rivers react to large earthquakes: Evidence from central Taiwan", *Geology*, vol. 38, no. 7, pp. 639–642, 2010.

[ZHA 17] ZHANG S., ZHANG L.M., "Impact of the 2008 Wenchuan earthquake in China on subsequent long-term debris flow activities in the epicentral area", *Geomorphology*, vol. 276, pp. 86–103, 2017.

[ZHA 19] ZHANG F., JIN Z., WEST A.J. et al., "Monsoonal control on a delayed response of sedimentation to the 2008 Wenchuan earthquake", *Science Advances*, vol. 5, no. 6, p. eaav7110, 2019.

10

Cumulative Deformation, Long-term Slip-rate and Seismic Cycle of Intra-continental Strike-slip Faults

Jérôme VAN DER WOERD
Institut Terre et Environnement de Strasbourg,
Strasbourg University, France

10.1. Introduction

One of the aims of morphotectonics is to characterize earthquake recurrence times along faults, in order to constrain seismic risk models and to estimate the probabilities related to the size and occurrence of future earthquakes. Knowing the seismic history of a fault is one of the ways of predicting its future behavior (see Chapter 11). Thus, conventionally, an average fault displacement rate over the long term is associated with a certain earthquake size, in order to develop slip models that could predict possible earthquake sequences. The fault slip-rate is the measurement of the rate of displacement of one side of the fault with respect to the other. A geological slip-rate is generally determined by an offset measurement of a relief form across a fault, accumulated over a long period of time (several thousand years

For a color version of all of the figures in this chapter, see www.iste.co.uk/rolandone/seismic.zip.

The Seismic Cycle,
coordinated by Frédérique ROLANDONE.

The Seismic Cycle: From Observation to Modeling,
First Edition. Frédérique Rolandone.

to several million years). A geodetic slip-rate is determined by measuring the ground displacement on either side of a fault at a certain distance from it, over a short period of time (a few years to a few decades), most commonly using a GPS system or radar interferometry (Figure 10.1, see Introduction and Chapter 13).

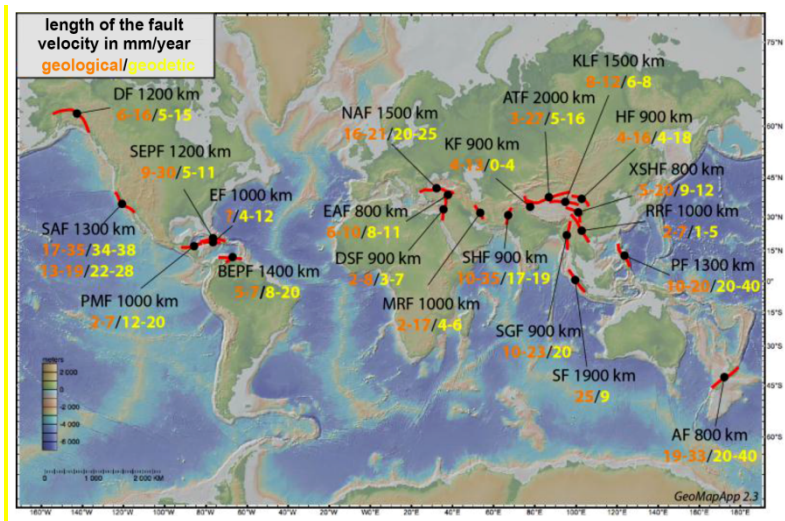

Figure 10.1. *Distribution on the Earth's surface of active continental strike-slip faults that are at least 1,000 km long, with length and geological/geodetic slip-rate bounds as per the literature*

While many faults remain under-studied, advances in knowledge make it possible to better characterize them. The question has now shifted from, "What is the fault slip-rate?" to "Is this rate constant over time? Does it vary over the seismic cycle or on the timescale of several cycles?" (see Introduction). Comparing rates resulting from different approaches (geodesy, geology) requires clearly defining what has actually been measured. Given this definition, we can discuss the possible origin for the differences or variations observed. These differences may be related to the fault's physical properties, or the evolution of the geometry of faults and their interactions over time, or even to changes in far-field boundary conditions imposed by plate tectonics.

These advances in knowledge are basically a result of the accumulation of slip-rate data resulting from various and constantly evolving dating methods of geomorphic markers, from paleoseismology and geodesy (GPS, InSAR), at various sites along faults, at different stages in their seismic cycle. For geological slip-rates,

there has been undeniable progress in dating through methods using cosmogenic isotopes (^{10}Be/^{26}Al/^{36}Cl/^{21}Ne) and also thermoluminescence (such as optically simulated thermoluminescence or optically stimulated luminescence (OSL)). We must also highlight the considerable contribution, in recent years, from high-resolution imaging (from Ikonos 1 m, Quickbird 0.60 m, SPOT5 2.5 m satellites, among others [LI 05, MÉR 05]) and high-resolution radar topography (airborne or terrestrial Lidar [ZIE 10, 15]), and also computer-based photogrammetric methods for the quick acquisition of digital elevation models, especially using drones.

In the following sections, we will focus on the definition and measurement of geological slip-rates from the cumulative deformation of geomorphological markers. We will address some commonly used methodologies and discuss some of their limitations. We will also look at the relationship between cumulative offset and earthquakes, the cumulative offset resulting from the addition of seismic displacements over time. Finally, we have chosen to restrict the discussion only to strike-slip faults.

10.2. From geomorphological offsets to fault slip-rate

10.2.1. *Tectonic offset of rivers*

The idea that it is possible to get a significant, quantitative measurement of some properties of earthquakes and faults from surface ruptures originated from the observation of deformations following some large earthquakes, notably the San Andreas earthquake of April 18, 1906 (see Introduction, [ZOB 06]). Not only was it possible to measure fault length (rupture) but also to characterize the co-seismic slip distribution along the rupture and quantify the deformation of the blocks separated by the fault. Although certain segments had been previously mapped, it took the 1906 earthquake to demonstrate the continuity of the San Andreas fault over hundreds of kilometers. Another aspect, clearly revealed by juxtaposing the recent rupture with morphologies inherited from earlier deformations, established the recurring nature of major seismic events. These conclusions supported similar observations made by Gilbert [GIL 84] in the late 19th century, along the Wasatch normal fault in Utah, of repeated shifts in the abandoned shorelines of the Bonneville paleo-lake.

A classic example of offset geomorphological markers is the Wallace Creek site along the San Andreas fault (Figure 10.2) [WAL 68, SIE 84, 87]. At this location, set in the relatively arid Carrizo plane, an intermittent stream, the Wallace Creek, flows down from the Temblor Mountains in the northeast. Crossing the San Andreas fault, this river incises the foothills forming a channel that is several meters deep.

The average rate of motion of the San Andreas Fault at this site has been constrained to 33.9 ± 2.9 mm/year for the last 3,700 years, and 35.8 ± 5.4 mm/year for the last 13,250 years, which is in good agreement with geodetic leveling measurements and GPS spatial geodesy measurements (35.9 ± 0.5 mm/year [MEA 05]).

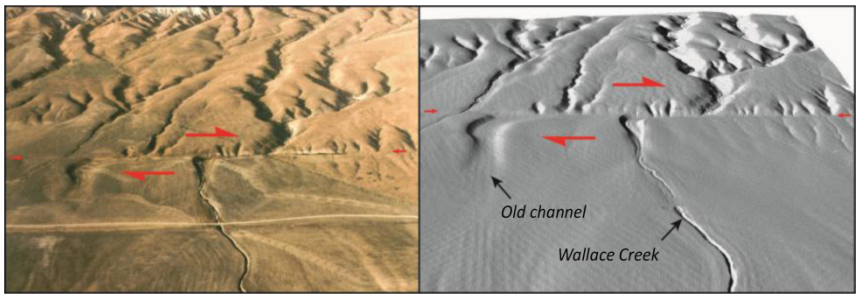

Figure 10.2. *a) Aerial photo of Wallace Creek site. b) Oblique view of a digital elevation model from airborne Lidar (https://opentopography.org/) showing relief details (B4 data, 25 cm resolution). The San Andreas fault follows a topographic escarpment, along which regressive channels form. Wallace Creek, the widest and deepest channel upstream, is offset right-laterally as it crosses the fault. Downstream (on the left), an ancient, abandoned channel, which is wider and has smooth risers, shows the earlier position of Wallace Creek*

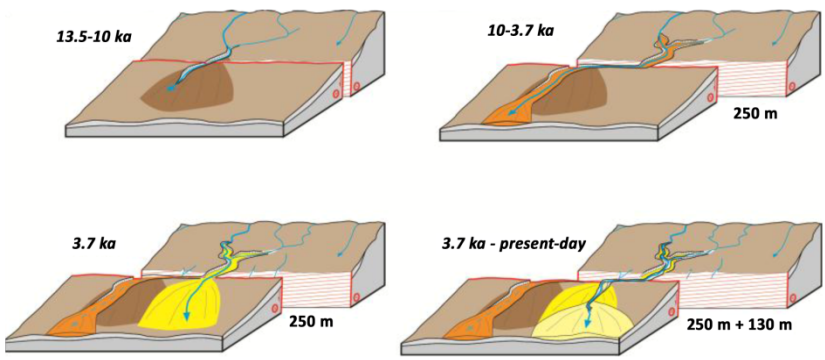

Figure 10.3. *Time progressive schematic representation of the evolution of the Wallace Creek site from establishments of colluvial deposits in foothills, incision of the Wallace Creek channel and phases of offset accumulation and of re-incision of the intermittent stream. Temporal constraints are derived from carbon-14 dating of sediments left behind in channels [SIE 84]*

10.2.2. *Average slip-rate determination from alluvial terrace edges (risers)*

In the following sections, we will focus on terrace risers as markers of deformation along strike-slip faults. Indeed, these are widespread markers and relatively numerous along the strike-slip faults. In many regions with active, obliquely converging tectonic plate activity, deformation is partitioned between strike-slip faulting and thrusting over distinct faults, with the strike-slip fault following the mountain range. This geometry of the structures almost automatically leads to the formation of drainage perpendicular to the direction of the strike-slip fault and these are the environments in which we hope to find many offset morphological markers.

These environments are ideal for quantifying recent displacements along the strike-slip faults, for several reasons:

– The perpendicular (or near-perpendicular) drainage makes it possible to reconstruct offset, natural geomorphological marker with high accuracy.

– These markers are associated with sediment deposits and can thus, potentially, be dated.

– The river incision and deposition phases lead to the formation of markers of various ages.

– The length of mountain ranges and of strike-slip faults (a few hundred kilometers to a thousand kilometers) increases the number of possible measurements.

These characteristics are the key points in the morphotectonic approach (or the tectonic geomorphology approach): measuring the offset, dating the offset, the temporal and spatial significance of the measurements.

Figure 10.4 schematically depicts the formation of a sequence of terraces concomitant with displacement along the strike-slip fault, inspired by situations seen along the Xidatan segment of the Kunlun fault [VAN 98, 02, TAP 01, RYE 06]. The accuracy of terrace riser horizontal offset measurements and the temporal relationships between incision and abandonment of different terraces makes it possible to recover the successive formation of the different deposits and the incision phases. This is done through a 3D approach using accurate topographical data. Depending on the situation, we must specify the relationship between the

incision of the terrace riser and the age of the adjacent terraces. This is sometimes complicated when certain terrace levels are not preserved on both sides of the fault due to erosion, or when the incision is progressive and the terrace risers are diachronic.

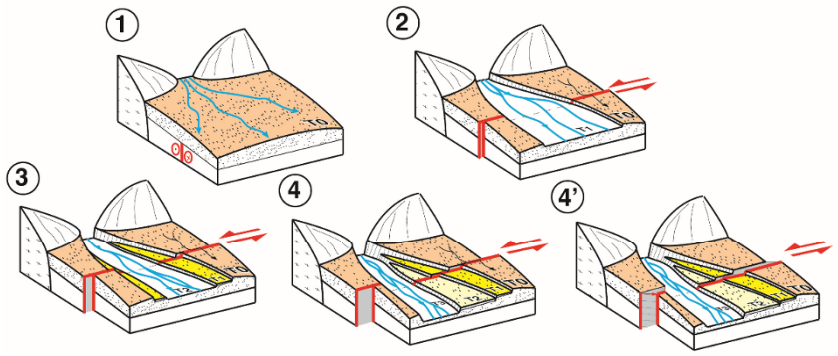

Figure 10.4. *Block diagrams showing a sequence of formation of alluvial terraces intersected by a strike-slip fault. (1) Formation of an alluvial fan T0 during a large sediment discharge. The fault trace is buried. (2) The river carves a bed, T1. Surface T0 is abandoned and begins to record movements of the fault, but its edge is constantly refreshed through lateral erosion. (3) During a new incision phase, T1 is abandoned and terrace riser T0/T1, which has become a passive marker, begins to record horizontal displacements. The age of abandonment of T1 dates terrace riser offset. (4) Successive episodes of deposition of terraces and incision lead to the formation of terraces whose risers have variable and incremental offsets. (5) A similar situation, but with a vertical component of motion. Vertical offset only accumulates when the surface is abandoned. Therefore, in this sequence, vertical offset of T1 (or T2) is correlated with the horizontal offset of T0/T1 (or T1/T2) and with the age of T1 (or T2). Modified from [VAN 02]*

In the Altyn Tagh fault example, some terraces have been completely eroded upstream of the fault (Figure 10.5) and consequently the terrace geometry changes drastically between upstream and downstream of the fault. Finally, there are some large (>5 m) incision phases between the terrace levels. The 3D reconstruction of the formation of deposits makes it possible to better understand the relationships between incision and the sinistral motion of the fault (Figure 10.6). In particular, it can be noted that the width of the active riverbed changes from 120 m to less than 20 m over the Holocene, after an incision of more than 15 m. In this case where the terraces are only preserved on one side of the fault, only the offset bounds of the

main channel are determined to estimate the left-lateral slip-rate rather than the terrace risers, whose ages are less well constrained (Figure 10.6).

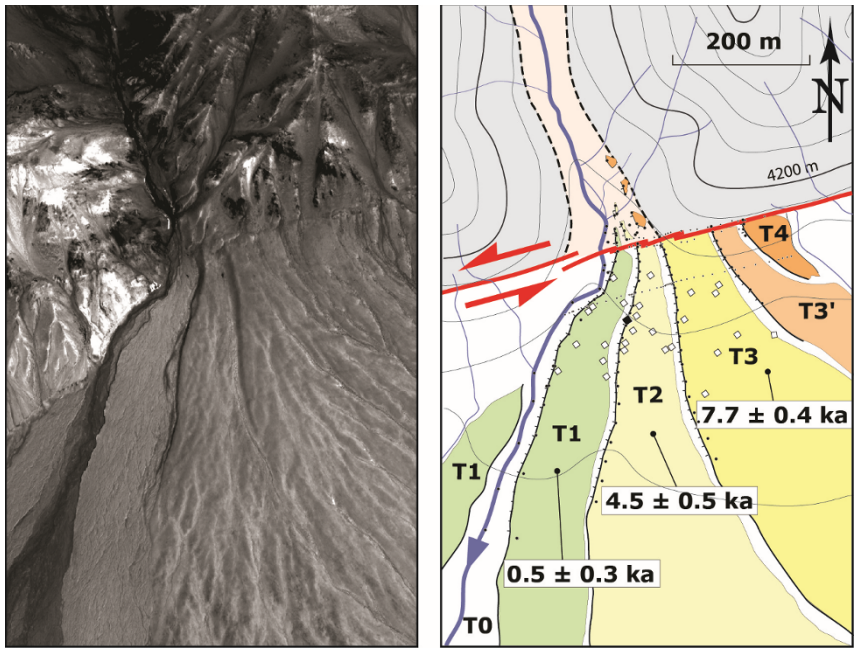

Figure 10.5. *Quickbird image and geomorphological interpretation of offset terraces along central part of Altyn Tagh fault Modified from [MÉR 12]*

The interpretation of the relationship between incision and offset is not straightforward and geological objects are complex. Contradictory studies have brought into question the role played by the interpretation of uncertainties related to determining the long-term slip-rate (epistemic uncertainty [SAL 15]). It is clear that considering the offset of a terrace riser that is never directly dated is a source of uncertainty in the determination of long-term slip-rate. In particular, the possibility that a terrace riser separating paired terraces may be diachronic across the fault has been considered a limitation in using terrace edges to characterize a tectonic offset [SUG 60, LEN 64, 68], with preference given to the offset of channels incised within the terraces. The combination of different dating methods, like carbon-14, thermoluminescence and cosmonuclides (see Box 10.1), leads to various scenarios being proposed with respect to the terrace types and the mode in which they were formed and abandoned, to fix the possible bounds on the offset ages [MÉR 05, COW 07, GOL 09].

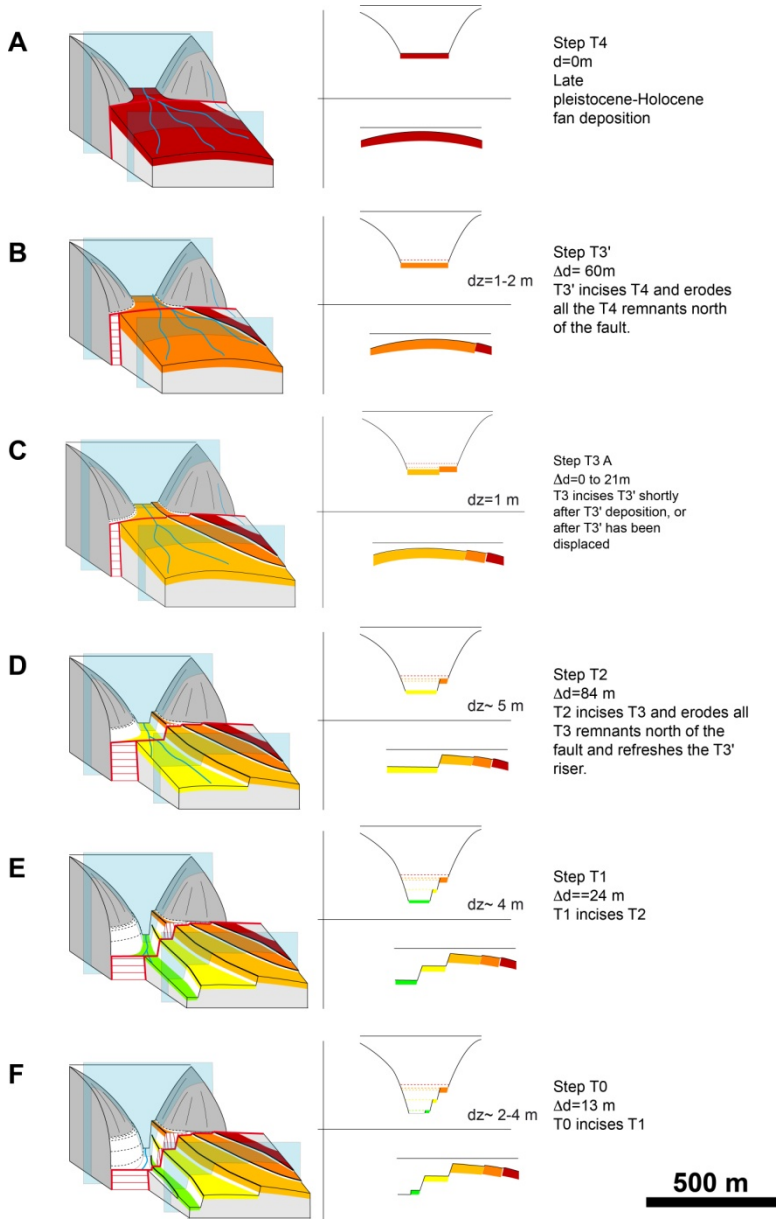

Figure 10.6. *Irregular complex evolution of interaction between horizontal tectonic movements and river dynamics, where the river incises by modifying its riverbed width. Here, four major terraces formed during climatic variations of the last 14,000 years. Modified from [MÉR 12]*

It is possible to determine the upper and lower bounds of the age of the terrace riser. Indeed, the incision only begins when the upper level is abandoned, and its offset may have started accumulating well before the lower terrace was abandoned. This approach remains valid if the terraces are of similar ages. We can also consider the maximum possible age alone, that is the age of the upper terrace, leading to an estimate of minimum slip-rates [COW 07].

Rocks on the Earth's surface are bombarded by cosmic particles, like high-energy protons. Nuclear interactions between these particles and the atoms in the rock minerals lead to the formation of radioactive isotopes, called cosmogenic isotopes, which remain trapped within the minerals. For example, these reactions lead to the formation of Beryllium-10 or Aluminum-26, from the silicon and oxygen atoms in quartz (SiO_2). The production rate of cosmogenic isotopes depends on the flow of the charged cosmic particles through the Earth's terrestrial atmosphere and their modulation by the Earth's magnetic field. It therefore depends on the altitude and latitude and must be known for each measurement site. This is the aim of international modeling and calibration programs, allowing a constant improvement in measurements. This cosmogenic isotope production rate also decreases with the thickness of the rock cross-section and, therefore, with depth. Quantifying the accumulation of these isotopes in the rocks on the surface and sub-surface is thus a way of measuring the exposure of the rock to cosmic radiation, as well as quantifying the erosion undergone by the surface being analyzed. Consequently, after a chemical isolation of the elements and the use of an acceleration spectrometer, it is possible to measure the quantity of isotopes accumulated in pebbles or blocks abandoned by the rivers or glaciers in terraces or moraines in order to determine their age [GOS 01, BEN 14].

Box 10.1. *Cosmogenic isotope dating*

10.3. Variation in space and time of the long-term fault slip-rate

To understand the role played by faults in the deformation of continents, we must know their rate of motion, especially whether this rate changes along the fault or over time. While on a small scale a fault is a simple linear (or planar) object, on a larger scale, a strike-slip fault is a series of segments with junctions and bifurcations that may sometimes be complex. The relationship between a segment and the entire fault system is not always a simple one. Furthermore, the sites where the geological rate can be determined are not uniformly distributed and it is rare to find situations where well-constrained geomorphological offsets can be precisely dated. If, in

addition, the rate varies over time as well as spatially along the fault, the kinematic balance of a fault becomes complex.

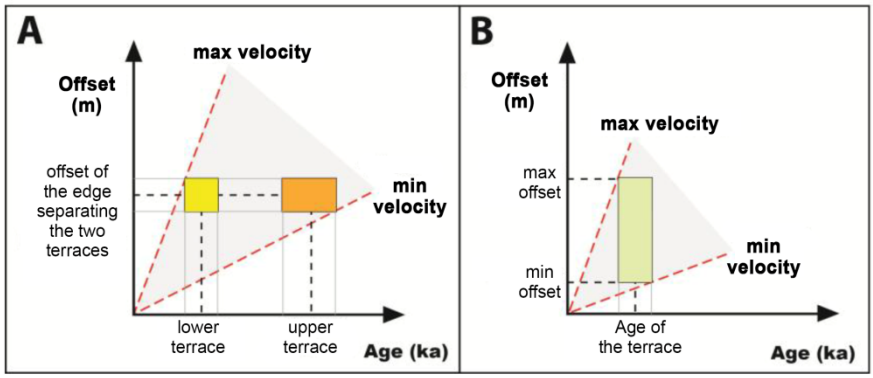

Figure 10.7. *Two approaches used to determine average fault slip-rate. a) The offset is well determined, but the timing of its accumulation is not clearly known and is bounded by the ages of lower and upper terraces. b) A different case where the age is well determined (here, age of a terrace) but offset is less well determined and lies between minimum and maximum bounds. Modified from [MÉR 12]*

The slip-rate of the Karakorum fault in western Tibet was determined at a dozen sites along the fault through the dating of offsets of alluvial deposits, terrace risers and abandoned moraines [CHE 15]. At certain places the fault is double and requires the integration of velocities over several segments. The rate is determined for various periods ranging from 10,000 to 15,000 years, up to 150,000 years, depending on the site. The rates determined vary from 2 to 8 mm/year, with a majority lying between 3 and 6 mm/year. If we add up the rates on the sites where the fault is double – ignoring the fact that rates are determined for different time periods – then the high bound of 8 mm/year for the rate is favored. If, on the contrary, we hypothesize that there are temporal variations, then the present-day rate of the fault is likely to be around 3–6 mm/year, with an increase toward the south. The comparison of the rate obtained through different methods, like geodesy, geomorphology and geology, shows some temporal consistency between 3 and 10 mm/year from the present day to 30 million years ago. However, the accuracy of the methods and uncertainties associated with the measurement of the considered objects also allows us to see temporal variations in rate and, perhaps, a decrease in rate over time.

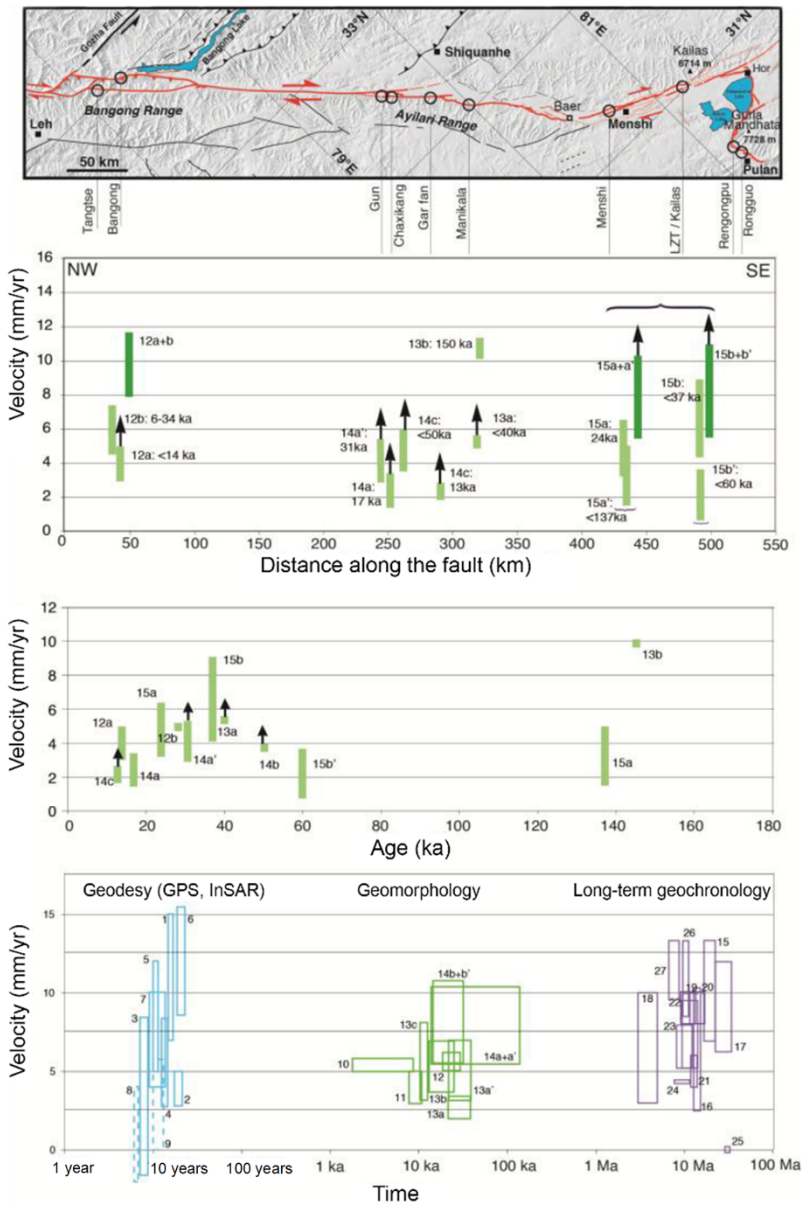

Figure 10.8. *Variation in long-term slip-rate along Karakorum fault for different time periods. Adding rates determined over different time periods presumes that rates do not vary temporally. Modified from [CHE 15]*

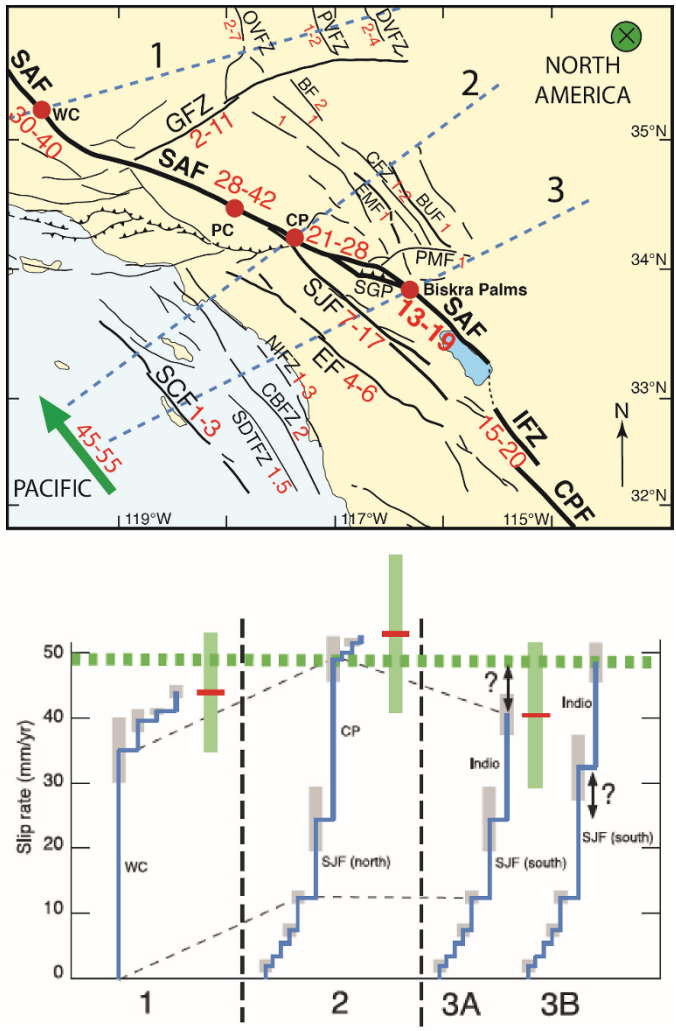

Figure 10.9. *At plate boundary scale, the San Andreas fault system, with its associated faults, accommodates the distant displacement, of the order of 5 cm/year, of Pacific and North American tectonic plates. We can see how the velocity is distributed over different faults along three sections perpendicular to the plate boundary. Along section 3, it has been proposed that the slip-rate variability along the San Jacinto fault (SJF) and San Andreas fault (SAF) results from the alternating seismic activity along these faults. Modified from [VAN 06]*

The boundaries of continental blocks or tectonic plates are rarely simple fault zones. While the San Andreas fault accommodates a large part of the displacement between the Pacific and the North American plates in Southern California, other faults also play a role. These faults can be distributed up to several hundreds of kilometers away from the main fault, defining a complex fault system whose geometry evolves in time with the progressive displacement of the micro-blocks limited by these faults. The low rate along some faults does not reduce the potential seismic risk, especially in densely populated regions.

In Southern California, the relative velocity of the Pacific and the North American plates is around 5 cm/year. The San Andreas fault and further south the San Andreas and San Jacinto faults accommodate over half of this relative plate motion. The remainder of the deformation is accommodated by other faults, generally smaller, but capable of producing earthquakes with a magnitude greater than 7. Knowing the respective rate of motion of all the faults is, therefore, one way to understand how the zone is deforming and also to look at the hazard that each fault zone represents. In this situation, with many sub-parallel faults close to each other, geodetic methods that require measurements at a certain distance from the faults cannot accurately solve how the deformation is distributed over each fault. When we add up the movement on each fault along three sections perpendicular to the plate boundary (Figure 10.9), we get the relative tectonic plate displacement of 5 cm/year. In detail, these reconstructions make it possible to discuss uncertainties over certain faults' slip-rates. In particular, the respective rates of the San Jacinto and San Andreas faults, to the east of Los Angeles, are the subject of debate [VAN 06]. While there is no doubt that the main San Andreas fault has accommodated most of the displacement accumulated over geological time, it seems that the San Jacinto fault is likelier to be the faster fault at present. Thus, the plate boundary system is likely to evolve with a change in active zones, with the San Jacinto fault becoming the main fault. It is not possible to say whether this current evolution is irreversible, from a geological point of view, or whether it is simply the result of the alternating seismic activity along these two faults.

10.4. Characteristic slip, earthquake size and seismic cycle

10.4.1. *Earthquake and cumulative offset: the Kunlun fault and Kokoxili earthquake*

The Kokoxili earthquake (Mw 7.9, November 14, 2001) is one of the largest known earthquakes on a strike-slip fault in Tibet (Figure 10.10, [KLI 05, LAS 05,

LI 05, VAN 06]). This earthquake ruptured one of the western segments of the Kunlun fault, over a length of around 450 km, in just a few minutes. Located in a region of the high Tibetan plateau, a high-altitude desert, it resulted in very little damage and there were no casualties.

Figure 10.10. *View to the west along the rupture of the magnitude 7.9 earthquake on November 14, 2001 in Kokoxili, along Kunlun strike-slip fault in Tibet. Paul Tapponnier's silhouette gives an idea of rupture width and size of co-seismic deformations*

The ground observations following the earthquake revealed the rapid, two- to four-fold variation in co-seismic slip during the rupture (Figure 10.11). Although the fault has a relatively simple geometry, consisting of a single fault on a regional level, part of these variations resulted from the complexity of the seismic rupture on the surface, which affected a large zone around the fault plane, and the difficulty involved in measuring the displacement precisely (Figure 10.10). However, it is likely that these variations are resolved with time over successive earthquakes. It is valid to wonder if these variations could accumulate over seismic cycles and whether they could bias the determination of long-term fault slip-rate.

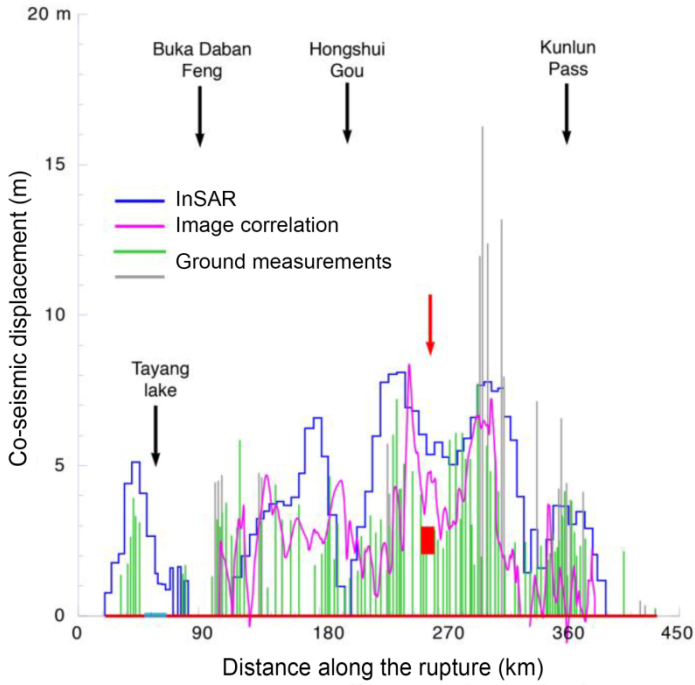

Figure 10.11. *Distribution of co-seismic slip along Kunlun fault during the magnitude 7.9 earthquake on November 14, 2001, determined using different methods. In red: position of study site, described below*

Regardless of the seismic slip model considered (characteristic slip, time predictable, etc. [SCH 84, SIE 96, TAP 01, WAR 97]), it is generally accepted that the displacement of blocks at distance from the fault ends up producing the same quantity of displacement on the fault. Although the determination of long-term slip-rates over time periods that are much longer than the return time of earthquakes (several thousand years) shows a relative consistency over distant sites along the Kunlun fault [VAN 02], it can be assumed that the fault accumulates the same displacement at any point on the fault. While this is true for accumulated displacements, it seems that this is no longer true for measurements of offset or temporal measurements, which are close to the values of the co-seismic displacement and the recurrence times of the earthquakes: there is thus likely to be a smoothing of disparities in slip over time and over successive earthquakes, at the same time as a temporal variation of the slip velocity over one or more seismic cycles [WEL 04].

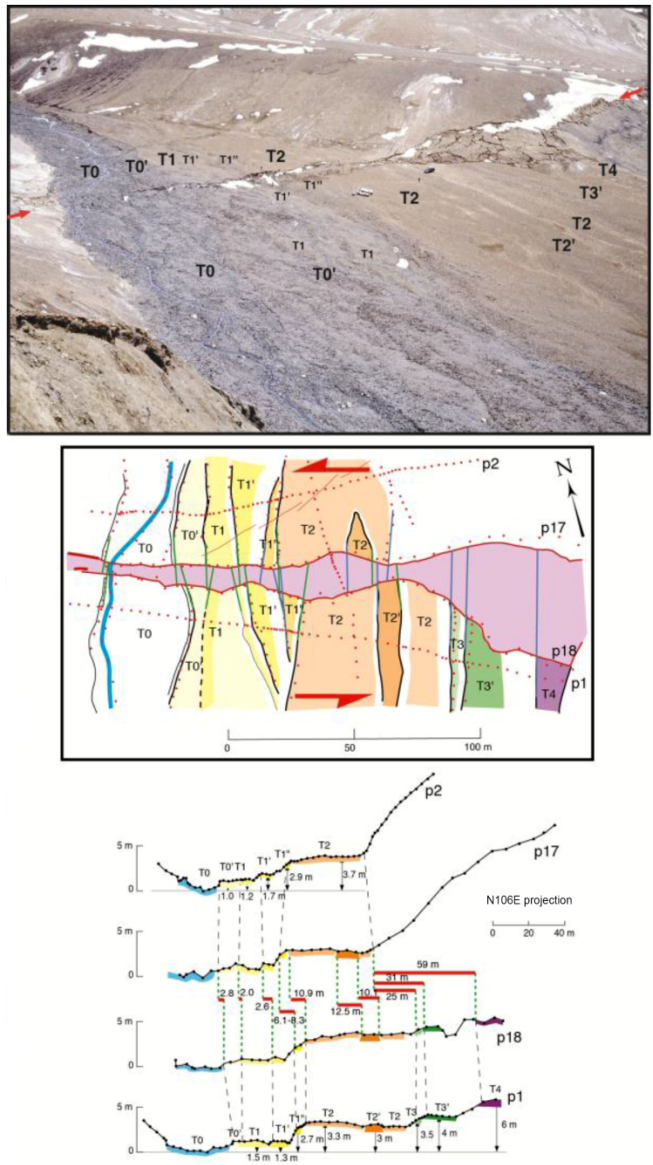

Figure 10.12. *Mapping of offset terraces and offset measurements from field observation, analysis of high-precision satellite images and topographic leveling in the field. Projections of topographic profiles leveled parallel to fault direction, with indication of terrace heights and sinistral offsets. The youngest ones are co-seismic and older ones are cumulative*

The Kokoxili rupture, with its exceptional length of 400 km, allows us to approach the problem of repeated earthquakes at a given site in the central part of the rupture (Figure 10.10) where the co-seismic displacement corresponds to a minimum average displacement of about 2.5 m. On either side of this site, the rupture reaches its maximum slip values of about 8–10 m [KLI 05, LAS 05]. A set of about 10 offset measurements, constrained by micro-topography measurements with a theodolite, takes into account the variation in co-seismic slip for four to five events of 1–5 m, with the possibility that the 5 m displacement results from two earthquakes with an average displacement of 2.5 m each (Figures 10.11 and 10.12).

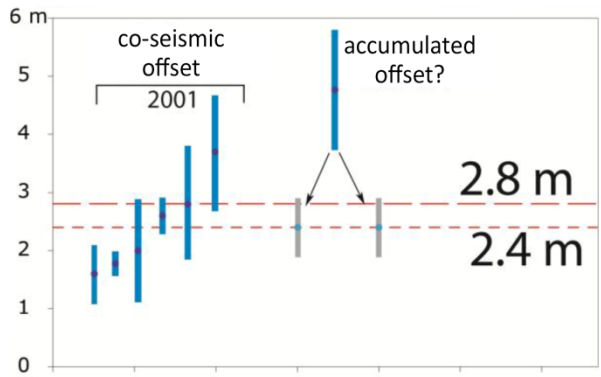

Figure 10.13. *Compilation of smallest geomorphological offset measurements and estimation of average co-seismic slip*

Cosmogenic isotope dating of some offset terraces makes it possible to put forth a scenario for the slip over the past 5,000 years that takes into account the variable measurements of co-seismic and accumulated slip, and implies a variation in slip-rate over time [WEL 04].

10.4.2. *Characteristic repetition of ruptures and earthquakes*

A compilation of the alluvial morphological offset measurements along faults gives us access to the fault's seismic history. As long as the erosion is moderate while incision events are relatively frequent (with respect to the occurrence of major earthquakes), then the channels incised across the fault are possible markers of deformation over time. The smallest morphological offsets correspond to the

co-seismic offset from the last seismic event, and the larger offsets result from the accumulation of displacement during earlier events. Along selected fault segments, the statistical analysis of the offset distribution makes it possible to show the repetition of events whose average slip is of the same amplitude. For example, along the Karakax fault segment on the Altyn Tagh strike-slip fault, a set of channel and terrace riser offsets is offset by about 6–7 m, thus determining the average displacement of the last large earthquake on this fault. Larger accumulated offsets become fewer, as might be expected due to erosion. However, their values suggest clusters of multiples of 6–7 m, at 14, 19 and 24 m. Similar observations have been made on other strike-slip faults, such as the San Andreas fault [ZIE 10, 15] or the Fuyun fault [KLI 11]. These offset distribution observations therefore suggest a seismic behavior where the quantity of slip in each major earthquake is similar, thereby characterizing the behavior of a fault segment. It is only through the additional use of dating methods that we can more accurately define the date of occurrence of seismic events, as there is no a priori evidence that these occur at regular intervals.

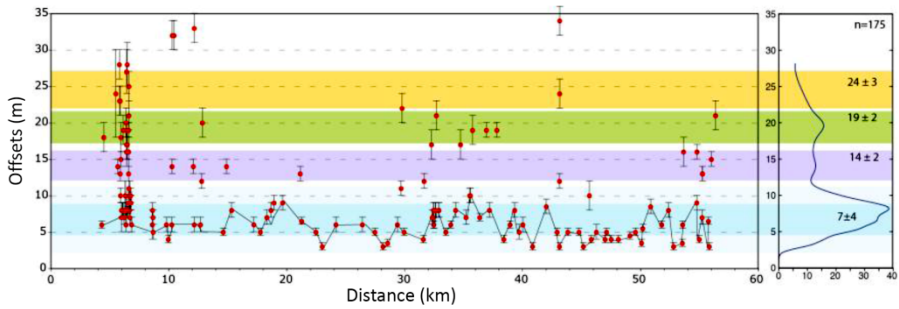

Figure 10.14. *Example of morphological offset distribution of channels and terraces along the Karakax – Altyn Tagh fault, in western Tibet. The curve on the right, or offset probability density function, shows average characteristic co-seismic displacements (here, multiples of 6–7 m). Modified from [LI 12]*

Thus, the cumulative deformation along the fault results from occasional seismic increments when the total displacement of the blocks takes place over a fault plane. This is not always the case when several faults define a complex damage zone. In this case, the deformation is accommodated over a larger zone with smaller displacements on each fault.

10.5. Conclusion

Variability in the geological slip-rate of a fault at different scales is directly related to the variability in displacement measured along a fault. For long periods of time, the average displacement velocity is better determined, but the number of earthquakes and their sizes become uncertain, while for shorter and more recent periods, the average velocity is less well determined, but the number and size of earthquakes are better determined. Combining measurements across different timescales, as well as the increase in the number of observations due to constantly developing tools and techniques, makes it possible to obtain ever-more reliable and significant datasets to understand how faults function.

10.6. References

[BEN 14] BENEDETTI L., VAN DER WOERD J., "Cosmogenic nuclide dating of earthquakes, faults and toppled blocks", *Elements*, vol. 10, pp. 357–361, 2014.

[CHE 15] CHEVALIER M.L., VAN DER WOERD J., TAPPONNIER P., et al., "Late Quaternary slip-rate along the central Bangong-Chaxigang segment of the Karakorum fault, western Tibet", *Geol. Soc. Am. Bull*, vol. 128, pp. 284–314, 2015.

[COW 07] COWGILL E., "Impact of riser reconstructions on estimation of secular variation in rates of strike-slip faulting: Revisiting the Cherchen River site along the Altyn Tagh Fault, NW Chin", *Earth Planet. Sci. Lett.*, vol. 254, pp. 239–255, 2007.

[GIL 84] GILBERT G.K., "A theory of the earthquakes of the Great Basin, with a practical application", *Am. J. Sci.*, vol. 27, pp. 49–53, 1884.

[GOL 09] GOLD R.D., COWGILL E., ARROWSMITH J.R. et al., "Riser diachroneity, lateral erosion, and uncertainty in rates of strike-slip faulting: A case study from Tuzidun along the Altyn Tagh Fault, NW China", *J. Geophys. Res.*, vol. 114, p. B04401, 2009.

[GOS 01] GOSSE J.C., PHILLIPS F.M., "Terrestrial in situ cosmogenic nuclides: Theory and applications", *Quaternary Science Reviews*, vol. 20, pp. 1475–1560, 2001.

[KLI 05] KLINGER Y., XU X., TAPPONNIER P. et al., "High-resolution satellite imagery mapping of the surface rupture and slip distribution of the Mw ~7.8, November 14, 2001 Kokoxili earthquake (Kunlun Fault, Northern Tibet, China)", *Bull. Seismol. Soc. Am.*, vol. 95, pp. 1970–1987, 2005.

[LAS 05] LASSERRE C., PELTZER G., CRAMPÉ F. et al., "Coseismic deformation of the 2001 Mw7.8 Kokoxili earthquake in Tibet, measured by synthetic aperture radar interferometry", *J. Geophys. Res.*, vol. 110, p. B12408, 2005.

[LEN 64] LENSEN G.J., "The general case of progressive fault displacement of flights of degradational terraces, New Zealand", *J. of Geol. and Geophys.*, vol. 7, no. 4, pp. 864–870, 1964.

[LEN 68] LENSEN G.J., "Analysis of progressive fault displacement during downcutting at the Branch River terraces, South Island, New Zealand", *Geol. Soc. Amer. Bull.*, vol. 79, pp. 545–556, 1968.

[LI 05] LI H., VAN DER WOERD J., KLINGER Y. et al., "Slip rate on the Kunlun Fault and recurrence time of great earthquake comparable to the 14/11/2001, Mw~7.8 Kokoxili earthquake at Hongshui Gou", *Earth Planet. Sci. Lett*., vol. 237, pp. 285–299, 2005.

[LI 12] LI H., VAN DER WOERD J., SUN, Z. et al., "Co-seismic and cumulative offsets of the recent earthquakes along the Karakax left-lateral strike-slip fault in western Tibet", *Gondwana Research*, vol. 21, no. 1, pp. 64–87, 2012.

[MEA 05] MEADE B.J., HAGER B.H., "Block models of crustal motion in southern California constrained by GPS measurements", *J. Geophys. Res.*, vol. 110, p. B03403, 2005.

[MÉR 05] MÉRIAUX A.-S., TAPPONNIER P., RYERSON F.J. et al., "The Aksay segment of the northern Altyn Tagh fault: Tectonic geomorphology, landscape evolution, and Holocene slip rate", *J. Geophys. Res.*, vol. 110, p. B04404, 2005.

[MÉR 12] MÉRIAUX A.-S., VAN DER WOERD J., TAPPONNIER P. et al., "The Pingding segment of the Altyn Tagh Fault (91°E): Holocene slip-rate determination from cosmogenic dating of offset fluvial terraces", *J. Geophys. Res.*, vol. 117, p. B09406, 2012.

[RYE 06] RYERSON F.J., TAPPONNIER P., FINKEL R.C. et al., "Applications of morphochronology to the active tectonics of Tibet", in SIAME L.L., BOURLÈS D.L., BROWN E.T. (eds), *Application of Cosmogenic Nuclides to the Study of Earth Surface Processes: The Practice and the Potential,* Geological Society of America Special Paper, Boulder, CO, 2006.

[SAL 15] SALISBURY J.B., HADDAD D.E., ROCKWELL T. et al., "Validation of meter-scale surface faulting offset measurements from high-resolution topographic data", *Geosphere*, vol. 11, pp. 1–18, 2015.

[SCH 84] SCHWARTZ D.P., COPPERSMITH K.J., "Fault behavior and characteristic earthquakes: Examples from the Wasatch and San Andreas Fault Zones", *J. Geophys. Res.*, vol. 89, no. B7, pp. 5681–5698, 1984.

[SIE 84] SIEH K., JAHNS R.H., "Holocene activity of the San Andreas fault at Wallace Creek, California", *Geol. Soc. Am. Bull.*, vol. 95, pp. 883–896, 1984.

[SIE 87] SIEH K., WALLACE R.E., "The San Andreas fault at Wallace Creek, San Luis Obispo County, California", *Geological Society of America Centennial Field Guide – Cordilleran Section*, vol. 1, pp. 233–238, 1987.

[SIE 96] SIEH K., "The repetition of large-earthquake ruptures", *Proc. Natl. Acad. Sci.*, vol. 93, pp. 3764–3771, 1996.

[SUG 60] SUGGATE R.P., "The interpretation of progressive fault displacement of flights of terraces, N. Z.", *J. Geol. Geophys.*, vol. 3, pp. 364–374, 1960.

[TAP 01] TAPPONNIER, P., RYERSON F.J., VAN DER WOERD J. et al., "Long-term slip rates and characteristic slip: Keys to active fault behaviour and earthquake hazard", *C. R. Acad. Sci*., series II, vol. 333, no. 9, pp. 483–494, 2001.

[VAN 98] VAN DER WOERD J., RYERSON F.J., TAPPONNIER P. et al., "Holocene left-slip rate determined by cosmogenic surface dating on the Xidatan segment of the Kunlun Fault (Qinghai, China)", *Geology*, vol. 26, pp. 695–698, 1998.

[VAN 02] VAN DER WOERD J., TAPPONNIER P., RYERSON F.J. et al., "Uniform postglacial slip-rate along the central 600 km of the Kunlun Fault (Tibet), from 26Al, 10Be, and 14C dating of riser offsets, and climatic origin of the regional morphology", *Geophysical Journal International*, vol. 148, pp. 356–388, 2002.

[VAN 06] VAN DER WOERD, J., KLINGER Y., SIEH K. et al., "Long-term slip rate of the southern San Andreas Fault from 10Be-26Al surface exposure dating of an offset alluvial fan", *J. Geophys. Res.*, vol. 111, p. B04407, 2006.

[WAL 68] WALLACE R.E., "Notes on stream channels offset by the San Andreas fault, southern Coast Ranges, California", in DICKINSON W.R., GRANTZ A. (eds), *Conference on Geologic Problems of the San Andreas Fault System, Proceedings: Stanford University Publications in the Geological Sciences*, vol. 11, pp. 6–21, 1968.

[WAR 97] WARD S.N., "Dogtails versus rainbows: Synthetic earthquake rupture models as an aid in interpreting geological data", *Bull. Seismol. Soc. Am.*, vol. 87, pp. 1422–1441, 1997.

[WEL 04] WELDON R., SCHARER K., FUMAL T. et al., "Wrightwood and the earthquake cycle: What a long recurrence record tells us about how faults work", *GSA Today*, vol. 14, no. 9, pp. 4–10, 2004.

[ZIE 10] ZIELKE O., ARROWSMITH J.R., LUDWIG L.G. et al., "Slip in the 1857 and earlier large earthquake along the Carrizo plain, San Andreas fault", *Science*, vol. 327, pp. 1119–1122, 2010.

[ZIE 15] ZIELKE O., KLINGER Y., ARROWSMITH J.R., "Fault slip and earthquake recurrence along strike-slkp faullts – Contribution of high-resolution geomorphic data", *Tectonophysics*, vol. 638, pp. 43–62, 2015.

[ZOB 06] ZOBACK M.L., "The 1906 earthquake and a century of progress in understanding earthquakes and their hazards", *GSA Today*, vol. 16, pp. 4–11, 2006.

11

Paleoseismology

Yann KLINGER
Institut de physique du globe de Paris, CNRS, Paris Cité University, France

11.1. Introduction

The objective of paleoseismology is to reconstruct the longest possible earthquake sequences in order to understand how deformation is accommodated over time for a specific fault system. Two aspects of paleoseismology can be identified: the first constrains the time series of earthquakes to study, for example, the return time of earthquakes over a given fault. In some cases, where there is rich historical documentation, either in archives or in the form of archeological evidence, paleoseismology may be associated with archeoseismology, which more specifically tries to recover traces of earthquakes in historical archives. The second aspect is that paleoseismology can also consist of determining the displacements associated with ancient earthquakes for a given site. Although the two approaches are clearly complementary, the time series construction is the approach that is most frequently used as it is easier to implement. Measuring the displacement associated with ancient earthquakes requires very specific conditions of preservation of morphology, which are more difficult to obtain. Indeed, a successful paleoseismological study first requires a carefully chosen work site. It is not only imperative (if difficult) to find a site that retains a distinct trace of successive past earthquakes in its geological record, but is also just as important that this site offers a good potential for dating the geological units that retain traces of these ancient earthquakes.

For a color version of all of the figures in this chapter, see www.iste.co.uk/rolandone/seismic.zip.

The Seismic Cycle,
coordinated by Frédérique ROLANDONE.

The Seismic Cycle: From Observation to Modeling,
First Edition. Frédérique Rolandone.

There is no need to prove how useful paleoseismology is in constraining the seismic cycle models when it comes to determining the time and displacement associated with a series of ancient earthquakes for a given site, or even in the best case, for a series of sites along the same geological structure. However, paleoseismology also has strong limitations and these must be kept in mind when undertaking this kind of study. Generally speaking, paleoseismology strives to identify and date co-seismic deformations associated with past earthquakes. This therefore implies that these deformations are visible in some way on the Earth's surface. This introduces a de facto threshold on the magnitude of the earthquakes that can be identified using paleoseismological methods and, with the exception of a few specific cases [LIU 15], it is generally accepted that only earthquakes of magnitude Mw 6–6.5 or higher can be detected. Further, paleoseismological methods are generally applied to the main geological structure and provide little or no information on the activation of secondary faults, or the deformation distributed around the main fault zone. This thus leads us to minimize the total deformation budget associated with an earthquake. Further, in the majority of cases where paleoseismological trenches are dug, we have no idea where these trenches lie with respect to the slip curve for an ancient rupture. It is therefore difficult, if not impossible, to interpret the quantity of slip measured in a trench and to know whether this is a representative measurement of the average, minimum or maximum slip without digging multiple trenches along the same structure. Consequently, we must be careful when interpreting and evaluating the magnitude of a paleoearthquake using paleoseismological data, especially with trench data. Dating problems must also not be underestimated. The distribution of samples over a study site is rarely optimal and may induce a strong bias in how results are interpreted [RIZ 19]. These difficulties, inherent to this kind of approach, can induce variability in the results for different sites along the same structure, which makes it difficult to carry out any comparison. This holds even truer when comparing the seismological behavior of different structures. In order to remedy this problem, the paleoseismological community has conventionally used a quantifier called the coefficient of variation, defined as the ratio between the standard deviation and the average for any specific dataset. For example, the set of recurrence times for successive earthquakes identified in a trench, or successive offsets in a population of earthquakes [ZIE 15]. This is a dimensionless quantifier and therefore lends itself well to comparisons between different structures which may have very different deformation rates.

In the rest of this chapter, we present the different methods used in paleoseismology. While we wish to differentiate between different methodological approaches, it is seen that very often the different methods also correspond to different types of earthquakes and different tectonic styles. The chapter is divided as

follows: section 11.2 focuses more specifically on paleoseismology for continental faults, followed by section 11.3, which describes the methods used for faults at sea. Finally, section 11.4 reviews a set of techniques based on secondary observations, which can give information on the occurrence of ancient earthquakes, although less accurately.

11.2. Paleoseismology for faults in a continental context

11.2.1. *Paleoseismological trenches*

Among paleoseismological tools, trenching is certainly the best-known and most widely used method. This method is used for faults in a continental context. As its name indicates, this consists of digging trenches (see Figure 11.1) across faults to determine the date of the last earthquake or earthquakes, which could have occurred on a given geological structure. This is, therefore, the main tool to determine whether or not a continental fault is active, in most seismic hazard studies.

Figure 11.1 *Paleoseismological trench opened across a fault. We distinguish a series of deposits that will be used to analyze seismological history. The theodolite, in the center, is essential for creating a grid on the wall that serves as a reference. Photo © Y. Klinger*

The principle of paleoseismological trenches is to find the trace of co-seismic disturbances (see Figure 11.2) in different, superficial sediment units. This disturbance may directly be the fossil trace of the co-seismic ground rupture, in the sense of a rupture whose morphology is preserved, buried by the later deposit of sediments that protects this trace from erosion. This can also be the trace of the fault that will offset geological units on either side of the fault, or a specific deposit associated with the collapse of a part of the co-seismic escarpment during or just after an earthquake. In this latter case, we speak of a colluvial wedge. In certain cases, it is also possible to find traces of liquefaction (thixotropy) when a unit rich in fluids is localized between two layers that are more impermeable and undergo overpressure due to the passage of seismic waves. In certain cases of very high overpressure, this effect can lead to the piercing of the impermeable layer, with the ejection of fluid and the surrounding material toward the surface, thereby creating a *sand blow*. A site that is favorable for a paleoseismological study is, therefore, a site where sediments can accumulate over time, in order to bury and protect these different traces. In an ideal site, each unit will be thin and distinct from the surrounding units and the sediments themselves will have fine granulometry. This makes it possible to obtain a high temporal resolution and, incidentally, this type of environment is particularly favorable for preserving samples of organic material used to date units. On the contrary, a coarse granulometry (gravel or pebbles, from 0.5 cm to a few decimeters) risks crushing samples during the deposition of sediments. Typically, environments that are highly favorable for a good-quality paleoseismological recording are lacustrine environments, flood zones (overbank deposits) and all counter-sloping depressions and escarpments along a fault, where water stagnates episodically with fine sediment deposit (sag ponds). It is preferable to avoid sites where sediments accumulated too rapidly, as this would require digging deeper trenches in order to distinguish between successive earthquakes.

The objective in a trench is to define, for every paleoearthquake, a level that is called the seismic horizon, which separates the sediment units that were deposited before the earthquake, and which were thus affected by co-seismic deformation, from those units that date from after the earthquake and are not affected by co-seismic deformation. The seismic horizon is, therefore, a virtual level, which does not correspond to a specific sediment unit, but most often corresponds to a contact between two units. We will define as many seismic horizons as there are identifiable earthquakes on a trench wall. It may be tricky to define a seismic horizon as it depends heavily on the quality of the sediment record. In general, we will give priority to a seismic horizon defined from multiple observations (e.g. many fissure and fault endings at the same stratigraphic level, but distributed laterally over the trench wall) rather than a level that is based only on an isolated observation, while keeping in mind that it is not proven that all fissures always reach the surface

during an earthquake [SCH 07]. Notably, fissures that do not accommodate displacement, but rather volume deformation are more sensitive to differences in the mechanical properties of the environment and may thus be more or less visible, depending on the affected material. In terms of dating, the goal is to be able to date samples that most closely surround the different seismic horizons.

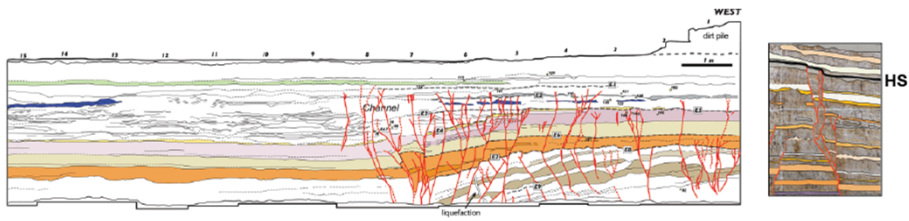

Figure 11.2. *Example of mapping in a trench. Different seismic horizons (HS) are defined based on the stratigraphic units that are intersected by the faults or, on the contrary, that seal a fault. In the case presented here, it is possible to distinguish nine successive earthquakes, labeled E1 to E9. The inset on the right shows a detail of the relationship between a fault, stratigraphic unit and the seismic horizon. From [KLI 15]*

11.2.1.1. *Trenches perpendicular to faults*

In a paleoseismological study, it is most common to dig trenches perpendicular to faults. Regardless of the type of fault (normal, reverse or strike-slip), a trench that is perpendicular to the structure is the conventional approach to establish the chronology of earthquakes. Trench analysis is based on the identification of different traces of deformations, which are visible in the stratigraphy (see Figure 11.2), and, notably, the identification of colluvial wedges (see Figure 11.3), which indicate the occurrence of an earthquake. Although each trench is unique, it can still be noted that there are several characteristics specific to each type of deformation:

– Normal faults: normal faults are particularly conducive to a paleoseismological approach. Each earthquake that ruptures the surface will create a vertical escarpment that may partially collapse during the earthquake to form a characteristic colluvial wedge at the foot of the escarpment (see Figure 11.3). In the case of normal faults, if the stratigraphy is detailed enough, or by using the size of the colluvial wedge [KLI 03], it is possible to assess the amplitude of the co-seismic displacement at the trench site (see inset Figure 11.3). In terms of dating, we will give priority to samples collected just below or just above the colluvial wedge, as this colluvial wedge is most likely to incorporate older material derived from faulted units.

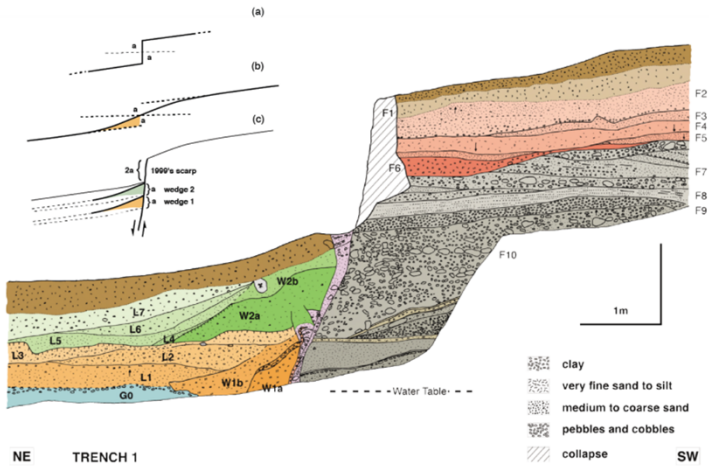

Figure 11.3. *Example of colluvial wedges (W1a, W1b and W2a) in the case of a normal fault. Their size may be used to locally deduce the amplitude of the vertical deformation associated with the ancient earthquakes. Adapted from [KLI 03]*

– Reverse faults: reverse faults can be difficult to interpret in paleoseismology, since in most cases the upthrusting wedge collapses in front of the fault escarpment, thereby masking it. Further, in the case of successive ruptures, a new rupture will most often go across and deform the deposits associated with earlier earthquakes [VAR 14], which can make the paleoseismological record difficult to interpret.

– Strike-slip faults: unlike normal or reverse faults, in the case of a strike-slip fault the main displacement occurs perpendicular to the trench and is therefore not directly visible. In this case, seismic horizons are thus identified chiefly from the observation of secondary deformations, most often vertical, which are due to the fact that the deformation is generally never purely strike-slip in nature. In the case of strike-slip faults, the choice of the site also often leads to the selection of a site where we know there will be vertical deformation in addition to the strike-slip deformation, like in a pull-apart basin, for instance. An important consequence of this is that it is generally impossible to use vertical offsets that are visible in a trench across a strike-slip fault for any information on the actual amplitude of the deformations associated with past earthquakes and, therefore, on the magnitudes of these earthquakes. Furthermore, in the case where the selected site corresponds to a relay zone, we must also consider the possibility that all the faults are not activated in each earthquake, or, on the contrary, that the faults within the relay are activated each time that one fault strand of the relay is activated.

11.2.1.2. *Trenches parallel to faults*

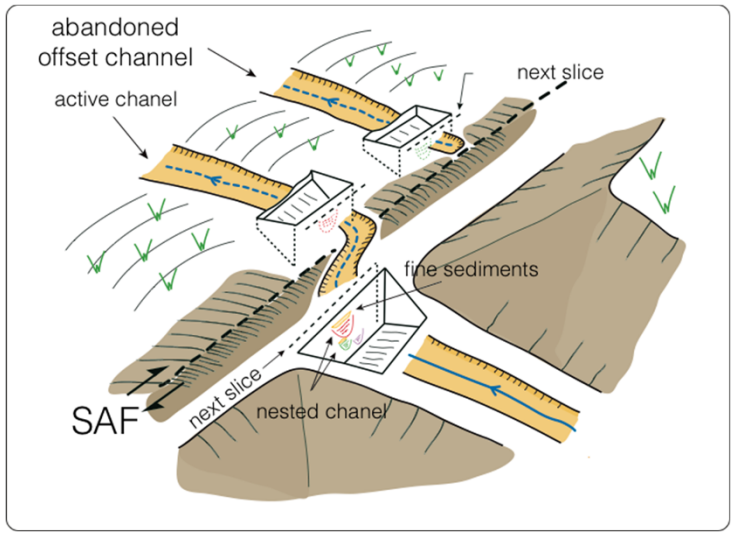

Figure 11.4. *Example of a 3D trench. In the upstream part, the channels are superimposed in the same riverbed. In the downstream part, each channel is individualized. During an earthquake, the flow in the upstream section may be blocked by the escarpment. This temporarily creates a pond, with the accumulation of sediments, until the erosion is large enough to hollow out a new downstream channel. The series of trenches on either side of the fault makes it possible to determine the geometry of the channels and accurately measure the horizontal displacement for each channel. In very favorable cases, it is possible to find several consecutive channels in the downstream compartment*

In the case of strike-slip faults, trenches can also be created parallel to the fault. The goal is to determine a time series of earthquakes and also determine, for each earthquake, the associated horizontal displacement. The principle consists of identifying a morphological marker that was horizontally offset during an earthquake and determining the initial geometry of this marker using trenches (see Figure 11.4). For example, in the case of the channel of a river flowing across a fault: during an earthquake, the downstream part of this channel is offset and when the offset becomes too large, the channel is abandoned by the river, which hollows out a new active channel opposite the upstream part. The abandoned channel (beheaded channel) will then be partially filled and buried by the sediments transported through surface runoff and wind transport. This process can repeat several times, leading to a series of abandoned channels downstream of the fault.

Reconstructing the detailed geometry of these channels makes it possible to measure the horizontal offset associated with each of these earthquakes. In general, this kind of approach requires many parallel trenches on either side of the fault, as well as perpendicular trenches that make it possible to follow and correlate the stratigraphic units between trenches. In this case, we speak of 3D trenches [WEC 18].

11.2.2. *Fault escarpments in the context of limestone*

In the context of a limestone environment, normal faults offer a particular opportunity to determine the history of ancient earthquakes. Indeed, when a normal fault that intersects a limestone massif is activated, the fault escarpment may be preserved intact for a long time, unlike an escarpment formed in looser material. In many cases, it is even possible to find the trace of accumulated escarpments that recorded the occurrence of several successive earthquakes [BEN 02] (see Figure 11.5). This is notably true in the Mediterranean basin, where limestone environments are particularly abundant.

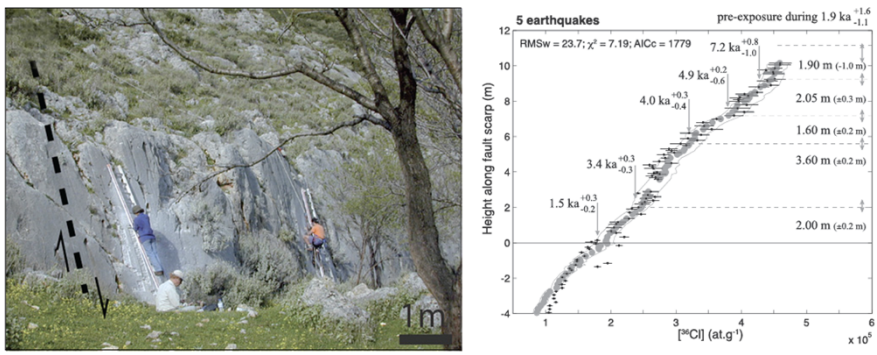

Figure 11.5. *The illustration on the left shows a limestone fault escarpment during a sampling session. A high density of samples along the escarpment is critical for obtaining the required resolution to distinguish between successive events. On the right, the graph indicates the concentration of the $_{36}Cl$ isotope depending on the height of the escarpment. Each bump in the samples indicates an ancient earthquake. The gray dots in the background correspond to a model of the evolution of the escarpment. Modified from [SCH 11, BEN 14]*

Several techniques have been tried, with mixed results, to distinguish between the different earthquakes that contributed to the creation of a visible, cumulative escarpment. For instance, the evolution of the roughness [STA 19], or the content of

some chemical species, depending on the height along the escarpment [MAN 10]. To date, the most successful approach consists of densely sampling the fault escarpment to measure the duration of exposure of the different parts of the escarpment to cosmic rays, using the cosmogenic isotope ^{36}Cl (see Chapter 10). Since the cumulative escarpment forms discretely during successive earthquakes, the exposure age, derived from the measurements of ^{36}Cl concentrations, should ideally increase from the base to the summit of the escarpment in steps, with each step corresponding to a new section of the escarpment being exposed during an earthquake. In reality, identifying these levels can be especially difficult, notably because cosmic rays penetrate the ground at the foot of the escarpment to a small depth and can cause a pre-exposure of the fault mirror. We must therefore use a modeling step to construct the earthquake sequences along the limestone escarpments [TES 19].

11.2.3. *Paleoseismology and satellite imagery*

While the initial objective of paleoseismology is to construct time series in order to be able to study the return times of earthquakes, aerial imagery, especially satellite imagery, makes it possible to specifically study the co-seismic deformations associated with ancient earthquakes, in particular for strike-slip earthquakes. In the case where the fault studied is in a climatic context where the erosion is not too great compared to the amplitude of the co-seismic deformations, it is quite possible to identify cumulative deformations associated with several earthquakes (see Chapter 10). This has been done for a long time in active tectonic studies, to quantify the average and long-term deformation rates [LEB 10]. The very high resolution of civil optical satellite data, with sub-metric pixels, now enables an accurate identification of details in ground morphology for a site with reasonably low plant cover. The most recent satellite constellations, which routinely capture multi-stereo images, also make it possible to locally calculate the topographic cover with a resolution that is of the same order as the resolution of source images that is, a few meters, without needing to physically visit the site. In the case of strike-slip faults, for which this technique is most often used, it is possible to use these images, and the deduced topography, to systematically measure the horizontal offset of the geomorphological markers perpendicular to the fault (see Chapter 10). These markers, also called *piercing lines*, are typically channels, ridge lines or edges of alluvial terraces, which are more or less oblique to the fault. Each successive earthquake will offset the parts on either side of the fault, going so far as to completely disconnect them when the accumulated offset becomes larger than the characteristic size of the marker. In the case of an active river channel, the river will then recreate a new channel in its

downstream part, in order to continue flowing, which will create a new marker that is ready to record the next offset. By identifying these markers on images and in the topography, it is possible to reconstruct the original geometry of the markers in each case. Since the markers may potentially be of different ages, the cumulative offsets associated with the different markers may be different. It is therefore possible to find out the cumulative offset associated with a number of different earthquakes and deduce from this the slip for a given earthquake. Each offset and its uncertainty can be described as a probability distribution, generally a Gaussian distribution, centered on the central offset value, whose limits are the maximum and minimum acceptable offsets for the marker concerned. For each fault section, it is then possible to sum up the probabilities associated with each measurement to calculate the *cumulative offset probability density function* for the set of measurements. In the case where the slip distribution along the same fault section is not too scattered for a given earthquake, the probability density curve shows peaks that make it possible to directly identify the offsets associated with ancient earthquakes. On the contrary, if there is large scattering, it may be more difficult to identify different peaks, beyond the peak corresponding to the most recent earthquake, and it may be necessary to carry out additional processing to separate the different data [KUR 18]. If the slip tends to repeat identically from one earthquake to another, we then speak of a characteristic slip [SIE 96, KLI 11].

11.3. Paleoseismology for faults in a marine context

The case of faults in the sea, especially faults associated with subduction zones, is very different from continental faults because, in general, we cannot directly observe the fault escarpment, which is underwater, often more than several kilometers from the coast. We must, therefore, use more indirect observations to study the history of earthquakes in this type of context. Two distinct approaches were developed and are described in the following sections. On the one hand, in the specific case of subductions, it is possible to study the vertical movements of the upper plate during a seismic cycle, especially during earthquakes. These vertical movements are expressed through a variation in the relative sea level at the coast that directly affects the flora and fauna living in coastal zones. On the other hand, in the case of subductions but not limited to them, it is possible to examine turbidity deposits, which can be found within and at the end of the submarine canyons that mark the continental talus. In some specific cases, these turbidity deposits can be associated with slope destabilizations caused by rather distant seismic sources.

11.3.1. *Subduction and vertical movements*

In subduction zones, the upper plate is vertically deformed in different ways depending on where you stand in the seismic cycle and on the distance from the subduction trench (see Figure I.1 in the Introduction). Over the inter-seismic period that corresponds to the tectonic loading, due to the fault being locked, the part closest to the subduction trench sinks down, causing progressive flooding in all coastal zones in this region. At the same time, at the rear of the subduction zone proper, the elastic response of the upper plate is expressed by an uplift and the concerned zone possibly coming out of the water. During the earthquake, the stresses are brutally released on the subduction front and the zone closest to the trench is uplifted almost instantaneously, while the rear zone sinks down just as quickly and may be invaded by seawater. If the deformation was perfectly elastic, the set of deformations would be perfectly compensated and would leave no trace in the topography. However, this is only partially true. From the paleoseismological point of view, therefore, we look for markers that could record the rapid variations in altitude, with adequate temporal resolution to be able to accurately date past earthquakes.

11.3.1.1. *Using coral as paleo-altimeters*

One approach that has been proven to be very successful is studying corals that live in shallow water. This technique was initially developed in the Pacific [TAY 87] and was then widely developed along the Indonesian subduction [PHI 17]. This subduction zone is characterized by a string of islands that are relatively close to the subduction trench, located in the zone that undergoes large deformation both in the inter-seismic period, as well as during earthquakes. These islands are surrounded by coral reefs where there are many species of coral growing, including a specific microatoll species called *Porites lutea*. These corals live at a specific depth, where they develop by growing concentrically, up to more than 1 m in diameter (see Figure 11.6). For each micro-coral, it is possible to define a minimum water depth called the *Highest Level of Survival (HLS)*. Above this depth, the parts of the microatoll that are too exposed to air and light die out. These microatolls are thus excellent indicators of the relative variation in altitude with respect to the sea level that is considered to be constant. During a subsidence event, the microatoll sinks and is therefore forced to grow upward to stay close enough to the surface. Conversely, in the event of an elevation, the upper part of the microatoll may be exposed and die, while the microatoll continues to grow laterally. By sampling coral slices along a radius of the microatoll and studying the shape of these samples, it is possible to study the phases when the coral grew upward and when it grew laterally, as well as the parts that died when part of the microatoll was lifted

out of the water. All of this helps to reconstruct the local curve of the variation in sea level with respect to the coral. This variation in sea level can then be interpreted directly as the vertical movement of the coral, in response to tectonic deformations. These vertical movements can then be combined with U/Th dating of the coral to place the variations in altitude of each microatoll within an absolute timeframe. By studying the history of many microatolls located on different islands along the Indonesian subduction, it was possible to reconstruct the history of earthquakes along this subduction over the last millennium to see how the earthquakes were organized spatially and temporally along this fault, and especially to test the hypothesis of a seismic super-cycle [PHI 17].

11.3.1.2. *Other markers of changes in sea level*

While coral has been largely used to study the Indonesian subduction, as well as a few other cases of subduction, their short lifespan does not allow the study of very long periods, which is a major handicap when studying a subduction zone whose convergence velocity is not very high. Further, the very existence of microatolls is strongly related to environmental conditions, like water temperature, which are not always conducive to coral growth. Consequently, other markers have been used to characterize vertical movements. Most often, the methods employed are directly adapted to the specific cases being studied and the work cited here must be considered as sources of inspiration rather than specific methods that can be directly applied in all contexts.

In some cases, it has been possible to find other living beings, apart from corals, that are just as sensitive to sea levels. For example, the case of the bioconstruction of coastal platforms by vermetid colonies that can be dated using carbon-14 and which made it possible to identify the major earthquake in 551 CE in the eastern Mediterranean basin [ELI 07]. On the contrary, along certain rocky coastal zones, living organisms lead to increased erosion in the foreshore zone, also called the intertidal zone, which ends up creating a marine notch, a characteristic of the average sea level at a given moment. In active tectonic zones, it is possible to identify marine notches that are today located above the average tidal level (see Figure 11.7), and which are proof of the rapid uplifting of the coast during earthquakes [BOU 15]. Similarly, a series of marine terraces have been identified along the coasts where there are active faults (subduction or normal faults) that can be used to characterize the vertical displacement associated with earthquakes [KOM 17].

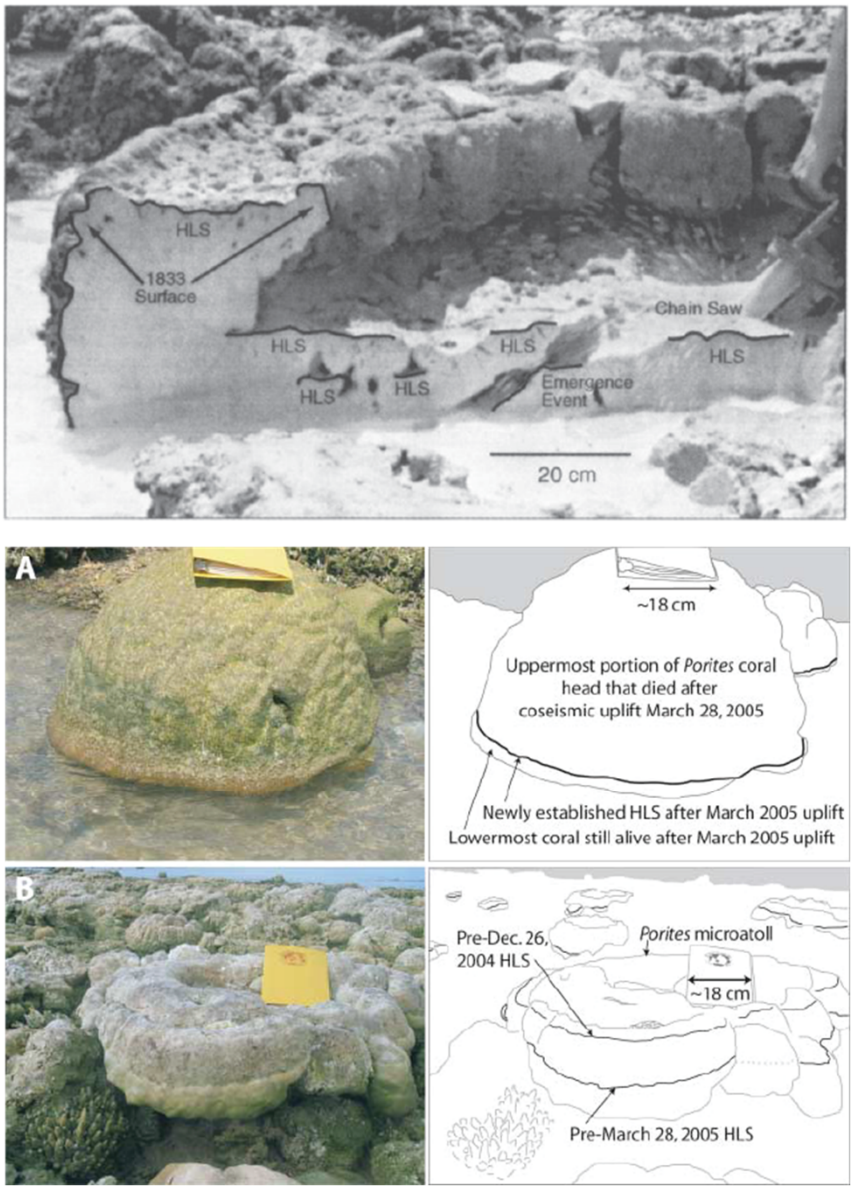

Figure 11.6. *Examples of coral microatolls affected by vertical movements due to subduction activity. The upper panel shows how the coral morphology varies depending on the variation in the HLS. The lower panel directly shows the aftermath of the coastal uplift associated with the 2004 and 2005 earthquakes in Indonesia. Modified from [ZAC 99, BRI 06]*

In the case where the coastal zone is not made up of cliffs, the vertical movements related to the subduction earthquakes can cause an instantaneous migration of the boundary between the zone irrigated by continental freshwater and seawater. These variations have a noticeable impact on the flora in these boundary zones. A prime example of such a change is the sudden death of coastal forests in the Cascades, in western North America, following a co-seismic subsidence event that caused these coastal zones to be flooded by seawater [ATW 92]. Typically in these zones, it is possible to observe the alternation of continental and marine deposits, in the stratigraphic sections, which indicate the different phases of the seismic cycle. These different deposits are most often rich in organic matter than can be dated using carbon-14.

Figure 11.7. *Succession of marine notches along a rocky coast of the island of Rhodes, in the eastern Mediterranean, associated with the uplift of the coast during historical and prehistoric earthquakes. Modified from [STI 14]*

11.3.2. *Turbidite record of earthquakes*

Certain coastal zones have a limited continental shelf followed by a continental talus that descends into a zone that is more distal from the coast. This talus may be traversed by submarine canyons that are generally perpendicular to the slope of the talus. The continental shelf, as well as the upper parts of the canyons are zones that are particularly prone to the storage of sand and silty sediments resulting from the

discharge of rivers that empty into the sea near these points. During large-magnitude earthquakes close to these coastal zones, ground vibrations can destabilize these sediments, which flow down the slopes in the form of submarine avalanches called "turbidity currents" or "turbidites". Most often, these turbidity currents follow the course of the canyons and the finest deposits may be transported over hundreds of kilometers in the abyssal plain. By coring sediment deposits from these canyons and basins at the foot of the continental talus, it is possible to recognize the turbidite deposits with a characteristic sedimentary signature. They are generally marked by erosive contact at their base and then a granoclassified sequence that includes a sequence of sand evolving toward silts and clays. The different turbidite sequences are generally separated by hemipelagic units that characterize a calmer deposition environment. These hemipelagic deposits may be rich in foraminifera, which can be dated using carbon-14, in addition to other organic elements (plant debris, charcoals, shell fragments) which are directly included in the turbidite deposit. The chief difficulty with this kind of an approach is being able to determine the seismic origin of the turbidity deposit with respect to turbidity that could have been triggered by another process. The non-seismic processes that could trigger turbidity currents include storms, with the influence of waves that can be felt up to a depth of a few hundred meters and could locally trigger turbidity currents, and exceptional sedimentary discharges linked to bad weather anywhere in the river basin of rivers flowing into the sea. A classic solution to identify the different processes is increasing the number of sediment cores along the zones of interest to differentiate between turbidites that appear local and temporally isolated, and the turbidites that can be correlated between many sediment cores along the coast and which seem to have been produced in the same time window. The latter kind of sediment is more certainly the signature of a large-magnitude earthquake that affected a significant part of the coast, while isolated turbidites are generally from other, more local causes. This type of approach consists of identifying successive turbidities in marine cores and has notably seen certain success along the western North American coast, in the Cascades region, where this approach made it possible to identify over 40 prehistoric earthquakes that occurred during the Holocene [GOL 07].

11.4. Indirect effects of earthquakes and paleo-seismicity

The different markers discussed until now are directly related to the activity of a specific structure and, in general, there is a direct correlation between a ground observation and the occurrence of an earthquake. However, there are many other, less direct markers that have also been used on and off to gain information on past seismic activity in some regions. In general, these markers do not directly record the rupture on the ground surface, as may be seen in a trench, but are more sensitive to

ground acceleration induced by the passage of seismic waves. The direct corollary is that in a region where there may be many seismogenic sources. It can be difficult or even impossible to use secondary deformations alone to decide which seismic source was responsible for the observed deformations. Further, we often find a case where a nearby earthquake of moderate magnitude will have the same effect as a larger magnitude earthquake occurring farther way, which again complicates the association between the observations and specific seismogenic sources. Among the observations typically used, we can list in particular (a non-exhaustive list) those that concern liquefaction in a broader sense:

– Similar to the triggering of turbidity currents in a marine context, ground acceleration associated with the passage of seismic waves can destabilize sediments on slopes in lakes and cause landslides. The very oscillation of the water in the lake, which could even generate a wave called a seiche, which breaks on the shore of the lake, could contribute to such destabilization. These landslides in a lacustrine environment are most often identified from the shallow seismic recordings, where they appear to be homogeneous (hence the name "homogeneity", also used in the marine context), unlike the more bedded sediment which is gradually deposited in a calm lacustrine environment. It is also possible to identify them in the cores, even if their sediment signature is often less distinct than in the case of marine turbidites. In certain cases, the geochemical signature of these sediments, which incorporate more terrestrial material than classic lacustrine sediments, can also be used to identify lake turbidite facies [AVŞ 15]. For instance, this kind of approach was successfully used to create seismicity catalogs based on observations in alpine lakes [BEC 09]. However, most often it is still difficult to identify the specific tectonic structures that were responsible for the earthquakes observed.

– In some cases, the sediments may simply be deformed and wrinkled while sliding on the slopes, without leading to a total destabilization and landslide. This is especially the case with sediments called varves that have a marked seasonal differentiation, with mechanical properties that are sufficiently different to promote decoupling and the sliding of one unit with respect to the surrounding units. Because of these differences in property, it is also possible to observe the liquefaction of one unit due to the fluid overpressure during the passage of waves, if this unit is restricted between impermeable units that do not allow the fluid to migrate in response to pressure changes. An example of this kind of disturbance, called seismite, can be seen in the Dead Sea basin, where tens of meters of varved lacustrine sediments are visible on outcrops, with alternation between the sediments in a normal position and units that are either pleated or show liquefaction indices (see Figure 11.8). The systematic mapping of these different horizons, coupled with U/Th dating of the aragonite contained within these varves, makes it possible to precisely reconstruct a part of the seismic history of the Dead Sea basin over the past

2,500 years, although even here it is still often difficult to determine, with certainty, the location of the seismic source responsible for the observed deformations [KEN 01].

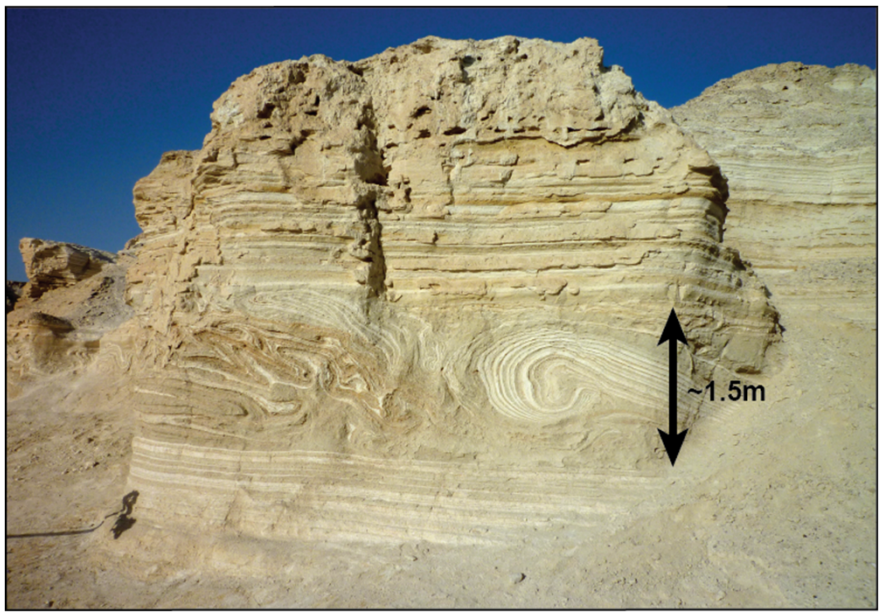

Figure 11.8. *Seismites in the Dead Sea basin. Flat, deposited varves surround the deposit that was disturbed by the seismic activity of the Dead Sea fault. Dating the units located directly above and below the deformed sequence makes it possible to narrow down the date of the event responsible for this deformation. Photo © Y. Klinger*

– In the same category, it is also important to mention the direct search for a liquefaction pattern, including in non-lacustrine contexts. In the case where there is a permeable, fluid-rich geological unit, typically sand, surrounded by significantly more impermeable units (typically clays), the passage of seismic waves can locally induce overpressure in the fluid that cannot migrate into the neighboring units. This overpressure can result in a destructuring of the unit containing the fluids with the formation of sedimentary figures that reflect the movement of turbulent fluids in the concerned layer. If there is sufficient overpressure and the overpressure layer is close to the surface, it is possible to puncture the covering layer to allow the fluid to be ejected toward the surface, creating sand blows on the ground surface. A stratigraphic level where we find many sand blows may therefore be interpreted as a seismic horizon, similar to rupture terminations in a trench. This type of approach

was used, for example, to study past seismic activity in the New Madrid zone in the United States [TUT 01].

Finally, the speleothems (chiefly stalactites and stalagmites) located in caves near active structures were also used to characterize past seismic activity. The main principle is that the speleothems can break after the effect of acceleration associated with the passage of seismic wave. Because speleothems can be dated in many ways, they show good potential for use in paleoseismology. If we can find caves where an entire population of speleothems broke at the same time, it is then possible to relate this observation with the occurrence of an earthquake in the zone being studied [KAG 05]. The chief difficulty, just as with liquefaction patterns, is that it is often difficult to characterize the seismic source with certainty.

11.5. References

[ATW 92] ATWATER B.F., MOORE A.L., "A tsunami about 1,000 years ago in Puget Sound, Washington", *Science*, vol. 258, pp. 1614–1617, 1992.

[AVŞ 15] AVŞAR U., HUBERT-FERRARI A., DE BATIST M. et al., "Sedimentary records of past earthquakes in Boraboy Lake during the last ca 600 years (North Anatolian Fault, Turkey)", *Palaeogeography, Palaeoclimatology, Palaeoecology*, vol. 433, pp. 1–9, 2015.

[BEC 09] BECK C., "Late Quaternary lacustrine paleo-seismic archives in north-western Alps: Examples of earthquake-origin assessment of sedimentary disturbances", *Earth-Science Reviews*, vol. 96, pp. 327–344, 2009.

[BEN 02] BENEDETTI L., FINKEL, R., PAPANASTASSIOU, D. et al., "Post-glacial slip history of the Sparta fault (Greece) determined by Cl-36 cosmogenic dating: Evidence for non-periodic earthquakes", *Geophys. Res. Lett.*, vol. 29, pp. 1–4, 2002.

[BEN 14] BENEDETTI L., VAN DER WOERD J., "Cosmogenic nuclide dating of earthquakes, faults, and toppled blocks", *Elements*, vol. 10, pp. 357–361, 2014.

[BOU 15] BOULTON S., STEWART I., "Holocene coastal notches in the Mediterranean region: Indicators of palaeoseismic clustering?", *Geomorphology*, vol. 237, pp. 29–37, 2015.

[BRI 06] BRIGGS R.W., SIEH, K., MELTZNER, A.J. et al., "Deformation and slip along the Sunda megathrust in the great 2005 Nias-Simeulue earthquake", *Science*, vol. 311, pp. 1897–1901, 2006.

[ELI 07] ELIAS A., TAPPONNIER, P., SINGH, S.C. et al., "Active thrusting offfshore Mount Lebanon: Source of the tsunamigenic, 551 AD Beirut-Tripoli earthquake", *Geology*, vol. 35, pp. 55–758, 2007.

[GOL 07] GOLDFINGER C., MOREY, A.E., NELSON, C.H. et al., "Rupture lengths and temporal history of significant earthquakes on the offshore and north coast segments of the Northern San Andreas Fault based on turbidite stratigraphy", *Earth and Planet. Sci. Lett.*, vol. 254, pp. 9–27, 2007.

[KAG 05] KAGAN E.J., AGNON A., BAR-MATTHEWS M. et al., "Dating large infrequent earthquakes by damaged cave deposits", *Geology*, vol. 33, pp. 261–264, 2005.

[KEN 01] KEN-TOR R., AGNON, A., ENZEL, Y. et al., "High-resolution geological record of historic earthquakes in the Dead Sea basin", *J. Geophys. Res.*, vol. 106, pp. 2221–2234, 2001.

[KLI 03] KLINGER Y., SIEH, K., ALTUNEL, E. et al., "Paleoseismic evidence of characteristic slip on the western segment of the North Anatolian Fault, Turkey", *Bull. Seism. Soc. Am.*, vol. 93, pp. 2317–2332, 2003.

[KLI 11] KLINGER Y., ETCHEBES M., TAPPONNIER P. et al., "Characteristic slip for five great earthquakes along the Fuyun fault in China", *Nature Geoscience*, vol. 4, pp. 389–392, 2011.

[KLI 15] KLINGER Y., LE BÉON M., AL-QARYOUTI M., "5000 yr of paleoseismicity along the southern Dead Sea fault", *Geophys. J. Int.*, vol. 202, pp. 313–327, 2015.

[KOM 17] KOMORI J., SHISHIKURA M., ANDO R. et al., "History of the great Kanto earthquakes inferred from the ages of Holocene marine terraces revealed by a comprehensive drilling survey", *Earth and Planet. Sci. Lett.*, vol. 471, pp. 74–84, 2017.

[KUR 18] KURTZ R., KLINGER Y., FERRY M. et al., "Horizontal surface-slip distribution through several seismic cycles: The Eastern Bogd fault, Gobi-Altai, Mongolia", *Tectonophysics*, vol. 734, pp. 167–182, 2018.

[LEB 10] LE BÉON M., KLINGER, Y., AL-QARYOUTI, M. et al., "Early Holocene and late Pleistocene slip rate of the southern Dead Sea fault determined by 10Be cosmogenic dating of offset alluvial deposits", *J. Geophys. Res.*, vol. 115, 2010.

[LIU 15] LIU-ZENG J., SHAO, Y., KLINGER, Y. et al., "Variability in magnitude of paleoearthquakes revealed by trenching and historical records, along the Haiyuan Fault, China", *J. Geophys. Res.*, vol. 120, pp. 8304–8333, 2015.

[MAN 10] MANIGHETTI I., BOUCHER E., CHAUVEL C. et al., "Rare earth elements record past earthquakes on exhumed limestone fault planes", *Terra Nova*, vol. 22, pp. 477–482, 2010.

[PHI 17] PHILIBOSIAN B., SIEH, K., AVOUAC, J.-P. et al., "Earthquake supercycles on the Mentawai segment of the Sunda megathrust in the seventeenth century and earlier", *J. Geophys. Res.*, vol. 122, pp. 642–676, 2017.

[RIZ 19] RIZZA M., BOLLINGER, L., SAPKOTA, S.N. et al., "Post earthquake aggradation processes to hide surface ruptures in thrust systems: The M8. 3, 1934, Bihar-Nepal earthquake ruptures at Charnath Khola (Eastern Nepal)", *J. Geophys. Res.*, vol. 124, pp. 9182–9207, 2019.

[SCH 07] SCHARER K.M., WELDON R.J., FUMAL T.E. et al., "Paleoearthquakes on the southern San Andreas fault, Wrightwood, California, 3000 to 1500 BC: A new method for evaluating paleoseismic evidence and earthquake horizons", *Bull. Seism. Soc. Am.*, vol. 97, pp. 1054–1093, 2007.

[SCH 11] SCHLAGENHAUF A., MANIGHETTI, I., BENEDETTI, L. et al., "Earthquake supercycles in central Italy, inferred from ^{36}Cl exposure dating", *Earth and Planet. Sci. Lett.*, vol. 307, pp. 487–500, 2011.

[SIE 96] SIEH K., "The repetition of large-earthquake ruptures", *Proc. Natl. Acad. Sci.*, vol. 93, pp. 3764–3771, 1996.

[STA 19] STAHL T., TYE A., "Schmidt hammer and terrestrial laser scanning (TLS) used to detect single-event displacements on the Pleasant Valley fault (Nevada, USA)", *Earth Surface Processes and Landforms*, vol. 45, no. 2, pp. 473–483, 2019.

[STI 14] STIROS S.C., BLACKMAN D.J., "Seismic coastal uplift and subsidence in Rhodes Island, Aegean Arc: Evidence from an uplifted ancient harbour", *Tectonophysics*, vol. 611, pp. 114–120, 2014.

[TAY 87] TAYLOR F.W., FROHLICH C., LECOLLE J. et al., "Analysis of partially emerged corals and reef terraces in the central Vanuatu arc: Comparison of contemporary coseismic and nonseismic with Quaternary vertical movements", *J. Geophys. Res.*, vol. 92, pp. 4905–4933, 1987.

[TES 19] TESSON J., BENEDETTI L., "Seismic history from in situ 36Cl cosmogenic nuclide data on limestone fault scarps using Bayesian reversible jump Markov chain Monte Carlo", *Quaternary Geochronology*, vol. 52, pp. 1–20, 2019.

[TUT 01] TUTTLE M.P., "The use of liquefaction features in paleoseismology: Lessons learned in the New Madrid seismic zone, central United States", *Journal of Seismology*, vol. 5, pp. 361–380, 2001.

[VAR 14] VARGAS G., KLINGER, Y., ROCKWELL, T.K. et al., "Probing large intraplate earthquakes at the west flank of the Andes", *Geology*, vol. 42, pp. 1083–1086, 2014.

[WEC 18] WECHSLER N., ROCKWELL T.K., KLINGER Y., "Variable slip-rate and slip-per-event on a plate boundary fault: The Dead Sea fault in northern Israel", *Tectonophysics*, vol. 722, pp. 210–226, 2018.

[ZAC 99] ZACHARIASEN J., SIEH K., TAYLOR F. et al., "Submergence and uplift associated with the giant 1833 Sumatran subduction earthquake: Evidence from coral microatolls", *J. Geophys. Res.*, vol. 104, pp. 895–919, 1999.

[ZIE 15] ZIELKE O., KLINGER Y., ARROWSMITH J.-R., "Fault slip and earthquake recurrence along strike-slip faults: Contributions of high-resolution geomorphic data", *Tectonophysics*, vol. 638, pp. 43–62, 2015.

12

Analog Modeling of the Seismic Cycle and Earthquake Dynamics

Stéphane DOMINGUEZ
Géosciences Montpellier, University of Montpellier, France

12.1. Introduction

When studying the seismic cycle in the context of subduction, we come up against several limiting factors related to the difficulties encountered when studying the kinematics of deformations in the marine context, to accessing the deep source of earthquakes, or when integrating the characteristic timescales for deformation processes that extend from a second to thousands of years (see Introduction, Chapters 1, 2, 3, 10, 11). First-order scientific questions remain unanswered, such as the role of friction heterogeneities on inter-plate mechanical and seismic coupling (see Chapter 4), the role played by the brittle-ductile transition, marking the down-deep limit of the seismogenic zone, on the variability in the inter-seismic phase (see Introduction and Chapter 6) and on the nucleation of megathrust subduction earthquakes (see Introduction and Chapter 5). The scientific analysis and use of geophysical and seismological data on subduction earthquakes are chiefly based on the use of analytical and numerical models that enable the study of deformation processes and their couplings. In parallel, and since the first applications of the seismic cycle theory (see Introduction), several experimental approaches have been developed to study the dynamics of earthquakes and the coupling between the physical properties of the faults and the rheology of the lithosphere [BRA 66,

For a color version of all of the figures in this chapter, see www.iste.co.uk/rolandone/seismic.zip.

The Seismic Cycle,
coordinated by Frédérique ROLANDONE.

The Seismic Cycle: From Observation to Modeling,
First Edition. Frédérique Rolandone.

BUR 67, BRU 73, OHN 73]. Other experimental studies have examined rupture dynamics to study the role of static and dynamic friction on fault slip kinematics, on seismic wave generation and propagation and on the production of heat through friction [ANO 94, 99]. More recently, Rosakis et al. [ROS 99] (Caltech) developed several experimental devices to study seismic rupture dynamics. Using a very high-speed camera (1 million images/second) they studied rupture propagation in a polymeric composite, Homalite. Their work made it possible to reveal deformation processes that explained the super-shear co-seismic velocities observed during major earthquakes [ROS 99]. Over the last decade, a new generation of analog models emerged (see [ROS 17] for a complete review). These models, based on more complex and better-dimensioned rheologies, seek to approximate the natural cases studied through more realistic simulations of deformation processes associated with the different phases of the seismic cycle. This work, which is currently at the forefront of research innovation, is carried out mainly by three European laboratories: the Geo-Forschungs-Zentrum in Potsdam (Germany), the Dipartimento Scienze Geologiche at the University of Roma TRE (Italy) and at Géosciences Montpellier (France). The German and Italian experimental laboratories have developed experimental models for the subduction zone [COR 17, ROS 19], while in France, several 2D and 3D analog models of a strike-slip fault and subduction zone are currently being operated [CAN 17, 20].

12.2. Principle and methodology

The experimental device used below to illustrate the scientific contributions of analog modeling corresponds to the 2D subduction model developed at Géosciences Montpellier [CAN 20]. It is made up of a 2 m long aluminum structure, supporting a fixed, inclined PVC plate atop which rest the various elements of the model (Figure 12.1). The part representing the subducting oceanic crust is fixed on a flexible aluminum plate and slides on the PVC plate via viscous contact. It is pulled at a low and constant velocity (0.5–2 cm/h) under a vertical rigid backstop by a computer-controlled mechanical system. The part of the model representing the upper plate has a general prismatic shape. Its frontal part rests on the subducting plate and its rear part on a reservoir of viscous material. It is also fixed against the vertical backstop (Figure 12.1). Since the analog model is not laterally confined, edge effects are absent.

The physical and mechanical properties of the analog materials are constrained based on the scaling theory [HUB 37, WEI 93]. The spatial dimensioning is generally imposed by considering the sizes of the natural object being studied and of the experimental device, that is, here, 1 cm = 2–3 km. The model to nature ratio

(4.10E-6) is then used to determine the mechanical and physical properties of the analog materials fulfilling the similarity criteria [CAN 15, CAN 20]. The temporal dimensioning is trickier to define since the velocity of the modeled deformation processes extends over several orders of magnitude (from s to Kyr). Taking into account the mechanical properties of the model viscous layer makes it possible to define a reliable temporal dimensioning for the inter-seismic and post-seismic phases of 1 s = 5–10 years. On the other hand, the co-seismic phase must be treated separately, since it corresponds to a high-speed deformation phase and inertial forces are no longer negligible. By comparing the durations of the experimental and natural earthquakes, it is estimated that 1 s = 100–1,000 s [CAN 15].

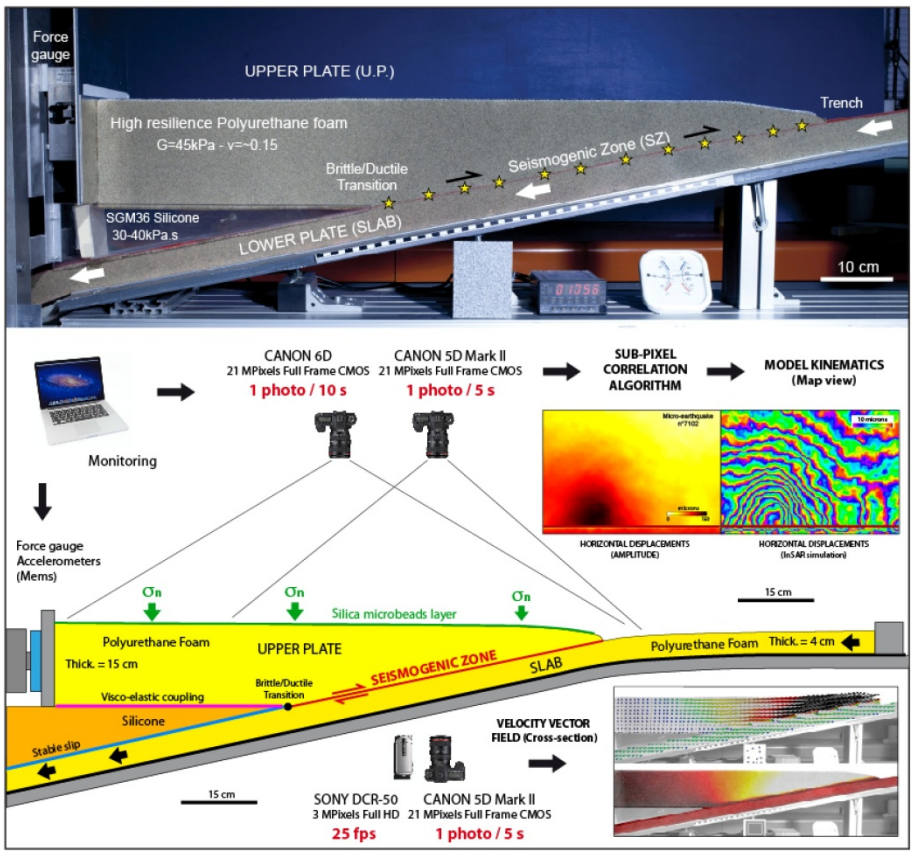

Figure 12.1. *Experimental device and protocol. The analog model is a first-order reproduction of the visco-elasto-plastic, multi-layer rheology of a subduction zone on the timescale of a seismic cycle. It allows us to reproduce all phases of deformation (pre-seismic, co-seismic, post-seismic and inter-seismic) with a striking analogy*

The rheology of the subduction model is identical to that used for the analog model for the seismic cycle on a strike-slip fault, developed earlier at Géosciences Montpellier [CAN 15, CAN 17]. It reproduces, to the first order, the mechanical and kinematic behavior of a subduction zone at the lithospheric scale. The visco-elastic rheology of the upper-plate lithospheric mantle is simulated by a silicone layer (PDMS-SGM36) that has a viscosity of 30–40 kPa.s. The elasto-plastic rheology of the upper-plate crust and, of the subducting plate (slab), is simulated by a high-resilience polyurethane foam (Young's modulus of 90 kPa, shear modulus of 40 kPa and Poisson's ratio of 0.1–0.2). The brittle-ductile transition is represented by a 0.5–1 cm thick zone where the silicone impregnates the polyurethane foam, to reproduce a shear rate-dependent visco-elastic coupling. The subduction plane is made up of the contact zone between the two polyurethane plates. It is inclined by 10–11° and is 50 cm long (equivalent to 150 km). It extends 25 cm below the silicone layer. To respect the dimensioning criteria (1 cm = 2–3 km, 1 s = 5–10 years) and the technical capabilities of the experimental device, the subduction velocity can be adapted within a range of 0.5–4 μm/s (0.2–1.5 cm/h), that is approximately 2–14 cm/year in nature. The normal stress along the seismogenic zone can be modified by depositing a thin layer (~1–2 mm) of granular material on the surface of the model. The frictional properties of the seismogenic zone are adjusted (static friction = 0.5–0.7 and dynamic friction = 0.2–0.4) by covering the surfaces in contact between the upper and lower plate with a thin layer (~3 μm) of epoxy resin [CAN 15]. It is also possible to simulate the asperities along the seismogenic zone by sprinkling silica microbeads or glass powder. The kinematic evolution of the model is quantified using a very high-resolution digital photography system, using a sub-pixel spectral correlation algorithm. It makes it possible to measure the instantaneous velocity field every 5 seconds, with millimetric spatial resolution and micrometric precision. Force sensors, accelerometers and a digital camera complete the system.

12.3. Experimental results

12.3.1. *Modeling the different phases of the seismic cycle*

The inter-seismic phase is characterized by an elastic deformation that chiefly affects the upper plate, and also, to a lesser extent, the subducting plate (Figure 12.2). It is modulated by spatial and temporal variations in the interplate mechanical coupling. At first order, the subduction of the slab at a constant speed and the frictional forces along the seismic zone cause a displacement of the upper plate toward the backstop. This motion induces a progressive increase in the compressional stress in the upper plate (elastic loading) as well as an increase in the shear stress along the plate interface (seismogenic zone). As shown by the

near-linear decrease in the horizontal velocity field, the upper plate shortens horizontally, the trench retreats, while the part of the upper plate that is located above the seismogenic zone subsides following the inclination of the subduction plane (Figure 12.2). Behind the brittle-ductile transition, and above the silicone corner, the horizontal compression of the upper plate causes it to thicken and a small uplift can be measured at the surface. During the inter-seismic phase, several types of transient slips disturb the general kinematics (creep, slow slip, low-amplitude co-seismic events), mostly affecting the lower half of the seismogenic zone. These events accumulate and modify the mechanical coupling and the stress distributions in this region, thereby affecting the frictional properties along the seismogenic zone.

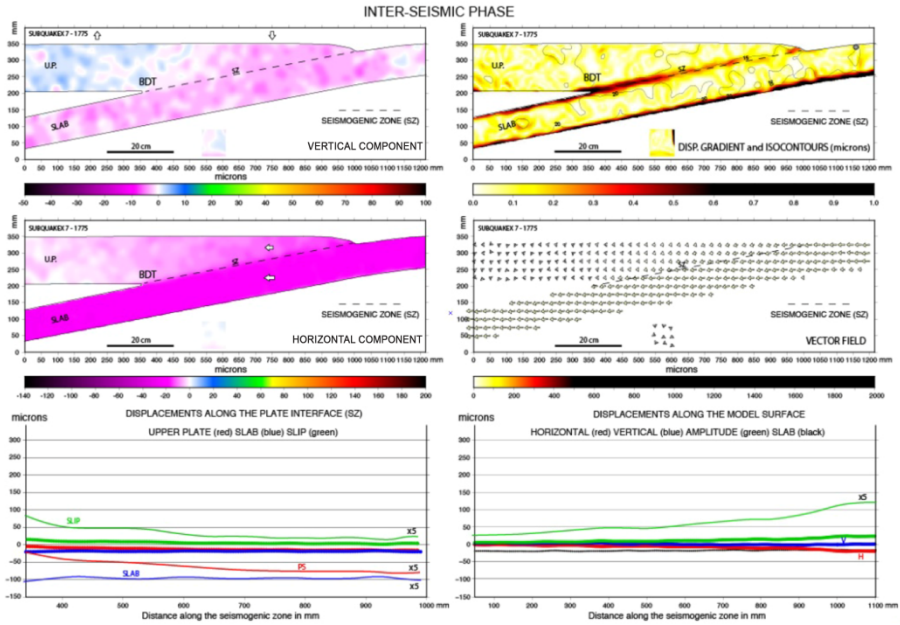

Figure 12.2. *Example of an experimental inter-seismic phase. Depending on the degree of mechanical coupling induced by frictional forces along the seismogenic zone, the upper plate undergoes elastic compressive deformation*

During the co-seismic phase (see Introduction, Chapters 1, 2, 5), the movements of the upper plate are reversed and a displacement pulse occurs toward the trench. Figure 12.3 shows a typical example of a strong co-seismic slip (megathrust subduction earthquake). As shown by the displacement profiles and the horizontal and vertical components of the velocity field, the displacements accelerate toward the trench. Along the seismogenic zone, they rapidly reach a maximum amplitude of

around 250 µm, while at the model's surface the horizontal displacements accelerate almost linearly, up to a maximum value of 270 µm near the trench. The vertical component, which has a smaller amplitude due to the low inclination (10–11°) of the subduction plane, exhibits a more complex evolution. We observe a subsidence of around 10–15 µm before the brittle-ductile transition and above the deep part of the seismogenic zone, as well as an uplift of more than 75 µm above the upper half of the seismogenic zone. These kinematics are controlled by the decompression of the upper plate, which lengthens horizontally and contracts vertically. The uplift of the front of the upper plate is controlled by the dip angle of the subduction plane and by the free-edge effect. Using the spatial scaling factor, we obtain average and maximum values for the co-seismic horizontal slip of ~30 m and ~70 m, respectively. For vertical movements on the surface, we obtain maximum subsidence and uplift values of ~5 m and ~20 m, respectively. These values are in good agreement with those measured for natural earthquakes, like in Japan [OZA 11].

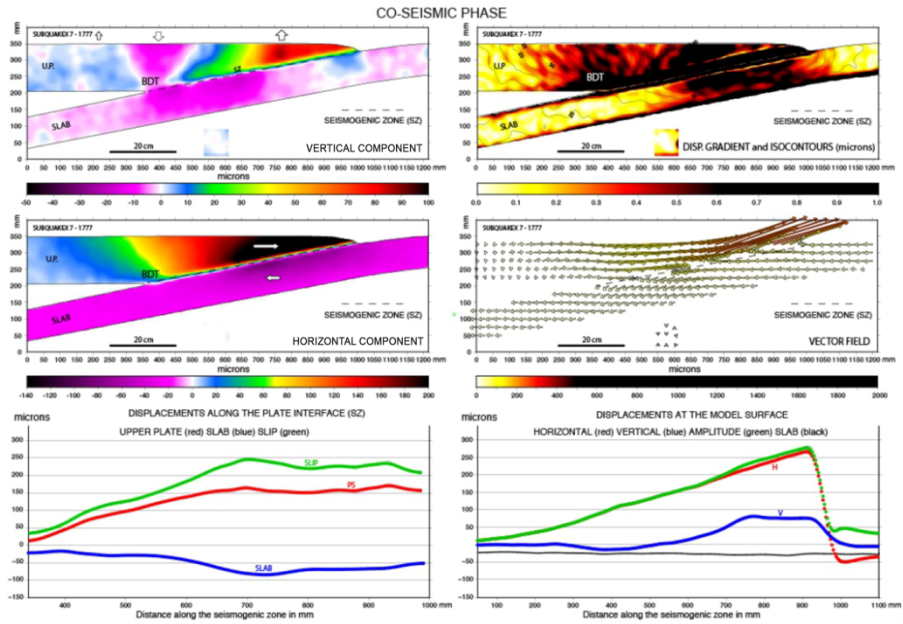

Figure 12.3. *Example of an experimental co-seismic phase. When the shear stress along the seismogenic zone becomes greater than the friction forces, a slip initiates and a part of the elastic deformation, accumulated during the inter-seismic phase, releases*

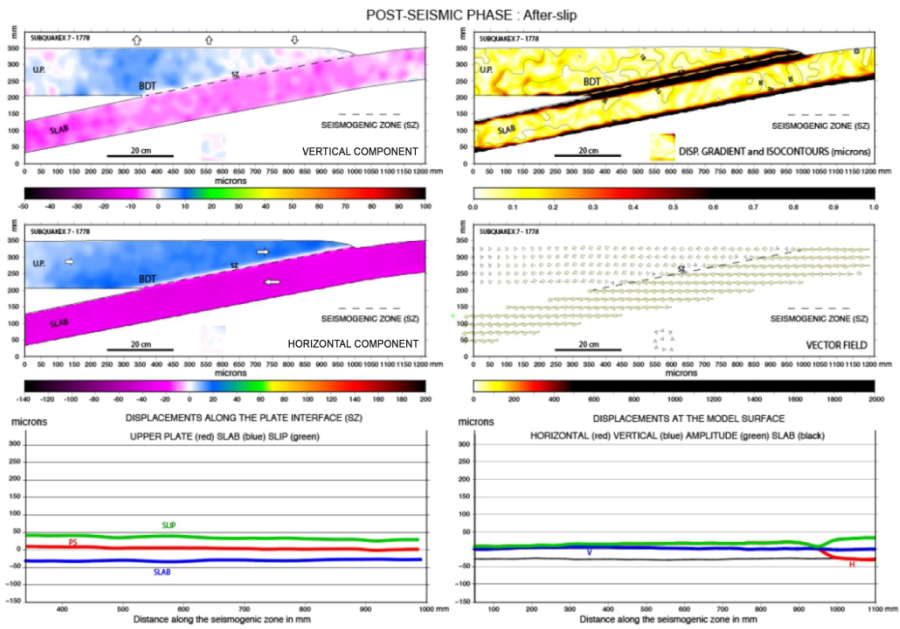

Figure 12.4. *Example of an early post-seismic phase (afterslip). The velocity field resembles that of the co-seismic phase but the displacement of the upper plate toward the trench is much smaller and more homogeneous. There is also a slight uplift zone close to the former co-seismic subsidence region*

After an experimental major earthquake (equivalent to M = 8–9), post-seismic deformation can be detected (see Introduction and Chapter 3). This phase, whose duration can exceed several tens of seconds (equivalent to hundreds of years in nature), can be divided into two parts: a short and generalized residual slip phase extending along the whole seismogenic zone (afterslip) followed by a phase of long-term visco-elastic readjustment during which the mechanical coupling between the two plates gradually increases again. During the first phase (Figure 12.4), it is seen that the upper plate continues to move homogeneously toward the trench. The cumulated amplitude of this displacement remains limited, being around one order of magnitude smaller than the co-seismic phase. Landward of the brittle-ductile transition, the upper plate moves toward the trench with a comparable velocity and a viscous shear is detected at the base of the crust (polyurethane foam). This motion tends to recompress the part of the upper plate that was stretched during the co-seismic phase causing a small uplift at the model's surface, located above the brittle-ductile transition and slightly to the rear of the co-seismic subsidence zone. This kinematics can be explained by the visco-elastic coupling between the silicone and polyurethane

foam, which buffers the decompression in the upper plate initiated by the co-seismic phase. This process delays the re-balancing of stresses in the whole region situated above and to the front of the silicone wedge. This early post-seismic phase fades quickly, in a few seconds (the equivalent of less than a few years in nature). For low to moderate earthquakes, this phase is not detected because, due to the monitoring sampling rate, it is included within the measurement of the co-seismic phase.

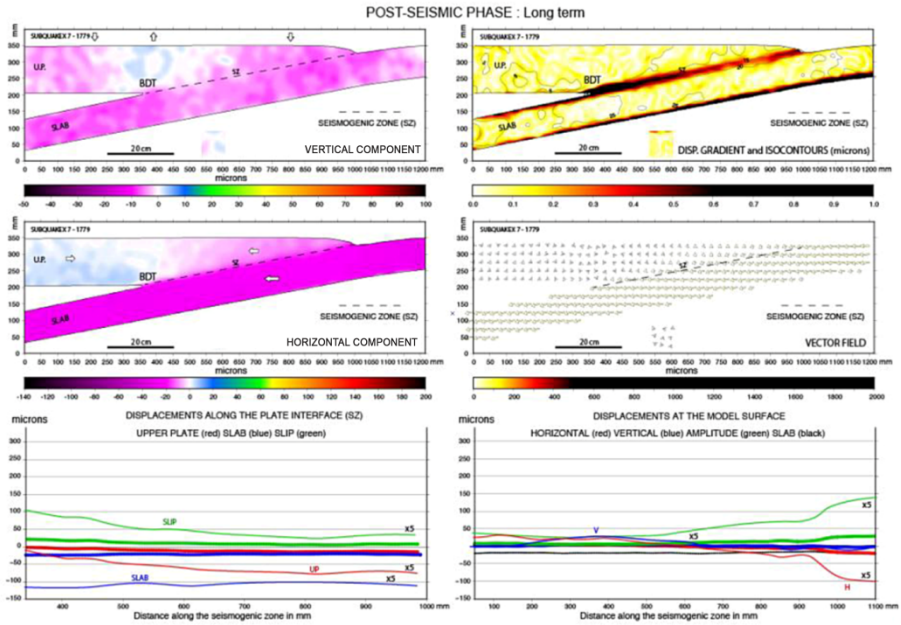

Figure 12.5. *Example of a long-term post-seismic phase. Above the seismogenic zone, the mechanical coupling increases, and the upper plate again accumulates elastic deformation. Landward of the brittle-ductile transition, the upper plate continues to decompress and move toward the trench*

During the next (long-term) co-seismic phase, the frontal part of the upper plate begins to move landward, toward the backstop, while the rear part continues to move toward the trench (Figure 12.5). This particular kinematics expresses the progressive re-locking of the seismogenic zone, which begins with the part that is situated farthest away from the part that continues to relax visco-elastically. Between these regions, that is just ahead of the brittle-ductile transition, we observe creep and low-amplitude slow earthquakes. The duration of this phase is proportional to the amplitude of the associated co-seismic phase. After the largest earthquakes, it may last between 15 and 20 s (equivalent to 100–200 years). The

post-seismic phase ends when the seismogenic zone re-locks as evidenced by the velocity field again showing a typical inter-seismic displacement pattern. The entire upper plate starts to experience a new phase of generalized elastic compression.

12.3.2. *Slip kinematics and the role of the boundary conditions*

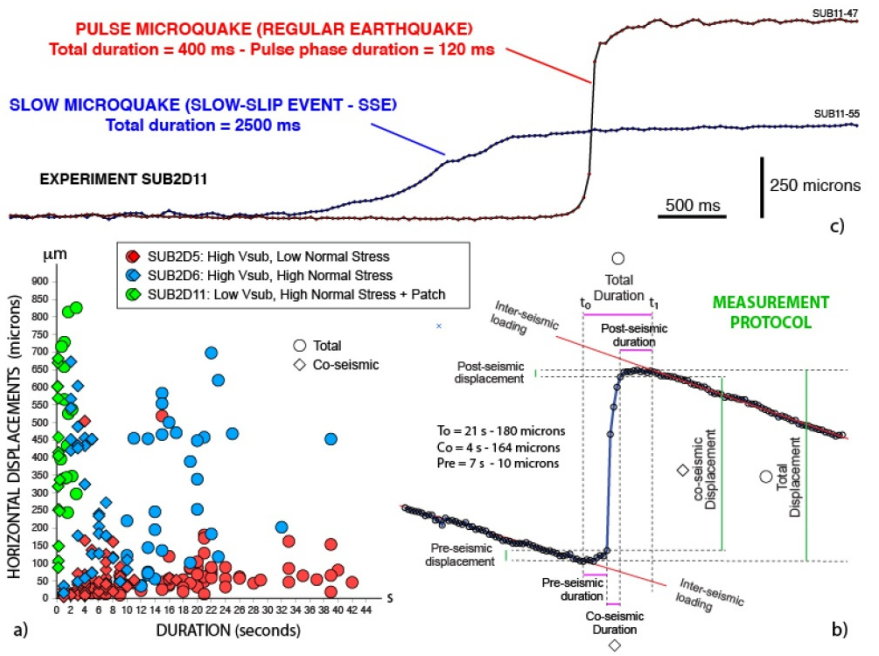

Figure 12.6 *The duration of experimental earthquake sequences can be highly variable (0.1–40 s), depending on the boundary conditions, even within the same experiment. This behavior is attributed to modifications in the frictional properties of the seismogenic zone induced by spatial and temporal variations in the interplate mechanical coupling*

High-speed camera monitoring reveals that the slip event durations may be variable and extend over several orders of magnitude (Figure 12.6(a) and 12.6(b), see Chapter 6). The fastest earthquakes last a few tens of milliseconds, while the slowest ones can extend over several tens of seconds. Boundary conditions play a major role, notably in modifying the mechanical coupling along the seismogenic zone. It is seen, for example, that for high normal stresses and slow subduction

velocities, the interplate coupling is higher, and the earthquake durations are shorter. On the contrary, for high subduction velocities and low normal stresses, the mechanical coupling becomes very low, favoring the occurrence of low-amplitude slow slips (Figure 12.6(b)). However, the boundary conditions do not explain everything, as impulsive slips (duration ~ hundreds of milliseconds) and slow slips (duration of a few seconds) can be detected during the same experiment (Figure 12.6(c)).

It can be hypothesized that the heterogeneities in stress (asperities) and friction (roughness) along the interface are responsible for these transient variations in the physical properties of the seismogenic zone. Indeed, in the absence of fluids, which is often used to explain the occurrence of slow earthquakes in nature, the kinematics of the experimental model is, a priori, only governed by friction forces along the interface between the foam plates and the visco-elastic coupling at the base of the seismogenic zone.

The analog model of the seismic cycle on a strike-slip fault [CAN 15] was able to demonstrate the decisive influence of the tectonic loading velocity at the boundaries on the properties of the seismogenic zone. Although the fault plane geometry and the position of the brittle-ductile transition are very different in the strike-slip and subduction models, a similar correlation can be shown. Figure 12.7 illustrates the effect of the subduction velocity (elastic loading) on the slip characteristics along the seismogenic zone by comparing two experiments carried out using the same analog model and two different velocities (0.6 and 1.26 cm/h).

In the case of a slow subduction velocity (0.6 cm/h), high inter-seismic mechanical coupling is observed all along the seismogenic zone, especially in its upper half. The inter-seismic phases are generally of long duration (>5 minutes) and, consequently, the model accumulates large elastic deformation which is released by high-amplitude co-seismic slips (Figure 12.7(a) and 12.7(c)). It can also be seen that the proportion of the co-seismic slip, with respect to the total convergence (~seismic coupling), is very small (<0.1) near the brittle-ductile transition (see left-hand side of Figure 12.7(a)) and reaches a maximum value close to 0.6 in the upper part of the seismogenic zone. For a high subduction velocity (1.26 cm/h), it can be seen that the mechanical coupling along the seismogenic zone is weaker. Consequently, the model accumulates less elastic deformation between two slip episodes, as shown by the significantly shorter duration (a few tens of seconds) of the inter-seismic phases (Figure 12.7(b) and 12.7(c)), even considering that the subduction velocity is twice as high. We also observe more frequent periods of aseismic slip (creep) and the coexistence of short earthquakes (duration < 1 s) and slow earthquakes (duration > 10 s) with low-to-moderate slip amplitudes (from 5 to 50 μm). The contribution of

the co-seismic events with respect to the total accommodated displacement along the seismogenic zone is also markedly smaller, about half as much as for the experiment at 0.6 cm/h. As with the strike-slip seismic cycle model [CAN 17], this difference in behavior can be explained by the rheology of the silicone whose mechanical resistance is strain rate-dependent. When the strain rate is high, as in the case of high subduction velocity, the silicone resists, limiting the storage of elastic deformation in the portion of the upper plate to which it is coupled. For a low strain rate (low subduction velocity), the silicone is very weak, thereby allowing the entire upper plate to store the elastic deformation. The volume available for the accumulation of inter-seismic elastic stresses is larger, the shear gradient along the seismogenic zone is lower and, consequently, the duration of the inter-seismic phase increases significantly. This results in an increase in the magnitude of experimental earthquakes and makes the co-seismic phases more impulsive (Figure 12.7(c)).

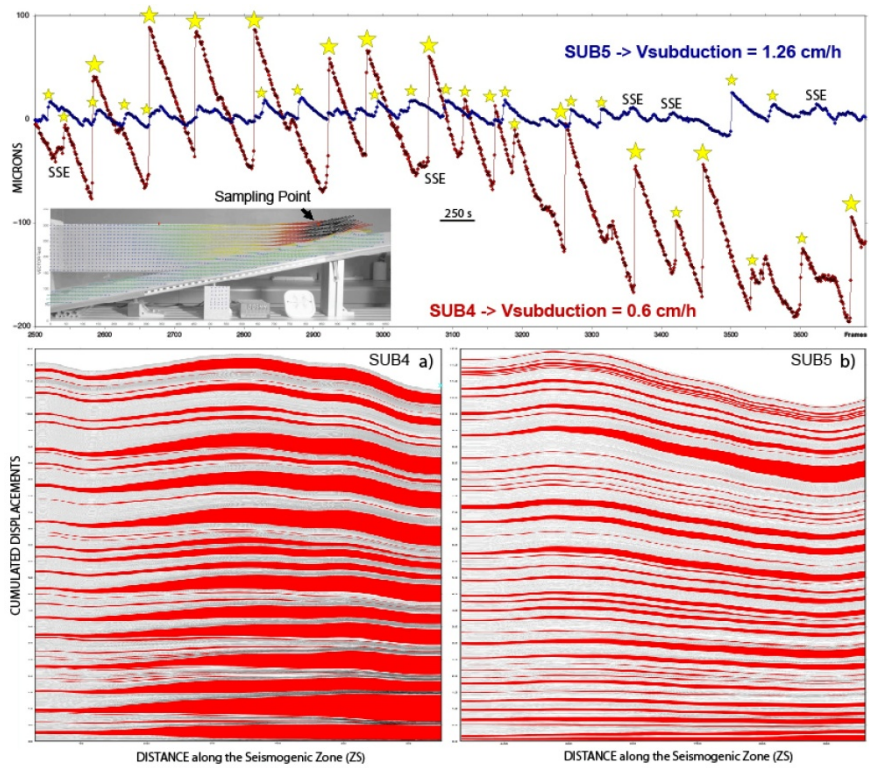

Figure 12.7. *Cumulated slip along the seismogenic zone for two different subduction velocities: a) 0.6 cm/h and b) 1.26 cm/h. The experiment extracts presented here correspond to a total of 12 mm of convergence. The major slips are identified in red. For more details refer to [CAN 20]*

These few examples of experimental results illustrate the success and potential of the analog modeling approach, which should be considered as an efficient tool for complementing other methods of investigation. Its greatest strength is that it is able to integrate processes that extend over wide scales of time and space, in both 2D and 3D. As with any modeling approaches, the extrapolation of experimental results to nature must be done taking into account all inevitable simplifications and limitations. We can look forward to new discoveries through the ongoing efforts to develop better-dimensioned models incorporating the latest concepts in earthquake dynamics.

12.4. References

[ANO 94] ANOOSHEHPOOR A., BRUNE J.N., "Frictional heat generation and seismic radiation in a foam rubber model of earthquakes", *Pageoph.*, vol. 142, pp. 735–747, 1994.

[ANO 99] ANOOSHEHPOOR A., BRUNE J.N., "Wrinkle-like Weertman pulse at the interface between two blocks of foam rubber with different velocities", *Geophys. Res. Lett.*, vol. 26, pp. 2025–2028, 1999.

[BRA 66] BRACE W.F., BYERLEE J.D., "Stick-slip as a mechanism for earthquakes", *Science*, vol. 153, no. 3739, pp. 990–992, 1966.

[BRU 73] BRUNE J.N., "Earthquake modeling by stick-slip along pre-cut surfaces in stressed foam rubber", *Bull. Seism. Soc. Am.*, vol. 63, pp. 2105–2119, 1973.

[BUR 67] BURRIDGE R., KNOPOFF L., "Model and theoretical seismicity", *Bulletin of the Seismological Society of America*, vol. 57, no. 3, pp. 341–371, 1967.

[CAN 15] CANIVEN Y., DOMINGUEZ S., SOLIVA R. et al., "A new multilayered visco-elasto-plastic experimental model to study strike-slip fault seismic cycle", *Tectonics*, vol. 34, pp. 232–264, 2015.

[CAN 17] CANIVEN Y., DOMINGUEZ S., SOLIVA R. et al., "Relationships between along-fault heterogeneous normal stress and fault slip patterns during the seismic cycle: Insights from a strike-slip fault model", *Earth Planet. Sci. Lett.*, vol. 480, pp. 147–157, 2017.

[CAN 21] CANIVEN Y., DOMINGUEZ S., "Validation of a multi-layered analog model integrating crust-mantle visco-elastic coupling to investigate subduction megathrust earthquake cycle", *Journal of Geophysical Research: Solid Earth*, 126, e2020JB020342, available at: https://doi.org/10.1029/2020JB020342, 2021.

[COR 17] CORBI F., FUNICIELLO F., BRIZZI S. et al., "Control of asperities size and spacing on seismic behavior of subduction megathrusts: Asperities and megathrust seismicity", *Geophys. Res. Lett.*, vol. 44, pp. 8227–8235, 2017.

[HUB 37] HUBBERT M.K., "Theory of scale models as applied to the study of geological structures", *Geological Society America Bull.*, vol. 48, pp. 459–1520, 1937.

[OHN 73] OHNAKA M., "Experimental studies of stick-slip and their application to the earthquake source mechanism", *J. Phys. Earth*, vol. 21, pp. 285–303, 1973.

[OZA 11] OZAWA S., NISHIMURA T., SUITO H. et al., "Coseismic and postseismic slip of the 2011 magnitude-9 Tohoku-Oki earthquake", *Nature*, vol. 475, pp. 373–376, 2011.

[ROS 99] ROSAKIS A.J., SAMUDRALA O., COKER D., "Cracks faster than shear wave speed", *Science*, vol. 284, pp. 1337–1340, 1999.

[ROS 17] ROSENAU M., CORBI F., DOMINGUEZ S., "Analogue earthquakes and seismic cycles: Experimental modelling across timescales", *Solid Earth*, vol. 8, pp. 597–635, 2017.

[ROS 19] ROSENAU M., HORENKO I., CORBI F. et al., "Synchronization of great subduction megathrust earthquakes: Insights from scale model analysis", *J. Geophys. Res.*, vol. 124, pp. 3646–3661, 2019.

[WEI 93] WEIJERMARS R., JACKSON M.P.A., VENDEVILLE B., "Rheological and tectonic modeling of salt provinces", *Tectonophysics*, vol. 217, pp. 143–174, 1993.

Conclusion

How Ideas Evolve from a Continual Confrontation Between Observations and Models

Cécile LASSERRE
UCBL, ENSL, UJM, CNRS, LGL-TPE, University of Lyon, Villeurbanne, France

The different chapters in this book illustrate the diversity of spatial and temporal scales involved in the seismic cycle, and the need for observations and models to develop together to enhance our understanding of how active faults behave. From the scale of the fine roughness of the fault plane, and the damage around it, to that of major fault systems cutting across tectonic plates and contributing in the long-term to how our landscapes are shaped, from super-shear rupture velocities during earthquakes, to low velocities of slow slip events during the interseismic period, there remains a wide range of spatial signatures and temporal behaviors associated with the seismic cycle to explore and take into account.

The many observations available today (geological, morphological, tectonic, geodetic, gravimetric, seismological) remain essentially observations on the surface of the Earth, collected from fieldwork and instruments on the ground or on board satellites. These allow precise mapping of fault zones and enable us to measure ground movements around faults associated with each phase of the seismic cycle or accumulated over several cycles. Only the inversion of these measures makes it possible to model (among other parameters) the amplitude, the spatial extent, and the temporal evolution of slip and deformation within and around the seismogenic zone,

The Seismic Cycle,
coordinated by Frédérique ROLANDONE. © ISTE Ltd. 2022.

The Seismic Cycle: From Observation to Modeling,
First Edition. Frédérique Rolandone.

given certain constraints or assumptions on the characteristics of the fault and the surrounding medium. Lithosphere imaging techniques with different resolutions, or drilling across faults, as well as analysis of the deep parts of faults that are today exhumed to the surface, all these offer additional information on the geometry and rheological properties of the fault zones. These characteristics are partly a result of the history of the redistribution of stresses over consecutive seismic cycles (the geological and tectonic history of the faults), and also govern this redistribution, both in the short term and over the long term.

This book offers an overview of the considerable advances made in the field of fault observations over the past century and especially in the past few decades. It shows how these observations have contributed to the evolution of ideas on the seismic cycle and improvement of models. These models seek to provide a conceptual framework for the observations (in this sense, the observations often appear "in advance" with respect to the models) and, in the case of analog or numerical models, they seek to isolate and test key parameters that govern the behavior of faults at different scales.

C.1. New observations, new advances

Most earthquakes are now systematically studied by combining seismological and field tectonic observations, GNSS data and aerial or satellite imagery (optical image correlation and InSAR data). This makes it possible to define the spatiotemporal characteristics of coseismic and postseismic deformations (mechanisms, slip distribution, dynamic source parameters, fault geometry and segmentation, rheological properties of the lithosphere), and thus their complementarity in terms of location, amplitude and duration (see Chapters 1–3). There is also increasing attention being paid to deformation away from the fault (off-fault deformation) [MIL 15]. An earthquake database can be progressively constructed with the accumulation of studies of individual events with increasingly refined resolutions. This database can be used to derive the generic properties of earthquakes and to study the relation between these properties, the structure and lithology of the fault zone and the deformation accumulated over the long term [WEL 94, CAN 11, PER 16]. Another objective is also to improve source models and the prediction of strong motion [CAU 14]. It also becomes possible to better quantify how earthquakes, based on their characteristics, impact the construction of the relief (see Chapter 9).

Despite a few local observations of aseismic slip along major, continental strike-slip faults [STE 60, AMB 70], the interseismic period has long been considered a simple and stationary period of deformation accumulation. The recent evolution in imagery and space geodesy toward high-resolution data and time series analysis, as well as developments in seismological networks and new data analysis techniques, all made it possible to reveal the complexity of interseismic deformation across space and time. The discovery of slow earthquakes in subduction zones

marked a major turning point in our understanding of the seismic cycle, forcing us to revise existing models. These aseismic events, whose physical mechanisms are still not well understood, have an impact on the seismic hazard, which can no longer be neglected (see Chapter 6). Depending on their depth, these events can, notably, modify the slip deficit in the seismogenic zone. This deficit is related to the interseismic coupling coefficient estimated through geodetic measurements. Many studies analyze the spatial distribution and temporal evolution of this interseismic coupling, the morphological and mechanical factors that control it, as well as its correlation with seismicity (see Introduction and Chapters 5–7). One of the important goals driving these studies is to evaluate the potential of monitoring interseismic coupling as a way to propose scenarios for future ruptures. However, one of the limitations of coupling maps is their "smoothing", both in space and time, related to the limited resolution of data and the small time window of observations, or again, related to the regularization and to the hypotheses used for the models [LOV 11]. More generally, the analyses of the partitioning and spatiotemporal interactions between aseismic and seismic slips, the respective scaling laws for these two slip modes as possible indices of their mechanisms [PEN 10] and their relation with the fault properties [BÜR 18] have become important research issues for seismic hazard assessment. The observations reveal transient, aseismic events that cause earthquake nucleation [BOU 11, KAT 12, SOC 17], or on the contrary, act as a barrier to earthquakes [VAC 18]. They also reveal earthquakes that trigger aseismic slips [ZIG 12].

For a synoptic view of the seismic cycle, the observations should ideally cover the largest time window possible and different phases of the cycle for the same fault system. These conditions are rarely fulfilled. The constant developments in methodology, however, make it possible to progress in this way and also to enable models to evolve. In tectonics, the major evolutions include the diversification and improvement of dating techniques [RYE 06], the more systematic use of high-resolution imagery and LiDAR and more recently the application of optical image correlation methods on archived or declassified images. These advances make it possible to quantify the morphology and long-term kinematics of the faults (see Chapter 10), which can differ from the current kinematics measured through geodesy, depending, for example, on the period of the seismic cycle being studied. It also makes it possible to revisit recent earthquakes, or even recent series of earthquakes, outside the instrumental period [KLI 11, MAR 18, STE 18]. In paleoseismology, 3D or non-invasive approaches [BEA 12] also give a better picture of the seismic history of a fault system in its entirety, by densifying the markers of past earthquakes. Finally, innovative methods at the boundary between paleoseismology and "paleogeodesy", based on the analysis of successive earthquake records in corals or fault scarps, allow for an extended spatiotemporal monitoring of the seismic cycle (see Chapter 11). The simple, characteristic earthquake model [SCH 84] thus seems outdated, except, it would appear, for certain immature faults

[KLI 11], while "super-cycle" models emerge in different tectonic contexts [GRA 94, SIE 08, SCH 11, NOC 17].

C.2. Models to understand observations and processes at different scales

In parallel, spurred on by these new observations and experimental data characterizing frictional properties of faults, more mechanical, analog and numerical models, as well as dynamic simulations of earthquakes or of a succession of earthquakes, were developed. These tried to reconcile short-term geodetic and seismological data with long-term geological and tectonic observations.

These models study how the properties of the lithosphere and of active faults (rheology, roughness at all scales, friction) can influence the timing, magnitude and spatial extent of slips and their modes (seismic or aseismic) in a fault system (see Chapters 4 and 12). A fault is most often considered as a simple interface governed by its frictional properties and the tectonic loading in a homogeneous medium. The geometric and structural complexities along and across the fault (its segmentation and degree of damage), the possibility of building permanent deformation (not compensated during the seismic cycle), or again the rheological contrasts on either side of the fault zone or within it, not yet widely studied by geologists and geophysicists, often remain neglected [BEN 03, COC 09]. Recent studies however have begun to better take these different aspects into account.

For regions (or laboratory experiments) where data has been able to capture different phases of the seismic cycle, the seismic cycle models have progressively included more realistic fault geometries and thermo-rheological structures [CAT 00, CAN 15], the seismic history and friction laws on the faults [HET 10, THO 17]. A formulation of the numerical models that follow a purely frictional vision can make it possible to reproduce the dynamics of a series of earthquakes [BAR 12] and account for certain effects of dynamic rupture propagation (whether or not barriers are crossed, for example [KAN 10]). Such formulation remains unsatisfactory, however, often being "ad hoc" and based very little on physical parameters, even if that evolves (see Chapter 4). Geometric variations along the faults can also induce seismic and aseismic slip sequences, without requiring the introduction of variations in friction [ROM 17]. The current trend is to move toward models (whether numerical or analog) that integrate the evolution of physical properties in the fault zone and the surrounding medium during the rupture [THO 18] and all through the seismic cycle (see Chapters 4 and 12).

One of the contributions of the models is also to bring out new ideas about potential precursors to slips on faults (slow and rapid earthquakes) [ARI 12], and, from a practical point of view, to bring in new observables to be created or extracted

from the noise of existing measurements. The models also allow us to look critically at surface observations and their interpretation. Displacement measurements across faults that are assumed to be purely interseismic can indeed be strongly affected by the effects of postseismic relaxation and interactions between faults over the long-term and over large distances [CHE 01, PER 04, TRU 13].

C.3. What comes next?

We must continue to look at the seismic cycle from multiple angles and on multiple scales. It is not possible to draw up an exhaustive list of all the future challenges in each domain of study, but there are a few priorities, nonetheless.

It is undoubtedly essential to understand the chronology and spatial distribution of seismic slips relative to aseismic slips (or other types of deformation, potentially non-elastic), on the scale of a nucleation zone, of the entire seismogenic zone, or of a fault system, in order to better decipher our current landscapes and anticipate future earthquakes. The paths for further study are related to:

1) The resolution and frequency content of the data, which is constantly improving, for spatial and aerial imagery as well as for GNSS and seismological networks. With InSAR, for example, we can now hope to access both the temporal dynamics of certain local phenomena [JOL 15], and deformations on the scale of plate tectonics [WEI 20]. The development of new techniques like seafloor measurements (of which the small number further biases the spatial distribution of data), fiber optics, inclinometers, multi-component strain gauges, etc., must also be encouraged.

2) The precision of measurements and the improvement in the signal-to-noise ratio. Several techniques have been developed recently in GNSS and seismology (this is "seismo-geodesy") to reduce the threshold for the detection of small, transient events (seismic and aseismic), to better localize them and describe their kinematics, in order to better constrain their mechanisms [FRA 18]. The separation of tectonic and non-tectonic signals (hydrological, climatic, see Introduction and Chapter 9) is also an important issue. Machine learning approaches, which are on the rise, are among the tools that can be used for this.

3) The combination of data of various types, and therefore of various resolutions and uncertainties, which must be taken into account in order to preserve the complementarity of the different data [PAG 21].

4) Modeling. It seems essential to introduce the complex structure and nonlinear properties of fault zones to cover a larger frequency range for the phenomena associated with the seismic cycle. Improvements in calculation methods and experimental devices allow this evolution (see Chapters 4 and 12).

5) Estimating uncertainties, not only in data, but also in the models resulting from data inversion. On this last, essential point, the Bayesian inversion approach offers the

possibility of discussing the robustness of the information brought in by the models (see Chapter 2).

C.4. References

[AMB 70] AMBRASEYS N.N., "Some characteristic features of Anatolian fault zone", *Tectonophysics*, vol. 9, nos 2–3, pp. 143–165, 1970.

[ARI 12] ARIYOSHI K., MATSUZAWA T., AMPUERO J.-P. et al., "Migration process of very low-frequency events based on a chain-reaction model and its application to the detection of preseismic slip for megathrust earthquakes", *Earth, Planets and Space*, vol. 64, no. 8, pp. 693–702, 2012.

[BAR 12] BARBOT S., LAPUSTA N., AVOUAC J.P., "Under the hood of the earthquake machine: Toward predictive modeling of the seismic cycle", *Science*, vol. 336, no. 6082, pp. 707–710, 2012.

[BEA 12] BEAUPRETRE S., GARAMBOIS S., MANIGHETTI I. et al., "Finding the buried record of past earthquakes with GPR-based palaeoseismology: A case study on the Hope fault, New Zealand", *Geophysical Journal International*, vol. 189, no. 1, pp. 73–100, 2012.

[BEN 03] BEN-ZION Y., SAMMIS C., "Characterization of fault zones", *Pure and Applied Geophysics*, vol. 160, no. 3, pp. 677–715, 2003.

[BOU 11] BOUCHON M., KARABULUT H., AKTAR M. et al., "Extended nucleation of the 1999 M-w 7.6 Izmit earthquake", *Science*, vol. 331, no. 6019, pp. 877–880, 2011.

[BÜR 18] BÜRGMANN R., "The geophysics, geology and mechanics of slow fault slip", *Earth Planet. Sci. Lett.*, vol. 495, pp. 112–134, 2018.

[CAN 11] CANDELA T., RENARD F., SCHMITTBUHL J. et al., "Fault slip distribution and fault roughness", *Geophysical Journal International*, vol. 187, no. 2, pp. 959–968, 2011.

[CAN 15] CANIVEN Y., DOMINGUEZ S., SOLIVA R. et al., "A new multilayered visco-elasto-plastic experimental model to study strike-slip fault seismic cycle", *Tectonics*, vol. 34, no. 2, pp. 232–264, 2015.

[CAT 00] CATTIN R., AVOUAC J.-P., "Modeling mountain building and the seismic cycle in the Himalaya of Nepal", *J. Geophys. Res.*, vol. 105, no. B6, pp. 13,389–13,407, 2000.

[CAU 14] CAUSSE M., DALGUER L., MAI P., "Variability of dynamic source properties inferred from kinematic models of past earthquakes", *Geophysical Journal International*, vol. 196, no. 3, pp. 1754–1769, 2014.

[CHE 01] CHERY J., MERKEL S., BOUISSOU S., "A physical basis for time clustering of large earthquakes", *Bulletin of the Seismological Society of America*, vol. 91, pp. 1685–1693, 2001.

[COC 09] COCHRAN E.S., YONG-GANG L., SHEARER P.M. et al., "Seismic and geodetic evidence for an extensive, long-lived fault damage zones", *Geology*, vol. 37, no. 4, pp. 315–318, 2009.

[FRA 18] FRANK W., ROUSSET B., LASSERRE C. et al., "Revealing the cluster of slow transients behind a large slow slip event", *Science Advances*, vol. 4, no. 5, p. 661, 2018.

[GRA 94] GRANT L., SIEH K., "Paleoseismic evidence of clustered earthquakes on the San Andreas fault in the Carrizo Plain, California", *J. Geophys. Res.*, vol. 99, no. B4, pp. 6819–6841, 1994.

[HET 10] HETLAND E.A., SIMONS M., "Post-seismic and interseismic fault creep II: Transient creep and interseismic stress shadows on megathrusts", *Geophysical Journal International*, vol. 181, no. 1, pp. 99–112, 2010.

[JOL 15] JOLIVET R., CANDELA T., LASSERRE C. et al., "The burst-like behavior of aseismic slip on a rough fault: The creeping segment of the Haiyuan fault, China", *Bull. Seismol. Soc. Am.*, vol. 105, pp. 480–488, 2015.

[KAN 10] KANEKO Y., AVOUAC J.-P., LAPUSTA N., "Towards inferring earthquake patterns from geodetic observations of interseismic coupling", *Nat. Geosci.*, vol. 3, pp. 363–368, 2010.

[KAT 12] KATO A., OBARA K., IGARASHI T. et al., "Propagation of slow slip leading up to the 2011 Mw 9.0 Tohoku-Oki earthquake", *Science*, vol. 335, no. 6069, pp. 705–708, 2012.

[KLI 11] KLINGER Y., ETCHEBES M., TAPPONNIER P. et al., "Characteristic slip for five great earthquakes along the Fuyun fault in China", *Nature Geoscience*, vol. 4, no. 6, pp. 389–392, 2011.

[LOV 11] LOVELESS J.P., MEADE B.J., "Spatial correlation of interseismic coupling and coseismic rupture extent of the 2011 Mw = 9.0 Tohoku-Oki earthquake", *Geophys. Res. Lett.*, vol. 38, no. 17, p. 306, 2011.

[MAR 18] MARCHANDON M., VERGNOLLE M., CAVALIÉ O. et al., "Earthquake sequence in the NE Lut, Iran: Observations from multiple space geodetic techniques", *Geophysical Journal International*, vol. 215, no. 3, pp. 1604–1621, 2018.

[MIL 15] MILLINER C., DOLAN J., HOLLINGSWORTH J. et al., "Quantifying near-field and off-fault deformation patterns of the 1992 Mw 7.3 Landers earthquake", *Geochemistry Geophysics Geosystems*, vol. 16, no. 5, pp. 1577–1598, 2015.

[NOC 17] NOCQUET J.-M., JARRIN, P., VALLÉE, M. et al., "Supercycle at the Ecuadorian subduction zone revealed after the 2016 Pedernales earthquake", *Nature Geoscience*, vol. 10, pp. 145–149, 2017.

[PAG 21] PAGANI C., BODIN T., MÉTOIS M. et al., "Bayesian estimation of surface strain rates from global navigation satellite system measurements: Application to the southwestern United States". *Journal of Geophysical Research: Solid Earth*, vol. 126, no. 6, p. e2021JB021905, 2021.

[PEN 10] PENG Z., GOMBERG J., "An integrated perspective of the continuum between earthquakes and slow-slip phenomena", *Nature Geoscience*, vol. 3, no. 9, pp. 599–607, 2010.

[PER 04] PERFETTINI H., AVOUAC J.-P., "Stress transfer and strain rate variations during the seismic cycle", *Journal of Geophysical Research*, vol. 109, no. B06402, 2004.

[PER 16] PERRIN C., MANIGHETTI I., AMPUERO J.-P. et al., "Location of largest earthquake slip and fast rupture controlled by along-strike change in fault structural maturity due to fault growth", *Journal of Geophysical Research: Solid Earth*, vol. 121, no. 5, pp. 3666–3685, 2016.

[ROM 17] ROMANET P., BHAT H., JOLIVET R. et al., "Fast and slow slip modes can emerge from fault geometrical complexities", *AGU Fall Meeting Abstracts T42A-04*, vol. 45, 2017.

[RYE 06] RYERSON F.J., TAPPONNIER P., FINKEL R.C. et al., "Applications of morphochronology to the active tectonics of Tibet", *Geological Society of America Special Papers*, vol. 415, pp. 61–86, 2006.

[SCH 84] SCHWARTZ D.P., COPPERSMITH K.J., "Fault behaviour and characteristic earthquakes: Examples from the Wasatch and San Andreas fault zones". *Journal of Geophysical Research*, vol. 89, pp. 5681–5698, 1984.

[SCH 11] SCHLAGENHAUF A., MANIGHETTI I., BENEDETTI L. et al., "Earthquake supercycles in Central Italy, inferred from 36Cl exposure dating", *Earth Planet. Sci. Lett.*, vol. 307, nos 3–4, pp. 487–500, 2011.

[SIE 08] SIEH K., NATAWIDJAJA D.H., MELTZNER A.J. et al., "Earthquake supercycles inferred from sea-level changes recorded in the corals of West Sumatra", *Science*, vol. 322, pp. 1674–1678, 2008.

[SOC 17] SOCQUET A., VALDES J.P., JARA J. et al., "An 8 month slow slip event triggers progressive nucleation of the 2014 Chile megathrust", *Geophysical Research Letters*, vol. 44, no. 9, pp. 4046–4053, 2017.

[STE 60] STEINBRUGGE K.V., ZACHER E.G., TOCHER D. et al., "Creep on the San Andreas fault", *Bulletin of the Seismological Society of America*, vol. 50, no. 3, pp. 389–415, 1960.

[STE 18] STEWART N., GAUDEMER Y., MANIGHETTI I. et al., "3DFaultOffsets, a Matlab code to automatically measure lateral and vertical fault offsets in topographic data: Application to San Andreas, Owens Valley, and Hope faults", *Journal of Geophysical Research*, vol. 123, pp. 815–835, 2018.

[THO 17] THOMAS M.Y., AVOUAC J.-P., LAPUSTA N., "Rate-and-state friction properties of the longitudinal valley fault from kinematic and dynamic modeling of seismic and aseismic slip", *J. Geophys. Res. Solid Earth*, vol. 122, no. 4, pp. 3115–3137, 2017.

[THO 18] THOMAS M., BHAT H.S., "Dynamic evolution of off-fault medium during an earthquake: A micromechanics based model", *Geophys. J. Int.*, vol. 214, no. 2, pp. 1267–1280, 2018.

[TRU 13] TRUBIENKO O., FLEITOUT L., GARAUD J.-D. et al., "Interpretation of interseismic deformations and the seismic cycle associated with large subduction earthquakes", *Tectonophysics*, vol. 589, pp. 126–141, 2013.

[VAC 18] VACA S., VALLÉE M., NOCQUET J. et al., "Recurrent slow slip events as a barrier to the northward rupture propagation of the 2016 Pedernales earthquake (Central Ecuador)", *Tectnophysics*, vol. 724–725, pp. 80–92, 2018.

[WEI 20] WEISS J.R., WALTERS R.J., MORISHITA Y. et al., "High-resolution surface velocities and strain for Anatolia from Sentinel-1 InSAR and GNSS data", *Geophysical Research Letters*, vol. 47, no. 15, p. e2020GL087376, 2020.

[WEL 94] WELLS D.L., COPPERSMITH K.J., "New empirical relationships among magnitude, rupture length, rupture width, rupture area, and surface displacement", *Bulletin of the Seismological Society of America*, vol. 84, no. 4, pp. 974–1002, 1994.

[ZIG 12] ZIGONE D., RIVET D., RADIGUET M. et al., "Triggering of tremors and slow slip event in Guerrero, Mexico, by the 2010 Mw 8.8 Maule, Chile, earthquake", *Journal of Geophysical Research: Solid Earth*, vol. 117, no. B9, 2012.

List of Authors

Harsha BHAT
Laboratoire de géologie
ENS
Paris
France

Nadaya CUBAS
ISTeP
Sorbonne University
Paris
France

Stéphane DOMINGUEZ
Géosciences Montpellier
University of Montpellier
France

Cécile DOUBRE
ITES
EOST
University of Strasbourg
France

Zacharie DUPUTEL
Observatoire Volcanologique du
Piton de la Fournaise
CNRS
Institut de physique du globe de Paris
Paris Cité University
France

Emilie KLEIN
Laboratoire de géologie
CNRS UMR 8538
Ecole normale supérieure –
PSL University
Paris
France

Yann KLINGER
Institut de physique du globe de Paris
CNRS
Paris Cité University
France

The Seismic Cycle: From Observation to Modeling,
First Edition. Frédérique Rolandone.

Cécile LASSERRE
UCBL
ENSL
UJM
CNRS
LGL-TPE
University of Lyon
Villeurbanne
France

Marianne MÉTOIS
UCBL
ENSL
UJM
CNRS
LGL-TPE
University of Lyon
Villeurbanne
France

Mathilde RADIGUET
ISTerre
Grenoble Alpes University
France

Frédérique ROLANDONE
ISTeP
Sorbonne University
Paris
France

Philippe STEER
CNRS
Géosciences Rennes
University of Rennes
France

Marion THOMAS
ISTeP
Sorbonne University
Paris
France

Martin VALLÉE
Institut de physique du globe de Paris
Paris Cité University
France

Christophe VIGNY
Laboratoire de géologie
CNRS UMR 8538
Ecole normale supérieure –
PSL University
Paris
France

Jérôme VAN DER WOERD
Institut Terre et Environnement
de Strasbourg
Strasbourg University
France

Index

The Seismic Cycle: From Observation to Modeling,
First Edition. Frédérique Rolandone.

M, N, O, P

R, S

T, V, W

WILEY END USER LICENSE AGREEMENT

Go to www.wiley.com/go/eula to access Wiley’s ebook EULA.

The study of the seismic cycle has many applications, from the study of faulting to the estimation of seismic hazards. It must be considered at different timescales, from that of an earthquake, the co-seismic phase (a few seconds), the post seismic phase (from months to dozens of years) and the inter-seismic phase (from dozens to hundreds of years), up to cumulative deformations due to several seismic cycles (from a few thousand to hundreds of thousands of years).

The Seismic Cycle uses many different tools to approach its subject matter, from short-term geodesic, such as GPS and InSAR, and seismological observations to long-term tectonic, geomorphological, morphotectonic observations, including those related to paleoseismology. Various modeling tools such as analog experiences, experimental approaches and mechanical modeling are also examined.

Different tectonic contexts are considered when engaging with the seismic cycle, from continental strike-slip faults to subduction zones such as the Chilean, Mexican and Ecuadorian zones. The interactions between the seismic cycle and magmatism in rifts and interactions with erosion in mountain chains are also discussed.

Frédérique Rolandone is Associate Professor at Sorbonne University, France, where she teaches both undergraduate and masters students. Her research focuses on the mechanics of faults and the seismic cycle based on the modeling of spatial geodesy measurements.

www.iste.co.uk

WILEY

9 781789 450385 90000